DOCTOR OF PHILOSOPHY

The hydrology of debris-covered glaciers

Fyffe, Catriona Louise

Award date:
2012

DOCTOR OF PHILOSOPHY

The hydrology of debris-covered glaciers

Catriona Louise Fyffe

2012

University of Dundee

The hydrology of debris-covered glaciers

Catriona Louise Fyffe

Doctor of Philosophy in Geography

University of Dundee

October 2012

Table of contents

Table of figures

Acknowledgements

This project has involved more people and equipment than I thought possible, and I very much thank everyone for being involved. My first thanks must go to Dr Ben Brock, without whom I would never have come to love Miage Glacier and want to go back in the first place! Ben, you are also brilliant at saying the right thing at the right time, whether keeping me positive when something is not going well, or making sure I stay on the right track. I am also unbelievably grateful for all of your time and effort; you have never turned me away or not emailed back…that's some commitment. So thanks Ben, for the hard work and enthusiasm. Thanks also to Dr Martin Kirkbride, you have a deep understanding of every type of physical process, and I feel privileged to have been taught by you. I am glad you have been there to help me make sense of things, and to not lose track of the question I'm trying to answer in the first place. Dr Tim Reid must also have a massive thanks; you can carry impossible loads, stride across the glacier, oh and abseil too! I am so glad you have been part of the Miage work and I'm superbly grateful for your help with Matlab. I must also thank Dr Doug Mair, for making sure I would make the best use of my time in the field. Many thanks are due to Dr Andrew Black for advice on practical hydrometry in difficult environments. I'm also very grateful for the emergency response pressure transducer service!

There were many students who helped on the Miage Glacier fieldtrips (a total of 18 from 4 Universities, Dundee, Northumbria, Aberdeen and Cambridge), who were always eager, hardworking and had an impressive ability to do whatever mad thing I asked of them, even if it meant getting covered in dye, rained on, or attacked by a rogue rock. I am grateful for their effort, the data they collected and shared with me, and their ability to cheer me up when work was hard – thanks guys! Thanks to David Barratt, Chris Harris, Freya Cowan, Will Holley, Lesley Hendry, Michael Lee, Thom Her, Jonathan Fuhrman, Craig Frew, Rebecca Douglas, Rebecca Crossley, Claire Ritchie, Scott Davidson, Stephen Hoare, Katie Metcalfe, Scott Barker, Chris Bennett and Ben Twiss. Also I can't forget Lynsey Gilbert, who made it through two Miage trips, including having to sleep on the dining table, putting up with insects (so long as they weren't above her bed), and my crazy driving. Thanks Lynsey!

Thanks must go to Marco Vagliasindi from the Fondazione Montagna Sicura, La Palud, for excellent logistical support and for the wind speed data from the Helbronner meteorological station from the Regional Functional Centre of Aosta Valley; to Claudia

Mihalcea and Claudio Smiraglia and all those from Milan University for help with logistics and sharing ablation data; to Fabio Brunier and Fabrizio Diotri from the Regional Functional Centre of Aosta Valley for air pressure data, and the 2005 LIDAR digital elevation model and the orthophoto of Miage Glacier, respectively. Many thanks to Lesley Foster for supplying and helping me use her debris thickness data. I also thank all those who lent equipment and advice. Thanks to Drs Doug Mair and Pete Nienow for their Kovax ice drill, and Pete for dye tracing advice, to Prof Joe Holden from Leeds University for the loan of the fluorometer, to the Scottish Crop Research Institute for the loan of a Campbell logger, and to Northumbria University for the loan of a fluorometer and Campbell loggers. Thanks to Chris Thomas for help with conduit closure calculations, and Craig Frew for calculating sky view factors in GIS.

I am grateful to the Department of Geography and Environmental Science at the University of Dundee for providing my studentship for this PhD, and for the support of everyone in the department. I thank the NERC Geophysical Equipment Facility in Edinburgh for a loan of two differential GPS receivers (loan number 917) and training on how to use them, and to Alan Hobbs from GEF for his advice. Many thanks to Craig Phillips and Alan Long who provided me with excellent laboratory and equipment support. I'm very grateful for all your help with everything from water chemistry analysis to figuring out the GPS. Thanks to Neil Lonie and the staff of the Dundee Satellite Receiving Station for allowing us to borrow the Ewing Building roof.

I must not forget to thank my Dad, who not only provided tools, advice on constructing things out of dexion, let me borrow his tripod, and showed me how to use a drill, but also put up with me testing my pressure transducer in the back bedroom. To Mum, thanks so much for letting me keep working, and for allowing me to work on a glacier with crevasses and moulins and not worry too much (I'm also sorry for when I filled the utility room sink with dye) – thanks and lots of love to you both.

I hereby declare that I am the author of this thesis, and unless otherwise stated I have consulted all references cited, and the work recorded within this thesis is my own and has not been previously accepted for a higher degree.

As the supervisor of the candidate, I hereby declare that the conditions of the relevant Ordinance and Regulations have been fulfilled.

Abstract

Studies of glacier-hydrology have focused on clean Alpine glaciers, and recently ice sheet outlet glaciers, but there are few studies on debris-covered glaciers. It is known debris affects ablation rates, and that debris-covered glaciers evolve differently to their debris-free counterparts, but how the debris influences the hydrology is poorly understood. This thesis aims to understand the influence of the debris on the hydrological system and water balance of Miage Glacier, Western Italian Alps. The supraglacial hydrology was studied by modelling ablation using a distributed energy balance melt model, and measuring supraglacial stream discharges; the structure and evolution of the englacial and subglacial network was investigated using dye tracing and water chemistry monitoring; and the proglacial runoff was examined through detailed hydrograph analysis. Glacier velocity measurements were used to investigate the debris' influence on the glacier dynamics. High ablation rates occurred on clean ice and beneath thin debris on the upper glacier, resulting in large supraglacial streams which led into an efficient drainage system. Glacier velocities had a greater magnitude and variability close to the upper glacier moulins. Thick debris on the lower glacier reduced ablation, and consequently the discharge of supraglacial streams and efficiency of the hydrological network. Despite locally inefficient subglacial drainage, glacier velocities on the lower glacier remained subdued, partly because the debris attenuated water inputs. This attenuation reduced the occurrence of high amplitude diurnal cycles in the proglacial runoff and confined them to particularly warm weather. Lag times from peak air temperature to peak runoff were long relative to comparable debris-free glaciers. Evaporation of rainfall from debris-surfaces was high, and dependant on the debris permeability, suggesting this is an important water balance component. Under climate warming, it is predicted the ablation of Miage Glacier will increase, but this may be negated given an increase in debris cover.

Symbols

Units are given in the text.

A_c	area under concentration curve
A_G	constant in Glen's flow law
A_s	cross sectional area of channel
A_{sm}	apparent mean cross-sectional area
a	ablation or melt rate
a_o	amplitude of obstacle
α	albedo
α_i	ice albedo
α_d	debris albedo
b	dispersivity of trace
C	subsurface heat flux
C_{pa}	specific heat capacity of air
C_{pd}	specific heat capacity of debris
C_{pw}	specific heat capacity of water
c	concentration
c_t	total concentration of component
c_i	dilute concentration of component
c_s	enriched concentration of component
c_d	dye concentration
c_{di}	dye concentration injected
c_{dp}	peak dye concentration
c_{ds}	dye concentration intended at site
D	dispesion coefficient
DDF	degree day factor or melt factor
ΔD	rate of change of heat stored in the debris
d	distance
d_d	distance travelled by dye
δd	distance between two GPS points
δd_1	distance between two GPS points at time 1
δd_2	distance between two GPS points at time 2
δz	elevation difference between two GPS points
δd_d	daily distance change
δz_d	daily elevation change
E_i	elevation of ice surface
E_b	elevation of subglacial bedrock
e_a	air vapour pressure
e_s	saturated vapour pressure
ε_{xx}	non-dimensional longitudinal strain rate
ε_d	debris surface emissivity
η	ice viscosity coefficient
F	function of
Φ_m	non-dimensional stability function for momentum
Φ_h	non-dimensional stability function for heat
φ	hydraulic potential
G	conductive heat flux
G_i	conductive heat flux reaching ice
g	gravitational acceleration
H	net sensible heat flux
h	depth
h_s	snowpack depth
h_d	debris depth or thickness
h_i	ice thickness
h_r	depth of runoff (stage)
h_l	calculation layer thickness
I	potential clear-sky direct solar radiation
J_v	vertical water vapour flux
K	debris thermal conductivity
k	constant
k_c	constant for channel conditions
k_t	constant relating to size of tank
k_v	von Karman's constant
κ	porosity
κ_s	snowpack porosity
κ_{es}	snowpack effective porosity
κ_v	molecular diffusion coefficient for water in air
κ_{vT}	thermal molecular diffusion coefficient for water in air
$\kappa_{v\theta}$	isothermal molecular diffusion coefficient for water in air
L	net longwave flux
$L\uparrow$	outgoing longwave flux
LE	latent heat flux
L_f	latent heat of fusion
L_m	mixing length
L_v	latent heat of vaporisation of water
λ	wavelength of obstacle
M	energy available for ablation
m	power function for channel conditions
μ	viscosity
μ_w	water viscosity
n	Manning's roughness coefficient/time step
n_G	constant in Glen's flow law
N	time steps per day
P	sensible heat from precipitation
P_{dr}	% dye recovered
Pr	pressure
Pr_s	separation pressure
Pr_o	overburden pressure

Pr_c	critical pressure
p	permeability
p_s	snow permeability
Q	discharge
Q_i	input discharge
Q_{damp}	daily discharge amplitude
Q_{dmax}	daily discharge maximum
Q_{dmin}	daily discharge minimum
Q_{dmean}	daily discharge mean
Q_{dsdamp}	daily discharge standardised amplitude
Q_{dstd}	daily discharge standard deviation
Q_i	discharge at time of dye injection
Q_{max}	maximum downstream discharge
Q_m	mean discharge between injection and detection point
Q_{mp}	mean discharge at proglacial stream while dye passes
Q_p	proglacial discharge at peak of dye concentration
Q_s	supraglacial stream discharge
Q_t	discharge from tank
q	specific humidity
q_a	specific humidity at measurement height
q_s	specific humidity at surface
$RF_{snow/ice}$	radiation coefficient for snow or ice
RH	relative humidity
RH_a	relative humidity at measurement height
RH_s	relative humidity at surface
R	debris thermal resistance
R_b	Richardson number
R_t	rate of water input to tank
R_r	rainfall rate
r	hydraulic radius of supraglacial channel
r_i	initial conduit radius
r_r	resulting conduit radius
ρ	density
ρ_a	air density
ρ_d	debris density
ρ_i	ice density
ρ_v	vapour density
ρ_w	water density
S	net shortwave flux
$S\downarrow$	incoming shortwave radiation
S_G	specific gravity of dye
SRF	shortwave radiation factor
σ	Stephan-Boltzmann constant
T	temperature
TF	temperature factor
T_a	air temperature
T_d	within debris temperature
T_f	melting point (O°C)
T_m	mean debris temperature
T_r	rain temperature
T_s	debris surface temperature
t	time
t_m	time to dye peak
t_i	time to half dye peak on rising or falling limb
t_t	time of discharge from tank
t_v	vertical travel time
t_1	time to half peak on rising limb
t_2	time to half peak on falling limb
Δt	model time step
θ	slope angle
θ_s	surface slope angle/flow angle down glacier
θ_b	angle of inclination at base of the glacier
τ	shear stress
u	velocity
u_d	dye trace velocity
u_r	runoff (stream) velocity
u_{rs}	supraglacial stream velocity
u_s	under snowpack water velocity
u_i	water velocity over ice
u_w	wind speed
u_o	annul velocity over the axis
V_t	volume of water in tank
V_d	volume of dye
V_{dr}	volume of dye recovered
V_{dg}	volume of dye required for gauging
V_{di}	volume of dye injected
W	half the glacier width
w	mass of salt injected
x	runoff coefficient
y	runoff coefficient
z	runoff coefficient
z_a	measurement height
z_o	aerodynamic roughness length
z_{oq}	surface roughness length for humidity
z_{ot}	scalar length for heat
z_d	depth in debris

1 Introduction

1.1 Rationale

The retreat of glaciers globally has illustrated the occurrence of climate change, but this retreat may also have impacts on society. Individual mass balance data compiled by the World Glacier Monitoring Service showed that despite local variations some clear trends have been observed. From the 1970s the majority of glaciers had a zero or slightly positive mass balance – showing they were in approximate equilibrium with the climate. Glacier retreat after this period is therefore very likely to be linked to a post-1970 global warming. This retreat is increasing, with mass loss being almost twice as much in period 1990/1991 to 2003/2004 as between 1960/1961 to 1989/1990 (Lemke *et al.,* 2007). Although the most up to date mass balance data (of the years 2007/08 and 2008/09) show a slightly less negative mass balance of -590 mm w.e. yr^{-1} compared to the 2000-2009 mass balance mean of -667 mm w.e. yr^{-1}, this is still greater than the mean mass balance of the 1980s by 165% (World Glacier Monitoring Service, 2011). There are exceptions, with Gardelle *et al.* (2012) revealing the glaciers of the southern Karakorum region in the Himalayas may be experiencing a slightly positive mass balance of $+0.11 \pm 0.22$ m yr^{-1}. The overall mass loss of glaciers and ice caps world-wide is clearly evident however, with mass loss from January 2003 to December 2010 estimated from GRACE derived satellite gravity fields of 148 ± 30 Gt yr^{-1} (Jacobs *et al.,* 2012).

This loss of mass and decrease in aerial extent of glaciers could have important consequences for water resources. The Greater Himalayan region is the headwater for some of the largest Asian rivers, providing a water resource for 1.3 billion people (Xu *et al.,* 2009). Meltwater from snow and glaciers provides a significant proportion of the runoff of many of these rivers. Meltwater from the Karakoram, eastern Hindu Kush and western Himalaya provides around half of the total flow of the Indus River in Pakistan. At periods outwith the monsoon season, melt provides around 70% of the runoff of the River Ganges, Indus, Tarim and Kabul. Furthermore, around a quarter of China's population is supplied with water from snow and glacier melt during the dry season (Xu *et al.,* 2009). Even when glacier melt occurs during the summer monsoon, Indian rivers such as the Ganga River at Rishekesh are composed of up to 40% glacier melt (mean 32%) (Maurya *et al.,* 2011).

Glaciers are an important water resource because of their innate ability to store water from winter snowfall and release it during the dry season (Jansson *et al.,* 2003). This

reduces the seasonal variability of rivers with a glacier melt component, with the dry season melt often contributing when the river would otherwise be in a low flow period. The Alps constitutes just 15% of the catchment area of the river Rhine, but in June alpine runoff accounts for 52% of the river's total discharge. This demonstrates the disproportionate effect melt has on summer streamflow (Weingartner *et al.,* 2007). Importantly, this meltwater is often delivered when the demand for water is highest, making its contribution more valuable, especially in arid or semi-arid areas where water deficits are already a problem (Beniston, 2003).

The impact of retreating glaciers on river runoff is therefore likely to be significant. In the future increased melt will initially increase river flows (with peak flow occurring earlier in the season), but ultimately a long term trend of a decreasing contribution to streamflow will emerge (Kundzewicz *et al.,* 2007). Modelling of runoff from the Bhagirathi River basin (containing the Dokriani Glacier) in the Garhwal region of the Himalayas by Singh *et al.* (2006a), revealed a 2°C increase in temperate would result in a 28% rise in summer flow. The loss of mass of the glaciers in the Tuotuo River basin, western China is likely to be contributing to an increase in streamflow. The glacier runoff since 1990 was modelled to increase by 9.4% due to increased melting (Zhang et al., 2007). Nevertheless, any short term runoff increases merely illustrate that stored water is being released at an increasing rate – further depleting the finite water reserve (Barnett *et al.,* 2005). This can already be seen in the Cordillera Blanca, where discharge records show the area has passed the period of increasing river flow and now has decreasing annual and dry season discharges, linked to the observed decrease in glacierised area. Runoff will continue to decrease, with the La Balsa catchment dry-season discharge decreasing by 70% if its glaciers disappear (Baraer *et al.,* 2012).

In a warming climate Stokes *et al.* (2007) reported that the thickness and aerial distribution of the debris layer of debris-covered glaciers is likely to increase. This is because debris-covered glaciers thin vertically rather than retreat due to the insulating effect of the debris. Ablation is concentrated on the margins of the debris, where cover is thinner, leading to the progressive thickening of the debris as material is released during melting. This was highlighted by measurements of the Pasterze Glacier where between the periods of 1964-1981 and 1981-2000 volumetric loss increased by 2.3 times, associated with an increase in debris cover from 4.4% in 1964 to 7.3% in 2001 (Kellerer-Pirklbauer *et al.,* 2008). Clearly, the significant impact debris has on a glacier's ablation rates will influence the overall runoff produced, and should be taken into account in future modelling (Zhang *et al.,* 2007). Furthermore, debris-covered glaciers are found in areas which are especially important for providing water downstream. For instance, many of the glaciers of the

Karakoram range in Pakistan are debris-covered, and they provide a significant proportion of the inhabitants of northern Pakistan with water (Mayer *et al.,* 2006). Understanding the runoff patterns from debris-covered glaciers is hugely important, as they are not only a source of vital water now, but they will become ever more valuable as climate change progresses.

Despite the need for an understanding of runoff patterns from debris-covered glaciers, the current level of understanding lags behind that of clean glaciers. The seasonal evolution of the glacier-hydrological system, following the retreat of the snowline, is well understood (Nienow *et al.,* 1998; Campbell *et al.,* 2006; Willis *et al.,* 2002). However, only one dye tracing study the author is aware of has been carried out on a debris-covered glacier (Hasnain e*t al.,* 2001), but this focussed on the autumn close up rather than spring evolution of the hydrological system, and did not explicitly deal with any influence of the debris. Considering the influence debris has on ablation, it would not be surprising if this impacts on the form and evolution of the hydrological system, but currently there are no data which look into this. There is also no knowledge of the influence of the debris on the supraglacial input hydrograph, apart from the known change in ablation with debris thickness.

The dynamic response of glaciers to meteorological forcing has been studied in detail, both in terms of how this varies seasonally, daily (especially in the spring time when the hydrological system is changing, as seen in the Alps (Mair *et al.,* 2001), and now in Greenland (Bartholomew *et al.,* 2011)), and even sub-daily (Mair *et al.,* 2008). But the difficulties of working on large and remote debris-covered glaciers means their velocity fluctuations tend to be studied using remote sensing methods. These methods reveal seasonal changes over months, but lack information on short term daily patterns, especially in the most dynamic regions of the glaciers where feature tracking is less reliable (Quincey *et al.,* 2009; Scherler and Strecker, 2012).

Often in glacier-hydrology the variations in certain water chemistry parameters (especially conductivity (Collins and Young, 1979), sulphate and bicarbonate ions (Tranter *et al.,* 1993b)) have been used to elucidate the temporal variations in the sources of water comprising proglacial runoff, both for temperate and cold-based glaciers (Hodgkins *et al.,* 1998). This can be used to understand the importance of different hydrological systems, and aids in the interpretation of runoff patterns. There are a few studies of the water chemistry of debris-covered glaciers, including one which attempted the separation of runoff components (Hasnain and Thayyen, 1994), but their findings were not related to the glacier-hydrological system. The debris may have an influence on the runoff water chemistry through superficial reactions of meltwater with debris, but there are opposing

views (Hasnain and Thayyen, 1999a and Hodson *et al.*, 2002), due to the lack of measurements of supraglacial water chemistry.

Even though there is a good understanding of ablation beneath debris-covered glaciers, their overall water balance (in terms of the contributions of melt, evaporation, precipitation and storage to runoff) is poorly understood. Only very recently has a fully distributed energy balance model been constructed and used to model the runoff from a debris-covered area of a clean glacier (Reid *et al.*, in press), and an energy balance model has not yet been applied to a mainly debris-covered glacier. Mihalcea *et al.* (2008b) did construct a distributed melt model but it was based on finding the debris surface temperature through statistical regression with global radiation, and the other energy balance components were not considered. Usually runoff models of debris-covered glaciers use an approach based on the relationship between debris thickness and degree day factor, and these are used to predict future runoff (Singh *et al.*, 2006a). Degree day models though are over dependant on air temperature, whereas the energy balance over debris suggests that because higher air temperatures result in higher debris surface temperatures, which increases the sensible heat loss to the atmosphere, sub-debris ablation is less sensitive to air temperature fluctuations than clean-ice ablation (Brock *et al.,* 2010). Accurate future runoff prediction therefore requires the development of a distributed energy balance melt model for debris-covered glaciers. There is a lack of data on the evaporation of water from debris, with just one study addressing this (Sakai *et al.*, 2004), and no studies looking at how water, either as a liquid or vapour moves within the debris layer.

There is also an absence of runoff records from debris-covered glaciers, which makes understanding their hydrological systems and water balance more difficult. One study compared the runoff between a clean and debris-covered glacier, but it did not include the spring evolution or a detailed hydrograph analysis (Mattson, 2000). There is also data on the runoff of the Gangotri Glacier (Singh *et al.,* 2006b), which has been analysed in detail, but data from the Lirung (Sakai *et al.,* 1997) and Dokriani Glaciers (Singh *et al.,* 1995), was not thoroughly explored. There is a need to increase the understanding of the runoff records of debris-covered glaciers, as this would make it more feasible to predict future runoff fluctuations.

Currently, there is a good understanding of the influence of debris on ablation (Mattson *et al.*, 1993; Reznichenko *et al.*, 2010)), the surface energy balance (Brock *et al.,* 2010), and how to model this (Reid and Brock, 2010), as well as on seasonal glacier dynamics. In terms of debris-covered glacier hydrology, there is now a good comprehension of supraglacial lakes and ponds (Richardson and Reynolds, 2000), and the formation of the englacial conduit network (Gulley and Benn, 2007). There is a tendency

for these parts of a debris-covered glacier to be understood in isolation, and there has only recently been an effort to put the understanding together into an (albeit theoretical) glacier mass balance model (Lefeuvre and Ng, 2012). Glacier-hydrology may be central to the integration of what is already known about debris-covered glaciers, and yet it is the least well understood part of the glacier system. It is also necessary to emphasise the links between the different parts of the hydrological system from supraglacial to proglacial (Figure 1.4), because it was in this way that the understanding of clean-glacier hydrology developed. Part of the reason for the lack of debris-covered glacier hydrology was mentioned by Hambrey *et al.* (2008, p 2373):

"The hydrology of Himalayan debris-mantled glaciers is poorly known in comparison with alpine glaciers, because the normal techniques such as dye-tracing, geophysical analysis of englacial and subglacial drainage and discharge monitoring are commonly impractical on account of the complex terrain, inhomogeneous debris content of the ice and difficulties of access."

Considering that the study glacier (Miage Glacier) has relatively easy access, an excellent research base covering its ablation, debris thickness, meteorology and energy balance (section 1.4), and has very similar characteristics to the (albeit much larger) Himalayan debris-covered glaciers, it is the ideal glacier for this study. Combining this with the apparent research gaps mentioned above provided the motivation for this study.

1.2 Aims and objectives

The aims of the thesis are numbered below, with the objectives of each aim given as subsections. The structure of the thesis is built upon the five aims, with each of the aims being dealt with in a results chapter. The order of the aims, and therefore results chapters, reflects the structure of the hydrological system (Figure 1.4), with the first aim referring to the supraglacial hydrology, the second and third aims referring to the englacial and subglacial routing of water through the glacier, and the resulting proglacial hydrograph. The fourth and fifth aims are used to understand the influence of the debris on the entire hydrological system, through investigating the catchment water balance and glacier dynamics, respectively.

1. Understand the influence of the debris on the spatial and temporal patterns of water inputs to the glacier
    a) Use mapping and measurement of supraglacial streams to understand the form of the supraglacial stream network
    b) Construct a distributed energy balance melt model to determine the spatial and temporal variations in ablation across the glacier
    c) Model how changes in air temperature and debris thickness may influence the pattern of ablation across the glacier
    d) Measure evaporation using lysimeters, and calculate the movement of water vapour within the debris, to understand the influence of debris on evaporation
2. Understand the influence of the debris on the structure and evolution of the englacial and subglacial water routing using dye tracing
    a) Use dye tracing to examine the structure of the hydrological system across the glacier
    b) Use dye tracing to examine how the hydrological system evolves over the season
3. Examine the temporal variations in bulk water routing using analysis of supraglacial and proglacial water chemistry, and analysis of the fluctuations of the proglacial stream
    a) Measure the supraglacial water chemistry to determine whether this is influenced by the presence of supraglacial debris

   b) Through measurements of proglacial stream water chemistry, determine the temporal variations in bulk water routing, how this changes seasonally, and what it reveals about the structure of the drainage system
   c) Analyse the proglacial hydrograph to determine how the debris' influence on the supraglacial hydrograph and englacial and subglacial drainage impacts on its timing and amplitude
4. Understand the influence of the debris on the water balance of the glacier
   a) Using the distributed energy balance model, quantify, and understand the relative importance of, the melt and rainfall inputs to the catchment
   b) Using measurements of evaporation and the proglacial hydrograph, quantify the outputs of the catchment
   c) Calculate the storage component as the difference between inputs and outputs
   d) Quantify the total influence of the debris on the melt and evaporation components of the water balance
5. Examine the spatial and temporal glacier velocity variations, to understand how the water inputs and hydrological structure influence the glacier dynamics
   a) Understand how the water inputs and hydrological structure result in the short term patterns of glacier velocity
   b) Understand the influence of the debris on the annual and seasonal glacier dynamics and the variability of glacier velocity

1.3 Hypotheses

Before data collection commenced several hypotheses were proposed, based on the current knowledge of glacier-hydrology and debris-covered glaciers. The broadest hypothesis was that the debris cover mantling a glacier would mean that its hydrological system, water balance and water chemistry was not analogous to that of a clean glacier. Starting with the supraglacial network, the uneven topography and perceived lack of supraglacial streams on debris-covered glaciers gave rise to the hypothesis that the debris cover discourages the formation of supraglacial streams, through the creation of small catchment areas and the capturing of melt into ponds. Linked to this hypothesis, and the known effect of snowcover on attenuating the supraglacial input hydrograph, it was thought the debris layer would attenuate and decrease the magnitude of the meltwater input hydrograph (due to decreased sub-debris melt and the storage of water within the debris). As there has been a lack of consensus regarding whether or not the debris can

provide a source of ions to the supraglacial meltwater, the next hypothesis states that the chemical reactions occurring between the debris and the water within the debris layer would provide a source of ions to runoff that has a supraglacial rather than a subglacial origin.

If the hypotheses on the influence of the debris on the input hydrograph were proved correct, then this might have an influence on the structure and evolution of the englacial and subglacial hydrological network. This led to the idea that removal of snow from the debris-covered region would not result in the input hydrograph increasing significantly enough to increase the efficiency of the englacial and subglacial network (the snowline would have to reach the clean ice area before this occurred). The lack of the change from an inefficient to efficient system, as well as the debris' influence on the input hydrograph, would mean the seasonal increase in the amplitude of diurnal fluctuations in proglacial runoff would not be observed until the snowline reached the clean ice region (i.e. would be later than a clean glacier with a similar climate). Similarly, if meltwater inputs from the debris-covered region have a more attenuated hydrograph, then this may form part of the stream's baseflow, meaning the baseflow would be a relatively large proportion of runoff. The diurnal runoff peak would also occur later (as this would be composed of clean ice melt from the upper clean ice areas).

Thinking about the water balance components, the influence of debris on ablation is likely to decrease overall runoff from the glacier, due to ablation beneath debris being significantly lower. Inputs from rainfall would also be decreased due to evaporation from debris being significantly higher than from bare ice.

1.4 Study area

Miage Glacier is a large compound valley glacier in the Western Italian Alps (Figure 1.1). It has four steep tributaries, Mont Blanc Glacier, Dome Glacier, and Bionassay Glacier, and the smaller Tête Carrée Glacier. There are also many smaller glaciers such as the Glacier du Col Infranchissable, and the hanging glaciers Col du Miage, Dômes de Miage and Aiguilles de Trélatête. Together these glaciers make up the Miage Glacier basin which follows the ridge crest from La Pointe Baretti (on the Breuillat arête) around to Petit Mont Blanc (Deline, 2005). These main tributaries combine into the main Miage Glacier tongue at the head of the main valley which trends north west to south east, and is over 1000 m deep and has gulleys that end in large avalanche cones. As the glacier enters Val Veny it bends around 90° so it now flows towards the north east, and shortly after it enters the main valley it splits into three lobes, the large northern and southern lobes, and the

much smaller central lobe. Once the glacier leaves the walls of the main valley it is flanked by large lateral moraines (up to 200 m high (Deline, 2005)), which bound the entire lower glacier except for the tips of the northern and southern lobes. In total Miage Glacier covers an area of 10.5 km^2, of which (in 2005) 4.5 km^2 was thickly debris covered, 5.4 km^2 was clean ice or snow, and 0.65 km^2 was dirty ice (for a description of how the different surface types were defined see section 3.2.4.2). The glacier's maximum elevation is around 4640 m a.s.l. in the highest snowfields above the Dome Glacier, with its lowest elevation around 1740 m a.s.l. at the end of the southern lobe. Overall Miage Glacier is one of the largest glaciers in the Alps, with only the Unteraargletscher in Switzerland of a similar size (Deline, 2005).

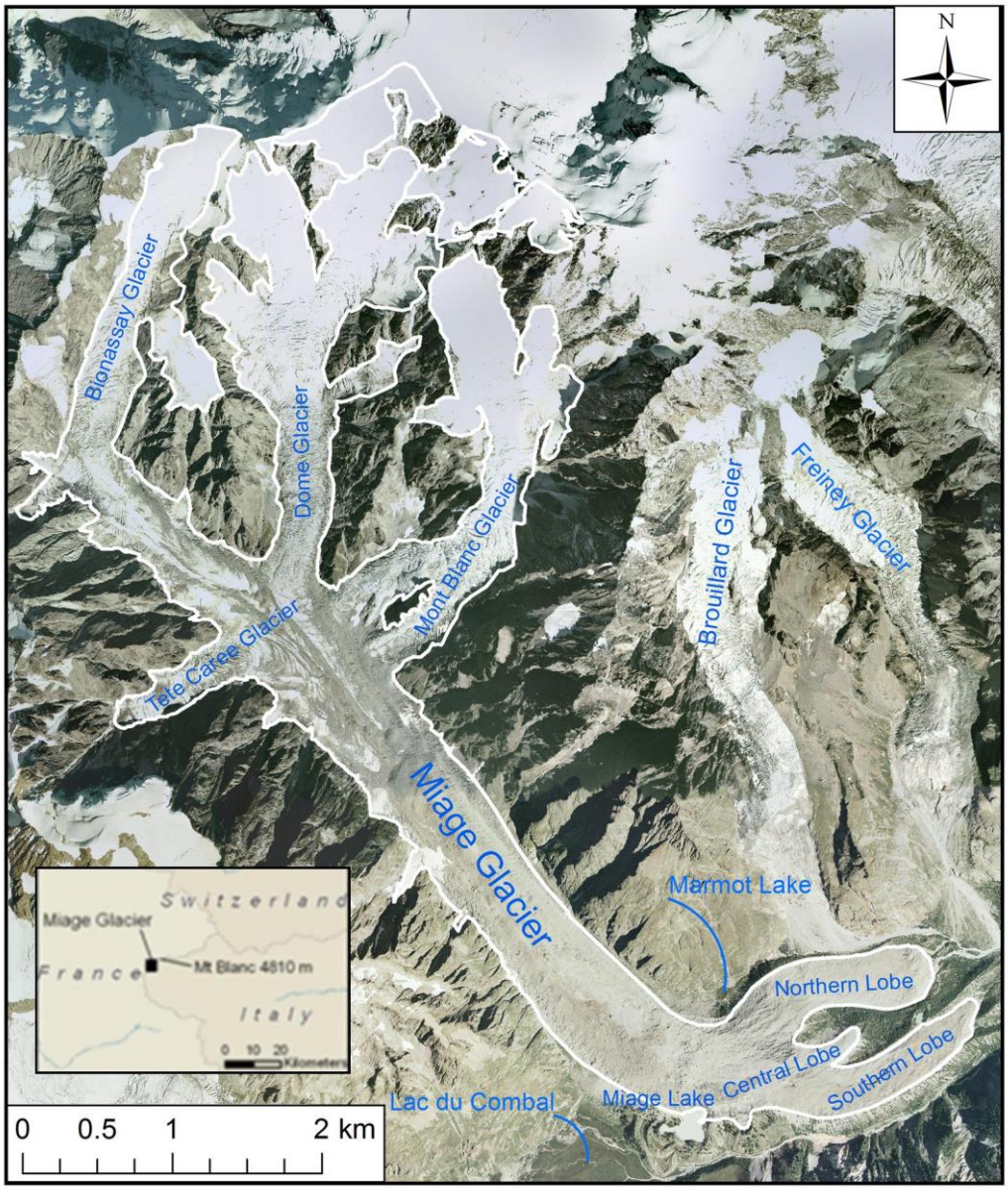

Figure 1.1 Aerial photograph of Miage Glacier, with its tributary glaciers named. Inset gives the position of the glacier in the Alps.

The debris cover on Miage Glacier begins as lateral moraines either side of the tributary glaciers, which merge to form medial moraines, and soon extend across the glacier so where the Mont Blanc Glacier confluences with the main glacier there is almost a completely continuous debris cover. On average the debris is 0.25 m thick, with the depth increasing towards the terminus (Foster *et al.,* 2012). The debris is derived from rock, and mixed snow and rock avalanches. Larger but less frequent rock falls are responsible for creating areas of particularly thick debris and large mega blocks (Figure 1.2). There have been around 10 rock falls or rock avalanches onto Miage Glacier in the 20th Century and, of those, three of the larger events will be described. The most recent was in May 1988 when 0.10 km^2 of subangular gneiss and granite was deposited from the Mont Blanc Glacier from an elevation of around 3300 m a.s.l (Chiuminatto, 2004, cited in Deline, 2009). In the late 1940s there was a second deposit whose source was from above the Tête Carrée Glacier and resulted in a 0.17 km^2 deposit of gneiss and slaty shist. It is now found on the western side of the glacier just above the bend (Deline, 2009). The oldest rock fall was in the early 1920s (Valbusa,1924, cited in Deline, 2009) and it also originated from above the Mont Blanc Glacier, but from an elevation of 4100 m a.s.l.. This deposit now resides on the northern lobe and consists mainly of gneiss, but also of blocks of granite, chlorite schist, and cataclastic breccia (Deline, 2009).

Figure 1.2 Large mega-blocks at the top of the northern lobe on Miage Glacier.

Miage Glacier has not always been a debris-covered glacier, with accounts and maps from the late 1700s suggesting the majority of the glacier was clean, and it remained so (at least above the bend) until 1820 during the second main advance of the Little Ice Age. By the 1840s a sketch map by Forbes (1843, cited in Deline, 2005) indicated the existence of two main medial moraines, which spread out to form a wide debris-cover on the lower lobes. The first detailed study of the glacier was performed by Baretti (1880, cited

in Deline, 2005) which showed the lower 2.5 km of the glacier was debris-covered, with the three main moraines continuing up-glacier. By the end of the nineteenth century the debris cover had expanded a further 2 km upglacier, but it quickly contracted by 1 km by around 1900 to 1915. The debris cover reached a similar extent to the present day by the 1930s (Deline, 2005). The geology of the debris cover reflects the geology of the surrounding mountains and Deline (2002) categorised Miage Glacier's debris cover into 8 lithotypes: rusty debris, Mont Blanc granite, microgranite, gneiss, schists (including chloritoschistes, black crystalline schists, ochre schists and white schists), slaty schists, amphibolite and tectonic breccia.

A layer of sediment exists beneath Miage Glacier, at least in the area above the bend (where it is around 10-15 m thick), and on the northern lobe (where it is 10-20 m thick), as identified by seismic reflection surveys performed in 1997 and 1998 (Pavan *et al.,* 1999, cited in Deline, 2002). The erosion-sediment index of Miage Glacier is 0.54, which implies it flows over a mixed bed in which sediment dominates (Deline, 2002). The erosion-sediment index is calculated by dividing factors related to debris production by factors related to the transport capacity of the meltwater stream. Values between approximately -2 and -0.3 indicate a hard bed, between -1.2 and 0 a mixed bed and greater than 0 a sedimentary bed (Haeberli, 1986, cited in Maisch *et al.,* 1999).

The recent changes of the debris cover and elevation of Miage Glacier were subject to study once digital elevation models could be compared. Thomson *et al.* (2000) constructed four digital terrain models (DTMs), to identify thickness changes along the lower glacier, revealing areas of thickening that migrated down glacier. These were interpreted as kinematic waves associated with episodes of increased mass flux. The first wave was caused by increased snowfall and lower temperatures from 1890 to 1940, resulting in the glacier advancing in 1930 - the debris cover retained the increase in mass to the terminus. Therefore, debris-covered glaciers do respond to climate, but because the debris protects the ice during unfavourable conditions, Miage Glacier experienced an increase in mass during the twentieth century, while nearby clean glaciers experienced a decrease. Smiraglia *et al.* (2000) studied the ice thickness variations on Miage Glacier between 1975 and 1991. They found a zone of thickening on the lower glacier (>40 m), which became less apparent up-glacier. Further up-glacier, at around 2100m, a zone of >40 m thinning was identified. This pattern was also attributed to a kinematic wave, caused by an increase in accumulation within the 1950s. The velocity measurements revealed a decrease in velocity with distance down-glacier (60 m a^{-1} at 2100 m, but 15 m a^{-1} at the terminus). The zone of thickening can be explained because a zone of longitudinal compression (occurring on the lower glacier) will amplify any thickening in a glacier cross-

section. Usually this would be compensated for by increased ablation at lower altitudes, but the debris cover decreases this ablation, preserving the area of thickening and magnifying the fluctuation in mass balance as it moves down-glacier. More recently Diolaiuti *et al.,* (2009) revealed that although Miage Glacier had increased in volume between 1975 and 1991 by 19.3 x 10^6 m^3, it had lost 36.2 x 10^6 m^3 between 1991 and 2003. The cross profile change between 1991 and 2003 showed the greatest lowering between 2010 m a.s.l. and 1970 m a.s.l., corresponding with an area of crevasses where the tongue becomes three lobes, with the only height increase being on the lower lobes. An inverse relationship was found between the debris altitude and the elevation change ($r = -0.7$ for 1975-2003), so greater elevations showed the most lowering, with the crevassed region being an exception. This was linked to the decreasing debris thickness (and hence increased ablation) with increasing altitude by combining the elevation change data with ASTER debris thickness data from Mihalcea *et al.* (2008a). Importantly, in comparison with other Italian clean glaciers, the thickness change of Miage Glacier was up to 30% less.

The debris thickness distribution across the glacier was studied by Mihalcea *et al.* (2008a), using ASTER surface temperature data to derive the debris thickness distribution. The details of this approach are given in section 2.4.3. The measured and calculated debris thicknesses compared well, and their map of debris thickness showed the general increase in debris thickness with decreasing elevation, and areas of thinner debris around 1901-2000 m a.s.l. associated with an area of crevasses, and areas of thicker debris associated with a rock fall at around 2101–2200 m a.s.l.. Further work to identify the debris thickness distribution of Miage Glacier, was performed by Foster *et al.* (2012), using meteorological and ASTER surface temperature data to solve the energy balance, and find the debris thickness. The debris thickness distribution was used in this thesis, and detailed methods are given in section 3.2.4.

Meteorological data has been collected on Miage Glacier by Brock *et al.* (2010) from up to two weather stations since 2005. This showed Miage Glacier has specific meteorological characteristics related to the shape of its valley and surface debris cover. The early morning air temperature lapse rate between the upper and lower weather stations is very steep (reaching an average of -12°C km^{-1} at 10:30 in 2006) because direct shortwave radiation warms the air at the lower weather station while the upper station remains shaded by the valley sides. There is also a daily cycle in wind speed and direction related to the air temperature lapse rate, so it switches from a wind down the main Val Veny overnight from west south west, to an up-glacier wind from the south south east by late morning due to the warming of the air by convection from the surface debris, although the fastest wind speeds are at 17:00 and from the south west as the wind direction veers back towards west

south west. The debris influences the radiation budget, with the spatial variations in debris thickness partly controlling the outgoing longwave radiation, sensible and latent heat fluxes, and air temperature. Annually averaged fluxes show little variation in their magnitude, except for the latent heat flux which was twice as high in the wetter year of 2007, compared to 2005. Brock *et al.* (2010) also studied the ice ablation and debris thermal characteristics on Miage Glacier. The sub-debris melt decreased exponentially with increasing debris thickness, with ablation rates falling to just 6 mm w.e. d^{-1} under 0.55 m of debris, with the highest ablation rates found near the margins of the debris cover. The effective thermal conductivity of the debris was a mean of 0.96 W m^{-1} K^{-1}, although it increased with increasing debris thickness, possibly because of air convection between the larger clasts of thicker layers.

One of the attractions of Miage Glacier is the ice marginal Miage Lake, which exists on the southern edge of the glacier, as it bends (Figure 1.3). Diolaiuti *et al.* (2005) studied the fluctuations and morphology of Miage Lake. The lake area increased by 24600 m^2 ± 4000 m^2 between 1893 and 1956, with it being stable since (although it drained in 2004). The lake had a complex configuration of two main basins separated by a submerged moraine. In the summer, the ice-contact basin had a thermal regime determined by melting icebergs, with a lower layer of warm water (2-5°C) melting the ice floor. The moraine dammed basin has a summer regime consisting of warmer water (7-12°C) overlying cooler water, although it could not influence melting as the basin was sediment-floored (Masetti *et al.,* 2009). Calving of the ice cliff accounted for a mass loss of 128 x 10^3 m^3 w.e., equating to around 2% of total glacier melt (Diolaiuti *et al.*, 2006). The lake drained suddenly in September 2004, exposing the lake floor and revealing the ice contact basin was composed of an ice-floored embayment. During lake drainage Masetti *et al.* (2009) found that along with the ice-floored northern basin there were three further ponds floored with fine glacial debris. These were fed by ice melt from the northern basin, although they do not have ice contact themselves. As the lake filled, englacial conduits provided water input into the northern basin, with this water filling the second pond through a subterranean connection, and this pond filling the third pond through a small channel. The fourth pond only changed in level in reaction to precipitation. Masetti *et al.* (2009) analysed the sediments in the bed of the ponds and found them to have a high percentage of fine particles (30-40 % clay and 40-45 % silt) and low permeability (3 x 10^{-7} m s^{-1}). A finite element mesh model of the bed of the sediment-floored ponds was constructed, allowing calculation of water loss through the bed (180 m^3 d^{-1}). Rapid drainage of the lake could not have occurred through the sediments comprising the basin floor, but must have occurred through an abrupt failure in the ice floor of the northern pond.

Figure 1.3 Miage lake in July 2010. The sub-basin in the distance is the northern ice-floored one, with the basin in the foreground fed from the northern basin.

Dendrochronology of the trees in front of the southern lobe was used to identify fluctuations in the southern lobe proglacial stream, and understand the stability of the frontal margin. Garvaglia *et al.* (2010) found that as the oldest trees in the area were about 30 years old, there has been no significant frontal advance or increase in stream activity, consistent with the known stability of debris-covered glacier termini, although some trees showed scars related to a period of positive glacier mass balance between 1975 and 1988 (Giardino *et al.,* 2001). Notably, the southern lobe proglacial stream decreased in flow during 2007, becoming completely dry by November that year (the main stream now exits from the northern lobe).

As Miage Glacier is an accessible Alpine glacier it has benefitted from a wealth of previous research on its ablation and debris thickness, mass fluctuations, meteorology, and its ice marginal lake. Despite this, little work has attempted to understand its runoff fluctuations or supraglacial, englacial or subglacial hydrology. This study is an opportunity to fill these knowledge gaps so a more complete picture of this glacier can be realised.

1.5 Thesis structure

The next chapter in this thesis is the literature review, which covers the structure of the glacier-hydrological system, and how it has been investigated using dye tracing, glacier velocity measurements and water chemistry fluctuations; the different techniques for modelling runoff on clean and debris-covered glaciers; the supraglacial streams and lakes on debris-covered glaciers, and how debris influences ablation and the glacier's response to

climate. This is followed by the methods chapter, which outlines the field, lab and analysis techniques employed to answer the thesis objectives. The five results chapters (chapters 4 to 8) are next, and their structure is based on the structure of the glacier-hydrological system (Figure 1.4), and the 5 aims of the thesis (see section 1.2). Each of the results chapters deals with an aim in turn. A discussion of the results found within the results chapters is given in summary sections at the end of the relevant chapter or subsection. The conclusions of the thesis and ideas for future research are given in chapter 9.

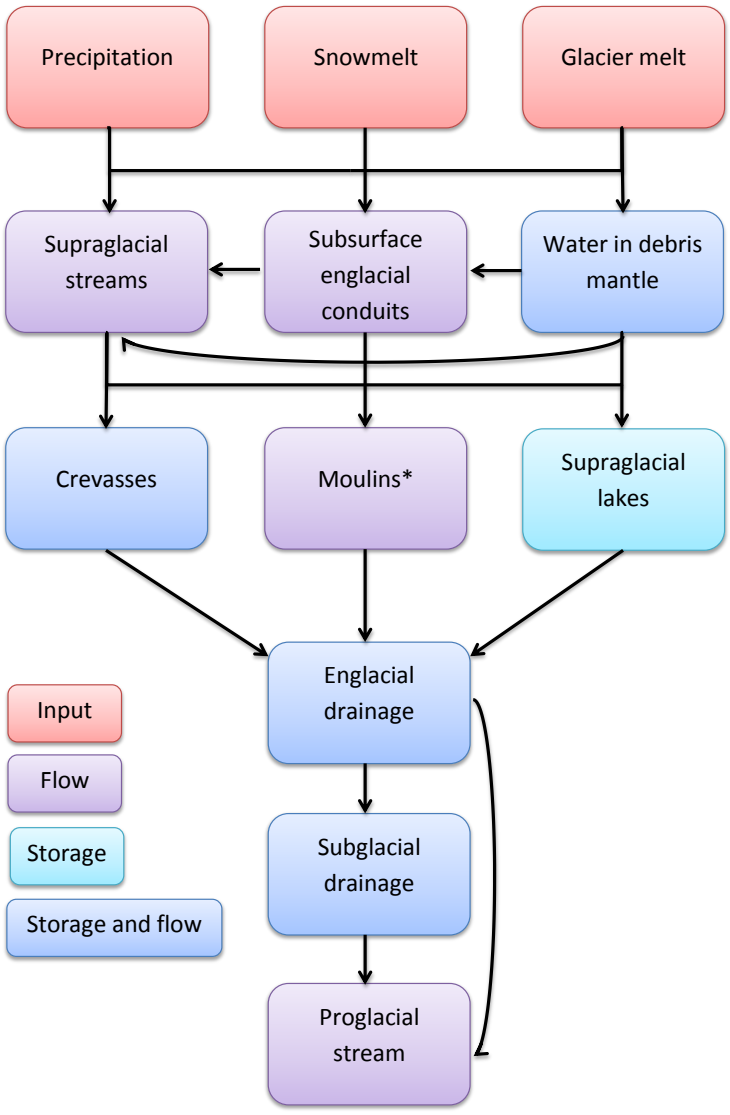

Figure 1.4 Diagram of the glacier hydrological system structure. *It is known moulins can occasionally store water and can be thought of as part of the englacial system, though they are usually just the beginning part of the englacial system.

2 Literature review

2.1 The influence of debris on glacier ablation and a glacier's response to climate: theory and modelling

The addition of a layer of debris onto a glacier has a profound influence on ablation. Understanding this influence, and the factors determining its magnitude, is the only way to allow the melt from a debris-covered glacier to be modelled. Quantifying this melt is essential to allow an accurate estimation of runoff from a debris-covered glacier, and is important for estimating how these glaciers react to climate fluctuations. Throughout this section reference will be made to the effective debris thickness which results in the maximum increase in ablation compared to clean snow or ice, and the critical debris thickness, which results in ablation equal to clean snow or ice, and above which ablation is reduced (Kirkbride and Dugmore, 2003).

2.1.1 Debris and its effect on glacial ablation

The pioneering study into the effect of a moraine cover on ice melting was carried out by Östrem (1959) who performed an experiment on Isfallsglaciären, which involved measuring its ablation under different thicknesses of sand and gravel. The ablation of the ice decreased when the thickness of the sand and gravel exceeded 5 mm, with thicker covers further decreasing ablation. This produced a relationship between debris thickness and ablation, creating a hyperbolic curve. Notably, Östrem (1959) mentioned that a layer thinner than 5 mm may increase ablation, but the erosion of thin layers of sand and gravel meant results were not obtained. Thermistor measurements revealed the mean temperature of the sand surface reached 9°C (much higher than the mean air temperature of 5.4°C), and this heat would be transferred as outgoing longwave radiation, as loss to heat the air, as loss to allow evaporation of melt water, and as energy to melt the ice below.

Mattson *et al.* (1993) conducted a similar experiment on Rakhiot Glacier, Punjab, India, but used the debris present on the glacier surface to construct artificial plots with differing debris thicknesses. Under a very thin debris cover (0-10 mm) ablation increased, with maximum increase found under 10 mm of debris (the effective thickness). This occurred due to the debris decreasing the albedo compared to uncovered ice (being 10-15% for debris, but 34-51% for clean ice (Benn and Evans, 1998)) – increasing the proportion of shortwave radiation absorbed, which due to the thin covering could be transferred quickly as heat energy to the ice-debris interface, resulting in increased ablation.

As the debris thickness increased above 10 mm, the amount of ablation increase above the bare ice rate decreased until a thickness of 30 mm was reached. Above this thickness ablation decreased further as thickness increased, because the debris insulated the ice from the incoming radiation, counteracting the increased albedo.

Mihalcea *et al.* (2006) investigated the influence of debris thickness on ablation, but they took account of the slope and aspect of the sites. A "stake farm" was constructed consisting of 23 ablation stakes drilled into sites covering different conditions on Baltoro Glacier, Karakoram, Pakistan. The ablation decreased as the debris thickness increased, matching the results of the above workers. Although higher elevation decreased ablation rates, it was superseded by the effect of the debris, and the slope angle and aspect of the site. Furthermore, with debris covers less than 0.1 m, slope and aspect effects could be greater than caused by debris thickness.

Kirkbride and Dugmore (2003) studied the response of glaciers in south Iceland to the 1947 eruption of Heckla, which deposited volcanic ash (tephra) over the Eyjafjallajökull ice cap. Gígjökull, a northern outlet glacier of this ice cap, advanced almost instantaneously in response to the tephra deposit. The speed of its reaction was associated with its fast velocity: the effect of the tephra cover on the magnitude of an advance depends upon the thickness and properties of the tephra, and the glacier's terminus velocity. Despite the insulation effect of the tephra predominating initially (decreasing ablation by 80% on the lower glacier), the overall effect was of a 30-37% decrease as the insulating effect reduced with time (tephra is reworked more easily than rock debris). Over longer time periods the darkening of the surface will result in a long term increase in ablation. The surrounding glaciers which received a thinner tephra covering only exhibited a negative mass balance change, with those closer to the eruption having a more negative response that took longer to return to equilibrium. Kirkbride and Dugmore (2003) created plots of tephra from the Heckla 1947 eruption of different thicknesses. The effective thickness was 2 mm, with the critical thickness being 5.5 mm. These values are less than reported by Mattson *et al.* (1993) for rock debris, due to the lower thermal conductivity of tephra. This was confirmed by Brock *et al.* (2007): the tephra from Villarrica Volcano lowered ablation rates below that of clean snow as soon as the cover was continuous (see Table 2.1 for a comparison of critical and effective debris thicknesses).

Adhikary *et al.* (2000) studied the influence of dust on ablation on the Lirung Glacier, Nepal Himalayas. They created plots of dust with differing thicknesses, while measuring the influence on ablation and albedo. On debris-covered glaciers, even areas of relatively clean ice (ice cliffs and crevasses) have a thin covering of dust. The effective thickness of the dust was 0.25 mm, with a critical thickness of 1.33 mm. Their test plot on

an ice cliff showed that relative to flat ice with the same debris thickness, ablation was doubled. When compared to bare ice, the flat site increased ablation 2.5 times, but on the ice cliff ablation increased four-fold. This was due to the albedo change on a sloping surface being greater than on a flat surface because of the greater radiation receipt on the east facing cliff. The dust particles form a small pit on the ice surface, and then flow downward because of gravity driven meltwater flow, allowing these pits to decrease albedo, and increase ablation.

Table 2.1 Critical (ablation equal to clean ice) and effective (ablation maximised relative to clean ice) debris thicknesses for a variety of glaciers and surface conditions, * denotes sources taken from Kirkbride and Dugmore (2003, p421).

Location	Critical Thickness (mm)	Effective Thickness (mm)	Surface Condition	Source
Villarrica Volcano, southern Chile	<5	-	tephra/ice	Brock *et al.* (2007)
Gígjökull, Iceland	5.5	2	tephra/ice	Kirkbride and Dugmore (2003)*
Breiđamerkurjökull, Iceland	4-7	-	tephra/ice	Lister (1953)*
Glaciar Pichillancahue-Turbio, southern Chile	<10	-	tephra/ice	Rivera *et al.* (2006)
South Cascade Glacier, Washington, U.S.A.	24	3	tephra/snow	Dreiger (1981)*
Isfallsglaciaren, Sweden	-	9	rock/ice	Östrem (1964)*
Kaskawulsh Glacier, Canada	-	15	rock/ice	Loomis (1970)*
Glacier de Tsidjiore Neuve, Switzerland	~30	10	rock/ice	Small and Clark (1974)*
Various (central Asia)	15	7	rock/ice	Konovalov (2000)*
Theoretical	-	20-30	rock/ice	Bozhinskiy *et al.* (1986)*
Barpu Glacier, Pakistan	-	~10	rock/ice	Khan (1989)*
Rakhiot Glacier, Pakistan	~30	~10	rock/ice	Mattson and Gardner (1991)*
Burroughs Glacier, Alaska, U.S.A.	<20	~7	rock/ice	Syverson and Mickelson (1995)*
Djankuat Glacier, Caucasus	70-80	-	rock/ice	Popovnin and Rozova (2002)
Lirung Glacier, Nepal	1.33	0.25	rock/ice	Adhikary *et al.* (2000)*
Khumbu Glacier, Nepal	50	3	rock/ice	Takeuchi *et al.* (2000)
Khumbu Glacier, Nepal	15	5	rock/snow	Fujii (1977)*
Various (central Asia)	20	7	rock/snow	Konovalov (2000)*

Unlike the above studies which have measured the influence of debris on ablation in the field, Reznichenko *et al.* (2010) set up an experimental study to investigate reduced melt beneath thick debris. They used blocks of ice with a cover of either sand or avalanche debris with a uniform thickness, which they subjected to either constant or diurnally cyclic radiation. Under constant conditions the debris delayed the onset of melt (by > 12 hours for a 130 mm thickness), with thicker covers increasing this delay. The absorption of heat by the debris also reduced melt rates initially, but importantly, this effect did not last and melt increased to a steady state so that ablation beneath all the debris thicknesses was similar, and 10% more than the clean ice rate (due to decreased albedo). Under a diurnal

cycle however, the steady state melt rate was never reached under a debris thickness > 50 mm, because the heat acquired was partially lost from the system during the cooling part of the cycle, and so the total heat transferred to the ice/debris interface was reduced. This effect is increased with increasing debris thickness, but steady state can be reached quickly on thinner covers, explaining the Östrem (1959) curve. Their findings imply that ablation beneath a given debris thickness (and thus the critical thickness for that glacier) is determined by the amplitude and duration of the cycle of radiation inputs to the debris surface. As these characteristics of the radiation cycle are determined by the altitude and latitude of the glacier, the critical thickness is also determined by the altitude and latitude (critical thickness decreases with increasing altitude and latitude), and this matched with measured data from several glaciers. The effect of rainfall on ablation under a debris cover depended upon the debris type, so that using sand (which has a low thermal inertia, and high permeability) the rain advects heat from the debris, increasing ablation, but under cyclic conditions and using rock debris (with a high thermal inertia, and low permeability) melt was delayed, and in their simulation did not occur at all. This was because it took a long time for the debris to become saturated with water, with the water in the saturated layer at the base of the debris freezing during the cool period. This frozen interstitial water then had to be melted within the next ablation period before melting of the 'glacier' ice could begin. Debris cover permeability is important in determining the influence of rainfall on sub-debris melt, as well as the duration of below zero night time temperatures.

2.1.2 Methods to model ablation under a debris layer

Ablation from the surface of a glacier will occur if there is a surplus of energy at the ice surface, and the ice is at the melting point (Benn and Evans, 1998). Whether there is a surplus of energy is determined by the surface energy balance:

$$S + L + H + LE + C + M = 0, \qquad (2.1)$$

(Pellicciotti *et al.,* 2008, p3987). Where S is the net shortwave radiation flux, L is the net longwave radiation flux, H is the sensible heat flux, LE is the latent heat flux, C is the subsurface heat flux and M is the energy available for ablation. All fluxes are in W m^{-2} and are positive downward. However, for debris-covered glaciers, any surplus energy at the surface has to be transferred through the debris before it can melt the ice. This transfer must be taken account of in the energy balance:

$$S + L + H + LE + P + G + \Delta D = 0, \quad (2.2)$$

(Brock *et al.,* 2010, p9). Where P is the sensible heat supplied or consumed due to precipitation, G is the conductive heat flux in the debris and ΔD is the rate of change in the heat stored within the debris. Using a surface energy balance model to calculate ablation from a clean glacier is well established, but early workers struggled to take account of all the components in the energy balance for a debris-covered glacier. For instance Nakawo and Young (1981) used an energy balance model to allow the ablation rate of ice under debris to be estimated from the debris surface temperature. They verified their model by conducting experiments similar to Östrem (1959), but they used Ottowa sand because it had a known thermal conductivity at different water contents – there being an increase in thermal conductivity as water content increases. This is important because the thermal resistance (R), determines the debris' effect on ablation, and this is calculated from the debris thickness (h_d) and thermal conductivity (K):

$$\boldsymbol{R = \frac{h_d}{K}}, \quad (2.3)$$

(Nakawo and Young, 1981, p87).

Their energy balance equation contained only S, L (combined into the radiation flux) H and LE, which required knowing T_s (the debris surface temperature), and estimating the surface vapour pressure by assuming either the surface of the debris was dry so evaporation did not occur and the surface and air vapour pressure was equal, or under wet conditions when the surface vapour pressure equalled the saturation vapour pressure at T_s. In reality, a condition between these extremes is likely. Once M is known from the energy balance equation it gives ablation (a) from:

$$\boldsymbol{M = L_f \rho_i a}, \quad (2.4)$$

(Nakawo and Young, 1981, p87), where L_f is the latent heat of fusion and ρ_i is the ice density. R can be calculated from M if T_s is given:

$$\boldsymbol{M = \frac{T_s}{R}}, \quad (2.5)$$

(Nakawo and Young, 1981, p87). As R is constant over time, M can be found without the energy balance equation if T_s is known. Any changes in the heat stored in the debris were not accounted for (it was assumed constant, which is correct if averaged over a 24 hour period (Nicholson and Benn, 2006)), and a linear temperature gradient through the debris was assumed.

Nakawo and Young (1982) tested the above model on Peyto Glacier, Canada, using plots of varying debris thicknesses. The modelled and measured ablation rates agreed well, but where they did not agree it was thought this was due to doubt over the value of R, as it was based on only two surface temperature measurements. Even a 0.5°C variation in temperature could change *R* significantly. Furthermore, there was a lack of confidence in the value of the coefficient of heat transfer, which is dependent upon the surface roughness.

Nicholson and Benn (2006) used a surface energy balance model to calculate melt beneath debris, although they only calculated S, L, H and LE, finding G as a residual. They take no account of P, and because of the difficulties in measuring the moisture content of the debris, the latent heat flux was calculated assuming either dry or saturated debris. They based their model over a 24 hour period to allow the assumption of a linear temperature gradient through the debris. Over smaller timescales this cannot be assumed because the temperature gradient is often not linear close to the surface (Conway and Rasmussen, 2000). Nicholson and Benn (2006) verified their model by measuring mean ablation at plots with differing debris thickness on Ghiacciaio del Belvedere in the Italian Alps, and Larsbreen in Svalbard. At Ghiacciaio del Belvedere where debris was assumed dry, melt rates were only within 27% of measured values, although where the debris was saturated calculated ablation was within 5% of measured melt. The model consistently over-estimated ablation, claimed due to not accounting for the conductive heat flux into the ice, but was probably because they calculated the sensible heat flux assuming stable atmospheric conditions (see Brock *et al.,* 2007).

Takeuchi *et al.* (2000) calculated the energy balance for bare and debris covered ice on Khumbu Glacier, Nepal Himalayas (without taking account of P, C or ΔD). They also estimated LE for dry or saturated debris. For bare ice the low wind speeds meant the turbulent fluxes were low, so the majority of energy used to melt ice was from net radiation. On the debris, as its thickness increased (above 20 mm), the proportion of solar radiation absorbed decreased – probably because of the higher albedo and drier debris surface (compared to thinner debris). Although, thicker debris has a higher surface temperature, meaning outgoing longwave radiation and the sensible heat flux are greater.

The thicker the debris, the more heat is stored during the day and although the total stored heat equated to zero over 24 hours, this heat warmed the air at night rather than melt the ice (night time ablation rates were negligible). This matches with the findings of Reznichenko *et al.* (2010).

The energy balance of the tephra-covered glacier on Villarrica Volcano in southern Chile) was studied by Brock *et al.* (2007). As the latent heat flux was assumed zero (due to the debris surface being dry), the sensible heat flux was found as a residual, to allow comparisons with calculated values. This was done because previously workers had calculated the sensible heat flux using the bulk aerodynamic approach, this assumes the atmosphere remains stable, and a bulk transfer coefficient can be used. This is likely incorrect, especially when the surface temperature is much higher than the air temperature during the day. To improve this, the bulk transfer coefficient was calculated for both stable and unstable atmospheric conditions using the Richardson number (R_b) found using:

$$R_b = \frac{2g(T_a - T_s)z_a}{(T_a + T_s + 546.4)u_w^2}, \quad (2.6)$$

(Brock *et al.,* 2007, p108) where g is acceleration due to gravity, T_a is air temperature, z_a is measurement height and u_w is wind speed. Assuming a stable atmosphere meant the sensible heat flux would be lower than the residual (by 55% in 2004, and 37% in 2005), but the method using the Richardson number matched the residual in 2005, but was 25% lower in 2004. Calculating the sensible heat flux as a residual was not perfect, due to errors in measuring the other fluxes, but taking into account the atmospheric instability increased the accuracy of the calculation of the sensible heat flux.

Brock *et al.* (2010) analysed the surface energy fluxes of the debris-covered Miage Glacier, Italian Alps. In contrast to Brock *et al.* (2007) the latent heat could be calculated due the availability of surface humidity measurements. The sensible and latent heat fluxes were calculated, taking into account unstable atmospheric conditions, using Brock *et al.* (2007)'s Richardson number approach. The residual energy flux for 2005 and 2007 was almost 0, lending confidence to the methods. Over the season, the latent heat (indicating evaporation) was a small negative flux, being highest in the mid-morning and late afternoon. However, there were large fluctuations, with the flux ranging from zero under dry conditions to 800 W m^{-2} if strong incoming shortwave radiation occurred after rainfall, or if the rain fell onto warm debris. At night condensation onto the debris surface was negligible. There were large differences in latent heat flux between years, with 2007 being especially high, due to a large rainfall total combined with high wind speeds. In this year

evaporation could reach rates of 1 mm h^{-1}. The high latent heat flux acts to reduce the energy available for ablation (as the energy would be needed for the latent heat of vaporization (2500 J g^{-1}), which is much larger than the latent heat of fusion (334 J g^{-1}) (Benn and Evans, 1998)) – which in 2007 was on average 4 W m^{-2} over 73 days. This may influence the effect of rainfall, as approximately 13-16% of rainfall was lost as evaporation – although the overall decrease in runoff due to evaporation was only 0.06 $m^3 s^{-1}$.

Apart from this study, there has been little account of evaporation from debris-covered glaciers, especially of direct measurement. The closest being Braun *et al.* (1994) who studied the water balance of the Linth-Limmern Head watershed in north-eastern Switzerland and used evaporation rates directly observed by Bernath (1991, cited in Braun *et al.* (1994)) to calculate the evaporation for the watershed within their precipitation-runoff model. The net evaporation figures used were:

- for snow and ice, 0.25-0.5 mmd^{-1} (October to May) or 0.5-1.8 mmd^{-1} of condensation (July to September)
- for rock/debris, 0.5-1 mmd^{-1} (June to September), same as snow for other months
- for vegetation, 2-3 mmd^{-1} (July to September), same as rock for other months

(Braun *et al.*, 1994, p17-18). Unfortunately, there was no mention of a glacier underlying the rock/debris surface but it gives an indication that evaporation rates could be twice as much as for snow and ice. Theoretically the existence of debris could influence the evaporation from the surface compared to clean ice due to the debris characteristics, as its lower albedo (10-15 %, compared to 34-51 % for ice (Benn and Evans, 1998)), increases the energy available for evaporation, and its greater surface roughness increases the turbulence at the debris/air interface and could prevent the overlying air becoming saturated with water vapour (Ward and Robinson, 2000). The high daytime temperature of the debris (Conway and Rasmussen, 2000) could increase the temperature of the water within it - increasing the evaporation rate (Thompson *et al.*, 2008). It may also influence the availability of water, with evaporation decreased if the debris is thick and only allows water to reach the surface via vapour flow rather than by capillary diffusion (Diaz *et al.*, 2004), whereas thin debris may store water and allow it to be available for evaporation, with rainfall events also providing water for potentially high evaporation rates (found by Brock *et al.* (2010)).

As it is now possible to quantify the energy balance at the surface of a debris-covered glacier, Reid and Brock (2010) constructed a physically based debris energy balance melt model (DEB-model). The model does not require the debris surface temperature;

instead the energy balance is solved numerically by varying the debris surface temperature until the energy flux at the debris surface is zero. The heat flux is conducted through the debris to give the melt at the ice/debris interface. This model is used in this thesis so detailed methods are given in section 3.2.4. The model successfully replicated the Östrem (1959) curve of ablation and debris thickness, and was found to match measured ablation well on both Miage Glacier ($r^2 > 0.94$) and the tephra-covered glacier on the Villarrica Volcano, Chile ($r^2 > 0.82$). This model has also been used in a distributed energy balance melt model constructed by Reid *et al.* (in press) for Haut Glacier d'Arolla, Switzerland, where DEB-model was used on areas of debris, and a clean ice model was used for the clean ice areas. The debris thickness distribution was modelled by fitting a probability density function to measured debris thickness data from each region of debris on the glacier. The functions were used to assign each debris-covered cell in the model with a debris-thickness value. Reid *et al.* (in press) mentioned that the air temperatures could be slightly higher above debris, and this effect needs more detailed study. Incorporating the DEB-model reduced runoff by 7% compared to treating the whole glacier as clean ice, despite the debris-covered area covering only 10% of the glacier area. This highlights the importance of including the influence of debris in melt models, even for predominantly clean glaciers.

However, taking account of all the energy fluxes requires detailed meteorological data that is often not available. Therefore Kayastha *et al.* (2000) developed a melt model using a positive degree day factor (see section 2.3), for the Khumbu Glacier, Nepal. Seven plots with differing debris thicknesses were constructed and their ablation, surface temperature and albedo measured. They then calculated the degree day factor for the different debris thicknesses. Areas with a greater ablation had a larger degree day factor, so it was highest with a debris layer of 3 mm, but lowest when the debris was 400 mm thick. To avoid calculating the ***DDF*** for different debris thicknesses for every glacier, Kayastha *et al.* (2000) found a ratio between the bare ice and debris-covered ice degree day factors and the debris' thermal resistance and its thermal resistance at its critical thickness (see Kirkbride and Dugmore (2003)). This allows ablation to be calculated on other glaciers with a similar debris geology, although it relies on the ratio developed being applicable to other glaciers. Hagg *et al.* (2008) used the degree day method to estimate ablation on Southern Inylchek Glacier, central Tian Shan. They found a good relationship ($R^2 = 0.85$) between debris thickness and degree day factor, allowing the modelling of the degree day factor (and hence ablation) for a given debris thickness. The modelled ablation was more

accurate (R^2 = 0.77) than if they had used the average degree day factor for all sites (R^2 = 0.70).

2.1.3 Using remote sensing to model sub-debris melt

Nakawo *et al.* (1993) investigated using remotely sensed data together with either Nakawo and Young (1981)'s or Nakawo and Takahashi (1982)'s model to calculate ablation over a whole debris-covered glacier. They used MESSR data from the MOS-1 satellite to delimit the land surface around Khumbu Glacier into snow, clean ice and debris using the maximum likelihood method. They used TM band 6 LANDSAT data to determine the surface temperature of the debris, which was used with meteorological data to work out the sub-debris ablation. Ice cliffs lower the average surface temperature given by each pixel, which reduces the calculated thermal resistance and increases ablation. This gives a more representative (i.e. higher) ablation, but means the thermal resistance is miscalculated over ice cliff areas, which are in reality partially debris-free.

On Khumbu Glacier, Nepal Himalaya, Nakawo *et al.* (1999) used the same method as above to calculate ablation. They revealed the downglacier temperature distribution: temperatures were 0°C at high altitudes where the ice was clean or covered with thin debris, with temperature increasing downglacier. As the thermal resistance (which is proportional to the debris thickness) is calculated from the surface temperature, this shows the debris thickness increases downglacier. However, an area of known thick debris cover was measured to have a relatively low temperature. This was because the debris was partially vegetated and had a wet surface – meaning evaporation occurred and removed energy from the debris as latent heat. They found ablation was low at high altitude, and increased downglacier to a maximum of 5 m a^{-1}. From here ablation decreased downglacier, showing the reversed ablation gradient typical of debris-covered glaciers (Benn and Evans, 1998).

Mihalcea *et al.* (2008a) attempted to prove the applicability of ASTER satellite data to the sensing of debris surface temperature by comparing measured temperatures (from thermistors and infrared thermometry) with the ASTER temperature on Miage Glacier, Italian Alps. There was a good correlation between measured and sensed surface temperature, but it was stronger in areas of more continuous debris cover (r = 0.8), compared to areas with crevasses and supraglacial ponds, giving an overall correlation of r = 0.69. This highlights the difference in spatial scale between point temperature measurements and the 90 m pixel scale of the ASTER data. Linear regression equations giving the relationship between the ASTER temperature and measured debris thickness

were found for each 100 m elevation band, because if the relationship was calculated over the whole glacier the correlation was lower ($r = 0.55$ compared to $r > 0.8$) than for individual bands. The correlation between debris thickness and thermistor temperature could reach around 0.95 between 03:00 and 04:00 hours, probably because at night the slope and aspect of the debris was no-longer influential. ASTER images cannot be used to acquire night-time temperature data, but this shows the possibility of using thermal imaging to sense the night-time debris temperature. This may be possible with terrestrial photography, as shown by work by Rivera *et al.* (2008) who used photography to determine the albedo distribution of Volcán Villarrica, southern Chile.

To combat the difficulty of the site specific relationship between surface temperature and debris thickness, Foster *et al.* (2012) developed a method of calculating debris thickness using the surface temperature from ASTER data and meteorological data to solve the energy balance at the surface. This gave the conductive heat flux into the debris, which along with the debris thermal conductivity, and the rate of change of heat stored in the debris as a fraction of the thermal conductivity, can be used to calculate the debris thickness. The air temperature was distributed across the glacier using a statistical relationship between the debris surface temperature and air temperature. As the resulting debris thickness map is used in this thesis as the input for the distributed melt model, details of the methods are given in section 3.2.4. The advantages of this approach were that it was successful using measured or reanalysis meteorological data, even without a DEM of the glacier surface. The debris thickness maps produced compared well with measured data and the map produced by Mihalcea *et al.* (2008a).

2.1.4 The influence of debris on how a glacier responds to climate, and how this results in the evolution of the debris cover

The above investigations showed that debris influences the ablation and runoff of a glacier. Therefore debris may impact on the glaciers response to climate. The variations in Miage Glacier are given in section 1.4. Mayer *et al.* (2006) analysed photographs to investigate the fluctuations of Baltoro Glacier, Karakoram, Pakistan. The differences in photographs between 1909 and 2004 revealed the margin of the glacier had remained at the same height – showing it had neither changed in length nor volume significantly. This stable behaviour was thought due to the thick debris cover.

Even though debris-covered glaciers have a stable terminus position, they still evolve, and most have exhibited an up-glacier increase of debris-covered area. The debris-cover of the Djankuat Glacier, in the Caucasus, Russia migrated up glacier and caused the

debris-covered area to increase by 7% between 1968 and 1999. This increase was greatest when the glacier had a more negative mass balance (Popovnin and Rozova, 2002). Stokes *et al.* (2007) studied the debris cover distribution of six glaciers in the Caucasus Mountains. The debris cover on all but one increased in area (by around 3-6 % from 1985 to 2000), caused by the up-glacier movement of the debris cover limit. Lambrecht *et al.* (2011) studied 6 glaciers in the Adyl-su basin, Caucasus, finding that although the area of supraglacial debris cover remained stable between 1971 and 1991 (16%), it increased to 23% by 2006, this corresponded with a glacier area reduction of 14.9% between 1971 and 2006.

Stokes *et al.* (2007) hypothesised the up-glacier migration of the debris cover was a result of the ablation on a debris-covered glacier being greatest at the debris margins, where the cover is thin and discontinuous. Focused ablation exposes more englacial debris, thickening the debris cover, and causing it to extend up-glacier. Furthermore, the surface lowering of a retreating debris-covered glacier could lead to slope instabilities along the glacier margins – enhancing the debris thickness. Despite the increasing debris thickness decreasing ablation, the glaciers studied were still retreating; the debris cover only slowed the retreat.

This highlights the finding that many debris-covered glaciers are downwasting in response to a negative mass balance. Bolch *et al.* (2008) studied the debris-covered glaciers in the Khumbu Himal, Nepal. Their debris-covered area increased (by almost 2.5% between 1962 and 2005), at the expense of clean-ice area (decreasing by over 10%), especially along the margins of the debris cover. All four glaciers were downwasting, and although the glacier's snouts showed slight downwasting (0.12-0.37 m a^{-1} for Khumbu Glacier), the area of transition from active to stagnant ice lowered the most (0.5 m a^{-1} for Khumbu Glacier), with areas with the thickest debris cover showing a less significant decrease. All the debris-covered glaciers exhibited the same pattern, with the downwasting in the middle of the glaciers possibly creating a hollow liable to be filled with a glacial lake (section 2.2.2).

The velocity of debris-covered glaciers may be influenced by unfavourable climatic conditions. On Tasman Glacier, New Zealand, Kirkbride (1995) noted a decrease in velocity with distance downglacier, with the highest velocities in the centre of the glacier where the ice was thickest, and velocities below measurable levels within the lowest 100 m. Velocities decreased over time, by 40-60% between 1957-1971 and 1971-1986. The decline in velocities was not related to a change in the terminus position, instead the area of debris cover increased (by 3.1 km^2 from 1890-1986), corresponding to an up-glacier migration of the debris cover by 4 km. Along the eastern lateral margin of the glacier, an area of thinner

ice was becoming detached from the main glacier, with the thicker, faster ice shearing past this slower shelf. Lower downglacier velocities were also found by Hubbard and Clemmens (2008) on the debris-covered Chacraraju Glacier, Peru, where velocities were less than 10 mm d^{-1} at the terminus compared to 100 mm d^{-1}, 1.7 km up-glacier.

Kellerer-Pirklbauer *et al.,* (2008) studied the influence of climate change on the Pasterze Glacier, Austria. The tongue of this glacier is clean along the left hand side, but has a covering of debris along the right hand side, allowing the comparison of the reaction of each side to the same changes. The glacier decreased in extent from 1964 to 2000, by 1.5 km^2, along with a corresponding loss in volume of 444 x 10^6 m^3 over the same period. However this ice loss did not occur equally over the glacier. Between 1981 and 2000, the surface lowering of the debris-covered part of the tongue decreased nearer the terminus, with the opposite trend identified on the clean part. Interestingly, the average lowering of the debris-covered area was greater than the clean ice lowering from 1964 to 1981. This was because although the debris-cover must decrease the ablation of the debris-covered area compared to bare ice, the emergence velocity (the "upward flow of ice relative to the glacier surface at a point fixed in space" (Paterson, 1994, p258, as cited in Kellerer-Pirklbauer *et al.,* 2008)) of the debris was measured to be 50-70% less than for clean ice between 1979 and 1986. From 1981 to 2000 however, the surface lowering of the debris-covered area was less than the clean ice, attributed to a reduction in emergence velocity for both parts. Although the thicker debris near the terminus counters the larger ablation at lower elevations, it had not yet reversed the ablation gradient. The effect of the debris is clear: the clean ice section terminus retreated 11 times more than the debris-covered one.

2.2 Supraglacial streams and lakes on debris-covered glaciers

This section focusses on the surface hydrology of debris-covered glaciers. The knowledge of the supraglacial stream network is limited, but those comments which have been found will be mentioned in the first section. This will be followed by an overview of the research on supraglacial lakes and ponds, which can be particularly prevalent on the lowermost regions of debris-covered glaciers.

2.2.1 Supraglacial streams on debris-covered glaciers

As far as the author is aware there is not a specific study of supraglacial streams on debris-covered glaciers, although they are mentioned occasionally in terms of part of the geomorphological characteristics of the glacier surface. Large supraglacial streams do exist on Khumbu Glacier, where they become englacial though the cut-and-closure mechanism

(Gulley *et al.,* 2009; see section 2.4). Iwata *et al.* (2000) and Watanabe *et al.* (1986) observed that on the middle part of Khumbu Glacier (around 3-5 km from the terminus) ablation is focussed around supraglacial streams and ice cliffs, with the ice cliffs eroded and shaped by the supraglacial streams. This results in the retreat of the ice cliffs, and a redistribution of the debris, which consequently gives rise to an irregular and uneven glacier surface. Watanabe *et al.* (1986) points out that the spatial differences in the ablation rate between the areas of supraglacial lakes and streams, and the debris-covered regions results in an increase in the height of surface undulations. Similar processes were found to occur on Baltoro Glacier, where although the along-glacier slope angle is only 3.9%, the roughness of the glacier surface is large perpendicular to the flow direction, with surface undulations of up to 25 m over a distance of 140 m being common. The cross section at Gore shows this clearly, with distinct valleys in the glacier surface associated with large supraglacial streams, although the combination of several tributary glaciers at this point also contributes to the uneven topography (Mayer *et al.,* 2006).

On the lowermost regions of debris-covered glaciers where the debris is usually thickest, supraglacial streams appear to be less common. Iwata *et al.* (2000) remarked that the streams seen on the middle part of Khumbu Glacier are hidden lower on the glacier, with the water only reappearing at the terminus. On Baltoro Glacier, Mayer *et al.* (2006) state that in the area of Urdukas (below the Gore cross-section) where almost the whole glacier surface is debris-covered, supraglacial streams, ponds and ice cliffs account for only a few per cent of the glacier surface area. When Hambrey *et al.* (2008) visited the Khumbu, Lhotse and Imja Glaciers they noted that few prominent supraglacial streams were seen, with the only one observed on Khumbu Glacier flowing within the trough of the lateral moraine, before following the terminal moraine to the valley floor. Hambrey *et al.* (2008) stated that supraglacial streams had a minor importance on these glaciers, but that there was still a significant network of englacial conduits. Kirkbride and Spedding (1996) implied the existence of englacial conduits beneath Tasman Glacier, through the identification of rounded, water-worked debris (abandoned conduit fills) on the glacier surface. This was despite the lack of supraglacial streams on the debris-covered lower 8 km of the glacier. Supraglacial streams on the upper and middle part of debris-covered glaciers can be large, and create uneven topography, but where the debris is thicker, supraglacial streams become scarce. Only Stokes *et al.* (2007) touched on the influence of the supraglacial hydrology on the rest of the glacier:

"In reducing melting during the ablation season, debris cover can reduce the infiltration of surface meltwater to the bed and thereby modify the subglacial hydrology and glacier flow" (Stokes *et al.,* 2007, p200), although they did not look into this further.

2.2.2 Glacial lakes and ponds on debris-covered glaciers

Glacial lakes are of particular interest on debris covered glaciers, where they exist both as transient features, and as expanding landforms that can be an important mechanism in the disintegration of glaciers, and a potential hazard if the dam enclosing them becomes unstable. This section deals with the threat of glacial lake outburst floods, the methods to locate potentially dangerous lakes, and the details of lake chemistry which causes lake growth. This growth may influence the ablation of the parent glacier, usually through the onset of calving, which could have consequences for how debris-covered glaciers recede. Miage Glacier also has an ice-marginal lake, details of which are given in section 1.4.

Debris-covered glaciers can be particularly susceptible to glacial lake outbursts because if a supraglacial lake forms it can be dammed by a potentially unstable ice-cored moraine. Kattelmann and Watanabe (1997) identified several potentially dangerous lakes in the Nepal Himalaya, with Tsho Rolpa and Imja Glacier Lake being highlighted. In 1997, Tsho Rolpa was 40 times larger than it was 20 years ago, whereas Imja Glacier Lake did not even exist in the mid-1960s but by 1992 it had grown to hold 28 x 10^6 m^3 of water. Kattelmann and Watanabe (1997) detailed the ways of reducing the possibility of floods from such lakes, although remedial action is not likely to be straightforward because artificial lowering of the lake level could cause the rest of the dam to fail. The growth and coalescence of lakes on debris-covered glaciers has also been observed by Ageta *et al.* (2000) on the glaciers in the Bhutan Himalayas where Rapsthreng Tsho has increased 0.5 km up-glacier between 1984 and 1998 and Lugge Tsho has grown 0.8 km between 1988 and 1993. Benn *et al.* (2000) studied the growth of a perched lake on the western side of Ngozumpa Glacier, Khumbu Nepal. The lake grew from three separate ponds in October 1998 to one large lake in October 1999, through a combination of water level rise and calving causing ice cliff retreat. Komori (2008) identified 50 ice contact lakes, of which 14 had increased in size in the Bhutan-China border region. The lakes formed grew in area and up-glacier extent faster on the southern range of the Himalayas (extending by 35-70 m a^{-1}, and <0.04 km^2 a^{-1}) than the northern range (extending by 10-40 m a^{-1} and <0.03 km^2 a^1). The slower lake growth on the northern range was likely due to lower glacier retreat and faster ice velocities compared to the southern range.

The existence of these lakes can be more dangerous if they form a sequence, for instance in the Lunana region, Bhutan Himalayas where three debris-covered glaciers form a sequence of termini, each with a lake. If the glacial lakes forming Thorthomi Tsho were to break through the moraine separating them from Raphsthreng Tsho down valley this

could cause an outburst from Raphsthreng Tsho (Ageta *et al.*, 2000). This risk is heightened by the risk of a rockfall event initiating the failure of one of the moraine dams. A rockfall was observed on Glacier Calafate, Chile in 2000, resulting in a flood that transported 2 x 10^6 m^3 of sediment (Harrison *et al.,* 2006). A rock avalanche also occurred onto Glacier Pucajirca in April 2002, causing 5 x 10^6 m^3 of sediment to be deposited into its proglacial lake, Laguna Safuna Alta, either from the rockfall or via associated erosion of the proximal face of the moraine dam. Significant erosion of the distal face also occurred, evidence that at least one displacement wave overtopped the dam. Although this event did not result in dam failure, it had been weakened and future failure due to gullying on the distal face was possible. Fortunately, a second lake down valley (Laguna Safuna Baja) had a capacity sufficient to capture any release from the upper lake, especially as it had a particularly wide (700m) and shallow moraine dam (Hubbard *et al.,* 2005). The difference between narrow end moraine dams which could be easily overtopped (Tsho Rolpa), and those which have thicker moraine dams and are less likely to fail (Thulagi Glacier lake, Central Nepal), is important in assessing the risk of lake outburst (Richardson and Reynolds, 2000).

To identify where new lakes may form in the future it is important to understand the factors which influence their occurrence. Reynolds (2000) found the glacier's surface gradient was a key factor. If the surface gradient was greater than 10°, no supraglacial lakes were found; if it was between 6 and 10° small, isolated and transient ponds may exist; if it was between 2 and 6° then ponds may form and cover a larger area, although they may still be ephemeral in nature; and if it was less than 2° the ponds may join to form a supraglacial lake. As well as the surface gradient Quincey *et al.* (2007) found that stagnant ice was necessary for lakes to form, and that the height of the drainage point was important. If a lake is growing on a glacier its level will be determined by the height at which the supraglacial and englacial drainage systems join. If the drainage point is relatively high then large scale ponding develops due to the low hydrostatic gradient, if the drainage point is low (for instance if the outlet channel is deeply incised) then the lake drains due to the high hydrostatic gradient. Whether or not the ponds that form grow appears to be due to their connection to the hydrological network (Röhl, 2008). This resulted in a classification of pond types based on their connection to the drainage network, along with whether currents or high flow velocities existed. An isolated pond only grew via calving if water temperatures and currents surpassed a specific threshold (around 1-2 °C and 0.1 m s^{-1} respectively) as this allowed deeper and progressive undercutting. This only occured if the pond grew large enough to join another pond or Tasman Lake (the proglacial lake of Tasman Glacier). Calving initiation is important as it accounts for much higher ice mass loss than the melting of subaerial and subaqueous ice. Therefore small ponds grow

horizontally through subaerial ice loss, which increases the area of bare ice available for melt. If they grow large enough to coalesce with another pond, ice loss increases as the main ablation mechanism switches from melting to calving, and they contribute to the disintegration of the glacier's terminus (Röhl, 2008).

One way to quantify the effect of ponds on ablation is to study their heat balance. Sakai *et al.* (2000) studied the heat balance of supraglacial ponds on the Lirung Glacier. Although the ponds absorbed a greater quantity of heat per meter (7 times the debris-covered area), the heat absorbed was only 3% of the total. Therefore, although ponds have a greater capacity to absorb heat their small size in comparison to the glacier area means their overall effect on ablation is lessened. Importantly, Sakai *et al.* (2000) discovered the lake outflow releases over half of the heat the ponds absorb, with the warm water expanding the associated englacial conduits.

Chikita *et al.* (1998) aimed to identify the mechanisms by which glacial lakes increase ablation on Tsho Rolpa Lake (a supraglacial lake on Trakarding Glacier). The lake contributed to ablation via ice melt at the bottom of the lake, and where the lake contacts the ice-cliff. The warmer surface water (>5°C) (present due to the low albedo of around 0.05, and strong density stratification of the upper layers (Chikita *et al.*, 2001)) was moved towards the glacier terminus via the strong valley wind, producing surface currents towards the ice cliff. Cold water from the ice cliff produced downward plunging counter-currents, completing the water circulation in the upper layer above the pycnocline. The continual transport of warm water to the terminus increased melting of the subaqueous cliff, encouraging calving of the associated aerial portion of the cliff face.

The importance of calving as a mechanism for lake growth was investigated by Richardson and Reynolds (2000), who found that the hummocky topography often found on debris-covered glaciers can lead to pond formation, which may be associated with regions of bare ice from crevasses. This bare ice can melt back to form an ice cliff, and if the ponded water melts a notch into the ice, the ice above can rotate and fail along the line of a relict crevasse. This process is exacerbated by further ponding above the same crevasse, which can drain through the crevasse, weakening the connection of the ice block and encouraging its collapse. The slope left after calving will likely be re-covered with debris if it is shallow enough, although backwasting of this slope and the opening of the next crevasse will result in the process being repeated: increasing the lake size and decreasing moraine stability.

The importance of crevasses to the calving rate of Tasman Lake, on Tasman Glacier was observed by Kirkbride and Warren (1999). The ice within 2 km of the terminus increased in velocity significantly compared to previous years, and this was associated with

increased crevassing linked to extending flow in the terminus area and the expansion of the proglacial lake. As the crevasses developed they increased the bare ice area available for melting, and became planes of weakness that encouraged calving. Glacier acceleration was therefore necessary before faster calving could commence, as without crevasses calving could only occur as fast as the thermo-erosional notch developed. At that time the glacier was still calving relatively slowly compared to the depth of the lake water (130 m), as deeper water is linked to faster calving. The lower 15 km of the glacier bed is grounded below the lake level, meaning a large portion of the glacier is susceptible to calving retreat. Faster calving due to the increased velocity and development of crevasses could mean the entire lower tongue is lost by 2008.

Supraglacial lakes therefore present a hazard to down-valley communities, and increase the ablation of debris-covered glaciers. Remote sensing has proved invaluable to find the factors governing their existence, as well as charting the growth in their number and size. Finding the mechanisms behind lake growth and drainage has required a detailed assessment of lake chemistry and morphology, highlighting the importance of calving as a mechanism for lake growth, and the link to the englacial network as a mechanism for drainage.

2.3 Modelling runoff from glaciers

Fundamentally, the discharge from a glacier is composed of melt from snow, ice, firn and liquid precipitation (Knight, 1999). The discharge will be slightly less than the sum of these components due to losses from evaporation, and it may be increased or decreased by the fluctuations in liquid water stored within the glacier (Jansson *et al.,* 2003). The proglacial hydrograph is the product of these components, but each has its own lag time based upon the distance the water has travelled from and the characteristics of the route it took (Richards *et al.,* 1996). Therefore, to model glacial runoff, knowledge is required of both the processes producing melt, and the meltwater routing (Baker *et al.,* 1982).

2.3.1 Techniques for modelling runoff from clean glaciers

Lang (1980, cited in Fountain and Tangborn, 1985) attempted to model glacier runoff using a multiple regression equation to calculate the discharge from Altschgletscher, Switzerland. Another option is to calculate the melt and use a reservoir model to account for the delays caused by meltwater routing. This method was adopted by Gottlieb (1980, cited in Fountain and Tangborn, 1985) who applied a degree day snow and glacier model (see Hock (1999), below) to Peyto Glacier, Canada. Lundquist (1982) used a degree day

method to model the melt from Nigardsbreen, Norway. A higher degree day factor was used for ice to account for its lower albedo, with the degree day factor varying seasonally using the application of a cosine function to replicate the fluctuation in net radiation receipt. Melt was routed via linear reservoirs for the upper and lower glacier.

A degree day melt model assumes daily melt is proportional to the sum of the positive air temperatures. The constant from which melt is calculated from temperature is the degree day factor, which varies depending upon the glacier surface covering, as well as diurnally and spatially. The classic degree day model is:

$$a = \begin{cases} \frac{1}{N} DDF_{snow/ice} T_a & : T_a > 0 \\ 0 & : T_a \leq 0 \end{cases}, \quad (2.7)$$

(Hock, 1999, p103). where a is the melt rate (mm h^{-1}), DDF is the degree day factor (mm d^{-1} $^{\circ}C^{-1}$), T_a is air temperature ($^{\circ}C$) and N is time steps per day. This is useful for calculating melt where the only available data is temperature, especially over longer periods when the DDF can be realistically assumed constant. However Hock (1999) found in comparison to measured discharge emanating from Storglaciären, Sweden (the melt translated into discharge using Baker *et al.* (1982)'s methods) the modelled diurnal discharge patterns were not satisfactorily accurate. A new model was conceived so the temporal and spatial variations in radiation receipt related to the glacier's topography could be accounted for. A digital elevation model (DEM) of the glacier was used to calculate the slope, aspect and topographic shading across the glacier. The potential direct clear-sky radiation reaching the glacier's surface can be calculated and inserted as a parameter into the model:

$$a = \begin{cases} \left(\frac{1}{n} DDF + RF_{snow/ice} I\right) T_a & : T_a > 0 \\ 0 & : T_a \leq 0 \end{cases}, \quad (2.8)$$

(Hock, 1999, p 103) where DDF is the melt factor (mm d^{-1} $^{\circ}C^{-1}$), $RF_{snow/ice}$ is a radiation coefficient for either snow or ice, and I is the potential clear-sky direct solar radiation at the glacier surface (W m^{-2}). This new model reproduced the diurnal discharge fluctuations much more accurately, even though the necessary meteorological data was only air temperature. A similar melt model was used to model runoff from the Tuotuo River basin, western China by Zhang *et al.* (2008).

However, Pellicciotti *et al.* (2005) criticised this model because of its simple estimation of albedo fluctuations (represented by the different *RF* values for snow and ice), and because both $RF_{snow/ice}$ and I were influenced by temperature when in reality they are

independent of it. Pellicciotti *et al.* (2005) compared several versions of degree day model with the melt calculated for Haut Glacier d'Arolla, Switzerland using the energy balance model developed by Brock and Arnold (2000). The model which reproduced melt most accurately required incoming and outgoing shortwave radiation, estimated snow albedo using an equation developed by Brock *et al.* (2000) which calculates albedo from air temperature and the timing of snowfall, and allowed only the temperature factor to be influenced by air temperature:

$$\boldsymbol{a} = \begin{cases} \boldsymbol{TFT_a + SRF(1-\alpha)\downarrow S : T_a > 1} \\ \boldsymbol{0} \qquad\qquad\qquad\qquad \boldsymbol{: T_a \leq 1}, \end{cases} \tag{2.9}$$

(Pellicciotti *et al.*, 2005, p 577) where TF is the temperature factor (mm h^{-1} °C^{-1}), SRF is the shortwave radiation factor (m^2 mm W^{-1} h^{-1}), $\downarrow S$ is incoming shortwave radiation (W m^{-2}) and α is albedo. Hock (1999)'s original model (2.13) gave r^2 = 0.769, whereas with Pellicciotti *et al.* (2005)'s model r^2 = 0.911 for the central weather station. By including the albedo parameterisation, the influences of snow metamorphism and the change from snow to ice was represented (during the transition from snow to ice model 2.8 did not match the reference melt rate but model 2.9 followed it fairly closely). Additionally, by allowing temperature to influence only the temperature-dependant sources of energy, the model was less sensitive to temperature fluctuations.

Instead of using a degree day model to estimate melt Baker *et al.* (1982) used a surface energy balance model (section 2.1.2) to calculate melt for an input to a linear reservoir model to calculate the runoff from Vernagtferner in the Oetzel Alps, Austria. Baker *et al.* (1982) routed the meltwater through one of three linear reservoirs depending upon whether melt was produced from ice, firn or snow, and added a constant value of 0.1 m^3 s^{-1} for groundwater. The reservoir represents the storage of water as a tank with a specifically sized "hole" in the bottom. The discharge (Q_t) from the tank at a specific time (t_t) is proportional to the volume of water within it (V_t):

$$\boldsymbol{V_t(t_t) = k_t Q_t(t_t)}, \tag{2.10}$$

(Baker *et al.,* 1982, p 106) where k_t is a constant related to the size of the "hole" in the tank. When water inflows into the tank the change of discharge over time is given by:

$$\boldsymbol{k_t \frac{dQ_t}{dt_t} = R_t - Q_t}, \tag{2.11}$$

(Baker *et al.,* 1982, p 106) which solves to give:

$$\boldsymbol{Q_t(t_t) = \int_0^t \frac{R_t(\tau)}{k_t} e^{(\tau - t_t)/k_t} d\tau + Q_t(0) e^{-t_t/k_t}}, \quad (2.12)$$

(Baker *et al.,* 1982, p 107) where $R_t(\tau)$ is the rate of water input. This allows the discharge at a specified time to be calculated if the inflow, storage constant and discharge are known at time 0. If the inflow and discharge are constant then k_t represents the time taken for water to leave the tank, so can be calculated from knowledge of the lag time between melt produced and reaching the gauging station (Baker *et al.,* 1982). The storage constant can be determined from semi-logarithmic plots of river discharge as when the river is in recession flow and follows the pattern of a depleting linear reservoir, the discharge plots as a straight line. Any break of slope indicates the flow is from a store with a different storage constant, although to calculate a specific reservoir's storage constant it must be separated from the others, by extrapolating the slowest recession flow back in time (Hannah and Gurnell, 2001). All the reservoir models mentioned are based on the same principles.

Hannah and Gurnell (2001) used the changes in the storage constants of linear reservoirs to elucidate the character of the hydrological system of the Taillon Glacier in the French Pyrénées. The melt was routed through two reservoirs, one representing inputs above the snowline (slow reservoir) and another for inputs below the snowline (fast reservoir). At the beginning of the season the majority of melt was routed through the slow reservoir, but as the season continued, more was routed through the fast reservoir and its associated storage constant decreased - creating increasingly peaked modelled hydrographs. Later in the season the storage constant of the slow reservoir decreased, until the storage constants for both reservoirs converged signifying the inputs were routed via one reservoir. This occurred because the snowpack decreased in area and storage capacity, and melt from the snowpack joined ice melt as it was routed through the glacier. Comparisons of their storage constants with those of larger glaciers revealed theirs were generally larger, indicating the hydrological system does not become as efficient (the lower glacier having a semi-distributed rather than a completely channelised network) because the smaller meltwater inputs are not sufficient to fully develop the network. This could have consequences for debris-covered glaciers, as smaller meltwater inputs could result if a thick debris cover decreases ablation.

Richards *et al.* (1996) used the distributed surface energy balance model developed by Arnold *et al.* (1996) to calculate the melt of Haut Glacier d'Arolla, Switzerland. When the basin geometry was known the melt of the catchment of a particular moulin or crevasse

could be calculated. This was routed via the US EPA sewer-flow hydraulic routing model - which routes the inputs into the moulins (drains) through the conduit (sewer) system, and allows the cross-sectional size, shape and roughness of the conduits to be varied. Richards *et al.* (1996) analysed the results of alternating the conduit characteristics within observed limits to discover which dimensions resulted in the closest match with observed discharge. They also simulated a distributed system by describing the conduit as very shallow, wide and rough, which was used when water was forced into the distributed system from the main conduits during high water pressures.

Arnold *et al.* (1998) improved this model by introducing a surface routing submodel and adjusting the subglacial submodel so the conduit system changed over the melt season. The surface routing model produced the hydrograph that inputs to a specific moulin or crevasse from the melt calculated by the surface energy balance model. It was constructed using the DEM to determine the position and length of the path taken by melt, assuming it flows following the steepest slope. The time taken for the water to pass through a cell was determined by the surface cover. If the cell was snow covered then the percolation time for the water to transfer vertically down through the snowpack, and the velocity of the water as it travels horizontally at the base of the snowpack was calculated from equations developed by Colbeck (1978):

$$\boldsymbol{t_v} = \frac{\boldsymbol{\kappa_{es} h_s}}{\left(\frac{(3\rho_w g)}{\mu_m}\right)^{\frac{1}{3}} \boldsymbol{p_s^{\frac{1}{3}} Q_i^{\frac{2}{3}}}}, \tag{2.13}$$

$$\boldsymbol{u_s} = \frac{\left(\frac{\rho_w g}{\mu_w}\right) \boldsymbol{p_s \theta_s}}{\boldsymbol{\kappa_s}}, \tag{2.14}$$

(Arnold *et al.*, 1998, p 194) where t_v is the vertical travel time (s), κ_{es} is the snowpack effective porosity, h_s is snowpack depth (m), ρ_w is water density (kg m^{-3}), g is gravitational acceleration (m s^{-1}), μ_w is water viscosity (Pa s), p_s is snow permeability (m^2), Q_i is the input melt from the surface energy balance model plus precipitation (m^3 s^{-1}), u_s is water velocity under snowpack (m s^{-1}), Θ_s is surface slope and κ_s is snow porosity. If the cell had an ice surface then the water was routed using Manning's equation:

$$\boldsymbol{u_i} = \frac{\boldsymbol{r^{\frac{2}{3}} \theta_s^{\frac{1}{3}}}}{\boldsymbol{n}}, \tag{2.15}$$

(Arnold *et al.*, 1998, p 194) where u_i is the water velocity over ice (m s^{-1}), r is the hydraulic radius of the supraglacial channel (m) and n is Manning's roughness coefficient ($m^{-1/3}$ s). These equations allow individual cell travel times to be summed to give the total time for melt to reach the moulin and produce a moulin hydrograph related to the catchment shape and surface cover. Arnold *et al.* (1998) improved the subglacial model by changing the conduit dimensions and roughness so the distributed configuration (represented by either eight small, rough conduits or a wide, shallow, rough one) is switched to a channelized system (of a singular circular conduit) as the snowline retreats. The conduit sizes were adjusted hourly based on the water pressure and velocity data produced by the sewer-flow routing model. This was based on the enlargement of conduits due to frictional heat, or the closure of them due to ice deformation (Röthlisberger (1972) in section 2.6).

Willis *et al.* (2002) worked on the supraglacial melt and routing model to analyse the changes caused by the removal of snow from a moulin catchment. They did multiple model runs with different albedos for snow and ice and changed the routing model so the meltwater input was no-longer routed through snow. In terms of the energy balance and melt rates, the loss of a snow cover increased ablation (from 31 mm day^{-1} to 45 mm day^{-1}), but the energy balance partitioning between the radiation and turbulent fluxes remained similar whether the surface was snow covered or not, although the change in weather conditions as the snowcover was removed could have hidden the albedo influence. The increase in melt rate with snowpack removal, coupled with a faster routing process, increased peak discharge into the moulin (which could initiate the switch between a distributed and channelised system (section 2.4)), and decreased minimum discharges (encouraging the drainage of water from marginal areas into the main channel network, increasing the efficiency of the drainage system in the channel margins). This identifies the importance of the moulin catchment hydrograph in influencing the englacial and subglacial drainage configuration, and highlights how both the melt rate and routing procedures are significant. This could have implications for debris-covered glaciers because of the smaller melt rates under debris, and the possible influence of the delaying effect of the debris on surface water flow. If this has significance similar to the snowpack on clean glaciers, it could change how the englacial and subglacial systems develop.

Flowers and Clarke (2002a) produced a glacier hydrology model which concentrated on the englacial, subglacial and groundwater system. Their theoretical model was composed of several layers: a degree day melt model; coupled to an englacial system composed of moulins, surface crevasses and basal crevasses which vary in density and volume; coupled to a subglacial system envisaged as a saturated layer of sediment beneath

the glacier which varies in porosity as the water flux varies; and a subglacial aquifer capped by an aquitard of till. The model was constructed within a grid so point values such bed elevation and fluid potential were calculated for the centres of the cells (nodes), whereas vector data on fluxes and the hydraulic conductivity was calculated between cells. Flowers and Clarke (2002a) also replicated the existence of a variable pressure axis (VPA) (Mair *et al.,* (2008), section 2.6) coinciding with the greatest fluctuations in pressure, with the pressure variations decreasing in magnitude with distance from the VPA. Flowers and Clarke (2002b) applied this model to Trapridge glacier, Yukon, Canada. In the spring, the existence of a saturated snowpack meant disproportionately more water was released compared to energy received – giving spring flood conditions. This coincided with high pressures subglacially as the glacier's bed flooded, with the pressure wave moving up-glacier over a period of 6 days, before water pressures subsequently decreased.

Flowers (2008) concentrated on the subglacial drainage and groundwater aquifer model components - based on the equations by Flowers and Clarke (2002a). The subglacial hydrology was conceived as either a distributed system consisting of a macroporous sheet, in which the hydraulic conductivity is influenced by the water-sheet thickness, or as a channelised system of parallel semi-circular conduits. Hard beds were associated with high amplitude diurnal variations and a short lag time, whereas soft beds had a lower diurnal amplitude and a longer lag time. Additionally, the glacier thickness was significant, with thicker glaciers favouring closure of conduits, but having higher water pressures favouring conduit growth - conduits are best developed under medium thickness glaciers. This could have implications for retreating debris-covered glaciers, as although thinner glaciers are less likely to develop a conduit system, if one is in place there is more chance it will be preserved. Flowers (2008) identified that the configuration of the subglacial system can have a large impact on the proglacial hydrograph, and factors such as the glacier's bed type, length, bed slope and thickness could influence the subglacial drainage network.

Contrary to Flowers' (2008) work, Covington *et al.,* (2012) isolated the influence of the subglacial drainage structure on the proglacial hydrograph, and found that in many cases the conduit geometry had little influence on the proglacial hydrograph – the recharge (input) hydrograph was more important. When a peaked (icemelt) hydrograph and a more gentle (snowmelt) hydrograph were input into either a conduit or distributed network, the resulting output hydrographs were almost identical. They tested different types of glacial drainage elements (conduits, crevasses and lakes) to clarify how they effected the output hydrograph – both conduits and crevasses were mainly recharge dominated (they did not alter the input hydrograph), with lakes mainly geometry dominated (they did influence the input hydrograph), with the reservoir size and constriction diameter being key parameters.

Although the proglacial hydrograph was usually recharge dominated, a complex system with multiple recharge points (each with its own lag time between the recharge point and hydrograph response), could create hydrographs with multiple or smeared peaks. Covington *et al.,* (2012) only tested one type of distributed system, and mentioned that its influence may be different if coupled to a conduit network (as in Flowers, 2008).

Modelling the runoff from glaciers can be achieved through degree day melt models of varying complexity, with routing through a reservoir system representing routing through slow (snow and firn associated with a distributed system in upglacier areas) and fast (over ice and through a channelised system lower on the glacier) reservoirs. More complex routing models have been developed to imitate the influence of the glacier's surface conditions, the changing nature of englacial conduits, and the configuration of the subglacial hydrology. The impact of debris is usually only mentioned in reference to its effect on ablation – its role in influencing routing is not discussed.

2.3.2 Runoff models for debris-covered glaciers

As the existence of a debris cover on a glacier influences melt (see section 2.1), it should be taken into account when producing a runoff model. Some models only do this by calibration with measure discharge. To model the proportions of different components of streamflow for the Gangotri Glacier basin in the Himalayas, Singh *et al.* (2008) used a degree day model to calculate the snow and glacier melt used as an input for SNOWMOD. All runoff from the glacier was routed through one reservoir, with non-glacial runoff being routed through two reservoirs. Despite the ablation area of the Gangotri glacier being debris covered (Singh *et al.,* 2006b) this was not mentioned, therefore model calibration allowed the adjustment of the degree day factor to account for the debris influence. This method was used by Singh *et al.* (2006a) on the debris-covered Dokriani Glacier in the Garhwal region of the Himalayas**.** A temperature increase of 2°C increased summer runoff by 28%, while varying the precipitation amounts between –10% and +10% resulted in a 7% runoff change. Caiping and Yangjian (2009) used the technique of artificial neural networks (ANNs) to model runoff on the debris-covered Keqikaer Glacier. The model is composed of three layers of nodes (an input layer with 8 inputs, a hidden layer with 13 nodes and an output layer giving the proglacial hydrograph) connected with links. The model was run forwards to produce runoff and then "backwards" so the strength of the links between different nodes could be changed to increase the model's accuracy.

Some workers take account of debris by adjusting an algorithm in their model. Tangborn and Rana (2000) used a precipitation-temperature-area-altitude (PTAA) model

on the Langtang Glacier, Nepal, which consisted of a suite of algorithms found through the regression of several mass balance variables. To account for the debris they added a factor representing the fraction of an elevation zone that was debris-covered, to one of the ablation algorithms. Braun *et al.* (1993) modified a conceptual precipitation-runoff model to allow for the 7% of the Langtang Khola basin, Nepal Himalaya containing a debris-covered glacier. They introduced a constant representing the contribution from geothermal melt and englacially stored water, along with a reduction factor to decrease the ice melt where debris occured. Adjusting this factor showed that when it equalled 0 the discharge was lower than modelled by 170 mm, although when melt was assumed equal to clean ice, discharge was 70 mm above that measured. A reservoir approach using a different parameter for water released from fast, intermediate or slow stores produced the runoff hydrograph. Zhang *et al.* (2007) used a different degree day factor in their degree day model which included direct clear sky solar radiation, depending upon whether the surface of Keqicar Baqi glacier, China consisted of ice, debris-covered ice or snow. The meltwater was routed depending upon its source so melt above the equilibrium line contributed to the firn reservoir; melt from clean and debris-covered ice contributed to the ice reservoir and snow out with the firn area contributed to the snow reservoir.

Some studies are based on knowledge of the characteristics of the debris cover. Rana *et al.* (1996) modelled runoff from Lirung Khola watershed (containing the debris-covered Lirung Glacier) by combining the HYCYMODEL precipitation-runoff model with Nakawo and Takahashi (1982)'s melt model (section 2.1.2). They estimated the debris thermal resistance by using literature values of the thermal conductivity (2 W m^{-1} °C^{-1}), and a uniform 0.5 m or 1 m debris thickness. The critical thickness was calculated using literature values of albedo, so the only measured data was temperature and global radiation. This is helpful where data is scarce, but the model had to be run with variations of debris thickness and albedo, with the results compared to measured discharge. The model indicated the debris was between 0.5 and 1 m thick, and that the debris thickness had a greater effect than albedo, with modelled results up to ±17% of measured discharge. Rana *et al.* (1997) applied the same HYCYMODEL, but used a Landsat 5 (Band 6) image to find the debris temperature, to give an average thermal resistance of the debris (using Nakawo and Young (1982)'s methods) of 0.14 m^2 °C W^{-1}. This allowed the sub-debris ablation to be calculated using surface temperature and meteorological data. Sub-debris melt was added to clean ice melt, snow melt and rainfall, and was routed via storage reservoirs to give total runoff. Simulated runoff matched measured best when sub-debris ablation was calculated (compared to the debris-free or no sub-debris melt scenarios), although modelled runoff could be up to 30% larger than measured.

Although not modelling runoff, Mattson (2000) studied the runoff of the debris-covered Dome Glacier in the Columbia Icefield, and compared it to the nearby clean Athabasca Glacier in the ablation seasons of 1994 (relatively dry and warm) and 1995 (cool and wet). The difference in runoff between the two years was much greater on the Athabasca Glacier (giving a total 1994 runoff volume of 16.74 x 10^6 m^3, but 12.55 x 10^6 m^3 in 1995) compared to the Dome Glacier (giving a total 1994 runoff of 9.45 x 10^6 m^3, and 9.48 x 10^6 m^3 in 1995). A warmer ablation season results in more melt on a clean glacier, but Mattson (2000) proposed the dry conditions of the debris cover (which would lower its thermal conductivity) on the Dome Glacier in 1994, meant the energy absorbed by the debris was used to increase the debris temperature, rather than melt the ice, with the debris loosing this heat to the air through the transfer of sensible heat and longwave radiation. Conversely, in 1995, the higher moisture content of the debris increased its thermal conductivity, so although cooler temperatures meant less energy was available, more of it was conducted to the ice. Therefore the debris cover regulated the runoff, reducing the variance between years. The runoff was compared from mid-July to the beginning of August – no study has looked at the influence of the debris cover on runoff patterns in the early ablation season.

2.4 Theory, dye tracing and direct investigations of the hydrological network

Shreve (1972) considered the channel characteristics to be determined by: the capacity of the system (which is adjustable, with a lag, to the inputs of water); the combination of ice pressure and rate of passage melting; and because large channels grow at the expense of small ones (there is more energy per unit area of wall available to melt the channel sides in a large channel than in a smaller one) – forming an arborescent network. The movement of water is determined by the differences in hydraulic potential, with the water moving "from regions of high hydraulic potential to regions of low hydraulic potential, following the steepest hydraulic gradient" (Benn and Evans, 1998, p 100). The hydraulic gradient is dependent upon the ice pressure, the gravitational potential caused by elevation, and the contraction and expansion of the passage (section 2.6, Röthlisberger (1972)). This means the englacial system would be in the form of a branching network, with the smallest passages near the surface, the orientation of which is perpendicular to lines of equal hydraulic potential (equipotentials), and with subglacial channels following the direction of ice flow.

Shreve (1972)'s work was mainly theoretical, with few observations supporting his conclusions. Stenborg (1969) used mapping of the supraglacial stream network and the strike of crevasses, along with dye tracing of the englacial and subglacial network, to elucidate the structure of the drainage system of Mikkaglaciären and Storglaciären, northern Sweden. Stenborg (1969) used sodium chloride solution as a tracer, injecting it into a moulin or crevasse on the glacier's surface and detecting the passage of the salt wave in the proglacial stream. The tracer travel time was not solely related to the distance between the injection and detection point. Mapping revealed the strike directions of crevasses to occur in a different direction depending upon whether they occurred on the east or west of the glacier. The strike direction of the crevasses along with the surface slope delimited the surface catchments, leading into two systems of englacial drainage.

Willis *et al.* (1990) conducted dye tracer tests using Rhodamine B on Midtdalsbreen, Norway. Their analysis of the tracer curves, and comparison of the measured velocities with those modelled for different channel types meant they could infer the drainage system type beneath the glacier. They calculated through-flow velocities (the distance from the injection to detection site divided by the time taken for the dye to reach a peak concentration) – finding them to be higher (0.086 to 0.228 m s^{-1} – signifying flow through larger conduits) on the eastern half of the glacier, compared to the western half (with velocities of 0.01 to 0.07 m s^{-1} – signifying flow in a distributed system). The shape of the return curves was revealing, with faster through-flow velocities associated with short asymmetrical peaks – showing a particularly steep rise, but more gradual fall. Slower velocities gave broader curves, often with multiple peaks. The percentage of dye recovered was higher (49.8 ± 31.3%) from the east of the glacier, compared to the west (29.9 ± 18.2%). The low rates of tracer recovery point to some dye being stored within the system, accounting for the multiple peaks as dye is released from storage. Willis *et al.* (1990) calculated the relationship between discharge and velocity, as how velocity varies with discharge is affected by the channel geometry, to give power functions for the eastern and western half of the glacier. The exponent (m in equation 2.18) of 1.0 from the eastern half reveals an increase in discharge results in the hydraulic gradient increasing, or the sinuosity of the channel decreasing (suggesting the channel is full, giving closed channel flow conditions (Nienow *et al.,* 1996)), the 0.6 exponent from the western half means an increase in discharge will result in an increase in channel cross sectional area along with a higher velocity (suggesting the channel is not full, giving open channel conditions (Nienow *et al.,* 1996)). Furthermore, the dispersion coefficient (D) of the tracer can be determined (as this

is "a measure of the rate at which the dye-concentration peak broadens relative to the rate at which it is transferred through the glacier" (Willis *et al.*, 1990, p93)) using:

$$\boldsymbol{D = \frac{d_d^2(t_m - t_i)^2}{4t_m^2 t_i \ln\left[2\left(\frac{t_m}{t_i}\right)^{\frac{1}{2}}\right]}}, \quad (2.16)$$

(Willis *et al.*, 1990, p93) where d_d is the travel distance, t_m is the time to the dye peak, t_i equals the time at which the dye concentration is half of the peak, either on the rising or falling limb of the dye return curve. The equation is solved iteratively for t_m, allowing D to be found. As the dispersion of the tracer is proportional to its velocity (u_d), the constant of this proportionality (or the dispersivity (b)) can be calculated:

$$\boldsymbol{D = bu_d}, \quad (2.17)$$

(Willis *et al.*, 1990, p96). If the channel system has interlinking passages then the dispersivity is a measure of the length of the passages, so a large dispersivity points to a more distributed network. Therefore, the decrease in dispersivity (from 71.1 to 13.1 m from the 13th to the 23rd of July) from one site on the eastern glacier shows the channel network became less distributed with time. Willis *et al.* (1990) compared their measured through-flow velocities with those calculated from equations developed for channels with a specific geometry. The velocities calculated for both a straight and sinuous semi-circular R-channel (which flows on top of the bedrock, but incises into the ice above) were higher than measured, with the velocities modelled for flow in a permeable sediment layer being too low. The possibility of a linked cavity system (a network of cavities joined by thin orifices, which occurs between the ice and bed) was investigated by using the measured velocities to determine the appropriate size of cavity, but the values returned were too large. Therefore, the observed velocities represented a network of both a linked cavity and discrete channel system.

However, some of the conclusions made by Willis *et al.* (1990) were challenged by Nienow *et al.* (1996) – specifically the power functions used to infer the channel conditions. These functions are built upon the relationships between velocity and discharge (Q), with m relating to the conditions in the channel, and k_c being a constant:

$$\boldsymbol{u_d = k_c Q^m}, \quad (2.18)$$

(Nienow *et al.*, 1996, p 1413). When the channel is full, discharge can only increase via an increase in velocity (assuming no change in channel dimensions), so velocity and discharge are directly related and $m = 1$. Under open channel conditions, the channel cross-sectional area can increase as well as the velocity, so that $m < 1$. The inferences made about the channels studied by Willis *et al.* (1990) are given above. These power functions do not account for the full complexity of the relationship between velocity and discharge. The variation in the relationship (which can be cyclic when plotted over time) is known as velocity-discharge hysteresis, which can mean inferences made about the channel environment from the m value are incorrect. To test the causes of hysteresis, Nienow *et al.* (1996) conducted dye tracing experiments, using Rhodamine-B dye on Haut Glacier d'Arolla, Switzerland. Those traces showing a clockwise velocity-discharge hysteresis were caused by the water flowing through a tributary channel before it reached the main channel. The dye velocity is therefore a product of the tributary and main channel velocity-discharge relationship; whereas often the relationship is constructed using the main channel discharge. The hysteresis is more pronounced the further the dye has travelled in a tributary channel. Furthermore, if the discharge of the tributary and main stream vary out of phase (one rises while the other falls) this causes clockwise hysteresis. The flow conditions could be determined if the tributary channel was short and the input discharge of the tributary channel varied in phase with the main channel discharge. Anti-clockwise hysteresis could be caused if water inputs into the moulin exceed its capacity – causing its water level to rise. This would result in a lower velocity, even if the discharge into the moulin was rising. As the input discharge decreased, the moulin could drain and the velocities would increase. This was confirmed by particularly high dispersivities in the morning and early afternoon when supraglacial discharge was rising, which were subsequently lowered in the evening. As channel geometry changes are unlikely to have caused this, the storage of water in the moulin probably caused the high dispersivities.

The influences on discharge-velocity hysteresis were investigated by Schuler and Fischer (2009), as they modelled the tracer transit velocity. They conducted repeated tracer injections every two hours over two days on Unteraargletscher, Switzerland – revealing systematic cyclic hysteresis within the relationship between discharge and velocity. They speculated that changes in the channel geometry could account for some hysteresis, but difficulties in the modelling of the channel (using the hydraulics of an R-channel) meant modelled velocities were higher than observed. They also accounted for the inflow modulation produced by the water entering a moulin before it entered the main stream. The overall velocity of dye passing through a moulin is a product of the inflow discharge

and the subglacial water pressure, the combination of which results in the water level in the moulin (its hydraulic head), and results in the overall discharge from the moulin. The outgoing discharge is used to model the tracer residence time by dividing it by the moulin's water volume. The effect of the moulin was greatest if it had a large cross-sectional area, as this resulted in a large moulin volume, decreasing the transit velocity (with the velocity varying out of phase with discharge and the moulin's water level). Although they could model the effect of inflow modulation, further measurements of the discharge-velocity relationship without the effect of the moulin would be needed (by tracing into a borehole directly into a subglacial channel), so the parameters explaining the channel roughness and sinuosity could be better defined. On Unteraargletscher, Schuler and Fischer (2009) identified one minimum and one maximum transit speed per day, however Werder *et al.* (2010) found on Gornergletsher there were two maxima and minima transit velocities each day. This was because when discharge in the channel was high, water pressures were high, increasing the fill level in the moulin, slowing dye transit through the moulin, and slowing the overall trace. Conversely, when channel discharge was low, the water level in the moulin was low and although the time water spent in the moulin was decreased, the trace was still slow. As the influence of the moulin and channel were equally important, and acted inversely to each other, maximum trace velocities occurred when the flow was moderate in the moulin and channel.

Nienow *et al.* (1998) conducted 415 dye traces into Haut Glacier d'Arolla, Switzerland during the ablation seasons of 1990 and 1991. They inserted dye into moulins or crevasses over a large area of the glacier's surface, and conducted repeat experiments from the same moulins to detect seasonal changes. For a specific injection site, the dye return curve evolved as the season progressed, with the curve becoming more peaked and less dispersed. The return time decreased and transit velocity increased over the season. They also calculated the channel average cross-sectional area, by dividing the discharge by the trace velocity. The difficulties in using this approach (due to averaging the velocity over a straight line) were acknowledged, but a relative decrease in channel area as the season progressed was identified. Therefore, they believed the drainage network had evolved from a distributed, multi-channel system, to a more efficient channelised system over the season. This switch occurred progressively farther up-glacier as the summer continued, signifying a gradual increase in the area in which flow occurred in the channelised system. Nienow *et al.* (1998) modelled the position of the channel head separating the distributed and channelised system and plotted its movement up-glacier - revealing the correlation between the channel head position and the summer snowline. This implied that it was the removal of the snowpack that resulted in the change in the channel network. This is because the

higher albedo of snow and its ability to slow the transfer of meltwater (see Campbell *et al.* (2006)) means when it is removed, the melt from ice produces a supraglacial inflow hydrograph with a much greater magnitude and amplitude than that from snowmelt (confirmed by modelling work by Willis *et al.* (2002), section 2.3.1). This causes an increase in water pressure in the distributed system, which causes the switch to a channelised network (section 2.6).

The effect of the snowpack on the meltwater delivery was investigated by Campbell *et al.* (2006). They sprayed dye onto the snow surface and allowed it to percolate through the snow and along the saturated layer above the ice. A snow pit was dug down-glacier and a fluorometer used to detect the dye emergence. They also injected the dye directly to the saturated zone via a borehole, so the influence of the flow at the ice-snow interface could be isolated. Ice layers in the early melt season prevented the percolation of water through the snow, but the effect of these diminished as the season progressed. Differences in the snow layers influenced the water flow through the snowpack and over time preferential flow paths developed which resulted in an increasing efficiency of meltwater transfer. The water velocity through the snowpack controls the hydrograph entering the englacial system, and influences the subglacial water pressures and consequent structure of the drainage network. If the debris layer has a similar effect on ablation and water flow to that of the snowpack (decreasing albedo and delaying the transfer of meltwater) it may also influence the development of the hydrological network.

Hasnain *et al.* (2001) used dye tracing to understand the drainage network beneath Dokriani Glacier, Nepal Himalayas. They investigated the switch of the drainage system from a channelised system to a distributed system, corresponding to a decrease in trace velocities from July to September. Interestingly, the Dokriani Glacier is debris-covered (Hasnain and Thayyen, 1999b), but in this study the form of the hydrological network was only studied later in the season, there does not appear to be a study on the spring evolution of the channel network on a debris-covered glacier.

Willis *et al.* (2009) combined dye tracing with the production of maps of the glacier's likely drainage network on the Brewster Glacier, New Zealand. A differential global positioning system (GPS) survey mapped the surface topography, and a ground penetrating radar (GPR) survey mapped the bed topography, with ArcGIS used to produce a digital elevation model (DEM) of the glacier's surface and bed, to create a map of the drainage system. Dye traces conducted into points close to the predicted main subglacial drainage routes travelled quickly to the snout, whereas input points farther from the subglacial drainage travelled more slowly. Their dye tracing showed four different types of drainage morphology, based on the velocities and dispersivities of each trace. Notably, the

velocities measured on Brewster Glacier (where the energy for melt is predominantly from turbulent fluxes) were less than on glaciers where radiative fluxes provide the most melt energy (for example Haut Glacier d'Arolla). The greater diurnal fluxes in meltwater delivery associated with glaciers whose melt is from radiative fluxes could result in a more efficient drainage network. The conductive heat flux resulting in melt on debris-covered glaciers could influence the efficiency of channels if it decreases the amplitude of diurnal melt inputs.

The dye tracing conducted on Midtalsbreen (see Willis *et al.,* 1990) was also used to understand the likely steady state water pressure at the ice/bed interface. Willis *et al.* (2012) modelled the form of the subglacial hydrological drainage system but varied the spatially uniform flotation fraction (water pressure over ice pressure). By comparing the resulting subglacial drainage network to that found by dye tracing, they deduced the long term average steady state pressure was about 70% of ice overburden pressure. Willis *et al.* (2012) compared the annual input fluxes calculated for each part of the subglacial network with measured trace velocities, and found areas with a lower input flux had slower transit speeds and vice versa. As the discharge decreases along the subglacial flowpath (and away from the axis of preferential drainage), channels became broader and lower, to the point they could be considered a distributed network, whereas closer to the main drainage axis, channels were narrow and high and therefore efficient. This has implications for areas under a thick debris cover, as it would reduce the input flux for a given part of the subglacial network.

Direct exploration of englacial conduits has been attempted by a number of workers (namely G. Vatne, J. Gulley and D. I. Benn) on glaciers where there is a well-developed conduit system that can be explored when water inputs are low. Their explorations revealed that supraglacial streams can become englacial by dropping into vertical moulins (for instance on Austre Brøggerbreen (Vatne, 2001)), and when supraglacial streams are captured by crevasses, as seen on Matanuska Glacier, Alaska (Gulley, 2009). An alternative process of englacial conduit formation is through the 'cut and closure' mechanism, which occurs when supraglacial streams incise into the ice at a rate greater than ablation. This process requires crevasse free glaciers with low ablation rates, and large supraglacial streams, and was observed on Khumbu Glacier (where the lower ablation rates are caused by the thick debris cover) and on Longyearbreen (where the cool climatic conditions reduce ablation). On Khumbu glacier, conduit closure was aided by the collapse of the overhanging banks of the supraglacial stream, formed as it meandered and migrated laterally. Once collapsed, more debris would be added from nearby slopes, decreasing ablation and encouraging a band of ice-cemented debris to form the roof of the now englacial conduit. This band of debris was observed in the roofs of both conduits

surveyed. On Longyearbreen closure involved snow bridging the roof of the supraglacial channel (Gulley *et al.,* 2009). On some glaciers (for instance the debris-covered Ngozumpa, Ama Dablam and Lhotse Glaciers, in the Khumbu Himal, Nepal) the 'cut and closure' mechanism was not observed but instead the formation of conduits originated from supraglacial ponds and tended to be related to crevasse traces (seen along conduit roofs). The supraglacial ponds formed the conduits by providing the high hydraulic gradient necessary, and they caused their evolution – with changes in lake level re-grading the conduit system, with associated incision creating steep-walled canyon type channels (Gulley and Benn, 2007).

The mechanism of conduit formation via hydrologically driven crevasse propagation (or hydrofracturing) (found on Hansbreen in Svalbard, Khumbu Glacier in Nepal and Matanuska Glacier, Alaska (Benn *et al.*, 2009)) seems to be key in the initiation of conduits either from water filled crevasses or supraglacial lakes. Where crevasses are involved it is the water pressure acting on the tip of the crevasse that allows it to reach greater depths, this was evident on Hansbreen, where one shaft penetrated much deeper than nearby dry crevasses (Benn *et al.*, 2009). This point was explored by Weertman (1973) who discovered that an isolated water-filled crevasse could theoretically penetrate to the base of a glacier (much deeper than a dry crevasse within a crevasse field), although at depth the upper part of the crevasse could be pinched shut by creep closure, forming a water-filled hollow. The importance of hydrofracturing is likely why crevasse traces tend to be found along conduit roofs (Gulley and Benn, 2007), and disproves the original hypothesis by Shreve (1972) that englacial conduits would form a branching network of passages aligned perpendicular to the equipotential surface. Shreve (1972) neglected to include fractures as weaknesses in the ice which, once exploited by water, become channels with a high hydraulic conductivity.

Explorations of the conduits revealed that their slope angle determined their form. Slope angles less than around 0.3 m m^{-1} resulted in a meandering channel, with greater slopes causing a sequence of waterfalls and plunge pools to develop, with the pools enlarging into large ice caves (Vatne, 2001). Gulley *et al.* (2009) measured the process of nick-point migration, and found incision rates during migration were much greater (0.35-0.47 m d^{-1}) than for channel floor incision (0.041 m d^{-1}), they also revealed the steepest sections migrated fastest, resulting in the formation of the waterfall and plunge pool morphology. The channels evolved over time, enlarging until they became blocked with ice, or closed via ice creep, at which time they could fill with water. While full, incision continued until a new route was found, often above the previous blockage. Therefore, these channel types may never reach the bed, and so cannot be responsible for supplying

water subglacially that influences glacier velocities (section 2.6). On the Ama Dablam Glacier, one of the explored conduits exhibited horizontal ice layers, with voids in between, with the water observed to be flowing below the lowest layer. These mark the water levels in the passage when it had become water filled and the surface had frozen (Gulley and Benn, 2007), and they have also been observed within a melted-out conduit on Miage Glacier.

Fountain *et al.* (2005) observed conduits by drilling holes into Storglacieren, Sweden and using a video camera to observe any dissected channels. Englacial conduits were relatively rare (being 4% of the features found), with most hydrological features (80%) being fracture-like, and exhibiting steep drops and slow flow velocities of around 0.01 m s^{1}. The fractures appeared connected, as tracers injected in one hole could be detected in those nearby. The conduits found existed as a pair, one above the other, which trended parallel to surface crevasses and had flow velocities of around 0.1 m s^{-1}. Fountain *et al.* (2005) concluded the majority of melt was transported via a distributed system of fractures, with conduits only forming where there is a concentration of discharge large enough to destabilize the fracture-like features. Although the peaked returns of dye traces points to most drainage occurring via conduits (Nienow *et al.*, 1998).

Overall, dye tracing has given an insight into the form of englacial and subglacial channels, although using it alongside measurements of glacier velocity and water chemistry can prove powerful, and this will be explored in the following sections. Direct exploration has filled in the details of the channelised system envisaged using dye tracing, although direct knowledge of the conditions at the glacier bed still requires proxy data. A debris cover influences the formation of englacial conduits, providing low melt rates which allow cut-and-closure mechanisms where crevasses are scarce, and providing supraglacial ponds to encourage crevasse propagation through hydrofracturing. Although it is still unclear whether debris influences the evolution of the subglacial system.

2.5 Using glacier hydrochemistry to understand glacier hydrology

Although dye-tracing studies give important insights into the nature and evolution of the pathways routing meltwater to the proglacial stream, they cannot provide information on the temporal fluctuations in the sources of meltwater, and how this relates to bulk runoff. Glacier hydrochemistry can partition the bulk runoff hydrograph into separate runoff components, determined by the meltwater's transit time and the hydrological environment it passes through (Brown, 2002). Collins and Young (1979) used measurements of electrical conductivity and discharge, to separate the runoff components

of Gornergletscher, Valais, Switzerland, and Peyto Glacier, Alberta, Canada. When meltwater is produced it is dilute, and if, after reaching the glacier bed via moulins, it travels slowly through the basal sediments within small channels or a film, then the solutes produced from the chemical reactions between the sediment and water become dissolved into the meltwater. Alternatively, meltwater is routed quickly within ice-walled conduits that do not provide a source of solute. This results in two flow routing components, so that the discharge and its resulting solute concentration, is a product of the varying quantities of the two components and their associated solute loads. The solute concentration given by each flow component to the total discharge is:

$$\boldsymbol{Q_t c_t = Q_i c_i + Q_s c_s,} \qquad (2.19)$$

(Collins and Young, 1979, p5) where Q is the discharge of the component, c is the solute concentration of the component and the subscripts t is total, i is dilute meltwaters and s is enriched subglacial meltwaters. This mixing model is only correct if the components have a uniform density and there are no chemical reactions upon mixing. Substituting $Q_i = Q_t - Q_s$ into the above equation allows the subglacial meltwater component to be calculated:

$$\boldsymbol{Q_s = \left[\frac{(c_t - c_i)}{(c_s - c_i)}\right] Q_t,} \qquad (2.20)$$

(Collins and Young, 1979, p5) where the parameters Q_t, c_t and c_i can be measured in the field, with c_s being approximated as the highest measured value of c_t. Young and Collins (1979) found subglacially routed meltwater provided a background discharge which decreased as the total discharge increased, with a sharp decline in the mornings due to the increasing water pressures at the glacier's bed, leading to a decrease in the release of stored meltwater. The dilute meltwater component increased with bulk discharge, forming an asymmetrical peak as it rose rapidly to a maximum around 15:00 to 18:00. All waters with a high solute load are taken to be part of the same component, whether the solute was gained as water passed through a moraine, or as it was transferred subglacially.

These assumptions led to criticism of two component mixing models. A more detailed approach was taken based upon an understanding of the weathering reactions occurring in the glacial environment, which lead to solute production. The key subglacial weathering reaction is acid hydrolysis, when rock minerals are weathered by acidic water, for instance carbonate hydrolysis:

$$CaCO^{3}_{(s)} + H^{+}_{(aq)} \rightarrow Ca^{2+}_{(aq)} + HCO_{3}^{-}{}_{(aq)}, \quad (2.21)$$

(Hubbard and Glasser, 2005, p88).

Therefore, hydrogen ions are required to drive the reaction, and so the availability of these, a measure of the acidity of water, determines the reaction rate. The concentration of the hydrogen ions in the water in glacial environments can be provided through the dissolution of atmospheric CO_2 into water, and its consequent dissociation into bicarbonate and hydrogen ions:

$$CO_{2(g)} \leftrightarrow CO_{2(aq)}, \quad (2.22)$$

$$CO_{2(aq)} + H_2O_{(aq)} \leftrightarrow H^{+}_{(aq)} + HCO_{3}^{-}{}_{(aq)}, \quad (2.23)$$

(Burton, 2000, p259 and 260). Alternatively, the oxidation of sulphide minerals can provide hydrogen ions, where pyrite oxidation is an example:

$$4FeS_{2(s)} + 15O_{2(aq)} + 14H_2O_{(aq)} \rightarrow 16H^{+}_{(aq)} + 4Fe(OH)_{3(s)} + 8SO_4^{2-}{}_{(aq)}, \quad (2.24)$$

(Hubbard and Glasser, 2005, p89).

Therefore the resulting proportions of the products of these two reactions (namely HCO_3^- and SO_4^{2-}) measured in the proglacial stream gives an indication of which reaction is the dominant source of the hydrogen ions driving the acid hydrolysis - suggesting the subglacial conditions. The hydrogen ions produced by the oxidation of sulphide minerals can increase the rate of carbonate hydrolysis, and so the two reactions can be coupled together (Hubbard and Glasser, 2005).

To compare the relative proportions of bicarbonate and sulphate ions, ratios have been devised to indicate which reaction dominates. For instance, the C-ratio [$HCO_3^-/(HCO_3^- + SO_4^{2-})$] was developed by Brown *et al.* (1996, cited in Brown, 2002), in which when the hydrogen ions for acid hydrolysis are entirely provided by carbonate hydrolysis there is a ratio of 1, but if the carbonate hydrolysis and sulphide oxidation reactions are coupled the ratio is 0.5. Tranter *et al.* (1998) uses the S-ratio [$SO_4^{2-}/(SO_4^{2-} + HCO_3^-)$], where the coupled reactions give a ratio of 0.5, but if hydrogen ions are only available from carbonate hydrolysis then a ratio of 0 is given (Brown, 2002).

Another indicator of the weathering environment is the partial pressure of carbon dioxide ($p(CO_2)$). The dissolution of gaseous CO_2 into solution may happen at a slower rate than the reactions using up the hydrogen ions formed when the CO_2 is dissociated. This diminishes the concentration of aqueous CO_2, as consumption of the hydrogen ions forces

the equilibrium to the right, consuming more CO_2. Therefore, whether or not the partial pressure of CO_2 in the atmosphere is equal to the partial pressure of CO_2 in solution, can indicate the strength of the weathering reactions compared to the supply of CO_2. When the partial pressure of the solution and atmosphere are equal then the system is open, suggesting an environment where; the rock: water ratio is low, or the minerals present are unreactive, the interface between the melt water and atmosphere is unrestricted, and there is a constant supply of unreacted meltwater. However, when the partial pressure of the solution and atmosphere are not equal the system is closed. This occurs when more hydrogen ions are used up by the weathering reactions than can be supplied, resulting in a low aqueous $p(CO_2)$ compared to the atmosphere. This indicates there is a large supply of fresh rock material and pure water. A closed system also results when there are more hydrogen ions available than are used, resulting in a high aqueous $p(CO_2)$ compared to the atmosphere (encouraging the equilibrium to use up the hydrogen ions and increase the CO_2 concentration). This occurs when hydrogen ions are added to solution from snowmelt or sulphide oxidation; when meltwater is refrozen and the CO_2 is excluded; or when carbonates act to neutralise the acidity of the melt water. Both types of closed system occur due to physical factors such as the absence of an air-water interface when channels are water-filled, or due to kinetic factors such as when the rate of dissolution of CO_2 is less than the use of hydrogen ions in weathering reactions (Brown, 2002).

Work by Brown *et al.* (1998) suggests further reactions occur after the mixing of the dilute and enriched flow components. When sediment was added to deionised water (replicating dilute meltwater) the concentration of Ca^{2+} increased (indicating carbonate hydrolysis, see equation 2.21) and HCO_3^- increased (indicating the dissociation of H_2CO_3), along with an increase in pH (hydrogen ions were consumed by the weathering reactions) – although the rates of increase decreased over time. Higher sediment concentrations led to a greater increase in pH and of the concentration of the ions mentioned. At larger sediment concentrations the aqueous $p(CO_2)$ was lowered significantly, suggesting more hydrogen ions were consumed than supplied. This implies the addition of suspended sediment to dilute meltwater results in chemical weathering reactions that increase the solute load. Kinetic factors probably resulted in this low $p(CO_2)$ as the solutions had free access to the atmosphere. Measurements of SO_4^{2-} ions imply melt waters spent time at the glacier bed, probably in a distributed system. This is because the release of SO_4^{2-} was limited, suggesting it happens slowly during the oxidation of pyrite.

Brown *et al.* (1998) used the understanding gained from laboratory work to elucidate the sources of meltwater sampled from the Haut Glacier d'Arolla, Switzerland. In July, discharges, SSC, and solute concentrations were variable, with the waters at higher

discharges having a lower solute concentration (suggesting the dilution of delayed flow by dilute quickflow), and lower $p(CO_2)$ and SO_4^{2-}/HCO_3^- ratio (suggesting solute was produced mainly from carbonation reactions). Although the delayed flow was diluted, by mid-July the higher velocity quickflow became able to entrain more sediment, meaning peak discharges had relatively high solute concentrations due to post-mixing reactions – compensating for the dilution effect. This effect was compounded in August, when discharge and SSC concentration variability was higher, but solute concentrations became less variable. This was because at peak discharge the SSC was highest due to higher velocities, which meant post mixing reactions resulted in a high solute concentration. This brings solute concentrations closer to that at minimum flow, when most solute is acquired through weathering reactions at the bed – reducing the fluctuation in solute concentration. Calculations by Brown *et al.* (1998) revealed up to 67% of the solute concentration measured in August might be due to post-mixing reactions. This undermines the assumptions of previous mixing models that the entire solute load was from delayed flow, and suggests the proportion of delayed flow could be overestimated, especially later in the season.

Further work on Haut Glacier d'Arolla by Tranter *et al.* (1998) focused on the fluctuations in the chemistry of subglacial meltwaters. They identified three modes of subglacial water. Mode 1 water was dilute and had a supraglacial or englacial origin. Mode 2 water was chemically similar to bulk runoff, but was more dilute (as post-mixing reactions have not taken place) and likely originated due to flooding of the channel marginal zone from a nearby subglacial conduit. Mode 3 waters were the most concentrated, with a high S-ratio (0.31) and $p(CO_2)$ – suggesting the solute was a product of coupled sulphide oxidation and carbonate dissolution, typical of the distributed system. However, within a distributed system the S-ratio should be 0.5, suggesting there is more HCO_3^- than predicted, possibly because of initial hydrolysis of $CaCO_3$, but this would be limited due to the finite supply of hydrogen ions. Tranter *et al.* (1998) suggest a subglacial source of CO_2 (from air trapped in cavities, gas bubbles or the oxidation of organic carbon) which could dissolve carbonate or aluminosilicate-silicate minerals, releasing more HCO_3^- ions.

Tranter *et al.* (1996) compared the hydrochemistry of the runoff from Haut Glacier d'Arolla (a warm-based glacier in Switzerland) with Austre Brøggerbreen (a polythermal glacier in Svalbard). Taking water samples from boreholes beneath Haut Glacier d'Arolla suggested high SO_4^{2-} concentrations and a high S-ratio, implying the existence of a distributed drainage system. The concentrations of SO_4^{2-} and HCO_3^- ions measured in the bulk runoff for both glaciers were compared (for Austre Brøggerbreen the non-snowpack concentration was used as there was a significant input of SO_4^{2-} from snowpack melting,

which cannot be attributed to weathering reactions). The similarity in the variation in SO_4^{2-} and HCO_3^- concentration between the two glaciers suggested a distributed system underlies Austre Brøggerbreen, and delayed flow contributes to the glacier's bulk runoff. This suggests a connection delivers the delayed flow through the thinner cold based ice between this distributed system and the glacier's terminus. Generally, the SO_4^{2-} concentration was higher at Haut Glacier d'Arolla than at Austre Brøggerbreen, even though there is little SO_4^{2-} in the bedrock of Haut Glacier d'Arolla – delayed flow supplies a larger fraction of the overall runoff at Haut Glacier d'Arolla than at Austre Brøggerbreen. There are concerns over comparison between alpine and sub-polar glaciers, as supraglacial streams of sub-polar glaciers tend to contain high suspended sediment concentrations. Reactions with this suspended sediment (from mud slumps and lateral moraine at Austre Brøggerbreen), likely to be sulphide oxidation and carbonate dissolution, could mean that entrained sediment could release SO_4^{2-}. This could complicate solute analysis and the links to glacier hydrology, especially on glaciers where there are sediment sources apart from the bed (for instance debris-covered glaciers).

Hodgkins *et al.* (1998) studied the hydrochemistry of the cold-based Scott Turnbreen, Svalbard. At this glacier the early melt season runoff had a high $p(CO_2)$, high non-snowpack SO_4^{2-} concentration and a high S-ratio, which is indicative of delayed flow through a distributed drainage system. The seasonal decrease in non-snowpack SO_4^{2-} concentrations suggested the development of channelized drainage – indicating a two component model would be appropriate. However, borehole measurements suggest the temperature at the glacier bed is lower than the pressure-melting temperature, moulins are not evident, and hydrochemically the S-ratio remains constant and does not vary with $p(CO_2)$, or out of phase with discharge – therefore an alternative hypothesis was required.

One source of solute identified by Hodgkins *et al.* (1998) was the proglacial icing, formed as meltwater refreezes between the terminus of the glacier and the end moraine, at the end of the melt season. The pore water trapped within the icing was very high in solute, caused by the long residence times; presence of sulphide minerals; the high sediment: water ratio and because the freezing of water acted to concentrate the solute into the remaining water. The main meltwater streams flow through this icing during the melt season, and the concentrated interstitial waters are released into them. Additionally, the ice marginal streams contain high solute concentrations, due to abundant and reactive (the available sediment has a high sulfide and organic content) sediment supply from moraine deposits available along the streams' length. This, along with free access to the atmosphere (allowing CO_2 to enter solution) could result in the high solute concentrations found subaerially. Although sulphide oxidation would have to be rapid and considerable to give the high

$p(CO_2)$ and S-ratio measured. A further explanation is the solute originates from weathering reactions within the saturated sediment surrounding the ice-cored lateral moraine. The high water: rock ratio and more reactive minerals available (some of the sediment in the subaerial stream will have become depleted due to previous reactions) give an environment suited to weathering reactions. The sediment pore water could then reach the streams through continual seepage, when the stream waters rise and entrain the accompanying sediment, or via frequent mass movements of the sediment directly into the stream. Interestingly, mass movements of this type occur into the supraglacial streams of Miage Glacier, and if this is a source of solute it could influence their hydrochemistry.

Separation of the proglacial discharge into its englacial and subglacial components was attempted on the debris-covered Dokriani Bamak Glacier, Garhwal Himalayas by Hasnain and Thayyen (1994). They used a simple chemical mixing model, finding as discharge increased, the electrical conductivity decreased, similar to clean glaciers. However, the problems with this approach, casts doubt on the accuracy of their hydrograph separation. A detailed chemical analysis of this glacier was achieved by Hasnain and Thayyen (1999a), although they did not elucidate the structure of the hydrological network. The Dokriani Glacier had a particularly high denudation rate of 4160 meq m^{-2} a^{-1}, compared to glaciers such as Haut Glacier d'Arolla (640-685 meq m^{-2} a^{-1}), suggesting the southern Himalayas have particularly high weathering rates. Intriguingly, although in June there was a strong positive correlation between the SSC and SO_4^{2-} and HCO_3^- (associated with water transport through subglacial sediments), this correlation usually diminished during the season. On this glacier the correlation between SSC and SO_4^{2-} remained high in July and August. Furthermore, the concentration of SO_4^{2-} as a proportion of $SO_4^{2-} + HCO_3^-$ actually increased with discharge (being 40-45% at 3 m^3 s^{-1}, but 40-63% at 10 m^3 s^{-1}). It was hypothesised pyrite oxidation could occur within the supraglacial debris during prolonged but low-intensity precipitation. High intensity precipitation events would leach the SO_4^{2-} from the debris, adding this to the runoff during high discharges - highlighting the importance of monsoon rains on the runoff chemistry.

Hodson *et al.* (2002) studied the hydrochemistry of the debris-covered Batura Glacier, Pakistan. Contrary to Hasnain and Thayyen (1999a) they found a clear negative correlation between SO_4^{2-} and discharge. Hence, chemical reactions at the glacier bed are probably the primary SO_4^{2-} source. The denudation rates were lower for the Batura Glacier than the Dokriani Glacier, being 1600 meq m^{-2} a^{-1}, although this is high compared with temperate and Arctic glaciers, possibly because high melt rates combine with monsoon rains resulting in high flushing rates of ions in the Himalaya. The rock types are also a significant factor – the denudation rates of Batura Glacier are much larger than the Chhota-

Shigri Glacier basin, even though Batura Glacier had a lower runoff total. Importantly, the monsoon is stronger over the Dokriani Glacier than the Batura Glacier, so perhaps this influences the proportion of SO_4^{2-} derived from the supraglacial debris. More work is required to understand which processes lead to solutes being released from the supraglacial debris layer.

The water chemistry of the debris-covered Gangotri Glacier, Garwhal Himalayas was investigated by Kumar *et al.* (2009). They found a weak negative relationship between discharge and the cation concentration in 2003, but in 2004 this was only applicable to Ca^{2+}, K^+ and Na^+. This was mirrored in the diurnal pattern with the total ion concentration decreasing as the discharge increased. They linked this inverse relationship to the mixing of dilute supraglacial water with concentrated subglacial water, although they did not expand on the relationship of SO_4^{2-} or HCO_3^- with discharge, or discuss the implications for predicting the glacier-hydrology. Therefore, there is scope for hydrochemistry studies that relate the ions and their relationship to discharge with the possible subglacial (and even supraglacial) weathering environment.

A novel approach to studying the runoff contributions from different reservoirs was employed by Bhatia *et al.* (2011), who used an isotope mixing model to differentiate runoff from the outlet of the Greenland Ice Sheet into snow melt, ice melt, and delayed flow waters. The used radon-222 as a tracer of delayed flow waters as it is present in soil, sediment and rocks. A higher degree of water-rock interaction causes radon enrichment and indicates the presence of delayed or groundwater flow. They also used the $\delta^{18}O$ (oxygen-18) and δD (deuterium) signatures to partition runoff into snow and ice melt, because the signature of snowmelt will be similar to present, low elevation conditions, whereas that of ice melt will reflect higher elevations and colder times, giving the snow and ice melt unique end-member signatures that are not varied by post-mixing. Furthermore, they used ^7Be (beryllium-7) to determine the transit time of melt water to the proglacial stream, as it is deposited on the surface through rainfall or aerosol deposition and has a short half-life of 53.3 days. It is therefore detectable in snow but not in glacier ice or delayed flow which is older than around 300 days. Their results indicated that supraglacial waters took around 7.5 days to travel to the stream from the surface, and that the proportion of delayed flow and snowmelt decreased from May (41% and 23%, respectively) to July (12% and 6%), whereas the contribution from ice melt increased (from 26% to 82%). If a particular isotope signature of melt beneath debris could be found then this could provide a useful way of finding the proportion of debris melt in runoff.

Hydrochemistry can be used to gain a better understanding of the environments through which meltwater flows. However, conclusions should be backed up with evidence from dye-tracing studies and borehole-measurements, as there are still uncertainties regarding the source of solutes measured in bulk runoff.

2.6 Glacier hydrology and its influence on glacier velocity fluctuations

Glacier motion is caused by the weight of the accumulated ice moving downwards due to gravity. Simultaneously, stress from the ice acting on the bed of the glacier causes strain to occur, resulting in ice movement through deformation of the ice or bed. Glaciers can also move by basal sliding between the ice and bed, which is controlled by the frictional drag between the two surfaces (Benn and Evans, 1998). One of the most important influences on the rate of glacier motion is the quantity and pressure of water at the ice-bed interface. An increase in water pressure over the majority of the glacier's bed reduces the effective pressure and increases the glacier velocity, either due to the existence of a linked cavity system which increases sliding rates if the glacier rests on bedrock, or due to increased pore water pressures in till beneath soft-bedded glaciers (Willis, 1995).

Iken and Bindschadler (1986) linked water pressure and velocity, and related this to a linked cavity system through their study of Findelengletcher, Switzerland. The borehole water levels corresponded with fluctuations in glacier velocity, with the boreholes connected to the drainage network showing diurnal fluctuations in June, with highest water levels in the evening. Velocities only fluctuated in phase with water level measurements if the subglacial hydrology consisted of water-filled cavities. This allows variations in basal water pressure to alter the sliding velocity, as it would act over a large area of the bed, rather than over a smaller area characteristic of channelised flow (Iken and Bindschadler, 1986). Water pressure influences basal sliding because sliding occurs due to the melting of water on the upstream of obstacles, as here high pressures lower the pressure melting point. The movement of water to the downstream side allows the ice to flow over the obstacle. Therefore, the addition of water to the bed increases sliding either through the creation of a water film surrounding obstacles, or through the transfer of stress from water filled cavities (which cannot accept shear stress) to areas of bed left in contact with the ice, further decreasing the pressure melting point. Alternatively, the traction force caused by the existence of pressurized water filled cavities acting on upstream facing ice, can increase sliding in the "hydraulic jack" mechanism (Benn and Evans, 1998).

Whether or not a linked cavity system can form, and influence basal sliding, is determined by whether the water pressure is higher than the separation pressure, which is given as:

$$\boldsymbol{Pr_s = Pr_o - \frac{\lambda\tau}{\lambda a_o}},\qquad (2.25)$$

(Willis, 1995, p85), where Pr_s is the separation pressure, Pr_o is the ice overburden pressure, λ is the wavelength of the obstacle, with a_o being its amplitude, and τ shear stress. This shows that a linked cavity system exists at lower pressures than overburden pressure, but if basal sliding is to be increased to the point it becomes unstable and the ice is completely separated from the bed, then water pressures must reach a critical pressure. This pressure is mid-way between the overburden and separation pressure:

$$\boldsymbol{Pr_c = 0.5(Pr_o + Pr_s)},\qquad (2.26)$$

(Willis, 1995, p86), where Pr_c is the critical pressure. As water pressures increase past the separation pressure, but below the critical pressure, basal sliding will increase stably, but if water pressures move towards the critical pressure, sliding increases unstably, so the velocity keeps increasing. When water filled cavities first grow is when increased water pressure has the greatest influence on basal sliding; once the cavities reach a maximum size the influence of water pressure deceases (Willis, 1995).

To increase subglacial water pressures there must be a water input, so water input fluctuations can result in fluctuations of water pressure. Röthlisberger (1972) noted water pressures remain low despite an increasing discharge, as channels grow to accommodate the water. This is only true if the increase in discharge happens at a rate slow enough to allow conduit adjustment. If the discharge increases at a rate faster than conduit expansion, water pressure increases with discharge. The growth of a conduit is caused by the frictional heat of the running water melting the conduit walls, but if ice pressure is greater than water pressure, ice deformation acts to close the conduit (Röthlisberger, 1972). The resulting water pressures then influence the glacier velocity.

Sugiyama *et al.* (2005) demonstrated how water input to the glacier bed influenced water pressures and sliding rates through measurement of surface strain changes, caused by the draining of a water-filled moulin on Koryto glacier, Kamchatka, Russia. The narrowing of conduits during the night meant that as the water input increased during the day, it exceeded the capacity of the subglacial system. The moulin consequently filled with water, trapping water up glacier. Above the moulin water pressures were higher than ice

overburden pressure - leading to the ice decoupling from the bed and increasing the glacier velocity. Once the moulin drained, the released water increased velocities in the lower glacier. The velocity increase above the moulin caused longitudinal compression of the ice below but, after moulin drainage, longitudinal extension occurred, as now the lower ice was flowing faster than the ice above it.

Mair *et al.*, (2008) compared ice velocity and deformation with proglacial discharge at Haut Glacier d'Arolla, Switzerland. They revealed average ice velocities were lower in the morning when discharge was minimum, and higher in the afternoon prior to maximum discharge. The greatest daily velocity variations were found in an area identified to have substantial water pressure fluctuations and thought to be above the subglacial drainage axis. In this area during high discharge, high subglacial water pressures caused low basal drag, which decreased the shear stress and ice deformation, resulting in a localised 'slippery spot' with greater basal motion and overall glacier velocity. This caused ice deformation to increase adjacent to the slippery spot, as the shear stress was transferred to where the ice and bed were in contact.

Shepherd *et al.* (2009) investigated whether the motion of the Greenland Ice Sheet was influenced by hydrological changes. They found a clear diurnal signal in ice motion – with a 110% velocity fluctuation measured at the lowest altitude GPS site. This, along with an observed diurnal surface uplift of up to 0.04 m, showed surface melt was transferred rapidly to the base of the ice sheet, where it increased water pressures and flow velocities through the hydraulic jack mechanism - giving consequences for how the Greenland Ice Sheet evolves in a warming climate. This depends however upon the future drainage structure, as this determines whether the ice sheet would increase or decrease in flow velocity when faced with a larger meltwater input. The velocity fluctuations were observed only during maximum water input at the first site, where the system was channelised, while at the third site the flow velocity decreased gradually, as the channelised network became more efficient (Shepherd *et al.*, 2009).

Further work by Bartholomew *et al.* (2011) also measuring glacier velocities on the Greenland Ice Sheet, revealed that although the network did become more efficient on the lower sites, and this did lead to lower velocities than during the initial formation of the channel network, the velocities of the lower stakes were still higher in the summer than during the winter. Also, as the summer progressed, speed up events (caused by supraglacial lake drainage) occurred progressively further upglacier as the area of melting reached further inland. Under a warmer climate, a greater area would be subjected to velocity variations and this would allow an increase in the dynamic mass loss of the ice sheet. Ultimately, a strong correlation was found between ablation and percentage change in

mean annual motion, implying higher ablation would increase ice velocities. This study also highlights the importance of supraglacial lakes for initiating channel formation, by allowing the accumulation of meltwater that can then propagate through thick ice to the bed.

At low discharges when most water at the bed is produced from frictional heat and geothermal energy, the water exists in a thin film, which has a steady state water pressure similar to ice overburden pressure. If the water film depth increases to above 0.004 m, the film becomes unstable. This creates areas with a pressure greater than the overburden pressure on the up-glacier side of bedrock bumps, with orifices forming a link to low pressure cavities on the down-glacier side. This linked cavity network remains stable as long as a moderate water input is maintained. Within this system, if the water inputs increase the water pressures will too, as the increased energy introduced to the system with a greater water input (which would melt the orifice and cavity surrounds) would dissipate over a large surface area, and so the closure rate due to ice creep would increase faster than the rate of opening. Therefore, the cavities grow gradually if meltwater inputs increase, but if melt of the surroundings of the cavities becomes greater than closure due to ice creep then the orifices grow unstably. This is encouraged by low sliding velocities and effective pressures (where the effective pressure is the difference between the ice overburden and subglacial water pressure), and by high discharges. At this point the orifices become tunnels parallel to ice flow, which evolve into a dendritic channel system. In a channel system the smaller surface area means the opening of the channels by frictional heat happens at a rate greater than closure, and so increased water inputs do not lead to higher water pressures (Willis, 1995).

The difference between the characteristics of linked cavity and channelised drainage systems was emphasised by Lappegard and Kohler (2005). They monitored the pressure at the bed, added pressure transducers to the base of boreholes, and pumped water into boreholes at a pressure above ice overburden. During the summer the time taken for the water cavities created initially to connect to the drainage network was very inconsistent, suggesting the network had a low surface to volume ratio. Once connected, the capacity of the system was large, and after pump shut-down the water pressures recorded were close to atmospheric: suggesting the existence of a channelised system. In winter, the initial water cavity connected to the drainage system consistently quickly, suggesting a network with a large surface to volume ratio, but once connected the discharge capacity was smaller and the pressures recorded an order of magnitude higher than the summer system: suggesting a system of connected cavities existed.

The switch between winter and summer drainage was captured by Mair *et al.*, (2001) on Haut Glacier d'Arolla, Switerland, during a short period of high velocity during the early

melt season or "spring event". Before the spring event, measured surface velocities were low, basal drag was high and the glacier was gradually lowering vertically. At this time the whole glacier was snow covered, with last summer's conduits having closed over the winter: the glacier had a distributed linked cavity drainage system. High temperatures, persistent rainfall and a strong föhn wind created large water inputs. During this period (22 to 28th of June) Mair *et al.,* (2001) measured high longitudinal velocities, which were particularly pronounced to the east of the centre line. The glacier uplifted initially, beginning to the east of the centre and spreading across the study area, which became lowering as the glacier slowed. Furthermore, a loss of areas of high basal drag and the instigation of upglacier longitudinal extension, followed by compression downglacier was reported. The increased discharge caused an increase in subglacial water pressures due to the existence of a distributed drainage system (see Willis (1995) and Lappegard and Kohler (2005) above), leading to the decoupling of the ice and bed, removal of basal drag, and increase in basal motion. The combination of horizontal velocity acceleration with vertical uplift (of up to 0.2 m) was observed after rainstorms on Maud Glacier, New Zealand by Kirkbride and Warren (1997). Mair *et al.,* (2001) observed that during the spring event the drainage system remained pressurised, but as it ended lower pressures corresponded with the high discharges, implying cavity enlargement from frictional heat and bed separation had begun. After the event, there was no-longer any fast flowing ice, with an area of low velocities corresponding with where ice had previously been fastest; with this area experiencing downwards motion of the ice surface and high basal drag. To the west and downglacier of this area a more gentle vertical decrease and zones of low basal drag were experienced. The glacier velocities remained low even when discharges rose later - suggesting a more efficient drainage network.

Bingham *et al.* (2006) observed high surface velocity events occurring on the polythermal John Evans Glacier, High Arctic Canada. The first high velocity event of the year (in 2000 and 2001) corresponded with the release of ponded supraglacial water as crevasses propagated to the bed by hydrofracture (see Benn *et al.* (2009) in section 2.4). Dye tracing revealed low water velocities (less than 0.15 m s^{-1}) and a large drainage network cross sectional area (over 6 m^2): indicating the existence of a distributed drainage network. The large water inputs led to high water pressures which spread downglacier, leading to the downglacier movement of high surface velocities. Similar events occurred in 1998 and 1999 (Copland *et al.,* 2003) – suggesting this is an annual occurrence.

On Fox Glacier, New Zealand, Purdie *et al.* (2008) discovered that the maritime nature of this glacier means even in winter the drainage system is relatively efficient. There are differences between summer and winter velocity (average daily surface summer velocity

is 0.87 ± 0.27 m d^{-1}, while in winter is 0.64 ± 0.24 m d^{-1}), but these are due to the smaller winter water input. Despite channelised drainage, this glacier showed incidences of short term velocity increases due to rainfall events. On the 22nd of January high melt combined with high rainfall led to an instantaneous increase in surface velocity. The meltwater was forced from the channelised system into the surrounding distributed system, resulting in high water pressures. Generally, the channelised system means rainfall events have to be significant even in winter (greater than 100 mm in 24 hours) to result in an increase in surface velocity. Purdie *et al.* (2008) mentioned the debris-covered part of the glacier lessened the effect of rainfall events on ablation (ablation rates were 44% less than on bare ice), because the debris protected the ice below from rainfall and decreased thermal melting. Rainfall events of a specific magnitude are less likely to instigate a velocity event on a debris-covered glacier than a clean one, as the volume of water transferred to the drainage system is lessened.

Quincey *et al.* (2009) found that the upper ablation zone of the debris-covered Baltoro Glacier, Pakistan could flow up to 65% faster in the summer than in the winter. The fastest flow velocities were found at the Concordia cross-section (~33 km from the terminus), coinciding with a region of moulins where large supraglacial streams reach the bed. Cross-profiles revealed the "blocky" nature of flow, with velocities being similar across the glacier but decreasing greatly near the margins. It was suggested the glacier moved by basal sliding in the upper 10 km, as this movement was linked with large meltwater inputs (the melting of the large snowpack in 2005 resulted in greater velocities than in 2004) which had created high water pressures within the subglacial system. However, the velocities measured on the lower 10 km were more consistent between summer and winter, so here flow via deformation was more likely.

These studies reveal how variations in the volume of water inputs and their timing, the position they reach the bed, and the type and evolutionary stage of the drainage system, influences whether high water pressures result. If these high water pressures are greater than the critical pressure then the ice and bed decouple, leading to increased sliding velocities. These factors can vary temporally (via daily, event based, or seasonal fluctuations) and spatially (from the position of the release of stored water to the local degree of connection to the drainage network). The velocity fluctuations influence the whole glacier through the creation of longitudinal compression and extension, or through the local transfer of stress creating "sticky spots". Surface velocity measurements can give an insight into the drainage system configuration, but knowledge of the water inputs and basal water pressures allows a more thorough understanding of the likely subglacial system.

3 Methodology

3.1 General chapter overview

3.1.1 Chapter outline

This chapter describes the methods used to collect and analyse data on the hydrology of Miage Glacier. It gives details of the fieldwork carried out, instruments used, laboratory analysis of the water chemistry samples, and the calculations performed to analyse the data. There were 4 main types of field data collected: meteorology and glacier ablation; dye tracing of moulins and streams; measurements of the proglacial stream discharge and water chemistry; and glacier velocity measurements, each of which is described in a subsection. They are organised to follow the same structure as the results chapters, so the meteorology and ablation measurements and models are given first (section 3.2) as they give information on the supraglacial melt rates, the dye tracing methods are next (section 3.3), followed by the proglacial water chemistry and runoff methods as they were used to understand the bulk water routing (section 3.4), and the glacier velocity measurements are given last in section 3.5. The data used in the water balance results chapter incorporates modelled ablation and evaporation data, the collection of which is described in section 3.2, and runoff data from section 3.4. Fieldwork was carried out in early June, between the end of July and beginning of August, and during the beginning of September of both 2010 and 2011, although a short visit was also made in October 2011. Details of the time periods of fieldwork and a general guide to data collection are given in Table 3.1. All day numbers mentioned in this thesis refer to the day-of-year or ordinal date, and all times use a 24 hour clock and are in local time unless otherwise stated.

Table 3.1 General guide to fieldwork dates and data collected. 'Dye' is dye tracing, 'Velocity' is glacier velocity measurements, 'Chemistry' is water chemistry measurements, 'Discharge' and 'Conductivity' measurements were of the proglacial stream.

Year	Months	Start day	End day	Measurements
2010	June	156	175	Dye, Velocity, Chemistry, Ablation
	July/Aug	209	218	Dye, Velocity, Chemistry, Ablation
	Sep	247	256	Dye, Velocity, Chemistry, Ablation
	June-Sep	156	175	Meteorology, Discharge, Conductivity
2011	June	155	166	Dye, Velocity, Chemistry, Ablation
	July/Aug	207	216	Dye, Velocity, Chemistry, Ablation
	Sep	254	259	Dye, Chemistry, Ablation
	Oct	284	284	Ablation
	June-Sep	155	259	Meteorology(to day 284), Discharge, Conductivity

3.1.2 Overview of instrument setup

Three meteorological stations were installed on the glacier (Figure 3.1a). The lower meteorological station (LOMET) was situated on the centre of the lower glacier (Figure 3.2a), with the upper meteorological station (UPMET) situated within the main trough, on the eastern moraine (Figure 3.2b). There was a further station (ICEMET) situated on the dirty ice between the central and western moraine in 2011 (Figure 3.2c). The main proglacial stream was monitored at the gauging station as it emanated from the northern lobe. All the proglacial stream instruments and measurements were found at this site (see section 3.4). Glacier velocity was measured at up to 22 positions on each day, with the 'C' points referring to those on the central moraine, the 'E' points those on the eastern moraine and the 'W' points those on the western moraine. 'SL' refers to the southern lobe and 'NL' to the northern lobe (Figure 3.1b). Only the 2010 points are shown, as the locations of some points differed slightly in 2011 (C4, C11 and C14), although their naming remains the same. There were 19 different dye injection points (Figure 3.1c and Figure 3.1d), named with an 'S', although those marked with a 'b' are points on a stream that flows into the numbered injection point. They were situated from 997 m from the gauging station (S1) up to 5867 m from the gauging station (S14b) (details of the calculation of the distance to the gauging station is given in section 3.3.1).

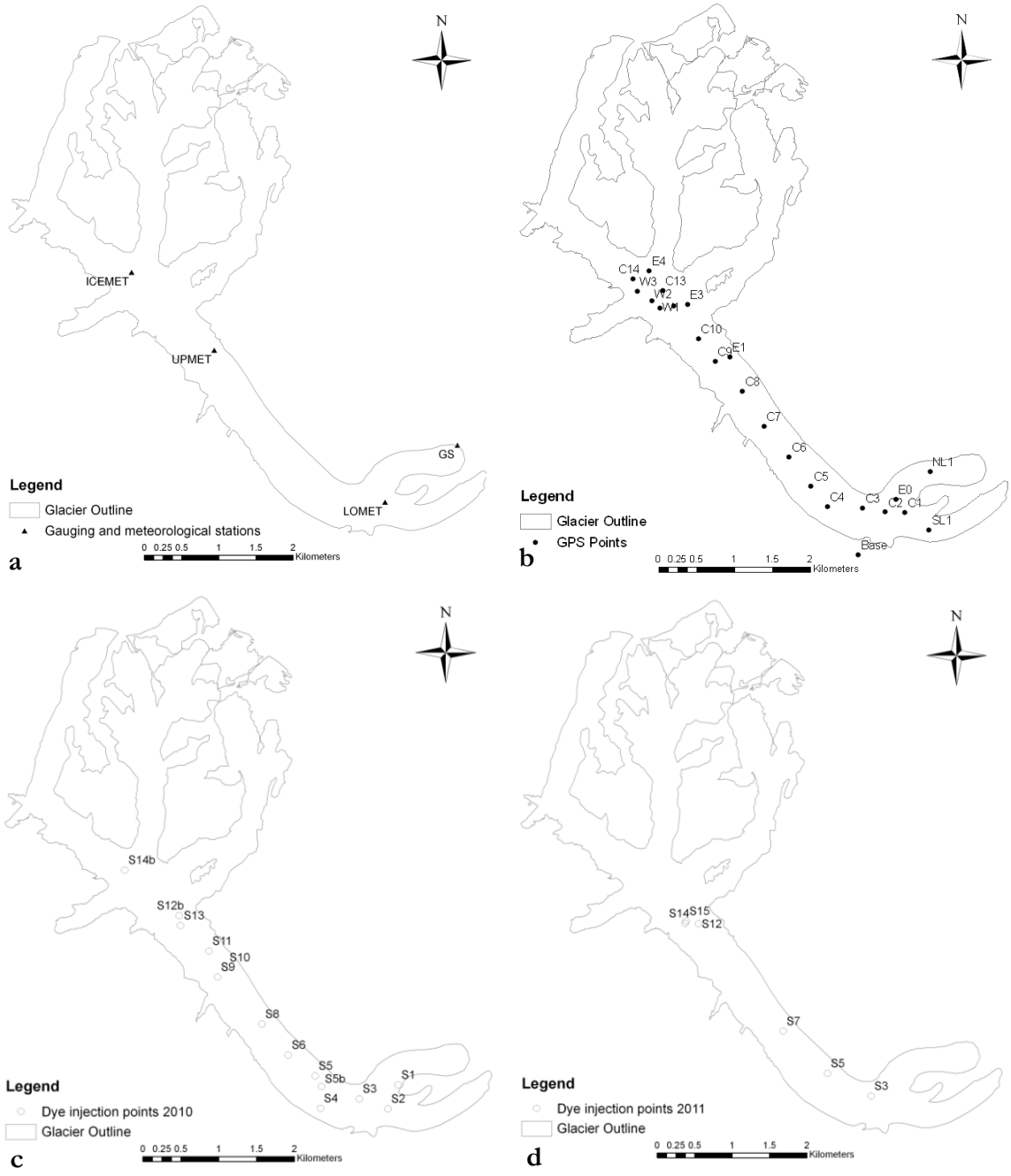

Figure 3.1 Maps of the instrument set up: a) gauging and meteorological stations, b) the GPS positions used in 2010, with the base station receiver situated at 'Base', c) dye injection points in 2010, d) dye injection points in 2011.

3.2 Meteorology and ablation

This section describes the setup of the meteorological stations and ablation stake network, as well as the construction of the distributed energy balance melt model. The meteorology measurements were essential as model inputs, but also gave context to the dye tracing, glacier velocity, and stream discharge and chemistry measurements. Debris temperature was measured to monitor the timing of the transfer of the temperature (and hence melt) cycle through the debris. Debris temperature and relative humidity data were used to calculate vapour flow through the debris. A distributed energy balance melt model was constructed to give information on the melt rates for different surface cover types (snow, ice and debris), and debris thicknesses, with measured ablation data used to verify the model. The melt model was also used to provide the quantity and timing of meltwater inputs into the hydrological system, and allow quantification of the 'melt' part of the water balance.

3.2.1 Meteorological stations

Details of the time periods and locations of the meteorological stations are given in Table 3.2 and the instruments used in Table 3.3. LOMET and UPMET were set up on an area of continuous debris cover (Figure 3.2a and Figure 3.2b, respectively), with the instruments and logger mounted onto a Campbell tripod, at a height of approximately 2.16 m. The instruments on LOMET and UPMET were recorded by a Campbell data logger, powered by a battery supplied by a solar panel. Both loggers recorded an hourly average, minimum, maximum or sum, as applicable, of measurements taken every 10 seconds. LOMET also recorded over the winter, but was limited to measurements of air temperature, relative humidity and incoming shortwave, to prevent damage to the anemometer and net radiometers when buried by snow. The instruments on UPMET were removed over winter.

Table 3.2 Overview of the deployment of the meteorological stations.

Met Station	Surface cover	Easting	Northing	Elevation (m a.s.l.)	Year	Start day	End day	Interval (min)
LOMET	debris	0335022	5072088	2066	2010	155	256	60
					2011	157	284	60
UPMET	debris	0332724	5074131	2356	2010	157	254	60
					2011	164	256	60
ICEMET	dirty ice	0331614	5075180	2411	2011	208	245	60

To measure the difference in air temperature caused by the change in surface cover from debris to ice, ICEMET was positioned over dirty ice to the west of the central

moraine on the upper glacier (Figure 3.2c). ICEMET only measured air temperature, using a Tinytag logger situated within a MET 20 Campbell radiation shield. The tip of the temperature probe was 1.47 m from the surface. Data was logged hourly, but unlike the Campbell loggers it captured one measurement at each hour, rather than an average over the hour. A higher logging frequency was not possible due to the limited logger capacity. The radiation shield was mounted as high as possible on a camera tripod.

Table 3.3 Details of instruments on meteorological stations. 'L' is LOMET, 'U' is UPMET and 'I' is ICEMET.

Quantity	Manufacturer	Type	Accuracy	Station
Air Temperature, °C	Vaisala	HMP45C	± 0.2°C	L, U
	Gemini Tinytag	PH-5001, 10K NTC thermistor	± 0.2°C in -5 to 65°C range	2011, I
Relative Humidity, %	Vaisala	HMP45C	± 2% in 0-90% range, ± 3% in 90-100% range	L,U
Wind Speed, m s^{-1}	Vector	A100L	1% ± 0.1 m s^{-1}, threshold 0.15 m s^{-1}	L,U
Wind direction, °	Young	05103	± 3%	L,U
Incident shortwave radiation, W m^{-2}	Kipp and Zonen	CM3, 0.305 < λ < 2.8 μm	± 10% for daily sums	L
	Skye	SP1 110, 0.35 < λ < 1.1 μm	± 3%	U
Reflected shortwave radiation, W m^{-2}	Kipp and Zonen	CM3, 0.305 < λ < 2.8 μm	± 10% for daily sums	L
Incoming longwave radiation, W m^{-2}	Kipp and Zonen	CG3, 5 < λ < 50 μm	± 10% for daily sums	L
Outgoing longwave radiation, W m^{-2}	Kipp and Zonen	CG3, 5 < λ < 50 μm	± 10% for daily sums	L
Debris temperature, °C	Gemini Tinytag	PH-5001, 10K NTC thermistor	± 0.2°C in -5 to 65°C range	L,U
Debris dew point °C	Onset	HOBO Temperature/RH Smart Sensor	± 4%	L
Precipitation, mm	Environmental Measurements	Plastic tipping bucket	-	2010, L 2011, U
	Unknown	Metal tipping bucket	-	2011, L
Evaporation, mm	Author	Lysimeter Mark 1	-	L

Figure 3.2 Photographs of meteorological stations: a) LOMET, b) UPMET, c) ICEMET, and d) EWMET.

Due to the differences in both the type of temperature probe and radiation shield found on the UPMET and ICEMET stations, a calibration experiment (EWMET) was set up to compare the temperatures measured by each sensor (Figure 3.2d). This was required because the temperature differences between UPMET and EWMET were used to calculate the lapse rate between these stations in the distributed melt model. Both probes and their radiation shields were attached to a tripod on the roof of the Ewing building, University of

Dundee, with the loggers set up in the same way as in the field. Data were recorded from day 301 at 10:00 GMT to day 334 at 10:00 GMT. The mean absolute difference between the Vaisala (UPMET) and Tinytag (ICEMET) probes was 0.39°C (relative 0.31 °C). As the Tinytag takes only one measurement per hour and the Vaisala records the average over the preceding hour, the Tinytag underestimates the temperature compared to the Vaisala when it is falling, and overestimates it when it is rising. The Tinytag temperature for each hour was therefore calculated as the average of that hour and the hour before, decreasing the mean absolute difference to 0.32°C (named the averaged Tinytag temperature). To ascertain whether there was a difference in the calibration of the sensors, the night time difference between the Vaisala and averaged Tinytag was found (night time was 18:00 to 5:00, applicable to Scotland from the 28th of October to the 30th of November). This eliminated the influence of warming from incoming shortwave radiation due to the different radiation shields. The average night time difference in temperature (Vaisala minus averaged Tinytag, relative) equated to 0.32°C. This was added to the averaged Tinytag temperature to give the adjusted Tinytag temperature (Figure 3.3a). The mean absolute difference between the adjusted Tinytag and Vaisala temperatures was now 0.15 °C (relative -0.02°C). The only other difference could be due to the different radiation shields or random sensor error. The plot of average relative hourly temperature differences between the Vaisala and Tinytag confirmed there was not a significant trend of higher temperatures at one of the sensors during the day (Figure 3.3b). As the manufacturer's accuracy for both temperature probes is ±0.2°C, the remaining difference is within measurement error.

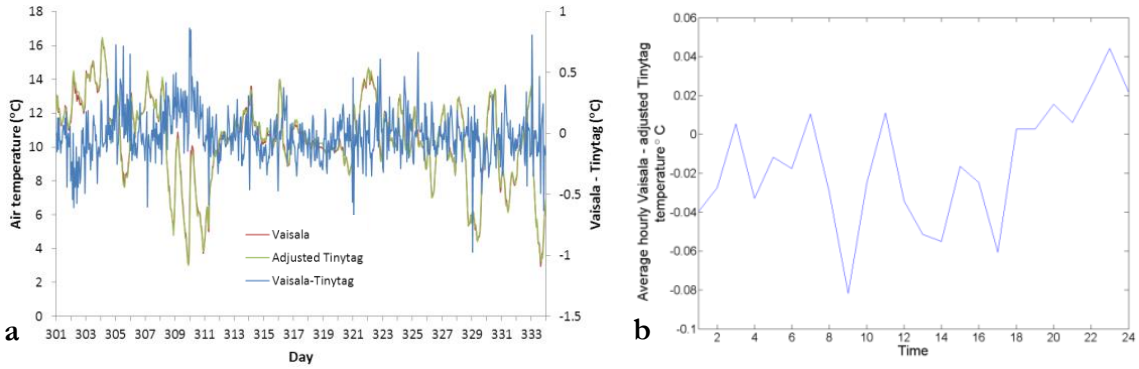

Figure 3.3 Graphs of calibration of Vaisala and Tinytag temperature probes: a) gives the Vaisala and corrected Tinytag air temperature data for the calibration period, with the difference in air temperature given on the right hand axis, and b) is the average hourly difference between the Vaisala and corrected Tinytag temperatures.

To measure evaporation from the debris a volumetric lysimeter (mark 1) was designed (following Sakai *et al.* (2004), Figure 3.4). It consisted of an upper cylindrical

section 0.12 m in diameter, the base of which was a funnel with the end covered by a layer of fine netting. This upper section was filled with debris, with the netting containing the debris, while allowing the passage of water. The water was captured in a lower container which was taped to the upper section. The lysimeter was buried so the rim of the upper cylinder was level with the debris surface. The volume of water within the lower container was measured with a measuring cylinder and translated into a water depth (mm) using the cross-sectional area of the cylinder. Subtracting the water depth in the lysimeter from the rainfall measured by the tipping bucket rain gauge gave the evaporation, which was calculated as a percentage of rainfall. Condensation of water onto the debris surface was assumed insignificant, if it percolated into the lower cylinder it would be counted as percolated rainfall (reducing calculated evaporation). A second lysimeter was designed (mark 2) so the base of the debris-filled container was in contact with the ice, with water flowing into a second container attached on the side of the first. This required the lysimeter to be buried on a slope which meant deployment was less successful, as sloping debris is often not stable. Both lysimeters were located at LOMET.

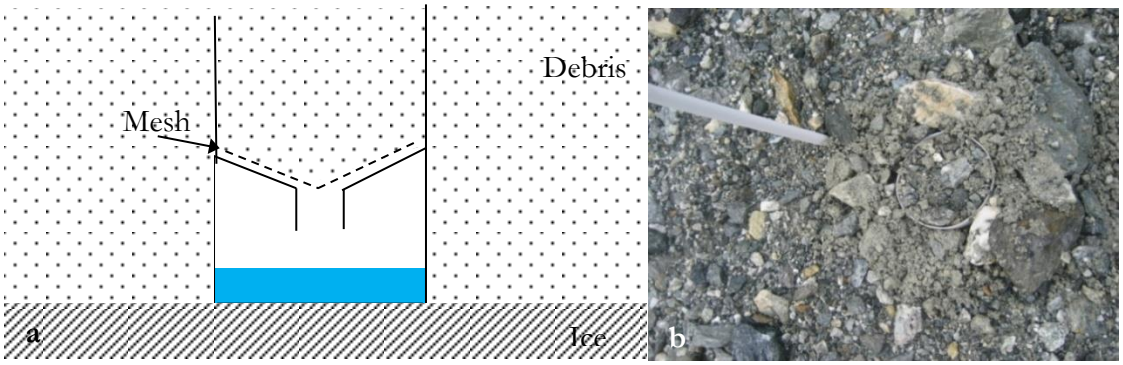

Figure 3.4 a) Diagram and b) photograph of mark 1 lysimeter in the debris near LOMET, 2011.

3.2.2 Debris temperature and relative humidity

The debris surface temperature was measured using Tinytag loggers which each had two probes. Each probe was attached to the upward facing surface of a flat, clean rock, with the probe's tip in contact with the rock, ensuring the probe measured the rock surface temperature. This is a standard method of measuring debris surface temperature, although average surface temperature is overestimated by about 3-4°C during the day, due to shaded debris having a lower temperature (Brock *et al.,* 2010). It is difficult to assess the representativeness of these point measurements compared to an area of debris, due to differences in rock type, aspect and shading found even over small areas. Details of the Tinytag temperature probes deployed are given in Table 3.4.

Table 3.4 Details of the deployment of the Tinytag temperature probes.

ID Number	Location	Nearby stake	Easting	Northing	Start day	End day	Interval (min)
1 and 2	C3	C3_0610	0334474	5072151	160 2010	256 2010	30
5 and 6	LOMET	La_0610	0335022	5072088	156 2010	256 2010	60
9 and 10	UPMET	-	0332724	5074131	160 2010	254 2010	30
1 and 2	LOMET	Lj_0711	0335022	5072088	207 2011	216 2011	10
5 and 6	LOMET	Lb_0611	0335022	5072088	154 2011	284 2011	30
9 and 10	LOMET	La_11	0335022	5072088	207 2011	216 2011	10
11 and 12	LOMET	Li_0711	0335022	5072088	207 2011	216 2011	10

The temperature, dew point and relative humidity within and at the surface of the debris were measured using HOBO loggers, deployed in 2010 and 2011 at LOMET, and by Brock *et al.* (2010) in 2005 at LOMET and on the southern lobe (Table 3.5). The data from the HOBO loggers is patchy due to occasional malfunction of one or more of the sensors. Thermistors tend to overestimate the surface temperature by 3-4°C compared to radiative temperature (found from the longwave radiation flux measured by the Kipp and Zonen CNR1 CG3 radiation sensor on LOMET) (Brock *et al.,* 2010). This meant the relative humidity measured by the HOBO loggers had to be corrected. The surface temperature derived from the CNR1 CG3 radiation sensor measurements gives a more representative temperature because its value is an average for the area under the upwelling longwave sensor. The HOBO sensor was not directly below the CNR1 sensor, but was within a couple of meters of it and on similar debris. This temperature and HOBO dew point data were used to calculate the surface relative humidity using the Magnus–Tetens approximation. During 2010, the sensor supposed to be at the ice/debris interface recorded average temperatures close to that at a depth of 16 cm, due to the sensor moving within the debris. In 2011, the sensors were taped to a length of plastic stake so they maintained their positions in the debris.

Table 3.5 Details of the deployment of the HOBO temperature and relative humidity probe. Probes were installed near LOMET, except * which was installed on the southern lobe.

Year	Debris depth (cm)	Sensor 1 depth (cm)	Sensor 2 depth (cm)	Sensor 3 depth (cm)	Sensor 4 depth (cm)	Start	End	Interval (min)
2005	0.23	0	8	15	23	165	204	10
***2005**	0.72	0	24	48	72	168	250	10
2010	20	0	7	16	20	156	239	60
2011	20	0	8	14	20	159	165	10
						215	258	10

3.2.2.1 Calculating vapour flow in the debris layer

The measured debris temperature and relative humidity within the debris layer was used to calculate the flux in water vapour within the debris. As mentioned, the overestimation of the debris surface temperature of the HOBO sensor meant this was derived from the CNR1 sensor on LOMET, and combined with the HOBO dew point data to give the surface relative humidity. Vertical water vapour flux within the debris (J_v) (kg m^{-2} s^{-1}) was calculated using the flux gradient relationship given by Oke (1987, p 65):

$$J_v = -\kappa_v \frac{\delta \bar{\rho}_v}{\delta z_d}, \quad (3.1)$$

where $\bar{\rho}_v$ is the mean vapour density (kg m^{-3}), κ_v is the molecular diffusion coefficient for water in air (m^2 s^{-1}), and z_d is the vertical distance within the debris (m). The molecular diffusion coefficient is dependent on temperature and a relationship derived from Oke's (1987) data was used:

$$\kappa_v = 1.5 \times 10^{-7} T_d + 2.122 \times 10^{-5}, \quad (3.2)$$

where T_d is temperature within the debris (°C). ρ_v was calculated from equation 3.3:

$$\rho_v = \frac{2.17 e_a}{T_d + 273.16}, \quad (3.3)$$

where e_a is the air vapour pressure (Pa) which is calculated from the product of saturated vapour pressure (e_s) (Pa) and the relative humidity (RH) as a ratio between 1 and 0:

$$e_a = e_s RH, \quad (3.4)$$

with e_s being found from the debris temperature using a standard empirical formula. These equations were written into MATLAB code and used to calculate the vapour flux between each sensor position, as well as the overall flux through the debris.

3.2.3 Ablation measurement

Ablation was measured using white plastic ablation stakes which were drilled into the ice (after removal of the surface debris if necessary) using a Kovex ice drill. The debris

was replaced as naturally as possible after stake installation. The length of the stake from the top to the debris (or ice) surface was measured, ideally daily during field visits, with the debris thickness recorded prior to stake installation (data from Milan University included debris thickness measurements with every monthly stake measurement). In total, 25 stakes were measured during 2010 and 29 during 2011, although not all were maintained throughout the season (Table 3.6 and Table 3.7).

Longer term stakes were situated across the debris-covered region of the glacier and used to for melt model validation. During 2010 many of the longer term thick debris stakes were installed and measured by the University of Milan. In 2011 they were installed along the glacier centreline and at LOMET. Furthermore, season long ablation data was also collected across the debris covered area in 2005 by Brock *et al.* (2010), and these data were used to verify the relationship between ablation and debris thickness.

Ablation of clean ice and snow on the upper glacier was also measured for model validation (snow in June, and clean ice in July or September). Snow stakes were measured at two locations from day 164 to 169 in 2010, and at three locations from day 159 to 165 in 2011. Ice stakes were measured at two locations from day 248 to 254 in 2010 and at 4 locations from day 209 to 214 in 2011. Measured ice and snow melt was converted to water equivalent ablation using literature densities of 890 kg m^{-3} and 461 kg m^{-3} respectively (Brock *et al.,* 2010; Fox *et al.,* 2008).

Table 3.6 Details of ablation stakes in 2010, the naming follows the form Aa_MMYY, where the 'A' relates to a location or stake type, with 'C3' being near the C3 GPS point (and so on for other GPS points), 'I' being an upper glacier clean ice stake, 'M' being a Milan stake on debris, 'S' being a snow stake, 'L' being a stake near LOMET, and 'U' being a stake near UPMET. The 'a' is used to distinguish stakes measured at the same location, and 'MMYY' gives the approximate measurement month and year, but if stakes were measured over the year without being re-drilled then only the year is given.

Name	Easting	Northing	Elevation (m a.s.l.)	Debris thickness (m)	Surface
2010					
C3_0610	334472	5072143	2110	0.28	Debris
C3_0810	334472	5072143	2110	0.16	Debris
Ia_0910	332114	5074757	2376	0	Clean Ice
Ib_0910	331549	5075203	2428	0	Small clasts on ice
La_0610	335019	5072096	2066	0.10	Debris
La_0810	335019	5072096	2066	0.08	Debris
M1_0610	332601	5074112	2265	0.28	Debris
M2_0610	333107	5073402	2224	0.24	Debris
M3_0610	333619	5072759	2139	0.11	Debris
M3_0710	333619	5072759	2139	0.11	Debris
M3_0810	333619	5072759	2139	0.11	Debris
M4_0610	333900	5072355	2098	0.13	Debris
M4_0710	333900	5072355	2098	0.14	Debris
M5_0610	334403	5071802	2047	0.08	Debris
M5_0710	334403	5071802	2047	0.08	Debris
M5_0810	334403	5071802	2047	0.10	Debris
M6_0610	335337	5071875	1966	0.16	Debris
M6_0710	335337	5071875	1966	0.12	Debris
M7_0610	335915	5072080	1878	0.14	Debris
M8_0610	334895	5072256	2001	0.19	Debris
M8_0810	334895	5072256	2001	0.16	Debris
M9_0610	335214	5072517	1959	0.23	Debris
M9_0810	335214	5072517	1959	0.15	Debris
Sa_0610	332558	5074013	2354	0	Snow
Sb_0610	331648	5075282	2483	0	Snow

Table 3.7 Details of ablation stakes in 2011, the naming follows the form Aa_MMYY, where the 'A' relates to a location or stake type, with 'C3' being near the C3 GPS point (and so on for other GPS points), 'I' being an upper glacier clean ice stake, 'M' being a Milan stake on debris, 'S' being a snow stake, 'L' being a stake near LOMET, and 'U' being a stake near UPMET. The 'a' is used to distinguish stakes measured at the same location, and 'MMYY' gives the approximate measurement month and year, but if stakes were measured over the year without being re-drilled then only the year is given.

Name	Easting	Northing	Elevation (m a.s.l.)	Debris thickness (m)	Surface
2011					
C11_11	331996	5074786	2441	0.2	Debris
C3_11	334491	5072146	2107	0.3	Debris
C3a_0711	334562	5072149	2107	0.24	Debris
C3b_0711	335061	5071965	2107	0.12	Debris
C5_11	333806	5072430	2166	0.22	Debris
C7_11	333195	5073205	2284	0.28	Debris
C9_11	332557	5074053	2377	0.23	Debris
Ia_0711	331614	5075180	2411	0	Ice
Ib_0711	331614	5075180	2411	0	Ice
Ic_0711	331614	5075180	2411	0	Ice
Id_0711	331614	5075180	2411	0	Ice
La_11	335032	5072093	2064	0.25	Debris
Lb_0611	335041	5072098	2064	0.22	Debris
Lc_0611	335041	5072098	2064	0.28	Debris
Ld_0611	335041	5072098	2064	0.3	Debris
Le_0611	335041	5072098	2064	0.14	Debris
Lf_0611	335041	5072098	2064	0.07	Debris
Lg_0611	335041	5072098	2064	0	Debris
Lh_0711	335027	5072099	2064	0.27	Debris
Li_0711	335002	5072089	2064	0.095	Debris
Lj_0711	334962	5072091	2064	0.22	Debris
Lk_0711	334920	5072070	2064	0	Ice
Sa_0611	331442	5075202	2501	0	Clean snow
Sb_0611	331442	5075202	2501	0	Dirty snow
Sc_0611	331442	5075202	2501	0	Semi-dirty snow
Ua_0611	332745	5074111	2351	0.013	Flat clasts
Ub_0611	332745	5074111	2351	0.01	Gravel
Uc_0611	332745	5074111	2351	0.03	Gravel
Ud_0611	332745	5074111	2351	0	Ice

3.2.4 Ablation modelling

To calculate the relative contributions of melt from different parts of the glacier (and different surface covers) a melt model for the entire glacier was required. A distributed energy balance model was therefore developed. As the variations in the melt rate may differ

under different surface covers for certain times of day and under certain weather conditions, it was decided an hourly melt model was necessary, as this would capture the detail of the spatial differences of melt over time, and help understand the proglacial runoff fluctuations. The total melt values were also required for the overall water balance. However, the production of a fully physically based state-of-the-art model was not the main focus of this thesis, and so some simplifications were necessary. The model philosophy was to use measured data as far as possible, and keep parameterisations to a minimum.

The model was scripted to run in the MATLAB programming environment using an hourly timestep over a 30 by 30 m grid over the melt season (days 159 to 253 in 2010 and days 165 to 255 in 2011). It required meteorological data from all three stations as an input, and base grids of the glacier's outline, elevation, debris thickness, surface cover (whether ice, dirty ice, or continuous debris) and the percentage snow cover for each day. It calculates ablation at the ice debris interface using the Reid and Brock (2010) model, which firstly numerically calculates the debris surface temperature from the balance of the fluxes at the debris surface, and then calculates the heat conducted through the debris. The ablation of clean ice, dirty ice and snow was calculated from a standard clean ice energy balance model, with the values of albedo, surface roughness and emissivity changed for each surface type.

3.2.4.1 Meteorological data

The meteorological data required by the model includes hourly incoming shortwave radiation, air temperature, wind speed, relative humidity, and total rainfall, all of which are acquired from LOMET and UPMET, with air temperature from ICEMET. It requires incoming longwave radiation and debris surface temperature (from the Kipp and Zonen CNR1 CG1 sensor) from LOMET and the dew point data from the HOBO sensor, to allow calculation of the surface relative humidity (section 3.2.2). In 2010 and part of 2011 the ICEMET temperature data was not available, so it was modelled using a statistical regression model developed from the 2011 data, which uses UPMET air temperature and relative humidity as inputs. The ICEMET data was required to account for the change in surface cover (and therefore air temperature) from debris to ice. There was also no rainfall data from UPMET in 2010 so the average LOMET to UPMET rainfall lapse rate from 2011 was used.

Table 3.8 Methods used to distribute the meteorological data over the glacier.

Parameter	Area	Year	Method to distribute
Air Temperature	Below UPMET	both	Hourly lapse rate from data between LOMET and UPMET
	UPMET-ICEMET	2010	Hourly lapse rate from statistical regression model from UPMET air temperature and relative humidity and 2011 ICEMET data
		2011	Hourly lapse rate from data, or as 2010 when no data
	Above ICEMET	both	Constant lapse rate (-0.0041 °C m^{-1}, Oerlemans (2010))
Air relative humidity	Below C6	both	LOMET data, no lapse rate
	Above C6	both	UPMET data, no lapse rate
Surface relative humidity	Glacier	both	LOMET data applied to glacier, no lapse rate
Wind Speed	Below C6	both	LOMET data, no lapse rate
	Above C6 until UPMET	both	UPMET data, no lapse rate
	Above UPMET	both	Repeated average hourly lapse rate from UPMET to Helbronner, calculated for 2010 and 2011
Incoming Shortwave	Below C6	both	LOMET data, no lapse rate, then adjusted for angle and aspect of slope
	Above C6	both	UPMET data, no lapse rate, then adjusted for angle and aspect of slope
Incoming longwave	Glacier	both	LOMET data lapsed using constant rate (-0.031 W m^{-2} m^{-1}, Marty *et al.,* (2002))
Rainfall	Glacier	both	LOMET data lapsed with 2011 mean LOMET to UPMET lapse rate (0.0026 mm hr^{-1} m^{-1})

The methods used to distribute the meteorological variables are in Table 3.8. The values were determined based upon the grid cell elevation, or the relation of the cell elevation to a threshold elevation. The threshold elevation for incoming shortwave radiation and wind speed values was C6 (elevation 2218 m), because this approximately marks the transition from the upper glacier which is confined within the glacier trough walls (where shading is increased and wind speeds are lower), and the lower glacier where there is less shading and higher wind speeds. These high wind speeds are caused by the Val Veny wind, which does not affect the upper glacier (Brock *et al.,* 2010). The wind speed above UPMET was increased upwards using the average lapse rate for each hour between UPMET and Helbronner (a meteorological station situated at 3460 m a.s.l. at Punta Helbronner, around 8 km from UPMET, data kindly provided by M. Vagliasindi from the Regional Functional Centre of Aosta Valley). This weather station is not on Miage Glacier, but is the only data at an appropriate altitude to capture the high elevation wind speeds where the glacier was not sheltered by the trough. This is important because of the sensitivity of the sensible and latent heat fluxes on wind speed.

The similarity of the sky view of points below and above C6 confirmed that, although a large simplification, the total incoming radiation across most of the lower and upper glacier should be reasonably represented by the measured data from the respective

meteorological stations (Figure 3.5). The calculation of the incoming shortwave radiation for each cell was based on methods by Brock and Arnold (2000). Measured incoming shortwave radiation was divided into direct and diffuse radiation using a cloudiness factor calculated as the ratio between measured and theoretical maximum incoming shortwave radiation for a cloud free sky. The calculation of direct and diffuse radiation required the slope aspect and angle to be calculated for each cell (found from the DEM (see below) in Arc GIS), and the sun height and azimuth for each hour (calculated using the 'sun_position' MATLAB function (Roy (2005), based on algorithms by Reda and Andreas (2008))). A full calculation of shading for each cell could be a future model refinement. Surface relative humidity was assumed constant over the glacier surface, and was required to identify when the debris surface was saturated and hence when latent heat was calculated.

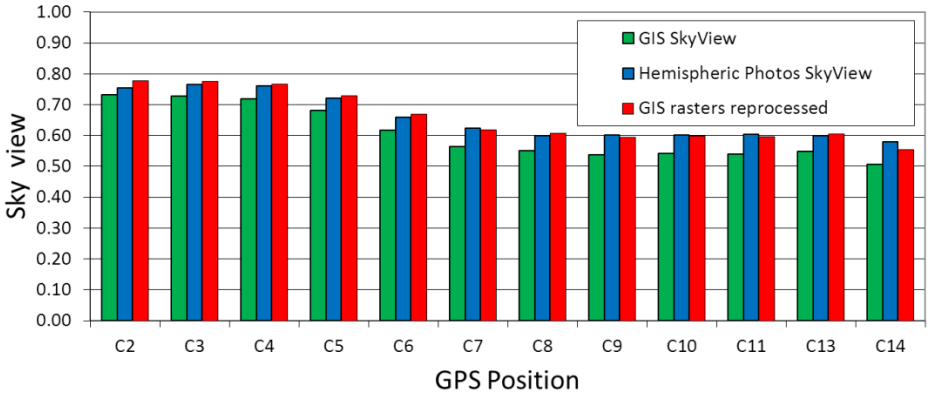

Figure 3.5 Sky view factors calculated for the GPS positions C2 to C14. Three different methods were used, the Sky View function of Arc GIS, processing of hemispherical photos, and the reprocessing of the Sky View rasters from Arc GIS using the software for the processing of the photos (analysis by C. Frew and T. Reid).

The air relative humidity was also taken from either UPMET or LOMET with no lapse rate. This is reasonable given that the relative humidity of the two stations was very similar. The LOMET relative humidity was on average higher than that at UPMET but in 2010 this was only by 3.8 %, small compared to the average daily variations in relative humidity of around 20 %.

There are a few caveats to the lapse rates used in Table 3.8. The first is that rainfall is assumed zero if the air temperature falls below 0°C, accounting for snowfall at higher elevations which is assumed not to runoff. Rainfall is calculated over the catchment area (Figure 3.6f), which follows the ridge around the glacier trough, rather than just over the glacier outline. The UPMET to ICEMET air temperature lapse rate is only used when the percentage snowcover on the UPMET cell is less than 50%, otherwise the air temperature difference between debris and ice will not be applicable as the debris is snow covered

(ICEMET data was collected only from July to September 2011). In this case the air temperature is lapsed upwards from UPMET using a constant lapse rate of -0.0041 °C m^{-1} (Oerlemans, 2010).

Evaporation is zero unless the rainfall is greater than 0 mm, and the current cell has a 'debris' surface type and a percentage snowcover less than 50%, in which case evaporation is 35% of rainfall (measured lysimeter data from 2010, section 4.4.1).

3.2.4.2 Remotely sensed data

The digital elevation model (DEM) was provided by the Agenzia Regionale per la Protezione dell'Ambiente (ARPA)(the Regional Agency for Environmental Protection, for the Aosta Valley), Italy and was produced from an airborne LiDAR survey in 2005, made of repeat aerial sorties (the ARPA DEM hereafter). It has a spatial resolution of 2 m, and a vertical accuracy of better than 0.5 m. It was resampled to a 30 m cell size and projected onto the WGS 84 UTM 32N coordinate system. It was clipped to cover the same area as the glacier outline to give a 329 by 216 cell grid (Figure 3.6c). All other grids have the same coordinate system and cell size, their bounding coordinates (representing the edge of the cells) are:

Top 5078798.49505

Left 329931.234071

Right 336411.234071

Bottom 5071628.49505

(WGS 84 UTM 32 N)

The 2005 orthorectified photo of Miage Glacier (provided by the University of Milan) was used to produce the glacier outline grid (Figure 3.6a). The outline of the glacier was digitised, which was a clear boundary along the majority of the main tongue and tributaries. Snow cones were included even if it was not known if they have glacier ice beneath them. At higher altitudes it was occasionally difficult to distinguish between snow patches and glacier ice, the snow was included if it was attached to the glacier, any snow patches or glacierets not attached to the main glacier were not included. On the lower glacier there may be areas of debris which do not have ice beneath them, but the thick debris cover makes this impossible to distinguish from debris-covered ice. The catchment outline (for calculating air temperature and rainfall) was produced similarly but the boundary used was the mountain ridge surrounding the glacier, and the outline of the lower glacier beyond the ridge. Separate streams drain the area outside the lateral moraines of the lower glacier, one of which collects water from Marmot Lake and the Brouillard Glacier to

the north of the glacier's bend, and another drains the Lac du Combal to the south-west of the lower glacier moraines, see Figure 1.1. However, the majority of rainfall which falls within the upper trough should drain into the glacier and the Miage Glacier proglacial stream.

The surface cover type was determined using the 2005 orthophoto. The glacier surface was described as consisting of debris, clean ice or dirty ice, with the outline of the glacier used as the outer limit (Figure 3.6b). A debris-covered surface includes areas where the debris is continuous (even if thin) and includes areas of snow from snow cones or patches which are otherwise below the mean transient snowline, as debris likely underlies snowcover here. The clean ice category includes areas of snow on the upper glacier. Areas of dirty ice were where the debris cover was discontinuous, although the boundary between mainly clean and dirty ice is difficult to determine, so the elevation limit at which the next elevation zone contained mostly clean ice (2600 m a.s.l.) was used as a boundary. The shapefile of the boundaries between the different surface covers was converted into a raster using the maximum area method.

As data on the snowcover over the glacier from the field is limited to photographs taken during field campaigns, MODIS snow cover data was used, as this is available daily and covers the entire glacier. An account of the change in snowcover over the season is necessary because it will change the quantity of melt produced, and provides information on when the melt from the dirty ice on the upper glacier occurs. Snowcover was found from analysis of the MODIS10A snowcover product, which generates daily percentage snowcover in 500 m tiles. MODIS snowcover tiles were downloaded from NASA and reprojected using the MODIS Reprojection Tool available from the USGS (https://lpdaac.usgs.gov/lpdaac/tools/modis_reprojection_tool). The spatial extent of each tile was changed so it matched the other grids, the coordinate system was changed from its sinusoidal projection into WGS84 UTM 32N, and the cell size was resampled to 30 m from 500 m (Figure 3.6e gives an example snow cover grid for day 159). No more data is produced by sampling at a smaller cell size, but it means the grid produced matches the other grids.

MODIS snow cover tiles can be unsuitable because of cloud covering the study area, or because of missing or erroneous data. Therefore tiles were chosen on days in which snow cover data was available for the entire study area. Individual cells can show large variations in percentage snow cover which are larger than likely caused by melting or snowfall. Therefore an average of two cloud free tiles which were within a few days of each other were used as a reference day, which was assigned to the middle day between the two measured days. Several reference days were identified for the summer of 2010, days 155,

174, 187, 210, 235 and 255, and for 2011 days 149, 178, 184, 228, 232, 251 and 265. Due to the absence of completely cloud free tiles near the end of the season, day 255 in 2010 was used without averaging with another tile, and despite some missing data. For any cells with missing data the percentage difference between day 235 and 255 was assumed zero. The percentage snow cover for each day in between the reference days was found by calculating the percentage difference in snowcover between each reference day and dividing this by the number of days between the reference days (the daily percentage difference). The daily percentage difference was subtracted from the first day, to give the second day's snowcover, and so on. As increases in snowcover were generally only a couple of percent and within the error of the MODIS data, the reference days were adjusted so a following reference day did not have more snow in a specific cell than the preceding reference day. The percentage loss of snow per day was calculated separately between each of the reference days. The rate of snow loss was greater earlier in the season, but became less later in the season as the remaining snow was confined to higher elevations. The resulting tiles of snow cover for each day were used as the daily percentage snow cover within the model.

Although a visual check of the snowcover with photographs in June matched well for both years, the end of July snow cover was greater on the snow cover grids than in photographs. To account for this in 2010, the average day 210 was modified to match the photographs taken on day 212, using an estimate of the elevation below which snow cover was negligible (using a feature such as a bend in the glacier or confluence of a tributary to identify the elevation). The glacier was deemed snowfree below 3000 m a.s.l. on the Mont Blanc and Dome Glaciers, and below 2600 m a.s.l. on the rest of the glacier. In 2011 there was not a reference day close to when photographs were taken, so a new reference day was created from the previous day 213 tile, and modified so the glacier was snowfree below 3000 m a.s.l. on the main tongue, 2600 m a.s.l. on Tête Carrée Glacier, 3070 m a.s.l. on Dome Glacier, and below 3200 m a.s.l. on Mont Blanc Glacier. The new average day tiles were used to recalculate the grids of snowcover for each day. It is unknown why mid-season snow cover was overestimated, but this highlights the difficulties in using MODIS snowcover data over relatively small glaciers.

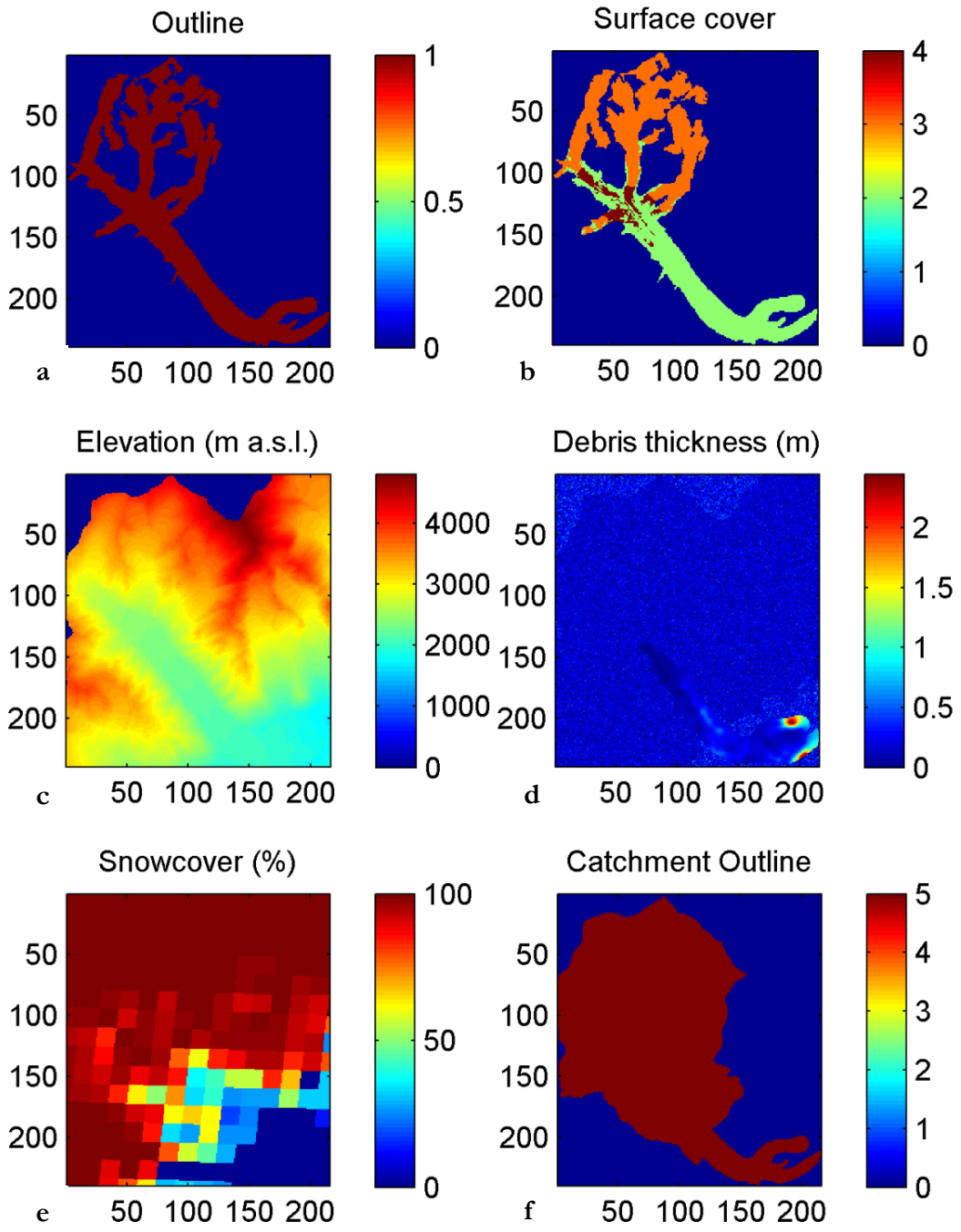

Figure 3.6 Graph of grids used as input data for the distributed energy balance melt model: a) is the glacier outline grid, a value of 1 signifies a glaciated cell, b) is the surface cover grid, a value of 2 is a debris covered cell, 3 is a clean ice or snow cell, and 4 is a dirty ice cell, c) the elevation grid used, d) the debris thickness grid used, e) an example snow grid (day 159 2010), and f) the catchment outline grid, a value of 5 signifies a cell within the catchment.

The debris thickness data used in the model was produced by Foster *et al.* (2012) using an energy-balance approach to estimate the debris thickness from ASTER AST08 thermal imagery and meteorological data. The energy balance components were distributed across the glacier for the time of image acquisition, and combined with remotely sensed debris temperature values to derive the debris thickness. The data used in the model were

calculated with an aerodynamic roughness length of 0.016 m. The point data provided by Foster *et al.* (2012) was interpolated onto a 30 m grid, and clipped to cover the same area as the other grids. Unfortunately, the data was only available to approximately 2370 m a.s.l. along the centre of the glacier, and to 2330 m a.s.l. and 2350 m a.s.l. on the western and eastern sides of the glacier respectively (Figure 3.6d). Above these elevations the debris thickness was modelled using a normal distribution with the mean and standard deviation of the distribution (mean 0.16 m, standard deviation 0.097 m) from the 2006 upper transect of debris thickness measurements made by Foster *et al.* (2012) at an elevation of 2334 m a.s.l.. A proportion of this distribution gives negative debris thicknesses, which were changed to zero.

3.2.4.3 Energy balance equations

The energy balance equations used are those used by Reid and Brock (2010), the code was kindly made available by T. Reid. The equations used will only be briefly replicated here; refer to Reid and Brock (2010) for details. The parameters used in the distributed energy balance model are given in Table 3.9. The energy balance equations and the calculation of the melt produced for debris-covered ice (equations 3.5 and 3.6) which is the DEB-model, and clean ice, snow and dirty ice (equation 3.7) which is the clean ice model, are given below:

$$M = S + L + H + LE + P + G \ , \tag{3.5}$$

$$a = \frac{G_i \Delta t}{\rho_w L_f} \ , \tag{3.6}$$

$$a = \frac{\Delta t}{\rho_w L_f} [(1 - \alpha_i) S\downarrow + L\downarrow + H + LE + P] \ , \tag{3.7}$$

where a is the ablation for the time step (m w.e.), M is the energy available for melt, S is the net shortwave radiation, L is net longwave radiation, H is sensible heat transfer, LE is latent heat transfer, P is the heat flux due to precipitation, G is the conductive heat flux beneath the surface, Δt the model time step, ρ_w the water density (kg m^{-3}), L_f the latent heat of fusion of water (J kg^{-1}), α_i is the clean ice/snow/dirty ice albedo and G_i is the conductive heat flux which reaches the ice. All radiation fluxes are in W m^{-2}. The equations for the surface fluxes of both models used are given below. The conduction of heat or

penetration of shortwave radiation into snow or ice was not modelled, and the snow or ice surface was assumed to remain at 0°C. The different surface types (clean ice, dirty ice and snow) modelled by the clean ice model are differentiated through the use of different emissivity, surface roughness length and albedo values. On the crevassed regions of the steep tributary glaciers, the Dome, Mont Blanc, Tête Carrée and Bionassay Glaciers, the surface roughness length was increased to 0.05 m (found over ice hummocks 1-1.5 m in height (Obleitner, 2000)). The crevassed regions were delimited using elevation bands derived from inspection of the 2005 aerial photograph and the ARPA DEM. As the surface roughness increases as snowcover reduces and ice surfaces are exposed, the increase in roughness was only applied when the percentage snowcover was less than 50%.

The DEB model firstly solves the energy balance at the surface, but to do this one needs the debris surface temperature. To solve this problem the model solves the energy balance numerically; so that it varies the debris surface temperature until the sum of the heat fluxes at the debris surface is zero, using the iterative Newton-Raphson method:

$$T_s(n+1) = T_s(n) - \frac{F(T_s(n))}{F\prime(T_s(n))}, \quad (3.8)$$

where $F'(T_s)$ is the derivative of the total surface flux with respect to T_s (the debris surface temperature, °C), and is calculated numerically by the central difference method. For each model time step $T_s(n=0)$ must have an initial value, so for the first time step it is equal to the air temperature, and for further timesteps it is the value from the previous time step. Equation 3.8 is repeated until $|T_s(n+1) - T_s(n)| < 0.01$. To calculate the conduction of heat through the debris to the ice/debris interface equation 3.9 is used:

$$\rho_d C_{pd} \frac{\partial T_d(z_d,t)}{\partial t} = \frac{\partial}{\partial z_d}\left(K \frac{\partial T_d(z_d,t)}{\partial z_d}\right), \quad (3.9)$$

which uses the partial derivatives of temperature, T_d, with respect to time, t and depth in the debris, z_d (m), where ρ_d is debris density (kg m^{-3}), C_{pd} is the debris specific heat (J kg^{-1} K^{-1}) and K is the debris thermal conductivity (W m^{-1} K^{-1}). The debris layer is split into 10 equally sized calculation layers and a numerical algorithm is applied which has boundary conditions of T_s and the debris temperature at the ice/debris interface (assumed the melting point T_f = 273.15 K). The equations for the surface fluxes are as follows; shortwave radiation:

$$S = (1 - \alpha_d)S\downarrow, \quad (3.10)$$

where α_d is the debris albedo and $S\downarrow$ is the incoming shortwave radiation derived from measured data and adjusted for the aspect and angle of the slope. Outgoing longwave radiation ($L\uparrow$) was calculated from the Stefan-Boltzmann law, equation 3.11:

$$L\uparrow = -\varepsilon_d \sigma T_s^4, \quad (3.11)$$

with ε_d the debris surface emissivity, and σ the Stefan-Boltzmann constant (W m^{-2} K^{-4}). The incoming longwave radiation was from measured data. The turbulent and sensible heat was calculated using the bulk aerodynamic method, using the Richardson number (R_b) to calculate the stability of the surface layer:

$$R_b = \frac{g(T_a - T_s)(z_a - z_0)}{T_m u_w^2}, \quad (3.12)$$

with $T_m = (T_a + T_s)/2$ and T_a is air temperature (°C), u_w is wind speed (m s^{-1}), g is gravitational acceleration (9.81 m s^{-2}), z_a is the height at which u_w and T_a are measured (always LOMET instrument height, m), and z_0 is the aerodynamic roughness length (m). The equation for sensible heat is:

$$H = \rho_a \frac{C_{pa} k_v^2 u_w (T_a - T_s)}{\left(ln\frac{z_a}{z_0}\right)\left(ln\frac{z_a}{z_{0t}}\right)} (\Phi_m \Phi_h)^{-1}, \quad (3.13)$$

where ρ_a is air density (kg m^{-3}) calculated using the ideal gas law, within which the air pressure is based on the elevation, C_{pa} is the specific heat capacity of air (1010 J^{-1} kg^{-1} K^{-1}; Oke, 1978) which is corrected for a humid atmosphere and k_v is von Karman's constant (k_v = 0.41). The scalar length for heat, z_{0t}, is considered equal to z_0. The non-dimensional stability functions for momentum (Φ_m) and heat (Φ_h) are expressed as functions of the bulk Richardson number (Brutsaert, 1982; Oke, 1978):
stable case, with momentum forces dominating and R_b positive:

$$(\Phi_m \Phi_h)^{-1} = (1 - 5R_b)^2, \quad (3.14)$$

unstable case, with buoyancy forces dominating and R_b negative:

$$(\Phi_m \Phi_h)^{-1} = (1 - 16R_b)^{0.75}. \quad (3.15)$$

Latent heat is calculated as:

$$LE = \rho_a \frac{L_v {k_v}^2 u_w (q_a - q_s)}{\left(ln\frac{z_a}{z_0}\right)\left(ln\frac{z_a}{z_{0q}}\right)} (\phi_m \phi_v)^{-1}, \quad (3.16)$$

where L_v is the latent heat of vaporisation of water (J kg^{-1}), q_a and q_s are the specific humidity at the measurement height and at the surface respectively, and z_{0q} is the surface roughness length for humidity, considered equal to z_0. During initial model runs it became apparent that under light wind conditions, and when the air was much warmer than the surface, R_b would become large and result in a very large positive sensible heat flux. This is because there is a critical Richardson number beyond which turbulence ceases (the air becomes stable) and the air flow is laminar. There is debate about the exact value of the critical Richardson number because of the difficulty in defining when turbulence ceases, with values between 0.2 and 1 suggested (Andreas, 2002). The generally accepted value is 0.2 (Essery, 2012, pers. comm.) and so when R_b is greater than this it is set equal to zero. R_b can also become very negative when the debris surface temperature is much greater than the air temperature, this is because when R_b is less than -1 free convection dominates (very unstable conditions) (Oke, 1978). Therefore if R_b is less than -1 it is set to zero. The latent heat flux is assumed to only occur if the surface relative humidity is 100%. The heat flux due to precipitation is calculated using:

$$P = \rho_w C_{pw} R_r (T_t - T_s), \quad (3.17)$$

where ρ_w is the density of water (kg m^{-3}), C_{pw} is the specific heat capacity of water (J kg^{-1} K^{-1}), R_r is the rainfall rate in m s^{-1} and T_r is the rain temperature (°C), which is set equal to T_a. The conductive heat flux, G, at the surface of the debris is approximated using T_s and the temperature of the debris at the first calculation layer, $T_d(1)$:

$$G = K\left(\frac{dT_d}{dz_a}\right)_{surface} \approx K\frac{T_d(1) - T_s}{h_l}, \quad (3.18)$$

where h_l is the calculation layer thickness (m), and K is the debris thermal conductivity (W m^{-1} K^{-1}). To calculate glacier melt the conductive heat flux which reaches the glacier ice, G_i, is calculated. This depends on the temperature gradient at the base of the debris:

$$G_i(t) = K\left(\frac{dT_d}{dz_a}\right)_{base} \approx K\frac{T_d(N-1)-T_f}{h_l}. \quad (3.19)$$

Table 3.9 Parameters used in distributed energy balance model. *As no other data available, dirty ice roughness length is the same as clean ice. **Value for 50% debris cover.

Parameter	Reference	Value	Units
Altitude of LOMET	Altitude of C1, 05/06/10	2066	m a.s.l
Altitude of UPMET	Altitude of E1, 07/06/10	2357	m a.s.l.
Altitude of ICEMET	Handheld GPS July 2010	2411	m a.s.l.
Air temperature, wind and RH measurement height (LOMET and UPMET)		2.16	m
Air temperature measurement height (ICEMET)		1.47	m
Debris thermal conductivity	Brock *et al.,* 2010, p 9	0.96	W m^{-1} K^{-1}
Debris density	Brock *et al.,* 2010, p 10	1496	kg m^{-3}
Debris specific heat capacity	Brock *et al.,* 2010, p 10	948	J kg^{-1} K^{-1}
Debris aerodynamic roughness length	Brock *et al.,* 2010, p 10	0.016	m
Debris albedo	Brock *et al.,* 2010, p 3	0.13	
Debris emissivity	Brock *et al.,* 2010, p 4	0.94	
Clean ice aerodynamic roughness length	Brock *et al.,* 2006 p 288	0.007	m
Clean ice albedo	Brock *et al.,* 2010, p 5	0.34	
Clean ice emissivity	Reid and Brock, 2010, p 906	0.97	
Dirty ice aerodynamic roughness length	Brock *et al.,* 2006 p 288	0.007*	m
Dirty ice albedo	Brock *et al.,* 2000, p 683	0.2**	
Dirty ice emissivity	Casey *et al.,* 2012, p 90	0.96	
Snow aerodynamic roughness length	Brock *et al.,* 2006, p 288	0.002	m
Snow albedo	Brock *et al.,* 2000, p 685	0.52	
Snow emissivity	Reid and Brock, 2010, p 906	0.97	

3.2.4.4 Model structure

The main model consists of a loop that runs over time, and then over the grid (Figure 3.7). It chooses the correct snow grid for the day, and then an 'if' loop selects grid cells within the catchment, for which the air temperature, rainfall and evaporation are calculated, then cells within the glacier outline are selected, for which the meteorological variables are calculated. The initial surface and within debris temperatures are set for use in DEB model. An 'if' loop distinguishes between completely snow covered, completely snow free, or partially snow covered grid cells. If the cell is completely snow covered then only the snow model is run (clean ice model with snow parameters). If the cell is partially snow covered then the snow model is run (called snow melt) as well as the appropriate melt model for the type of surface cover (clean ice (clean ice model with clean ice parameters), dirty ice (clean ice model with dirty ice parameters) or debris covered ice (DEB-model),

called ice melt). The overall melt is the snow melt multiplied by the fraction of snow cover plus the ice melt multiplied by the snow free fraction. If the cell is snow free then the appropriate melt model for the type of surface cover (clean ice, dirty ice or debris-covered ice) is run and gives the melt for the cell. Although melt for debris-covered cells will usually be modelled by DEB-model, the very high melt rates generated by very thin debris are unrealistic, and so if the debris thickness of a cell is less than 0.01 m, the dirty ice model is run instead.

Melt is summed for each time step to give total melt over the season for the entire glacier. A time series of melt is the sum of all cell values multiplied by 900 (to account for the 30 m cell size) for each hour divided by the number of seconds in an hour to give a value in $m^3 s^{-1}$. Time series of individual fluxes and meteorological variables are calculated by summing the values for all cells and dividing by the number of cells within the glacier outline or catchment as applicable, to give a mean for each hour.

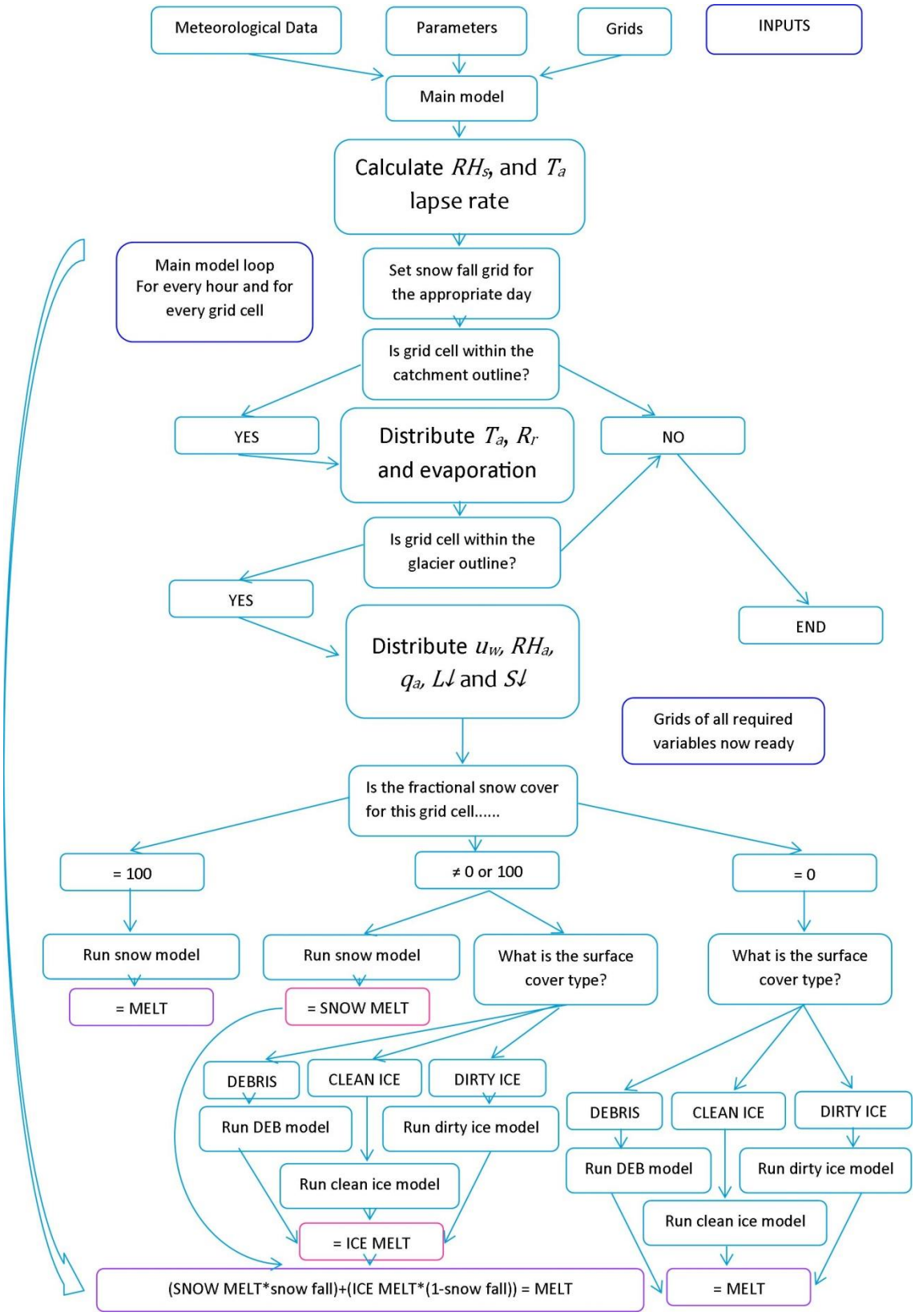

Figure 3.7 Diagram of melt model structure. Note that melt is calculated in either one of three ways, to give only one melt value (shown in purple). Symbol definitions are given at the start of the thesis.

3.3 Dye tracing and supraglacial streams

Dye tracing was carried out to ascertain the efficiency of the englacial and subglacial drainage system at different times of year and from different parts of the glacier. This was to answer the second aim of the project of understanding the structure and evolution of the hydrological drainage system. The discharge and velocity of supraglacial streams was measured to give the characteristics of the input hydrograph entering different parts of the glacier.

3.3.1 Dye Tracing

All dye traces were carried out using Rhodamine WT liquid dye which had a concentration of 21% by weight (Keystone Aniline Corporation, 2002). The quantity of dye to be injected was estimated initially using equation 3.20:

$$V_{di} = 3.14 \times 10^{-4} \left(\frac{0.305 Q_{max} d_d}{0.045 u_d} \right)^{0.94} C_{ds}\,, \qquad (3.20)$$

where V_{di} is the volume of Rhodamine (l), Q_{max} is the maximum stream discharge at the downstream site ($m^3\ s^{-1}$), d_d is the distance to the downstream site (km), u_d is the mean stream velocity ($m\ s^{-1}$) and C_{ds} is the peak concentration at the downstream sampling site (ppb) (adjusted to SI units from Kilpatrick and Wilson (1989)), as well as knowledge of the quantity of dye used by other investigators. Apart from the first 'test' trace the quantity of dye used was between 40 and 280 ml per injection. The dye was transferred into small 40 ml bottles, with the number of bottles filled giving the quantity of dye injected. The dye from these small bottles was transferred into up to two larger glass bottles prior to injection, so all dye was injected simultaneously. It was ensured that as much of the dye as possible entered the stream, although where access was difficult some dye was lost on nearby ice or rocks. The time of injection, quantity of dye injected, and GPS position of the injection site was noted after each injection.

The dye trace was detected at the gauging station on the northern lobe proglacial stream using a Seapoint Rhodamine fluorometer (during all of 2010 and June 2011) or a Turner Cyclops-7 fluorometer (July, August and September 2011). The fluorometers were recorded by a Campbell logger (mainly a CR500, until 14/06/11 when it was replaced with a CR10X) at either 5 or 1 minute intervals. The fluorometers were calibrated in the field using stream water measured into two buckets and dye measured using an accurate μml

pipette. A measure of the background fluorescence was taken prior to addition of dye. The calibration was repeated for each fluorometer and dye lot, with the relationship forced through zero so the background fluorescence gave a concentration of zero (Figure 3.8). The fluorometers were calibrated in the field to insure the water temperature was similar to during a trace, because water temperature is the most significant factor that varies the relationship between fluorescence and dye concentration (Wilson *et al.,* 1986). The fluorescence of Rhodamine WT is stable within a pH range of 5.5 to 11 (Keystone Aniline Corporation, 2002), none of the pH values measured at the gauging station or supraglacial streams had a pH above 11, there was one day in 2010 when the pH dropped below 5.5 but there were no dye traces conducted on this day. Dye can be adsorbed onto sediment and organic material (Wilson *et al.,* 1986), although the tendency of Rhodamine WT to stain suspended matter is low (Keystone Aniline Corporation, 2002). The background fluorescence measured by the fluorometer is positive and varies, probably because of the presence of suspended sediment which can fluoresce within the same wavelength band used for dye detection (Hubbard and Glasser, 2005). This was taken into account when interpreting traces, see section 5.

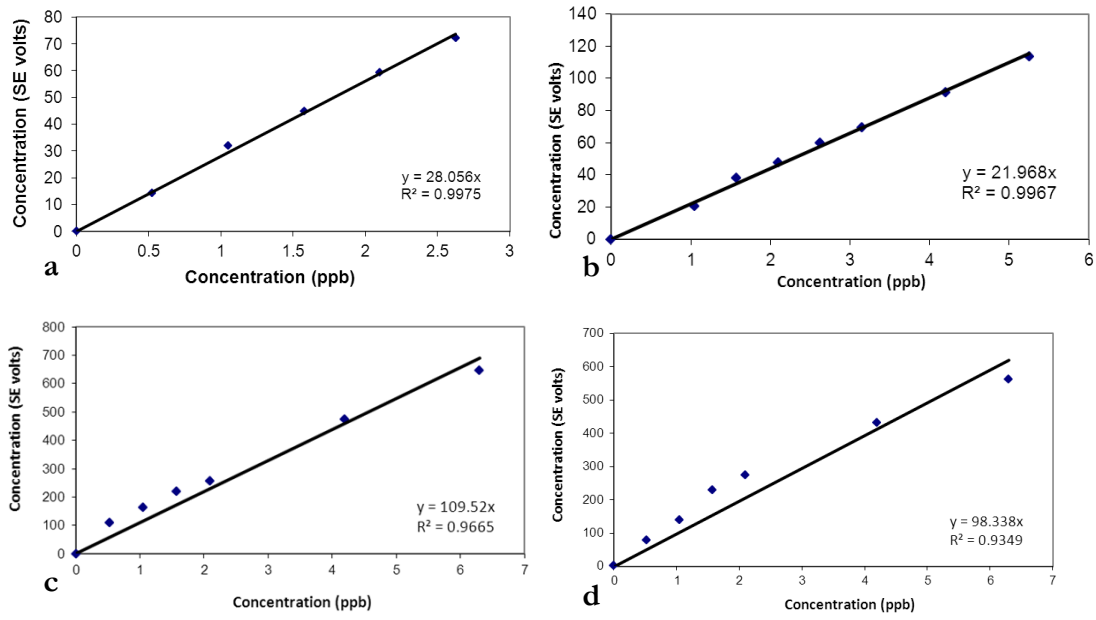

Figure 3.8 Calibration relationships between dye concentration and SE volts as measured by the fluorometer: a) Seapoint fluorometer and dye lot 1, b) Seapoint fuorometer and dye lot 2, c) Cyclops fluorometer and dye lot 2, and d) Cyclops fluorometer and dye lot 3.

Injection points during 2010 were chosen to cover as much of the glacier as possible, and although efforts were made to repeat injections during different field visits, this was only possible for one injection point. While it was intended to use injection points which led directly into a moulin, this often was not possible, especially where debris was thick. Streams often flow beneath the debris, making it difficult to inject dye, and they may

only be visible for a short section, with no indication of where they become englacial. In some cases the difficulty in reaching a moulin due to the stream or moulin forming within steep ice cliffs, meant an injection point was found further upglacier. A total of 23 dye injections were carried out during 2010, using 14 injection points. However, only 13 traces were successfully detected. Of the unsuccessful traces, 5 were due to missing logger data, and 2 traces were unsuccessful because the fluorometer malfunctioned. There were 3 traces which were not detected, even though the fluorometer and logger were working. In these cases, one was unsuccessful because the quantity of dye injected was too low, and the dye from the other two likely emerged from the small southern lobe stream (this was much smaller than the northern lobe stream, and all other traces were detected emerging from the northern lobe).

During 2011 the execution of repeat injections at individual points was emphasised. Five injection points were chosen, two on the lower glacier debris zone, and three on the upper glacier debris zone. The three upper points were intended to be spread equally along the glacier, but following an extensive search the only moulins found were all in a relatively small area, with no other moulins found a considerable distance above this area (up to above the join of the Dome glacier with the main glacier (Figure 3.1d, note S14b was a stream that led into S14.)). The two lower debris zone points had small input streams compared to two of the three upper points, this was not intentional, but purely due to the difficulty in finding large streams on the lower glacier. In 2011, 25 dye injections were carried out, of those 5 were unsuccessful. Two traces were unsuccessful because of logger data loss, during one trace the fluorometer had to be removed before the trace had arrived, and two traces had very variable background fluorescence, making it impossible to distinguish the trace from the background fluorescence.

Once the dye trace had been obtained the background fluorescence was calculated and removed and the appropriate calibration applied depending upon the dye lot and fluorometer. Several parameters were calculated from each trace. First the time to peak (t_m), and time to half the peak on the rising (t_1) and falling (t_2) limb of the trace was found. From the time to peak the minimum trace velocity was calculated using equation 3.21:

$$u_d = \frac{d_d}{t_m}, \tag{3.21}$$

where u_d is the trace velocity (m s^{-1}), d_d is the straight line distance to the injection site (m) and t_m is the time taken between injection and the peak of the return curve (s) (Nienow *et al.,* 1998, p 828). Due to the bend in the glacier as it leaves its trough, a straight line

distance could not be used for the upper traces. For all traces below S4 the direct distance from the injection site coordinates and the gauging station was used, for all traces above this point the distance between the injection point and S4 was used and added to the distance between S4 and the gauging station to give the total distance. The velocity is a minimum because the actual distance the water travelled will be greater than measured due to stream sinuosity. The dispersion coefficient (D) and dispersivity (b) which give a measure of the dispersion rate of the dye return curve and the dispersion relative to the trace velocity respectively, were also calculated (section 2.4 and equations 2.16 and 2.17). The apparent mean cross sectional area (A_{sm}, m^2) was calculated (during 2011 only) using equation 3.22:

$$A_{sm} = \frac{Q_m}{u_d}, \tag{3.22}$$

where Q_m is the mean discharge between the injection and detection point, calculated as the average of the supraglacial and proglacial stream discharge over the time of the test (from injection until the end of the trace return curve) (Nienow *et al.,* 1998, p 828). Using the mean discharge decreases the possibility of overestimating the cross sectional area, although a slightly different method was used to calculate Q_m compared to Nienow *et al.* (1998), because in this study the input supraglacial discharges were measured (section 3.3.2) and were assumed constant over the time of the test. If there was a gap in the proglacial stream discharge data the detection point discharge was derived from the nearest noted stage measurement. To find the volume of dye recovered (V_{dr}, ml) the equation used to calculate the discharge of a stream from the slug-injection method (Kilpatrick and Cobb, 1985, p6) was rearranged (equation 3.23):

$$V_{dr} = \frac{S_G^{-1}\left(\frac{1}{1.649\times10^{-8}}(Q_{mp}A_c)\right)}{C_d}, \tag{3.23}$$

where S_G is the specific gravity of the dye used (1.15), Q_{mp} is the average discharge during the time taken for the dye curve to pass through ($m^3\ s^{-1}$), A_c is the area under the dye curve in ppb $minute^{-1}$, and C_d is the concentration of the dye prior to injection (ppb).

3.3.2 Supraglacial stream measurements

The discharge of the supraglacial streams in which dye was injected during 2011 was measured immediately before or after the dye injection. Two methods were used, either the velocity-area method, or salt dilution gauging. Dilution gauging was preferred, but field conditions meant this was not always possible.

The velocity area method involved measuring the width of the channel, and its depth at preferably 10 equally spaced points across the channel. The spacing of the depths was approximate due to the difficulty in securing a tape to the far bank of the stream. Velocity was measured by timing the passage of a float over a measured distance. This was repeated 10 times, but the trapping of a float by rocks in the channel meant the average number of velocity measurements was 8 (minimum 3). This surface velocity is an overestimate of the mean velocity averaged over the depth of the channel (found at 0.6 of the depth if measuring from the surface) due to the drag at the bed decreasing velocities (Dingman, 2002). Observations suggest the floats followed the stream thalweg and so travelled faster than the average route considering all possible paths. This was partly systematic, as floats which found slower routes would become trapped by rocks. The measured distance was sometimes underestimated due to being unable to completely follow the channel. The stream discharge is the average depth multiplied by the width, multiplied by the average float velocity.

To perform a salt dilution gauging the width of the channel was measured and used to inform the mixing length. An appropriate mixing length is 10 channel widths in turbulent channels to 100 channel widths for smoother flowing streams (Hubbard and Glasser, 2005), although the maximum mixing length was sometimes constrained by safety concerns or an upstream lake or confluence. The mixing length was kept consistent to improve comparability between gaugings. The salt (60 g) was measured volumetrically in a pre-calibrated container. Stream water was added to the container so the salt was dissolved before injection, with the container rinsed during injection to ensure all salt was injected. The conductivity was measured using a Hanna HI 9033 portable conductivity probe (Table 3.10) at 5 second intervals from before the time of injection (to give a background conductivity) to when the conductivity had returned to background levels. The exact time of the injection to the nearest second was noted. The conductivity probe was calibrated in the laboratory using 13 solutions of known concentration, composed of deionised water and the same salt as used in the field (Figure 3.9). The discharge was calculated using equation 3.24:

$$Q = \frac{w}{(1000A_c)}, \qquad (3.24)$$

where Q is the discharge ($m^3\ s^{-1}$), w is the mass of salt injected (mg) and A_c is the area under the concentration curve (mg l^{-1} s^{-1}), which is found by calculating the sum of all concentration values that constitute the curve (minus the background) and multiplying this by the time interval (5 s).

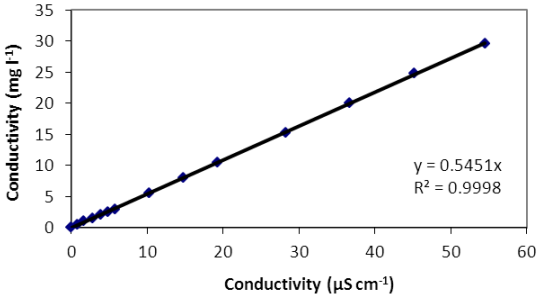

Figure 3.9 Calibration relationship between salt concentration and conductivity as measured by the conductivity probe.

To assess the precision of the dilution gauging method three gaugings were performed successively on the S15 stream. These gaugings gave an average absolute error from the mean of 0.00054 $m^3\ s^{-1}$, which was 4.08% of mean discharge. This gives confidence the technique can be reproduced accurately. A velocity-area gauging was performed at the same time but gave a discharge around twice that measured using dilution gauging (the velocity-area discharge was 0.022 $m^3\ s^{-1}$, but for dilution gauging was a mean of 0.013 $m^3\ s^{-1}$). This was because the stream velocity was overestimated using the float method as the mean stream velocity from the dilution gaugings (the distance between injection and detection point divided by the time between injection and peak of the concentration curve) was 0.27 m s^{-1}, but the mean float velocity was 0.65 m s^{-1}. The dilution gauging velocity is a better measure because it gives the average water velocity. Using the dilution gauging velocity with the velocity-area cross-sectional area gives a more comparable discharge of 0.0093 $m^3\ s^{-1}$. Therefore, to allow comparisons of the discharge variations for a particular stream one cannot compare discharges using two different methods. When a stream was only measured using the velocity-area method the stream velocity was altered using a ratio of dilution to float velocity found when a dilution and float velocity were performed simultaneously. This follows the method of multiplying surface velocities by a ratio (usually 0.85) to give the mean velocity across the channel's depth (Dingman, 2002). S14 however could only be measured using the velocity area

method, and sometimes only float velocities were measured, in this case they were multiplied by the stream's average cross sectional area, to give an estimate of discharge.

3.3.3 GIS analysis

GIS analysis was performed to understand the surface topography of the glacier and how this relates to the formation of the supraglacial stream network. This was used to increase the understanding of the input meltwater hydrograph for different parts of the glacier. The bed topography was digitised and used along with a digital elevation model of the glacier's surface to calculate the ice thickness. This was used to calculate conduit closure rates.

3.3.3.1 Surface topography analysis

A series of standard hydrological GIS analyses were performed in Arc GIS on a 2 m digital elevation model (the ARPA DEM) of the glacier's surface (Figure 3.10). Firstly, a filled DEM was produced which fills any depressions in the DEM. This is standard practice prior to hydrological analysis, although from a glaciological perspective means water will not be lost down moulins. Without this step however, supraglacial lakes would not be able to overflow and supply water downglacier, as they have been observed to do so. From the filled DEM a flow direction raster was produced which gives the direction of flow from each pixel. This raster was used to produce a flow accumulation raster, in which the number of pixels which drain to each pixel is computed, so pixels with a high value indicate the location of surface streams. The flow direction raster was also used to produce a flow length raster which gives the length of the flow line that ends at each pixel. The pixels with higher values suggest longer flow lengths, and therefore the location of streams. A watershed raster can be computed from the flow direction raster and a pour point (the catchment outlet). The watershed rasters for each dye injection point were found to determine the catchment size of each stream. Due to the 'filling' of the DEM, the watershed outlines produced from the lower glacier moulins included the catchments of the upper glacier moulins. Nesting the catchments accounted for this affect, although it assumes there are no other moulins apart from those used as injection points. For the maps produced see section 4.3.

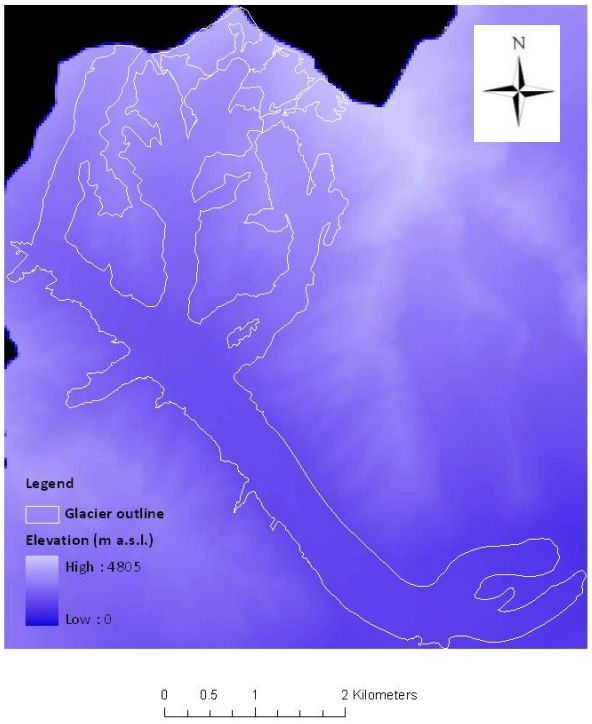

Figure 3.10 Map of the digital elevation model of Miage Glacier.

3.3.3.2 Bed Topography and conduit closure rates

The bed topography of Miage Glacier has been measured by several workers. In August 1957 4500 m of longitudinal profile was surveyed using seismic reflection by Carabelli (1961). Further seismic reflection work was carried out by Casati (1998) in October 1997 covering a 450 m longitudinal section just upglacier of the bend and again in June 1998, along the northern lobe. An indirect determination of the glacier ice thickness was performed by Lesca (1974) using a formula proposed by Somiglia (1972, cited in Deline, 2002), based on the glacier velocity (found from aerophotogrammetry of boulder displacement) and the glacier's bed slope. From these surveys Deline (2002) produced a bed topography map. This map was scanned and georeferenced so the outline of the bed map matched with the digitised glacier outline (section 3.2.4.2). It was difficult to achieve a good match between the outlines due to the lack of clear control points used to join the datasets. Rock outcrops and the position of the edges of the tributaries were used as control points, which provided a reasonable fit along the main tongue, but the lower lobes could not be well matched. The bed topography of the lower lobes must therefore be treated with caution. The bed contours were digitised into a point shapefile which was interpolated into a raster with a 25 m cell size (Figure 3.11a). The 2005 ARPA DEM was resampled to 25 m using a bilinear technique to allow calculations using both rasters.

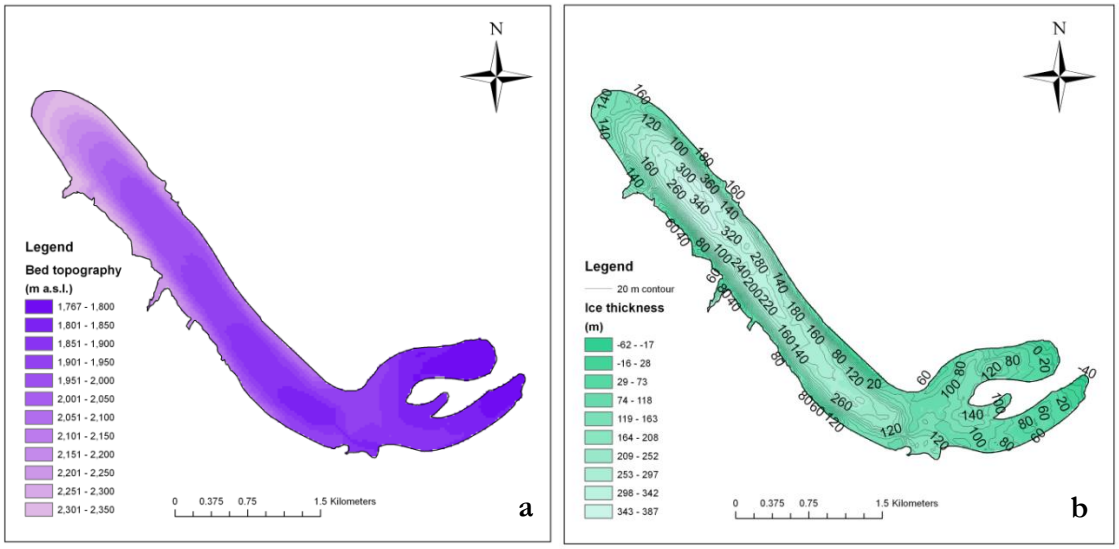

Figure 3.11 a) Map of the bed topography (based on data in Deline (2002)) and b) map of ice thickness.

An ice thickness map was produced by subtracting the bed topography raster from the surface DEM raster (Figure 3.11b). However, the ice thickness is overestimated by the depth of the debris, with the ice thickness overestimated most where the debris depth is greatest. Nonetheless, there are some areas where the ice thickness is negative on the edges of the lower lobes, due to the poor fit between the surface and bed rasters. It is presumed the elevation of the bed has stayed the same since the surveys were carried out, if this is the case then the ice thickness map is relevant to 2005 when the surface DEM was produced.

Conduit closure rates were calculated to give an indication of how far upglacier the main subglacial conduit system would remain open over winter. Following Hooke (1984, cited in Nienow *et al.,* 1998) the time, t (s) for a conduit to close to a given radius, r_r (m) is given by:

$$t = \frac{\ln(r_r) - \ln(r_i)}{\left(\frac{\rho_i g h_i}{n_G A_G}\right)^3}, \qquad (3.26)$$

where ρ_i is the ice density (920 kg m^{-3} at 0°C, Oke (1978)), g is gravitational acceleration (9.81 ms^{-2}, Oke (1978)), n_G =3 and A_G = 5.8 × 10^{-7} Pa s$^{-0.5}$, both constants in Glen's flow law (Nienow *et al.,* 1998). The ice thickness, h_i (m) was derived from the ice thickness map (Figure 3.11b) by extracting a profile of thickness measurements (at approximately 25 m intervals) from the proglacial stream portal, up the northern lobe and along the glacier centreline. The initial conduit radius r_i (m) was derived from linearly interpolating the measured input (0.20 m^3 s^{-1}) and proglacial stream discharge (6.38 m^3 s^{-1}) of the S12 stream

in September 2011, and dividing this by the trace velocity on this day (0.59 m s^{-1}) to give the channel cross sectional area (A_s, m^2) along the entire stream length. The radius of the assumed semi-circular channel was given by:

$$r_i = \sqrt{\frac{2A_s}{\pi}}. \quad (3.27)$$

The initial radius may be underestimated due to using only the input discharge of one of the main supraglacial streams (only the supraglacial stream velocity of S14 was measured in September 2011), and it is not known what distance the S12 channel travels before it confluences with the S14 conduit (or any other subglacial conduits). The resulting radius cannot be zero because of the logarithmic relationship between the time passed and the decrease in conduit radius, therefore a negligible conduit radius (0.01 m) was chosen.

3.4 Proglacial stream measurements

The third aim of the thesis was to understand the temporal variaitons in bulk water routing. This was achieved through analysis of the variations in the proglacial stream hydrograph and water chemistry. The discharge of the proglacial stream was also measured to quantify the runoff part of the water balance. The supraglacial water chemistry was measured to elucidate the debris' impact on the chemistry of the supraglacial streams.

3.4.1 Runoff

3.4.1.1 Stage measurement

The runoff from Miage Glacier was measured at a gauging station (GS, UTM 32 T 0335997 5072853, elevation 1777 m a.s.l., Figure 3.1a) set up just downstream of where the stream emerges from the glacier. Where the stream emerges it is broad and does not have a tall portal, but instead the water's surface is very close to, or in contact with, the ice forming the roof of the channel. The gauging station consisted of a plastic stilling well held onto a dexion frame bolted onto a very large boulder (Figure 3.12). The boulder did not move at any point during the field campaign. The stilling well had stage board markings which enabled stream stage to be measured by hand, allowing calibration and checking of the instrument measured stage. The stream at the gauging station was contained within one channel, although both upstream and downstream it was braided in places. There is no obvious control at this point on the stream, which made the creation of a rating curve

difficult. There were few large boulders in appropriate positions near the channel, and no bedrock outcrops, which constrained the location of the gauging station. The bed of the stream is composed of sediment ranging in size from silt to boulder. Sand sized sediment was mobile within the flow near the bed. The gauging station is located before any streams from other glaciers confluence with the Miage Glacier northern lobe stream. Another stream emanates from the southern lobe of Miage Glacier, but this is considerably smaller than the northern lobe stream and from dye tracing results has only a local catchment covering the southern lobe, while the northern lobe stream catchment covers the rest of the glacier (see section 5).

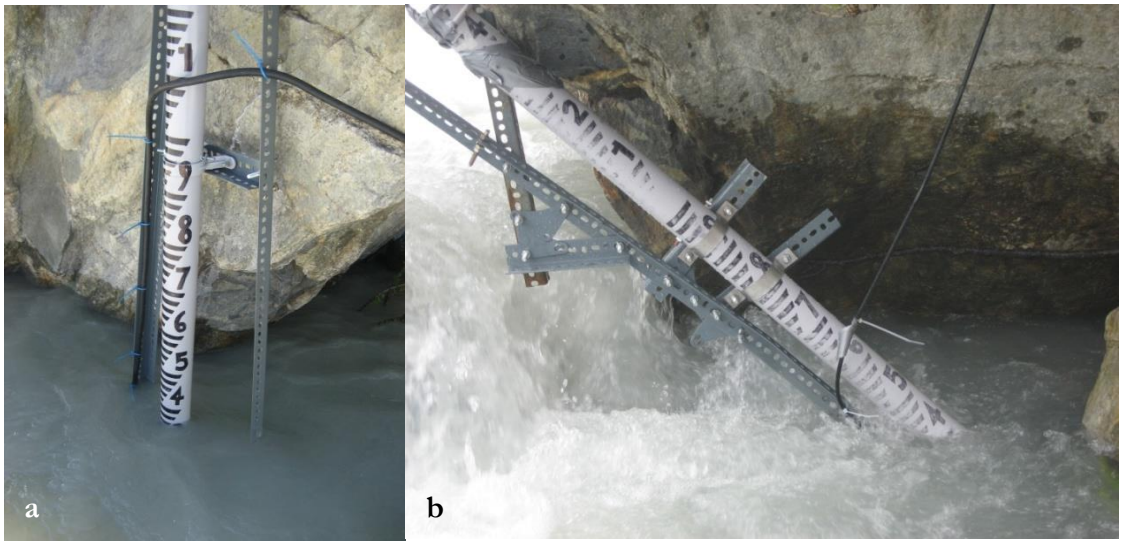

Figure 3.12 Photographs of the gauging station set up: a) during 2010 and June 2011, and b) from July 2011 onwards.

To measure stream stage a Druck PTX 1830 pressure transducer (Table 3.10) was hung within the stilling well. The Druck measures atmospheric pressure as well as total pressure to give the water depth in metres above a standard datum (ma SD). It was logged by a battery powered Isodaq logger. During 2010 data were stored every 15 minutes from day 156 at 19:30 until day 173 at 12:00 when it was changed to every 30 minutes, until day 251 at 14:45 when it logged every 15 minutes until day 255 at 12:45. There were some missing data due to configuration problems, day 174 at 12:30 until day 175 at 12:30, and occasionally when the water level was below the lowest point of the logger. High water levels between the August and September 2010 trips resulted in the stilling well becoming knocked out of its brackets, probably due to a boulder impact. This was obvious in the stage record, and happened on day 239 at around 16:30. This resulted in data loss until the stilling well reached a stable position (the data were corrected for the lower sensor height).

Table 3.10 Details of proglacial stream and water chemistry instruments.

Quantity	Manufacturer	Type	Accuracy
River level	GE Sensing	Druck PTX1830	±0.1% full scale (or ±0.06% full scale)
	Onset	HOBO U20 -001-04	±0.075% full scale, ±0.3 cm
Conductivity and temperature	Campbell	CS547A	±5% of reading 0.44 to 7.0 mS cm^{-1}, ±10% of reading 0.005 to 0.44 mS cm^{-1} ±0.4°C
	Hanna	HI9033 with HI 76302W probe	± 1% full scale(excluding probe)
pH	Hanna	HI 98140	±0.01 pH
	Hanna	HI 98128	±0.01 pH
Turbidity	Hanna	HI 93703	±0.5 FTU or 5% whichever is greater

During 2011 the Druck pressure transducer was reinstated within the stilling well, which was in the same position as in 2010, but at a slightly different height. The stage was logged every 15 minutes from day 155 at 14:15 to day 166 at 12:30, after which it logged at 30 minute intervals. Unfortunately at around 22:00 on day 169 there were very high water levels, during which time the Druck continued to record, but afterwards levels fell to a lower level than reasonable. During day 173 and 174 water levels rose again but the levels recorded were not stable, until at around 24:00 on day 174 when the level logged dropped suddenly. When the Druck was next visited (day 207) the bottom of the stilling well and the Druck were completely out of the water (despite the well having fallen in its brackets). The data from day 169 at 22:00 (corresponding with the peak of the flood) were therefore removed. By comparing the distance to the bed in June and July 2011 in relation to the same position on the dexion which had remained bolted onto the rock it was calculated that 0.34 m of bed scour had occurred. However this bed scour cannot be accounted for in the stage measurements because the rate and timing of scour was unknown. The stream morphology also changed so where there was calm water in the vicinity of the stilling well this was now turbulent. The dexion was reconfigured and the well attached at an angle, with the bottom of the well in calmer water nearer the bank edge (Figure 3.12b). The Druck had been damaged during the event and was replaced on day 215 at 13:00 by an Onset HOBO pressure transducer (Table 3.10). This instrument measures only total pressure but logs to its own internal memory. It measured at 15 minute intervals until day 259 at 10:00. To convert measured pressures into a water level in maSD, the effect of variations in air pressure were compensated for using the Onset HOBOware compensation tool. The air pressure data used was hourly and from Mont de la Saxe, near Courmayer (UTM 32T 0343098 5075613, 2076 m a.s.l., around 7.6 km from the gauging station), and were kindly made available by Fabio Brunier from Regione Autonoma Valle d'Aosta. The air pressure data were adjusted to account for the elevation difference between the gauging

station and the air pressure measurement site using the difference in standard air pressure at the two elevations.

The stage was also measured by observing and taking multiple photographs of the stilling well. This allowed logged stage to be checked, and was used to fill gaps in the logger data. This is particularly true in late July 2011 before the HOBO logger was installed. This means the daily average stage (and therefore discharge) data for these days are based on just a few (sometimes only one) measured stages. Measured stages were also used to calibrate the Druck and HOBO record so that values either recorded or later calculated (respectively) could be given in maSD. Measured stages are accurate to approximately ± 1 cm (the mean absolute difference between observed stage and the average stage taken from 3 to 5 photographs was 0.011 m in 2010, and for 2011 using 1 to 14 photographs, was 0.010 m). The accuracy of observed stage measurements is much less during high flow conditions and vice versa.

3.4.1.2 Discharge measurement

To construct a stage-discharge rating curve the discharge of the stream as it passed the gauging station was measured. This was achieved using dye dilution gauging (using Rhodamine WT dye) due to the fast nature of the stream. The length of stream used for the dilution gauging is the mixing length, which needs to be long enough to ensure the dye has mixed evenly across the channel, so the area under the dye curve at the bank where it is measured will be the same as in the centre of the channel (Kilpatrick and Cobb, 1985). For proglacial streams a rough rule is to use either 10 times the channel width for turbulent sections to 100 times the channel width for smoother reaches (Hubbard and Glasser, 2005), using an estimate of the channel width of 6 m this gave a 60 m mixing length. Another option is to use equation 3.28:

$$L_m = 260\sqrt{A_s}\,, \qquad (3.28)$$

where L_m is the mixing length (m), and A_s is the cross sectional area of the channel (m^2) (estimated as 3 m^2) (Kite, 1993, cited in Hubbard and Glasser, 2005). This gave a mixing length of 450 m. Unfortunately, the mixing length was constrained upglacier by the position of a tributary channel that entered the main channel at about 150 m from the gauging station, and so a point just downstream of this was chosen. The proglacial stream emerged from the glacier snout 20-30 m above this point. This position was advantageous as the stream was relatively narrow, which meant the dye could be injected across the

channel as far as possible. The position of dye injection for dilution gauging was kept consistent, although the distance was re-measured at the beginning of each field visit. The volume of Rhodamine WT 20% dye (V_{dg}, ml) required to carry out a successful dilution gauging can be found from:

$$V_{dg} = \frac{1.354 \times 10^{-3} Q L_m}{u_r} c_{ds} \,, \qquad (3.29)$$

where Q is the stream discharge ($m^3\ s^{-1}$), u_r is the stream velocity ($m\ s^{-1}$) and c_{ds} the intended concentration at the sampling site (ppb) (converted to SI units from Kilpatrick and Cobb, 1985, p 8). Using estimates of the stream discharge and velocity and an intended concentration of 10 ppb a value of just over 5 ml was given. This was successful in producing a clear peak in the dye return curve, although it was increased to 10 ml during high flow conditions.

To perform a dilution gauging 5 (or 10) ml of dye was measured into a small bottle accurately using a μml pipette, and this was poured into a bucket of stream water, with the bottle washed in the bucket. The bucket of water was added to the stream, ensuring the dye mixture went into the main flow as much as possible, and that the bucket was washed with stream water. The time was noted to the nearest second. The dye was detected at the gauging station with either a Seapoint Rhodamine fluorometer or Turner Cyclops fluorometer. The sensed measurements were noted every 10 seconds from a few minutes before the injection (to ensure accurate background fluorescence) until after the fluorescence returned to background. Equation 3.30 was used to calculate the discharge from the dye return curve:

$$Q = 1.6492 \times 10^{-8} \left(\frac{S_G V_{di} c_{di}}{A_c} \right), \qquad (3.30)$$

where S_G is the specific gravity of the dye used (1.15 in this case), V_{di} is the volume of concentrated dye injected in ml (5 or 10 ml), c_{di} is the concentration of the dye solution injected in ppb (21 x 10^7 ppb), and A_c is the area under the dye return curve in ppb $minute^{-1}$ (Kilpatrick and Cobb, 1985, p 6). The area under the curve was found by removing the background fluorescence and applying the correct calibration to convert fluorometer values into ppb (see section 3.3.1) and then all positive values were summed and multiplied by the time interval between each measurement.

3.4.1.3 Defining a rating curve

In total 29 dilution gaugings were performed throughout the 2010 and 2011 ablation seasons. However, not all could be used to construct the final rating curve. The first 8 dilution gaugings carried out during June and the beginning of August 2010, used 5 ml of Rhodamine WT dye measured using a plastic dropper. This was not thought accurate, but the other pipette was not reading correctly due to becoming clogged with dye. These 8 gaugings were discarded, but the dye for all other gaugings was measured using a µml pipette. Also, due to problems with the fluorometer (usually high background fluctuations, or erroneous readings) a further 5 gaugings were discarded. The stages at which dilution gaugings were performed was limited by the variation in river stage during each field visit. Separate curves for different times of year could not be created, as there were not enough gaugings covering a reasonable range of flows for each time period. It was thus not possible to ascertain whether the rating had changed between fieldtrips. Therefore, the stage of all gaugings was adjusted to correspond with the stage on the June 2010 stilling well. This included adjusting the September 2010 stage by the addition of 0.042 m, and adjusting the June 2011 stage by the addition of 0.025 m. The significant bed scour between the June and July 2011 meant the stage positions from July 2011 onwards cannot be directly related to the June 2010 well. However, at a stage of 0.397 maSD there were two gaugings performed during September 2010 with discharges of 3.77 $m^3 s^{-1}$ and 4.05 $m^3 s^{-1}$, and in September 2011 there was a gauging of 3.89 $m^3 s^{-1}$, which lies between these two. The September 2011 stage was higher than the 2010 stage by 0.032 m. All of the stage values from July 2011 onwards were lowered by this amount, after the stage values (if taken from measured stages) were converted from inclined to vertical measurements. This resulted in a second point from September 2011 also matching well with a point from the 2010 record, which suggests this adjustment was reasonable.

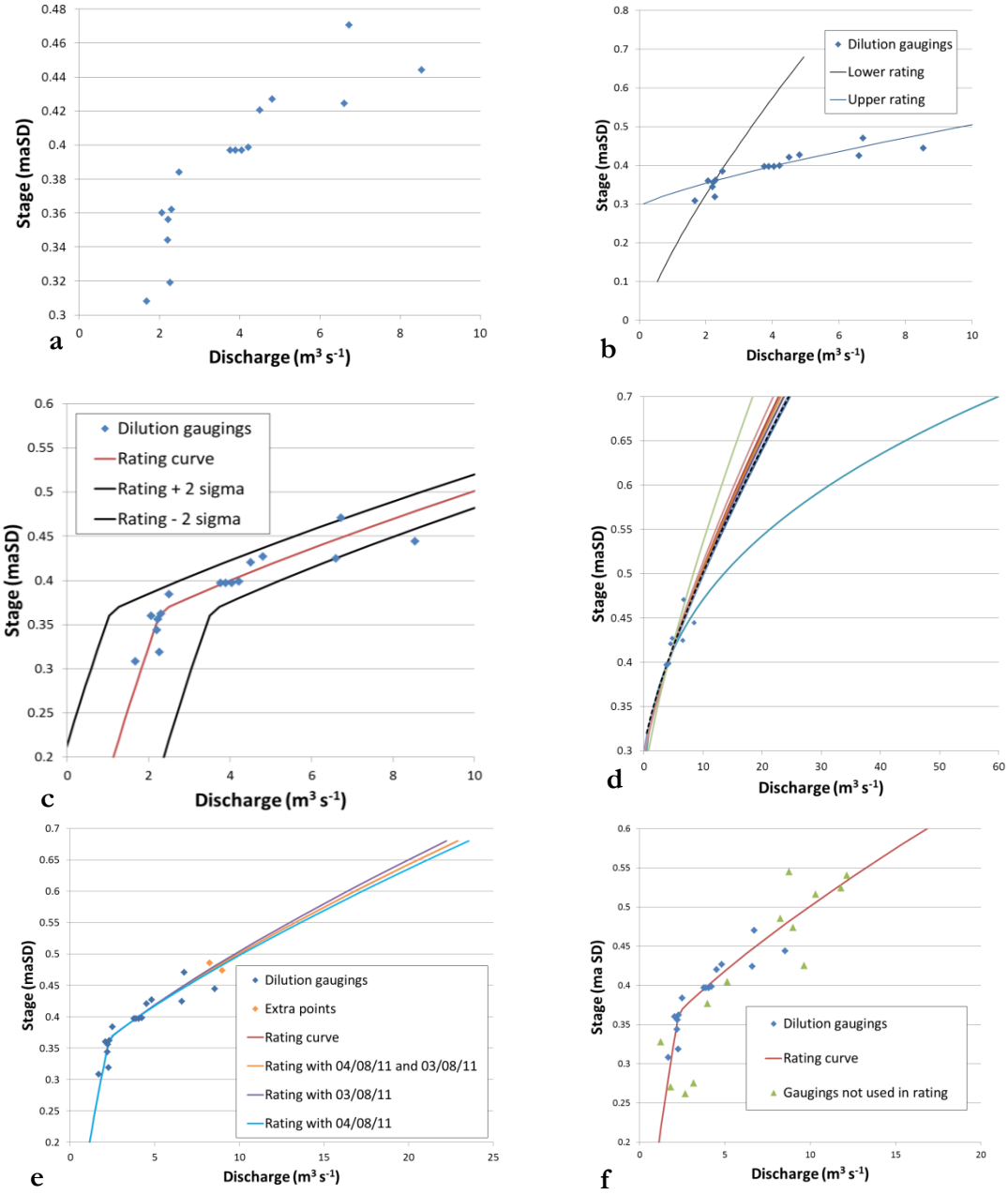

Figure 3.13 Graphs of the development of the rating curve: a) scatter graph of the river gaugings used in the production of the rating curve, b) the lower and upper ratings, showing their point of intersection, c) the final rating curve with error bounds of 2σ, d) sensitivity analysis, showing how the upper rating changed if one point was removed at a time, and e) the influence on the rating of the addition of two extra points at higher flows.

From the points in Figure 3.13a, there is a region of lower stages which has a rating relationship at a steeper angle than the upper points, suggesting the existence of a change in the rating between the upper and lower points. This is not unusual in river rating curves. The software Hydata (from the Centre of Ecology and Hydrology) was used to construct the curve. To find a reasonable position of the intersection between the lower and upper ratings, separate ratings for the two sets of points (separated around 0.39 maSD) were established (Figure 3.13b). In Hydata, this allowed the intersection point to be confirmed at

around 0.36 maSD (the second top point in the lower set of gaugings), as this is user controlled. The resulting rating curve (Figure 3.13c), was a power function of the form:

$$\boldsymbol{Q = x(h_r + z)^y}\ , \qquad (3.31)$$

where h_r is stage (ma SD), and for stages below 0.366 maSD it has the coefficients:

$x1$) 7.73 $y1$) 1.3 $z1$) 0.029,

and for stages above 0.366 maSD the coefficients are:

$x2$) 80.81 $y2$) 1.3 $z2$) -0.301.

In Hydata, the power coefficient, y, is constrained to between 1.3 and 2.8, to keep it within reasonable values for rivers, and both these curves were constrained in this way. This rating gives a standard error of the estimate of 0.76 $m^3\ s^{-1}$, which gave a percentage error of 14.6% using the average daily discharge in 2010 of 5.37 $m^3\ s^{-1}$. The standard error of the rating curve is 0.61 (following DHV Consultants (1999)) (Figure 3.13c). There was a larger spread of the gauged points at higher discharges, partly due to the difficulty in measuring an undulating stage during high flows. The stage used was usually from the pressure transducer. Due to limited gaugings at higher discharges, two of the high flow gaugings which were previously excluded due to producing less clear gaugings, were introduced to the rating one at a time, to see how this influenced the discharge at high flows (Figure 3.13e). The original rating curve lies almost exactly beneath the rating which includes both extra gaugings. The discharge at 0.7 maSD (a stage reached only very occasionally, the maximum stage in the 2010 record being 0.734 maSD) ranges from 23.8 $m^3\ s^{-1}$ to 25.2 $m^3\ s^{-1}$. This is a reassuringly small variation, but is probably due to the intersection point being defined, and also because the majority of points remain unchanged. To further study the variability at higher flows, each of the upper points was removed in turn and a new curve calculated. The resulting plot (Figure 3.13d) shows most curves were very similar giving a range of discharges at 0.7 maSD of between 18.4 $m^3\ s^{-1}$ and 24.7 $m^3\ s^{-1}$, with the upper curve of the chosen rating reaching 24.5 $m^3\ s^{-1}$ (dashed black). One of the ratings has a discharge at 0.7 maSD of 59.9 $m^3\ s^{-1}$, this was when the point on the 12th of September 2011 was removed, because this was the uppermost point which lay above the rating curve. It could be argued the rating should follow the lower curve, but considering that if the rating is shown alongside the gauged points which were not used to construct the rating (see Figure 3.13f), it matches well. The adjustments to the stage records were applied and this single rating equation used to calculate discharge for the full record of stage measurements in 2010 and 2011.

3.4.2 Water chemistry

3.4.2.1 Field measurements

The water chemistry of the northern lobe proglacial stream was measured at the gauging station. As well as measurements collected by hand, continuous conductivity and water temperature data were collected by a Campbell CS457A Conductivity and Temperature Probe (Table 3.10). This was logged by either a Campbell CR500 (during 2010 and until 14/06/11) or a Campbell CR10X (remainder of 2011) at one minute intervals during field visits, and 30 minute intervals between field visits. Unfortunately, the probe often became clogged with sediment, resulting in large periods when the conductivity data were erroneous. The water temperature data were not as affected by this problem, but gave erroneous readings if the probe was out of the water. Throughout 2010, conductivity data were collected from day 174 at 14:00 to day 179 at 9:00, from day 209 at 14:00 to day 235 at 16:00, and from day 249 at 15:00 to day 255 at 13:00, although there are gaps within these periods. During 2011 the conductivity probe recorded from day 156 at 14:00 to day 177 at 14:00, from day 207 at 19:00 to day 236 at 4:00, and from day 255 at 12:00 to day 258 at 16:00, also with gaps.

During field visits water chemistry measurements were taken every morning and evening, although the most continuous series of measurements was in June 2010, throughout the other field trips twice daily measurements are only available every second or third day. The average time of morning measurements in 2010 was 10:44 and in 2011 was 10:06, with the average time of afternoon measurments 16:54 in 2010 and 16:43 in 2011. Ideally measurements would have been taken at a time corresponding with minimum and peak discharge (following Brown *et al.,* 1996), but since proglacial runoff peaked at 23:00 on average in 2010 and 01:00 the next day in 2011, afternoon measuremetents are more representative of rising rather than peak flow. Minimum runoff occurred around 11:00, so morning measurements represent conditions at minimum flow. At each measurement time the conductivity, water temperature, turbidity and pH (with a Hanna HI 9033 during 2010 and June 2011, and a Hanna HI 98128 during the rest of 2011) of the proglacial stream was measured (see Table 3.10 for probe accuracy specifications), and a water sample was taken from the proglacial stream. This involved rinsing a 500 ml bottle in the stream, and filling it with stream water, which was filtered using a Nalgene field filter holder and receiver and hand pump, and a pre-weighed Whatman cellulose nitrate membrane filter (0.45 μm pore size and 47 mm diameter). The upper part of the filter unit was rinsed twice with sample, which was discarded, and the lower part of the filter unit was rinsed twice with filtrate

which was discarded before the sample to be stored was filtered (following Hubbard and Glasser (2005)). The total volume of water that passed through the filter (including that used for rinsing) was noted to allow the calculation of the suspended sediment concentration (SSC). The sample was stored in a labelled acid-rinsed bottle which was stored in a cool bag before return to the accommodation, where it was stored either in a cool bag with ice pack (June both years) or in a fridge (July/August and September trips of both years) until return to the UK. Some sample bottles were posted back and this took a few days. The bottles were filled to the brim as far as possible. During days 160, 172, 214 and 251 in 2010 water chemistry measurements were taken from the proglacial stream at hourly intervals during the day. During 2011 water samples, and conductivity and pH measurements were taken from the supraglacial streams used for dye tracing, as well as from supraglacial ponds, supraglacial lakes and some other supraglacial streams.

3.4.2.2 Laboratory work

In the laboratory samples were refrigerated prior to analysis. Each sample was tested for the concentration of sulphate, bicarbonate and (in 2010) chloride ions present. During analysis of the water samples pipette nibs, 50 ml mixing bottles, conical flasks, vials and droppers were all rinsed with deionised water and sample before the sample to be tested was used. Each test was carried out on each sample twice, and if the two tests were not similar within certain parameters the test was repeated. If two of the three tests did not agree within the parameters then the result was not included. The sulphate concentration was found by measuring 10 ml of sample into a mixing bottle, and adding a powdered sulphate reagent, the bottle was gently agitated until the powder had dissolved and the sample was left for 5 minutes while the colour developed. The test has a stated measurement range of between 2 and 100 mg l^{-1}. The sample absorbance (A) was tested in a CECIL CE 4002 spectrophotometer (accuracy of $\pm$ 0.005A or 1%, whichever is greater) at 450 nm wavelength. This absorbance was related to the sulphate concentration in mg l^{-1}, using a calibration curve of absorbance against sulphate concentration (Figure 3.14a). Values in mg l^{-1} were converted into μeq l^{-1}. The calibration was performed by producing samples of a known concentration from a sulphate standard solution, and then subjecting each to the test above. For the sulphate tests the results were not accepted if they differed by more than 100 μeq l^{-1}, of the remaining samples the mean absolute difference between samples was 21.8 μeq l^{-1} (28.7 μeq l^{-1} in 2010 and 9.3 μeq l^{-1} in 2011), this equates to a mean percentage difference of 29% (18% in 2010 and 51% in 2011). The percentage difference is larger in 2011 due to the increased number of lower concentration supraglacial samples.

The chloride concentration was found by measuring 10 ml of sample into a mixing bottle, and adding two chloride reagents, one at a time, ensuring each one had dissolved. The sample was left for two minutes for the colour to develop before the absorbance was measured at a wavelength of 450 nm using the CECIL spectrophotometer. This test has a stated measurement range of 0.5 to 25 mg l^{-1}. The absorbance measured was converted into a concentration of chloride ions in mg l^{-1} using a calibration curve created by preparing solutions of known concentration from a chloride standard solution, and subjecting them to the test above (Figure 3.14b). The calibration produced did not go through zero, and when a fifth point was added independently at 0.5 mg l^{-1} this confirmed the angle of the relationship. Most sample absorbances gave a negative chloride concentration, meaning the chloride concentrations were lower than detectable. Of those that were positive (7 samples) the mean absolute difference between tests was 50.0 μeq l^{-1} (119%). The chloride test was therefore not performed in 2011. Some workers have used the chloride concentration of water samples to proportion the sulphate concentration into ions derived from the snowpack (i.e. from snowfall scavenging of sea salt or other atmospheric aerosols), and those produced from the reactions of water with sediment (Hodgkins *et al.,* 1998). The low chloride ion concentrations meant this was not possible or necessary, as the proportion of the sulphate concentration derived from the snowpack was small. This was confirmed by measurements of the sulphate concentrations of the upglacier streams in June 2011. The input stream of S14 (which had a mainly snow covered catchment) gave a sulphate concentration of 0 μeq l^{-1} (i.e. less than measureable), and the input stream of S15 gave a sulphate concentration of 0.88 μeq l^{-1} on day 159 and 9.70 μeq l^{-1} on day 164. The sulphate concentrations measured at the proglacial stream are considerably larger than this (see section 6.2).

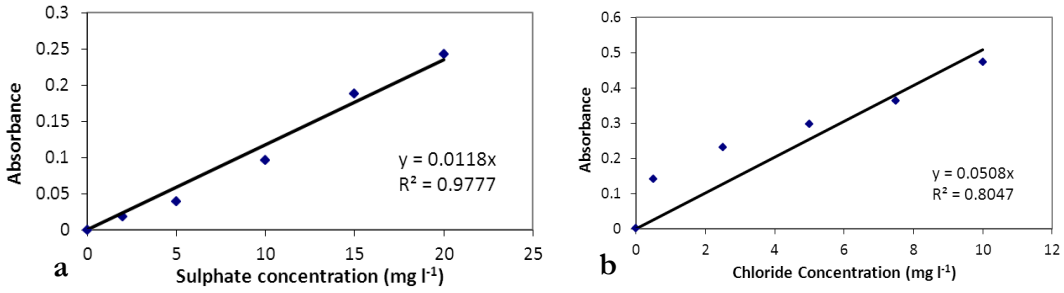

Figure 3.14 Calibration between the concentration of a) sulphate and b) chloride solutions and the absorbance measured on the spectrophotometer.

The concentration of bicarbonate was found by titrating 20 ml of sample with 0.01 mol l^{-1} hydrochloric acid. Kittiwake pH 4.5 indicator was used to ascertain when the correct volume of hydrochloric acid had been added to the sample. Two titrations were carried out

on each sample, and they were accepted if the volume of hydrochloric acid added agreed within 2 ml (59.8 μeq l^{-1} of bicarbonate). If not then a third test was performed, and if two of the three tests agreed then their values were used instead. Equation 3.32 was used to calculate the concentration of bicarbonate in the sample ($cHCO_3^-$, g l^{-1}):

$$cHCO_3^- = \frac{vHCl\ cHCl}{vHCO_3^-}, \qquad (3.32)$$

where $vHCl$ is the volume of hydrochloric acid (l) used to reach the end point, $cHCl$ is the concentration of hydrochloric acid in g l^{-1} (0.365 g l^{-1}), and $vHCO_3^-$ is the volume of sample in l (0.02 l). The concentration of bicarbonate in the sample was converted from g l^{-1} to μeq l^{-1}. The average absolute difference between the tests was 24.7 μeq l^{-1} of bicarbonate (5%). Once both the sulphate and bicarbonate concentrations had been found in μeq l^{-1} they were used to calculate the C-ratio for each sample (section 2.5).

The partial pressure of CO_2 was calculated from equation 3.33:

$$\log \rho(CO_2) = \log(HCO_3^-) - pH + \rho KCO_2 + \rho K_1\ , \qquad (3.33)$$

(Brown, 2002, p 865) where ρKCO_2 is equal to 1.12 and ρK_1 is equal to 6.58 if the water has a temperature of 0°C (Ford and Williams, 1989, cited in Brown, 2002). The concentration of HCO_3^- is in mol l^{-1}, with the value of $\log \rho(CO_2)$ calculated being the exponent of 10 which gives the partial pressure in atm (Brown *et al.,* 1998).

The filter papers used were folded and retained in labelled bags. The filters were dried in an oven for several hours, and were weighed using Acculab 110 scales (reproducibility of ≤ 0.0001 g). The difference in weight of each filter paper before and after use gave the mass of sediment in each sample. This was divided by the total volume of water passed through the filter to give the suspended sediment concentration in mg l^{-1}. The greatest error in this analysis is the volume of water filtered as this was measured using the graduations on the filter receiver.

3.5 Glacier velocity measurements

Measurements of the glacier velocity were performed to determine how the configuration of the hydrological system and water input variations affected the glacier dynamics. Daily velocities were used to pinpoint the timing and location of short term

speed up events while monthly and seasonal velocities were calculated to give an overview of the influence of the debris on the glacier dynamics.

3.5.1 Field procedures and data processing

The glacier's surface velocity was measured by repeat survey of boulder positions using a Leica differential GPS (dGPS) system. On each survey day one dGPS receiver was set up as the reference station, with the tribrach screwed onto a control point situated on stable moraine overlooking Miage Lake (Miage 1), within a few hundred metres of the glacier margin ('Base' in Figure 3.1b, and Figure 3.15a). This control point was previously occupied onto the WGS84 network by the University of Milan. During July and August 2011 the reference station was set up on a different rock near Miage Lake, but at a location which made the system less visible to tourists (the Miage 2 and Miage 3 reference positions (the Miage 2 reference rock was shifted inadvertently)). A network of survey points was established along the glacier centreline with the aim of covering the entire ablation zone, with additional lateral points located at confluences and divisions making a total of 22 survey points (Figure 3.1b) during 2010. That year two Leica dGPS systems were borrowed from the Geophysical Equipment Facility (NERC GEF loan 917, 2010), so separate teams could cover different parts of the glacier on each day. During 2011 the number of points was reduced to 10, following the upper centreline (from C4 to C14) as there was only one dGPS roving antenna. Three of the points were relocated in 2011, C4, C11 and C14, as the original points could not be reused or located. They remained at a similar altitude to the 2010 points. Survey points were located on the flat tops of stable boulders, onto which the outline of the GPS's tribrach was spray painted (using a template of the tribrach's base). The tribrach was positioned within this outline and the antenna was fixed and levelled onto the carrier as usual ('spray template method', Figure 3.15b). The rover tribrach was not fixed onto the rock, but remained stable on the rock during the occupation period. Most points were surveyed on most days but weather conditions and fieldwork logistics meant this was not always possible. Each point was measured on static mode and occupied for 3 minutes. Static mode was used because of the long distance and indirect sight lines between the reference station and rover, meaning radio coverage was unreliable. Certain points were also occupied more than once a day, to increase the temporal resolution of the glacier velocity data. Glacier-wide surveys were carried out most days between days 156 and 169, 210 and 218, and 248 and 253 in 2010, and between days 155 and 165, and 209 and 214 in 2011. Data were processed using Leica GeoOffice software.

Figure 3.15 Photographs of the dGPS set up, a) the base station receiver overlooking Miage Lake, and b) the roving receiver, sitting within the spray painted outline.

Post-processed positional quality reported in Leica GeoOffice was sub-centimetre for most points (the average position quality, height quality and combined position and height quality over the season for all points for which the ambiguity had been resolved are 0.0012 m, 0.0019 m and 0.0023 m for 2010 and 0.0011 m, 0.0017 m and 0.0020 m for 2011, respectively). The points processed using the Miage 3 reference during August 2011 were adjusted to match those using the Miage 2 reference using the change in the measured position of a boulder on a stable moraine which occurred due to the change in reference position. This is a standard method of adjusting points with different reference positions (A. Hobbs, personal communication). However, the same stable boulder was not measured with the Miage 1 reference position, so the average surface velocity between the June and July/August 2011 visits cannot be calculated.

All points were processed a second time on return to the UK using the daily precise ephemeris as downloaded from the International GNSS Service. Only points for which the ambiguity could be resolved were used in analysis of the glacier velocity.

Errors resulting from sliding or 'melting in' of the boulders on which survey points were located are likely insignificant. The boulders chosen were large and considered stable. Furthermore, any slippage would have resulted in boulder rotation and problems levelling the tribrach. The tribrach was levelled successfully at most points, except C11 which slipped between the August and September 2010 trips. Some of the smaller rocks used on the western side above the snowline in 2010 (W2 and W3), were discarded due to suspected rock movement. These rocks were smaller because of the difficulty in locating suitable rocks in deep snow. To quantify the errors associated with the repositioning of the tribrach within the spray painted outline, the position of a boulder on a stable moraine near Miage Glacier was measured three times using the 'spray template' method. The root mean

squared errors of the easting and northing measurements were 0.0032 m and 0.0015 m, respectively (Table 3.11, point M). The same procedure was repeated for five stable points (large rocks or paving slabs) situated around the University of Dundee campus, using a local base reference station (Table 3.11, points A to E). The average distance and height error for all points was 0.0045 m and 0.0057 m, respectively. This error includes uncertainties due to the differential GPS system and the positioning of the tribrach within the spray painted outline, and means horizontal velocity variations greater than ± 5 mm and vertical velocity variations greater than ± 6 mm are interpretable.

Table 3.11 Data quality statistics for the dGPS, for stable points A-E in Dundee, and M on a rock on the lateral moraine on Miage Glacier.

	RMSE (m)		**Mean (m)**	**RMSE (m)**	**Mean (m)**	**Mean (m)**	**Mean (m)**
Point	Easting error	Northing error	Distance error	Height error	Position Quality	Height Quality	Position and Height Quality
A	0.00301	0.007062	0.007192	0.009572	0.0012	0.001467	0.001867
B	0.00086	0.003519	0.003385	0.006701	0.0011	0.0012	0.001633
C	0.001657	0.001451	0.001992	0.005435	0.001067	0.001433	0.001767
D	0.002185	0.005725	0.005927	0.004446	0.000867	0.001467	0.0017
E	0.002004	0.005258	0.005349	0.00298	0.001167	0.001567	0.001967
M	0.003184	0.001528	0.003309	0.004961	0.000567	0.001	0.001167
Mean	0.00215	0.004091	0.004526	0.005683	0.000994	0.001356	0.001683

3.5.2 Analysis of point data

For each point the short term surface velocity (usually over a day or two) was calculated by dividing the net horizontal distance travelled by the time between each point occupation to give a velocity in cm d^{-1}. The mean velocity over a fieldwork period (e.g. days 156-169, 2010) was calculated by finding the net horizontal distance travelled between the first and last point occupations in the period, divided by the time difference. The short term velocities were normalised so as to highlight whether a certain GPS position had travelled faster or slower than average on a particular day. To do this the mean velocity for the period of interest (for instance June 2010) was subtracted from the short term velocity so intervals which showed faster than average velocities would give positive values and vice versa. The normalised short term velocity was divided by the standard deviation for the appropriate GPS position and fieldwork period, giving the difference from average velocity in units of standard deviation (σ). The vertical velocity was calculated as the difference in vertical height between each survey divided by the time difference. The vertical movement of a point will be caused by a combination of its downslope movement following the glacier's flow angle, the strain acting on the glacier in the vicinity of the measured point,

downward movement due to melt beneath the boulder, and cavity opening at the ice/bed interface due to pressurisation of the water at the bed. To find the horizontal distance each GPS position would have moved downwards due to the glacier's downwards flow, it is necessary to find the flow angle (ϑ_s) for each GPS position (e.g. C5). This was calculated using equation 3.34:

$$\vartheta_s = \tan^{-1}\left(\frac{\delta z}{\delta d}\right), \tag{3.34}$$

where δz is the elevation difference between a certain GPS position (e.g. C5) and the one downglacier (e.g. C4) (m a.s.l), and δd is the distance between the specified GPS position and the one downglacier. The elevation data was taken from the 2005 ARPA DEM so the downward slope angles from the lowest GPS positions could be found by choosing an arbitrary position on the DEM 500 m downglacier from the specified GPS position. It is assumed the flow angle for a given position on the glacier has not changed since 2005. This is likely because the flow angles were also found using the measured average June elevation for each position, and ignoring the lowest positions for which the slope angle could not be calculated, the mean absolute difference between the ARPA DEM flow angles, and those calculated from the measured GPS data was 0.66°. The flow angles were also calculated using the distance between each GPS position and the mid-point between that position and the one downglacier, but this resulted in a more undulating profile which captured the surface topography rather than the flow angle, and so was not used. The daily elevation change (δz_d, cm) due to the movement of the GPS position downslope (negative if the elevation decreases) was found from:

$$\delta z_d = \delta d_d \tan \alpha , \tag{3.35}$$

where $\delta d_d$is the distance the GPS position moved each day (cm). The time between GPS measurements was used to turn δd_d into a rate in cm d^{-1}, which was subtracted from the raw vertical velocity to give the vertical velocity corrected for the slope angle. As the GPS points were on top of large boulders, ablation beneath the boulder may result in the point moving downwards. It was assumed this melt was negligible as melt beneath a thick debris cover is generally less than 10 mm d^{-1} w.e. (the C7_11 stake with a debris thickness of 0.28 m had an average ablation over June 2011 of 8 mm w.e.). It is difficult to substantiate this due to the impossibility of measuring ablation beneath large boulders.

Although a full analysis of the strain acting on the ice near the GPS points is not possible, due to the network mainly following the glacier centre line, the longitudinal strain rate was calculated to ascertasin which areas of the glacier experienced compressional or extensional flow. The non-dimensional longitudinal strain rate (ε_{xx}) was calculated from equation 3.36:

$$\varepsilon_{xx} = (\delta d_2 - \delta d_1)/\delta d_1 \,, \qquad (3.36)$$

(Ramsey, 1967) where δd is the distance between a GPS position and the one downglacier, with the subscript 1 referring to the distance at time 1, and the subscript 2 referring to the distance at time 2. The distance was always calculated between positions occupied on the same day, and the two positions involved were usually occupied within half an hour of each other. The strain was then divided by the number of days between measurements to give the strain per day (non-dimensional). The strain rate was negative if the line had become shorter over time (compression), and was positive if the line had become longer over time (extension). The GPS positions are assumed to follow the glacier centre line, and so give the longitudinal strain, although it is understood this does not account for any transverse, shear or vertical strain.

4 The influence of debris on the input meltwater hydrograph

This chapter aims to explain how the debris cover influences the ablation rate, and therefore the quantity, distribution and timing of meltwater inputs from different parts of the glacier. The influence of debris on ablation was investigated using a distributed energy balance melt model, the development of which is discussed in section 4.1, with the model results shown in section 4.2. The next section seeks to identify how the debris influences the form of the supraglacial stream network, by understanding how the topography and melt rates combine to influence the form and discharge of the supraglacial streams on the debris-covered and debris-free regions. How the magnitude of evaporation may differ from clean glaciers is then covered, as well as the fluctuations of water vapour within the debris layer, since these processes may influence the proportion of rainfall or melt that runs off.

4.1 Development of a surface melt model incorporating the effects of the debris cover

Due to a lack of suitable previously developed models for debris-covered glaciers (section 2.1.2) a distributed energy balance model was constructed to allow the calculation of the spatial differences in the magnitude of ablation, and therefore runoff. These differences may then influence the englacial and subglacial hydrology. Some of the model methods required some consideration, and they will be discussed first. This will be followed by the details of the sensitivity analysis and model validation. The spatial differences in ablation are discussed in section 4.2.1, followed by the effect of the debris on the timing of the melt cycle. Next the fluctuations in the source of melt are mentioned to understand the relative importance of the different surface cover types and how this changes during the day and during different weather conditions. Lastly, in section 4.2.4 the sensitivity of the model to variations in air temperature and debris thickness is investigated.

4.1.1 Discussion of model methods

A detailed account of the model methods are given in section 3.2.4, this section only discusses some particular aspects of the methods used.

4.1.1.1 Debris thickness distribution

The model grid cells were classified as debris-covered based on whether they were delimited as continuously debris-covered from inspection of the 2005 aerial photograph. Debris thickness values for most cells was provided by Foster *et al.* (2012), but the region of the glacier above 2370 m a.s.l. was not included, and so above this the debris thickness was determined by giving each cell a value from a normal distribution of debris thickness values (with the mean and standard deviation from measured values from a transect on the upper glacier measured by Foster *et al.* (2012)). This method was employed by Reid *et al.* (in press) to model the debris thickness of debris patches on Haut Glacier d'Arolla, although they used exponential probability functions, with each debris patch having its own function based on measured debris thicknesses. This accounts for the differences in debris thickness between different areas while also allowing each cell to be allocated a debris thickness value. This was not possible on the upper region of Miage Glacier because of the lack of detailed debris thickness measurements, and so while the overall magnitude of sub-debris melt should be realistic here, the exact location of areas of thinner or thicker debris covers cannot be determined. The debris thickness distribution using measurements over the entire glacier was normal, with a mean of 0.25 m (Foster *et al.,* 2012). The debris thickness distribution from the upper transect was similar, with the greatest frequency of thicknesses in the 0.20 m or 0.24 m 'bin', but the distribution was bi-modal with a high frequency of 0 m debris thicknesses (Figure 4.1). This lowered the mean to 0.16 m (Figure 4.1). Inclusion of zero debris thicknesses in the distribution decreased the mean compared to the mode, and meant a proportion of the cells had negative debris thicknesses. The normal distribution will have a lower proportion of zero debris thicknesses than in reality, but conversion of the negative thicknesses to zero (modelled using the dirty ice model), and the lower mean compared to modal debris thickness should partially compensate for this. As only 20 measurements were taken, it was decided a normal distribution was most appropriate as this was the form of the distribution for the entire glacier. Debris is likely interspersed with patches of debris-free ice, so perhaps future model development should proportion debris-free and debris-covered areas where debris is thinner. The most frequent debris thickness measured on Haut Glacier d'Arolla debris-patches was at or close to 0 m, hence why Reid *et al.* (in press) used an exponential function. The differences in the distribution shapes are due to the thicker and more continuous debris on Miage Glacier compared to Haut Glacier d'Arolla.

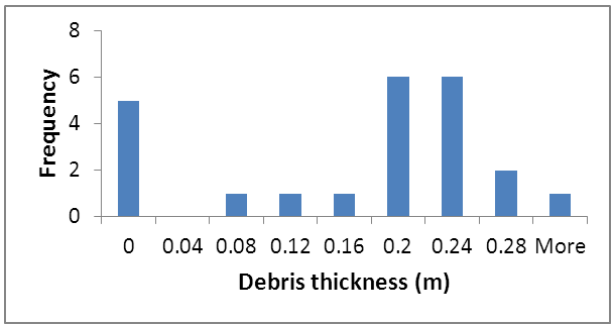

Figure 4.1 Debris thickness distribution of 23 measurements made along a transect at an elevation of 2334 m a.s.l. in 2006 (Foster *et al.,* 2012). The 'bin' size is 0.04 m.

4.1.1.2 2m air temperature extrapolation

In the model the air temperature is extrapolated across the whole glacier from the air temperature measured over debris at LOMET (see Table 3.8 for details). It is important to account for the differences in air temperature above debris compared to ice due to the release of sensible heat and longwave radiation from the debris to the air during the day. This was achieved by situating a meteorological station on mainly debris-free ice (ICEMET) and creating a lapse rate from UPMET, situated on debris. Although the ICEMET data were corrected to account for the differences in sensors used on UPMET and ICEMET (section 3.2.4.1), the ICEMET temperature probe was situated 0.69 m closer to the surface than the UPMET probe. However, the slight decrease in the ICEMET air temperature due to its lower sensor height will be much smaller than the average air temperature difference between UPMET and ICEMET of 2.4°C (Figure 4.2). The mean 'lapse rate' with elevation between UPMET and ICEMET was -0.044°C m^{-1}, an order of magnitude larger than a standard clean glacier air temperature lapse rate of -0.0041°C m^{-1} (Oerlemans, 2010). The decrease in air temperature is not a lapse rate with elevation, but rather a step change in air temperature between the debris-covered and debris-free regions. Figure 4.2 shows the air temperature difference is largest during the day when the debris temperature, and its effect on air temperature, is greatest. The ICEMET data was therefore used because it captured the air temperature difference caused by the different surface covers, and this was important to reproduce in the model.

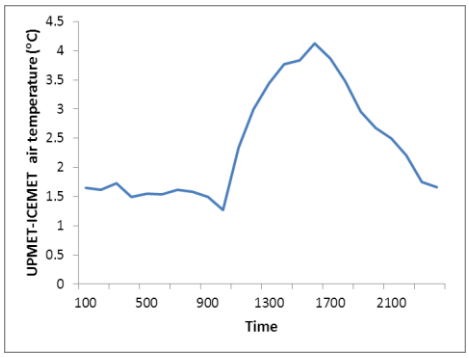

Figure 4.2 Average hourly UPMET minus ICEMET air temperature in 2011.

4.1.1.3 Precipitation extrapolation

Precipitation was a large proportion of runoff (section 7.1), but there are uncertainties in its distribution which must be considered. The rainfall rate increased upglacier with a mean lapse rate of 0.0026 mm hr^{-1} m^{-1}, determined from measured data at UPMET and LOMET. The total rainfall at LOMET and UPMET between days 167 and 219 in 2011 was 243 mm and 385 mm respectively, giving a total rainfall lapse rate of 49 mm per 100 m. Some of the increase in rainfall is due to the increase in intensity but occasionally rainfall occurred at UPMET and not LOMET, and so the rainfall frequency also increases with altitude. The measured rainfall lapse was lower than the average rate found at altitudes between 400 m and 3800 m of 75 mm per 100 m for the Valais and north-eastern ranges of the Swiss Alps, although in the north-eastern range the rate decreased at higher altitudes to 57 mm per 100 m between 1700 m and 3810 m (Lang, 1985, cited in Barry, 2008). The calculated lapse rate is therefore reasonable and should be applicable at higher altitudes than the UPMET station.

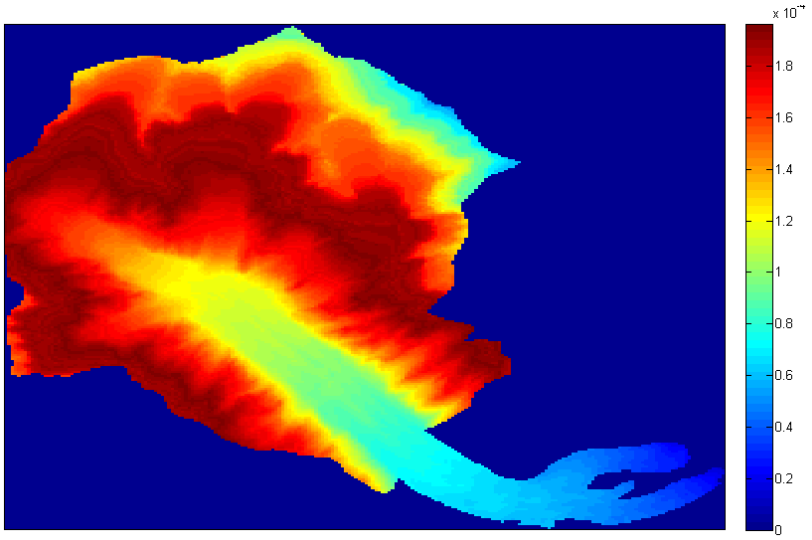

Figure 4.3 Average daily rainfall (mm d^{-1}) across Miage Glacier catchment for 2010.

The transition from rain to snow fall was assumed to occur at 0°C, but the threshold temperature varies between studies with Farinotti *et al.* (2011) using a range between -1°C to +1°C, Bocchiola *et al.* (2010) a threshold of 0°C, while Hock and Holmgren (2005) and Huss *et al.* (2008) used 1.5°C. Figure 4.3 shows the average daily rainfall distribution resulting from rainfall extrapolation and freezing level position. The elevation of the mean 0°C isotherm marks the transition from an increasing to decreasing trend in precipitation with altitude. Increasing this threshold would increase the quantity of rainfall that contributes to runoff. All rain gauges can suffer from undercatch, with even the difference between standard raingauges, and ground-flush gauges in Britain being estimated at 2-7% (Marsh and Dixon, 2012), although this is expected to be much larger at higher altitudes. There are considerable ranges in undercatch corrections, with values from 10-90% for selected catchments in the Swiss Alps (Farinotti *et al.,* 2011) to 35% for Storglaciären, Sweden (Hock and Holmgren, 2005) and to 45% for the uppermost valley of Zinal, Valais, Switzerland (Huss *et al.,* 2008). Due to the variability in undercatch and the lack of specific data for Miage Glacier, the rainfall values were not corrected.

4.1.2 Sensitivity analysis and model validation

The sensitivity of the DEB-model and Clean Ice Model to the debris and ice properties will be discussed, followed by model validation using stake data. The locations of stakes used in model validation and for assessing the spatial variability of ablation are shown in Figure 4.4.

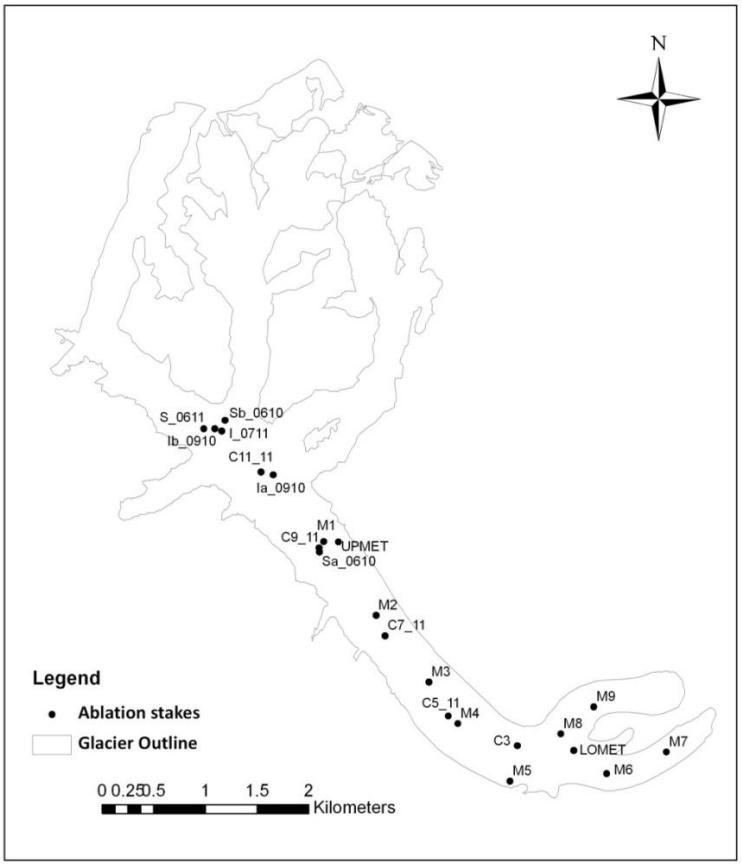

Figure 4.4 Location map of ablation stakes in 2010 and 2011. Where more than one stake was positioned at a similar location, only one marker is shown. All 'L' stakes were positioned at LOMET, and all 'U' stakes at UPMET. Stake names are in the form 'A1a_mmyy', where 'A1' denotes the location or surface type, 'a' delimits different stakes at the same location or surface type, and 'mmyy' is the month and year of measurement.

4.1.2.1 Sensitivity analysis

A sensitivity analysis was performed by Reid and Brock (2010) on the parameters of the DEB-model which described the debris properties (Table 4.1). Changes in the debris thermal conductivity and emissivity have an almost 1:1 influence on melt, whereas the model is less sensitive to changes in the debris volumetric heat capacity, surface roughness and albedo. Spatial differences in debris thermal conductivity (due to a different proportion of pore space or degree of saturation) could result in ablation variations on the ground which were not modelled. To test the Clean Ice Model sensitivity, the parameters for the dirty ice surface were varied and the change in ablation at a dirty ice cell near ICEMET was calculated (Table 4.1). Since the Clean Ice Model was used to model ablation of snow and clean ice as well as dirty ice, but with different parameter values, the results are applicable to these surface types, although the initial values were different. The Clean Ice Model is sensitive to variations in emissivity, and albedo, but much less sensitive to surface roughness variations. Nevertheless, the percentage change of albedo is almost 10 times the consequent change in ablation. For both the DEB-model and the Clean Ice Model the

percentage change of emissivity was lower than 10% because the emissivity cannot be greater than 1. Both models were directly sensitive to changes in emissivity, but as the natural variability of emissivity is small it is less likely to be responsible for large differences between modelled and measured ablation.

Table 4.1 Sensitivity analysis of DEB-model and the Clean Ice Model. * The value of k_d in this study was 0.96 as it was an average value for 25 sample points (Brock *et al.,* 2010). ** The sensitivity of the DEB-model to the debris albedo was tested in this study using the ablation at the LOMET cell.

Debris parameters (DEB-model) from Reid and Brock (2010) at LOMET				
Parameter	Change	Initial value	Units	mm w.e. d^{-1} as a % of initial ablation
k_d	± 10%	0.94*	W m^{-1} K^{-1}	-9.9 to +8.1
C_d	± 10%	1418208	J m^{-3} K^{-1}	-0.55 to +0.50
ε_d	± 5 %	0.94		+4.5 to -5.2
z_{0d}	± 10%	0.016	m	+0.49 to -0.44
α_d**	± 10%	0.13		-0.48 to +0.45
Dirty ice parameters (Clean Ice Model), this study at ICEMET				
Parameter	Change	Initial value	Units	m w.e. d^{-1} as a % of initial ablation
α_m	± 10%	0.2		-1.5 to +1.3
z_{0m}	± 10%	0.007	m	+0.43 to -0.65
ε_m	± 3%	0.96		-2.6 to +2.4

4.1.2.2 Model validation

Modelled melt was validated using stake measurements of individual cells and the relationship between seasonal melt and debris thickness using all modelled cells. Modelled ablation for each stake was calculated from the cell containing the named stake, and over the same time period as the measured data. Since stake debris thicknesses were not always the same as the debris thickness of the appropriate model cell, the model thickness was changed to match that of the stake. Model runs to validate sub-debris and dirty ice melt were carried out with the snowcover set to 0 %, and those to validate snowmelt were carried out assuming a 100% snowcover.

The melt of debris covered cells will be discussed first, with the difference between modelled and measured ablation given in Table 4.2. Overall the melt of the debris-covered stakes was underestimated, with the average relative difference between measured and modelled melt -0.003 m w.e. d^{-1}, or a 16% underestimation relative to measured melt (Table 4.2). The standard error of the estimate of ablation equated to 0.005 m w.e. d^{-1}. There were no significant relationships between stake error and the distance of the stake to the relevant

meteorological station, the stake's elevation or its debris thickness (Figure 4.5). This suggests that model errors were not related to the distribution of the meteorological variables across the glacier.

An alternative method to assess the reliability of the debris melt model is to plot daily average ablation for all cells against debris thickness and compare this with measured data (Figure 4.6). In 2005, season long ablation data was collected from 25 stakes (Brock *et al.,* 2010), and so these were used to compare with modelled data. The relationship between ablation and debris thickness was similar in the modelled and measured data but modelled data had less variability than measured data. This was likely due to differences in modelled debris properties which remain constant (debris thermal conductivity, emissivity, volumetric heat capacity and surface roughness length for momentum), but vary in reality. An underestimation of melt at a certain stake could be due to the thermal conductivity being lower than modelled (0.96 W m^{-1} K^{-1}), due to more air voids between the debris (~0.025 W m^{-1} K^{-1}), or a greater proportion of water in the debris layer (~0.58 W m^{-1} K^{-1}) (Reid and Brock, 2010). Measured thermal conductivity varied from 0.71 W m^{-1} K^{-1} to 1.37 W m^{-1} K^{-1} (Brock et al., 2010), a 16% increase in ablation could therefore be produced with an increase in thermal conductivity to 1.11 W m^{-1} K^{-1}, within the measured range. Conversely, a 16% decrease in emissivity (which increases ablation due to decreasing outgoing longwave radiation) is unlikely, as natural variability of emissivity is much less. There also appears to be a shift in the relationship between ablation and debris thickness in Figure 4.6. This may be because the ablation of the lower glacier (thicker debris) cells was calculated from incoming shortwave radiation from LOMET, while ablation of the upper glacier (thinner debris) cells used shortwave radiation data from UPMET.

Table 4.2 Measured (meas) and modelled (mod) ablation (a) for all stakes in 2010 and 2011.

Stake	Start Day	End Day	Surface	Debris thickness	Meas a	Mod a	Mod a - meas a	Mod a - meas a
				m		m w.e. d^{-1}		%
C3_0610	162	171	Debris	0.28	0.009	0.009	0.000	-1.4
C3a_0711	211	216	Debris	0.24	0.021	0.014	-0.007	-34.1
C5_11	166	212	Debris	0.22	0.016	0.013	-0.002	-15.8
C7_11	166	211	Debris	0.28	0.008	0.010	0.002	21.1
C9_11	165	212	Debris	0.23	0.009	0.011	0.002	21.2
La_0610	159	171	Debris	0.1	0.022	0.021	0.000	-1.0
La_11	209	216	Debris	0.25	0.024	0.015	-0.009	-38.2
Lh_0711	209	216	Debris	0.27	0.017	0.013	-0.005	-26.8
M1_0610	159	214	Debris	0.28	0.015	0.009	-0.005	-36.1
M2_0610	159	214	Debris	0.24	0.016	0.011	-0.005	-30.4
M3_0610	159	195	Debris	0.11	0.033	0.025	-0.009	-26.5
M3_0710	195	214	Debris	0.11	0.031	0.024	-0.007	-22.6
M4_0610	159	195	Debris	0.13	0.020	0.022	0.002	12.1
M4_0710	195	214	Debris	0.14	0.022	0.021	-0.001	-4.7
M5_0610	159	195	Debris	0.08	0.033	0.033	0.001	2.0
M5_0710	195	214	Debris	0.08	0.031	0.033	0.002	7.8
M6_0610	160	195	Debris	0.155	0.021	0.014	-0.007	-34.5
M6_0710	195	214	Debris	0.12	0.021	0.017	-0.004	-20.4
M7_0610	160	214	Debris	0.14	0.021	0.023	0.003	12.9
M8_0610	160	214	Debris	0.185	0.020	0.018	-0.002	-12.1
M9_0610	160	214	Debris	0.225	0.021	0.015	-0.006	-27.5
Ia_0711	209	214	Dirty ice	0	0.067	0.046	-0.021	-31.3
Ib_0711	209	214	Clean ice	0	0.049	0.051	0.001	3.0
Ib_0910	248	249	Small clasts on ice	0	0.075	0.052	-0.023	-30.6
Ic_0711	209	214	Supraglacial stream	0	0.063	0.051	-0.012	-19.8
Id_0711	209	214	Dirty ice	0	0.064	0.051	-0.014	-21.4
Sa_0610	164	169	Snow	0	0.024	0.029	0.005	20.8
Sa_0611	165	165	Snow	0	0.031	0.030	-0.002	-5.2
Sb_0610	164	169	Snow	0	0.013	0.026	0.013	105.6
Sb_0611	165	165	Snow	0	0.026	0.030	0.004	13.7
Sc_0611	165	165	Snow	0	0.034	0.030	-0.004	-13.0

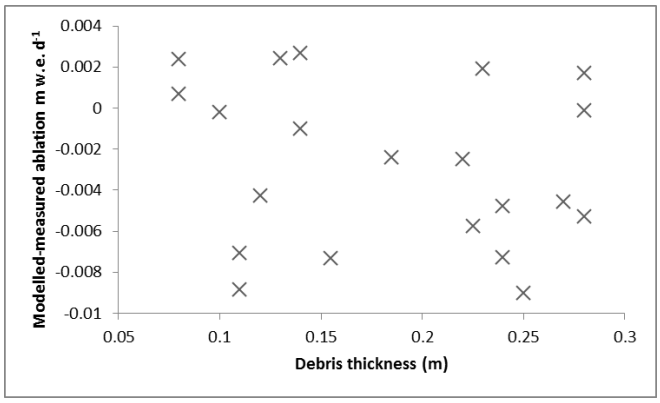

Figure 4.5 Relationship between model error and debris thickness for all debris-covered stakes in 2010 and 2011.

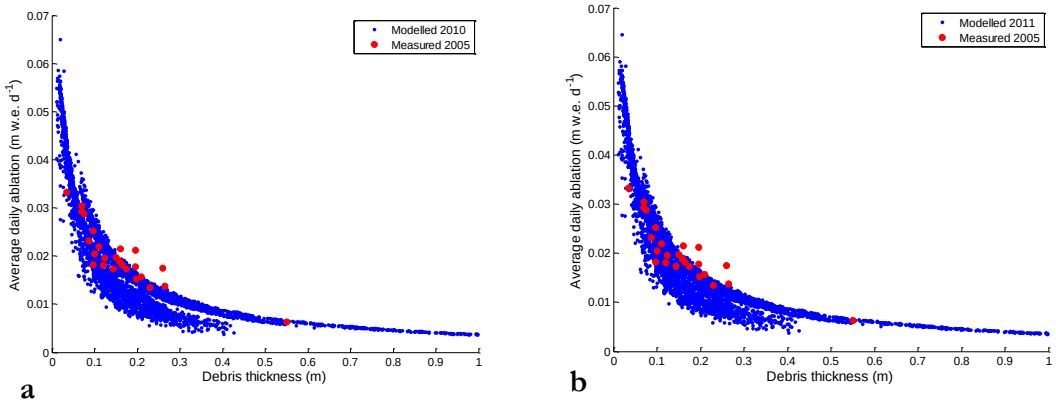

Figure 4.6 Scatter graphs of average daily modelled ablation against debris thickness, a) with 2010 modelled data and 2005 measured data and b) with 2011 modelled data and 2005 measured data. The x axis has been limited to focus on the measured data; there are therefore some modelled points out with the graphed area.

To confirm whether the debris melt model could sufficiently capture the timing of ablation, the modelled debris temperature was compared with that measured at LOMET within 0.2 m debris (Figure 4.7). Measured within debris temperatures were from HOBO temperature probes between days 215 and 259 in 2011. The measured debris surface temperature was from the longwave sensor at LOMET, since thermistors tend to overestimate surface temperature compared to that measured radiatively (Brock *et al.,* 2010). Modelled and measured surface temperatures matched well ($R^2 = 0.95$), although the 14 cm probe matched the modelled temperatures at 16 cm most closely ($R^2 = 0.95$), this may be due to the probe moving down slightly within the debris after installation, and is within the expected error of positioning such a probe. The 20 cm probe gave temperatures between that modelled at 18 cm and 20 cm (assumed 0°C in the model), reasonable given the difficulty in ensuring the probe remained in contact with the ice. At the surface, modelled and measured average peak temperature, and the timing of the peak were the

same (to 0.1°C), and the 16 cm (modelled) and 14 cm (measured) data had very similar average peak temperatures (4.5°C and 4.2°C, respectively), which occurred just one hour earlier at the measured probe. Therefore the model replicates the temperature cycle within the debris well.

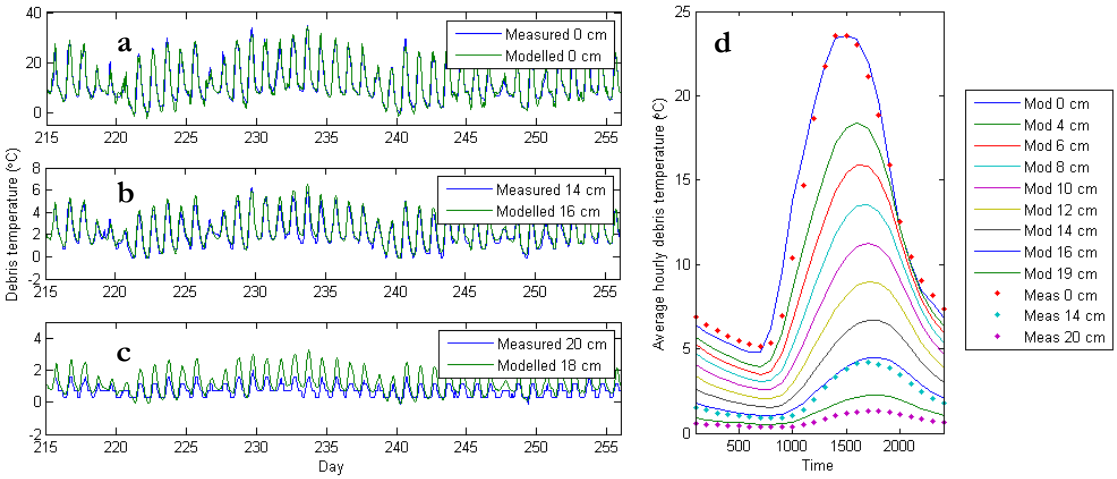

Figure 4.7 a) to c) are timeseries of measured and modelled debris temperatures for 0.2 m thick debris near LOMET in 2011, with d) the measured (Meas) and modelled (Mod) average hourly debris temperatures over the same period.

The difference between measured and modelled ice ablation can be seen in Table 4.2, although all stakes measured were within the 'dirty ice' area and were modelled as such. There was a reasonable underestimate of ablation (-0.014 m w.e. d^{-1} on average), with the standard error of the estimate equating to 0.016 m w.e. d^{-1}. The Ib_0711 stake was situated on relatively clean ice within the dirty ice area, the other stakes were situated on partially debris covered ice, with the Ic_0711 stake in a small supraglacial stream. It is very difficult to measure 'representative' ablation of dirty ice where melt rates vary substantially between regions of clean, slightly debris-covered ice, under boulders, or ice with a thin dust covering (Figure 4.13). Underestimation of melt could be due to the model albedo or surface roughness being too low (Table 4.1). The surface roughness value was the same for clean and dirty-ice, although the value given was an average over a range of ice surfaces, including rougher ice (Brock *et al.,* 2006). Dirt cones, cryoconite and other surface roughness elements caused by variations in debris cover are common to melting ice surfaces, but the debris concentration on this region of Miage Glacier could be higher, and the surface roughness elements more pronounced, meaning surface roughness was underestimated. The sensitivity analysis showed ablation was relatively insensitive to variations in surface roughness (Table 4.1) but more sensitive to changes in albedo, although a large albedo change would be needed to result in an appreciable difference in ablation. The albedo used in the model approximates that of a 50% debris cover (Brock *et*

al., 2000), with the relationship between debris cover and albedo suggesting a greater percentage debris cover has a lower albedo and vice versa. Monitoring the spatial differences in albedo across the glacier would be beneficial, maybe using Landsat TM data, as carried out by Klok *et al.* (2003) on the Vadret da Morteratsch.

Unfortunately, as no stakes were measured within the clean ice area, the melt model could not be validated here. However, the only difference between the clean and dirty ice models was the use of higher albedo and emissivity values for clean ice. The albedo is a measured value from Miage Glacier, taken at the foot of the Dome Glacier.

To validate the snow model ablation was calculated for the cells with snow stakes, presuming a 100% snowcover (Table 4.2). Snowmelt was well modelled with the standard error of the estimate equating to 0.007 m w.e. d^{-1}. On average melt was overestimated, although this was due a large difference at one stake (Sb_0610). The measurement periods of the snow stakes in 2011 are rather short, but the lack of UPMET data from the beginning of the season meant the model could only be run from day 165.

4.2 The influence of debris on the distribution and timing of ablation, and its sensitivity to future changes

This section deals with what the distributed melt model reveals about the influence of debris on ablation: firstly looking at the spatial variation in ablation; then how the debris effects ablation at an hourly resolution; before considering the variation in ablation from the different surface cover types. Finally, the melt model is used to understand the sensitivity of different parts of the glacier to air temperature and debris thickness changes.

4.2.1 The spatial variation of ablation

This section describes the spatial variation of ablation, as modelled by the distributed melt model. The relationship between ablation and elevation is given in Figure 4.8 and Figure 4.9, with the average daily modelled ablation shown in Figure 4.10 and Figure 4.11. Average daily ablation of all modelled cells mentioned includes the influence of snowcover over the season.

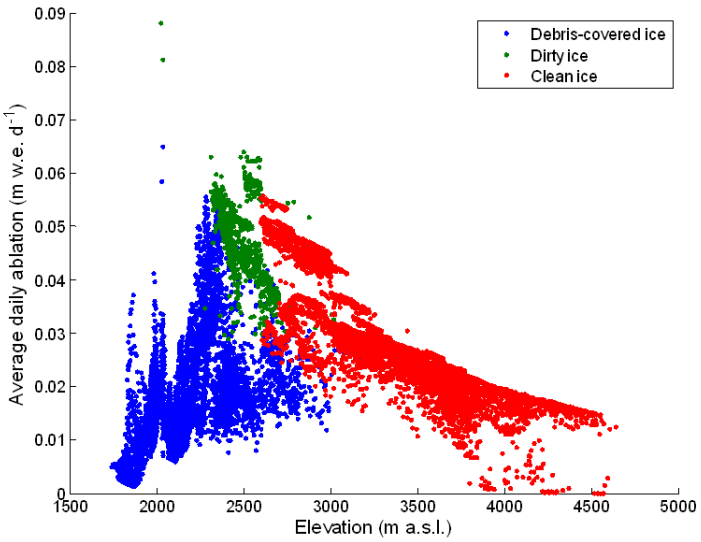

Figure 4.8 Average daily modelled ablation against elevation for 2010, for each glacier cell in the distributed model, split by surface cover type. The melt stated includes the influence of snowmelt for each cell.

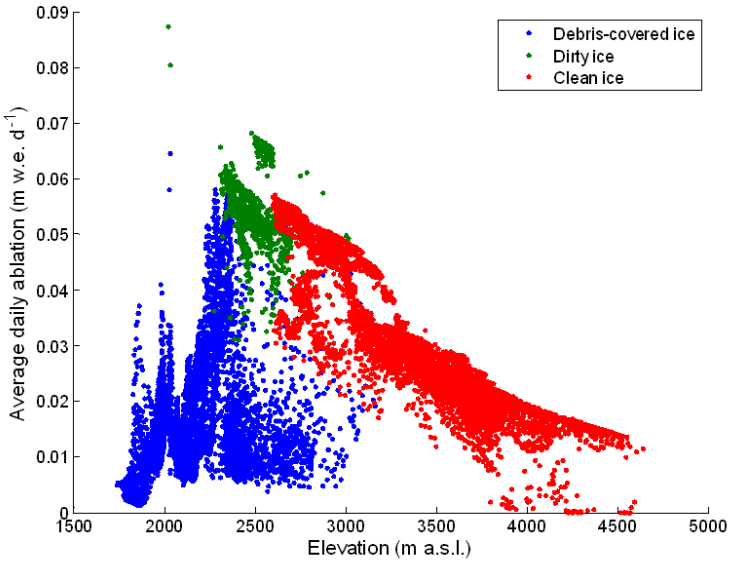

Figure 4.9 Average daily modelled ablation against elevation for 2011, for each glacier cell in the distributed model, split by surface cover type. The melt stated includes the influence of snowmelt for each cell.

The ablation of clean ice is small at the top of the ablation zone, but all cells experience some melt over the season (up to 4673 m a.s.l.). Average daily ablation increases downglacier (Figure 4.8 and Figure 4.9) due to warmer air temperatures which are above the 0°C isotherm more often, as well as a decrease in snowcover. Figure 4.10b and Figure 4.11b shows the main factor determining clean ice ablation (apart from elevation and air temperature) is the quantity of incoming shortwave radiation, which is governed by the aspect and slope angle of the glacier surface. Higher ablation areas are therefore on south

and east facing slopes. Ablation rates at 3500 m are around 0.02-0.03 m w.e. d^{-1}. On the ice falls of the Dome and Mont Blanc Glaciers melt rates are higher (around 0.05 m w.e. d^{-1}), due to a favourable aspect, steep decrease in elevation and increase in surface roughness. The upper margin of the region of higher surface roughness was defined from visual inspection of aerial photography, and so was a clearer and more static boundary than in reality. Parts of the Bionassay and Tête Carrée Glaciers also had regions marked with a higher surface roughness but as their elevation and aspect is not as favourable to ablation, the difference in ablation was less marked. On the lower parts of the Dome and Mont Blanc Glaciers, where the ice becomes dirty, this decrease in albedo adds with the aforementioned effects to give the region of the highest ablation rates on the glacier (over 0.06 m w.e. d^{-1} on average).

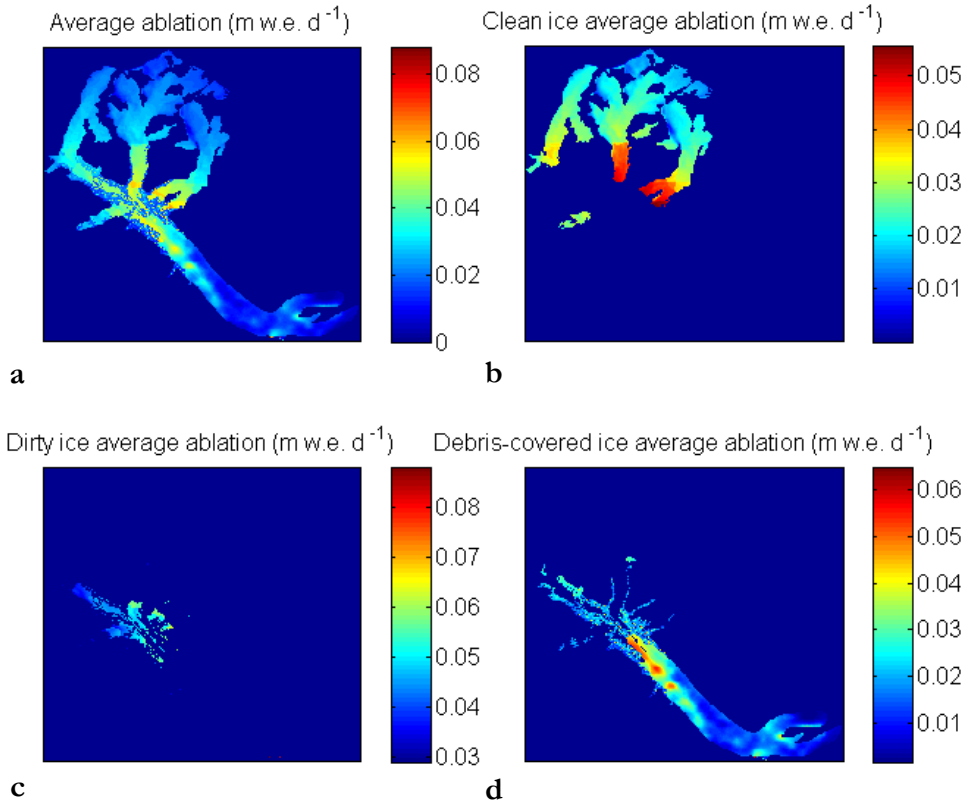

Figure 4.10 Average daily modelled ablation in 2010 for a) all cells, b) clean ice cells, c) dirty ice cells and d) debris-covered cells. The values of ablation include the effect of snowcover for each cell. Colourbars for each subplot are different to highlight the differences in ablation within each surface cover type.

The mid-part of the glacier has a large range of ablation rates which are determined more by the surface cover type and debris thickness than elevation or aspect. Debris covered regions following the lateral and medial moraines have the lowest ablation rates of around 0.02 m w.e d^{-1}, but individual cells with very low debris thicknesses have high ablation rates, for instance one cell with a debris thickness of 0.014 m had an average ablation of 0.05 m w.e. d^{-1}. Unrealistically high ablation could have occurred if the debris

thickness was <0.01 m because the DEB-model does not reproduce the decrease in ablation for debris covers thinner than the 'effective thickness' (Reid and Brock, 2010), which occurs as the effect of the debris to decrease the albedo diminishes, probably because the debris becomes patchy rather than specifically thinner. This was prevented by calculating ablation for cells with a debris thickness < 0.01 m using the dirty ice model rather than DEB-model. The regions of dirty ice in between the debris-covered regions have ablation rates around 0.05 m w.e., although this hides the great variation in small scale ablation rates in this region which were not modelled due to the complexity of the processes involved (e.g. boulder table and cryoconite formation).

Figure 4.12 shows hourly ablation for four adjacent cells, one dirty ice, one clean ice and two debris-covered cells with different debris thicknesses, at an elevation of around 2700 m a.s.l.. Total melt was much higher for the clean ice cell than under 0.12 m debris (0.042 m w.e. d^{-1}, compared to 0.014 m w.e. d^{-1}), caused by much larger ablation in the middle of the day when maximum ablation of clean ice was around three times that under debris. The dirty ice cell exhibited the greatest ablation with a mean daily ablation of 0.050 m w.e. d^{-1}, due to the lower albedo compared to clean ice. Note sub-debris ablation increases more gradually, and peaks later than dirty ice or clean ice ablation, this will be discussed in section 4.2.2.

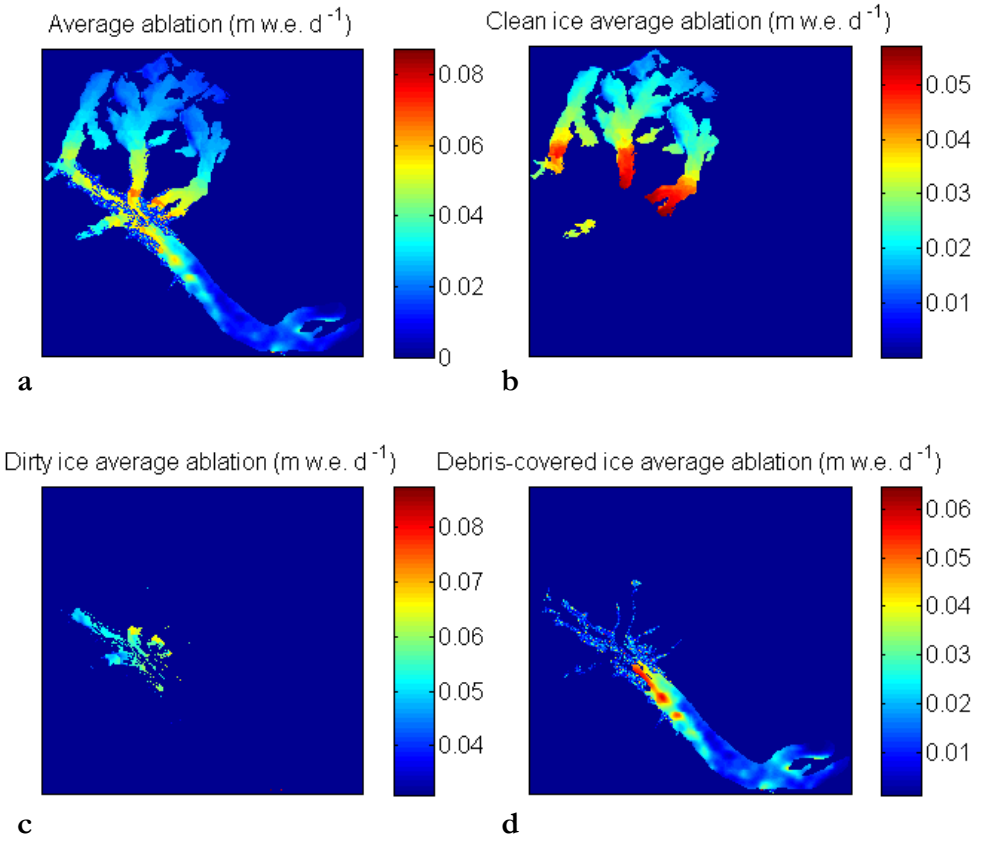

Figure 4.11 Average daily modelled ablation in 2011 for a) all cells, b) clean ice cells, c) dirty ice cells and d) debris-covered cells. The values of ablation include the effect of snowcover for each cell. Colourbars for each subplot are different to highlight the differences in ablation within each surface cover type.

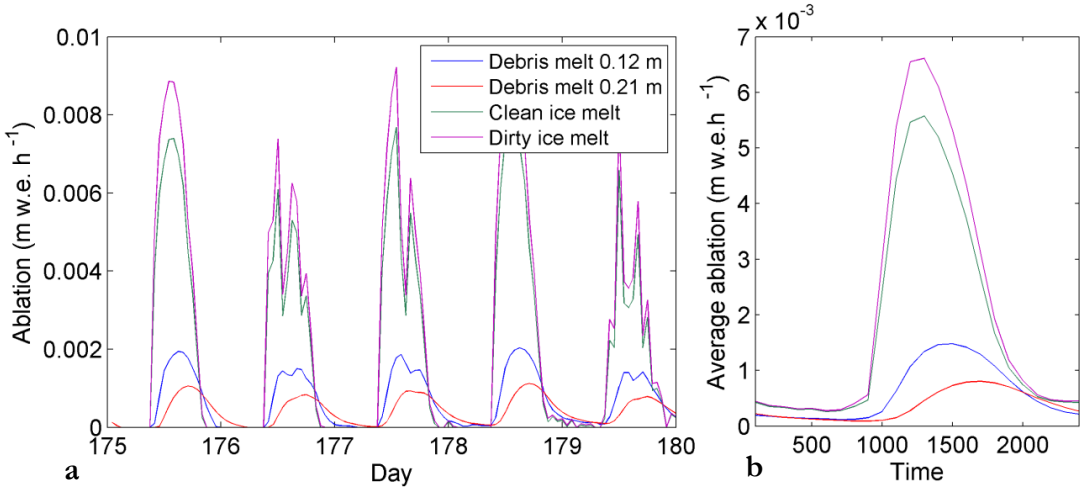

Figure 4.12 a) Hourly ablation of 4 adjacent cells with different surface covers, and b) average hourly ablation for the same cells over the season. The legend in a) is appropriate for both figures.

Figure 4.13 a) Photo of differential ablation on upper glacier due to partial covering of debris, July 2011, and b) rock table on upper glacier, July 2010.

Figure 4.14 Scattered debris cover at stake Ib_0910, September 2010.

To determine how ablation of snow would compare to that beneath a debris cover three of the cells used to validate the modelling of snow were also modelled assuming 0% snowcover. All of the cells were within the debris surface cover type, and had debris thicknesses of 0.01 m (Sa_0611), 0.03 m (Sa_0610) and 0.13 m (Sb_0610). Of the two cells where the debris thickness was very thin sub-debris melt was greater than snowmelt on average during June (by 0.02 m w.e. d^{-1} and 0.002 m w.e. d^{-1} for Sa_0611 and Sa_0610 respectively). Conversely at Sb_0611 snowmelt was greater than sub-debris melt, with the average difference in June being 0.02 m w.e. d^{-1}. The similarity of the sub-debris and snowmelt at Sa_0610 suggests, at least at the elevation of Sa_0610, that sub-debris and snowmelt would result in similar inputs into the hydrological system where the debris was around 0.03 m thick. Over the majority of the main tongue and especially on the lower glacier debris thickness are generally much greater than this. Therefore melt inputs are likely to be much greater when snow overlies thick debris, compared to after the snow has melted back. This could have implications for the development of the hydrological system.

Downglacier of 2300 m a.s.l. the majority of the glacier has a continuous debris cover, and so ablation is determined by the variations in debris thickness. The increase in

debris thickness with distance downglacier leads to ablation decreasing near the snout, but Figure 4.10d and Figure 4.11d show the situation is more complex, with regions of thinner cover especially along the western side of the main tongue, and regions of thicker cover along the central moraine and on the western edge of the glacier as it turns. In the areas of thickest debris cover ablation is very low, so on the lowest part of the northern lobe average daily ablation is only 0.002 m w.e. d^{-1}. There are also regions of anomalously high ablation at 1850 m a.s.l. and 2000 m a.s.l., associated with thin debris near Miage Lake and on the southern edge of the northern lobe.

Table 4.3 Minimum, average and maximum modelled values of average daily ablation for each surface cover type in 2010 and 2011. These values include the influence of snowcover for each cell.

	Dirty ice	**Clean ice**	**Debris-covered ice**
2010		m w.e. d^{-1}	
Min	0.029	0.00002	0.002
Mean	0.047	0.025	0.019
Max	0.088	0.056	0.065
2011		m w.e. d^{-1}	
Min	0.031	0.000008	0.001
Mean	0.054	0.028	0.018
Max	0.087	0.057	0.065

The current ablation profile of Miage Glacier shows the reversed ablation gradient typical of debris-covered glaciers. Moreover, the melt model highlights the large spatial variations in ablation on the mid-glacier where the debris is discontinuous, as well as regions at higher altitudes where factors such as the elevation, solar radiation receipt and surface roughness influence ablation. In terms of contributing area, the clean ice section is the largest (51%), followed by the debris-covered (42%) and dirty ice (7%). Looking at Table 4.3, the high altitude clean ice cells have the smallest ablation rates, with maximum ablation found on dirty ice cells. On average, debris-covered cells have the lowest ablation, with dirty ice consistently highest. The area of the glacier which contributes most melt to supraglacial streams will be the mid-glacier where there is a greater area of dirty and thinly debris-covered ice, whereas the lowest melt inputs are at high altitude or on the lower lobes where the debris is thickest.

4.2.2 Timing of ablation

The debris cover also influences the timing of the onset and peak of melt. Debris temperature data was collected at LOMET where the debris was 0.2 m thick, from day 215 to 259 in 2011. This revealed the influence of the debris on the diurnal debris temperature

signal as it passes from the surface to the ice-debris interface. The maximum and minimum daily temperature was found at depths of 0 cm, 8 cm, 14 cm and 20 cm in the debris (the 8 cm sensor malfunctioned occasionally), which allowed calculation of the diurnal temperature amplitude. Measurement of surface temperature using thermistors overestimates by 3-4°C compared to when measured radiatively (Brock *et al.,* 2010). The mean amplitude of the temperature of the debris surface was 27.3°C; of the sensor at 14 cm depth was 3.4°C; and at 20 cm depth was 1.0°C. This shows the reduction in the diurnal temperature amplitude with depth (Figure 4.15).

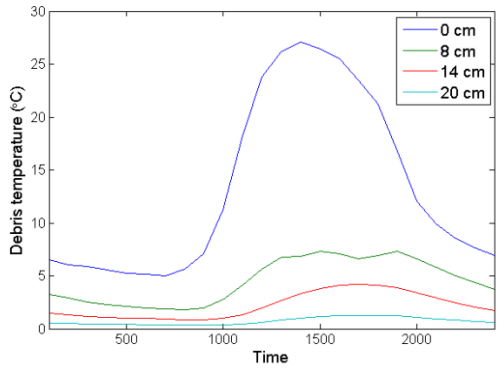

Figure 4.15 Average temperature at depth within the debris over a daily cycle, near LOMET in 2011. The lowest sensor should measure 0°C continuously, but was not completely in contact with ice.

The time of the maximum temperature at each depth gives the lag time between peak temperature at the surface and at depth in the debris. This analysis uses the time the maximum value is reached first, so lag times are minimums. Using the average hourly temperature cycle the lag time of the peak from the surface to 14 cm was 2 hours 30 minutes (velocity of 1.6×10^{-5} m s^{-1}) and from the surface to a 20 cm was 2 hours 40 minutes (velocity of 2.1×10^{-5} m s^{-1}). If the second velocity is used to extend this to the mean debris thickness on Miage Glacier of 25 cm (Foster *et al.,* 2012) then it would take 3 hours 20 minutes for the surface temperature peak to reach the ice. Assuming the time of peak temperature corresponds with peak melt, this shows peak melt is delayed by over 3 hours for the average debris thickness. The heat is conducted slightly faster through the lowermost part of the debris, due to the saturated conditions of the lowest layer increasing the debris thermal conductivity (Nicholson and Benn, 2006). The timing of melt onset is represented by the beginning of the rise in temperatures after the minimum. Using the average hourly temperature cycle, the lag time between the beginning of the rise in temperature at the surface and 14 cm is 1 hour 10 minutes (velocity of 3.3×10^{-5} m s^{-1}); and between the surface and 20 cm is 1 hour 30 minutes (velocity of 3.7×10^{-5} m s^{-1}). If this is extended to 25 cm debris using the lag time to 20 cm this gives a lag to melt onset of

1 hour 53 minutes. Again, the temperature signal is transferred more quickly in the lower debris layer.

The temperature cycle within the debris can be used to understand the timing of melt because the quantity of melt produced is determined by the conductive heat flux at the base of the debris, which is a product of the temperature gradient between the ice and the debris just above it. In DEB-model the debris cover is split into 10 calculation layers, with the conductive heat flux calculated for each, and the heat flux between the lowest debris layer and the ice used to calculate the melt for that debris thickness. The use of several calculation layers allows the assumption of a linear temperature gradient within each layer, but the non-linearity of the overall temperature gradient is maintained, meaning melt can be modelled hourly. The time of maximum melt occurs when the temperature gradient within the lowest layer of debris is at its steepest, shown in the debris temperature measurements by the time of maximum temperature at the deepest probe. To investigate this, melt of 14 adjacent cells close to LOMET with different debris thicknesses, was extracted from the model outputs for the first 36 days of the 2010 season. Their average hourly melt cycles (Figure 4.16) show both the onset and peak of melt is delayed by the debris, with thicker debris resulting in longer lag times. The lag time to peak melt for each cell was calculated from the time of peak incoming shortwave radiation at LOMET (13:00) (Figure 4.17a). The lag time to melt onset was calculated as the time difference between the first substantial flux of incoming shortwave radiation (07:00) and the hour after the minimum melt beneath the debris (Figure 4.17b). For the mean debris thickness (0.25 m) the lag time to peak melt would be around 5 hours, and to melt onset would be around 2 hours.

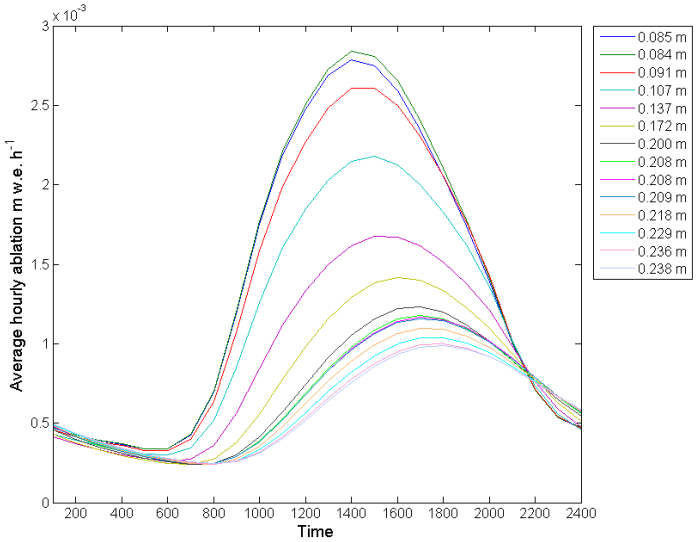

Figure 4.16 Average hourly modelled ablation for different debris thicknesses near LOMET. Ablation was averaged over days 159 to 195 2010.

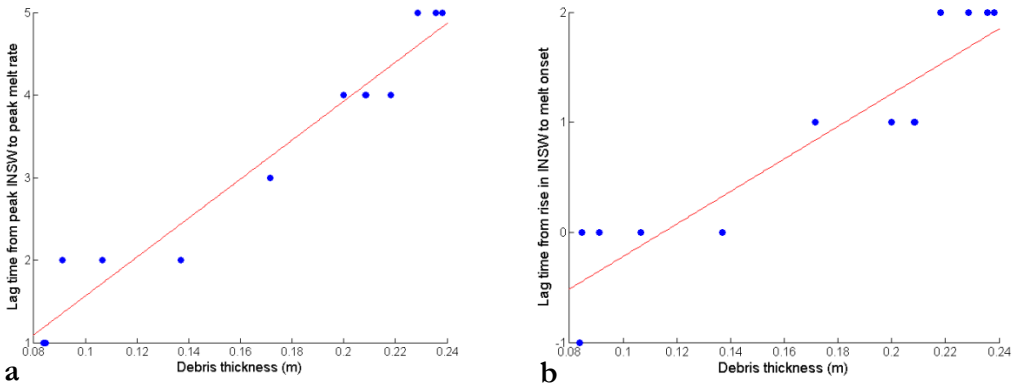

Figure 4.17 a) Lag time from peak INSW to peak melt and b) lag time from rise in INSW to melt onset using the average hourly modelled melt cycles of cells near LOMET with different debris thicknesses. Note that a few cells will have the same lag time because of the hourly model timestep, a shorter timestep would have given a greater resolution of the relationship between debris thickness and lag time.

Therefore, the diurnal cycle that reaches the ice debris interface will be primarily dependent upon the daily air temperature signal, but also depends on the debris thickness and thermal properties, which may be influenced by the level of saturation of the debris. The debris properties influence the timing as well as the magnitude of sub-debris melt, by causing a lag between the temperature cycle at the surface and the ice-debris interface. Since more melt is produced beneath thinner debris, the mean lag time between peak incoming shortwave radiation and peak sub-debris melt which is reproduced in the runoff will be skewed towards that of thinner debris, reducing the lag time. If one compares the time of maximum total melt from each surface type (Figure 4.18), peak melt of snow and dirty ice occurs at 13:00, of clean ice occurs at 14:00, and of debris-covered ice occurs at 15:00. Therefore the lag to peak melt is less than for the mean debris thickness. This analysis does not account for how far melt travels to the proglacial stream, or the magnitude of lags in the supraglacial, englacial or subglacial hydrological system. Overall, when comparing clean ice melt and sub-debris melt, there is a lag to melt onset and peak, the amplitude of the diurnal melt signal is reduced and melt occurs later into the evening.

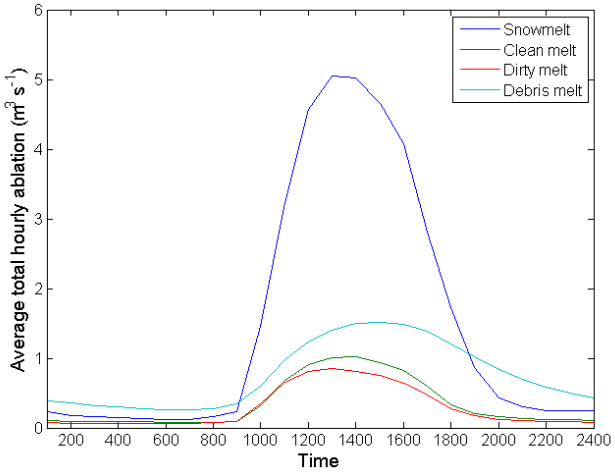

Figure 4.18 Average hourly total modelled ablation for each surface cover type in 2010.

Analysis of the movement of the temperature cycle through the debris suggests this adds a delay in the production of melt beneath a debris layer, with this delay determined by the debris properties. This could have implications for the rest of the hydrological system, as it would reduce the diurnal amplitude of supraglacial stream discharges and result in a later input discharge peak. This could be translated into a later and less pronounced daily peak in the proglacial runoff record.

4.2.3 The fluctuations of the source of melt

It is important to understand the seasonal variations in the quantity of melt from the different surface cover types. This allows the understanding of the relative contribution of different parts of the glacier to runoff as the season progresses, and under specific weather conditions.

At the beginning of June 2010, total melt was composed mainly of snow melt (over 80%), with the rest from the debris covered region, and a very small quantity from the dirty ice area (Figure 4.19). The progressive melting back of the snowline meant the proportion of snow melt decreased gradually until around day 213. The snowmelt component is replaced by sub-debris melt until day 190, when the sub-debris component reached a consistent 30% of runoff. There are gradually increasing contributions from dirty ice and clean ice with these increasing (to around 15% each) until day 210 when they vary around an average, and by which time snowmelt contributes 30-40%. Aside from seasonal trends, on specific days the proportion of snowmelt is decreased and replaced by sub-debris, clean ice and dirty ice melt, for instance days 171, 211 and 226. Figure 7.1 shows these days are associated with relative runoff lows. On these days, low air temperatures meant the elevation of the 0°C isotherm was lower than usual, decreasing the contributing area of snowmelt, and increasing the proportion of clean, dirty and sub-debris melt to runoff.

These days result in recession flows, for instance day 171 also had particularly high sulphate and bicarbonate concentrations, and a low C-ratio, indicative of melt from delayed flow dominating runoff (section 6.2.1.1). Although on day 211 measured discharge remained high despite low melt inputs, because of earlier rainfall.

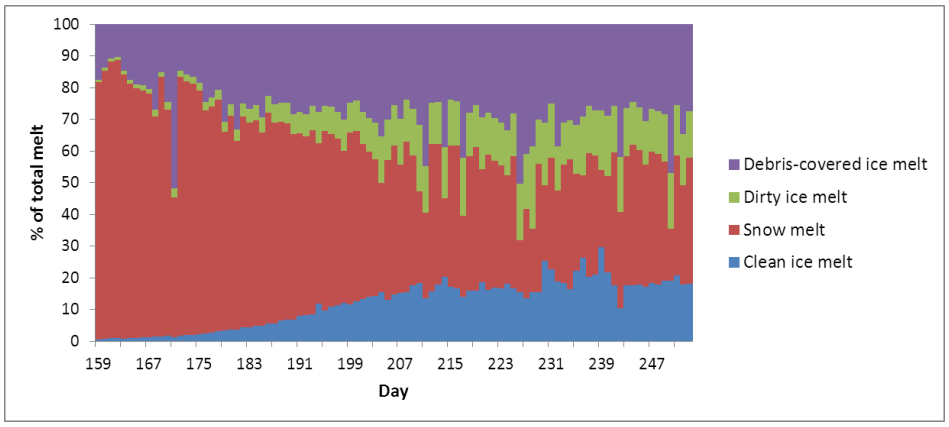

Figure 4.19 Daily variations in the proportions of debris-covered ice, dirty ice, snow and clean ice of total melt. Values are daily averages for 2010.

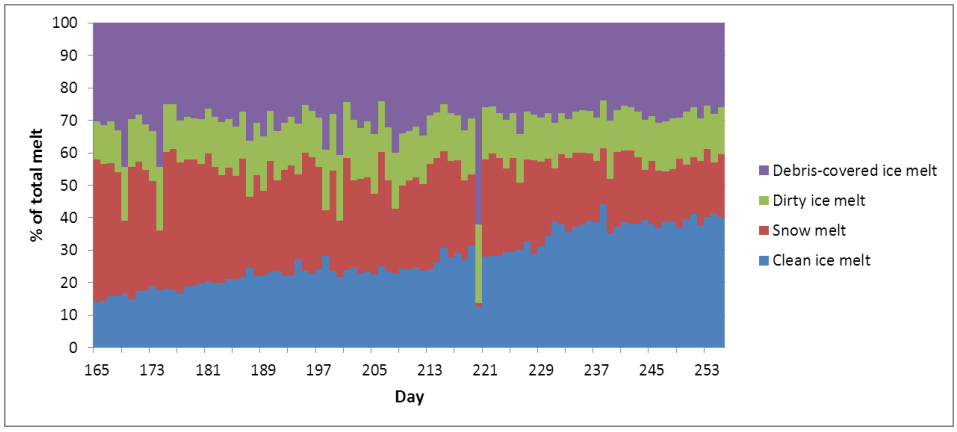

Figure 4.20 Daily variations in the proportions of debris-covered ice, dirty ice, snow and clean ice of total melt. Values are daily averages for 2011.

During the beginning of the 2011 season the snow cover was less extensive than in 2010, with the early June contribution of snowmelt being just 44%, with the remainder of melt composed of sub-debris melt (30%), clean ice melt (14%) and dirty ice melt (12%), Figure 4.20. The contribution from sub-debris melt and dirty ice melt stayed relatively consistent over the season, implying snowcover was limited over these regions in June. This was due to very warm conditions prior to the June fieldtrip – April air temperatures in northern Italy reached record levels, with positive temperature anomalies of over 10°C over the northern plains. This was caused by a warm air mass from North Africa (Società Meteorologica Italiana, 2011), shown in the LOMET record by a peak temperature on day 99 of 13.8°C, which was not exceeded again until day 128. There was still a gradual decrease in the proportion of snowcover, until around day 231 when the snow cover was

16% and clean ice 39% of total melt, so the decrease in snowmelt was due to the exposure of clean ice. As in 2010, there were certain days when cooler conditions reduced snow melt and increased the contribution from clean ice, dirty ice, and sub-debris melt. There was a particularly strong anomaly on day 220 when sub-debris melt constituted 62% of total melt, with clean ice 24%, dirty ice 13% and snow melt only 1%. Average air temperatures were not significantly low, but decreased during the day, so mid-day air temperatures were 9.3°C at LOMET and 6.7°C at UPMET. This corresponded with a distinct low flow in the discharge record on day 221, which was matched well by the model due to its hourly timestep.

Table 4.4 Proportion of melt from different surface cover types in 2010 and 2011.

% of total melt	Clean ice	Snow	Dirty ice	Debris-covered ice
2010	11.9	50.4	10.3	27.4
2011	27.4	27.4	15.0	30.2

The contributing area of the clean ice cells (which contain most snow covered cells by mid-summer) constitute 51% of the glacier area, with dirty ice cells contributing 7% and debris-covered cells 42%. This is unlike the average contribution from each surface cover type (Table 4.4). The apparent disconnect between the contributing area of each surface cover type and their contribution to total melt is due to the differences in melt rates between the different areas, with clean ice and snow melt, and dirty ice contributing a greater proportion of runoff than their area, and the debris-covered region contributing a smaller proportion of runoff than its contributing area. This is due to reduced melt beneath thick debris-cover on the lower glacier, and the high melt rates on the upper glacier where the lower albedo of the dirty ice, and favourable aspect and increased surface roughness of the crevassed clean ice of the tributary glaciers, increases melt rates (section 4.2.1).

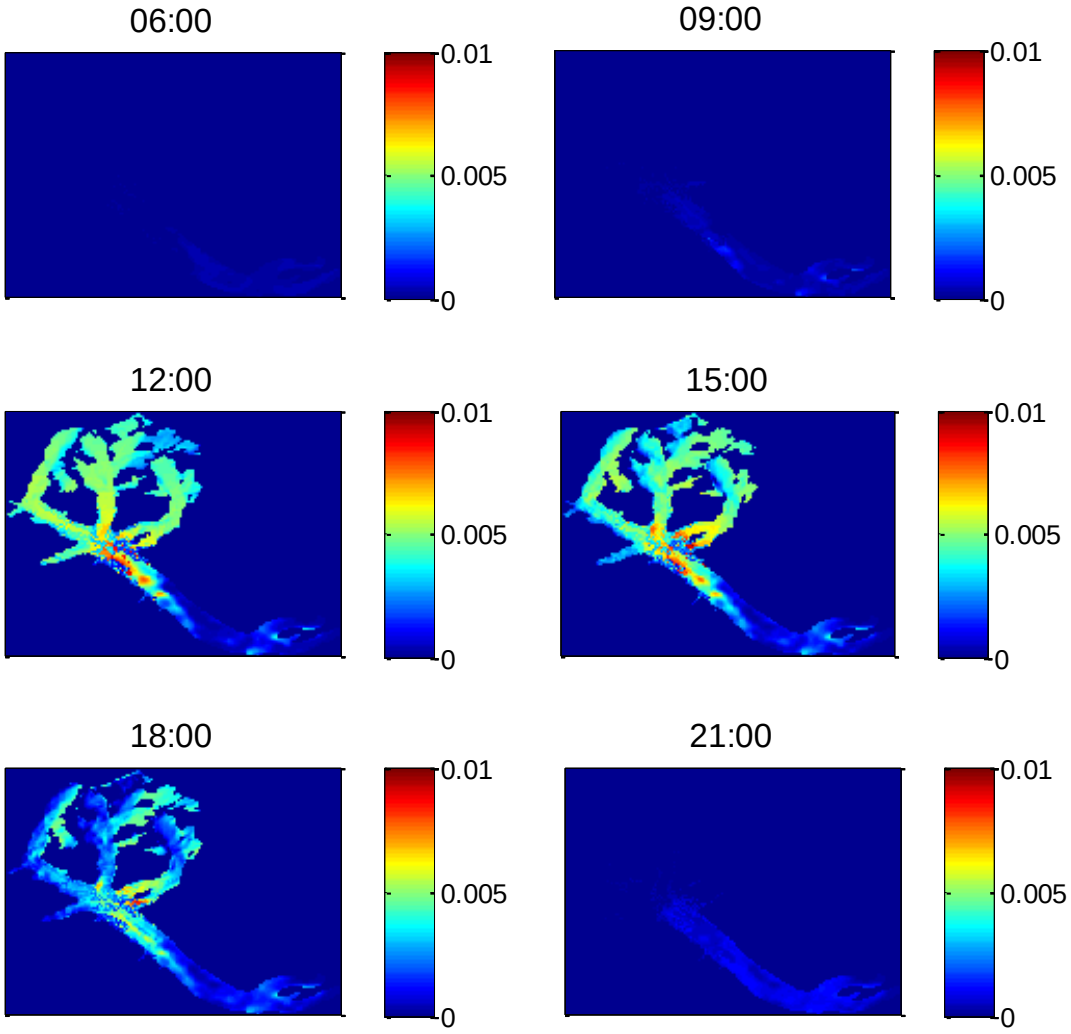

Figure 4.21 Grids of hourly ablation (values in m w.e. h^{-1}) at three hour intervals on day 187 2010, which was a dry day with average weather conditions. The colourbars have been adjusted so they all have a maximum of 0.01 m w.e. h^{-1}, with some values at 15:00 exceeding this (maximum ablation was 0.011 m w.e. h^{-1}).

Looking at the hourly contributions from different parts of the glacier (Figure 4.21), the debris-covered region produces the most overnight melt, because air temperatures remain high enough for melt because of its lower elevation, unlike debris-free ice at higher elevations. In the morning melt from the debris-covered region increases after clean and dirty ice, but continues longer into the evening due to the lag caused by the conduction of the heat from the surface to the base of the debris. The highest melt rates at 15:00 are found on areas of dirty and thinly debris-covered ice, and during most of the day the areas of snow, clean ice and dirty ice even at high elevations have higher melt rates than the ice beneath the debris.

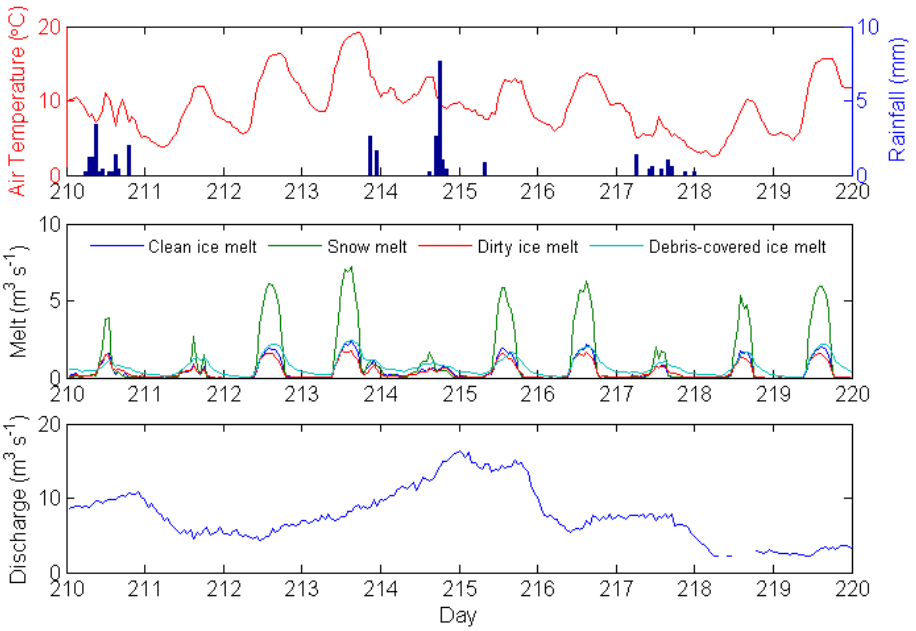

Figure 4.22 Meteorological data from LOMET, total modelled melt from each surface cover type, and proglacial discharge for days 210 to 220 in 2010.

If hourly contributions are studied over periods of variable meteorological conditions (Figure 4.22), days with clear diurnal air temperature signals (e.g. days 212 and 213, 2010) are dominated by snowmelt, followed by debris-covered and then clean and dirty ice. However on cooler or rainy days (e.g. days 214 and 217) melt from the debris-covered region dominates for most of the day, with snowmelt much reduced, although it may become a slightly larger component in the middle of the day. There was a period of warmer days when the discharge was diurnal in 2011 (Figure 4.23). This was late in the season in 2011, when there was little snow cover, so melt from clean ice dominated along with snowmelt. The greater proportion of clean ice to snowmelt coincides with the diurnal proglacial discharge patterns, and may suggest a causal link (related perhaps to the faster runoff from ice compared to snow, though this effect would be assumed smaller by mid-summer), but the quantity of melt from all regions was increased. The debris-covered region still contributed less melt than either clean ice or snow, but was greater than the dirty ice melt, and still dominated overnight. The shape of the daily peaks are interesting, with the debris-covered and dirty ice regions having relatively flat peaks (e.g. days 232 and 233) on the warmest days, because the entire area of the debris-covered and dirty ice cells will be melting on warm days by mid-day so any further increase in melt will be due to greater afternoon air temperatures and incoming shortwave receipt. However, for clean ice and snow-covered regions, the contributing area expands as the afternoon proceeds. The shapes of the individual components add together to give the proglacial hydrograph shape, for instance the clear double peaks of all components on day 231, translate to a double

peaked hydrograph that evening. On the other days the lack of a clear peak in proglacial discharge may be due to the different melt components having different mean lag times, usually sub-debris melt peaks later than other surface types (by 1 to 2 hours on average, section 4.2.2), although notably it occurred within the same hour as the clean ice peak during these days, perhaps explaining the unusually diurnal runoff.

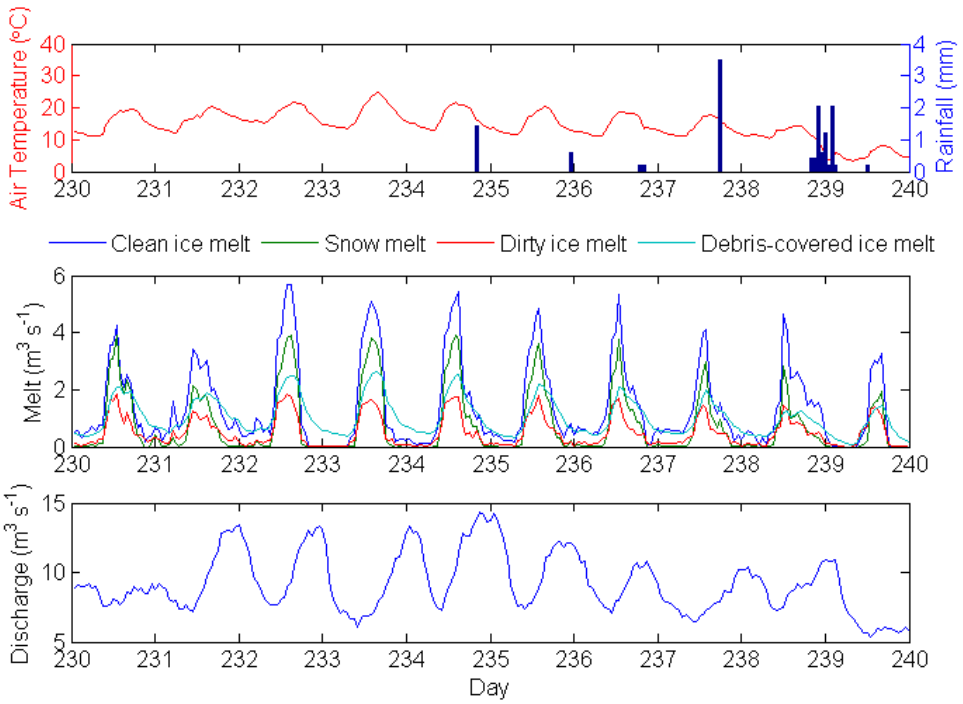

Figure 4.23 Meteorological data from LOMET, total modelled melt from each surface cover type, and proglacial discharge for days 230 to 240 in 2011.

Hourly melt is given in Figure 4.24 alongside proglacial runoff and precipitation data for each of the fieldwork periods. This is to provide the background meteorological, runoff and melt data to allow the interpretation of the dye tracing, proglacial water chemistry and glacier velocity data later in the thesis.

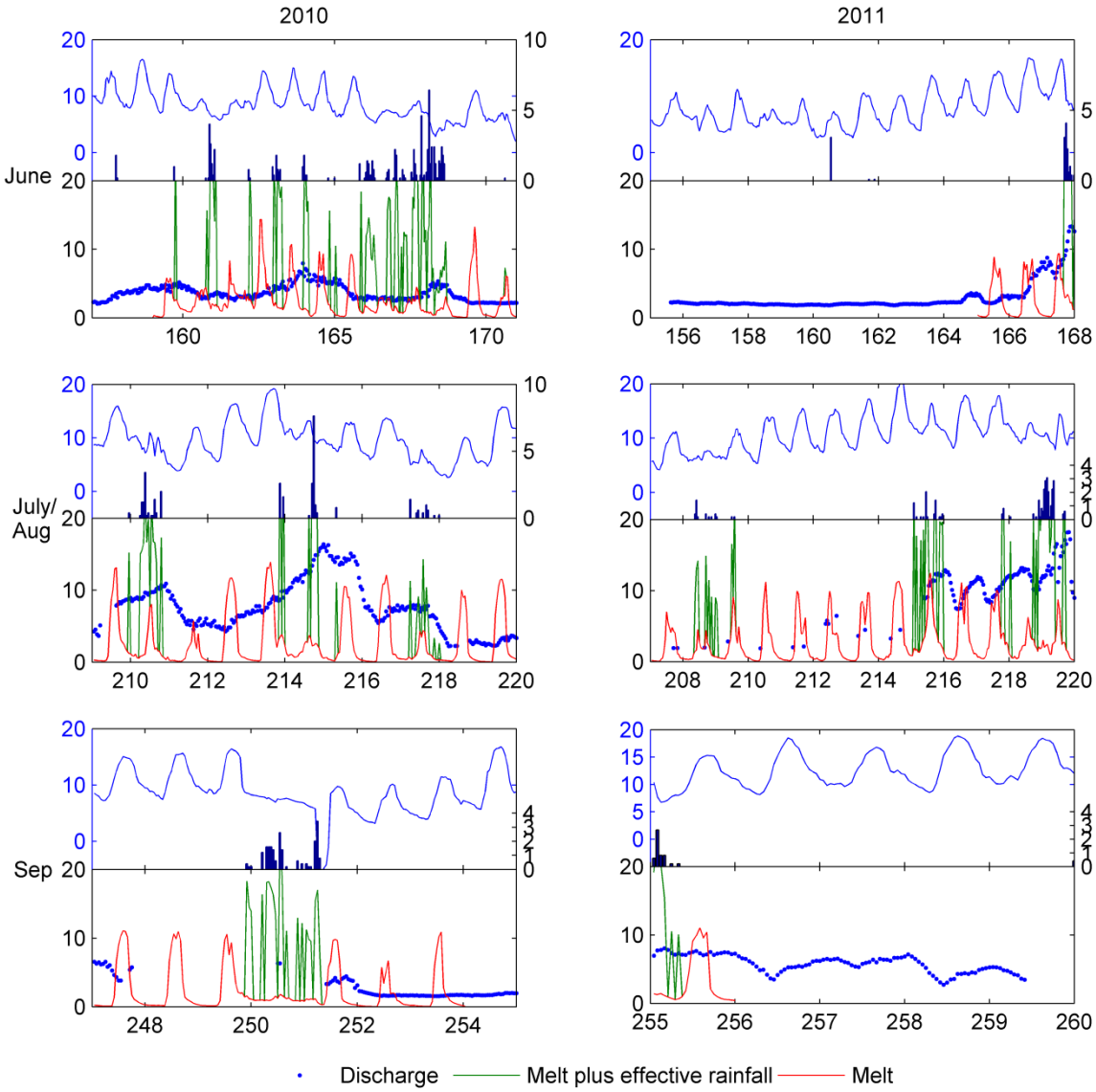

Figure 4.24 Meteorological conditions and water inputs and outputs into the glacier within each of the monitoring periods. The top plot of each set gives the LOMET air temperature (line, °C) and rainfall (bar, mm), with the bottom plot giving the melt and melt plus effective rainfall (rainfall minus evaporation) as modelled by the distributed model and the measured proglacial discharge (all m^3 s^{-1}). The y-axis on the lower plots has been constrained to 20 m^3 s^{-1} so that variations in proglacial discharge can be seen more easily. The x-axis gives the day number. Please note model values were not available on days 157, 158 and 254 of 2010, and days 155 to 164 and days 256 to 259 in 2011. There were no rainfall data before day 160 in 2011.

4.2.4 Sensitivity to air temperature and debris thickness variations

To understand the sensitivity to the model to air temperature and debris thickness changes, the model was modified and the results compared with those from the original dataset. The first model scenario involved increasing or decreasing the air temperature of the LOMET and UPMET records in 1°C increments. The scenarios were run in 2010 when the ICEMET temperature was estimated from the UPMET temperature. The debris

thickness was also varied by applying a uniform change to the debris thickness grid in increments of 0.01 m. The boundaries of the different surface cover types remained constant, but when the debris thickness was increased by 0.01 m, individual cells which were classed as dirty ice (due to a thickness < 0.01 m) were now above the threshold and modelled as debris-covered (essentially increasing the debris-covered area). The changes in air temperature and debris thickness were combined to determine to what degree the debris thickness changes compensate for the air temperature changes.

Looking at the spatial difference in total seasonal melt (Figure 4.25a), a 1°C increase in air temperature increases melt over the whole glacier, but the change was spatially variable. The smallest increase in ablation occurred where the debris was thickest (the melt increase was less than 0.05 m over the season), and at very high altitudes, with the change greater as the debris cover thins upglacier. The largest increase in melt was for areas with a high surface roughness (the Dome and Mont Blanc Glaciers) and even above this region the Mont Blanc Glacier experienced high melt rates because of its south facing aspect. The areas of clean ice, even at high elevations, had a larger increase in melt than the majority of the debris-covered tongue. Therefore regions of thin debris and clean ice, and especially crevassed regions, are relatively sensitive to air temperature changes. Conversely, ice beneath thick debris is relatively insensitive to air temperature changes.

An increase in the debris cover thickness (Figure 4.25b) generally decreases ablation over the main tongue, with the change in seasonal melt usually less than -0.1 m. Areas of thinner debris have a greater decrease in ablation, as the relationship between debris thickness and melt is steeper. Where the debris was previously <0.01 m it was modelled using the dirty ice model, and a small increase in debris thickness meant it was modelled with DEB-model which gives very high melt rates for very thin debris. Conversely, a small increase in the thickness of debris which was previously just thick enough to be modelled by DEB-model will result in a large decrease in melt rates, due to the steep relationship between melt and thickness. This does not exactly replicate real-world conditions, but gives the correct broad result that a small change in debris thickness where previously thicknesses were small or zero can either result in a large change in ablation. A large increase in ablation can occur if the thickness is increased to become similar to the effective thickness (where ablation is highest relative to clean ice (Kirkbride and Dugmore, 2003)), or a large decrease in ablation can occur if the orginal thickness was close to the effective thickness and the debris thickness was increased. Further model development should focus on correctly replicating the decrease in melt as the debris thickness decreases from the effective thickness to clean ice, because it is this region of thin debris cover that experiences the most significant changes in melt.

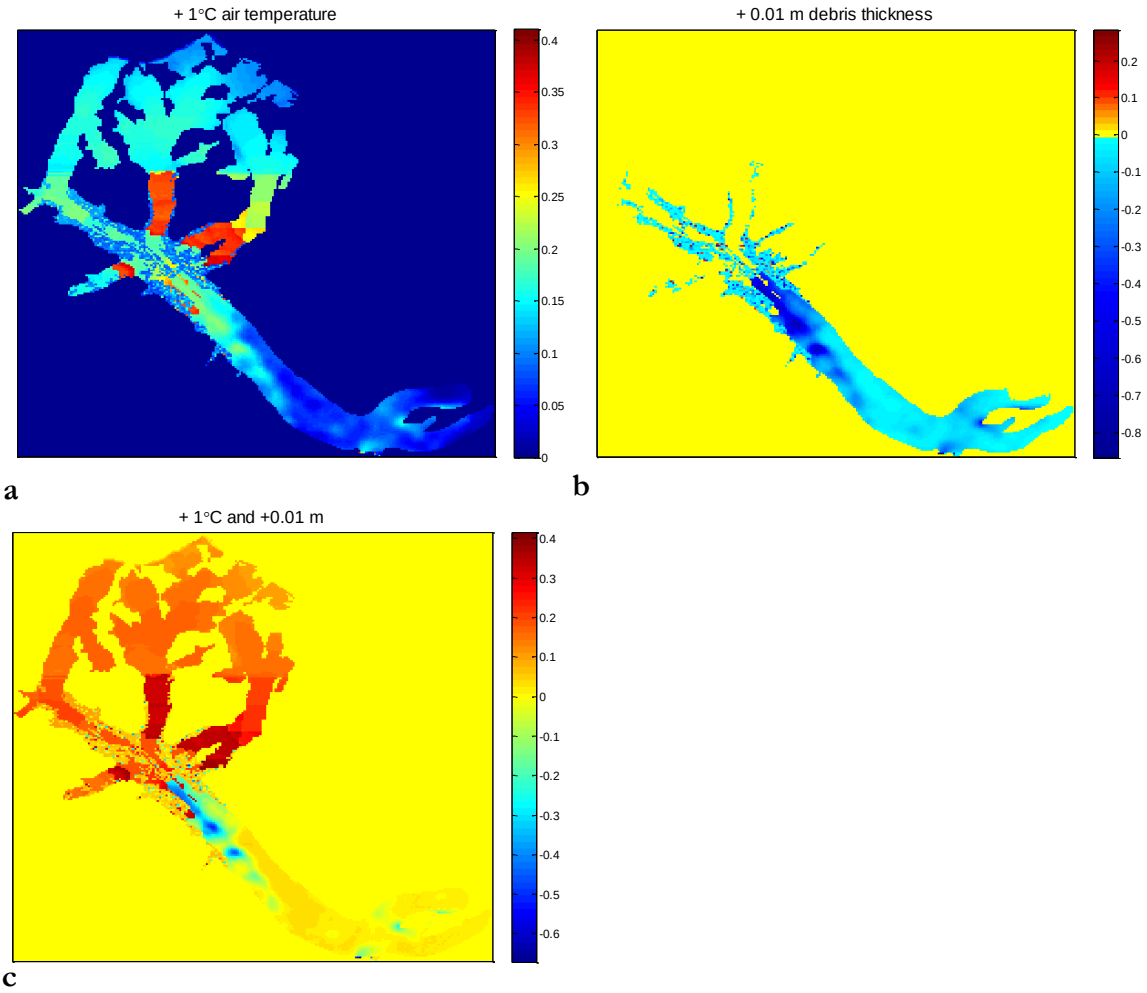

Figure 4.25 Difference in total melt for the season in m w.e., for 2010 for different climate change scenarios; a) when air temperature is increased by 1°C, b) when the debris thickness is increased by 0.01 m and c) when scenarios a) and b) are combined. Note that the colour bar for b) was adjusted so that zero is yellow.

When an increase in air temperature and debris thickness are combined (Figure 4.25c), the overall influence varies across the glacier. On regions of thick debris the influence of the increased temperature overcomes that of an increased debris thickness, to give an overall increase less than 0.04 m over the season. The opposite effect is apparent for thinly debris-covered regions, where the decreased melt due to thicker debris is dominant. On some cells which had zero or very thin debris thicknesses originally, and where the increase in debris thickness significantly increased ablation, melt was further increased by the warmer air temperature. Cells which had a debris thickness >0.01 m originally and experienced a large decrease in ablation due to the increased debris thickness still showed an overall decrease in melt but this was counteracted by the increase in air temperature. If there was a combination of increased air temperature and debris thickness, regions of clean or very thinly debris covered ice (much less than the effective thickness)

would experience the greatest increase in ablation. Where debris was moderately thin a small increase in air temperature could be compensated for by an increased debris thickness.

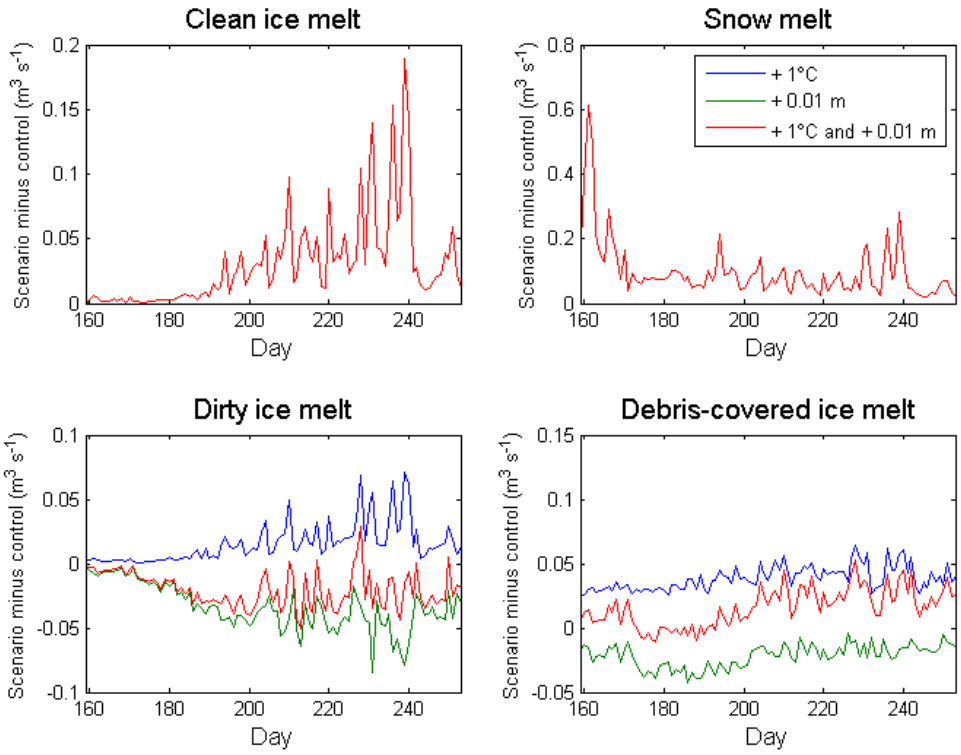

Figure 4.26 The difference in daily melt for each surface cover type under each of the climate change scenarios. The effect of the increase in air temperature and the combined effect of the increase in air temperature and debris thickness results in the same change for snow and clean ice melt (the red and blue lines overlap, with the green showing zero change). The legend in the snow graph is relevant for all subplots.

Figure 4.26 shows the temporal differences in the quantity of daily melt produced for different regions of the glacier, concentrating on an increase in air temperature and/or debris thickness. Under warmer conditions the increase in melt is greater later in the season and for warmer days for clean ice, because more ice is exposed, and also because the warmer the air temperature the greater the contributing area of clean ice melt, which increases the number of cells with increased ablation. For snow, the largest increase in melt is early in the season when there is a larger snow covered area. When the snow is on top of debris it counteracts the insensitivity of the sub-debris melt. This means the overall increase in ablation is greatest in the early spring and suggests an increase in spring air temperatures may result in a larger increase in ablation than an equivalent increase in summer temperatures. For dirty ice there is an increase in melt with increased air temperature but this does not give as large a difference in total ablation because of its smaller area. The lower total melt of dirty ice when the debris thickness is increased is due

to a number of cells becoming classed as debris-covered and no-longer counted as dirty ice. Sub-debris ablation does increase with an increase in air temperature but the magnitude is smaller and the fluctuations not as pronounced as for clean ice. The impact of an increase in debris thickness results in lower ablation over the entire season, even though there were now more debris-covered cells. When both effects are combined the influence of the air temperature to increase ablation dominates, but in the summer the greater melt (and number of cells) especially on the upper glacier means total melt is even greater.

Table 4.5 Model sensitivity to air temperature and debris thickness variations.

Average daily melt (m^3s^{-1})		**-1**	**0**	**1**	**2**
% difference		**Air temperature change (°C)**			
-0.01	**Debris thickness change (m)**	2.79 -3.7 %	2.97 +2.2 %	3.15 +8.5 %	3.34 +15.2 %
0		2.73 -6.0 %	2.90 -	3.09 +6.3 %	3.28 +12.8 %
0.01		2.68 -7.8 %	2.85 -1.9 %	3.03 +4.3 %	3.22 +10.7 %
0.02		2.63 -9.5 %	2.80 -3.7 %	2.98 +2.4 %	3.16 +8.8 %

An increase in air temperature of 1°C results in a 6.3% increase in ablation over the whole glacier (Table 4.5). Doubling the air temperature increase does not increase melt by double, however. The ablation increase with air temperature was not linear, but slightly exponential, with the increase in daily average total melt rising by 0.01 m^3s^{-1} with each 1°C increase in air temperature. This was unexpected given the insensitivity of sub-debris melt to air temperature variations (Brock *et al.,* 2010), but was due to the non-linear response of the dirty ice cells. Increasing the debris thickness by 0.01 m resulted in a small (-1.9%) reduction in ablation, but the sign of the change for a particular cell varied depending upon its original debris thickness. The spatial variation in debris thickness and its change is therefore important in determining the overall impact of a change in debris thickness on ablation. The change in ablation with debris thickness was also non-linear, but this was complicated by the switch of certain cells between being modelled as debris-covered or dirty ice. This analysis does not account for changes to the surface cover type boundaries,

which have been observed to occur on debris-covered glaciers, for instance an up-glacier movement of the debris-covered ice boundary (Stokes *et al.,* 2007) and the increase in dirty ice, at the expense of clean ice (Bolch *et al.,* 2008).

Figure 4.27 The snout of the Mont Blanc glacier as it (partly) joins Miage Glacier, September 2012. Where the ice does reach Miage Glacier it is thin and dirty, most mass transfer is via dry calving.

Figure 4.28 The collapse of the western edge of the Dome Glacier 17th June 2012. Photo courtesy of Fondazione Montagna Sicura.

This corresponds well with what is known about the evolution of debris-covered glaciers, and what has been seen on Miage Glacier recently. Since the 2005 aerial photo there has been considerable change at the base of the Dome and Mont Blanc Glacier ice falls, with the most noticeable difference being the disconnection of the Mont Blanc Glacier tongue with the main glacier (Figure 4.27). Only a very thin section of ice joins the main tongue, with most mass transferred through dry calving. Just this year (2012) there was a massive collapse of part of the western edge of the Dome Glacier, probably caused

by very warm weather. The ice at the top of this region must have become too thin and crevassed to support that below it (Figure 4.28). These regions of the most drastic short term change were identified in the model as having firstly some of the highest ablation rates, and also being most sensitive to increased temperatures. If warming continues then both these tributaries will probably become completely unattached from the main glacier. A similar situation occurred on the Brenva Glacier, just down valley from Miage Glacier, where avalanche deposits in the 20th century magnified a period of advance so that it extended down to the main valley (Deline, 2005). However, ablation of the clean ice on the steep ice fall meant the upper glacier became disconnected with the lower debris-covered part, leaving stagnant ice in the lower valley.

High melt rates (identified as regions of thinning) in the thinly debris-covered region just upglacier from the edge of the debris cover have been observed on glaciers such as the Khumbu Glacier (where thinning was greatest near Everest Base Camp where the ice was clean or dirty (Nakawo *et al.,* 1999), and 6 Glaciers in the Adylsu valley, Caucasus (where the greatest ablation was found at the up-glacier edge of the debris-cover (Stokes *et al.,* 2007). The lower melt rates beneath thick debris is also well known (Östrem, 1959), but often there are a significant number of supraglacial lakes which are not prevalent on Miage Glacier but are common on glaciers in the Bhutan Himalayas (Reynolds, 2000; Ageta *et al.,* 2000) and Ngozumpa and Imja Glaciers in the Khumbu Himal (Benn *et al.,* 2000; Chikita *et al.,* 2000). They may start small but can coalesce into large lakes with calving ice fronts which can dramatically increase ice mass loss (Röhl, 2008), although even small ponds increase ablation by exposing ice cliffs in otherwise thickly debris-covered regions (Benn *et al.,* 2001). To model the evolution of glaciers where ponds are common they should be included in a future version of the distributed melt model.

4.3 The influence of debris on the supraglacial topography and stream network

This section deals with the supraglacial stream network, in terms of the morphology, size and velocity of supraglacial streams and how they are distributed across the glacier. Results are produced from a combination of observations, measurements and GIS analysis of the ARPA DEM of the glacier.

On the upper glacier above C10, the surface topography is controlled by the existence of the main central and lateral moraines. The differential ablation between these areas of thicker debris cover, compared to the clean or slightly debris covered ice between them results in the ice surface beneath the moraines being relatively high. Meltwater collects into supraglacial streams on the clean ice in between the moraines. The main stream between the central and eastern moraine could be followed up to the base of the Dome glacier, and is thought to drain into the S12 moulin. The main western stream could be followed up to around 500 m northwest of ICEMET and likely drains into the S14 moulin. There were several moulins around C10: S11, S12, S14 and S15, although S11 was only actively used by a stream in 2010, and not 2011.

Measurement of supraglacial stream discharges suggests the S14 stream was the largest and fastest stream on the glacier (of those observed) with a mean discharge of 0.62 $m^3 s^{-1}$ and velocity of 1.52 m s^{-1}. The S12 stream was the second largest measured and was the main stream draining the eastern side of the upper glacier, (mean discharge 0.18 $m^3 s^{-1}$ and velocity 0.46 m s^{-1}). The S15 stream had smaller discharges and slower velocities (mean of 0.017 $m^3 s^{-1}$ and 0.36 m s^{-1}), so likely had a local catchment.

Downglacier from these moulins the elevation difference between the moraines and the valleys in between them increases with distance downglacier, until the region close to C8. The valley system in between the moraines can be seen on both the DEM of the glacier (Figure 4.29) and on the map of flow length (Figure 4.30, top inset). The regions of high flow length indicate the presence of supraglacial streams and highlight the parallel valleys running along glacier where flow is focussed by the moraine's topography. The valley is particularly steep either side of C9 (Figure 4.31a), and although the streams were not measured they were observed to be fast flowing. This valley system is occasionally interrupted, for instance by the presence of C8 lake. Gradually this valley system becomes less apparent downglacier from C7. The decrease in the prominence of the valley system downglacier is caused by debris cover redistribution, which occurs when the sides of the moraine exceed 27-29° and the debris slides down the flanks of the moraine and into the

trough at the bottom (Deline, 2002). This mechanism increases the debris thickness at the foot of the moraine, and decreases the thickness at the top, decreasing the ablation gradient, and resulting in a flatter topography with a more even debris coverage. The downglacier evolution of the debris cover influences the glacier's surface topography and the supraglacial stream network. This is why there is a difference between the upper glacier stream network which follows the troughs between the moraines (Figure 4.30, top inset), and the lower glacier where the stream network is less coherent because the local relief is smaller and there is no-longer a preferential valley to capture drainage (Figure 4.30, bottom inset).

The more hummocky topography on the lower glacier (Figure 4.31b) results in a decrease in catchment size compared to the upper glacier. The catchments of the dye traced moulins and streams were delimited from the ARPA DEM (see section 3.3.3.1). The catchment sizes can only be used as a guide because the analysis fills the sinks in the DEM and takes no account of moulins. Despite these caveats the catchments of the lower glacier streams and moulins generally remain small with the mean catchment size for the S1 to S4 streams being 0.025 km^2 (Figure 4.32 and Table 4.6). This demonstrates the topography is constraining the catchment size, even without accounting for other moulins. The catchments of S5 to S8 are calculated as the largest in area, but the catchments extend farther upglacier than in reality because there is no account of upstream moulins. The size of most of the upper glacier catchments are not constrained by topography (apart from S9 and S10, which have relatively small catchments), but simply are smaller for streams further upglacier, although they are an order of magnitude larger than the lower glacier catchments. The mean modelled catchment size for the S11 to S14 streams is 1.42 km^2. This analysis is consistent with the stream measurements of the upper glacier streams, in that the S15 stream has a much smaller catchment area (0.006 km^2) than S14 and S12 (1.33 km^2 and 1.15 km^2), and it had a smaller discharge.

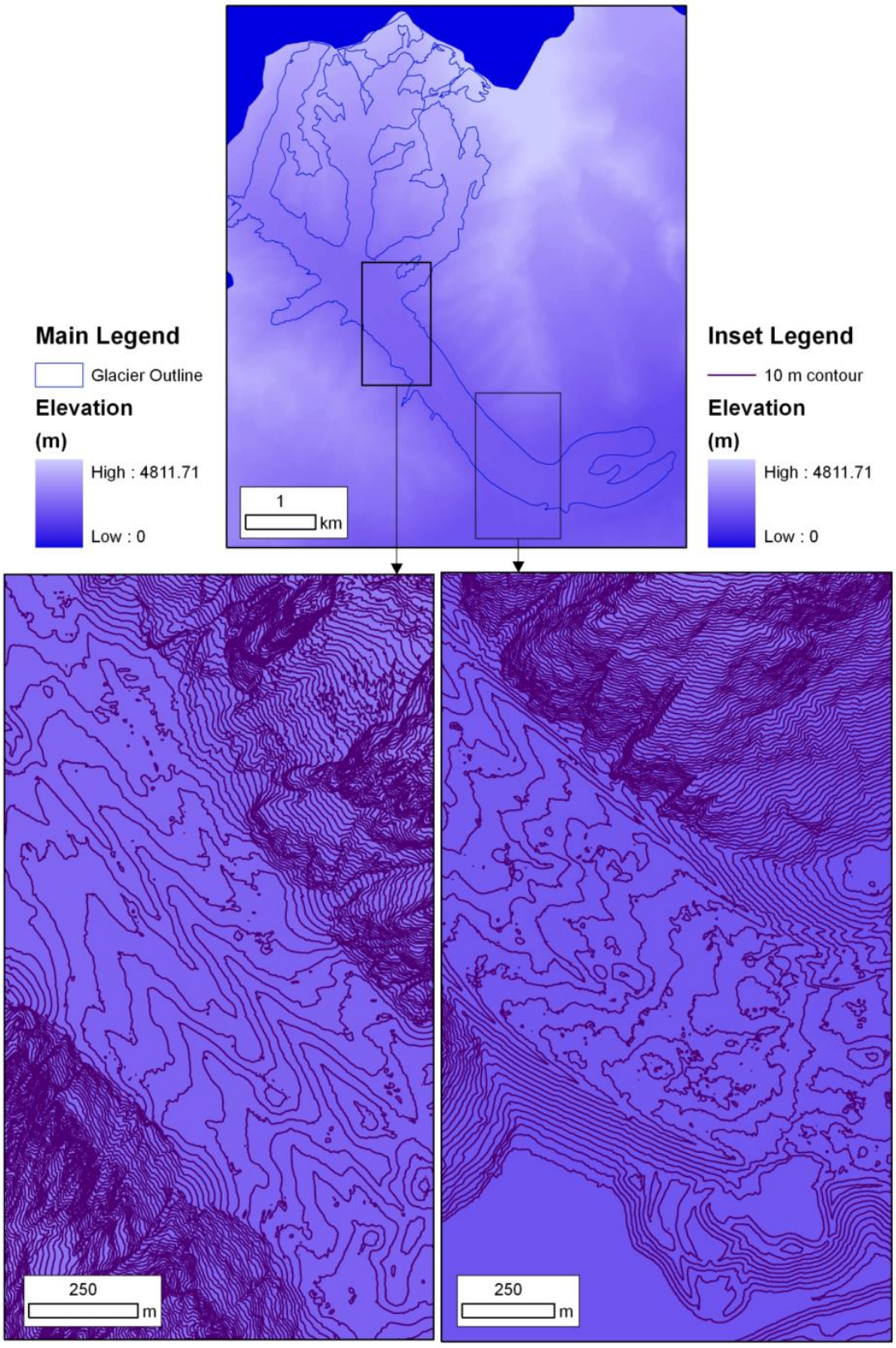

Figure 4.29 Map of the 2005 ARPA digital elevation model. The left inset shows the clear peaks in elevation associated with the central, eastern and western moraines on the upper glacier, and the valleys in between. The right inset shows the more hummocky topography on the lower glacier. Both insets show contours at 10 m intervals.

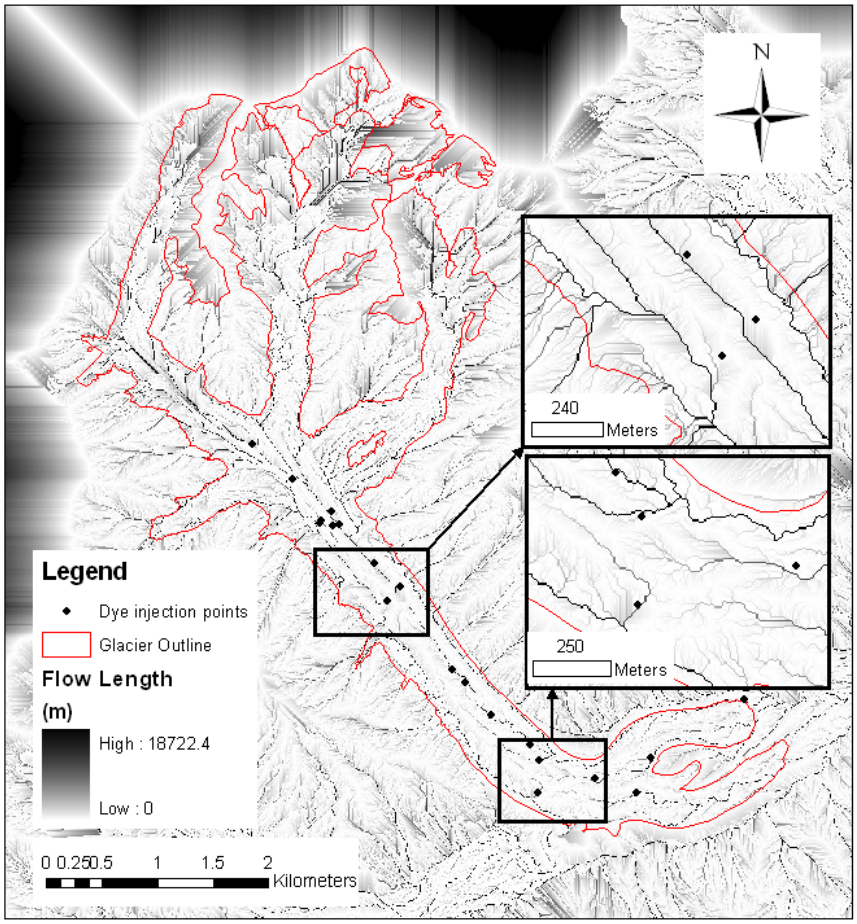

Figure 4.30 Supraglacial flow length map, where high values are indicative of the position of supraglacial streams. The top inset shows the 'valley system' in between the moraines on the upper glacier, and the bottom inset shows the less coherent network on the lower glacier. See section 3.3.3.1 for an explanation of how this map was produced.

Figure 4.31 Photographs of supraglacial topography: a) Shows the valley in between the eastern and central moraine, this photograph was taken just to the east of C10 in September 2011, and b) looking downglacier from C7, shows the hummocky topography of the lower glacier, June 2011.

Table 4.6 Catchment areas as delimited using analysis of the 2005 ARPA DEM. The catchment areas may be overestimated because the analysis does not account for the occurrence of moulins.

Injection Point	Catchment Area (km^2)
S1	0.05
S2	0.03
S3	0.02
S4	0.01
S5	2.13
S5b	0.02
S6	2.12
S7	2.10
S8	2.10
S9	0.002
S10	0.21
S11	2.06
S12	1.15
S12b	1.15
S13	1.15
S14	1.33
S14b	0.59
S15	0.006
S16	1.09
Gauging Station	2.70

There are many areas on the lower glacier where very few streams were seen, for instance on most of the northern lobe apart from the southern flank which is drained by S1, and between C3 and C5, where only the S5 stream system is present towards the eastern edge of the glacier. The S5 stream network is probably the largest on the lower glacier. It's discharge was very consistent, ranging from a minimum of 0.027 $m^3\ s^{-1}$ on day 157 to a maximum of 0.032 $m^3\ s^{-1}$ on day 163. Input velocities were slow, but faster in June (June mean 0.24 m s^{-1}, and July/Aug mean 0.14 m s^{-1}). The S7 stream discharges were also small and ranged from 0.006 $m^3\ s^{-1}$ on day 258 to 0.032 $m^3\ s^{-1}$ on day 215, with velocities similar to S5 with a mean of 0.24 m s^{-1}. Most lower glacier streams flowed slowly, because of the small discharges and gentle gradient of the lower tongue. Another observation was the lack of well-defined moulins on the lower glacier.

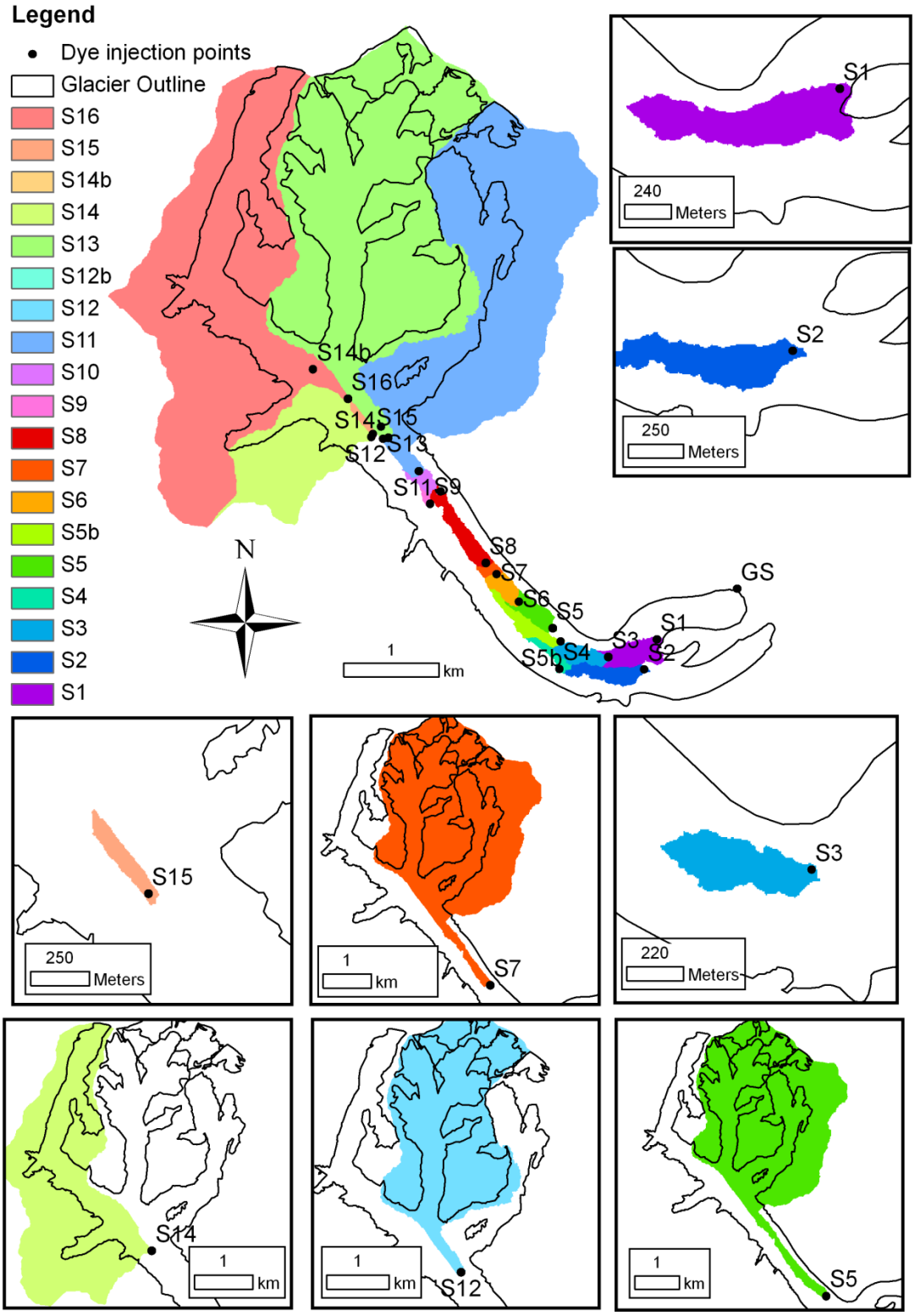

Figure 4.32 A map of the supraglacial stream catchments as delimited by ArcGIS using the ARPA DEM and the Hydrology Toolbox. The catchment outlet is the injection point used for dye tracing. This analysis does not account for the occurrence of moulins, and so catchment sizes may be overestimated. The catchments have been overlain on top of one another in the main figure.

This analysis suggests there is a difference between the upper and lower glacier in the discharges entering moulins. On the upper glacier, high melt rates create large meltwater inputs which are funnelled by the moraine system into a few large streams. Inputs into the moulins around C10 are therefore relatively large. Lower on the glacier (from approximately C7 downglacier), the redistribution of the debris produces a more hummocky topography. Supraglacial stream catchment areas are constrained by the topography, which when combined with low ablation rates beneath the thick debris (section 4.2) results in supraglacial streams with small input discharges.

The impact of the debris on input stream discharges is important because the stream discharge determines whether or not a particular stream causes the switch between a distributed and channelized network when it reaches the glacier's bed (Hewitt and Fowler, 2008), which could influence the evolution of the subglacial channel network. Relatively small inputs also reduce the likelihood of pressurisation of the subglacial drainage system, limiting the impact on glacier velocity variations.

4.4 Evaporation and vapour flow in the debris layer

The evaporation of water from a debris-cover is rarely studied, but could result in an important reduction in runoff from rainfall. This section looks at whether this is the case, and also studies the details of water vapour flow within the debris layer, as condensation or evaporation of water at the ice/debris interface could have implications for the energy balance at the ice surface.

4.4.1 Measured evaporation

In both 2010 and 2011 a lysimeter was installed near the lower weather station (section 3.2.1). The evaporation calculated over each of the measurement periods is given in Table 4.7. The evaporation from the mark 1 lysimeter in 2010 was consistent, as the evaporation as a percentage of rainfall was around 35% for both measurement periods. This was slightly higher than the 25% of rainfall calculated by Sakai *et al.* (2004) for the Lirung Glacier. In contrast, the values for 2011 using the same lysimeter design were much larger, with evaporation as a % of rainfall being around 90%. In 2011 the lysimeter was situated in a slightly different position where the debris was thicker and more level. The debris at this site had a greater proportion of fines, and the debris size distribution was smaller on average (compare Figure 4.33a and Figure 4.33b). The debris became consolidated over time, forming a dense matrix with low permeability. This could only have happened if there was a significant quantity of clay and silt sized sediment that caused

cohesion of the individual sediment grains (Mehta and McAnally, 2008). Such fine grained debris would have resulted from melt out of a medial englacial debris septum, as this would have allowed the debris to be comminuted at depth (Gomez and Small, 1985). Cohesion of the grains would have decreased the rate of water percolation, and increased the proportion of rainfall evaporated. Similarly, Sakai *et al.* (2004) found the percentage of rainfall evaporated was higher from an area of soil than from debris, which was attributed to the difference in permeability between the two sites. Furthermore, if infiltration rates were very low then rainwater may have spilled over the top of the lysimeter and onto the surrounding debris, decreasing that collected and overestimating evaporation. Debris permeability is therefore important in governing the percentage of rainfall evaporated, assuming air temperature and wind speed is similar. The relatively small diameter of the lysimeter opening compared to the size of the debris meant smaller clasts on average were used. This may have resulted in an overestimation of the evaporation rates. The evaporation as a percentage of rainfall was very high for the mark 2 lysimeter (91%), but there were problems during its installation (section 3.2.1). The water also had to percolate through twice the depth of debris, and flow into a collecting bottle, possibly reducing the amount of percolated water.

Table 4.7 Lysimeter measurements from 2010 and 2011, both types of lysimeter were located next to LOMET, but in slightly different locations in the debris.

Lysimeter	Days	Year	Percolation (mm)	Rainfall (mm)	Evap. (mm)	Evap. as a % of rainfall	Rainfall coefficient
Mark 1	211-217	2010	12	19	7	36	0.64
Mark 1	218-252	2010	52	80	28	35	0.65
Mark 1	163-208	2011	24	222	198	89	0.11
Mark 1	208-258	2011	7	104	97	93	0.07
Mark 2	165-258	2011	29	324	295	91	0.09

Figure 4.33 Lysimeter mark 1 near LOMET: a) in September 2010 (it was buried originally so the top was level with the debris surface), and b) in September 2011. Note the cemented appearance of the debris surface.

These results are likely too few to allow detailed inferences about the exact quantity of evaporation of rainfall from the debris. However, evaporation of rainfall can be considerable, especially where the debris permeability is low. This means a given rainfall event is less likely to result in high water inputs to the glacier hydrological system beneath areas of debris. This reduces the quantity of rainfall reaching the proglacial stream, and decreases the peak discharge. Overall, evaporation of rainfall from debris is likely higher than evaporation of rainfall onto clean ice because of: higher surface temperatures (mean debris surface temperature at LOMET in 2011 was 12°C, compared to 0°C for ice) increasing the rainwater temperature; higher surface roughness (aerodynamic roughness length over debris for Miage Glacier is 0.016 m (Brock *et al.,* 2010) compared to 0.007 m over clean ice (Brock *et al.,* 2006)) reducing saturation of overlying air (Ward and Robinson, 2000); and the low permeability of debris causing storage of rainfall and increasing the proportion evaporated. Unfortunately, measured evaporation cannot give information on the evaporation of meltwater, because melt could not enter the lysimeter and its base was not in contact with the ice. This makes it difficult to understand the fluxes in liquid water over the whole debris column. However, measurements of temperature and relative humidity within the debris can be used to understand the flow of water vapour, and this is discussed next.

4.4.2 Water vapour flow in the debris

The flow of water vapour within the debris was modelled using simple flux gradient relationships based on the variations of temperature and relative humidity in the debris layer. Unfortunately continuous data from 2010 and 2011 is limited to three of the four

sensors from the 2011 HOBO, and the vapour flow fluxes from these data will be studied first. Some examples will also be given from data collected by Brock *et al.* (2010) in 2005.

4.4.2.1 Interpretation of patterns of water vapour flow

The daily flux cycle can be seen in the average hourly data (Figure 4.34). Overnight temperatures in all layers are low, although the surface temperature is much warmer (around 6°C) than the lower two sensors. The relative humidity was also high for all sensors, but only the surface sensor remains unsaturated, at around 90%. Under these conditions the vapour flow is very slightly negative (downwards), with the surface to 14 cm flux being about double between 14 and 20 cm. From about 8:00 onwards, the surface temperature rises, but this is not reflected in a rise in temperature at 14 cm for at least 2 hours. Meanwhile the relative humidity of the surface decreases, although the lower two layers remain saturated throughout the day. The vapour flow between the surface and middle layer becomes more negative, with the flow in the lower layer also becoming more negative, but, as for the temperature increase this doesn't occur until a couple of hours after the upper layer. The vapour flow in the top layer reaches its greatest magnitude at 12:00, of -1.18×10^{-6} kg m^{-2} s^{-1}, before it becomes less negative during the afternoon, even though the surface temperature is still increasing. Air temperatures peak at the surface at 15:00, with the relative humidity reaching its lowest level at 16:00. By this time the vapour flow in the top layer is still decreasing, but the lower layer is just reaching its greatest flux magnitude of -5.54×10^{-7} kg m^{-2} s^{-1} at 17:00. During the evening, the debris temperatures decrease, the surface relative humidity increases and the magnitude of the vapour fluxes in both layers decreases.

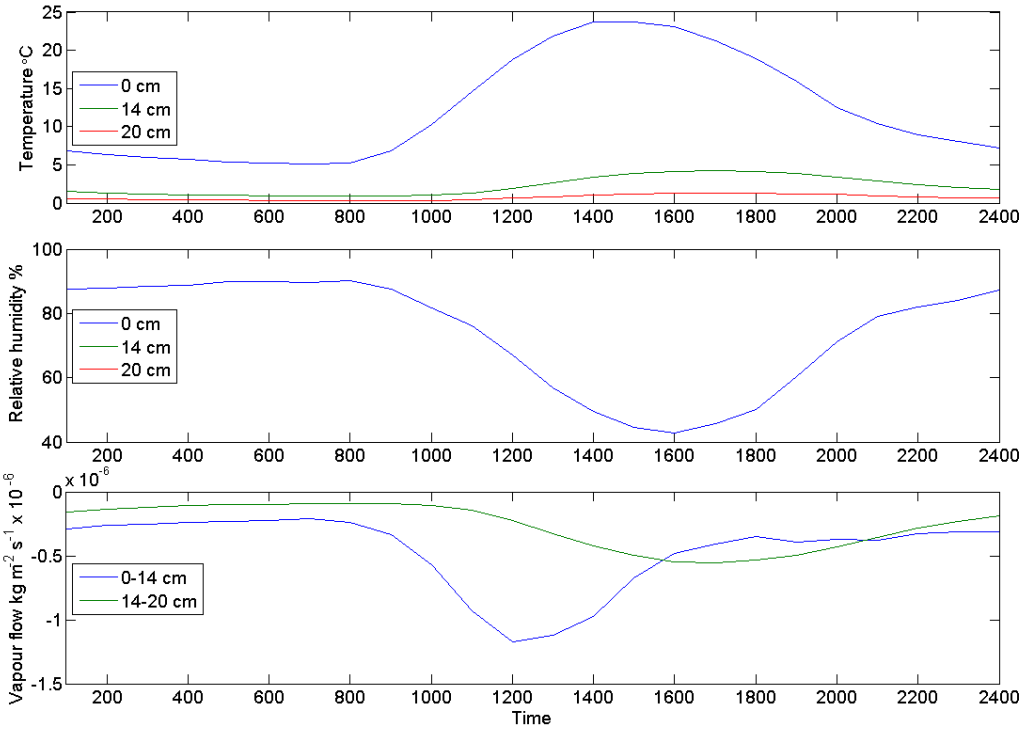

Figure 4.34 Average hourly debris temperature, relative humidity and modelled vapour flow, with the temperature and relative humidity measured by sensors within 0.20 m debris near LOMET during days 215 to 258 in 2011.

To explain the fluctuations in the vapour flow it is helpful to refer to the theory of water transport in soils developed by Philip and de Vries (1957). The vapour flow is driven by the vapour density gradient, and the saturated water vapour density (a function of temperature). Philip and de Vries (1957) split the vapour flow (J_v) (g cm^{-2} s^{-1}) into two components: the first due to the temperature gradient (thermal), and the second due to the moisture gradient (isothermal) to give,

$$\frac{J_v e_a}{\rho_w} = -\kappa_{vT} \nabla T_d - \kappa_{v\theta} \nabla \theta, \qquad (4.1)$$

(Philip and de Vries, 1957, p224) where e_a = the partial pressure of water vapour (mm Hg), ρ_w is the liquid water density, κ_{vT} is the thermal molecular diffusion coefficient (cm s^{-1}), $\kappa_{v\theta}$ is the isothermal molecular diffusion coefficient (cm s^{-1}), T_d is the soil (or debris) temperature, and θ is the moisture content (cm^3 of liquid water per cm^3). The discussion refers to thermal and isothermal flow, although the calculated vapour flow includes both components.

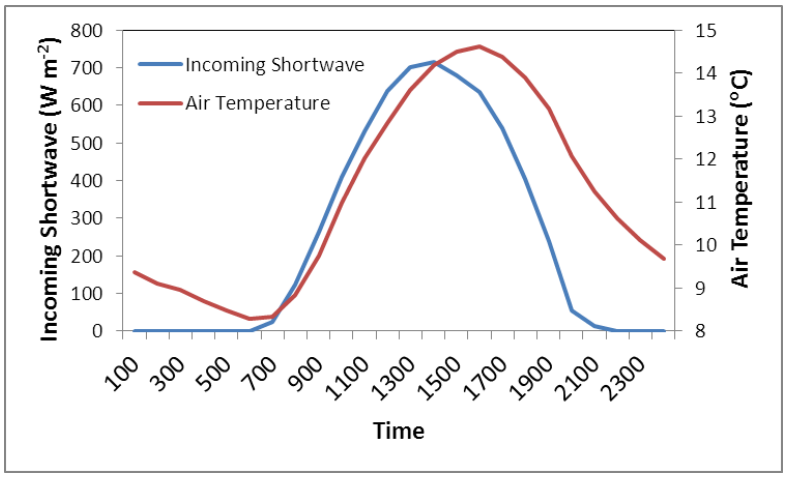

Figure 4.35 Average hourly air temperature and incoming shortwave radiation measured at LOMET during 2011.

The thermal vapour flow occurs because if a steep temperature gradient is experienced within a soil (analogous to the processes in the debris), water vapour flows from hot to cold (Marshall and Holmes, 1988). This is because the saturated vapour pressure is dependent upon temperature, so if there is not a large variation in relative humidity (which influences the actual vapour pressure), then temperature drives the vapour density gradient. As vapour density is low when temperatures are low, the vapour moves towards cooler layers. In the morning a temperature gradient is caused by the difference between the surface debris, warmed by incoming shortwave radiation (Figure 4.35), and the ice. The top layer experiences a downward (negative) thermal vapour flow, which increases as the temperature gradient increases during the morning. In the afternoon the temperature difference between the surface and 14 cm decreases, therefore reducing the magnitude of the downward vapour flow. This agrees with that modelled for soils experiencing a temperature gradient. Grifoll *et al.* (2005) modelled the vapour flow for an Adelanto loam soil in Arizona and within the wet region 0.5-0.01 m deep, downward vapour flow occurred, associated with a temperature gradient between 15.5˚C and 40.4˚C at the surface. Scanlon (1992) calculated there would be a downward vapour flow during the summer below 1 m (corresponding to the evaporation front), within the soils of the Chihuahuan Desert, Texas. Furthermore, Saito *et al.* (2006)'s numerical model predicted that below the drying front during the day, there would be a downward thermal vapour flow. The drying front is the depth above which water vapour flow rather than liquid water flow dominates the total water flux (Saito *et al.,* 2006).

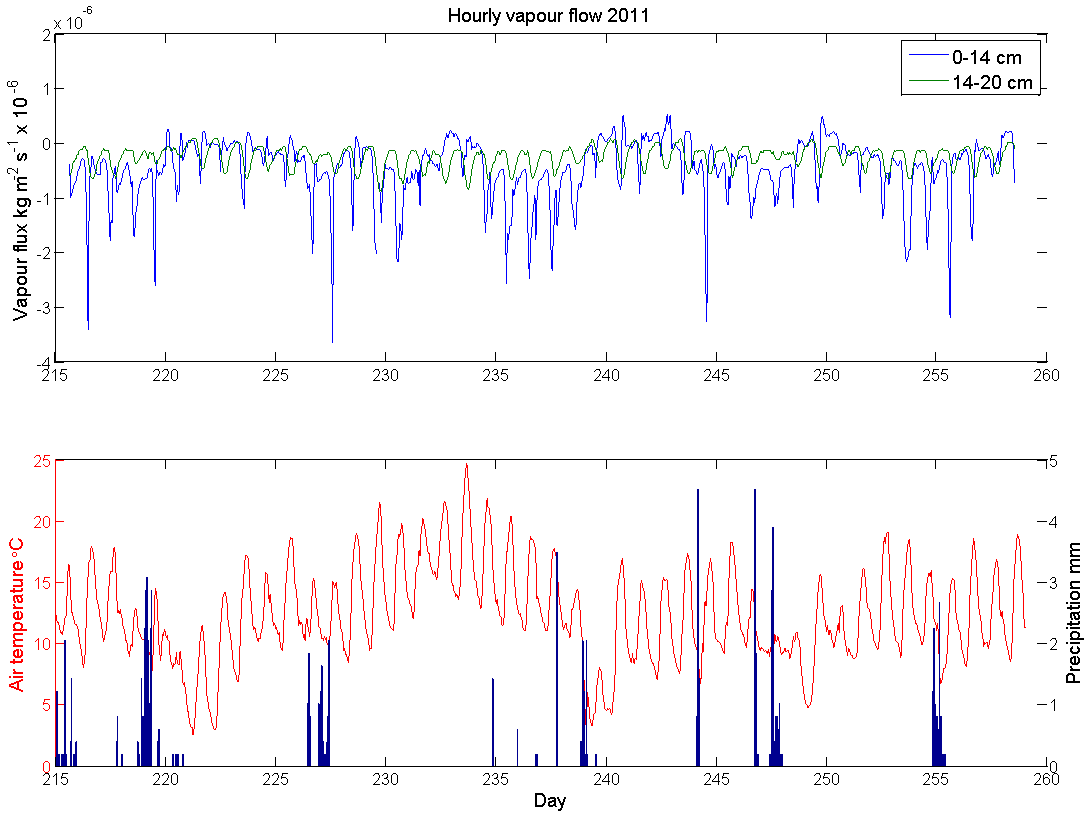

Figure 4.36 Timeseries of vapour flow modelled from data from the sensor in 0.20 m debris near LOMET in 2011, and the air temperature and precipitation over the same period.

If the whole 2011 series is studied (Figure 4.36), then pronounced downward spikes in vapour flow in the upper layer become apparent, which are larger than on an average day. These spikes occurred on days 216, 219, 227, 244 and 255, and occur in the middle of the day following rainfall during the preceding morning or evening. For instance on day 255 the surface layer vapour flow peaked at -3.2×10^{-6} kg m^{-2} s^{-1}, following heavy rainfall in the morning of day 255 which saturated the upper layer. When the entire profile is saturated and there is a steep temperature gradient (e.g. the morning following rainfall), the thermal vapour flow dominates within the entire profile and the large temperature gradient gives a pronounced negative flux.

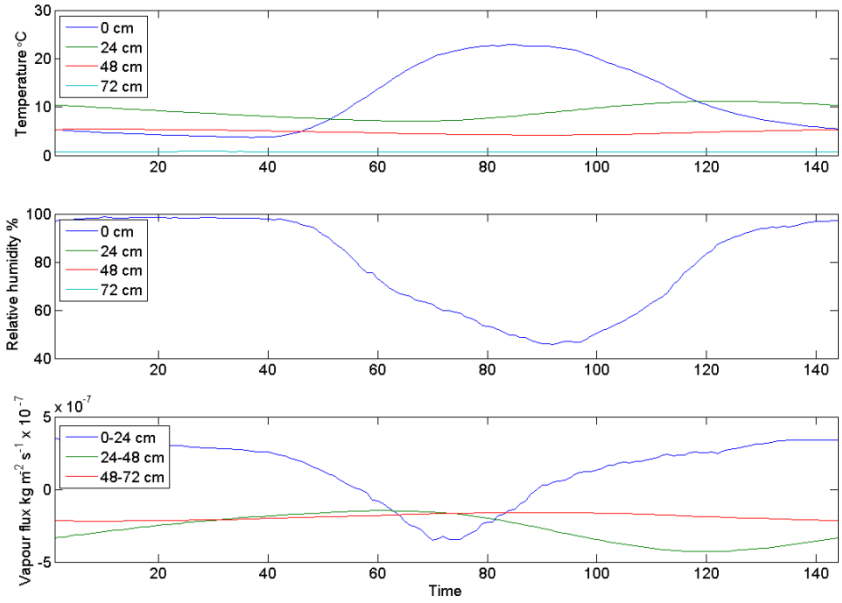

Figure 4.37 Hourly average debris temperature, relative humidity and modelled vapour flow from sensors in debris 0.72 m thick on the southern lobe from day 168 to 250 in 2005. The time is the 10 minute period within the day.

In a profile from 2005 with a debris thickness of 72 cm (Figure 4.37), there is an increasingly negative flux in the lower layers during the afternoon and evening, although the increased depth means the most negative flux occurs later. However, the top layer (0 to 24 cm), has an inverse night time temperature gradient, so surface temperatures are cooler than at depth, possibly due to sensible heat loss and radiative cooling from the debris surface. During the night the relative humidity gradient between the surface and 24 cm is small (only a couple of %) so thermal vapour flow dominates, vapour flows towards the cooler surface, and instigates positive vapour flow of up to 3.5×10^{-7} kg m^{-2} s^{-1}. The flow becomes negative as the temperature gradient reverses during the day and the surface warms, but despite this the flow becomes positive again by mid-afternoon. This is because although there is a temperature gradient, the relative humidity gradient dominates and this causes isothermal vapour flow.

This isothermal vapour flow occurs in the upper debris layers because there is a steep relative humidity gradient, between the surface debris that contains relatively dry air, compared to the saturated air at depth. Despite the steep surface layer temperature gradient, the flow of vapour is upward (positive), and it increases as the surface relative humidity decreases. This upward flux in the upper layer occurs in conjunction with the downward flux within the lower layers: there is a flux divergence associated with the sensor second from the top of the profile. This flux divergence probably happens in most debris thicknesses (it was not evident in the 2011 profile because the sensor 2nd from the surface malfunctioned). Looking at the pattern of vapour flow from a 23 cm profile from 2005

(Figure 4.38), the 0 to 8 cm layer exhibits a small downward spike in vapour flow in the early morning (when the temperature gradient dominates), but by 10:40 the vapour flow has become positive as the relative humidity gradient increases.

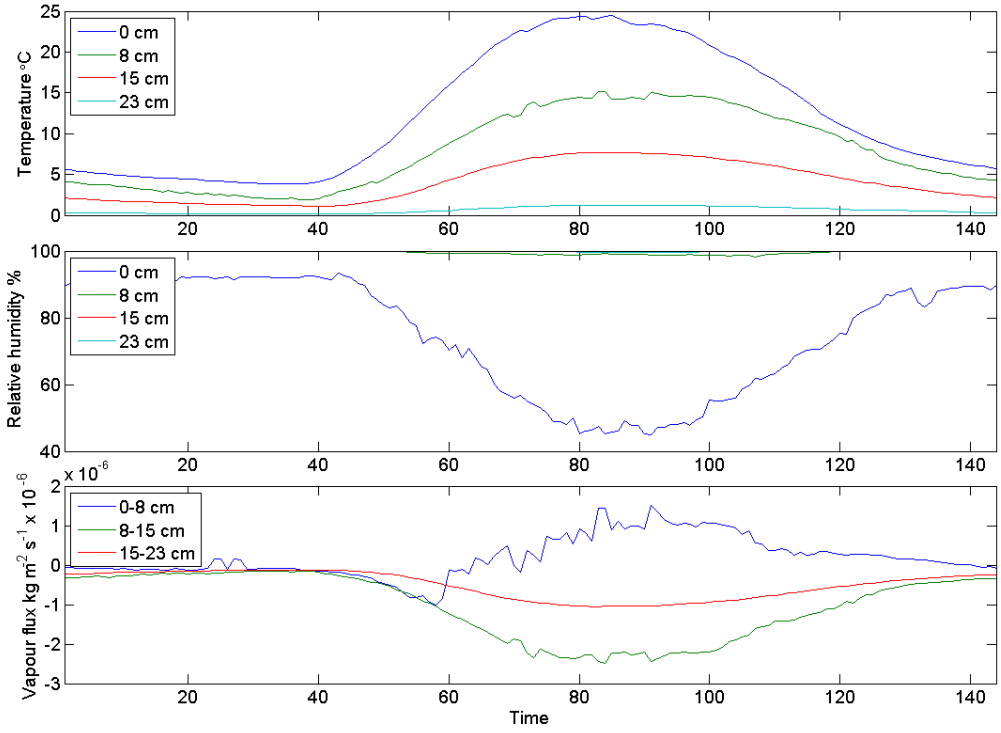

Figure 4.38 Hourly average debris temperature, relative humidity and modelled vapour flow from sensors near LOMET in debris 0.23 m thick from day 165 to 204 in 2005. Bottom plot is the calculated vapour flow. The time is the 10 minute period within the day.

The position of the flux divergence corresponds with the boundary between the lower granule layer, and the upper clast layer. As the source of the water vapour required to move upward cannot be from below this sensor (vapour here moves downward), the vapour must be released by evaporation of liquid water at the clast/granule interface. This explains why following a downward thermal vapour flow spike the flow becomes upward dramatically: at this point evaporation occurs and dries the debris, decreasing the surface relative humidity, causing a relative humidity gradient, and isothermal vapour flow. This will be why the soil literature only relates downward thermal vapour flow to positions below the evaporation front: above this front isothermal vapour flow dominates (Saito *et al.,* 2006; Scanlon, 1992). This upward flux is greater where the depth of the upper layer is thinner (the maximum upward flow between 0-8 cm was 1.5 x 10^{-6} kg m^{-2} s^{-1}, but between 0-24 cm was 3.5 × 10^{-7} kg m^{-2} s^{-1}), because the humidity gradient acts over a smaller distance.

4.4.2.2 Implications for the energy balance and liquid water flow

When the vapour flow over all layers is summed to give a total vapour flow it is negative (Table 4.8). There is a net transport of water to the debris/ice interface, where the water vapour may condense to liquid water. The condensation of water vapour would act as a source of energy at the ice surface (Table 4.8), providing a mechanism along with heat conduction to melt the ice. The energy released is negligible in comparison to that received through conduction of heat however.

Table 4.8 Total vapour flow for all layers in the debris and the energy released if this condensed to water for 3 records of vapour flow.

Sensor	Depth of profile (m)	Number of days of data	Average daily total vapour flow through all layers (kg m^{-2} s^{-1})	Energy released if all vapour condenses to liquid water (W m^{-2})
HOBO 1, LOMET 2005	0.23	8	-9.35×10^{-7}	2.34
HOBO 2, southern lobe 2005	0.72	82	-3.14×10^{-7}	0.79
HOBO, LOMET 2011	0.20	44	-7.22×10^{-7}	1.81

The accumulation of liquid water at the ice/debris interface could not continue without the entire debris profile becoming saturated. A simultaneous upwards liquid water flux would provide a mechanism to remove this water. Liquid water tends to flow towards cold regions in response to a temperature gradient, but the existence of a matric potential gradient could override this (Marshall and Holmes, 1988). Philip and de Vries (1957) noted that at low moisture contents vapour flow dominates as the moisture transport mechanism, but as the moisture content increases above θ_K(the moisture content when the unsaturated hydraulic conductivity is a small proportion of its saturated value) the flow of liquid commences in the opposite direction to the vapour flow. In the models constructed by Grifoll *et al.* (2005) and Saito *et al.,* (2006), this occurred below the drying front. Here the liquid water flow was upward as the gradient in the moisture content was great enough to surmount gravity. This liquid water then evaporated at the drying front, above which upwards isothermal vapour flow dominated. Importantly, the phase change occurred below the surface. Within the debris condensation of water at the ice/debris interface, and evaporation at the clast/granule interface could cause a moisture content gradient through the profile, driving liquid water upward. Perhaps the clast/granule boundary acts as the evaporation front. The present data does not allow the quantification of such a flux, although the need for a source of liquid water at the clast/granule interface for evaporation points towards its existence. Observation of the debris layer during fieldwork in 2005

revealed that at the ice/debris interface the lowest few centimetres of debris remains permanently water saturated. This layer did not dry out, even after several warm days (Brock, B., pers. comm.). The net downward vapour flow, along with ice melt, may be responsible for the continued saturation of this layer.

4.5 Summary

There are a few key findings from this chapter on the influence of the debris on the supraglacial input hydrograph and water chemistry:

1. The area of highest melt rates corresponds with the region of dirty ice and thin debris near the upper limit of the debris-cover, and extends to the lower portions of the Dome and Mont Blanc tributary glaciers where a favourable aspect and increased surface roughness increases melt rates. Melt from these regions provided the greatest proportion of runoff during the day and under average weather conditions. Conversely the lowest melt rates were found either at high altitudes or under very thick debris on the lower lobes. Only in the early morning/late evening or under cooler weather conditions did sub-debris melt provide a greater proportion of total melt than the debris-free areas.
2. The conduction of heat from the surface to the ice/debris interface imparts a delay on the timing of the initiation and peak of sub-debris melt compared to the air temperature cycle at the surface.
3. Areas of crevassed and dirty ice were the most sensitive to air temperature changes, but conversely sub-debris ablation was less sensitive to air temperature changes. An increase in debris thickness increased melt most where debris was added to previously zero or very thin debris thicknesses, but would decrease melt most where the debris was previously just above the threshold between dirty and debris-covered ice (0.01 m). When the two scenarios were combined the greatest increase in ablation occurred where the debris was originally zero or very thin, but the increase in thickness of moderately thin debris could reduce the impact of an increase in air temperature.
4. A 1°C increase in air temperature would result in a 6.3% increase in average daily melt, with an increase in debris thickness of 0.01 m resulting in a 1.9% decrease.
5. The valley system created by the medial and lateral moraines on the upper glacier leads to relatively large supraglacial catchment sizes, which together with high melt rates mean supraglacial streams on the upper glacier are relatively large. The

hummocky topography on the lower glacier means catchment sizes are limited by the topography, which when combined with low melt rates reduces the discharges of the supraglacial streams.

6. There is evidence the bicarbonate concentration of supraglacial streams may be enriched due to the reaction of meltwater with debris, but there is not evidence for the debris enhancing the supraglacial sulphate concentration, apart from within small ponds.
7. Evaporation of rainfall from the debris does occur, and is likely approximately 35% of rainfall, but its magnitude is dependent upon the debris permeability.
8. The overall water vapour flow within the debris is downward, and if this vapour was to condense at the ice surface would provide a source of energy to melt the ice (although this is negligible compared to conduction). Counter to this, liquid water moves to the top of the granule layer, where it may evaporate. This would reduce the debris temperature and decrease the energy for melt by the same amount.

5 Spatial patterns of water routing using dye tracing

This chapter aims to address the second aim of the thesis to understand the influence of the debris on the englacial and subglacial water routing. The structure of the system over the whole glacier was determined using dye tracing into the hydrological network at locations across the glacier. In 2011 repeat injections of specific moulins were performed to understand the evolution of the hydrological network. Results of the dye injections will be given in section 5.1, with interpretation and discussion in section 5.1.4. All dye trace parameters are given in Table 5.1 for 2010 and Table 5.2 for 2011, with the injection site details given in Table 5.3 and Table 5.4. For details of the methods used in dye tracing see section 3.3.1.

5.1 Results

The results of the dye tracing are partitioned into early season, mid-season and late season, which were the three monitoring periods of both years. The days within each period are given in Table 3.1. An overview of all of the traces is given in section 5.1.4.

5.1.1 June

The results of the dye tracing in June will now be described. Traces conducted into S9 and above were considered upper glacier traces and will be described first, with details of the lower glacier traces (S8 and below) being described next.

5.1.1.1 The englacial and subglacial structure from the upper glacier

The earliest trace from upglacier in June 2010 was S13_162 (the trace injection site and day number). This moulin was in a hollow left by a supraglacial lake (Figure 5.1). This trace had a velocity of 0.83 m s^{-1}, low dispersion parameters, and was one clear peak, followed by a secondary but much smaller peak. Figure 5.2 shows the June 2010 upglacier traces. The second upglacier trace in 2010 was S10_164, it was slower than the S13 trace but still had a fast trace velocity of 0.60 m s^{-1}. The trace had one clear peak with no shoulder, although the spread of the trace was larger than for S13. The percentage dye recovery was 86% for the S13_162 trace but a much lower 36% for the S10_164 trace.

Figure 5.1 S13 injection point June 2010.

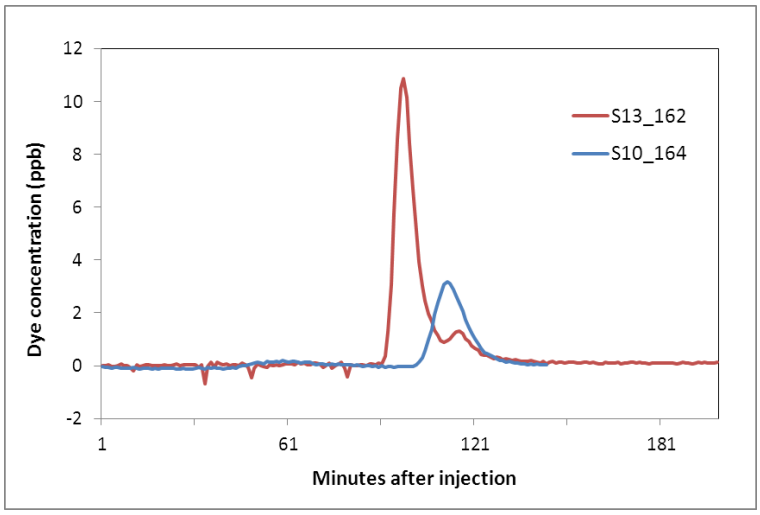

Figure 5.2 Upper glacier traces in June 2010.

The earliest June 2011 trace carried out upglacier was into S12. Figure 5.3a gives the June 2011 upglacier traces. The S12_161 trace had a fast velocity of 0.51 m s^{-1}, and the lowest value of dispersivity for all S12 and S14 traces. The trace was one smooth peak with no shoulder, and had a high dye recovery of 87%. The next upglacier trace was on day 164 into S15. Despite a well formed and large moulin, this stream was small compared to the other upglacier injection points (input discharge 0.013 m^3 s^{-1}) and had a local catchment area of thinly debris covered ice between the central and western moraines. The S15_164 trace had its slowest velocity (0.28 m s^{-1}) and highest dispersion coefficient of the year, although the dye recovery was high (93%). The rising limb of the trace rose sharply, but the falling limb lowered gradually, with concentrations remaining high for around 100 minutes. This pronounced shoulder was followed by a small secondary peak about 557 minutes after injection. The other upglacier injection in June was into S14 (Figure 5.3b), the largest

moulin on the glacier. The S14_165 trace was the fastest of the June upglacier traces, had low dispersion parameters and a high dye recovery of 87%. Its trace was one discrete peak.

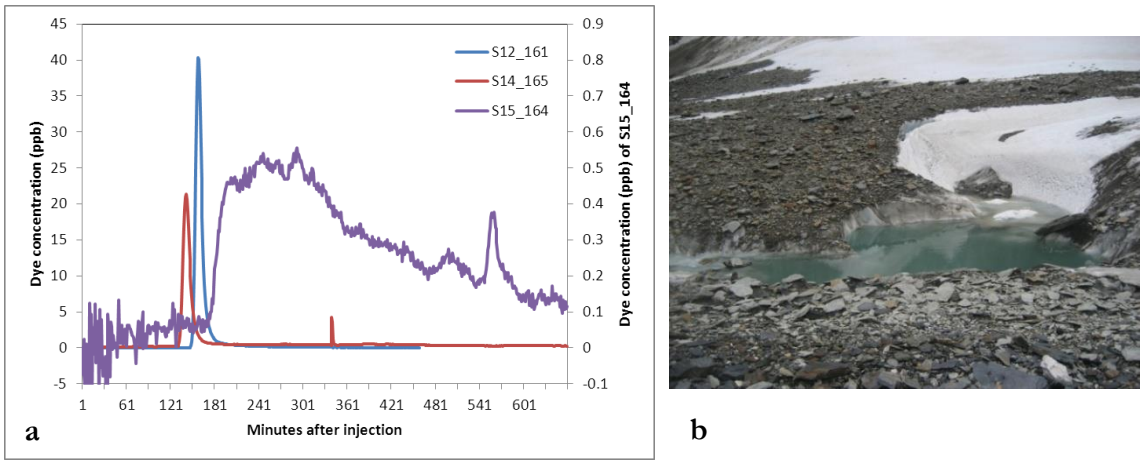

Figure 5.3 a) Upper glacier traces, June 2011, b) S14 in June 2011.

5.1.1.2 The englacial and subglacial structure from the lower glacier

There were four successful lower glacier traces during June 2010, Figure 5.4. The first was S6_160, which had a fast trace velocity of 0.58 m s^{-1} (similar to the S10 velocity of 0.60 m s^{-1}), and small dispersion parameters, but a low dye recovery of 21%. It was a single-peaked trace with no shoulder. The next trace was into an englacial conduit S8_161 (Figure 5.4c), which had a slower trace velocity of 0.43 m s^{-1}. It had the same dispersion coefficient as the S13_162 trace, but its dispersivity was larger (4.15 m) because the trace was slower. The trace had a single peak and was similarly shaped to that of S13_162. The percentage dye recovery was 28%. The nearest injection point to the terminus was S1, traced on day 163. It had a very slow trace velocity of 0.024 m s^{-1} and a low dye recovery of 17%, although the dispersion parameters were both small. The dye recovery was slightly lower because the background fluorescence decreased after the injection time, so there may be a larger area under the return curve than measured. The trace had one main peak but the increase in dye concentration was small and the curve was not smooth.

The S3_165 trace was conducted next but was not clear because the background fluorescence increases in the morning and falls later, so if the background fluorescence was the average over the morning, the trace was barely above background. Therefore the background fluorescence from the hour before injection was used. This gives a trace with a first very small peak, after which concentrations fall below background, followed by a second, higher and more convincing peak, with concentrations falling and then rising for around 130 minutes before falling below background. Assuming this is a dye trace and not

due to other factors influencing the background fluorescence, it has a slow velocity of 0.19 m s^{-1}, but low dispersion parameters. The dye recovery was only 4%.

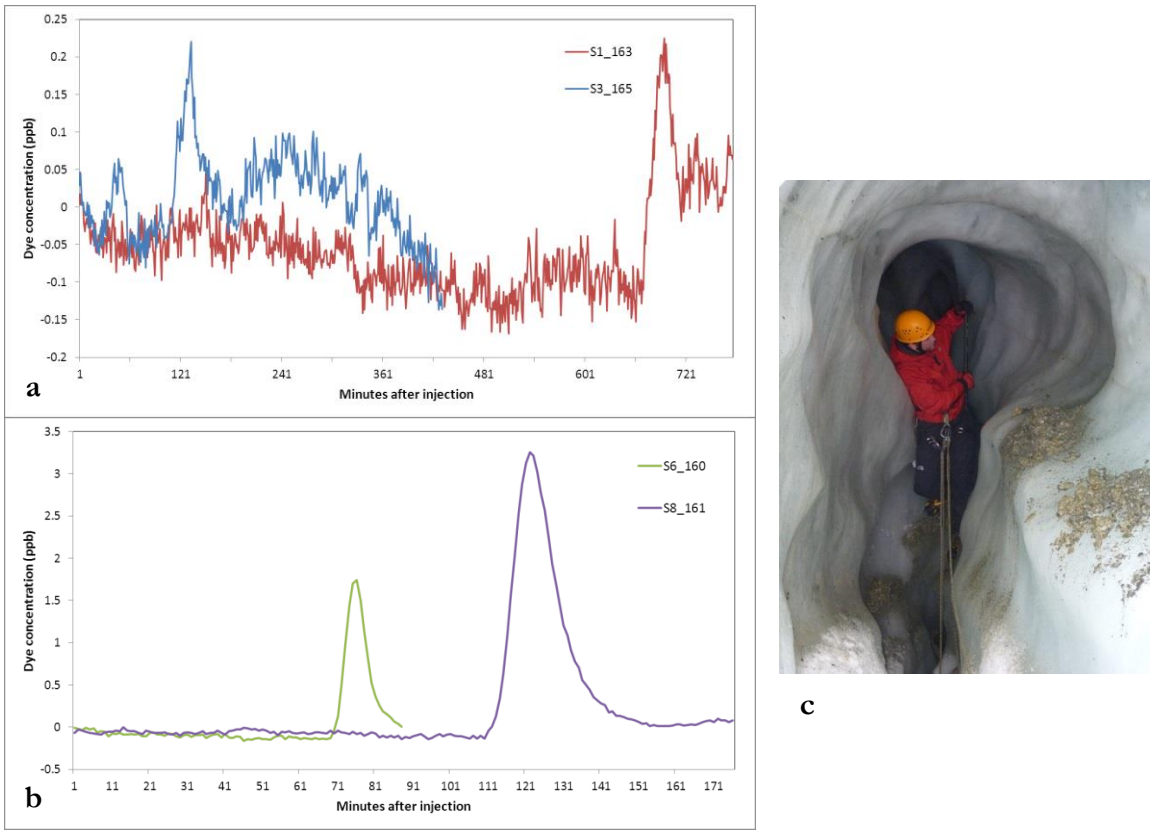

Figure 5.4 Lower glacier traces, June 2010, a) those of low dye concentrations, S1 and S3, b) those of high dye concentrations, S6 and S8, and c) the englacial conduit above the S8 stream.

The earliest lower glacier traces during 2011 were into S7 and S5 (Figure 5.5, Figure 5.6, and Figure 5.7). The S7_156 injection had a slow velocity of 0.073 m s^{-1} and a low dye return of 16%. The trace was broad and low, with the dye concentration rising to a first peak which falls almost back to background before rising again where it exhibits several smaller less distinct peaks which are overlain on a generally rising dye concentration. The concentration falls to background but the tail end of the trace is less clear, probably due to a greater variability in fluorescence caused by the fluorometer working less effectively. The S5 stream is the main stream on the eastern side of the lower glacier, although it is small compared to the upper glacier streams having a day 157 discharge of 0.027 m^3 s^{-1}. The injection point was into a stream 446 m upstream of the moulin (using a straight line). As the distance between the injection site and the S5 moulin is known, as well as the stream velocity (from salt dilution gauging), the time the dye spent in the supraglacial stream can be calculated, assuming the stream velocity measured is indicative of the velocity of the stream along its length. This time was taken off the time to the peak dye concentration, to give an adjusted trace velocity and dispersivity. Henceforth, only adjusted trace velocities

and dispersivities are given. The S5_157 trace was slow (0.070 m s^{-1}) and had a low dye recovery of 37%. The trace was very broad, taking around 700 minutes to pass through. It rose reasonably steeply initially, and then more gently over around 3 hours. There were 6 individual peaks evident during the second half of the trace, of which the last three were more distinct, with levels returning to background around 860 minutes from injection.

S5 and S7 were both traced again later in June 2011. Their traces will be compared to see if there is evidence of evolution of the hydrological network. The S5_163 trace velocity was 0.070 m s^{-1}, exactly the same as the S5_157 trace, and the percentage dye recovery for both traces was very similar (37% and 38%). The input discharge (0.032 m^3 s^{-1}) was the highest recorded for S5, although only 0.005 m^3 s^{-1} larger than for the S5_157 trace. The trace had a steeper rising limb than the S5_157 trace, and had three much more distinct peaks, superimposed on a gradually falling limb. This suggests three preferential flow paths were in use, each with a characteristic velocity. It appears the system has become more efficient, because the smaller less distinct peaks of the S5_157 trace have become more distinct, with the first containing the majority of the water. However, the characteristics of S5_163 trace still suggests the hydrological system was inefficient, and the beginning of the rising limb, overall trace velocity, and time taken for the trace to pass the gauging station was similar to the S5_157 trace.

The S7 stream was injected again on day 162 (Figure 5.7). The S7_162 trace was slightly faster than the S7_156 trace, and the first peak on the S7_162 trace arrived earlier than the first peak of the S7_156 trace, with the many smaller peaks on the S7_156 trace being replaced by one much higher and clearer peak which had a steep rising limb, with the other peaks before and after this main peak being much smaller. This is indicative of the multiple flow paths observed on the earlier trace evolving into one preferential flow path, with the other paths carrying a smaller portion of meltwater. The input discharge into S7_162 was 0.011 m^3s^{-1}, although there was no measurement on day 156 with which to compare. The percentage dye recovery increased from 16% to 32%.

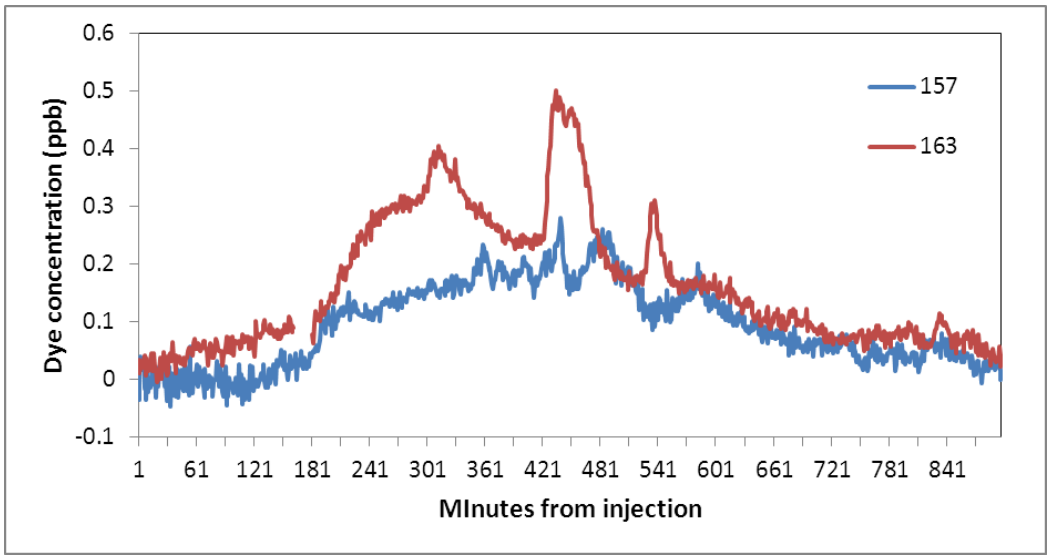

Figure 5.5 Dye traces into the S5 injection point in June 2011.

Figure 5.6 a) injecting the S5 stream and b) the S7 stream, both June 2011.

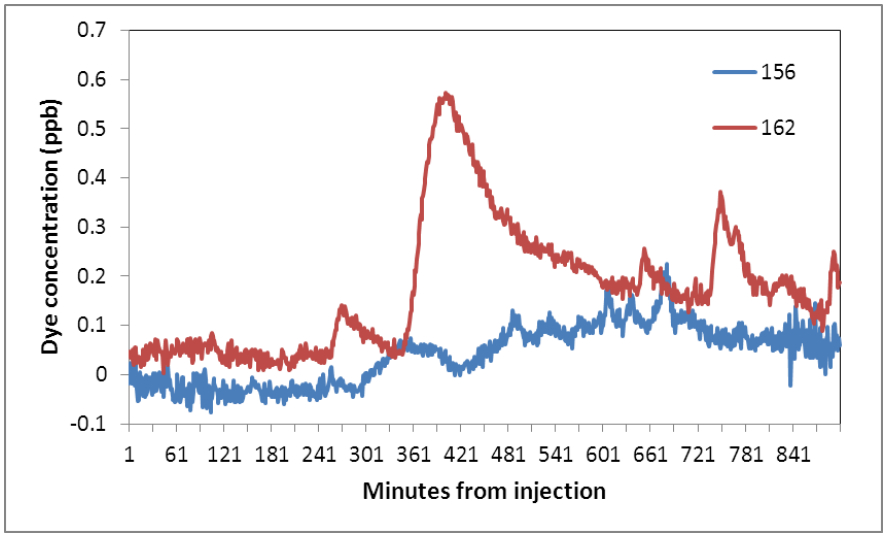

Figure 5.7 June 2011 dye traces into the S7 injection point.

Table 5.1 Dye trace parameters for all injection points in 2010. Please refer to the thesis symbols for definitions of the parameters listed.

Name	Day	V_{di} (ml)	Trace?	C_{pd} (ppb)	u_d (m s^{-1})	D (m^2 s^{-1})	b (m)	Q_{mp} (m^3 s^{-1})	Q_i (m^3 s^{-1})	Q_p (m^3 s^{-1})	A_c (m^2)	P_{dr} (%)
S1	156	~4	N	-	-	-	-	-	-	-	-	-
S2	159	40	N	-	-	-	-	-	-	-	-	-
S6	160	40	Y	1.74	0.583	1	1.72	2.88	2.74	2.69	12	21
S8	161	120	Y	3.26	0.434	1.8	4.15	2.90	2.86	2.89	47	28
S13	162	200	Y	10.9	0.830	1.8	2.17	3.36	3.16	3.41	204	86
S1	163	40	Y	0.23	0.024	0.0016	0.07	5.97	5.28	6.30	4.4	17
S10	164	160	Y	3.17	0.602	2.3	3.82	5.70	6.40	5.59	40	36
S3	165	80	Y	0.22	0.192	0.23	1.20	2.84	2.84	2.84	4.3	4
S9	169	120	N	-	-	-	-	-	-	-	-	-
S3	170	80	N	-	-	-	-	-	-	-	-	-
S5	171	80	N	-	-	-	-	-	-	-	-	-
S3	210	80	Y	3.08	0.345	0.86	2.50	10.71	10.50	10.96	51	170
S5	211	120	Y	0.40	0.226	9.47	41.9	5.63	4.81	6.22	47	55
S9	212	120	N	-	-	-	-	-	-	-	-	-
S11	213	120	Y	1.79	0.442	3.55	8.03	7.80	7.16	7.95	940	92
S13	215	160	N	-	-	-	-	-	-	-	-	-
S16	216	200	N	-	-	-	-	-	-	-	-	-
S5b	218	80	Y	0.19	0.207	-	-	2.98	-	2.98	3.7	3
S13	248	160	N	-	-	-	-	-	-	-	-	-
S14b	249	200	Y	7.84	0.613	1.77	2.89	-	-	-	130	-
S3	252	80	Y	2.84	0.265	1.86	7.01	1.65	1.61	1.67	79	41
S4	253	80	N	0.12	-	-	-	-	-	-	-	-
S12b	254	100	Y	1.31	0.318	8.3	26.1	1.93	1.91	2.01	210	102

Table 5.2 Dye trace parameters for all 2011 dye injections. Refer to thesis symbols for definitions of the parameters listed. The Q_s and u_{rs} type is either 'D', dilution gauging, 'V', the velocity area method (timing of floats), or 'AdD', adjusted to dilution gauging (see section 3.3.2 for details). *Indicates traces with multiple peaks for which the D and b parameters are less reliable.

Name	Day	V_{di} (ml)	Trace?	C_{pd} (ppb)	u_d (m s^{-1})	D (m^2 s^{-1})	b (m)	Q_{mp} (m^3 s^{-1})	Q_i (m^3 s^{-1})	Q_p (m^3 s^{-1})	A_c (m^2)	P_{dr} (%)	Q_s (m^3 s^{-1})	Q_s type	u_{rs} (m s^{-1})	u_{rs} type	Q_m (m^3 s^{-1})	A_{sm} (m^2)
S7	156	160	Y	0.23	0.073	2.8*	38*	2.14	2.18	2.10	47	16	-	-	-	-	-	-
S5	157	120	Y	0.28	0.070	15*	209*	2.08	1.99	2.09	84	37	0.027	D	0.24	D	1.03	15
S15	159	280	N	-	-	-	-	-	1.92	-	-	-	0.027	D	0.44	D	-	-
S14	160	280	N	-	-	-	-	-	1.98	-	-	-	0.535	V	1.14	V	-	-
S12	161	280	Y	40.3	0.510	0.7	1.37	2.09	2.05	2.10	467	87	0.025	AdD	0.44	AdD	1.05	2.1
S7	162	240	Y	0.57	0.124	2.65	21.4	2.01	2.02	2.00	150	32	0.011	AdD	0.17	AdD	1.01	8.1
S5	163	200	Y	0.49	0.070	1926*	27476*	2.21	2.15	2.24	137	38	0.032	D	0.25	D	1.11	16
S15	164	200	Y	0.56	0.283	84	296	3.00	2.60	3.43	247	93	0.013	D	0.27	D	1.51	5.4
S14	165	200	Y	21.3	0.583	1.2	2.06	2.35	2.22	2.48	480	84	0.438	V	1.24	V	1.40	2.4
S3	166	80	Y	0.34	-	-	-	3.78	3.08	4.91	25	30	-	-	-	-	-	-
S5	208	200	Y	1.82	0.229	1.98	8.63	1.98	-	1.98	207	52	0.031	D	0.13	D	1.01	4.4
S15	209	240	Y	7.25	0.439	1.57	3.57	2.85	-	-	196	59	0.010	D	0.27	D	1.43	3.2
S14	210	160	Y	3.13	0.470	2.6	5.54	1.87	-	-	75	22	0.874	V	2.13	V	1.37	2.9
S12	211	160	Y	1.89	0.487	11	23	2.16	-	2.16	474	27	0.341	D	0.43	D	1.25	2.6
S7	212	200	Y	-	-	-	-	6.46	-	-	1457	1181	0.028	D	0.24	D	3.24	-
S14	213	120	Y	4.71	0.731	1.24	1.70	4.47	4.47	4.47	41	38	0.888	V	2.16	V	2.68	3.7
S15	213	120	Y	3.55	0.576	1.23	2.13	4.47	4.47	-	43	40	0.014	D	0.30	D	2.24	3.9
S12	214	160	Y	6.51	0.699	1.44	2.06	4.47	4.47	4.47	70	49	0.147	AdD	0.50	D	2.31	3.3
S7	215	190	N	-	-	-	-	-	11.13	-	-	-	0.032	D	0.28	D	-	-
S5	216	195	N	-	-	-	-	-	7.28	-	-	-	0.028	D	0.14	D	-	-
S5	255	200	Y	0.58	0.280	0.28*	1.00*	7.20	7.16	7.28	14	13	-	-	-	-	-	-
S15	256	240	Y	9.62	0.578	4.5	7.78	5.16	4.94	5.25	135	73	0.022	D	0.50	D	2.56	4.4
S14	257	120	Y	5.20	0.697	1.4	2.01	6.02	5.90	6.16	45	62	0.378	V	0.92	V	3.20	4.6
S12	257	160	Y	3.13	0.593	3.5	5.97	6.34	6.10	6.66	99	99	0.196	D	0.49	D	3.29	5.5
S7	258	200	Y	0.73	0.107	50	466	4.53	4.48	5.08	165	94	0.006	D	0.25	D	2.39	22

Table 5.3 Description of the injection points S1 to S8.

Name	Easting	Northing	Elevation (m a.s.l.)	Distance to GS (m)	Description of injection site	Location
S1	335154	5072320	1980	997	A small, shallow, slow flowing stream, unclear when it becomes englacial.	On the southern edge of the northern lobe, originates from the ice cliffs in between the central and northern lobe.
S2	335020	5072004	-	1295	A small stream at the base of an area of ice cliffs.	On the southern lobe, to the south of the central lobe and the C1 GPS point.
S3	334624	5072131	2038	1560	Very small stream, which appears to go down a moulin as there is no trace of the stream past this point, but the stream is covered by substantial boulders which hide the moulin.	In between the C2 and C3 GPS points on the lower glacier.
S4	334130	5072011	2053	2050	Dye into a very small stream that was believed to lead into a much larger moulin which could be heard beneath some large boulders.	On the top part of the southern lobe, on the bend of the glacier.
S5	334061	5072440	1511	2161	The largest stream network on the lower glacier, but the stream is still small and slow flowing, with a shallow gradient. It meanders beneath high ice cliffs, and is occasionally covered by debris. The moulin could not be directly traced because of access difficulties.	The S5 stream is the main stream on the eastern side of the lower glacier, which flows from east of C5 down to a moulin located 446 m from the injection point (straight line distance).
S5b	334143	5072298	2085	2024	Small supraglacial stream with a shallow gradient, high debris content, and meanders beneath short ice cliffs.	Is a tributary of the S5 stream, it flows from the area just downglacier of C4 through fairly flat debris to the confluence with the S5 stream just downglacier from the S5 injection point.
S6	333704	5072716	-	2620	Small, slow flowing stream, some water ponded upstream.	Between C5 and C6 GPS points, above the bend of the glacier.
S7	333470	5073005	2025	2987	A small, shallow stream that flows at the base of some ice cliffs, with the stream disappearing into the ice as the gap between the ice cliff and the ice on the other bank of the stream close together. This may be analogous to the 'cut and closure' mechanism (Vatne, 2001). It is fairly certain the stream becomes englacial but it may not reach the bed for some time.	Is on the eastern side of the glacier in between C6 and C7.
S8	333356	5073124	2077	3149	Dye was poured into an englacial conduit, within which a stream could be heard flowing from above.	Situated in between the central and eastern moraines to the south east of the C7 GPS point.

Table 5.4 Descriptions of the injection points S9 to S16.

Name	Easting	Northing	Elevation (m a.s.l.)	Distance to GS (m)	Description of injection site	Location
S9	332772	5073747	2270	4001	A fast flowing supraglacial stream.	In the valley between the central and western moraines, to the west of the C8 GPS point.
S10	332885	5073872	2077	4012	A fast flowing stream that disappeared into a moulin just after the injection site.	In the valley between the central and eastern moriaines, to the east of the C8 GPS point.
S11	332656	5074088	2286	4326	A fast flowing stream that reaches a moulin before the elevation of C8 (530 m downglacier) because here the central and eastern moraines join.	In the valley between the central and eastern moraine, parallel to UPMET and just downstream of the C9 GPS point.
S12	332336	5074440	2417	4804	A large, fast stream which leads directly into a vertical moulin.	In the valley in between the central and eastern moraine, just to the north-east of the C10 GPS point.
S12b	332261	5074556	2340	4938	A fast flowing supraglacial stream, believed to lead to the S12 moulin.	In the valley between the central and eastern moraine, leads into the S12 moulin, about 140 m downstream.
S13	332280	5074427	2353	4830	A fast stream that leads directly into a moulin, and which was fed by ponded water emanating from the snowpack. The stream was within a conical hollow which had collapsed snow around the edges, indicating it was once filled by a lake.	To the west of the central moraine, upglacier from C10, and immediately below the S15 moulin.
S14	332158	5074447	2353	4932	A large, fast stream which enters the largest moulin on the glacier. In June 2011 its input stream emanated from saturated snow which led into a pool, and then the moulin. By July 2011, it had evolved into a wide, straight channel leading into a vertical moulin. The stream still disappeared beneath a snow roof, but likely reappears upglacier as the main stream between the central and western moraine.	A hundred metres to the west of the S15 stream, to the west of the central moraine, and to the south of the confluence of the Tête Carée glacier with the main glacier.
S14b	331546	5075159	2476	5867	A fast flowing supraglacial stream, which meanders along the eastern edge of the upper part of the western moraine, and likely leads into the S14 moulin.	Main stream between the central and western moraines, parallel with C14 GPS point. Becomes partly englacial between C10 and C11, probably flows into S14 around 940 m from the injection site.
S15	332172	5074477	2342	4943	A fast flowing but small stream which leads directly into a conical shaped moulin.	Immediately to the west of the central moraine (the moulin cliff cuts into the moraine), north of C10 and the S13 injection point.
S16	331911	5074848	2387	5390	Fast flowing supraglacial stream on a dirty ice area, possibly leads into the S12 moulin.	Flows in between the central and eastern moraine, to the east of C11.

5.1.2 July/August

In the July/August fieldtrip of 2010, 7 dye traces were conducted, of those 3 were successful, and 1 resulted in a half trace, with only the rising limb captured. The unsuccessful traces were because of missing data or the fluorometer not working correctly. There were two successful lower glacier traces, the first on day 210, was into S3. It had a trace velocity of 0.35 m s^{-1}, dispersion coefficient of 0.86 m^2 s^{-1} and dispersivity of 2.50 m. The trace (Figure 5.8) had one peak with no shoulder. The second lower glacier trace S5_211 was into the same S5 steam that was injected in 2011, although the parameters have not been adjusted for time spent in the supraglacial stream. The trace had a velocity of 0.26 m s^{-1}, and large dispersion characteristics. Although Figure 5.9 shows the trace rises quickly about 140 minutes after injection, it has a flat top and long tail, which rises into a second peak about 400 minutes after injection. Another injection was performed into S5b (Figure 5.9), a tributary of the main S5 stream. Only the rising limb of the trace was recorded so the S5b_218 velocity is a maximum of 0.21 m s^{-1}. The dye concentration rises at about the same time as the S5_211 trace, but with a shallower gradient.

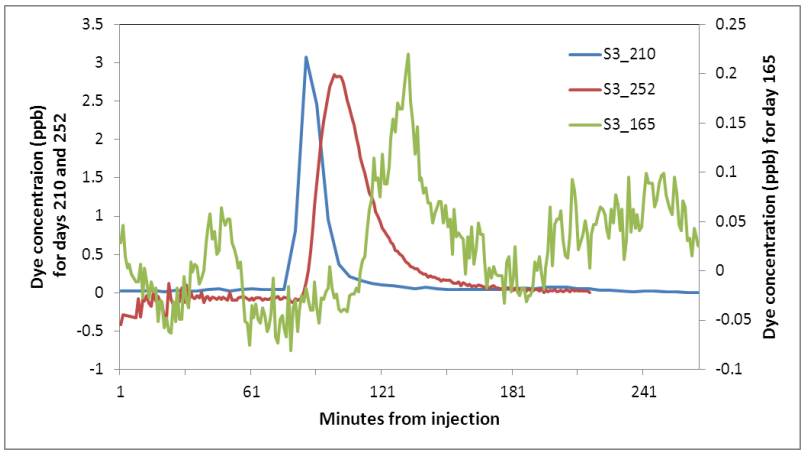

Figure 5.8 Dye traces into S3 in June, July and September 2010.

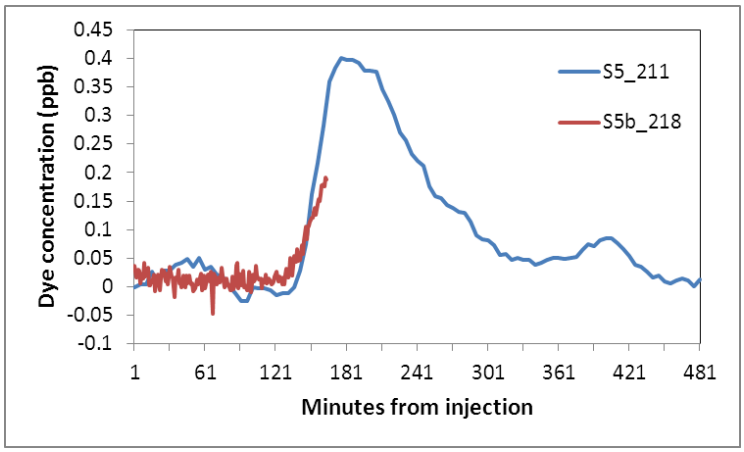

Figure 5.9 Dye traces into S5 and S5b during in July and August, 2010.

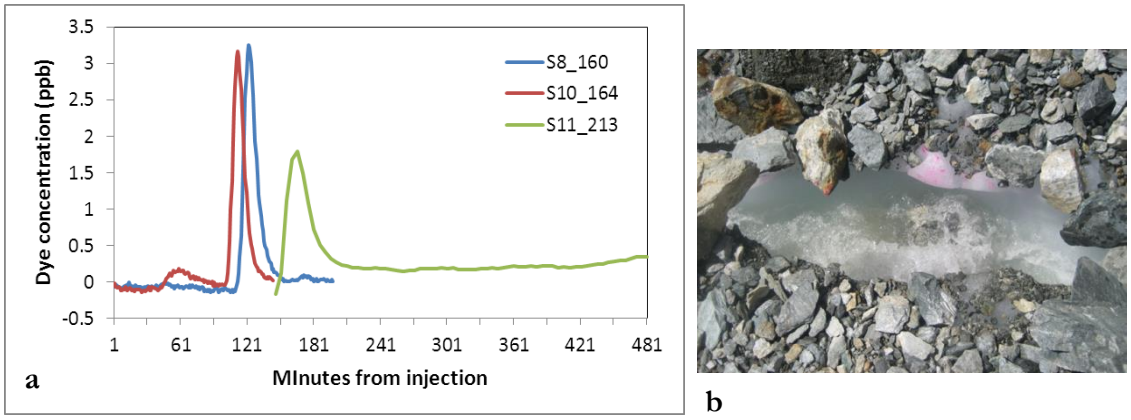

Figure 5.10 a) Comparison of the S11 trace in August with the S8 and S10 traces in June 2010, and b) the S11 stream, it has a width of approximately 0.3 m.

The only upper glacier trace was into S11 (Figure 5.10). The S11_213 trace had a velocity of 0.44 m s^{-1}, and moderate dispersion parameters. The percentage dye recovery was 92% (not including the long tail). The trace has one peak, but also a long tail of raised dye concentrations (although there may have been a rise in the background fluorescence). This trace was slower and had a greater spread than the S13, S10 and S6 traces in June 2010, and although its velocity was only slightly slower than the S8_161 stream, its dispersion coefficient and dispersivity were greater.

Next, the results of the repeat traces carried out in July and August 2011 will be given, the trace onto the lower glacier will be mentioned first, followed by the upper glacier traces. The first dye injection was into S5_208, which had a velocity of 0.23 m s^{-1} (Figure 5.11). As for June 2011, the trace parameters have been adjusted to account for the time the dye spent in the supraglacial stream. The trace velocity increased substantially since June (both June traces had a velocity of 0.07 m s^{-1}), even though the input discharge was similar to day 163. The mean cross sectional area decreased in July, from 14.7 m^2 and 15.9 m^2 on day 157 and 163 respectively, to 4.4 m^2, with the drop due to an increase in trace

velocity. The percentage dye recovery increased to 52%. The rising limb of the trace was relatively steep and rose to the main peak about 50 minutes earlier than in June. The falling limb was still gentler, and has a second peak before it fell to background, and it took around 200 minutes for the trace to pass through. The same return curve shape was exhibited in July 2010 (Figure 5.12), and although the 2010 trace was smoother and had a more prominent main peak, it had an almost identical trace velocity (0.23 m s^{-1} S5_211 2010, and 0.20 m s^{-1} S5_208 2011, both uncorrected for supraglacial travel time) and percentage dye recovery (53% in 2010 and 52% in 2011).

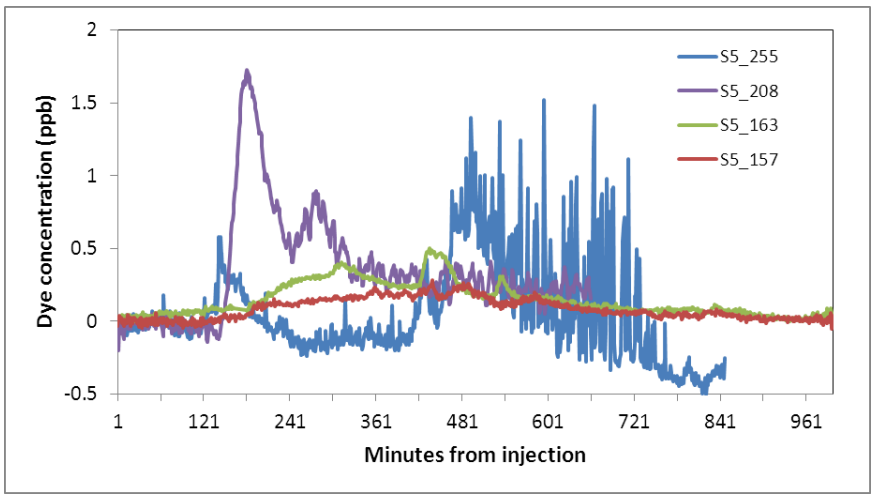

Figure 5.11 Dye traces into S5 in June, July and September, 2011.

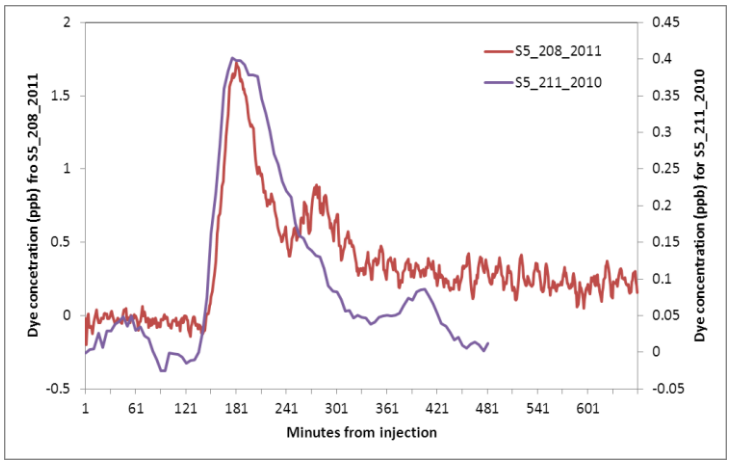

Figure 5.12 Traces into S5 in July/August in 2010 and 2011.

The next dye injection was S15_209 (Figure 5.13), and it had a velocity of 0.44 m s^{-1}. The velocity increased significantly since June (0.28 m s^{-1}), and although the timing of the beginning of the rising limb correlates closely with day 164, the peak came much earlier because there was no longer a flat top to the trace. This caused a drop in dispersion coefficient and dispersivity. This was despite the input discharge of the S15_209 trace being less than in June (0.010 m^3 s^{-1} compared to 0.013 m^3 s^{-1}). There was a decrease in the mean

cross sectional area of the channel compared to June. The S15_209 trace was one clear peak with no shoulder.

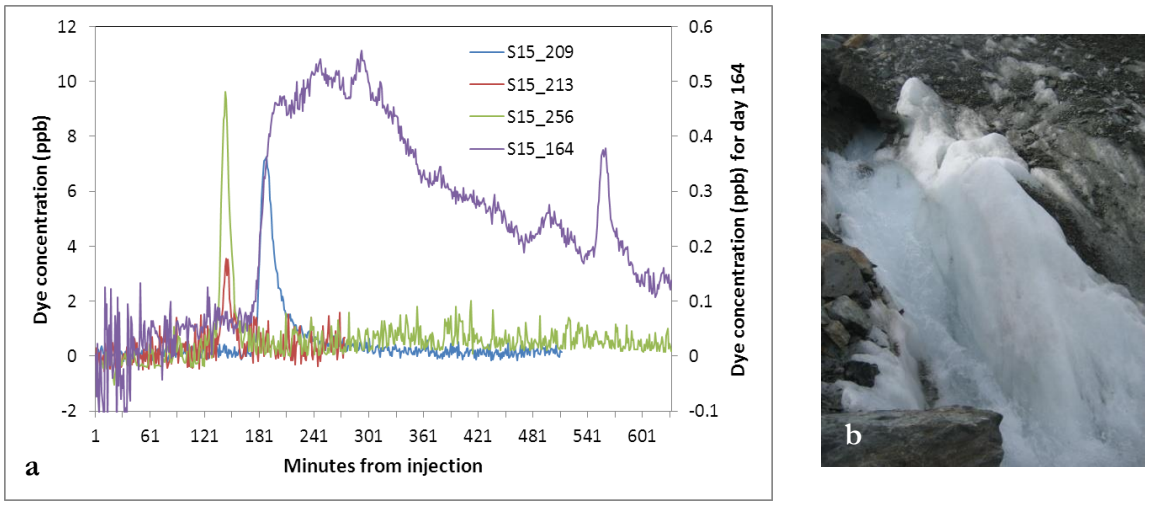

Figure 5.13 a) Dye traces into S15 in June, July, August and September, 2011, and b) the S15 stream just before it enters its moulin. The gauging section was on a flatter reach upstream.

S14 (Figure 5.14 and Figure 5.15) was traced on day 210, but contrary to the above traces, its trace velocity (0.47 m s^{-1}) decreased since June, and the dispersion coefficient doubled. This increased the dispersivity to 5.53 m, the highest measured for S14. This was despite the input discharge being double June values. The mean channel cross sectional area increased from 2.39 m^2 in June to 2.92 m^2 in July. Although the trace in Figure 5.14 is one distinct peak, it was noticeably later and broader than any other traces into this moulin. A similar situation occurred at S12 (Figure 5.16 and Figure 5.17) on day 211. This trace had a slower velocity than June, although more significantly the dispersion coefficient and dispersivity were almost 20 times larger. The input discharge into S12 was much greater though (0.34 m^3 s^{-1} on day 211, 0.025 m^3 s^{-1} on day 161). If only the peak was included, the percentage dye return decreased from 87% to 27% and the mean cross-sectional area increased slightly. The trace detected still had a steep (if not as steep) rising limb (Figure 5.16), but had a gentle falling limb, so although the timing of the beginning of the rising limb was similar to June, the peak was later and followed by a long tail of higher concentrations.

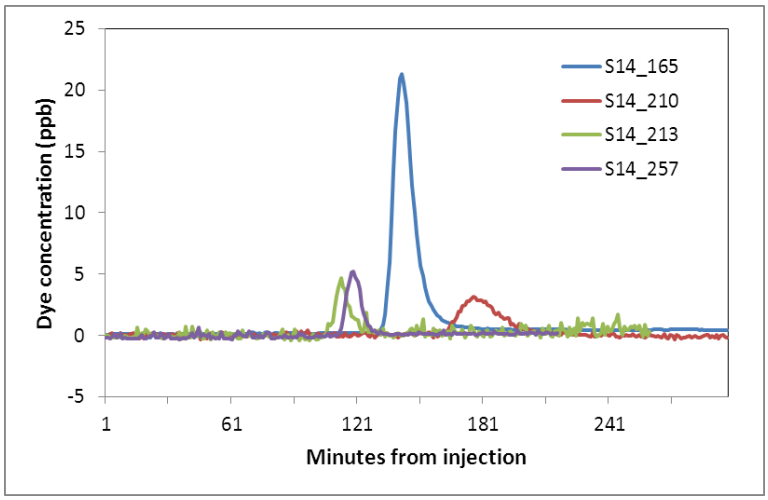

Figure 5.14 Dye traces into S14 in June, July, August and September, 2011.

Figure 5.15 a) the S14 moulin in July 2011, and b) dye tracing S14 in July 2011.

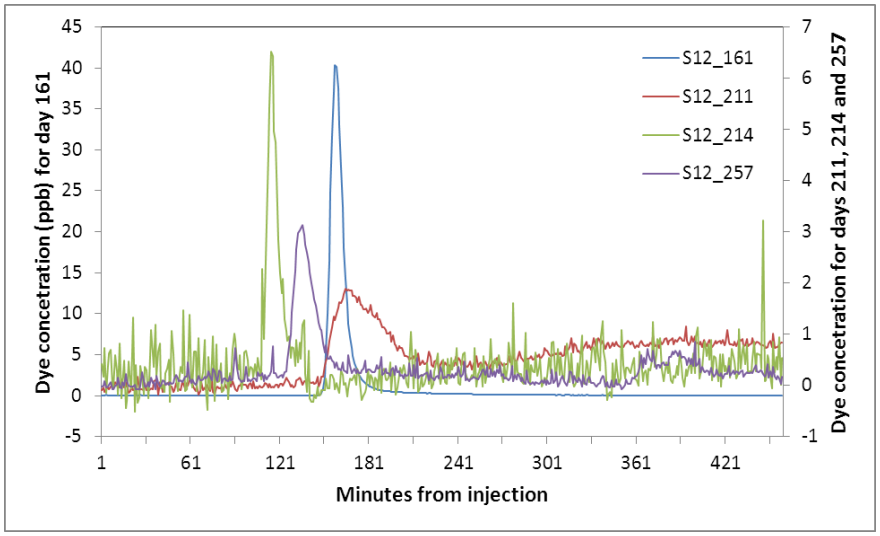

Figure 5.16 Dye traces into S12 in June, July, August and September, 2011.

Figure 5.17 Dye tracing the S12 stream in September 2011.

Two traces were carried out on day 213, into S15 and S14. The S15_213 trace had a velocity of 0.58 m s^{-1} (faster than the S15_209 trace of 0.44 m s^{-1}), and it had a slightly lower dispersion coefficient and dispersivity. The input discharge was higher than on day 209, but only by 0.004 m^3 s^{-1}. The mean cross sectional area increased slightly due to the increase in average discharge not being entirely accommodated within the increase in velocity. Although the background fluorescence was rather variable, the trace was still one clear peak (Figure 5.13a), with the trace velocity faster than on day 209.. The S14_213 trace also had an increased velocity of 0.73 m s^{-1} (the highest recorded this year for all injection points). The dispersion coefficient was lower than for the S14_210 trace, but similar to the S14_165 trace, and along with the fast velocity, resulted in the lowest dispersivity for S14. The input discharge was slightly higher than on day 210 (0.888 m^3 s^{-1} and 0.874 m^3 s^{-1} on days 213 and 210 respectively). The percentage dye recovery was higher for the S14_213 trace compared to the S14_210 trace, but the values were lower than expected because of the variable background fluorescence. The dye trace from S14_213 (Figure 5.14) was one distinct peak.

The S12 site was injected on day 214, and gave a velocity of 0.70 m s^{-1} (the highest for S12), and was similar to the velocity of the S14_213 trace. The dispersion coefficient and dispersivity were about 10 times smaller than they were on day 211, but still higher than the values for the S12_161 trace. The input discharge (0.15 m^3 s^{-1}) was around half the discharge on day 211. Neglecting the tail of the S12_211 trace, the percentage dye recovery increased from 27% to 49%. The mean channel cross sectional area increased to 3.3 m^2 since day 211. The trace was still one peak, which was narrower than the S12_211 trace, and came through before any other traces at this site (Figure 5.16).

5.1.3 September

To understand whether the structure of the englacial and subglacial system changes later in the season, the dye tracing from September in both years will be studied, firstly by looking at the lower and then upper glacier traces.

On the lower glacier the S3_252 trace was slower (0.27 m s^{-1} compared to 0.35 m s^{-1}) and had double the dispersion coefficient of the S3_210 trace in 2010 (Figure 5.8). Also, although the S5_255 2011 trace had the fastest trace velocity of the season, the trace parameters were from the first peak of the trace (Figure 5.11) which only gave a percentage dye recovery of 13%. Since including the second peak of the trace brought this to 74%, it is suggested both peaks are part of the trace and the drainage system is composed of a faster, smaller path, and a separate slower, but larger secondary path. A trace was also carried out into S4 on the southern lobe in 2010. No trace was returned, probably because the stream routed down the southern lobe and into the southern lobe proglacial stream, so was not detected at the northern lobe gauging station.

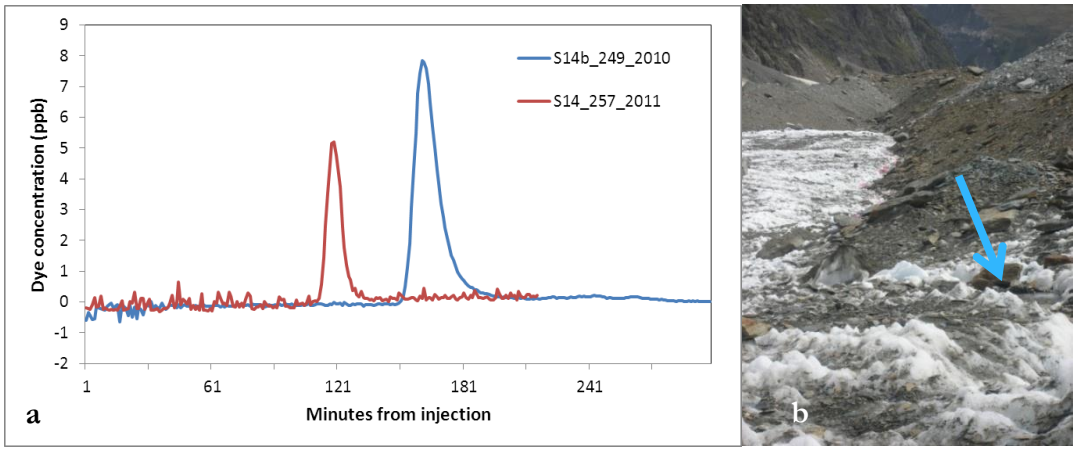

Figure 5.18 a) Dye traces into S14b in 2010 and S14 in 2011, and b) the S14b stream, the stream channel is marked by the arrow.

On the upper glacier three traces were conducted in 2011, into S12, S14 and S15. The September traces into these moulins were faster than their traces in June and the end of July, but similar or in the case of S12, slightly slower than their early August traces (Figure 5.13a, Figure 5.14 and Figure 5.16). The dispersion coefficient of the traces was also greater than their early August traces, and in the case of S12 and S14 greater than their June traces. Both the S12b_254 and S14b_249 traces in 2010 can be compared with the traces conducted into the same moulins in September 2011 (Figure 5.19 and Figure 5.18). Both the 2010 traces were slower than their 2011 counterparts, and in terms of dispersion coefficient were similar (S14b and S14) or larger (S12b and S12) than in 2011. There may

have been some influence of the increased travel distance in supraglacial streams but both streams were fast flowing.

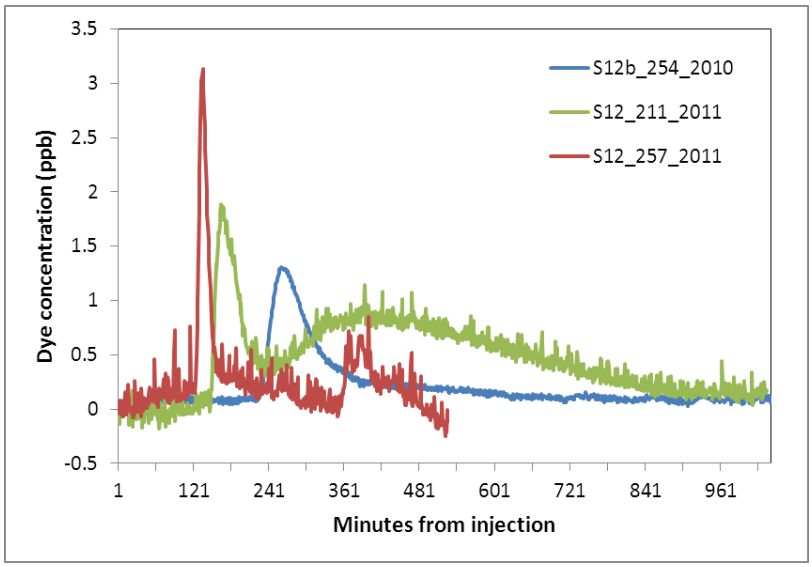

Figure 5.19 Dye traces into S12 in September 2010, and July and September 2011.

5.1.4 Overview of dye tracing results

The most striking result from the dye tracing experiments was that the trace velocity increases with distance upglacier. If the average trace velocity from all injection points is correlated with the distance from the gauging station (using the distance measured using the pivot point on the bend of the glacier, section 3.3.1), then the relationship is significant with a p-value of 0.004, and is positive, giving a Pearsons correlation coefficient of 0.759, and an R^2 of 0.534 (Figure 5.20a). Generally, the water entering the glacier via the main moulins around C10 (S12, S13, S14 and S15) travelled quickly to the proglacial stream, with the mean travel time in 2011 for S12, S14 and S15 being 143 minutes, 137 minutes and 191 minutes respectively. These traces also had high percentage dye returns, confirming that the majority of the water was routed efficiently, as little of it was stored or returned at too low a concentration to be detected.

This highlights another relationship between the percentage dye recovered and the distance from the gauging station. This was a significant (p-value of 0.024) and positive relationship, with a Pearsons coefficient of 0.644 and R^2 of 0.356. When plotted (Figure 5.20b), the traces from S11 upwards have dye returns around 80%, and the lower glacier traces have returns of 20 to 40%. This is except for the trace into S3 which has an anomalously high percentage dye recovery of 72%. This stream must enter the glacier close to the main conduit system because its return was peaked even though the input discharge was very small. The trace velocity of this injection point was lower than for the

upper-glacier streams, because the small input stream transports water slowly before it reaches the main channel system.

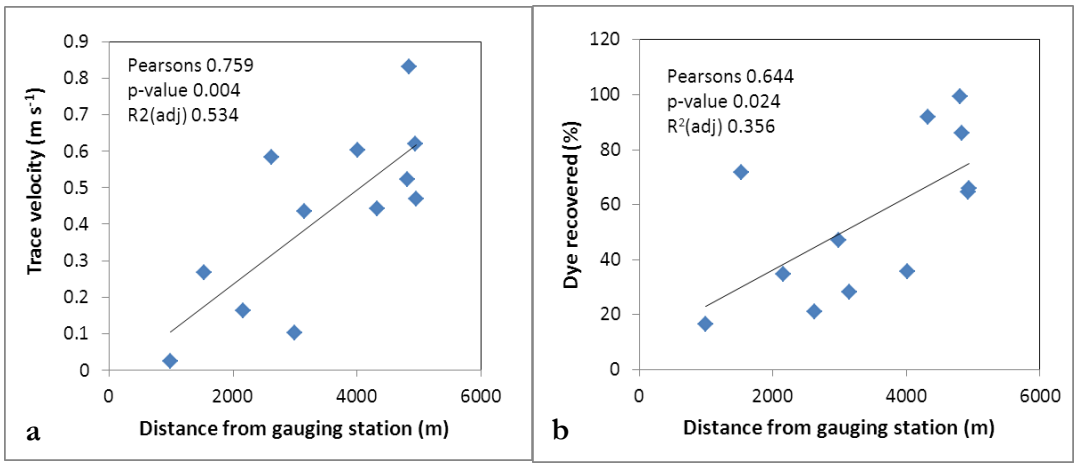

Figure 5.20 Relationship between the distance to gauging station and a) average injection point trace velocity, and b) average injection point percentage dye recovery, including all 2010 and 2011 data.

The trace velocity of the lower glacier points was on average lower, and the percentage dye recovery was also relatively low. The variability of the lower glacier trace parameters was high however, with velocities ranging from 0.024 m s^{-1} (S1) to 0.58 m s^{-1} (S6). Overall, water from the lower glacier has a longer travel time to the proglacial stream, with the average travel time in 2011 for S7 being 515 minutes, and for S5 being 299 minutes, despite the shorter travel distances. Meltwater produced on the upper glacier could therefore reach the proglacial stream before meltwater produced at the same time on the lower glacier.

5.2 Interpretation and discussion

This section will briefly interpret the dye tracing results and discuss how the hydrological system was influenced by the debris cover. For each part of the glacier (upper then lower) the dye tracing results will be used to infer firstly the structure of the hydrological system, and secondly the degree of evolution of this system over the season. Then reasons will be discussed for the mechanisms behind the creation and development of the system.

5.2.1 Upper glacier

Traces from the upper glacier indicated that a channelized system existed a large distance from the glacier's terminus, even in early June when the upper glacier was snow-covered – this is unlike the clean glacier model of the gradual upglacier advance of the channelized system. The system remained channelized throughout the season but the

efficiency of water routing could be decreased in mid-summer if cooler weather was followed by an increase in inputs. In this section the upglacier dye traces will be interpreted to identify the drainage structure, followed by the theories explaining the early channelization of the drainage system. Then the evolution of the network and the causes of this will be discussed.

The dye traces from the majority of the upper glacier traces had fast trace velocities (all greater than 0.4 ms^{-1}), low dispersion coefficients and dispersivities and high percentage dye returns (see Figure 5.2, Figure 5.10, Figure 5.13, Figure 5.14, Figure 5.16, Figure 5.18 and Figure 5.19). The mean velocity of the four streams which led into moulins around C10 (S12, S13, S14 and S15) was 0.61 m s^{-1}, with the mean percentage dye return being 79%. These trace characteristics, along with a steeply peaked trace shape, indicate the water followed an efficient flow path (Nienow *et al.,* 1998), envisaged as a discrete channel system. Traces indicative of a channelized network were returned even very early in the season when, especially in 2010, the upper glacier was still snow-covered (from S13_162 in 2010, 4830 m from the gauging station, and from S12_161 in 2011, 4804 m from the gauging station). The exception to this was the S15_164 trace which had a pronounced shoulder of high dye concentrations (Figure 5.13), suggesting water was being delayed. This may be because of a constriction or pool in the channel or moulin meaning water was being released gradually into the rest of the network. The S15 and S14 moulins were very close to each other, but the S14 trace had a sharp peak - therefore, although the main conduit network emanating from the larger moulins (S12 and S14) was open by day 161, the connection between the main conduit network and smaller streams such as S15 had not yet fully evolved.

The evolution of the glacial hydrological system occurs when pressure fluctuations caused by increasing discharges within the hydrological system become large enough to destabilise the hydraulically inefficient distributed subglacial system so drainage becomes concentrated into fewer channels, before a major channel develops. Usually, this transition follows the snowline as it moves upglacier, because this marks the division between lower and less peaked inputs from snowmelt, and the higher and more peaked inputs from icemelt, with the channels forming downglacier from a moulin in which the critical discharge is exceeded (Nienow *et al.,* 1998). This results in a hydrological system which is efficient below the snowline, but less efficient above it. This is dissimilar to the situation on Miage Glacier when upper glacier traces suggested an efficient system early in the season.

A channelized network may exist early in the season because the channels did not completely close over the winter; because meltwater inputs entering the main upglacier

moulins were sufficiently large, or because of supraglacial lake drainage. Each of these possibilities will be discussed in turn.

Conduit closure calculations were performed for Miage Glacier (section 3.3.3.2), which revealed that after 8 months channels would close to a negligible size (radius of 0.01 m) 561 m from the gauging station, but after 4 months would be closed 857 m from the gauging station. As a test, the input discharge was doubled, this resulted in the distance from the gauging station over which the channel remained open after 8 months remaining the same, but if conduit closure occurred for only 4 months then the conduit remained open 964 m further upglacier. This was because the ice was not quite thick enough to cause channel closure in the overdeepening just up from the glacier's bend. Even in this case the conduit would not remain open far enough upglacier to reach the S12, S13 and S14 moulins (>4800 m from the gauging station). Therefore, the main conduit system beneath the upper glacier will close over the winter.

The channelisation of the drainage system is linked to the upglacier advance of the snowline because of the change in the input discharges between snow (high albedo and long within-snowpack travel time (Campbell *et al.,* 2006) gives an attenuated and lower input hydrograph) and ice (lower albedo and faster runoff leads to a more peaked and higher input hydrograph) (Willis *et al.,* 2002). The large catchment areas of the largest moulins on Miage Glacier (S14 and S12) could mean the input discharges (section 4.3) were large enough to open the channel network even if the input was from snowmelt. This may be aided by the system of moraines and valleys which concentrate runoff into large streams either side of the central moraine. The channelisation of the subglacial system could be initiated after a particularly large rainstorm (Barrett and Collins, 1997) which suggests the switch from snow to ice melt is not the only mechanism that initiates channel formation. Favourable spring weather conditions could lead to inputs large enough to destabilise the distributed system.

However, spring snowmelt is less likely to lead to an input meltwater hydrograph with a high diurnal amplitude. This would mean the pressure perturbations needed to destabilise the subglacial system would be absent (Nienow *et al.,* 1998), and the system could adjust to the gradually varying meltwater inputs. However, Mair *et al.* (2002) found an area downstream of several moulins on Haut Glacier d'Arolla experienced uplift during periods of high melt input, caused by separation of the glacier from its bed and enlargement of subglacial cavities along the axis of preferential drainage. This cavity enlargement increased the hydraulic efficiency of the subglacial hydrological system, thereby increasing the proportion of subglacial discharge in this area of the bed, and increasing the possibility subglacial channels formed here when the snowpack melted.

Kamb's (1987) theory of channel evolution involves the presence of large pressure perturbations which initiate the growth in the channel network due to the frictional melting of the cavity walls. However, Mair *et al.* (2002) suggested cavity growth, caused by variations in horizontal and vertical glacier velocities, may increase the efficiency of subglacial drainage and allow it to accommodate the discharges required to open a channelized network without the need for large pressure perturbations. Therefore, it is probably the relatively large input discharges of the upper glacier supraglacial streams, combined with the fact they enter the glacier near a region of high glacier velocity variability (see sections 4.3 and 8.2.3, respectively) that allows a channelized system to be formed upglacier early in the season.

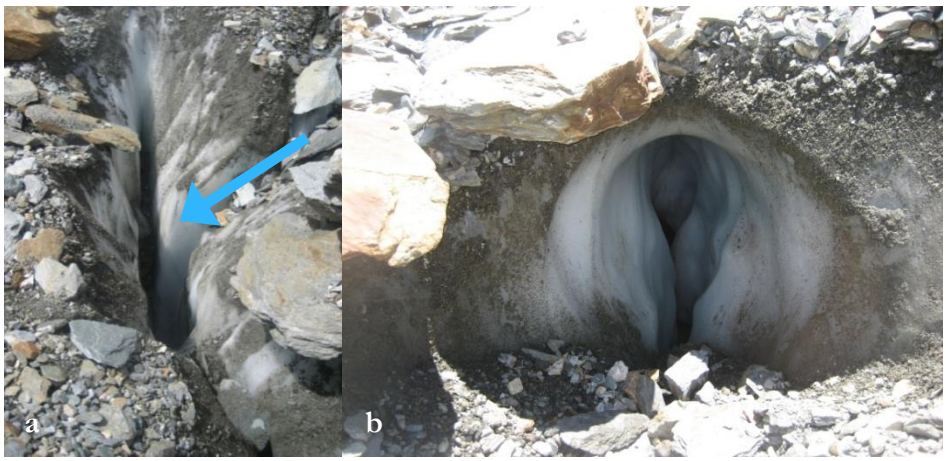

Figure 5.21 a) the S13 injection point, in July 2010, showing the east-west trending crevasse, the arrow marks where the stream entered the moulin, and b) melted out englacial conduit, downglacier from C5.

Another mechanism that can lead to channel formation is supraglacial lake drainage. There were two large lakes on Miage Glacier (near C4 in 2011 and near C8 in both years). These lakes drained during the ablation season, but after June, and so would not have caused channelisation of the network during June. However, there is evidence lake drainage led to moulin development. S13 was within a hollow which in June had evidence for collapsed snow which could have been held on top of the frozen surface of a supraglacial lake (Figure 5.1). Later in the season it could be seen the moulin intersected a transverse crevasse (Figure 5.21a), suggesting the moulin formed when water pressure from the supraglacial lake caused hydrofracturing (hydrologically driven crevasse propogation), with the lake drainage enlarging the crevasse into a moulin. If the lake drained suddenly it would cause phreatic (pressurised) conditions subglacially, leading to the creation of a channel network downglacier of the lake outflow moulin. There is evidence for phreatic conditions occurring englacially within Miage Glacier from observations of keyhole shaped conduits melted out at the surface (Figure 5.21b). Conduit systems created by the drainage

of supraglacial lakes have been found on the debris-covered Ngozumpa and Khumbu Glaciers in Nepal (Gulley and Benn, 2007; Benn *et al.,* 2009). If the C4 and C8 supraglacial lakes drained suddenly conduit systems would form downglacier from their drainage points. Although this was not confirmed by dye tracing, the large portals formed at the base of the empty lake hollows suggest a conduit system was created (Figure 5.22). Supraglacial lake drainage will therefore aid in the formation of the conduit system, but since not all moulins had evidence of lake formation this is likely a secondary mechanism.

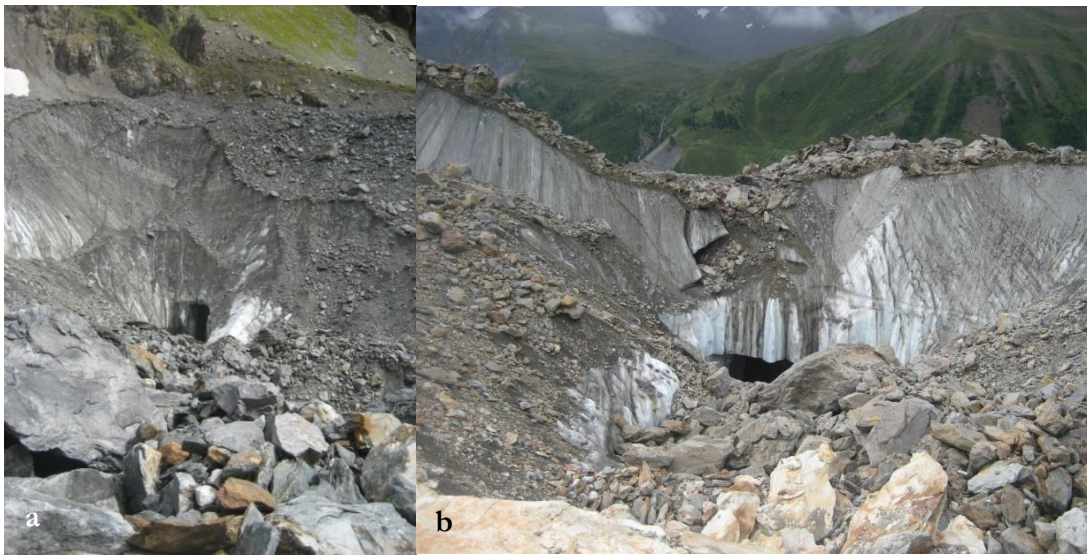

Figure 5.22 Drained supraglacial lakes in July 2011, a) the C8 lake and b) the C4 lake.

To understand whether the efficiency of the hydrological network was maintained into the summer the mid-season traces were studied. As shown in Figure 5.23a below, the velocity of the traces from the upper glacier moulins in 2011 (S12, S14 and S15) remained higher than those from the lower glacier (S5 and S7) throughout the season. The trace velocity of the S11_213 trace in 2010 was 0.44 m s^{-1}, again still indicative of a discrete channel system.

However, compared to June the traces S12_211 and S14_210 in 2011 were slower and had larger dispersion coefficients, although the traces still had singular peaks (Figure 5.16 and Figure 5.14 respectively). This indicates the efficiency of the channel system had reduced since June. Usually, increased melt inputs during July would result in a more efficient channel network. For S14 and S12 this doesn't appear to be the case, possibly because of the particularly cold weather between days 198 and 208, when maximum daily temperatures were generally below 10°C, and air temperatures fell below zero at UPMET during the mornings of day 205 and 206 (Figure 5.24). This resulted in low ablation (modelled average daily melt between days 198 and 208 was an average of 0.017 m d^{-1}, a third less than the seasonal average of 0.025 m d^{-1}), thereby reducing input discharges. The size of a glacial conduit is determined by the balance between the widening of the channel

due to the friction of meltwater acting on the channel sides; and its closure due to ice deformation resulting from the difference between overburden and water pressure (Röthlisberger, 1972). Reduced input discharges lead to lower water pressures - enabling conduit closure. This reduced the conduit's capacity to evacuate meltwater when the weather warmed and the discharges rose again, from day 209 onwards, and explains the slower and more dispersed traces from these moulins.

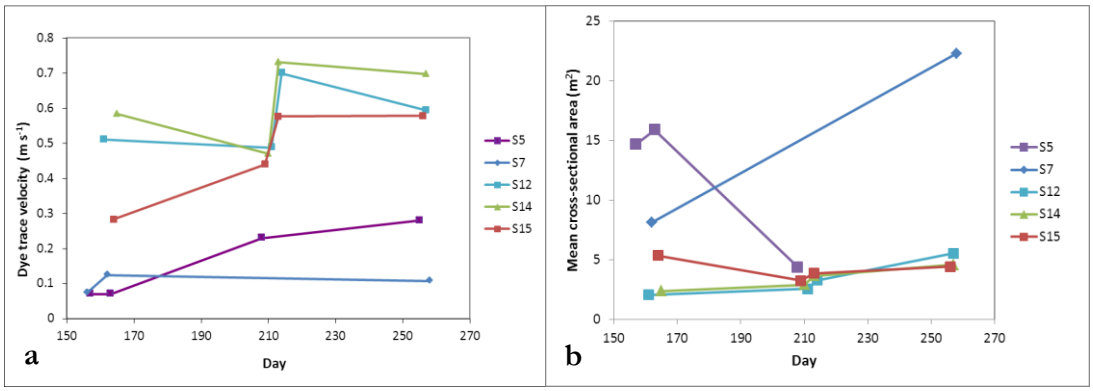

Figure 5.23 a) Dye trace velocity variations over the 2011 season, and b) mean cross-sectional area variations over the 2011 season.

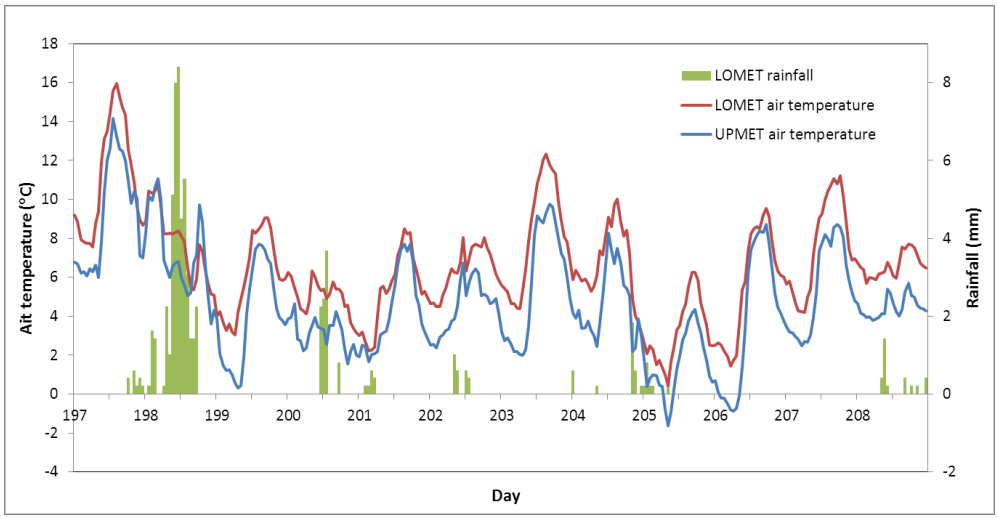

Figure 5.24 Meteorological conditions prior to the July/August fieldtrip, 2011.

However, it may not be correct to say that the conduit diameter was less in July than in June, since the input discharges into both moulins were greater in July, but it is likely the conduit diameter was not great enough to efficiently evacuate the quantity of meltwater entering the system (i.e. warmer weather meant discharges increased at a rate greater than conduit growth, causing water to back up in the system and reduce trace velocities (Nienow *et al.,* 1996)). This can lead to an increase in water pressures (Röthlisberger, 1972), which can increase sliding velocities (Iken and Bindschadler, 1986). Faster glacier velocities were observed on days 212 and 213, implying that the conduit network had indeed been overwhelmed (section 8.1.4). Since the source of the melt inputs

for the main moulins are from relatively high upglacier there may be a greater chance of cooler weather reducing melt inputs sufficiently to allow a decrease in conduit diameter, even in mid-summer.

The early August traces into S12, S14 and S15 in 2011 all showed an increase in trace velocities (Figure 5.23a), a decrease in dispersion coefficients and dispersivities, and a slight increase in channel cross sectional area (Figure 5.23b), compared to the traces before day 212. This suggests the conduit network was now able to accommodate the increased discharges. Frictional melting of the channel walls would have occurred during the period of rising discharges prior to day 212, allowing the conduits to expand and efficiently evacuate an increased meltwater input (Röthlisberger, 1972).

The late season traces and how they compare to the mid-season traces will now be discussed. In 2011, the September traces into the upper glacier moulins (see Figure 5.13, Figure 5.14 and Figure 5.16), suggested that the drainage system remained more efficient than in late July but less efficient than in early August. This may be because air temperatures remained high throughout August compared to July (mean LOMET air temperature in July was 9.4°C, but 12.6°C in August), so the drainage system efficiency was maintained. Proglacial discharges were all higher in September than they were during any traces earlier in the season. On the contrary, when September traces into S12b and S14b were compared with their 2011 counterparts, the 2010 traces were slower (Figure 5.18 and Figure 5.19). Air temperatures during August and September (until day 253) were much cooler in 2010 compared to 2011 (average August LOMET air temperature in 2010 was 10.5°C, but in 2011 was 12.6°C, similarly in September 2010 it was 8.8°C compared to 11.5°C in 2011). Consequently, input discharges later in 2010 would have been smaller, leading to slower water velocities and increased conduit closure rates.

Comparing the efficiency of water routing from different moulins, the S14_210 trace in 2011 implied the system had become less efficient than in June, but this was not by as much as the S12 trace, and in 2010 the S12b trace had a much less efficient signature than the S14b trace in September after a cooler August. This implies the hydrological system emanating from the S12 moulin (between the central and eastern moraine) is more liable to closure than that of the S14 moulin (between the central and western moraine), probably because the input discharge into S12 was consistently smaller than into S14 (mean S12 input discharge was 0.18 $m^3 s^{-1}$, but for S14 was 0.62 $m^3 s^{-1}$).

5.2.2 Lower glacier

The traces from the lower glacier revealed that the drainage system was less efficient than expected. The existence of the thick supraglacial debris cover, possibly combined with the layer of sediment at the bed of the glacier, appears to inhibit the formation of a completely channelized network. The evidence for this and the arguments for the debris influencing the glacier-hydrology will now be given.

Traces into some of the lower glacier moulins (S6 and S8, Figure 5.4), were characterised by fast velocities, low dispersion coefficients and single peaked return curves. These features indicate that the water was routed through an efficient channelized network. However, traces into S1, S3, S5, S5b and S7 had slower velocities, larger dispersion coefficients, and in some cases (especially S5 and S7, Figure 5.5 and Figure 5.7) displayed multiple peaks. These features indicate the water spent at least some time within a less efficient hydrological network, with the multiple peaks indicating multiple flow paths characteristic of a distributed system. On average, injection points S8 and below had a relatively slow average trace velocity of 0.26 m s^{-1}, and a low average percentage dye recovery of 37%.

Traces into S5 and S7 showed evidence of evolution of the hydrological network (Figure 5.11 and Figure 5.7), with certain peaks becoming more prominent and suggesting certain flow paths began to dominate. The multiple peaks of the S5 traces earlier in the season converged to one broad peak by mid-summer of both years (Figure 5.12), although trace velocities were still much lower than those of a completely channelized system. Therefore the hydrological network did increase in efficiency, but not to the extent that water was transferred as quickly as from the upper glacier moulins. The traces into S3 also changed from less clear and multi-peaked to a relatively fast single peaked trace in mid-summer, although again trace velocities were lower than expected for a completely channelized system (Figure 5.8).

Later in the season the slower trace velocity and greater dispersion coefficient of the S3_252 trace compared to the S3_210 trace pointed towards the efficiency of the hydrological network decreasing. For S5 in 2011 the situation was more complex, with the trace being composed of two peaks, of which the first came though faster than the mid-season main peak. Despite this, the divergence of the flow suggests the system was reverting back to the more distributed configuration found early in the season.

Given dye tracing suggests the hydrological system emanating from the main moulins is efficient, it seems strange traces from the lower glacier during the same period are indicative of a less efficient system, even though the lower glacier was mainly snow free

even in June of both years. However, this may be caused by the low ablation rates under the thick debris cover on the lower glacier (section 4.2). The lower melt rates along with the uneven topography of the lower glacier leads to small and attenuated supraglacial stream discharges (section 4.3). The transition from a distributed system to a channelized system occurs when the water pressure in the cavities reaches close to the ice overburden pressure. This causes the rate of cavity closure to fall relative to the rate of cavity opening, and means the cavities become unstable and are replaced with a channel system (Walder, 1986). For the pressure in the cavities to reach close to overburden the discharge through the system must be large enough to mean the size of the cavities would be too large to be stable. This results in a glacier specific critical discharge above which channels develop (Hewitt and Fowler, 2008). The reduced input discharges (caused by the supraglacial debris cover) must not be large enough to initiate the formation of a channelized system. Small and non-peaked inputs of meltwater can be accommodated within a less efficient subglacial system. This work has therefore identified that the debris cover's role in reducing input discharges into the system acts to inhibit the formation of a completely channelized drainage network.

There is evidence a distributed system can exist at the same time as a channelized system exists on other parts of a glacier, for instance on Haut Glacier d'Arolla not close to the preferential axis of drainage (Nienow *et al.,* 1996), on the western side of Midtalsbreen, southern Norway (Willis *et al.,* 1990), or within the smaller drainage catchment of the South Cascade Glacier, USA (Fountain, 1993). It is more unusual for a less efficient drainage system to occur downglacier of the channelized network, and within the same catchment area (i.e. all traces mentioned drain to the northern lobe proglacial stream), as found on Miage Glacier.

Instead, it is envisaged that on the lower glacier, it is the link between where the supraglacial stream enters the glacier, and where the water enters the main subglacial channel, which is the inefficient part of the system. It is this part which is poorly developed and causes the decrease in trace velocities and multiple peaks of the S5 and S7 streams. On Haut Glacier d'Arolla, borehole experiments by Hubbard *et al.* (1995) revealed adjacent to the main channel along the variable pressure axis, there was an area of distributed drainage which supplied water to, and was the recipient of, water from the main channel, depending upon whether the pressure in the main channel was higher or lower than the adjacent distributed system. A distributed and channelized system probably occurs simultaneously under Miage Glacier, with the distributed system draining to the main channel system. Unlike Hubbard *et al.* (1995) however, the distributed system beneath Miage Glacier contains water irrespective of the pressure gradient between the channel and distributed

system (i.e. the distributed system does not need to be supplied with water from the channel system during high flow periods), because water enters the distributed system from the surface.

At the bed of Miage Glacier (specifically above the bend and on the northern lobe) a thick layer of sediment is believed to exist (Deline, 2002). Conduit formation can be inhibited if the sediment layer is thick and highly porous. Flowers (2008) modelled the influence of different bed types on the formation and evolution of the subglacial hydrological system and found if a glacier had a mixed bed where the bed was hard up-glacier, but became progressively 'softer' downglacier then the sediment wedge would stall conduit formation. Conduits would form on the hard bed first, where high water pressures would result until the conduits found an outlet at the glacier terminus. Rates of debris supply to the margins of a glacier are generally higher if it is debris-covered, resulting in the build-up of large lateral moraines which constrict the glacier during periods of positive mass balance, when it instead thickens. Gradually sediment builds up so the glacier becomes perched above the valley floor (Benn and Evans, 1998). A sediment layer may therefore be common beneath other debris-covered glaciers, and may have a similar effect on the formation of the subglacial hydrological system.

Some of the water may also travel as porewater through the sediment, with this accounting for the lower percentage dye returns on the lower glacier. As discharges in the porewater system rise, porewater flow would become insufficient to route meltwater and a distributed system would develop (Benn and Evans, 1998). This distributed system may be in the form of a linked cavity system, which can exist over a soft bed so long as there are enough immobile large boulders or bedrock hummocks to provide areas for cavities to form (Kamb, 1987). Given a main channel does flow through the lower glacier which exhibits fast transit times, and that other glaciers with a subglacial sediment aquifer do have channel systems (e.g. Haut Glacier d'Arolla, Hubbard *et al.,* 1995), it is concluded the sediment layer beneath Miage Glacier works in conjunction with the smaller input discharges on the lower glacier to inhibit channel formation.

However, other injection points such as S6 and S3 did give peaked traces, even early in the ablation season. This does not appear related to the input discharge of these streams as S3 was the smallest stream traced, and S5 was one of the largest on the lower glacier (and it gave broader and slower traces compared to S3). Therefore, it must be related to the efficiency of the individual channel's link to the main conduit network. This may be determined by the discharge and diurnal amplitude of the input stream, the distance between the moulin and main subglacial channel, or the existence of a crevasse transecting the stream.

5.2.3 Summary

From the overview of the dye traces over the season (section 5.1.4) it was apparent that on Miage Glacier the water flow velocities increase with distance upglacier, and this was linked to a higher percentage dye return from the upper glacier. This was due to the existence of the channelized system on the upper glacier (section 5.2.1), and the locally distributed system on the lower glacier (section 5.2.2). There was a greater variability in the trace velocity from lower glacier moulins though, reflecting the difference in the efficiency of the join between each of the injection sites and the main channel system. This is unlike the clean glacier model of water routing where the trace velocity decreases up-glacier, with this happening most markedly at the channel head position in between the conduit and the up-glacier distributed system, as marked by the position of the snowline (Nienow *et al.,* 1998).

The main findings from this section on the structure and evolution of the water routing through the glacier are as follows:

1. A channelized system exists emanating from the upper glacier early in the season – this will have been opened due to the large size of the supraglacial streams on the upper glacier, with supraglacial lake drainage also resulting in conduit formation for certain moulins.
2. Traces into the lower glacier indicate a distributed system exists between some supraglacial streams and the main conduit system, this system does become more efficient but water velocities do not reach those of the upper glacier. This is due to a combination of the debris cover on the lower glacier attenuating inputs and the existence of a sediment layer beneath the ice.
3. The structure and evolution of the hydrological system of Miage Glacier is not analogous to that of a temperate clean glacier – the channelization of the system is not related to the snowcover and water velocities are faster from moulins on the upper compared to lower glacier.

Now that the spatial differences in the hydrological system and its development over the season have been characterised it is important to understand how the quantity of water travelling in different parts of the hydrological system changes over the season. The next section looks at the bulk water routing in terms of how the hydrological system affects the chemistry and timing of the water flow, and the impact this has on the proglacial hydrograph.

6 Temporal variations in bulk water routing using analysis of water chemistry and proglacial runoff

In this chapter the routing of different components of runoff are studied using supraglacial and proglacial water chemistry and analysis of the proglacial runoff hydrograph. The supraglacial water chemistry was used to determine the influences on the chemistry of the water before it enters the glacier, aiding in the interpretation of the proglacial water chemistry. The proglacial water chemistry was used to identify the short term variations in the hydrological conditions through which the majority of water has travelled through, as well as the likely overall drainage structure, through comparisons with measurements on other glaciers. Finally, the proglacial runoff analysis was used to understand how the overall hydrological system impacts upon the proglacial hydrograph, in terms of the hydrograph shape, its amplitude and the lag times between meteorological variables and runoff. The delimiting of the hydrograph into phases also allowed the identification of the meteorological and glaciological conditions which give rise to particular hydrograph forms.

6.1 Supraglacial water chemistry

This section deals with the water chemistry characteristics of the supraglacial streams, ponds and lakes on the glacier (Table 6.1), and whether any parameters are influenced by the debris cover. The chemistry of samples of melted snow was compared to see if a change from snow to ice melt could change the proglacial runoff chemistry.

6.1.1 Snow samples

Three snow samples were melted and analysed in 2010, from near S1, S5, and C14. The SSC was generally low (mean of two samples 26 mg l^{-1}), and the bicarbonate concentration was low compared to the supraglacial streams (mean of three samples 145 μeq l^{-1}). The sulphate concentration for near S5 was 25 μeq l^{-1} and for C14 was 127 μeq l^{-1}, which is a large difference and makes inferences difficult. Nevertheless, the value for C14 is the highest value measured of all of the supraglacial samples and suggests snowmelt can be a source of sulphate. This results in a considerably lower C-ratio for this sample (of 0.45) than measured in any of the supraglacial or proglacial samples. This higher sulphate concentration will be because of the scavenging by snow or dry deposition of sulphate

aerosols (Brown, 2002). The mean absolute difference between the duplicate samples of sulphate was 21.8 μeq l^{-1}, so differences within this range could be due to measurement error.

Table 6.1 Supraglacial stream, lake (C4 and C8 Lakes), pond (SP5) and snow water chemistry measurements. * denotes values are an average from more than one measurement. Q_s is the supraglacial stream discharge, and u_r is the supraglacial stream velocity.

Name	Cond. (μ S cm^{-1})	SSC (mg l^{-1})	pH	Temp. (°C)	HCO^{-}_3 (μeq l^{-1})	SO^{2-}_4 (μeq l^{-1})	C-ratio	S-ratio	$p(CO_2)$	Q_s (m^3 s^{-1})	u_r (m s^{-1})
C4 Lake	-	17	-	-	314	47	0.87	0.13	-	-	-
C8 lake*	-	8	-	-	292	30	0.92	0.08	-	-	-
SP5	56.8	15	9.79	2.7	658	87	0.88	0.12	-5.27	-	-
Snow*	-	26	6.70	-0.3	145	76	0.66	0.34	-2.78	-	-
E4*	-	0	-	-	254	57	0.83	0.17	-	-	-
LOMET streams*	12.3	256	8.50	0.3	309	22	0.93	0.07	-4.30	-	-
SS1	7.6	60	8.39	0.54	254	-	-	-	-4.28	-	-
S1	16.1	266	7.66	0.13	464	2	1.00	0.00	-3.29	-	-
S5*	10.2	54	7.53	0.6	258	12	0.96	0.04	-3.42	0.03	0.17
S7*	28.0	55	8.20	-	408	6	0.98	0.02	-3.90	0.02	0.26
S8	-	277	-	-	269	21	0.93	0.07	-	-	-
S12*	4.0	18	7.75	-	187	10	0.95	0.05	-3.73	0.18	0.46
S14	-	1	-	-	135	0	1.00	0.00	-	0.53	1.14
S15*	18.4	32	8.86		278	6	0.98	0.02	-4.71	0.02	0.32

6.1.2 Supraglacial streams

For some supraglacial stream measurements multiple samples were taken, and these included the 2011 dye tracing streams (S5, S7, S12, and S15, see Figure 6.2 to Figure 6.4) as well as the E4 stream (at the foot of the Dome glacier and which leads to the S12 moulin, Figure 6.1). Samples were taken from three different but small streams near LOMET (SS2, SS3 and SS4), and another very small stream on the northern lobe (SS1). Only one sample was collected from each of S1, S8 and S14.

Figure 6.1 Supraglacial stream near to E4, emanating from the base of the Dome glacier in June 2010.

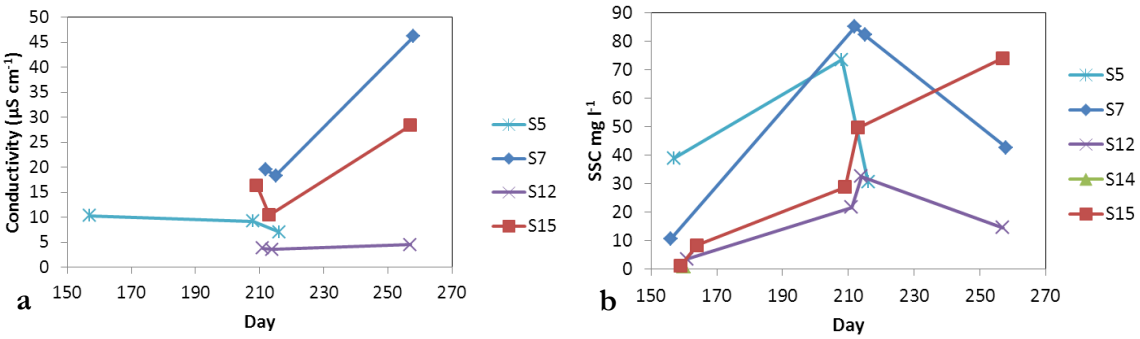

Figure 6.2 a) Supraglacial stream conductivity variations, and b) SSC variations, for the 2011 season.

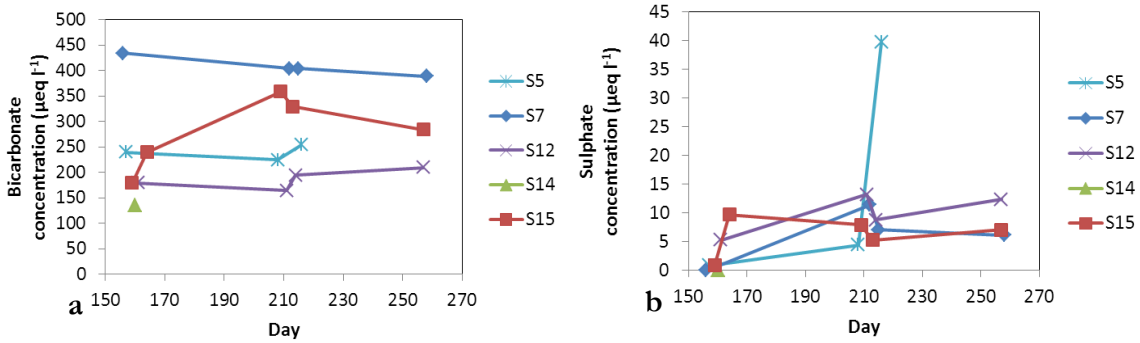

Figure 6.3 a) Supraglacial stream bicarbonate and b) sulphate ion concentration variations over the season in 2011.

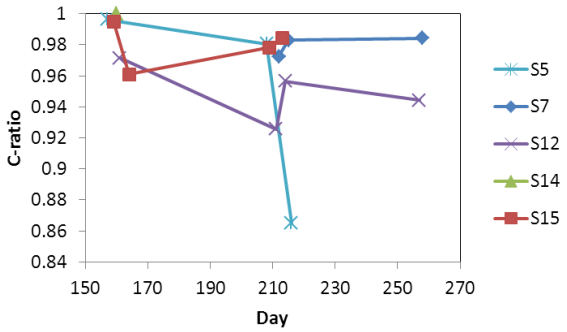

Figure 6.4 Supraglacial stream C-ratio variations over the season in 2011.

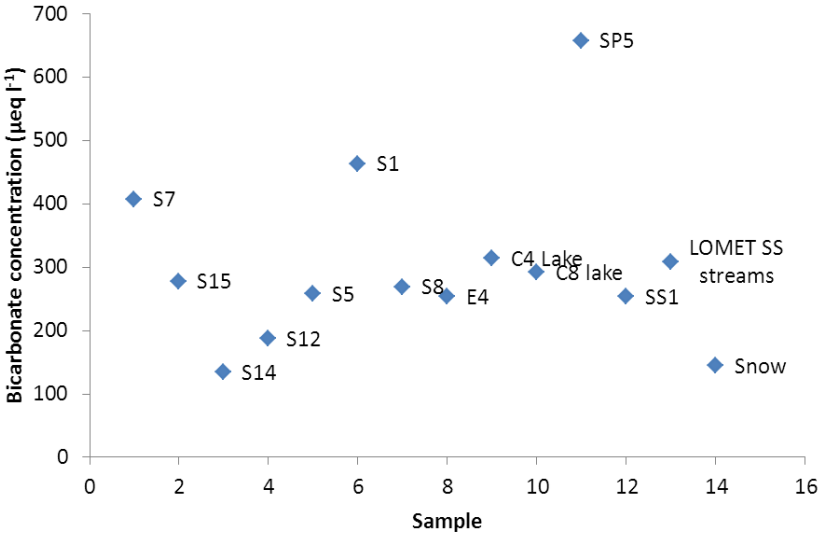

Figure 6.5 Bicarbonate concentrations of all supraglacial samples. Where more than one sample was taken from a location, the average is given.

The supraglacial water chemistry data will now be discussed in terms of what it reveals about the meltwater sources of each of the streams. The S14 stream is situated near C10, had the largest discharge and velocity of those streams measured (section 4.3), and had the lowest bicarbonate and sulphate concentration, and lowest SSC of all the 2011 streams (only E4 was lower, with 0 mg l^{-1}). The source of water for this stream was from ice and snowmelt that has had little chance to react with sediment. Similarly the S12 stream, had the second largest discharge and velocity, the lowest conductivity, the next lowest SSC, and the next lowest bicarbonate concentration. The stream water was therefore dilute ice or snowmelt that had spent limited time in contact with sediment. This was understandable because both these streams had large catchments draining areas of clean ice (section 4.3). The E4 stream had a very low SSC because it was composed of melt from the clean Dome glacier tributary. It also had a high sulphate concentration, suggesting snowmelt was a higher proportion of the sample (the snowpack can contain atmospherically derived sulphate (Tranter *et al.,* 1996)), due to the thick snow cover in June 2010 when this sample was taken. All of the other supraglacial stream measurements had low sulphate concentrations, implying icemelt dominated as the meltwater source. The sulphate concentrations measured in the supraglacial streams were an order of magnitude lower than those measured at the gauging station (mean 2010 sulphate concentration was 200 µeq l^{-1}, and in 2011 was 215 µeq l^{-1}, compared to the mean of supraglacial stream measurements of 15 µeq l^{-1}), implying the majority of the proglacial stream sulphate must be produced by reactions of water with sediment at the bed.

Figure 6.6 Looking upglacier from just above the S15 moulin, shows this stream's catchment is mainly debris covered.

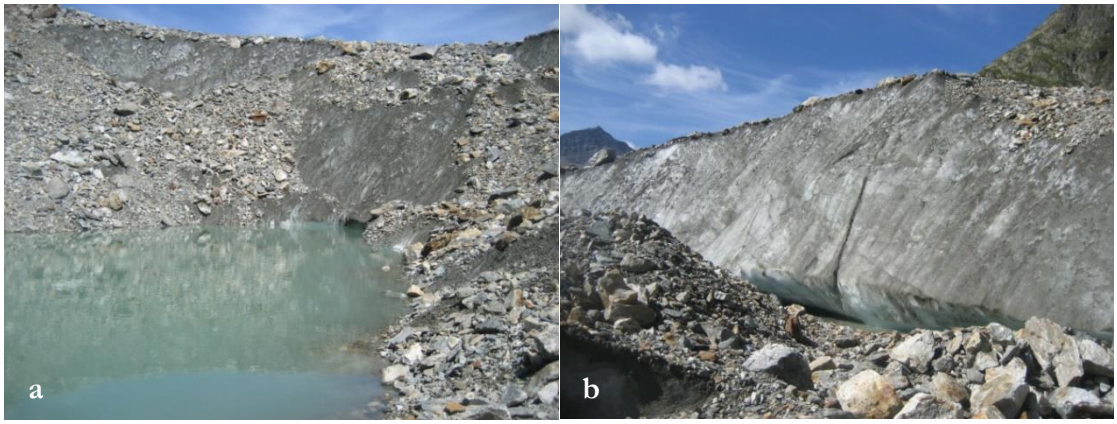

Figure 6.7 a) The supraglacial lake just upstream of the S5 injection point, this lake water drains into the stream, and b) is the ice cliff overhanging the S5 stream, both taken July 2011.

Despite being close to S14 and S12, the S15 stream had a higher conductivity, SSC and bicarbonate concentration than those streams. This is likely because this stream had a smaller catchment than S14 and S12, which was mainly debris covered in mid-summer (Figure 6.6). The stream water was therefore in contact with and transported more sediment, increasing the chance of water-rock interaction and allowing acid hydrolysis which leads to the production of bicarbonate ions, and an increase in conductivity. This suggests the S14 and S12 stream water was mainly from further upglacier where the area of clean ice was greater. The bicarbonate concentration and SSC of S15 was similar to S12 in June 2011 though, suggesting the S15 stream water was composed of snowmelt early in the season. As the snow melted and was replaced with a debris-covered surface the water-rock interaction increased.

The S7 stream had the highest conductivity and bicarbonate concentration of any of the 2011 streams, and had a SSC higher than the upper glacier streams and similar to that of S5 and SS1. It was a small stream with a low velocity on a thickly debris-covered

region of the lower glacier. The supraglacial meltwater could have interacted with suspended sediment within the stream, or with sediment as it travelled within the debris, which resulted in acid hydrolysis and the production of bicarbonate ions. This stream was similar to the S1 stream which had a high bicarbonate ion concentration and conductivity, as well as reasonably high SSC. This was also a small stream which drained a thickly-debris covered region of the lower glacier.

However, there was not a clear relationship between conductivity, bicarbonate ion concentration and the degree of debris-cover in a stream's catchment. The S5 stream was a small stream on the debris-covered lower glacier, but it had an intermediate bicarbonate concentration and conductivity (lower than S15 but higher than S12), although its SSC was similar to S7. This stream was partly fed by a small ice walled pond (Figure 6.7a) which remained all season, with water also provided by melt of tall ice cliffs surrounding the stream (Figure 6.7b). The pond conductivity was the lowest of those measured in 2011 (19 $\mu S\ cm^{-1}$), probably due to the ice cliffs surrounding this pond providing dilute meltwater, reducing the conductivity and bicarbonate ion concentration. The other ponds measured were generally ephemeral and did not have well-developed ice cliffs. Although there were ice cliffs associated with the S7 stream they were only in evidence near where the stream entered the glacier, and were not as tall or extensive as those near the S5 stream. The very small streams measured (SS1 and the SS2 to SS4 streams next to LOMET), had intermediate bicarbonate concentrations and conductivities. Two of the streams had relatively high SSC, but the other two had a SSC close to the main supraglacial streams, although the SSC was not closely related to the conductivity or bicarbonate ion concentration. As these streams were so small, the water would have only travelled a short distance over a short period of time, limiting its contact with sediment. Despite this the water still had a bicarbonate concentration much greater than the S12 and S14 streams, suggesting the debris can enrich the bicarbonate concentration of supraglacial water, even over short distances. Therefore, although the increased contact sub-debris melt has with rocks and debris may increase the conductivity and bicarbonate concentration of the stream it flows into, this is complicated by dilution of this water with ice cliff meltwater.

There does appear to be a relationship between the distance from the gauging station and the bicarbonate concentration of the streams, although it was not statistically significant at the 95% level (Figure 6.8) (p-value 0.098, R^2 0.22), implying local influences have a more significant effect on the supraglacial stream water chemistry than the surrounding debris thickness. Nevertheless, the debris cover may enrich the supraglacial stream waters with bicarbonate ions where there are limited sources of dilute melt from ice cliffs. Acid hydrolysis reactions can occur in-stream if the water reacts with suspended

sediment (Tranter *et al.,* 1993b), and so bicarbonate ions could be produced within streams with relatively high SSC even if they are ice-walled. The average supraglacial stream bicarbonate concentration of 282 μeq l^{-1} was still considerably lower than the average gauging station concentration of 783 μeq l^{-1} in 2010 and 603 μeq l^{-1} in 2011 though. There must therefore be a significant proportion of the proglacial bicarbonate concentration produced due to reactions at the bed.

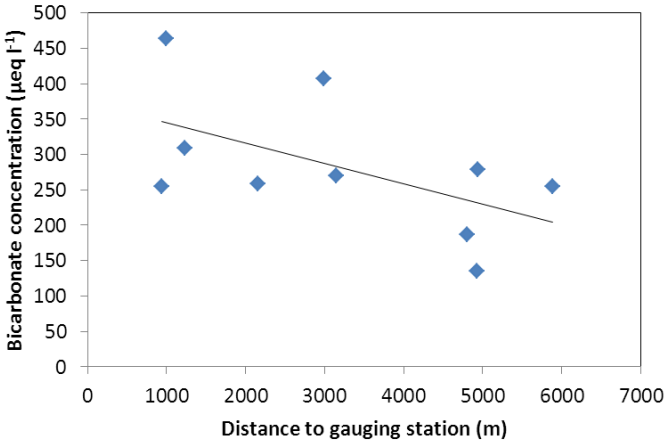

Figure 6.8 Relationship between the bicarbonate ion concentration of supraglacial streams, and the distance to the gauging station. If more than one bicarbonate concentration measurement was taken then the value given is an average, the distance to the gauging station is a straight line, but uses a pivot point at S4 to account for the glacier's bend.

Comparing the bicarbonate concentrations of the supraglacial streams on Miage Glacier with those from other glaciers, confirms that the reaction of meltwater with debris may enrich supraglacial waters with bicarbonate compared to the debris-free area. Tranter and Raiswell (1991) measured the bicarbonate ion concentration of supraglacial melt water of Gornergletscher, Switzerland, and found a range of 36 μeq l^{-1} to 72 μeq l^{-1}, lower than any of the Miage Glacier supraglacial streams. Raiswell and Thomas (1984) took two supraglacial samples from the Fjallsjökull Glacier, draining the Vatnajökull ice cap in Iceland which had values of 180 μeq l^{-1} and 290 μeq l^{-1}, of which the lower value was similar to the upper glacier supraglacial measurements on Miage Glacier, and the higher value closer to those on the lower glacier. Raiswell and Thomas (1984) suggested the higher solute levels in their supraglacial compared to precipitation measurements were due to supraglacial chemical reactions of the meltwater (possibly with rock debris, but this was not mentioned explicitly). In terms of sulphate, Tranter and Raiswell (1991) found values were very small (<0.01 μeq l^{-1}), and Raiswell and Thomas (1984) measured values of 13.4 μeq l^{-1} and 20.2 μeq l^{-1}. The latter values were similar to those found at S5 and S8 on Miage Glacier. The fact there was not a clear distinction in sulphate concentrations between the upper and lower glacier samples (Table 6.1), suggests the debris does not have a significant

influence on the sulphate ion concentration. This was contrary to Hasnain and Thayyen (1999a) who suggest the strong correlation between proglacial sulphate concentrations and SSC implied enhanced weathering of the supraglacial debris during the monsoon elevated sulphate concentrations on the Dokriani Glacier, Garhwal Himalaya. However, Hodson *et al.* (2002) found this not to be the case on the Batura Glacier, Pakistan, as they found a strong negative correlation between proglacial discharge and sulphate concentrations, and suggested the elevated sulphate concentrations were most likely due to sulphate oxidation reactions at the bed of the glacier. The generally low supraglacial sulphate concentrations on Miage Glacier similarly suggest the majority of the proglacial sulphate is not of a supraglacial origin (apart from the snowmelt contribution in the early season).

6.1.3 Supraglacial ponds and lakes

A few water samples from ponds and lakes on the glacier were taken for comparison with the stream measurements, they included one from C4 lake (Figure 6.9b), two from C8 lake (Figure 6.9a) (one from each year), and one from a very small pond (SP5). Generally the SSC of the lakes and pond was low compared to that measured in the streams, being between 2 and 17 mg l^{-1}. The conductivity of the lakes was not measured, but the conductivity of 6 ponds (including SP5) was, and their conductivity was high compared to the stream measurements, ranging from 19 to 58 μS cm^{-1}, with a mean of 35 μS cm^{-1}, much higher than the supraglacial stream mean of 14 μS cm^{-1}. Their mean pH of 9.4 was also much higher than for the supraglacial streams of 8.1. Part of the increased conductivity in the small ponds was due to an elevated bicarbonate and sulphate concentration, because the sample taken from SP5 had a bicarbonate and sulphate concentration (658 μeq l^{-1} and 87 μeq l^{-1} respectively) which was higher than any of the other supraglacial samples taken, with the bicarbonate concentration similar to the proglacial stream. The larger lakes had a bicarbonate concentration similar to the supraglacial streams of around 300 μeq l^{-1}, because both had large ice cliffs which provided dilute meltwater, whereas SP5 was a much smaller ephemeral feature without ice cliffs. The small ponds, although common, were not so prevalent as to be viewed as a significant source of input meltwater on the glacial scale, so it is unlikely they are a significant bicarbonate source. The C4 and C8 lakes also had particularly high sulphate concentrations of 47 μeq l^{-1} and 30 μeq l^{-1} respectively. This demonstrates that the long residence time of the lake water, where it is in contact with sediment in suspension or on the lake bottom, is conducive to coupled sulphide oxidation and carbonate dissolution reactions which produce sulphate ions (Brown, 2002). The lake sulphate concentrations were still much

lower than for the proglacial stream, and so likely only provide a significant source of ions to proglacial runoff over short periods when the lakes drain. On some of the large Himalayan glaciers (e.g. Khumbu Glacier (Watanabe, 1986) and Ngozumpa Glacier (Benn *et al.,* 2001)) supraglacial lakes are very common, and in these cases supraglacial lake water may provide a larger proportion of proglacial ions than on Miage Glacier where large lakes are less widespread. Of course factors such as the residence time of the water in the lake, the degree of ice cliff melt input, and the reactivity of the local geology will also be important in governing the water chemistry of any lake water.

Figure 6.9 a) C8 lake and b) C4 lake, both in June 2011.

6.2 Proglacial water chemistry

In this section the proglacial water chemistry will be studied in order to firstly gain an understanding of the short term variations in the likely flow path of the majority of runoff (whether dilute or quickflow), and secondly to be used as a proxy to identify the overall configuration of the drainage system, and the extent to which this varies over the season.

6.2.1 Results

The results of the proglacial water chemistry will now de described, divided by the measurement period in which they were collected. The dates of each of the measurement periods are given in Table 3.1.

6.2.1.1 June 2010

To look at the relationships between the water chemistry variables and discharge, as well as between the variables, the June data was split into two sections: early June from day

156 to day 165, and late June from day 166 to 175, this was done arbitrarily to identify if there were any changes between early and late June (see Table 6.2 and Table 6.3 for p-values and R^2 statistics). The water chemistry values used were from all samples collected. Relationships will only be mentioned if they were significant (p-value less than 0.05), looked reasonable when plotted, and are not due to one of the variables being calculated from another. In early June the only direct relationship between any of the water variables and discharge was with $\varrho(CO_2)$ whereas most other variables (SSC, conductivity, pH, sulphate and bicarbonate) had their strongest relationship with discharge if it was lagged by 18 hours (the hourly discharge was moved forward 18 hours and replaced the original discharge in the correlation – lags of 6, 12, 18 and 24 hours were used). Furthermore, when relationships between the different water chemistry variables were calculated, there were strong relationships between the SSC and conductivity, pH, sulphate concentration, bicarbonate concentration and a negative relationship with the C-ratio. There were also strong relationships between conductivity, sulphate concentration, bicarbonate concentration, and the C-ratio, and between the concentration of sulphate and bicarbonate ions. This implies the SSC, conductivity, sulphate and bicarbonate concentration were varying together.

In late June the results were different, with many variables (pH, sulphate, bicarbonate, SSC, C-ratio and $\varrho(CO_2)$) not having a significant and convincing relationship with discharge at any lag time. The relationship between water temperature and discharge gave the best (negative) relationship with a 12 hour lag. Conductivity had the strongest (negative) relationship with discharge with no lag. There were few significant relationships between water chemistry variables (Table 6.3), with the only convincing relationships being between SSC and conductivity and the water temperature and $\varrho(CO_2)$.

Further analysis was performed on the hourly conductivity and water temperature data, with hourly discharge data (Table 6.4 and Table 6.5). This data was split into early June (day 156 to 164), mid-June (day 166 to 175) and late June (176 to 179), with the last period shorter because it had the most data. These periods are different from those using twice daily data since more data was available, and were designed so that there was approximately the same amount of data in each group (around 10 days). There were gaps between groups later in the season due to data gaps. In early June the strongest relationship between conductivity and discharge was positive and with an 18 hour lag (confirming the twice-daily data), and in mid-June was negative with no lag. Later in June the strongest (and only convincing) relationship with conductivity was positive and with discharge lagged by 12 hours. For water temperature, there were no significant relationships in early June,

whereas in mid-June and late-June there was a significant negative relationship with discharge with no lag.

Table 6.2 Relationships between discharge and lagged discharge and water chemistry parameters. The top value is the Pearsons correlation coefficient, the middle value the p-value, and the bottom value the R^2 coefficient. R^2 values are only given if the relationship is significant (p-value <0.05). Bold highlighted values indicate the strongest relationship for that water chemistry parameter, and are only used when the relationship looks reasonable when plotted. All further tables follow the same layout.

Early June						**Late June**					
156-165	**Q**	**Q+6**	**Q+12**	**Q+18**	**Q+24**	**166-175**	**Q**	**Q+6**	**Q+12**	**Q+18**	**Q+24**
SSC	0.198	0.426	0.564	**0.801**	0.704	**SSC**	0.27	0.173	0.323	0.454	0.54
	0.378	0.061	0.01	**0**	0.001		0.255	0.466	0.165	0.044	0.012
			28	**62**	46.6					16.2	25.4
Cond.	-0.084	0.289	0.298	**0.64**	0.634	**Cond.**	**-0.847**	-0.775	-0.794	-0.754	-0.622
	0.709	0.216	0.202	**0.003**	0.004		**0**	0	0	0	0.003
				37.5	36.7		**70.3**	57.8	61	54.4	35.4
pH	0.425	0.502	0.404	**0.518**	0.194	**pH**	**0.228**	0.325	0.382	0.298	0.236
	0.048	0.024	0.077	**0.023**	0.425		0.32	0.162	0.096	0.203	0.317
	14	21		**22.6**							
Water temp.	-0.242	-0.33	-0.054	-0.172	-0.436	**Water temp.**	-0.473	-0.563	**-0.637**	-0.533	0.53
	0.278	0.155	0.821	0.48	0.062		0.03	0.01	**0.003**	0.015	0.016
							18.3	27.9	**37.3**	24.5	24.1
SO_4^{2-}	-0.192	0.296	0.25	**0.557**	0.513	**SO_4^{2-}**	-0.168	-0.004	0.156	-0.445	-0.383
	0.424	0.249	0.334	**0.025**	0.042		0.535	0.886	0.579	0.111	0.159
				26.1	21.1						
HCO_3^-	0.08	0.613	0.772	**0.859**	0.675	**HCO_3^-**	-0.247	-0.236	-0.248	-0.27	-0.315
	0.723	0.004	0	**0**	0.002		0.357	0.416	0.392	0.351	0.252
		34.1	57.4	**72.2**	42.4						
C-ratio	0.223	-0.19	-0.107	-0.428	-0.448	**C-ratio**	0.091	-0.07	-0.371	0.341	0.265
	0.359	0.446	0.684	0.098	0.082		0.789	0.848	0.291	0.37	0.459
$\varrho(CO_2)$	**-0.427**	-0.433	-0.312	-0.414	-0.093	**$\varrho(CO_2)$**	-0.177	-0.3	-0.338	-0.224	-0.11
	0.047	0.057	0.18	0.078	0.704		0.529	0.297	0.237	0.442	0.707
	14.2										

Table 6.3 Relationships between water chemistry variables in early (155-165), and late (166-175) June 2010.

155-165	SSC	Cond.	pH	Temp.	SO_4^{2-}	HCO_3^-	C-ratio
Cond.	**0.732**						
	0						
	51.2						
pH	**0.498**	0.318					
	0.018	0.149					
	21						
Water temp.	-0.334	-0.385	-0.407				
	0.128	0.077	0.06				
SO_4^{2-}	**0.643**	**0.772**	0.245	-0.407			
	0.003	**0**	0.312	0.084			
	37.9	**57.2**					
HCO_3^-	**0.692**	**0.731**	0.25	-0.243	**0.527**		
	0	**0**	0.262	0.276	**0.02**		
	45.3	**51.1**			**23.5**		
C-ratio	**-0.556**	**-0.716**	-0.196	0.371	-	-	
	0.013	**0.001**	0.422	0.118	-	-	
	26.8	**48.3**					
ϱ(CO_2)	-0.443	-0.254	-	0.391	-0.199	-0.161	0.163
	0.039	0.254	-	0.072	0.415	0.473	0.504
	15.6						
166-175	**SSC**	**Cond**	**pH**	**Temp.**	**SO_4^{2-}**	**HCO_3^-**	**C-ratio**
Cond.	**-0.527**						
	0.012						
	24.2						
pH	0.379	-0.345					
	0.09	0.126					
Water temp.	-0.35	0.436	-0.434				
	0.12	0.048	0.049				
		14.7	14.5				
SO_4^{2-}	-0.273	0.304	-0.133	0.084			
	0.307	0.253	0.637	0.767			
HCO_3^-	-0.149	0.334	-0.28	0.287	0.025		
	0.582	0.206	0.312	0.3	0.943		
C-ratio	0.119	-0.153	-0.08	0.106	-	-	
	0.778	0.653	0.827	0.771	-	-	
ϱ(CO_2)	-0.36	0.257	-	**0.614**	0.009	0.346	0.111
	0.187	0.355	-	**0.015**	0.98	0.2	0.761
				32.9			

Table 6.4 Relationship between hourly logged conductivity and discharge, with varying discharge lag times, for all season in 2010. Note that there are no July relationships due to lack of data. The days containing the analysed data are given in brackets.

Conductivity	Q	Q+6	Q+12	Q+18	Q+24
Early June	-0.084	0.289	0.298	**0.64**	0.634
(156-164)	0.709	0.216	0.202	**0.003**	0.004
				37.5	36.7
Mid June	**-0.798**	-0.672	-0.547	-0.396	-0.301
(166-175)	**0**	0	0.001	0.014	0.047
	62.5	43.4	27.7	13.3	6.9
Late June	-0.234	0.32	**0.667**	0.217	0.141
(176-179)	0.035	0.004	**0**	0.06	0.245
	4.3	9.1	**43.7**		
Early	**-0.403**	-0.181	0.054	0.185	0.251
August	**0**	0.023	0.509	0.022	0.002
(209-219)	**15.8**	2.7		2.8	5.7
Mid-August	**-0.378**	0.048	0.237	0.161	0.022
(220-227)	**0**	0.511	0.001	0.026	0.758
	13.8		5.1	2.1	
Late August	-0.4143	-0.259	-0.129	-0.107	0.142
(228-236)	0	0	0.08	0.147	0.055
	16.6	6.2			
September	0.125	0.15	0.236	0.133	-0.251
(249-255)	0.209	0.146	0.025	0.227	0.026
			4.5		5.1

Table 6.5 Relationship between hourly logged water temperature and discharge, with varying discharge lag times, for all season in 2010. The days containing the analysed data are given in brackets. The July group is large since no other data was collected during this period with which to compare it with.

Water temperature	Q	Q+6	Q+12	Q+18	Q+24
Early June	-0.242	-0.33	-0.054	-0.172	-0.436
(156-164)	0.278	0.155	0.821	0.48	0.062
Mid June	**-0.633**	-0.551	-0.443	-0.255	-0.21
(166-175)	**0**	0.001	0.009	0.122	0.171
	38.1	28.1	17.1		
Late June	**-0.37**	-0.071	0.274	-0.096	-0.304
(176-179)	**0**	0.493	0.007	0.365	0.005
	12.7		6.5		8.1
July	**-0.322**	-0.289	0.076	0.188	-0.027
(182-208)	**0**	0	0.052	0	0.488
	10.2	8.2		3.4	
Early August	-0.394	**-0.46**	-0.385	-0.177	-0.083
(209-219)	0	**0**	0	0.015	0.256
	15.1	**20.8**	14.4	2.6	
Mid-August	-0.312	-0.263	-0.055	0.089	-0.062
(220-227)	0	0	0.45	0.219	0.395
	9.3	6.4			
Late August	-0.399	-0.394	-0.309	-0.202	-0.166
(228-236)	0	0	0	0.005	0.021
	15.5	15.1	9.1	3.6	2.3
September	-0.322	-0.375	-0.192	0.125	0.249
(249-255)	0.001	0	0.07	0.256	0.028
	9.5	13.1			5.0

The fluctuations in the water chemistry variables will now be studied. During days 156 to 158 discharge rose steadily, and was accompanied by a rise in conductivity, SSC and pH, and an overall fall in $\varrho(CO_2)$ (see Figure 6.10 and Figure 6.12). Both the bicarbonate and sulphate concentrations rose too (Figure 6.11), but from day 157. The discharge rose gradually and with lots of variation during day 159, peaking in the evening of day 159/morning of day 160, before it decreased in the middle of day 160. This relative fall in discharge was associated with a distinct peak in conductivity, SSC, pH, bicarbonate (913 $\mu eq\ l^{-1}$ at 10:05) and sulphate concentrations (474 $\mu eq\ l^{-1}$ at 14:05), as well as a decrease in the C-ratio.

As the discharge fell on day 161 and 162, the conductivity, bicarbonate and sulphate concentrations decreased, with the pH and C-ratio remaining steady. The SSC fell on day 161, but rose again on day 162. As the discharge rose on the evening of day 163, the conductivity, bicarbonate and sulphate concentrations remained low, suggesting the rising discharge was dilute quick flow. The $\varrho(CO_2)$ was the lowest measured during June, possibly due to post-mixing chemical reactions. On day 164, although the sulphate concentrations remained low, the conductivity rose slightly, along with a rise in the bicarbonate concentration. Figure 6.10 shows the SSC rose during days 163 and 164, but did not reach as high as on day 160, even though the discharge on days 163 and 164 was higher (the highest SSC on day 160 was 1216 mg l^{-1} at a discharge of 3.43 $m^3\ s^{-1}$, and on day 164 the SSC was 899 mg l^{-1} at a discharge of 4.86 $m^3\ s^{-1}$) - implying the availability of particles limited the SSC on day 164 (Clifford *et al.,* 1995).

The steady proglacial discharge on days 166 and 167 was associated with an increase in conductivity, bicarbonate and for day 166, sulphate concentration. On days 170 to 173 the gradually decreasing discharge (Figure 4.24) was associated with rising sulphate concentrations, very high bicarbonate concentrations on day 172 (peaking at 1187 $\mu eq\ l^{-1}$), a rising conductivity, generally low SSC and low C-ratio (Figure 6.10 and Figure 6.11). While discharge rose during days 174 and 175, the conductivity, sulphate and bicarbonate concentration decreased, and the C-ratio rose to its highest level since day 164 (0.88). The SSC rose too, but remained lower than earlier in June.

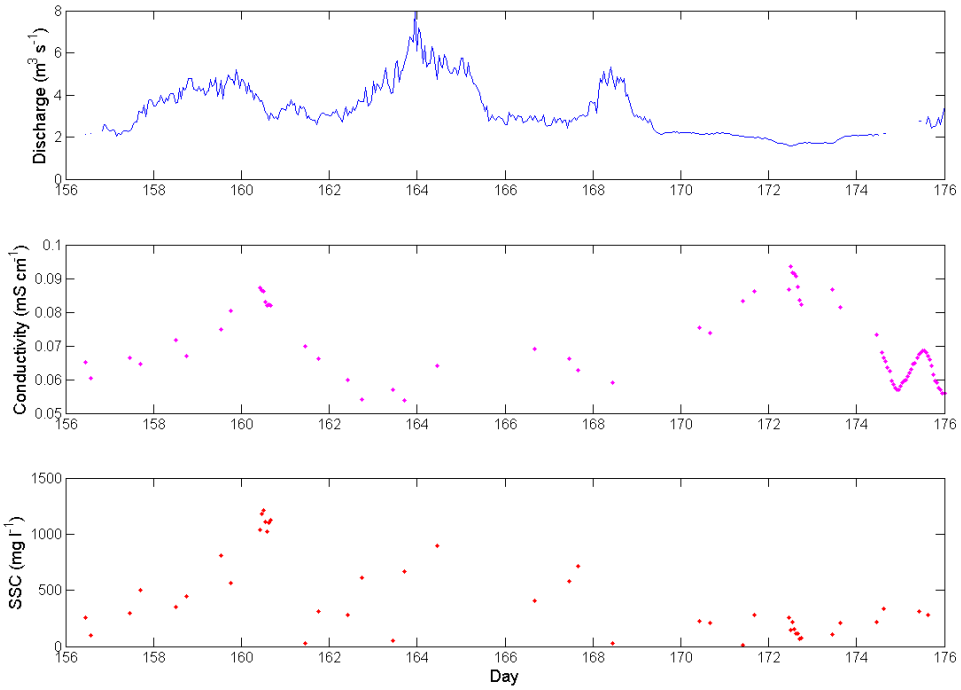

Figure 6.10 Fluctuations in discharge, conductivity and SSC at the proglacial stream, June 2010.

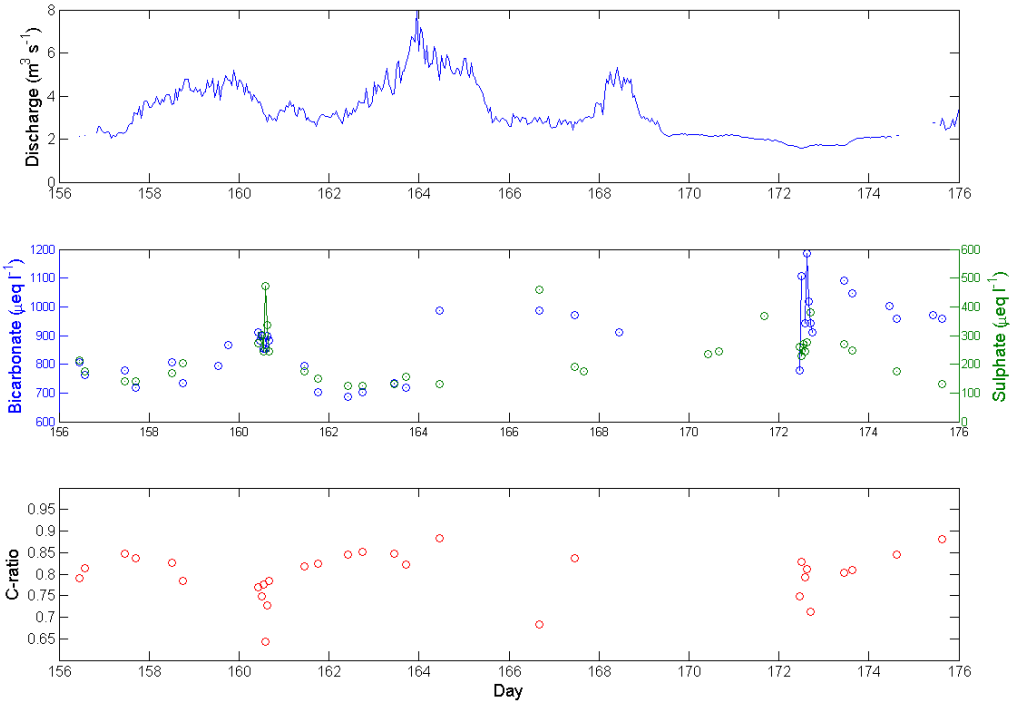

Figure 6.11 Fluctuations in discharge, sulphate and bicarbonate concentration, and C-ratio, June 2010.

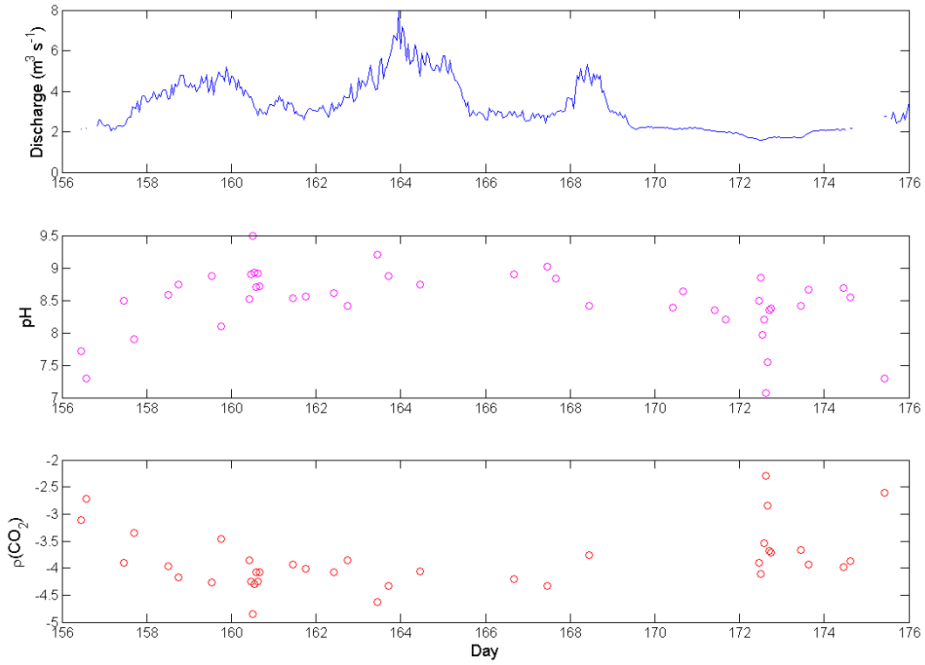

Figure 6.12 Fluctuations in discharge, pH and ϱ(CO2) at the proglacial stream, June 2010.

6.2.1.2 June 2011

The variations in the water chemistry parameters can be seen in Figure 6.13, Figure 6.14 and Figure 6.15. When particular values are referred to as being above or below average, the average is the average of that parameter over the season.

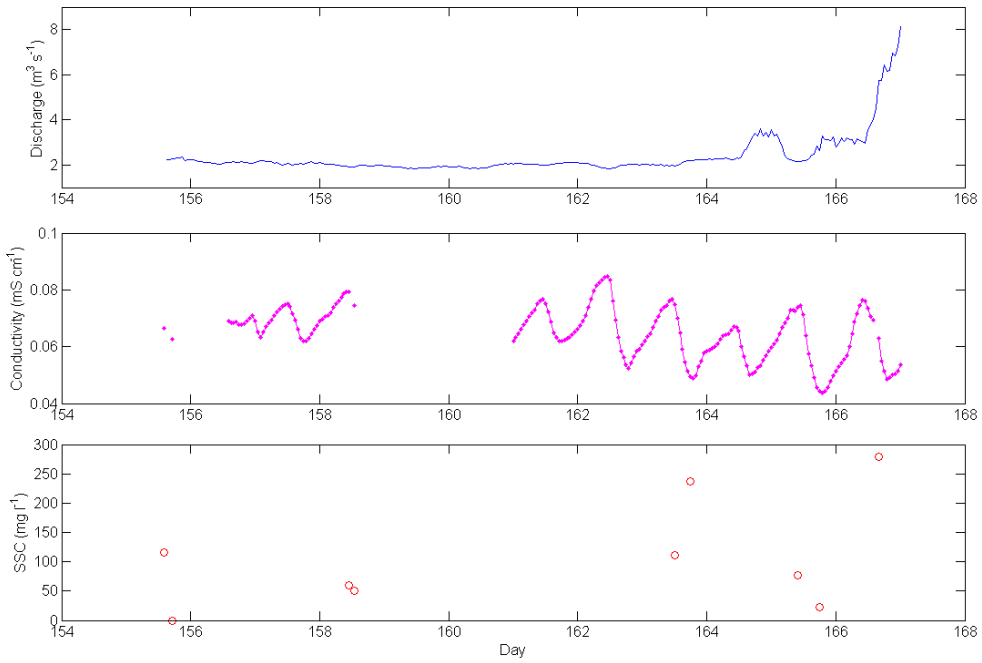

Figure 6.13 Discharge, conductivity and SSC fluctuations at the proglacial stream, June 2011.

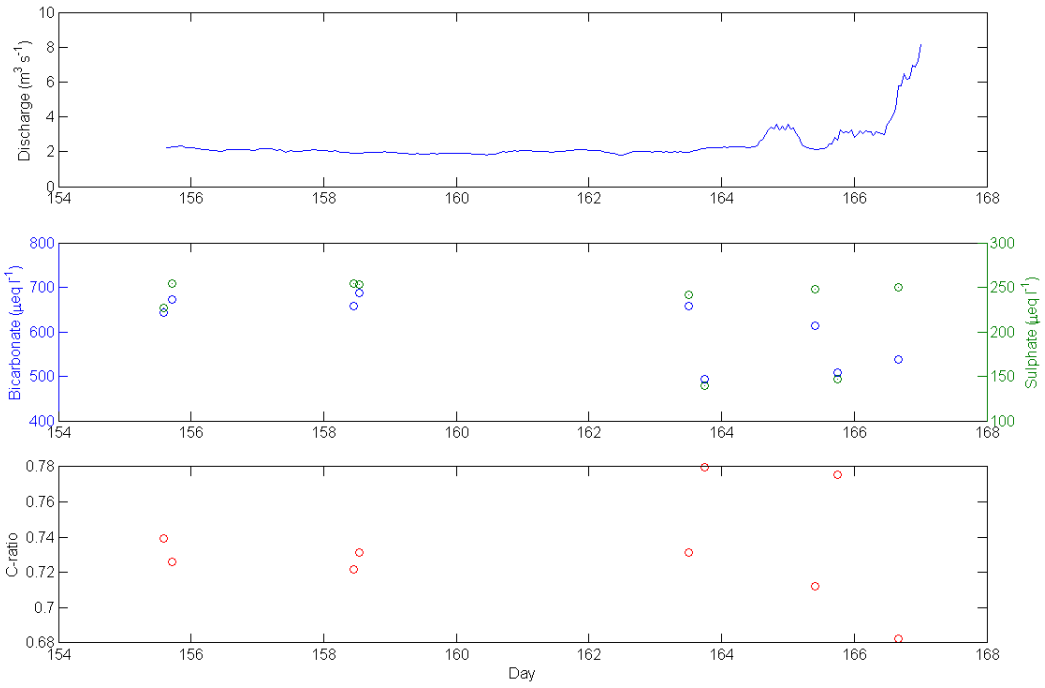

Figure 6.14 Discharge, bicarbonate and sulphate concentrations, and C-ratio at the proglacial stream in June 2011.

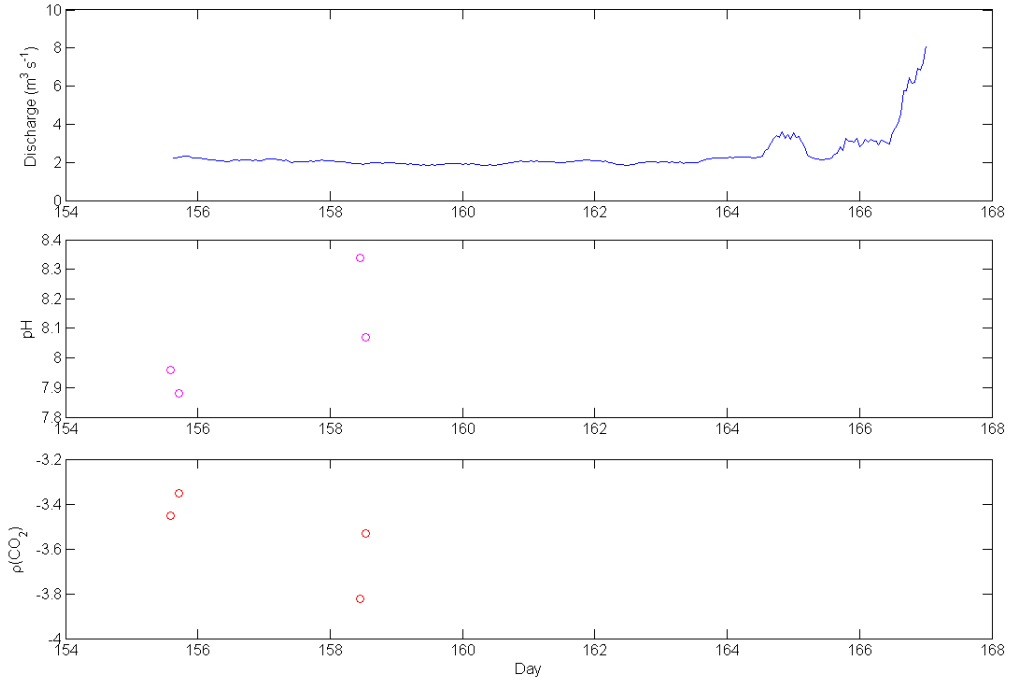

Figure 6.15 Discharge, pH and $\rho(CO_2)$ fluctuations at the proglacial stream, in June 2011.

At the beginning of June (days 155 and 158) discharges were low and had small diurnal fluctuations, with the small fluctuations and above average values of conductivity suggesting runoff was mainly delayed flow. The SSC was lower than average due to the low discharges. Sulphate concentrations were around average, but the bicarbonate concentrations were slightly higher than average, giving a C-ratio just below 0.75, indicative of delayed flow dominating runoff.

Later in June (days 163 to 166) the discharges increased (especially near the end of day 164 and day 166), with the hourly conductivity below average in the late afternoon. On day 163, when discharge was still low, the morning measurement was associated with high conductivity, lower than average SSC, high bicarbonate concentration, and around average sulphate, with a C-ratio below 0.75. By the afternoon, the conductivity was lower, SSC higher (due to higher discharge), and both the bicarbonate and sulphate concentrations were below average, with the C-ratio greater than 0.75. A similar change in water chemistry characteristics between morning and evening can be seen on day 165. On day 166, the discharge increased steeply, resulting in an above average SSC. Conductivity still fell as discharges rose which indicates that the runoff increase was mainly composed of dilute quickflow.

Looking at the relationships between variables, the only convincing and significant relationship of any of the variables with discharge was conductivity when lagged by 24 hours (Table 6.6). This suggests there was not a noticeable difference between the sources of water at different discharges, and was related to the subdued hydrograph. The fluctuations in conductivity were related to those of sulphate and bicarbonate though (Table 6.7).

Overall, the water chemistry parameters show a clear change from when runoff was mainly from delayed flow (days 155 and 158), to a period when the afternoon runoff was mainly quickflow. The latter period was associated with firstly warmer air temperatures, and by day 164, increasing discharges (Figure 4.24).

Table 6.6 Relationships between proglacial water chemistry variables and discharge at different lag times, in June and July/August 2011. The July/August discharge could not be lagged due to a lack of data.

June 2011						**July/Aug 2011**	
155-166	**Q**	**Q+6**	**Q+12**	**Q+18**	**Q+24**	**207-216**	**Q**
SSC	0.649	0.559	0.311	0.039	-0.016	**SSC**	0.398
	0.048	0.192	0.497	0.934	0.973		0.329
	33.9						
Cond.	-0.464	-0.320	-0.061	-0.314	**-0.599**	**Cond.**	**-0.716**
	0	0	0.401	0	**0**		**0**
	21.1	9.8		9.4	**35.5**		**49.6**
pH	-0.809	-	-	-	-	**pH**	**0.982**
	0.191	-	-	-	-		**0.003**
							95.2
Water temp.	-0.149	-0.212	0.073	0.215	-0.315	**Water temp.**	-0.325
	0.040	0.003	0.318	0.003	0.062		0.075
	1.7	4.0		4.1	1.3		7.5
SO_4^{2-}	0.093	0.224	0.343	-0.059	-0.378	**SO_4^{2-}**	**-0.802**
	0.812	0.629	0.451	0.9	0.403		**0.017**
							58.4
HCO_3^-	-0.455	-0.387	-0.192	-0.458	-0.632	**HCO_3^-**	-0.436
	0.219	0.391	0.680	0.302	0.128		0.280
C-ratio	-0.536	-0.647	-0.665	-0.275	0.066	**C-ratio**	**0.847**
	0.137	0.116	0.103	0.550	0.887		**0.008**
							67.0
ϱ(CO_2)	0.775	-	-	-	-	**ϱ(CO_2)**	**-0.987**
	0.225	-	-	-	-		**0.013**
							96.2

Table 6.7 Relationships between water chemistry variables in June 2011.

155-166	SSC	Cond.	pH	Water temp.	SO_4^{2-}	HCO_3^-	C-ratio
Cond.	-0.202 0.602						
pH	0.178 0.822	0.948 0.052					
Water temp.	-0.259 0.574	**0.392** **0** **14.9**	- -				
SO_4^{2-}	-0.198 0.610	**0.871** **0.002** **72.4**	0.343 0.657	0.597 0.157			
HCO_3^-	-0.568 0.111	**0.823** **0.006** **63.1**	-0.084 0.916	0.742 0.056	**0.804** **0.009** **59.6**		
C-ratio	-0.179 0.645	-0.648 0.059	-0.559 0.441	-0.332 0.467	- - -	- - -	
$\varrho(CO_2)$	- -	-0.933 0.067	- -	- -	-0.293 0.707	- - -	0.533 0.467

6.2.1.3 July/August 2010

Water chemistry variations in July and August 2010 can be seen in Figure 6.16, Figure 6.17 and Figure 6.18. During days 209 and 210 the discharge rose gradually and was associated with a subdued and below average conductivity cycle, with a relatively high C-ratio (0.88 on day 209), suggesting dilute meltwater was the main runoff component. The cold weather on days 210 and 211 caused discharge to fall, and this was associated with a rise in conductivity and decrease in the C-ratio to levels corresponding with delayed flow (0.73 in the morning of day 211).

Day 214 was characterised by a sharp rise in discharge which peaked at the end of the day. The SSC was above average, although there was a trend of falling SSC until a value of 378 mgl^{-1} at 14:50, before it rose to 859 mgl^{-1} at 16:50 – the highest SSC measured during this field trip. Although variable, the C-ratio increased over the day due to the falling sulphate concentrations, implying the proportion of dilute meltwater had increased. Notably, the pH was unusually high, reaching 9.16 at 13:50. This was associated with low values of $\varrho(CO_2)$ (minimum -4.60 at 13:50), the lowest since day 160.

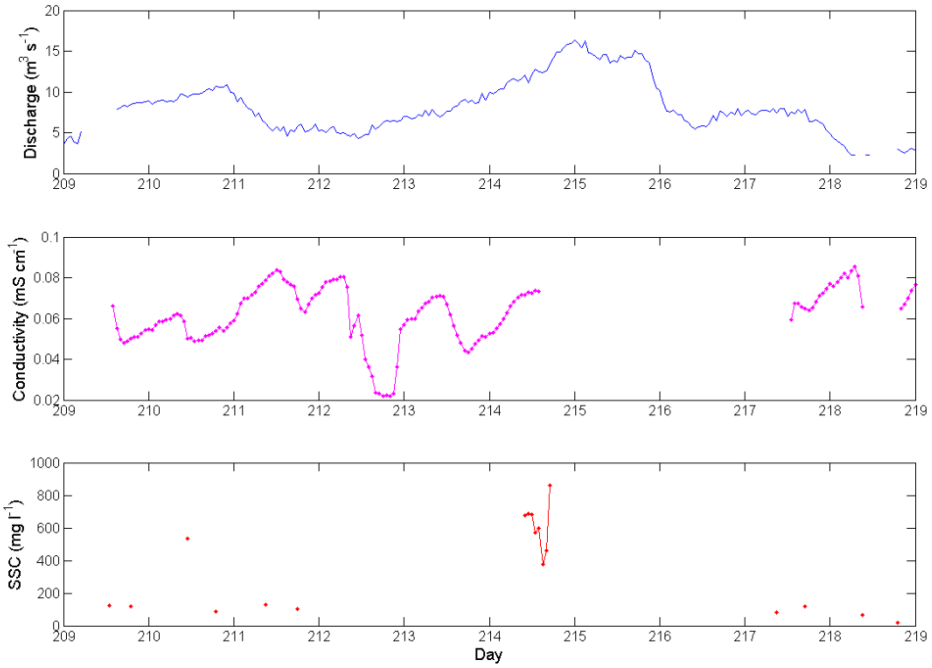

Figure 6.16 Discharge, conductivity and SSC fluctuations at the proglacial stream in July/August 2010.

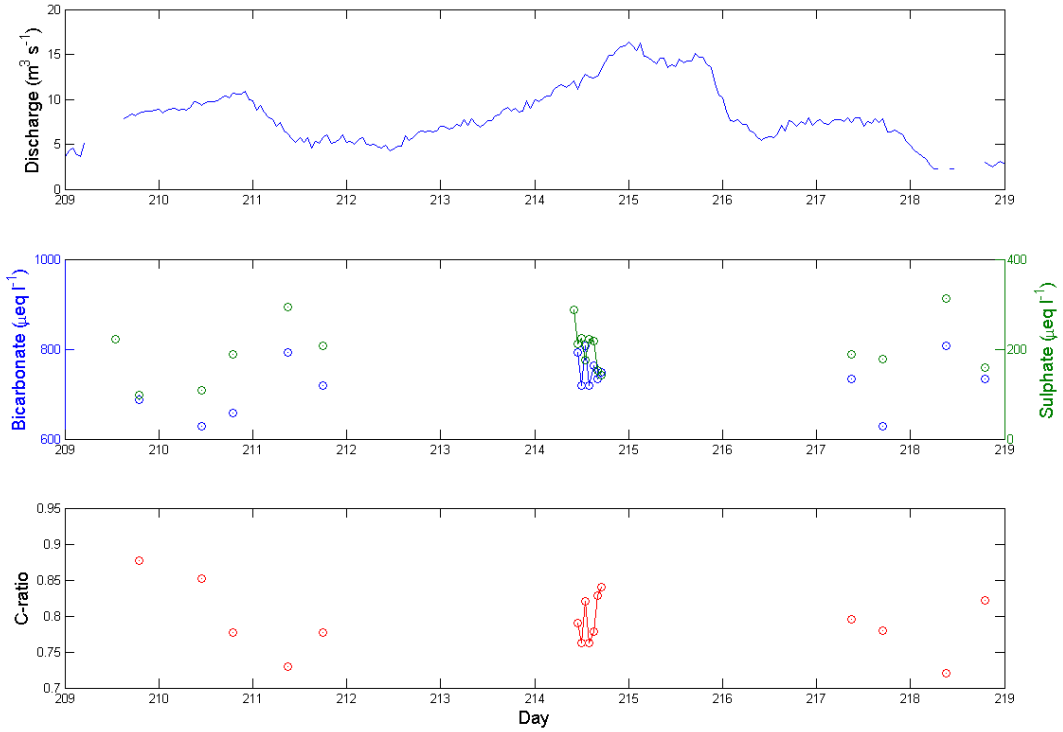

Figure 6.17 Discharge, bicarbonate and sulphate concentration and C-ratio fluctuations at the proglacial stream in July/August 2010.

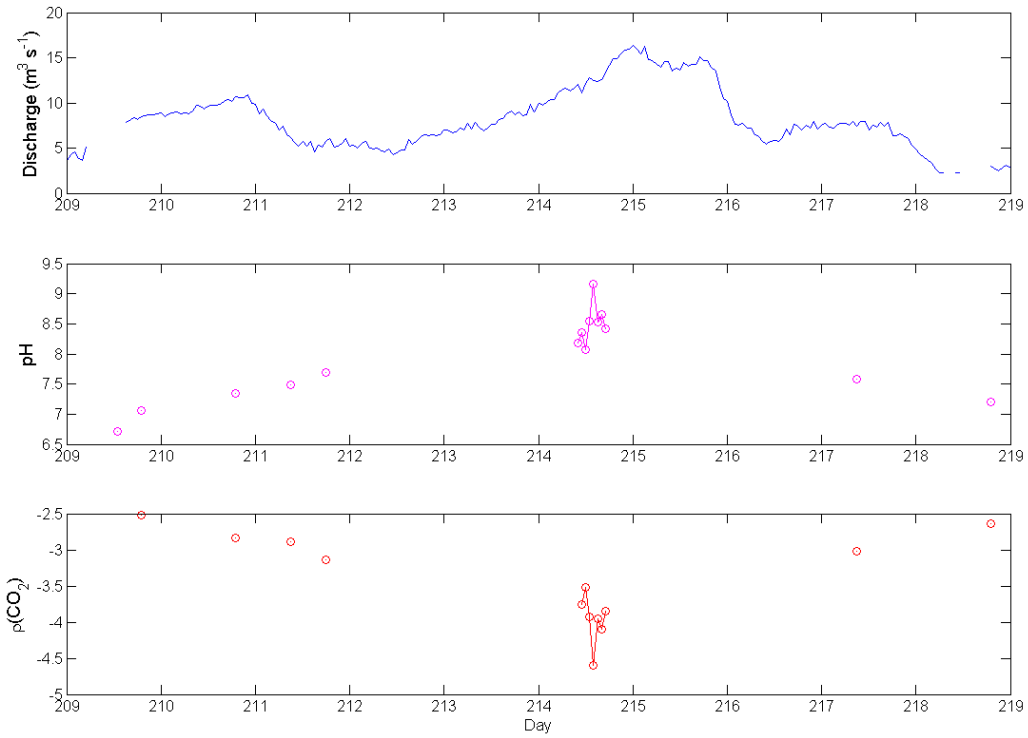

Figure 6.18 Discharge, pH and $\varrho(CO_2)$ fluctuations at the proglacial stream in July/August 2010.

Discharge fell from day 215 onwards and this was associated with a rising conductivity, low SSC, below average pH and a falling C-ratio (caused by an above average sulphate concentration) on days 217 and 218. Since the C-ratio fell to 0.72 in the morning of day 218 this suggests the dilute meltwater which composed most of the runoff on day 214 had been replaced by delayed flow.

The relationships between the water chemistry variables and discharge will now be compared (Table 6.8). The SSC and pH had a positive relationship with discharge with no lag, and the $\varrho(CO_2)$ had a negative relationship with discharge with no lag. The water temperature did have a significant relationship with discharge but it was negative and had a 12 hour lag. There were no significant relationships between discharge and either conductivity, sulphate concentration, bicarbonate concentration, or the C-ratio. The best relationship with discharge and hourly conductivity was in early August and was negative and with no lag, and for hourly water temperature the best relationship was negative with a 6 hour lag (Table 6.4 and Table 6.5). The significant relationships between variables were between SSC and pH and $\varrho(CO_2)$; between conductivity and sulphate, bicarbonate and C-ratio; and between sulphate and bicarbonate (Table 6.9). This implies that the SSC may have been partly driving the pH and $\varrho(CO_2)$ changes and these were influenced by changes in the magnitude of discharge. However, conductivity, sulphate and bicarbonate did not vary with discharge, but did vary together.

Table 6.8 Relationships between proglacial water chemistry variables and discharge at different lag times, in July/August and September 2010.

July/Aug						**Sep**					
209-218	**Q**	**Q+6**	**Q+12**	**Q+18**	**Q+24**	**247-253**	**Q**	**Q+6**	**Q+12**	**Q+18**	**Q+24**
SSC	**0.811**	0.735	0.677	0.472	0.042	**SSC**	0.564	0.864	**0.985**	0.693	0.555
	0	0.002	0.003	0.055	0.882		0.029	0.006	**0.002**	0.307	0.332
	63.3	50.5	42.3				26.5	70.5	**95.9**		
Cond.	0.068	0.203	0.452	0.672	0	**Cond.**	0.388	0.945	0.962	0.757	0.89
	0.861	0.63	0.261	0.047	1		0.191	0.004	0.038	0.243	0.043
				37.4				86.7	88.9		72.2
pH	**0.769**	0.725	0.726	0.587	0.107	**pH**	-0.288	-0.488	-0.292	-0.23	-0.832
	0.001	0.008	0.003	0.027	0.728		0.299	0.22	0.633	0.77	0.081
	55.7	47.9	48.7	29							
Water temp.	-0.576	-0.176	**-0.595**	-0.337	0.162	**Water temp.**	-0.42	-0.027	-0.401	0.558	0.563
	0.031	0.578	**0.025**	0.239	0.596		0.119	0.95	0.503	0.442	0.323
	27.6		**30**								
SO_4^{2-}	0.048	-0.353	0.029	0.403	0.013	**SO_4^{2-}**	**-0.652**	-0.747	-0.525	0.326	-0.319
	0.86	0.197	0.912	0.109	0.963		**0.016**	0.053	0.364	0.674	0.601
							37.3				
HCO_3^-	0.174	0.033	0.094	0.282	-0.03	**HCO_3^-**	-0.1	0.477	0.311	0.339	-0.437
	0.534	0.91	0.738	0.29	0.918		0.735	0.233	0.611	0.661	0.462
C-ratio	0.076	0.455	0.005	-0.401	-0.138	**C-ratio**	0.459	**0.841**	0.7	-0.353	0.175
	0.787	0.102	0.985	0.124	0.638		0.114	**0.018**	0.185	0.647	0.779
								64.9			
ϱ(CO_2)	**-0.778**	-0.725	-0.627	-0.579	-0.126	**ϱ(CO_2)**	0.241	0.514	0.322	0.259	0.835
	0.002	0.012	0.029	0.038	0.697		0.407	0.193	0.598	0.741	0.079
	56.9	47.3	33.3	27.5							

Table 6.9 Relationships between water chemistry variables during July/August 2010.

209-218	SSC	Cond	pH	Water temp.	SO_4^{2-}	HCO_3^-	C-ratio
Cond.	0.305 0.426						
pH	**0.773** **0.001** **56.7**	0.652 0.08					
Water temp.	-0.338 0.217	0.199 0.637	-0.529 0.043 22.4				
SO_4^{2-}	-0.073 0.774	**0.842** **0.004** **66.7**	0.105 0.709	-0.201 0.474			
HCO_3^-	0.168 0.535	**0.871** **0.005** **71.8**	0.388 0.19	0.32 0.287	**0.58** **0.019** **28.9**		
C-ratio	0.232 0.388	**-0.758** **0.029** **50.3**	-0.142 0.644	0.22 0.47	- -	- -	
ϱ(CO_2)	**-0.787** **0.001** **58.4**	-0.618 0.139	- -	0.408 0.166	-0.163 0.594	-0.355 0.234	0.138 0.654

6.2.1.4 July/August 2011

The water chemistry variations in July and August 2011 can be seen in Figure 6.19, Figure 6.20 and Figure 6.21. From day 207 to 211 the conductivity, bicarbonate and sulphate concentrations were higher than average during the whole day and the C-ratio remained below 0.75. This indicates the majority of runoff was from delayed flow. The discharge was very low over this period (around 2 m^3 s^{-1}) and was accompanied by a low SSC. The pH on day 207 was very low for Miage Glacier and this led to a correspondingly high ϱ(CO_2) of -2.13, this situation of a high ϱ(CO_2) is another typical characteristic of delayed flow waters (Tranter *et al.,* 1993b).

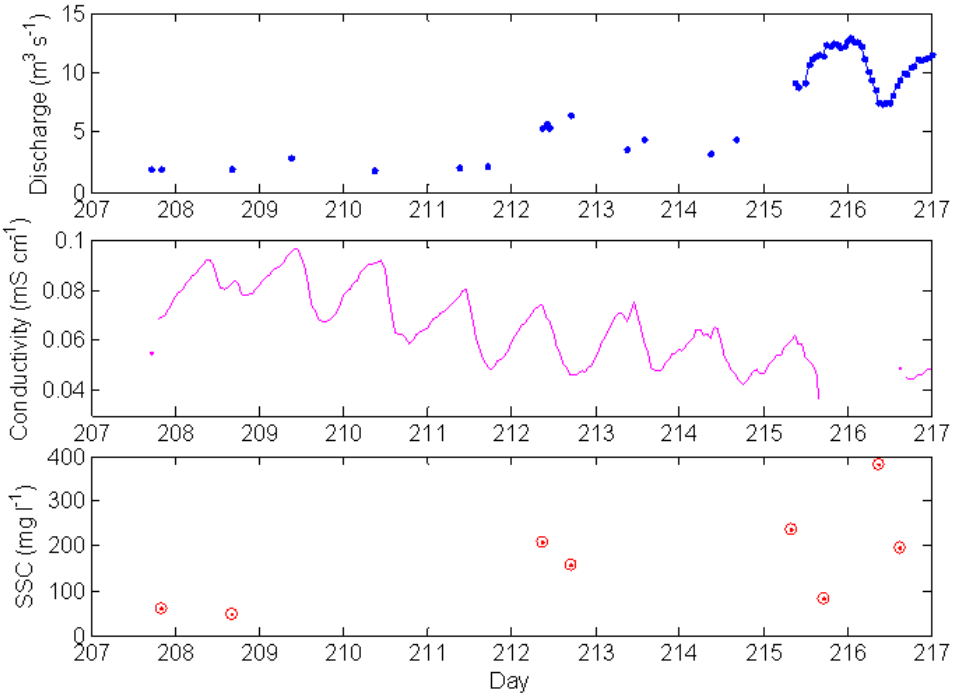

Figure 6.19 Fluctuations in discharge, conductivity and SSC at the proglacial stream in July/August 2011.

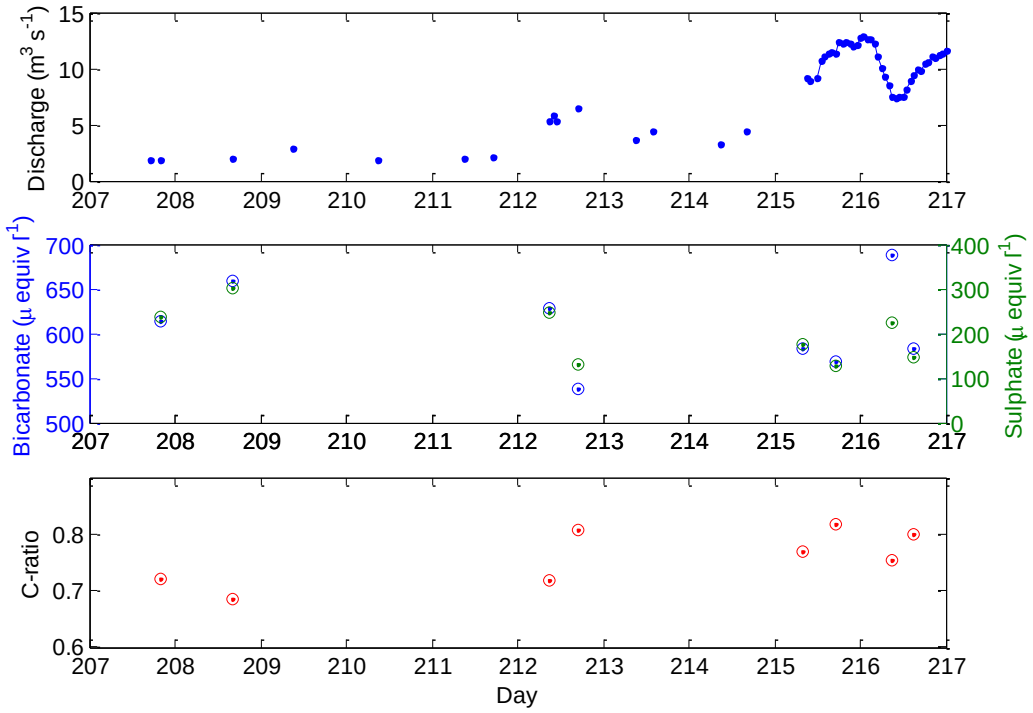

Figure 6.20 Fluctuations in discharge, bicarbonate and sulphate concentrations and C-ratio at the proglacial stream, July/August 2011.

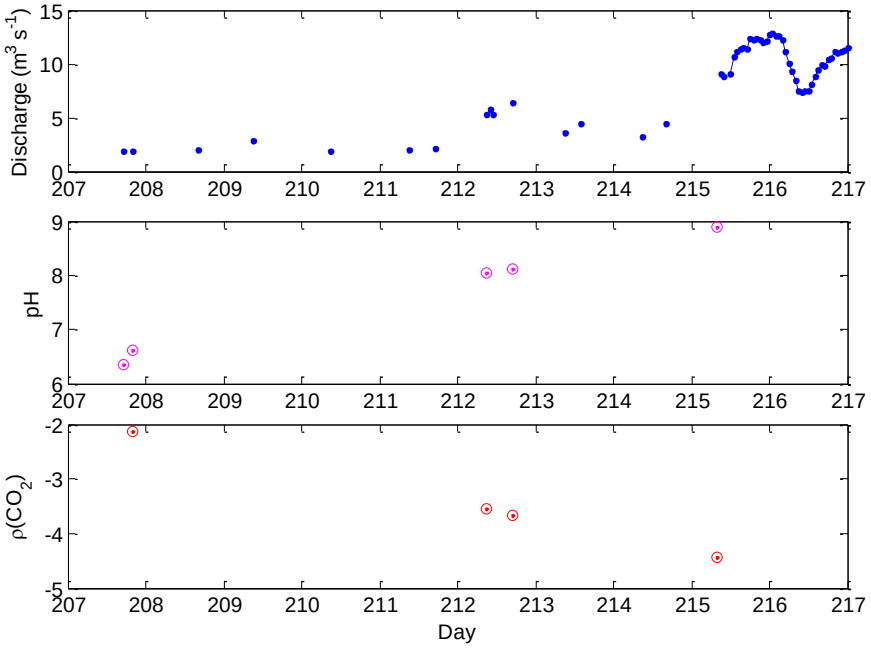

Figure 6.21 Fluctuations of discharge, pH and $\rho(CO_2)$ at the proglacial stream, July/August 2011.

The afternoon measurement of day 212 had below average conductivity, sulphate and bicarbonate concentrations, and a high C-ratio of 0.81, indicating an increase in dilute meltwater. The much higher discharge on days 215 and 216 (average of 11.3 m^3 s^{-1} and 10.1 m^3 s^{-1}) resulted in the conductivity remaining below average and the C-ratio remaining above 0.75 even in the morning of both days. This indicates dilute quickflow dominated throughout the day. The day 215 morning pH was very high (8.89), and was associated with a very low $\varrho(CO_2)$. The distinct drop in afternoon SSC suggests it was supply limited, and so the afternoon runoff had little access to sediment.

Using the July/August data there were strong relationships between discharge and conductivity, pH, sulphate concentration, C-ratio and $\varrho(CO_2)$ (Table 6.6). This confirms the change from the delayed flow signature when discharges were low (and so low pH and C-ratio, high conductivity, sulphate and $\varrho(CO_2)$) during days 208-211; to when dilute flow dominated during high discharges (and so pH and C-ratio was high, and conductivity, sulphate and $\varrho(CO_2)$ was low) from day 212 onwards. Similar to the results in July/August 2010, there were significant relationships between the SSC and pH and $\varrho(CO_2)$ (Table 6.9), this means that under high SSC conditions the pH is high ($\varrho(CO_2)$ low), indicating an increase in weathering reactions (the concentration of hydrogen ions had been depleted). This indicates high SSC at high discharges leads to post-mixing chemical reactions (Tranter *et al.,* 1993b).

Table 6.10 Relationships between water chemistry variables in July/August 2011.

207-216	SSC	Cond.	pH	Water temp.	SO_4^{2-}	HCO_3^-	C-ratio
Cond.	-0.529 0.281						
pH	**0.955** **0.045** **86.8**	-0.099 0.874					
Water temp.	-0.030 0.955	0.119 0.095	-0.110 0.890				
SO_4^{2-}	-0.106 0.803	**0.993** **0** **98.3**	-0.507 0.494	-0.364 0.477			
HCO_3^-	0.337 0.414	**0.954** **0.003** **88.7**	-0.373 0.627	-0.233 0.658	**0.821** **0.012** **62.0**		
C-ratio	0.175 0.678	**-0.994** **0** **98.6**	0.519 0.481	0.448 0.373	- -	- -	
ϱ(CO_2)	**-0.947** **0.053** **84.5**	0.409 0.591	- -	0.090 0.910	0.532 0.468	- -	-0.543 0.457

6.2.1.5 September 2010

The September 2010 water chemistry data is given in Figure 6.22, Figure 6.23 and Figure 6.24. There was a prolonged period of rainfall during day 250 and the morning of day 251 totalling 21 mm. The conductivity decreased on day 250 from around 0.06 mS cm^{-1} to 0.03 mS cm^{-1} around 16:00, after which time it remained low until 12:00 on day 251, when it rose to 0.06 mS cm^{-1} again. This may indicate when the runoff from rainfall reached the proglacial stream (Figure 6.22), and acted to dilute the ion concentration of the rest of the runoff. The first two measurements of day 251 were within this period of low conductivity, which gave sulphate concentrations of 197 μeq l^{-1} and 209 μeql^{-1}, both of which were below average. The C-ratio of the measurement at 10:25 was particularly low (Figure 6.23), because of an unusually low bicarbonate concentration. During days 252 and 253 in 2010, the low discharge (around 1.7 m^3 s^{-1}), SSC, C-ratio (average 0.75) and high sulphate concentrations (average 230 μeql^{-1}) are indicative of baseflow conditions.

Table 6.11 Relationships between water chemistry variables in September 2010.

247-253	SSC	Cond.	pH	Water temp.	SO_4^{2-}	HCO_3^-	C-ratio
Cond.	-0.039 0.9						
pH	0.246 0.377	**-0.778** **0.002** **56.9**					
Water temp.	-0.343 0.21	0.469 0.1	-0.403 0.136				
SO_4^{2-}	-0.522 0.067	-0.3 0.344	0.262 0.386	0.298 0.322			
HCO_3^-	0.044 0.881	0.325 0.303	-0.136 0.643	0.633 0.015 35.1	0.359 0.228		
C-ratio	0.331 0.27	**0.608** **0.036** **30.7**	-0.354 0.236	0.181 0.554	- -	- -	
ϱ(CO_2)	-0.237 0.414	**0.805** **0.002** **61.3**	- -	0.412 0.143	-0.242 0.426	0.203 0.487	0.377 0.205

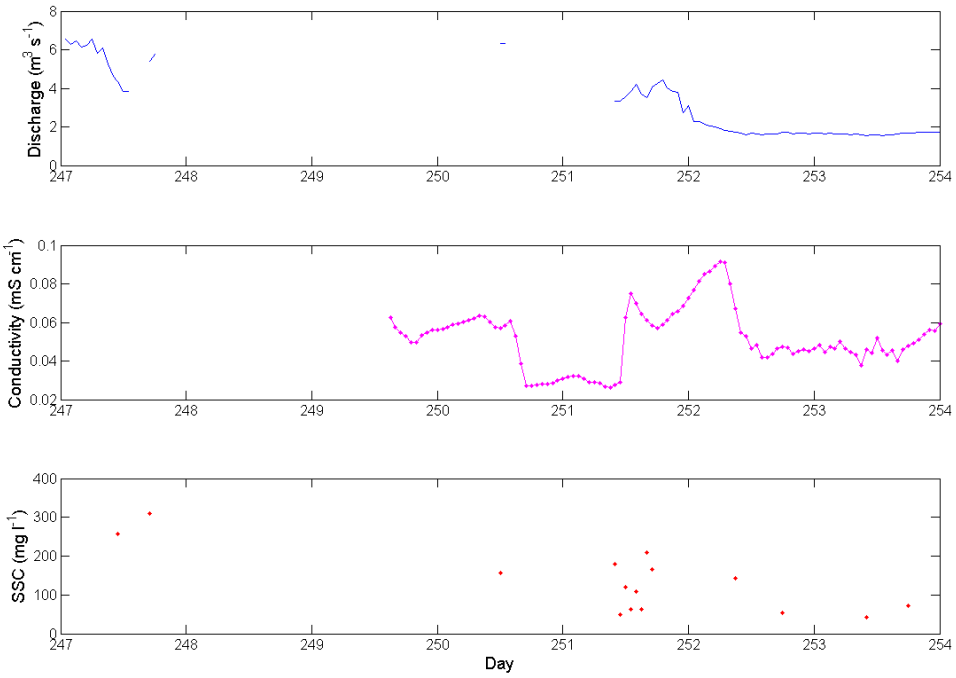

Figure 6.22 Fluctuations of discharge, conductivity and SSC at the proglacial stream, September 2010.

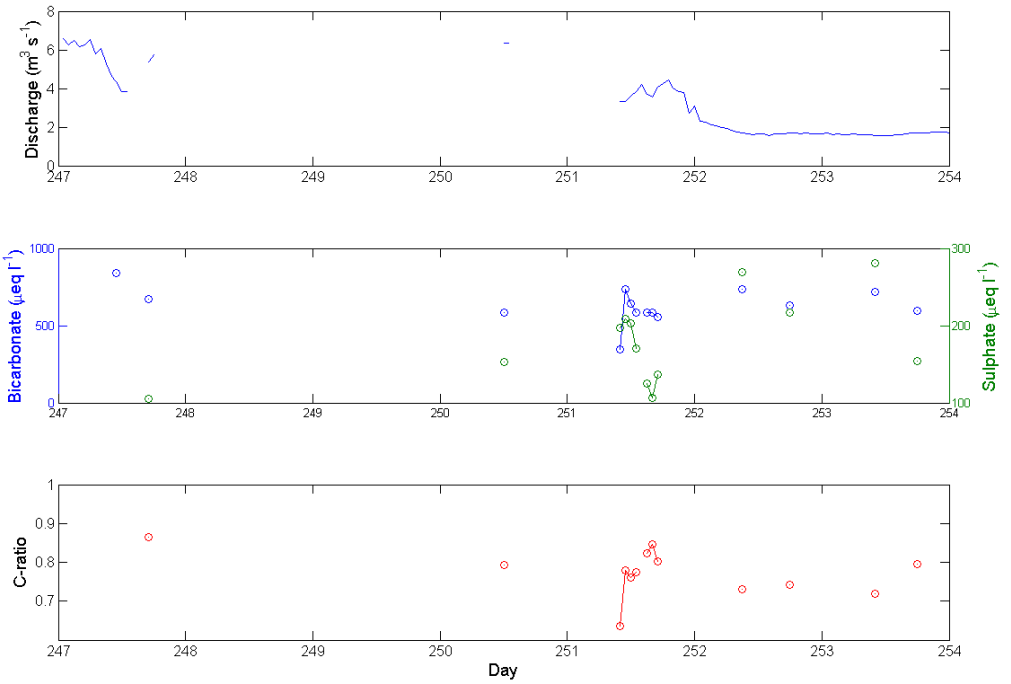

Figure 6.23 Fluctuations of discharge, bicarbonate and sulphate concentration, and C-ratio at the proglacial stream, September 2010.

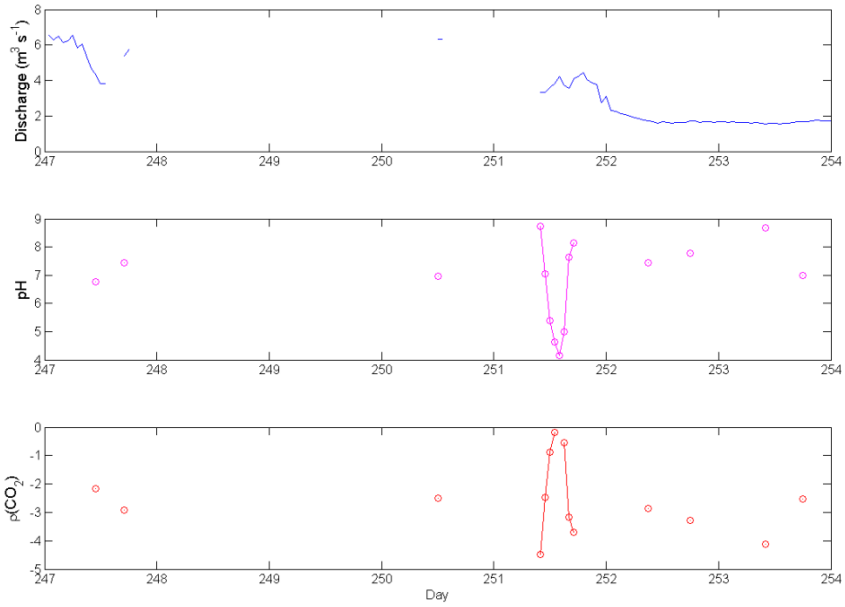

Figure 6.24 Fluctuations in discharge, pH and $\rho(CO_2)$ at the proglacial stream, in September 2010.

There were no significant relationships between discharge and logged conductivity or water temperature in September (Table 6.4 and Table 6.5), and the only direct relationship with discharge was with sulphate (Table 6.8). Conductivity did have significant relationships with pH, C-ratio and $\rho(CO_2)$ (Table 6.11), but unlike in July/August did not have relationships between SSC, pH, $\rho(CO_2)$ and conductivity, sulphate and bicarbonate.

This may be due to there being less of a change in the magnitude of discharge over the period compared to July/August, and the influence of a large rainfall input.

6.2.1.6 September 2011

In September 2011 (Figure 6.25, Figure 6.26 and Figure 6.27), there was a clear negative relationship between discharge and conductivity, but it is the troughs of discharge and their relationship with peaks of conductivity that are most clear. The discharge troughs signify a greater proportion of the runoff was baseflow, and this was confirmed by the above average sulphate and bicarbonate concentrations and low C-ratio (0.63, the lowest for the year) measured in the morning of day 258. The decrease in conductivity, sulphate and bicarbonate concentrations, and increase in C-ratio in the afternoon shows there must have been an increase in dilute quickflow.

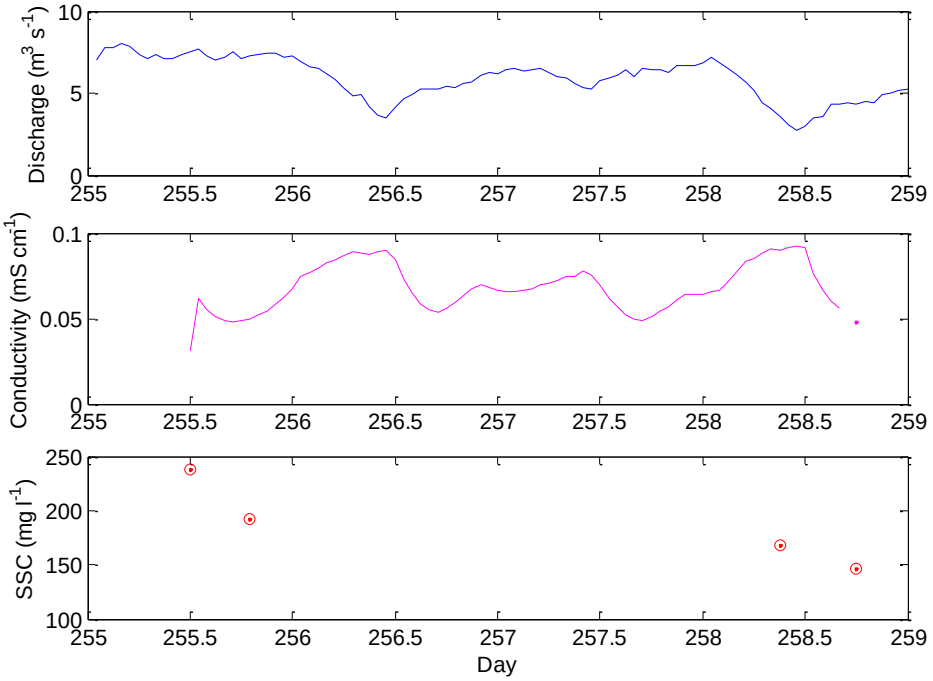

Figure 6.25 Fluctuations of discharge, conductivity and SSC at the proglacial stream, September 2011.

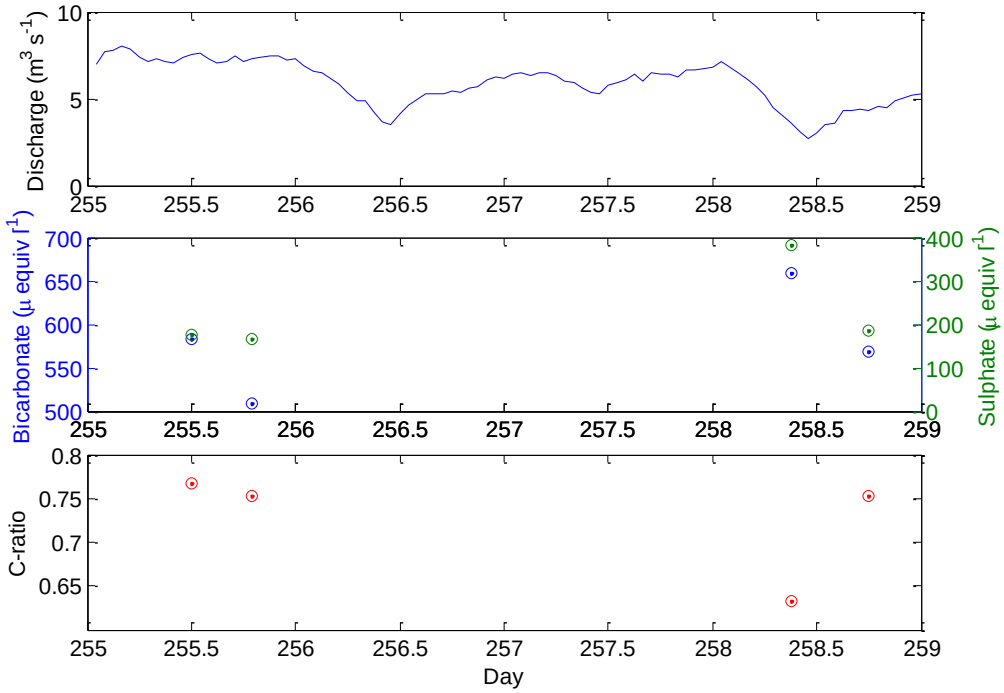

Figure 6.26 Fluctuations of discharge, bicarbonate and sulphate concentration, and C-ratio at the proglacial stream, September 2011.

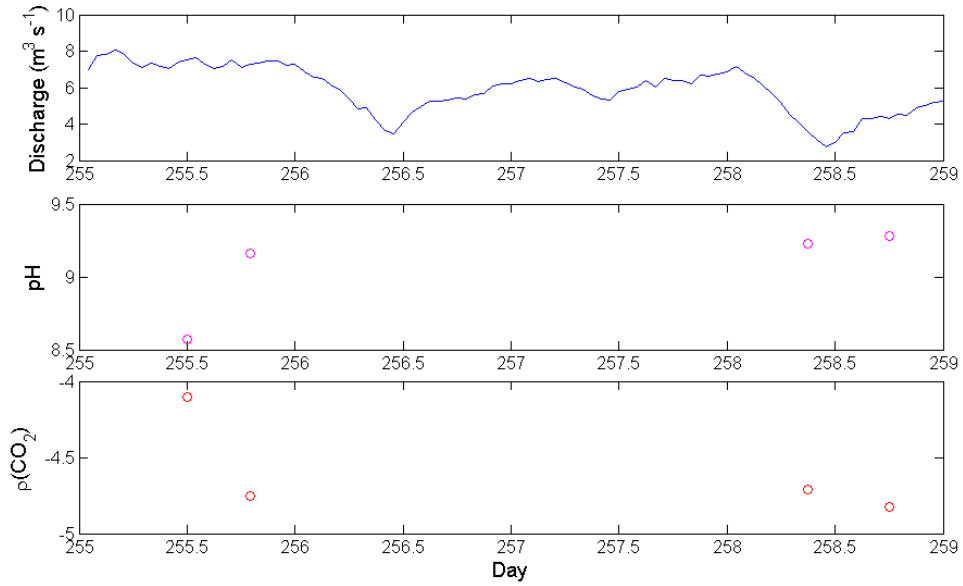

Figure 6.27 Fluctuations in discharge, pH and $\rho(CO_2)$ at the proglacial stream, in September 2011.

6.2.1.7 Seasonal overview

Generally the quantity of sulphate ions measured at the proglacial stream was high compared to other glaciers (Table 6.13), with values most similar to the debris-covered Dokriani Glacier outside of the monsoon season. The highest values of sulphate on Miage Glacier were either when there was a pulse of ion and sediment rich water (on day 160 in 2010), or when discharges were low during cold weather conditions (on days 171, 218 and

253 in 2010, and on days 208 and 258 in 2011). Although the highest sulphate concentration measured was on day 160 in 2010, the delayed flow sulphate concentrations were still high even in mid-summer. The variation between different times of year was not particularly great with the difference between mean June, and mean July/August concentrations being only 5 μeq l^{-1} in 2010, and 25 μeq l^{-1} in 2011 (Table 6.12). This was contrary to Haut Glacier d'Arolla and Austre Brøggerbreen where June sulphate concentrations were at least twice those later in the season (Tranter *et al.,* 1996). The relationship between sulphate and discharge was generally weak, so in 2010 the only direct relationship with discharge was in September when the sulphate concentration increased as discharge decreased (p-value 0.016, R^2 37.3), although in 2011 this negative relationship was also found in June (p-value 0.009, R^2 27.4), and more strongly in July and August (p-value 0.017, R^2 58.4).

Although there was evidence for some of the bicarbonate ions on Miage Glacier being generated supraglacially, even if this is take into account then the mean and range of values was still high (Table 6.13). The values were most similar to the debris-covered Batura Glacier and Dokriani Glacier during the monsoon season, and were slightly above the values for Grimsvötn, and below those from the icing at Scott Turnbreen. As for sulphate, bicarbonate concentrations tended to be highest either in June 2010 when there was a pulse of sediment and ion rich water, or during recessional flow, for instance during the morning of day 173 in 2010 when the bicarbonate concentration was 1092 μeq l^{-1}, corresponding with particularly low discharges (Figure 6.11). The bicarbonate concentration decreased over the season in 2010, but this was not mirrored in 2011 (Table 6.12). Unlike sulphate, the bicarbonate concentration never had a significant and convincing relationship with discharge in 2010 or 2011. There were strong relationships between bicarbonate and sulphate both in 2010 (using all samples p-value 0.000, R^2 19.2) and in 2011 (using all samples p-value 0.000 R^2 47.9), which suggests the temporal variations in the concentrations of both ions were determined by similar mechanisms. High sulphate and bicarbonate concentrations were found during low flow periods throughout the year, although the magnitude of discharge was not particularly low. The high sulphate concentrations measured on days 171, 218 and 253 in 2010 were associated with discharges of 1.97 m^3 s^{-1}, 2.26 m^3 s^{-1} and 1.56 m^3 s^{-1}, but the mean daily discharge during 2010 was only 5.37 m^3 s^{-1}.

Table 6.12 Average values of water chemistry parameters during each of the field visits in 2010 and 2011. All values from the northern lobe proglacial stream.

Parameter	Q ($m^3 s^{-1}$)	Cond. ($mS cm^{-1}$)	SSC ($mg l^{-1}$)	pH	SO_4^{2-} ($\mu eq l^{-1}$)	HCO_3^- ($\mu eq l^{-1}$)	C-ratio	$\varrho(CO_2)$
	2010							
June	3.1	0.071	381	8.5	204	856	0.82	-3.8
July/Aug	7.8	0.062	242	7.5	199	714	0.80	-3.0
Sep	3.5	0.048	153	7.7	189	630	0.76	-3.2
	2011							
June	2.7	0.069	106	8.1	224	608	0.73	-3.5
July/Aug	6.2	0.047	172	7.6	199	608	0.76	-3.4
Sep	5.5	0.052	186	9.1	228	580	0.73	-4.6

Table 6.13 Comparison of sulphate and bicarbonate ion concentrations between different glaciers. All values are in $\mu eq\ l^{-1}$, with the mean in brackets and the range giving the maximum and minimum values recorded. * represents studies cited in Brown (2002).

Glacier	Source	Non-snowpack SO_4^{2-}	HCO_3^-
Miage Glacier, Italy in 2010	This study.	(202) 97-473	(777) 344-1186
Miage Glacier, Italy in 2011	This study.	(215) 128-323	(603) 494-688
Haut Glacier d'Arolla, Switzerland	Brown *et al.* (1996)*	30-240	180-460
Austre Brøggerbreen, Svalbard	Tranter *et al.* (1996)	10-140	145-520
Scott Turnbreen, Svalbard	Hodgkins *et al.* (1998)	(130) 96-200	(170) 110-260
Scott Turnbreen, Svalbard (icing)	Hodgkins *et al.* (1998)	(830) 0-3200	(1800) 350-4600
Dokriani Glacier, India (pre monsoon)	Hasnain and Thayyen (1999a)	160-418	159-397
Dokriani Glacier, India (monsoon)	Hasnain and Thayyen (1999a)	85-1140	128-1053
Dokriani Glacier, India (post monsoon)	Hasnain and Thayyen (1999a)	137-431	168-384
Nigardsbreen, Norway	Brown (2002)	7-40	1.4-8.5
Tsanfleuron, Switzerland	Fairchild *et al.* (1994)*	118	627
Fjallsjökull, Iceland	Raiswell and Thomas (1984)*	26-66	190-300
Chamberlain, USA	Rainwater and Guy (1961)*	29-310	150-200
Engabreen, Norway	Ruffles (1999)*	0-142	51-675
Grimsvötn, Iceland	Steinpórsson and Óskarsson (1983)*	132	573
Batura Glacier, Pakistan	Hodson *et al.* (2002)	160	730
Bench Glacier, Alaska	Anderson *et al.* (2000)*	262	427
Gangotri Glacier, India	Kumar *et al.* (2009)	(673) 333-1186	(1138) 17-4130

6.2.2 Interpretation and discussion

The water chemistry variations will now be considered in terms of what they reveal about the conditions through which water was travelling. Certain periods were characterised by proglacial runoff being composed of mainly delayed flow (which has a longer travel time, and greater sediment contact) or quickflow (which has travelled quickly through the glacier, usually with less sediment contact). The reasons for these short term variations will be discussed first. Then the average chemical characteristics of the proglacial runoff on Miage Glacier will be discussed to identify what this reveals about the overall drainage structure and its development.

6.2.2.1 Short term variations

In general, periods when discharges were high were associated with low conductivity due to the dilution of the supply of ions by an increasing quantity of dilute meltwater. The sulphate ion concentration was also lower because the contact with sediment at the bed had been lessened (Tranter *et al.,* 1993b), and this leads to a C-ratio above 0.75 – indicative of periods of quickflow (Brown *et al.,* 1996). High discharges were also associated with a high SSC since it usually increases with discharge due to the increased ability for faster water to transport sediment particles (Lefrançois *et al.,* 2007). The pH also tends to be high ($\varrho(CO_2)$ low) which is a signature of post-mixing chemical reactions between the dilute water and the increased suspended sediment, since the hydrogen ions required to allow acid hydrolysis are used at a greater rate than they can be replaced by the dissociation of dissolved CO_2 (which is limited in subglacial environments) (Tranter *et al.,* 1993b). All of these characteristics indicate that most water travelled in a channelized system, where although the possibility of reactions with the sediment at the bed is lessened (due to fast water transit times), post-mixing chemical reactions can occur in-stream with the suspended sediment.

These conditions were seen on days 163 and 214 in 2010 (sections 6.2.1.1 and 6.2.1.3) and days 215 and 216 in 2011 (section 6.2.1.4), although afternoon measurements during periods of moderately high discharges could also show these characteristics. These days were associated with high melt or rainfall inputs (see Figure 4.24) which resulted in the rising discharge. Days 163 and 214 in 2010 were also associated with an increase in glacier velocities, especially on the upper glacier (see sections 8.1.1 and 8.1.3). This would imply some of the water had travelled within the distributed system (which would increase water travel times and the contact with sediment), however the large water inputs during this time must have meant that the majority of water was still transported within a channelized system.

Periods when discharges were very low and stable were associated with high conductivity, bicarbonate and sulphate concentrations, and a low C-ratio. These conditions suggest the water has had a greater basal residence time, which increases the sediment contact time and allows the production of sulphate (Tranter *et al.,* 1993b). This then decreases the C-ratio to below 0.75 (Brown *et al.,* 1996). Despite an increased sediment contact, the SSC of the stream water is lessened due to the lower discharge (Lefrançois *et al.,* 2007). The pH tends to be low ($\varrho(CO_2)$ high) – which occurs if coupled sulphide oxidation and carbonate dissolution reactions take place, as this produces bicarbonate and hydrogen ions. Sulphide oxidation reactions are thought limited to a distributed system

where the highly reactive sulphide minerals are available within freshly comminuted rock flour (Tranter *et al.,* 1993b).

These conditions were observed on days 170 to 173, and 252 and 253 in 2010 (sections 6.2.1.1 and 6.2.1.5), and on days 155, 158, 207 and 208 in 2011 (sections 6.2.1.2 and 6.2.1.4). On these days low discharges were related to periods of low melt input and no or small quantities of rainfall (Figure 4.24). The characteristics of the water chemistry parameters suggest a larger proportion of the water had spent time in the distributed system where contact with freshly comminuted rock flour is common (Tranter *et al.,* 1993b). When dilute melt or rain input is low therefore, water transferred through the distributed system becomes a larger proportion of runoff.

However, in early June 2010, as discharge increased during days 156 to 159, the conductivity, SSC, sulphate and bicarbonate concentration and pH all increased. The discharge then reached a peak on the evening of day 159/morning of day 160, and as it began to fall these chemistry parameters reached a peak. For the conductivity to rise in phase with discharge the supply of ions must have increased at a rate that overcame the effect of dilution (Richards, 1982), confirmed by the rise in bicarbonate and sulphate ion concentrations. The conductivity and bicarbonate ion concentration could increase with discharge due to post-mixing chemical reactions of water with suspended sediment. However, sulphate is not thought to be produced in large quantities during post-mixing chemical reactions – only if water has spent long periods at the bed (Brown *et al.,* 1998). The C-ratio also decreased to levels associated with delayed flow. Furthermore, although a high SSC is usually associated with high discharges, the SSC concentrations on day 160 were the highest recorded all season, even though the SSC of much higher discharges was measured. Particularly high SSC are associated with high subglacial water pressures because there is an increase in sediment supplied to the meltwater from subglacial sources (Clifford *et al.,* 1995).

Therefore runoff during days 157 to 160 likely had an increasing component of ion and sediment rich water that had spent some time in contact with sediment at the bed. This was possibly caused by the rising input of water (suggested by the rising discharge) causing high subglacial water pressures which flushed water out of the subglacial distributed system. High subglacial water pressures can lead to more of the cavities becoming hydraulically linked and able to provide sediment (and presumably ions) to the rest of the system. High pressures are also associated with the switch of part of the network to a channelized system, resulting in the increased flow of water from the distributed system into the main network (Willis *et al.,* 1996). This is supported by the relationships of SSC, conductivity, pH, sulphate and bicarbonate with discharge being strongest with an 18 hour

lag, as well as the positive relationships between variables, which did not exist later in June. These parameters were therefore varying together, and are a signature of a specific pulse of water. This pulse reached the gauging station as discharges fell on day 160, one to two days after a period of faster velocities on day 158 (see section 8.1.1, Figure 8.3a). This could suggest that either the water flow through the distributed system was slow enough to result in these long travel times, or that high pressures in the main network prevented water that entered the distributed system from being released into the channelized system until discharges fell (Hubbard *et al.*, 1995). Presuming the water did flow in the distributed system (at 0.07 ms^{-1} a velocity characteristic of the S5 and S7 traces which were indicative of a distributed system, section 5.1.1.2), from the main moulins around 4900 m from the gauging station, this would take around 19 hours for the water to reach the gauging station – it is therefore likely that an increased delay was caused by high pressures in the main system.

Looking at evidence for the evolution of the hydrological system, there was a clear change in the relationship of SSC with discharge: it rose to much higher values during day 160 than it did during subsequent periods of higher flow, suggesting sediment supply had reduced. This suggests the channel network had become more efficient during the first episode of rising discharge on day 159, and since then meltwater was transferred within a conduit system where the contact with sediment was lessened. Since the relationships between the water chemistry variables and discharge changes between early and late June (from a positive relationship of most variables with discharge if it is lagged by 18 hours, to only conductivity relating inversely to discharge), it is likely the hydrological system did become more efficient between early and mid-June.

6.2.2.2 Seasonal trends

The concentration of sulphate and bicarbonate ions was measured to be relatively high on Miage Glacier when compared with other glaciers, and remained high during low flow periods throughout the year (section 6.2.1.7) The concentration of sulphate ion concentrations can be influenced by the amount of supraglacial sulphate derived from the snowpack from deposition of mainly the sea salt aerosol (Tranter *et al.,* 1996) (measured to be very low on Miage Glacier, see section 3.4.2.2); or by the time water has spent in contact with sediment at the bed of the glacier where sulphide oxidation results in the production of sulphate (Tranter *et al.,* 1993a); or by the influence of groundwater in the proglacial stream. One measurement of the groundwater, from a spring close to the main valley river, the Dora d'Veny had very high concentrations of sulphate and bicarbonate – 2959 $\mu eq\ l^{-1}$

and 1361 μeq l^{-1} respectively, which gave a C-ratio of 0.32. Some of the sulphate or bicarbonate could come from groundwater, especially during low flow conditions when the proportion of groundwater of total flow would be larger. However, if the entire contribution of sulphate and non-supraglacial bicarbonate was from groundwater then during low flow conditions the C-ratio would be much lower. The lowest C-ratio measured was 0.63 on day 258 in 2011, considerably higher than the groundwater. Even if the bicarbonate concentration is artificially dropped by 250 μeq l^{-1} to account for the average supraglacial input of bicarbonate ions (section 6.1.2), the C-ratio is still 0.52. Therefore it is less likely the ions provided to the proglacial stream are derived from groundwater. There must therefore be some sulphate ions derived from reactions at the bed in a distributed system. This confirms the dye tracing results which suggested a distributed system underlies parts of the lower glacier.

Furthermore, although bicarbonate ions can be produced within post-mixing chemical reactions (Tranter *et al.,* 1993b), as well as supraglacially (section 6.1.2), the bicarbonate and sulphate ion concentrations tend to vary together (although the only significant relationship was in July/August 2010). They also tend to be high during low flow periods, suggesting that at least a portion of the bicarbonate concentration is produced at the bed.

Since high sulphate and bicarbonate concentrations were found during low flow periods throughout the season, the delayed flow component of discharge was probably relatively large. If the sulphate was not from groundwater sources there may be other reasons why the concentrations were particularly high. Higher sulphate concentrations could occur because of a higher quantity of reactive minerals in the rocks beneath Miage Glacier, or because the water has spent extended periods in contact with sediment. The valley geology is composed of mainly gneiss, mica-schists and granite (Deline, 2002), although it's the reactive minerals (which can be present in only trace amounts) which control most weathering reactions (Tranter *et al.,* 1996). The layer of sediment at the bed of the lower glacier (Pavan *et al.,* 1999, cited in Deline, 2002, see section 1.4) could act as a subglacial aquifer, increasing the water-rock contact time and causing favourable conditions for ion production.

Heavy rainfall was determined by some studies to lead to the leaching of sulphate ions from the supraglacial debris (Hasnain and Thayyen, 1999a). The 2010 water chemistry data however does not support this (Figure 6.22, Figure 6.23 and Figure 6.24). A greater concentration of bicarbonate ions was found on Miage Glacier in the supraglacial streams where the debris cover was thick (section 6.1.2) but higher concentrations of sulphate were not found. There was a prolonged period of rainfall during day 250 and the morning of day

251 2010 totalling 21 mm. A period of low conductivity occurring during these days, thought caused by the runoff from rainfall reaching the proglacial stream, was actually associated with below average values of sulphate. Therefore a large rainstorm dilutes the ion concentration of stream water, whether the ions originate supraglacially or subglacially, unless the rainwater overwhelms the subglacial conduit system, and enters the surrounding distributed system. It cannot be ruled out that supraglacial debris could be a source of sulphate, similar to the proglacial icing which gave high sulphate concentrations at Scott Turnbreen Glacier in Svalbard (Hodgkins *et al.,* 1998), but high sulphate concentrations could also be derived from reactions at the bed.

6.3 Proglacial runoff analysis

In this chapter an analysis of the proglacial hydrograph is presented, which gives an understanding of the diurnal runoff amplitude and timing, and its response to meteorological forcing. The results are discussed in relation to the glacier morphology and debris cover. The full 2010 and 2011 runoff hydrographs are given in Figure 6.28 and Figure 6.29 respectively.

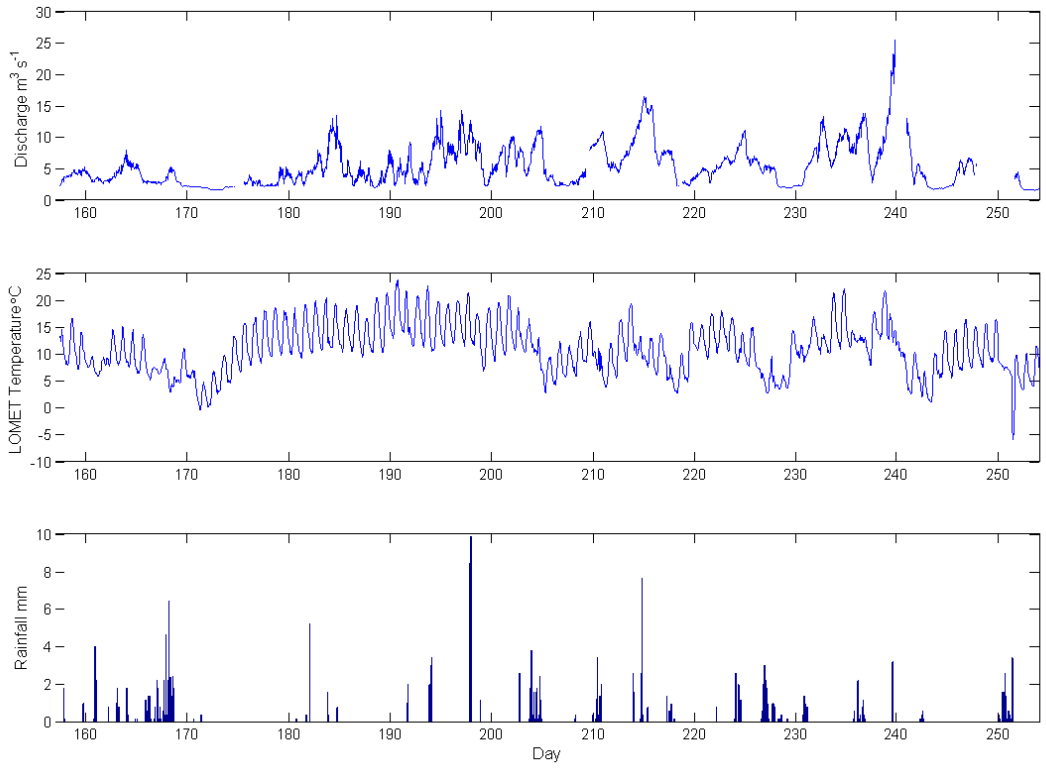

Figure 6.28 Runoff and meteorological record for the summer of 2010.

The June 2010 runoff is composed of discharge fluctuations that occur over periods of a few days, with peaks driven by periods of warmer weather or heavy rainfall. This is followed by cold weather which gives a distinct recession period. Runoff

magnitudes then increase in response (with a few days lag) to the increase in air temperatures, with discharge remaining high and with noticeable diurnal fluctuations during warm weather. The air temperature becomes more variable and there is a greater rainfall frequency from around day 210, and this corresponds with discharge fluctuations which occur over a few days and lack a clear diurnal signal. Very warm weather around day 239 gives rise to the largest flow of the season, followed by recessional flow during particularly cold conditions.

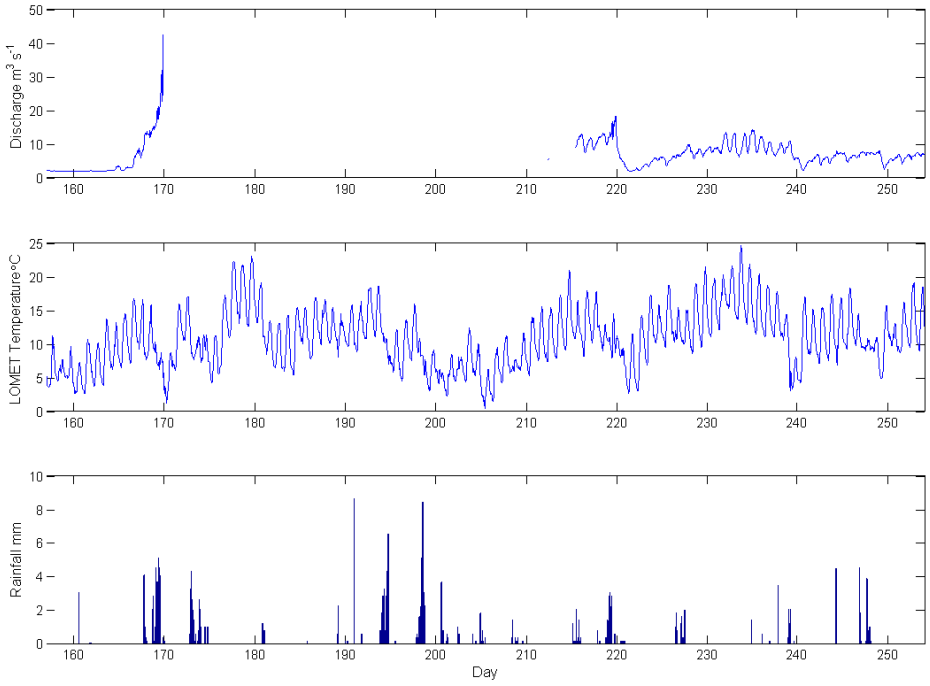

Figure 6.29 Runoff and meteorological record for the summer of 2011.

The early 2011 runoff is very low and stable, and corresponds with low air temperatures. The following rise in air temperatures, as well as heavy rainfall leads to a dramatic rise in discharge. Runoff data is missing until the end of July, after which time it rises to a peak on day 219 caused by heavy rainfall. The following cool weather results in low flows which gradually increase with air temperature in the following days. When the air temperature is particularly high the runoff has clear diurnal fluctuations (days 232 to 240), but returns to a more subdued pattern of a gradually rising then more steeply falling hydrograph when the weather is colder.

6.3.1 The influence of the debris cover on the amplitude and timing of diurnal runoff fluctuations, and how these relate to meteorological forcing

Understanding how the daily meteorological cycle is translated into the runoff hydrograph, in terms of the magnitude and timing of the diurnal runoff signal, can be used to understand the overall efficiency of the hydrological system. It is necessary therefore to separate the days with diurnal hydrographs from the rest of the record where other events such as rainfall, or the release of water from storage may have influenced the hydrograph.

To analyse the daily hydrographs the runoff record was split into days with the beginning of the 'day' being the average time of minimum runoff (for complete days with no rain) of 11:00 in 2010. The day is numbered according to the day at the beginning of the daily hydrograph.

Each day's hydrograph was categorised by eye as to whether it was i) diurnal (a peak in the middle of the day, and lower flows at the beginning and end), ii) rising (flow increased over the day), iii) falling (flow fell over the day), or iv) was unknown (hydrograph steady or could not be differentiated into one of the other categories). Some hydrographs fell within two categories (usually rising and diurnal or falling and diurnal), and in these cases the most prominent feature of the hydrograph in terms of the magnitude of the runoff change and the location of the peak flow determined the hydrograph category. Mean hydrographs for categories i) to iii) are in Figure 6.30.

.

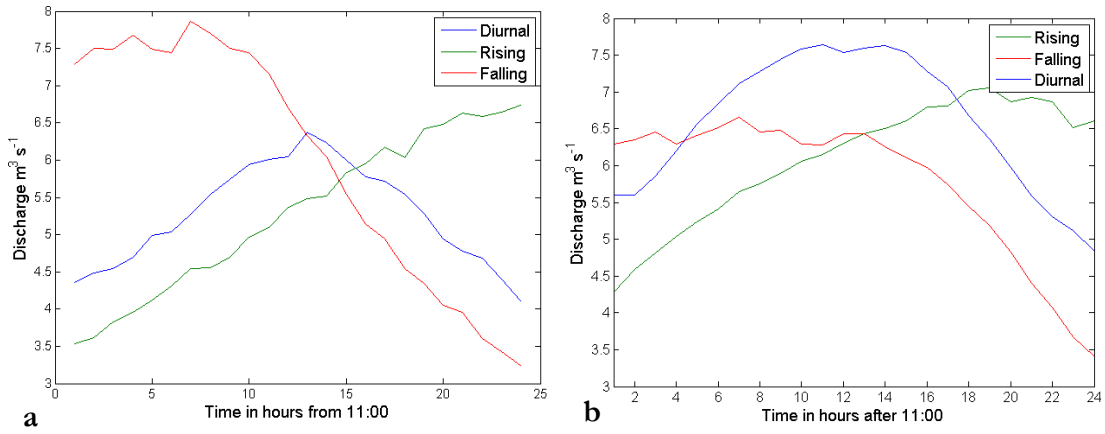

Figure 6.30 Mean diurnal, rising and falling hydrographs, a) for 2010 and b) for 2011.

Following Swift *et al.* (2005) specific parameters were calculated for each of the hydrographs classified as diurnal, as well as averages for each year. They include:

- Q_{damp} diurnal discharge amplitude (maximum minus minimum runoff)

- Q_{dmax} diurnal discharge maximum (runoff peak)
- Q_{dmin} diurnal discharge minimum (either before or after the peak)
- Q_{dmean} diurnal discharge mean
- Q_{dsdamp} diurnal discharge standardised amplitude (the diurnal runoff amplitude expressed as a proportion of the diurnal minimum flow ((maximum flow-minimum flow)/minimum flow), which can be thought of as the ratio of rapidly routed to long residence time melt)
- Q_{dstd} diurnal discharge standard deviation

In addition, the times of maxima and minima runoff were found as the hour number for the day, with hour 1 being 11:00. The times of maxima and minima meteorological variables and proglacial conductivity was found in the same way (their day also started at 11:00), and this allowed the lag time between maxima and minima of different variables to be calculated. For conductivity only daily cycles which were categorised as diurnal were included in the analysis to remove the effect of specific outburst or rainfall events.

6.3.1.1 The amplitude of diurnal runoff hydrographs

The occurrence of clearly diurnal runoff hydrographs, and the amplitude of the diurnal cycle can reveal the proportion of efficiently routed quickflow to more slowly routed baseflow. This can be used to infer the likely peakedness of the supraglacial input hydrograph, as well as the efficiency of the englacial and subglacial system.

The categorisation of the runoff hydrographs (Table 6.14) revealed that the majority of hydrographs were diurnal in both years, followed by rising and then falling hydrographs. Looking at individual months, diurnal hydrographs dominated only in July 2010 and August 2011. Rising hydrographs dominated in August 2010 and June 2011, and during June and September 2010 rising and diurnal hydrographs both occurred with the same frequency. Falling hydrographs did not dominate during any months, but in September 2011 they did occur more often than diurnal hydrographs, although only 15 days were measured.

Table 6.14 Gives the number 'N' and percentage '%' of hydrograph types in 2010 and 2011.

2010	All		June		July		August		September	
Hydrograph type	N	%	N	%	N	%	N	%	N	%
Rising	26	30	7	30	5	17	11	41	3	43
Falling	15	17	4	17	5	17	5	19	1	14
Diurnal	32	37	7	30	14	48	8	30	3	43
Unknown	13	15	5	22	5	17	3	11	0	0
2011	**All**		**June**		**July**		**August**		**September**	
Hydrograph type	N	%	N	%	N	%	N	%	N	%
Rising	20	36	7	54	-	-	8	29	5	33
Falling	7	13	0	0	-	-	3	11	4	27
Diurnal	25	45	6	46	-	-	16	57	3	20
Unknown	4	7	0	0	-	-	1	4	3	20

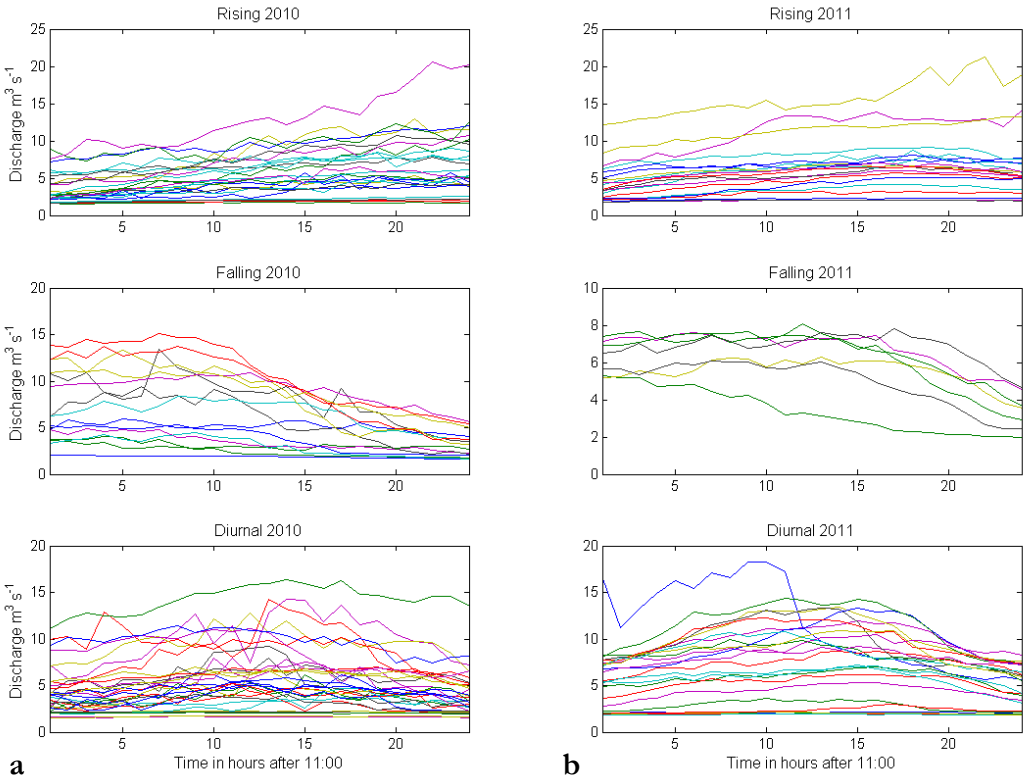

Figure 6.31 Individual hydrographs classified as diurnal, rising and falling for a) 2010 and b) 2011.

Figure 6.31 shows the diurnal hydrographs for each year. There is a reasonable variability in the amplitude of the diurnal runoff signal between different days, and individual runoff hydrographs generally do not smoothly rise or fall and can exhibit a flattened or variable peak. Part of the reason for a less smooth hydrograph could be due to the variability of the stream level when it was measured, particularly when discharges are

high and the accuracy of stage measurement decreases, but smooth runoff changes were measured on some days, which indicates this cannot account for all variability.

Table 6.15 Statistics of the runoff hydrograph analysis, calculated from diurnal and all hydrographs.

Statistic	2010 diurnal hydrographs ($m^3 s^{-1}$)	2010 all hydrographs ($m^3 s^{-1}$)	2011 diurnal hydrographs ($m^3 s^{-1}$)	2011 all hydrographs ($m^3 s^{-1}$)
Q_{dmean}	5.27	5.25	6.59	6.43
Q_{dstd}	0.96	1.09	1.17	1.03
Q_{dmax}	6.98	7.03	8.26	7.91
Q_{dmin}	3.57	3.43	4.64	4.51

The main runoff hydrograph statistics are in Table 6.15. The 2010 mean discharge was slightly lower than in 2011, although the standard deviation of runoff in 2010 was only lower than 2011 for diurnal hydrographs. The average maximum runoff was higher in 2011 than in 2010 for both all and diurnal hydrographs.

The diurnal runoff amplitude may increase in the middle of the season but there is considerable day to day variability (Figure 6.32a). In 2010 the diurnal amplitude increases during the middle part of the summer (around days 194 and 196), with smaller amplitudes in early June and September. However, there was considerable variability in the runoff amplitude. The 2011 data (Figure 6.32b) shows a stark increase in diurnal amplitude between early June and August, with day 219 having the largest diurnal amplitude of over 12 $m^3 s^{-1}$. There is still considerable scatter (2 to 7 $m^3 s^{-1}$) in the diurnal amplitudes in August. Warmer days result in an increase in the diurnal runoff amplitude. When the diurnal amplitude was plotted against maximum daily temperature at LOMET (Figure 6.33) there was a clear relationship in both years ($p = 0.000$, $R^2 = 0.441$ for 2010, and $p = 0.001$, $R^2 = 0.348$ for 2011) so as the maximum temperature increases the diurnal runoff amplitude increases. Therefore warmer days result in greater melt inputs, increasing the proportion of quickflow and the diurnal runoff amplitude.

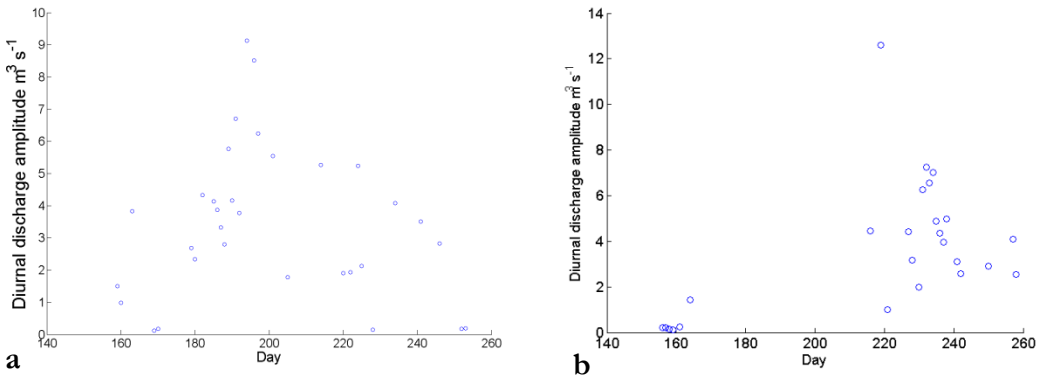

Figure 6.32 Diurnal amplitude of discharge against day number for a) 2010 and b) 2011.

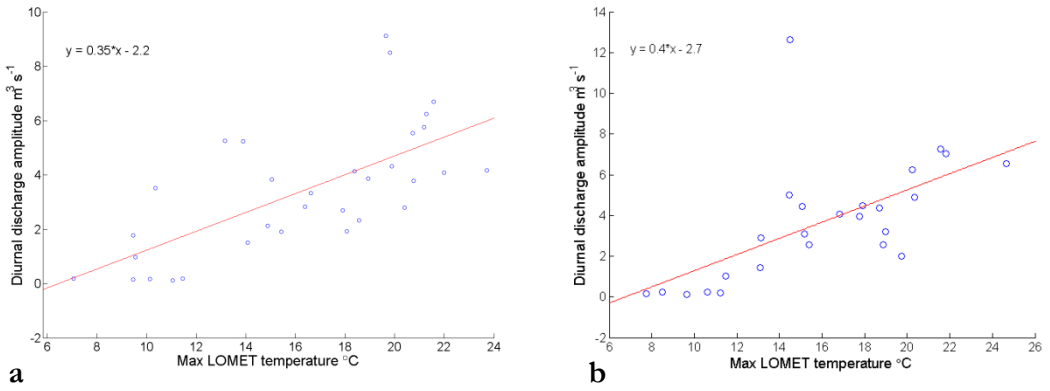

Figure 6.33 Diurnal amplitude of discharge against the maximum air temperature at LOMET for a) 2010 and b) 2011.

To look at the change in the hydrograph shape over time the runoff hydrograph was averaged over a period of a few days (usually 10 days). All runoff data were included and in this analysis the beginning of the day is at 01:00. This allows an overview of the mean hydrograph including all hydrograph types, and shows when diurnal patterns dominate. For most periods in 2010 the overall runoff pattern is not diurnal (Figure 6.34), at least not in terms of a consistent pattern prominent when averaged over several days. Only in 3 periods is a diurnal pattern apparent, during days 176-185, 186-195 and 196-205 of 2010. These periods are during the end of June, and most of July, and correspond with the high percentage of diurnal hydrographs during July 2010. The same analysis was performed on the 2011 data (Figure 6.35), with the 10 day periods remaining the same for comparison purposes (though some are missing due to incomplete data, and for some periods there were not 10 full days of data). Many periods also do not show a clear diurnal signal, although the hydrographs are clearer in 2011 than 2010. This is likely because most of the data in 2011 was from August, when diurnal hydrographs dominated, and this corresponded with days 226-235 which had the clearest averaged diurnal signal. In June the hydrograph is particularly flat, and during the end of August and beginning of September (days 236-245 and 246-255) the less clear diurnal signal corresponds with when diurnal hydrographs were least common.

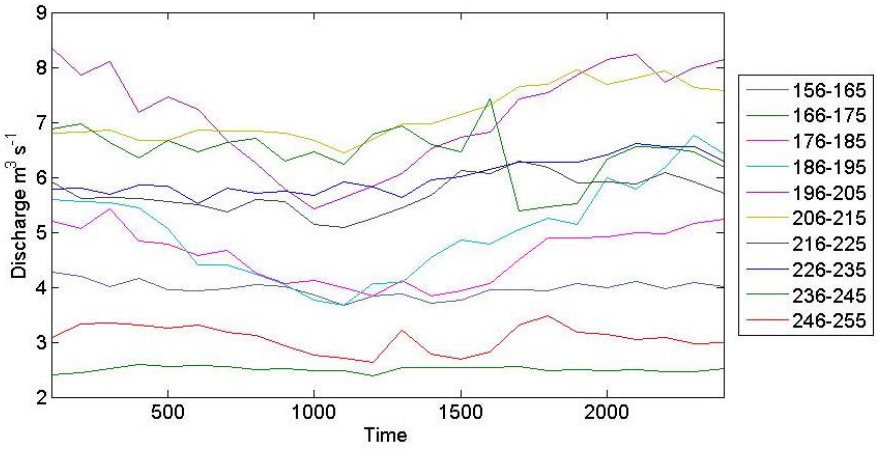

Figure 6.34 Average diurnal hydrographs for 10 day periods in 2010.

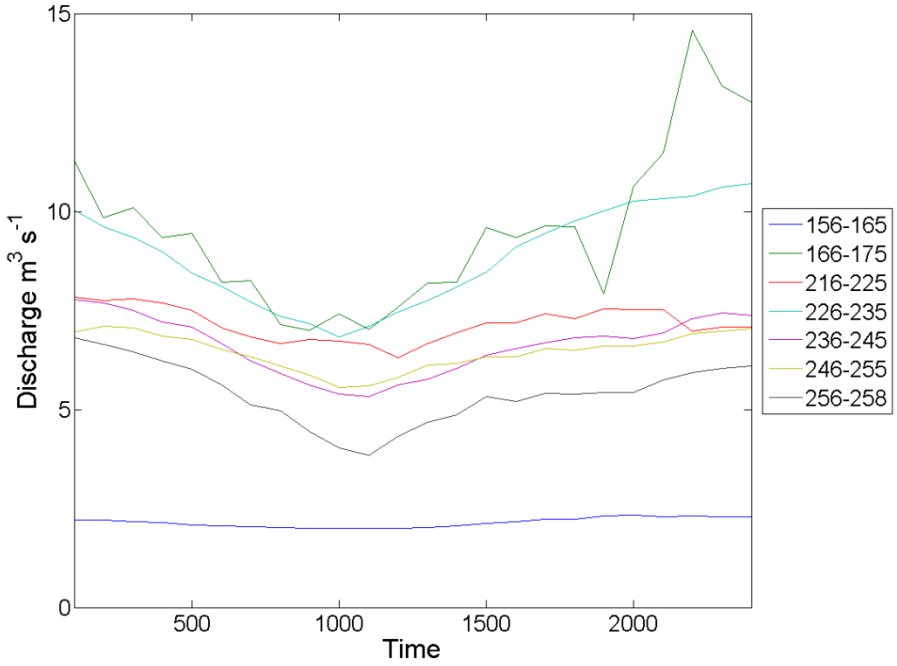

Figure 6.35 Average diurnal hydrographs for 10 day periods in 2011.

The diurnal runoff amplitude can be compared to other glaciers (Table 6.16) especially if one studies Q_{dsdamp} and the ratio of Q_{dmax} to Q_{dmin}. Generally the Q_{dsdamp} of July 2010 was similar to the hydrographs classed as 'High' for the Taillon Glacier (Hannah *et al.,* 1999), and is between the 'Medium' and 'High Peaked' classes for Haut Glacier d'Arolla (Swift *et al.,* 2005). In 2011, the period of peaked hydrographs gave a Q_{dsdamp} similar to the 'Low' of the Taillon Glacier runoff, although the September 2011 Q_{dsdamp} was higher than in June. The value of Q_{dsdamp} in June of both years, and in September 2010 is rather low compared to the values for the other two glaciers, with these values much lower than the 'Low peaked' Haut Glacier d'Arolla hydrographs, and only similar to the 'High Baseflow' hydrographs from Taillon. The statistics calculated above were only for hydrographs classed as diurnal.

Table 6.17 shows Miage Glacier has fewer diurnal hydrographs over the season than was classified for Haut Glacier d'Arolla (46% for Miage Glacier, 61% for Haut Glacier d'Arolla (Swift *et al.,* 2005)), which is consistent across both years. Taillon Glacier has a similar number of diurnal hydrographs (48%, Hannah *et al.* (1999)), but looking at the classification scheme for this glacier's runoff, some of the 'Building/Late peaked' hydrographs may have been classed as diurnal for Miage Glacier, as they show a rise to a peak around 24:00, generally the Taillon classification is not as similar to that used for Miage Glacier runoff, as the Haut Glacier d'Arolla classification.

In terms of the discharge ratio, this is larger than for the Gangotri Glacier, with the values for Miage Glacier during periods of peaked hydrographs (2.62 in 2010 and 1.77 in 2011) being higher than the highest values for the Gangotri (1.38-1.41 (Singh *et al.,* 2006b)). This is understandable given the Gangotri Glacier is much larger than Miage Glacier (glacierised area of the Gangotri Glacier is 286 km^2 (Singh *et al.,* 2006b), compared to 10.5 km^2 for Miage Glacier). The longer travel times for melt from high altitudes which has travelled long distances to the gauging station would increase the baseflow compared to the quickflow component, and reduce the ratio between the maximum and minimum runoff.

The proportion of quickflow to baseflow on Miage Glacier during warm weather periods was similar to other temperate glaciers. This was shown by the similarity of the diurnal discharge amplitude to Haut Glacier d'Arolla and Taillon Glaciers during periods when diurnal hydrographs dominated.

Under lower discharge conditions however, the base flow of Miage Glacier was a larger component of runoff than exhibited by these glaciers – shown by the smaller amplitude of diurnal fluctuations in spring on Miage Glacier. This corresponds with the lower overall percentage of diurnal hydrographs. The presence of a larger baseflow component will be due to either a less clear diurnal input hydrograph, or attenuation of this input hydrograph by a less efficient englacial and subglacial system. The attenuation of the input hydrograph (section 4.2.2), and local inhibition of the evolution of the subglacial system (section 5.2.2), thought due to the presence of the debris cover, may combine to reduce the proportion of water routed rapidly to the proglacial stream. This would increase the baseflow component of proglacial discharge.

Table 6.16 Diurnal amplitude statistics for selected glaciers. Please see section 6.3.1.3 for a description of how the phases in the Miage Glacier runoff record were delimited.

Phase/Period	Q_{damp} ($m^3 s^{-1}$)	Q_{dsdamp} ($m^3 s^{-1}$)	Q_{dmax}/Q_{dmin}
Miage Glacier 2010 - diurnal hydrographs only (all hydrographs)			
June/phase 1	1.66	0.56	1.56
July/phase 2/peaked	5.00	1.62	2.62
Aug	3.03	0.62	1.62
Sep	1.06	0.32	1.32
Phase 3	2.67 (3.86)	0.60	1.60
Mean	3.41 (3.60)	1.01	2.01
Miage Glacier 2011 - diurnal hydrographs only (all hydrographs)			
June	0.40	0.20	1.20
July	-	-	-
Aug	4.91	0.83	1.83
Sep	3.19	0.99	1.99
Phase 1	0.40	0.20	1.20
Phase 2/peaked	4.99	0.77	1.77
Phase 3a	6.03 (4.09)	1.12	2.12
Phase 3b	3.05 (3.00)	0.89	1.89
Mean	3.62 (3.39)	0.70	1.70
Haut Glacier d'Arolla 1998/1999 (Swift *et al.,* 2005)			
Low-peaked	0.91	0.83	-
Medium peaked	2.19	0.89	-
High peaked	3.63	2.40	-
Taillon Glacier 1995/1996 (Hannah *et al.,* 1999)			
Low	0.079	0.776	-
Intermediate	0.168	2.649	-
Intermediate Late Peak	0.087	0.929	-
High Intermediate	0.326	2.611	-
High	0.27	1.224	-
High Baseflow	0.117	0.434	-
Gangotri Glacier 2000-2003 (Singh *et al.,* 2006b)			
May	4.6	-	1.08-1.09
June	17.8	-	1.18-1.22
July	42.6	-	1.38-1.41
Aug	30.2	-	1.31-1.35
Sep	1.1	-	1.19-1.20
Oct	3.8	-	1.12-1.15

Table 6.17 Table of hydrograph classification statistics for selected glaciers, with 'N' the number of hydrographs and '%' the percentage of total.

Hydrograph classification	**Miage Glacier**				**Haut Glacier d'Arolla (Swift *et al.,* 2005)**				**Taillon Glacier (Hannah *et al.,* 1999)**	
Year	2010		2011		1998		1999		1995+1996	
	N	%	N	%	N	%	N	%	N	%
Rising (*Building/Late Peaked for Taillon)	26	36	20	38	21	13	30	19	41*	35*
Falling	15	21	7	13	27	17	28	18	12	10
Peaked Falling (Arolla only)					11	7	5	3		
Peaked/Diurnal Attenuated (Taillon only)	32	44	25	48	97	62	91	59	56 8	48 7

6.3.1.2 The lag time between peak temperature and runoff

The lag time between the air temperature and proglacial runoff peak gives the mean time between melt production and its exit from the glacier, and hence a glacier average water travel time. However, where the glacier is debris-covered it also incorporates the time lag associated with the conveyance of the surface temperature cycle to the ice debris interface, which increases with increasing debris thickness (section 4.2.2).

To find the relationship between the discharge and air temperature, a lag correlation was performed between hourly discharge and air temperature records from LOMET and UPMET. The discharge record was moved back in time in hourly increments and the correlation repeated up to a lag of 24 hours, with the lag time with the highest correlation coefficient giving the average lag time. The discharge and air temperature record was also split into 10 day periods and the process repeated, to reveal any changes over the season. Only the 2010 record was used in the statistical analysis, due to its completeness, and all hydrograph types were included, Table 6.18.

Most correlations were stronger with the UPMET rather than LOMET temperature, suggesting the proglacial stream hydrograph shape was determined more by the weather conditions (which determine the timing of melt) on the upper, rather than lower glacier. The lag time for the whole discharge series was between 9 and 10 hours, indicative of the mean meltwater travel time to the proglacial stream. In late June (days 166 to 175) the lag time was higher than average (15 hours), associated with a period of recessional flow from days 169 to 175. The lag time decreased below average during July to 7 hours during days 186 to 205. During this time the weather conditions were consistently warm, and the discharge exhibited a larger proportion of diurnal hydrographs. In August

there were three periods (days 206 to 235) in which the lag time increased to 24 hours. This is unusual and points towards the runoff being driven more by meteorological changes over timescales longer than one day and may be related to the lack of diurnal hydrographs in August. By the end of the season the lag time decreased to 14 hours (UPMET relationship), suggesting although the discharge was reacting to meteorology that day, there was still a considerable lag between melt generation and proglacial runoff.

Table 6.18 Lag correlations between discharge and air temperature at LOMET and UPMET in 2010.

Time period (days)	**LOMET air temperature and lagged discharge**			**UPMET air temperature and lagged discharge**		
	Lag of best correlation (hours)	Pearsons correlation (p-value < 0.05)	R^2 (adj.)	Lag of best correlation (hours)	Pearsons correlation (p-value < 0.05)	R^2 (adj.)
All (156-255)	9	0.436	18.7	9/10	0.490	24.0
156-165	10	0.343	11.3	11	0.413	16.6
166-175	14/15	0.437	18.7	15	0.400	15.6
176-185	9	0.310	9.2	8	0.397	15.4
186-195	7/8	0.282	7.6	7	0.383	14.3
196-205	7	0.613	37.3	7	0.582	33.6
206-215	24	0.547	29.6	24	0.577	33.0
216-225	24	0.451	20.0	24	0.433	18.4
226-235	24	0.721	51.8	24	0.738	54.2
236-245	19	0.713	50.7	13/14	0.729	52.9
246-255	18	0.378	13.5	15	0.492	23.5

Analysis of individual daily hydrographs of both years was performed to find the lag time between melt and runoff. In 2010 the average time of maximum air temperature was just before 17:00, with time of maximum runoff (diurnal hydrographs only) just after 22:00. The mean lag time for each day with a diurnal hydrograph was 6.34 hours. Figure 6.36a demonstrates the lag time decreases slightly with time. There is large scatter between days, between -15 hours (likely an anomaly, not shown) to 14 hours. Table 6.19 shows the average values for different months, which indicates a decrease over the season, although the shortest lag times were in August when the percentage of diurnal hydrographs was lowest. Unlike the runoff amplitude data, there was no relationship with maximum daily air temperature (Figure 6.37a). So although warmer days result in a greater proportion of quickflow, the water does not travel to the proglacial stream any quicker.

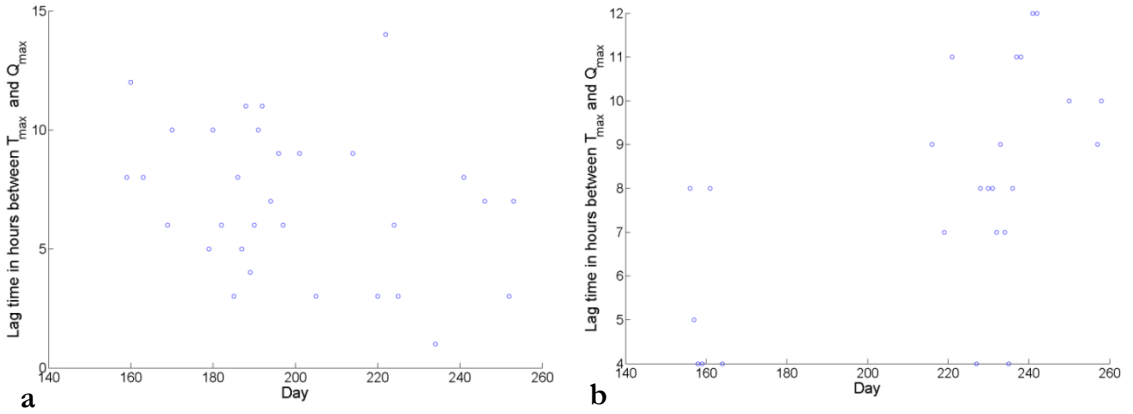

Figure 6.36 Lag time between maximum air temperature at LOMET and maximum discharge against day number for a) 2010 and b) 2011.

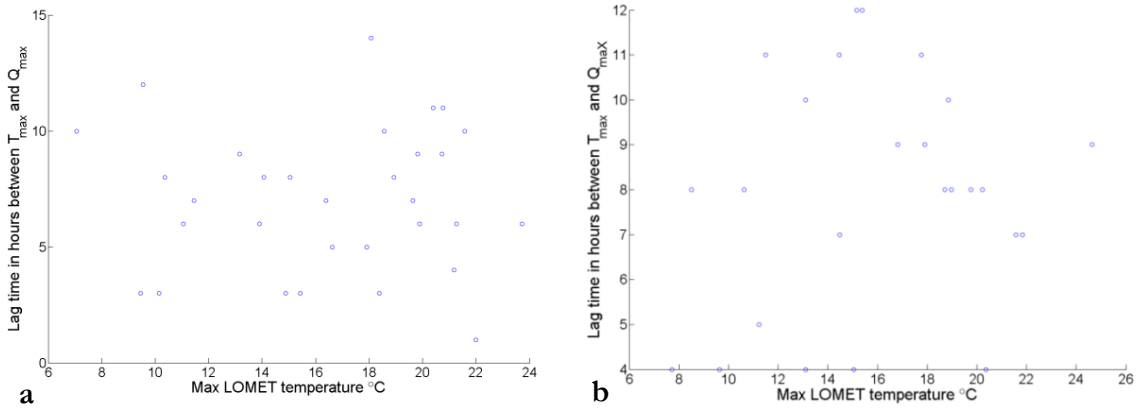

Figure 6.37 Lag time between maximum air temperature at LOMET and maximum discharge against maximum LOMET air temperature for a) 2010 and b) 2011.

Table 6.19 Monthly average lag times from maximum air temperature to maximum discharge.

Month	2010 lag time T_{max} to Q_{dmax} (hours)	2011 lag time T_{max} to Q_{dmax} (hours)
June	8.43	5.50
July	7.00	-
August	3.63	8.50
September	5.67	9.67

Table 6.20 Monthly average lag times from maximum air temperature to minimum conductivity.

Month	2010 lag time T_{max} to $Cond_{min}$ (hours)	2011 lag time T_{max} to $Cond_{min}$ (hours)
June	6.00	3.29
July	3.00	2.5
August	2.92	2.67
September	3.00	1.50

The average time of maximum runoff in 2011 was roughly 23:30, and the average time of maximum LOMET air temperature was 16:45. The mean daily lag time was 7.92 hours, with a minimum of 4 hours and maximum of 12 hours. Figure 6.36b demonstrates that in 2011 there may be an increase in the lag time over the season, and this is also shown by an increase in the monthly average lag times shown in Table 6.19, so contrary to 2010

the water travel time increased over the season. Therefore, there is not a clear trend in the variations of lag time over the season. There is no relationship between the maximum daily temperature and the lag time to runoff (Figure 6.37b), confirming warmer days do not result in faster travel times.

Table 6.21 Maximum and minimum lag times for selected glaciers. See section 6.3.1.3 for a description of how the phases in Miage Glacier runoff were delimited.

Glacier	Method	Year	Reference	Max. lag time T_{max} to Q_{dmax} (hours)	Phase of max. lag time	Min. lag time T_{max} to Q_{dmax} (hours)	Phase of min. lag time
Miage Glacier	Statistically derived	2010	This study.	24	D206-235 /Aug/Phase 3	7	D196-205 /July/phase 2
Haut Glacier d'Arolla (uses $log_{10}Q$)	Statistically derived	1998	Swift *et al.* (2005)	10	D153-158 /June/Phase 2	0	D217-221/ Aug/Phase 8
Haut Glacier d'Arolla (uses $log_{10}Q$)	Statistically derived	1999	Swift *et al.* (2005)	9	D168-173/ June/Phase 1	3	D201-204/ July/Phase 5
Austre Brøggerbreen	Statistically derived	1991	Hodson *et al.* (1998)	29	D185-194 /Phase 2	4	D218-228 /Phase 5
Austre Brøggerbreen	Statistically derived	1992	Hodson *et al.* (1998)	10	D175-186 /Phase 1	5	D198-215 /Phase 4,5,6
Gangotri Glacier	Diurnal hydrographs	2000-2003	Singh *et al.* (2006b)	6.30-7.30	Oct	4	July
Miage Glacier	Diurnal hydrographs	2010	This study.	8.43	June/Phase 1	3.63	Aug
Miage Glacier	Diurnal hydrographs	2011	This study.	9.67	Sep/Phase 3b	5.5	June/Phase 1

In comparison to other glaciers (Table 6.21), the statistically derived minimum lag time was greater than either for Haut Glacier d'Arolla, or Austre Brøggerbreen, whereas the maximum lag time is longer than for Haut Glacier d'Arolla, but similar to Austre Brøggerbreen in 1991. The long lag times at the high Arctic Austre Brøggerbreen were due to the glacier's shallower gradient and more gradual melting of the snowpack, combined with meltwater ponding within the snowpack. The tortuous nature of the ice marginal channels (water was not routed subglacially) may have contributed to the long travel times (Hodson *et al.,* 1998). Miage Glacier is temperate though, so an alternative explanation is required. The lag times from hydrograph analysis are similar to Gangotri Glacier, but as the Gangotri data was from analysis of 4 'clear weather' days in each month (Singh *et al.,* 2006b), it does not give a good representation of the lag times of the entire runoff hydrograph.

To further understand the changes in lag time and runoff amplitude in terms of the source of water, lag times between peak temperature and minimum conductivity were studied. The minimum conductivity indicates the timing of the dilute quickflow peak, with the lag time from peak air temperature highlighting the mean water travel time through the

channelized part of the hydrological system. In 2010 the average time of minimum conductivity occurred just before 20:00, and the mean daily lag time from peak air temperature to minimum conductivity was 3.47 hours. Figure 6.38a and the monthly average lag times in Table 6.20 suggest lag times decreased from June to August, but this was based on just 3 days of June conductivity data. Overall, lag times were less than between peak temperature and peak runoff. There were few days in which both diurnal proglacial discharge and diurnal conductivity data existed, but the available data occasionally showed a gap between the time of lowest conductivity and highest discharge, resulting in a few hours when discharge and conductivity rose in phase (Figure 6.39 and Figure 6.40). The mean time between minimum conductivity and maximum discharge was 2.5 hours, although one day exhibited peak discharge an hour before minimum conductivity (day 234). Generally, when runoff first rises it is composed of increasingly dilute meltwater, as the runoff rises further the meltwater becomes increasingly ion rich.

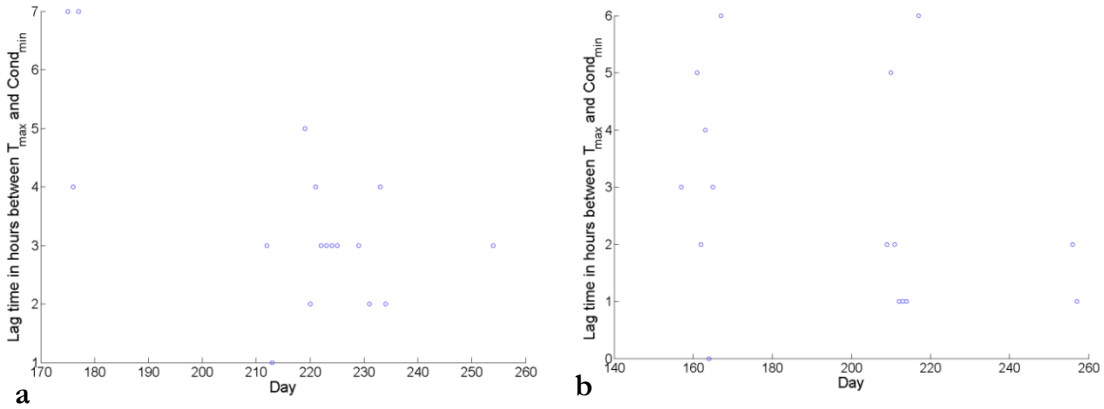

Figure 6.38 Lag time between peak air temperature at LOMET and minimum conductivity against the day number, for a) 2010 and b) 2011.

The same analysis was performed on the 2011 conductivity data. The average time of minimum conductivity occurred at around 18:30, with the average daily lag 2.75 hours, with a minimum of 0 and maximum of 6 hours. There does not appear to be a trend of increasing or decreasing lag time over the season (Figure 6.38b and Table 6.20), but this confirms the 2010 results that the lag time to peak conductivity from peak temperature is usually less than to peak runoff. Figure 6.41 and Figure 6.42 show conductivity and discharge data for individual days, with the period of rising discharge and conductivity tending to last a few hours (average time between minimum conductivity and maximum discharge was 4.25 hours), although on day 257 they rose in phase for 8 hours.

These individual days of conductivity and discharge data can be plotted to show the temporal change in the relationship of conductivity and discharge (Figure 6.40 and Figure 6.42). These graphs show some degree of hysteresis in the relationships, with the clearest cyclic hysteresis being anticlockwise (days 222 and 224 in 2010 and 161 and 164 in 2011). On these days the short period of increasing conductivity with discharge (or in some cases high but variable discharge and increasing conductivity) can be seen.

The lag times of conductivity and discharge will now be discussed in terms of what they reveal about the components of runoff. Generally a proglacial hydrograph shows an inverse relationship between discharge and conductivity, as afternoon quickflow dilutes the baseflow component, decreasing the stream conductivity (Brown, 2002). There can be more than two proglacial hydrograph components however, and Figure 6.43 is a conceptual diagram of those for Miage Glacier runoff. The stars indicate where water could acquire solute; this could be supraglacially when reacting with debris (measured to occur on Miage Glacier, section 6.1.2), or subglacially if the meltwater spends time within an inefficient network where water reacts with subglacial sediment. Dye tracing indicated some of the lower glacier subglacial drainage pathways were inefficient and this was confirmed by a significant concentration of sulphate ions in the proglacial stream (sections 5.2.2 and 6.2.2.2). Supraglacial water chemistry measurements indicated clean ice melt from the upper glacier does not tend to acquire solutes (section 6.1.2), and the short travel time to the proglacial stream signified an efficient englacial and subglacial route (section 5.2.1). Snow and ice melt from the highest parts of the glacier will have longer travel distances and therefore travel times and, although not measured, there is a possibility the hydrological system very high upglacier may also be less efficient.

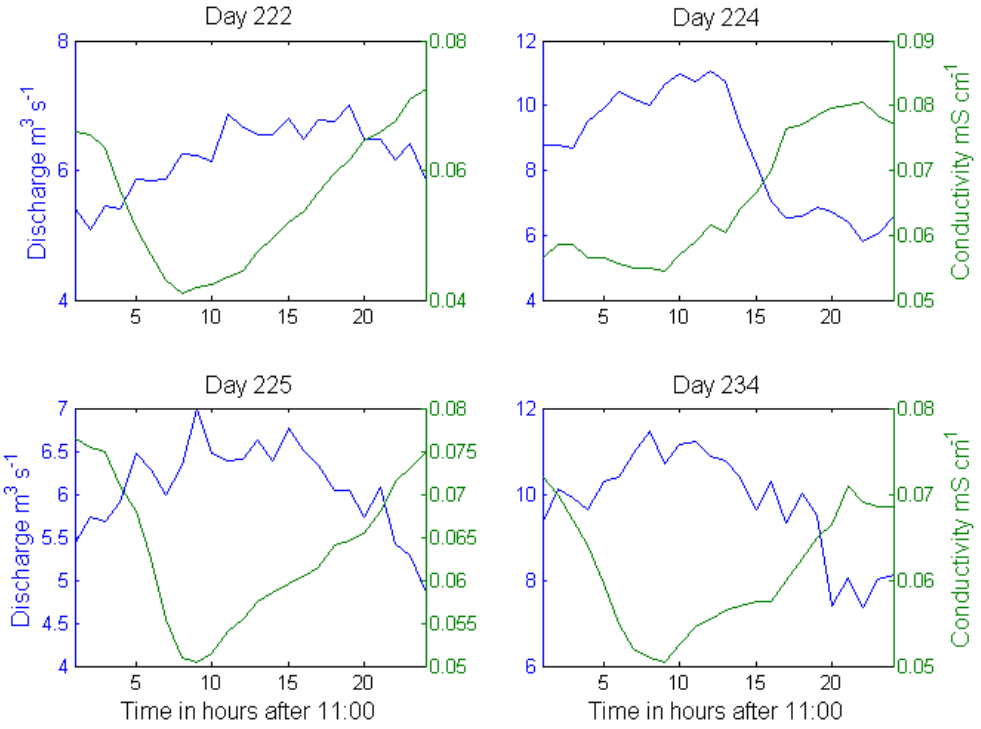

Figure 6.39 Selected days of hourly discharge and conductivity data, in 2010.

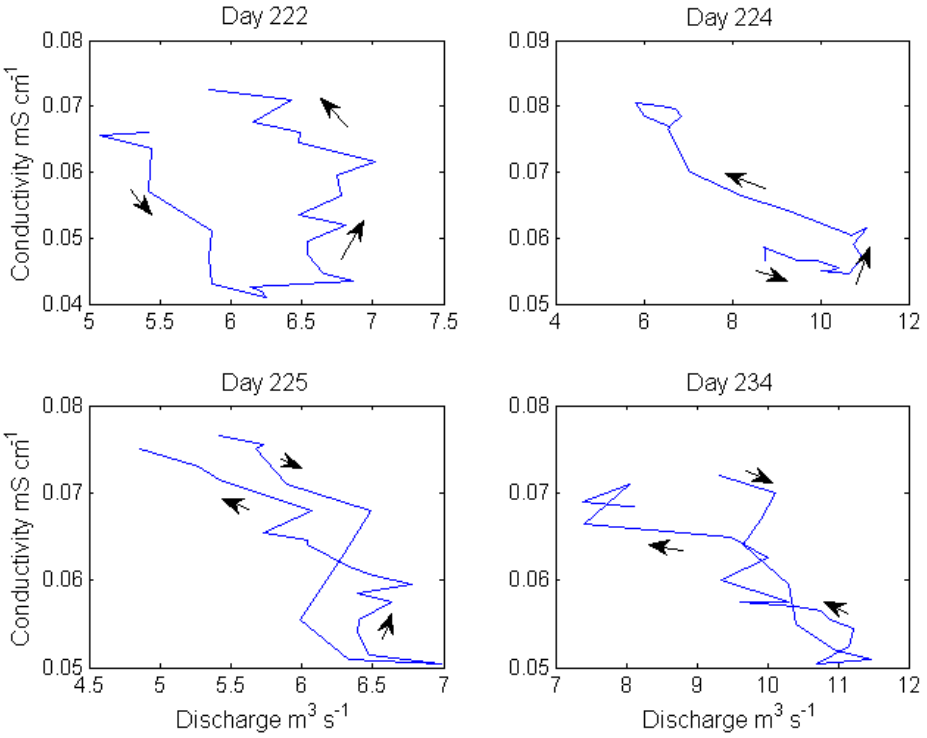

Figure 6.40 Plots of the temporal relationship between hourly discharge and conductivity on individual days in 2010.

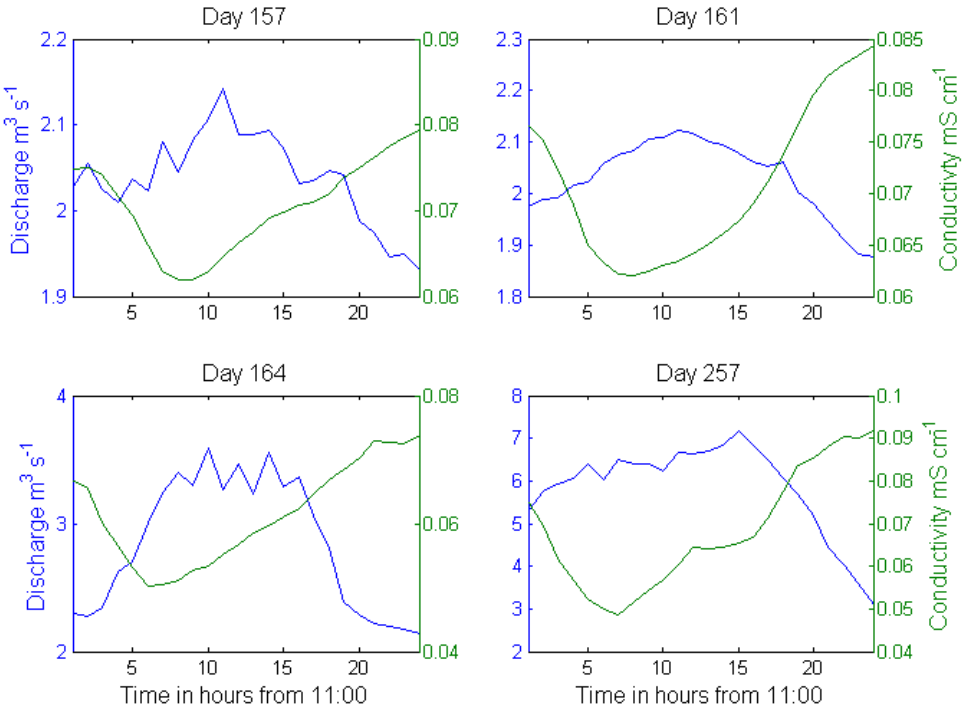

Figure 6.41 Selected days of hourly discharge and conductivity data, in 2011.

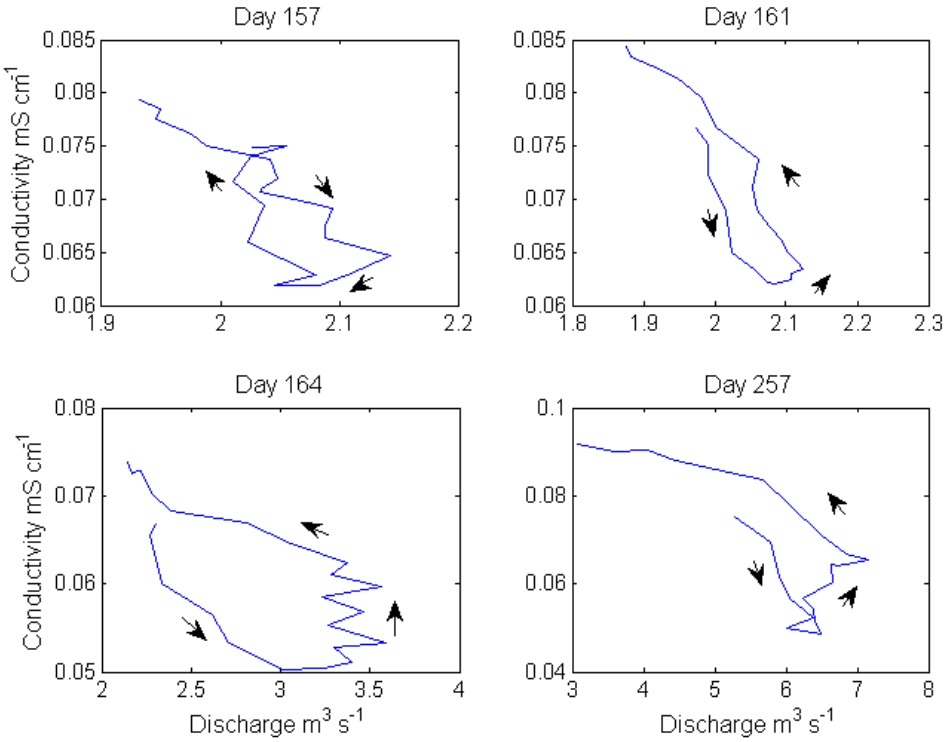

Figure 6.42 Plots of the temporal relationship between hourly discharge and conductivity on individual days in 2011.

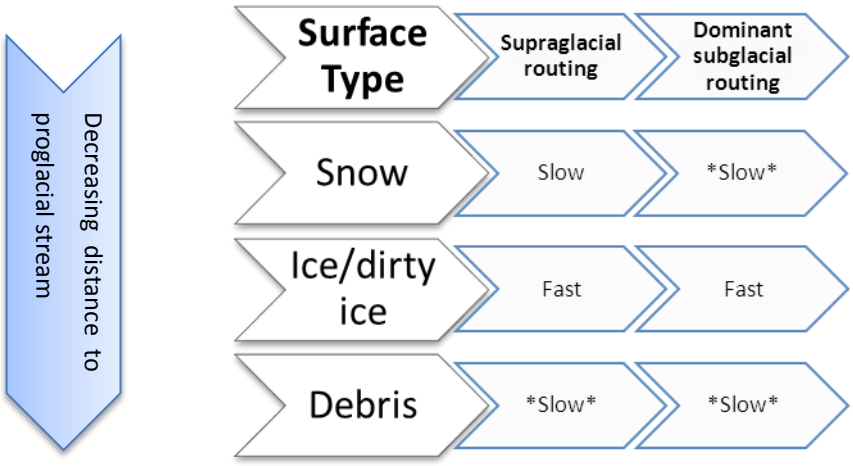

Figure 6.43 Conceptual diagram of runoff components, and their relative travel time class for a debris-covered glacier. The stars indicate where solute could be acquired by the meltwater.

Although post-mixing chemical reactions can increase the solute component of runoff as discharge increases, due to the increased ability for water to transport sediment, this resulted in only a reduction in the amplitude of the diurnal conductivity cycle – minimum conductivity still corresponded with maximum discharge on Haut Glacier d'Arolla (Brown *et al.,* 1998). Therefore the rise of conductivity with discharge may not be due solely to post-mixing chemical reactions, and the longer lag to discharge peak may also be important. It is likely that the later peak is composed of an ion rich meltwater component. This component could be composed of sub-debris melt, which has both longer travel times and a higher solute load (see Figure 6.43). However since modelling suggested melt from the debris-covered region provided only 27-30% of total melt it is likely that that melt from the tributary glaciers very high upglacier may constitute the rest of the discharge peak. This water would have travelled further, and may have passed through a less efficient system than found emanating from the main C10 moulins, increasing the solute concentration, although post-mixing chemical reactions may also be important. There is little fieldwork evidence of this component, but streams from the margins of the Dome and Mont Blanc Glaciers were seen to enter the glacier, and melt was modelled to occur much higher than the highest traced moulins. The combination of the 'debris' and 'tributary' components may create the observed late peak in discharge. Since travel times and solute loads of the melt from the dirty ice region near the main moulins were low this component likely peaks when discharge begins to rise and conductivity is at a minimum.

6.3.1.3 Summary of runoff fluctuations and their relation to meteorological variations

To understand why certain periods have certain hydrograph characteristics it is useful to study the hydrograph in relation to the weather patterns (see Figure 6.28 and Figure 6.29). The 2010 and 2011 hydrographs were delimited into phases with certain characteristics, based on the dominance of hydrograph types. To do this objectively the percentage of each hydrograph type (diurnal, rising or falling, not including unknown hydrographs) was calculated for a running 10 day period (Figure 6.44 and Figure 6.45). The early season period before diurnal hydrographs become dominant is early season runoff (phase 1). Periods when the dominant hydrograph type is diurnal (more than 50% of the days) are classified as a diurnal runoff stage (phase 2). Later periods which do not have a dominant hydrograph type over a long period, or are dominated by falling or rising hydrographs tend to have a saw-toothed appearance and are called saw-toothed runoff or phase 3 (although phase 3 runoff could come before phase 2 runoff). The mid-day of the 10 day period is used as the bounding day between phases, see Table 6.22 for the time periods of each of the phases. This method does not follow other workers who split the record into several numbered phases (for instance Swift *et al.,* 2005; Hannah *et al.,* 1999) based on the dominant diurnal hydrograph type and the climatic regime. This is because of the apparent distinct periods of peaked, and saw-toothed hydrographs, which warrant specific discussion.

Table 6.22 Boundaries of the phases of proglacial runoff.

Year	Phase 1	Phase 2	Phase 3
2010	Days 156-181	Days 182-197	Days 198-254
2011	Days 156-169	Days 227-240	a Days 216-226
			b Days 241-258

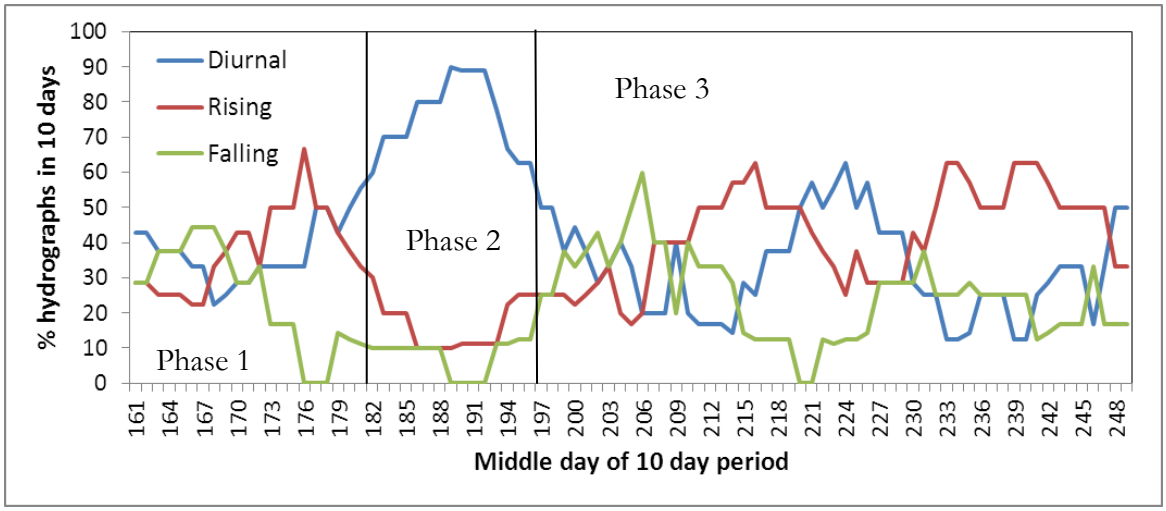

Figure 6.44 Graph of the % of diurnal, rising or falling hydrographs in running 10 day periods in 2010.

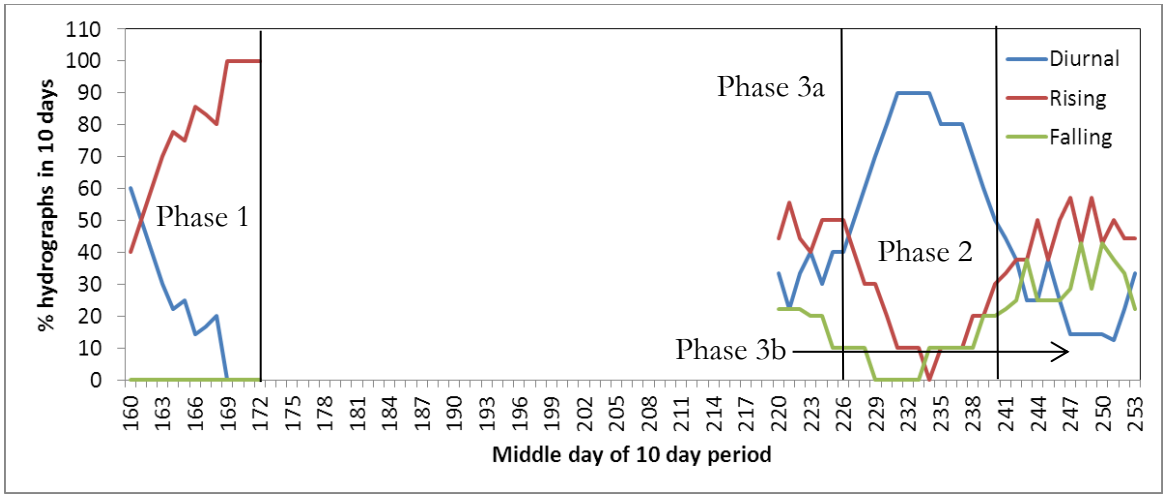

Figure 6.45 Graph of the % of diurnal, rising or falling hydrographs in running 10 day periods in 2011.

6.3.1.3.1 Phase 1: Early season runoff

During phase 1 in 2010 discharges remain low (average 3.2 m^3 s^{-1}), and although diurnal hydrographs dominate, their diurnal amplitude is low (1.7 m^3 s^{-1}), meaning on average there was not a clear diurnal hydrograph (Figure 6.34). Statistically derived lag times suggest melt water travel time was longer than average. Variations over a few days have a larger magnitude than diurnal fluctuations. The details of individual fluctuations and their link to glacier velocity and water chemistry variations are described in sections 8.1.1 and 6.2.1.1 respectively. Air temperatures were low on average being 9.4°C at LOMET compared to the summer mean of 10.8°C, and this cooler weather was associated with a smaller diurnal temperature amplitude (mean of 6.9°C for June compared to the summer

mean of 7.7°C). June was a wet month (see lower subplot, Figure 6.28) with rainfall totalling 77 mm.

Phase 1 in 2011 is really composed of two sections, the period up to the end of day 164, and the period after this when discharges first rise, and then rise again to a very large peak flood flow. The beginning of the record is characterised by very low discharges (mean until end of day 164 was 2.1 m^3 s^{-1}), and although most days are diurnal and have a relatively short average lag time from peak temperature to peak runoff of 5.5 hours, the diurnal amplitude of 0.4 m^3 s^{-1} was very low. Air temperatures were cold, being an average of 6.7°C at LOMET, more than 3°C lower than average. Discharges rose on day 164 but did not rise substantially until day 166, followed by the large flood event on day 169. The flow increase was caused by very heavy rainfall (totalling 45 mm at LOMET, and 72 mm at UPMET on day 169, the largest daily rainfall total at the UPMET gauge). This resulted in an approximate discharge peak of 42 m^3 s^{-1} at 21:00 on day 169. Prior to this the runoff was rising due to increased air temperatures from day 163 to 166.

The subdued hydrographs in phase 1 of both years could be due to two factors: having a less peaked supraglacial input hydrograph, or a less efficient englacial and subglacial system. As discussed in section 5.2.1, the main subglacial channel system was open and efficient from as early as day 160 in 2010 and day 161 in 2011. However, there was still substantial snowcover on the upper glacier in June 2010, and it is known a snowpack can reduce the amplitude of the input hydrograph, and increase the meltwater travel time (Campbell *et al.*, 2006; Willis *et al.,* 2002). This meant even though the main conduit system was efficient early in June in both years, the proglacial stream hydrograph was still subdued. Given efficient conduit systems are unlikely to modify hydrographs on short timescales (Covington *et al.,* 2012) the input (recharge) hydrograph would be the main determinant of the proglacial hydrograph form. As the snow cover was thinner and in places saturated in June 2011, it would be expected runoff would have a shorter lag time compared to 2010 (which it did), however a larger runoff magnitude would also be expected. This was not the case but can be explained by the cooler climatic conditions in June 2011 compared to 2010 (LOMET air temperatures days 155 to 165 were 10.2°C in 2010 and 7.1°C in 2011, Figure 6.46).

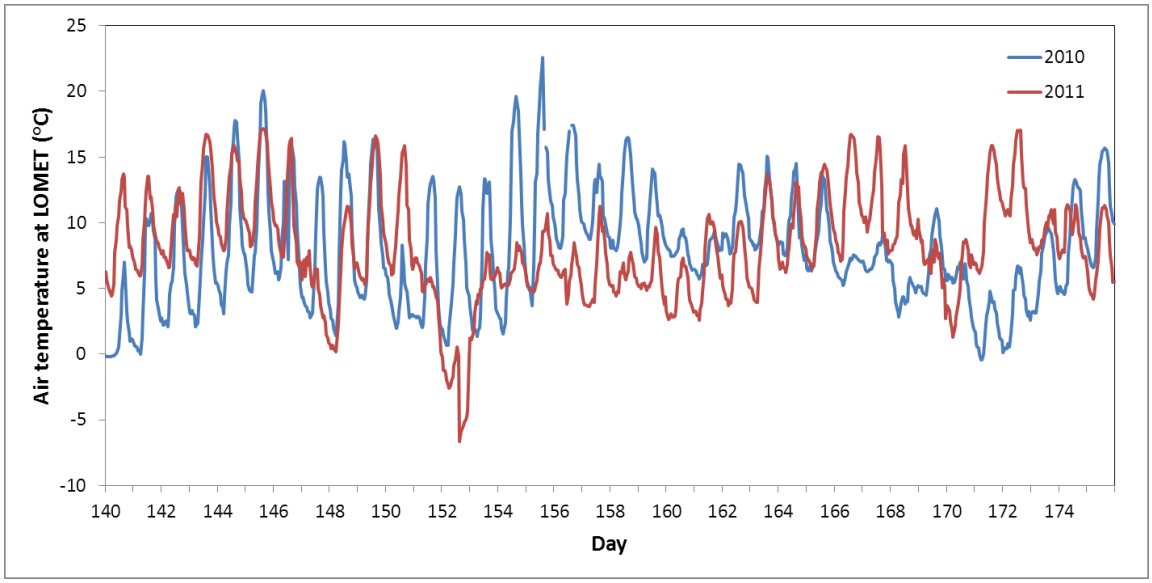

Figure 6.46 Spring air temperatures at LOMET in both 2010 and 2011.

The snowcover in both years meant there was little clean or dirty ice exposed, as at lower altitudes where snowcover was minimal the ice was debris-covered. It has been shown the debris attenuates the air temperature signal as it is conducted through the debris (section 4.2.2). This results in decreased melt beneath thick debris covers (Östrem, 1959; Mattson *et al.,* 1993; Mihalcea *et al.,* 2006), with Miage Glacier data suggesting this leads to smaller supraglacial stream discharges when combined with small supraglacial catchments. Therefore the supraglacial input hydrograph from the debris-covered region will be moderated by the debris-cover. The early season dye tracing, especially from 2011, suggested some of the lower glacier streams had particularly inefficient englacial and subglacial systems, with these becoming more efficient over the season. Meltwater from the debris-covered region will have a subdued hydrograph, and if the stream does not have a close link to the main channel system, may be delayed englacially and subglacially too.

This means that a proglacial hydrograph with a smaller amplitude and longer lag from peak air temperature can result even if a large proportion of the lower glacier is snowfree, if the snowfree region is instead debris-covered.

6.3.1.3.2 Phase 2: Diurnal runoff

During the second phase of the 2010 runoff record the discharge increased, with the mean peak discharge in July being 8.5 $m^3 s^{-1}$, more than double in June (4.1 $m^3 s^{-1}$). This is accompanied by an increase in the percentage of diurnal hydrographs, and an increase in their mean amplitude from 1.7 $m^3 s^{-1}$ in June to 5.0 $m^3 s^{-1}$ in July. Although there is not

much of a decrease in the lag from peak temperature to runoff using the diurnal hydrographs (from 8.43 hours in June to 7 hours in July), the statistically derived lag time does decrease to a below average 7 hours.

Figure 6.28 shows these changes were driven by consistently fine weather with increased air temperatures and only occasional rainfall. Mean LOMET air temperature increased by almost 4°C compared to June, to 13.1°C, with the increase in UPMET air temperature slightly larger (mean of 10.6°C). The increased discharge at the proglacial stream did not instantly follow the air temperature increase, with around three days (days 176 to 179) where air temperatures were high but there was not a response at the proglacial stream. This may indicate part of the runoff generated during this period was stored, at least temporarily. Alternatively, the snowcover may not have melted back above the debris-covered region by this time in the season, reducing melt inputs. However, the discharge did become more responsive to meteorological changes, as shown by the close-up of days 190 to 200 in Figure 6.47. This demonstrates the shape of the hydrograph peak may partly be driven by the daily pattern of air temperature, and especially incoming shortwave. For instance, the twin peaks of incoming shortwave on day 190 are echoed in the hydrograph, and the earlier peak on day 195 may be due to the decrease in afternoon incoming shortwave.

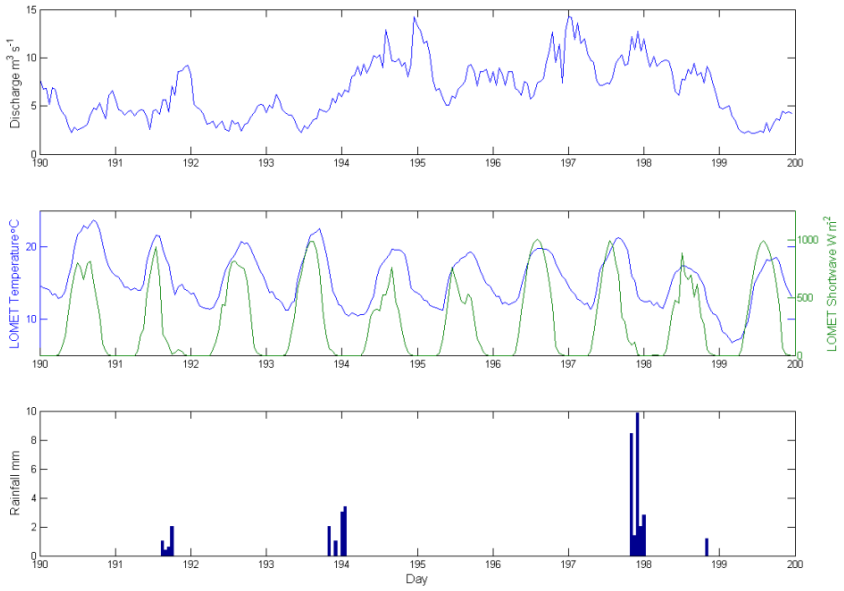

Figure 6.47 Close-up of the runoff, air temperature and rainfall (from LOMET) of days 190 to 200, 2010.

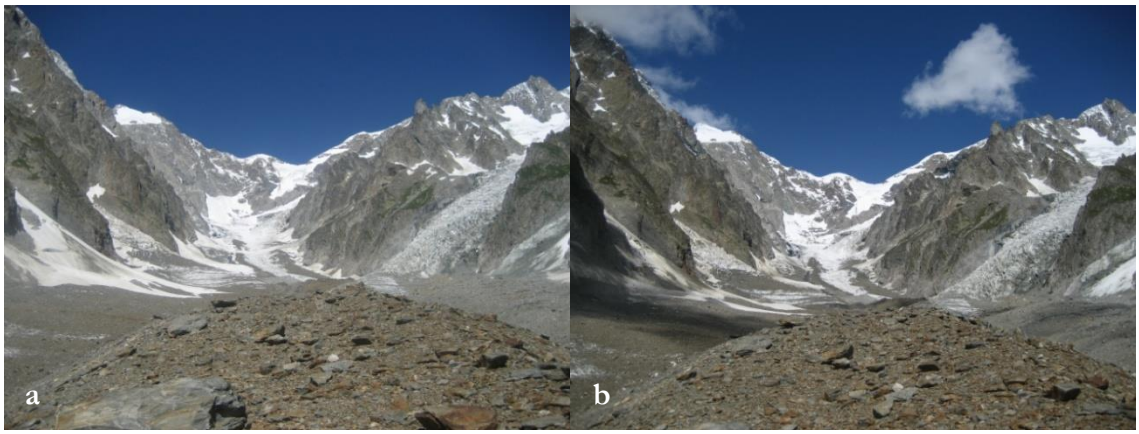

Figure 6.48 Photographs of the upper glacier snowcover taken looking upglacier from C10, a) was taken on 31/07/10 and b) on 29/07/11.

By the end of July 2010 (day 212) on Miage Glacier the snowcover had melted back to approximately the base of the Bionassay Glacier, with the ice falls of the Dome and Mont Blanc Glaciers, and the lower part of the Tête Carrée glacier being snow-free (Figure 6.48a). Modelled snow cover suggested these areas were mainly snow-free (<10% snow cover) for at least the previous week. The dye tracing in July/August 2010 revealed the lower glacier injection points were more efficient than June, and spent at least some time in an efficient drainage system, and although the one trace from the upper glacier had a single peak, it travelled more slowly than the upglacier traces in June (section 5.1.2). Trace velocities ranged between 0.23 and 0.44 m s^{-1}. The removal of snowcover from the debris-free area probably increased the magnitude and amplitude of meltwater inputs to the upper glacier moulins (e.g. S12 and S14) (Willis *et al.,* 2002). Considering these moulins were efficient in June, it would be expected they remained so and allowed the more peaked supraglacial hydrograph to be translated into a more peaked proglacial hydrograph, with greater amplitude and decreased lag time. The warmer weather resulted in greater melt inputs on the lower glacier where the internal drainage had increased in efficiency, further increasing the diurnal hydrograph amplitude.

Data from July 2011 was missing but a phase 2 period where diurnal hydrographs dominated occurred in August from days 227 to 240. Within this period diurnal hydrographs occurred on 79% of the days, with an average diurnal amplitude of 5.0 m^3 s^{-1} (greater than the season average of 3.6 m^3 s^{-1}). The mean and maximum diurnal days discharge was greater in magnitude than average too (mean discharge 9.2 m^3 s^{-1}, compared to the seasonal average of 6.6 m^3 s^{-1}, and maximum discharge 11.5 m^3 s^{-1}, compared to the seasonal average of 8.3 m^3 s^{-1}). These larger discharges were caused by warmer weather, with air temperatures being on average 3.1°C warmer than usual. Figure 6.49 shows the consistently warm and dry weather. The time from peak air temperature to peak runoff was

similar to average being 7.73 hours, an increase since June. The snowcover observed at the beginning of July was similar to 2010, but there was less snow at the foot of the Bionassay Glacier, and the snowcones on the valley sides covered a smaller area (Figure 6.48b). By mid-August the snowcover would have decreased further. The dye tracing in July and August showed although some injection points on the upper glacier gave slower and more dispersed traces at the end of July, by the beginning of August upper-glacier trace velocities had increased to between 0.58 m s^{-1} and 0.73 m s^{-1}. The lower glacier trace into S5 indicated the lower glacier local drainage had become more efficient. Although this does not demonstrate the early to mid-summer transition, it does allow comparison of the hydrograph between the early season when the glacier was snow-covered, and the mid-season when it was snow-free. It is strange these peaked hydrographs do not lead to a decrease in the lag time from peak air temperature to peak runoff. This may be because the main conduit system opens early on Miage Glacier, and so later in the season if air temperatures are warm and melt occurs at increasingly higher altitudes, meltwater travels increasingly longer distances. This increases the time for melt to reach the proglacial stream, even if the drainage system is efficient. There may also be short term velocity hysteresis within the moulin/conduit system during high discharges, which can increase meltwater travel times (Nienow *et al.,* 1996).

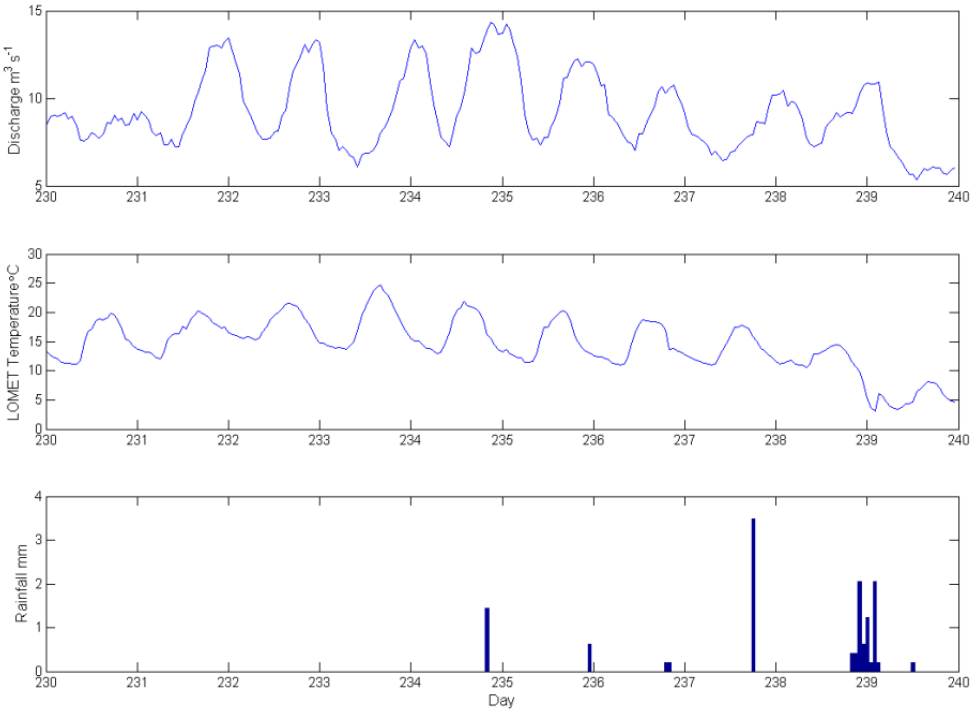

Figure 6.49 Close-up of the runoff, air temperature and rainfall (from LOMET) from days 230 to 240 in 2011.

It is evident in both 2010 and 2011 that periods of clearly diurnal hydrographs with a large discharge amplitude require consistently warm and dry weather. The loss of

snowcover from the upglacier clean ice is likely also required to increase the amplitude of the supraglacial hydrograph (Willis *et al.,* 2002). The change to a hydrograph with a larger diurnal amplitude as the snowpack receded was also seen on Haut Glacier d'Arolla (Swift *et al.,* 2005), Gangotri Glacier (Singh *et al.,* 2005) and Taillon Glacier (Hannah *et al.*, 1999), although the first two also exhibited a decrease in the lag time to peak runoff which was not apparent in the Miage data (Figure 6.36). Periods of dominant diurnal hydrographs were less common than expected, with periods of slightly cooler weather patterns not producing clearly diurnal hydrographs. These periods are the focus of the next section.

6.3.1.3.3 Phase 3: Saw-toothed runoff

The phase three runoff in 2010 begins around day 197, after which time one particular hydrograph type doesn't dominate for a significant period. The hydrograph statistics suggest the diurnal discharge amplitude is larger than average using both only diurnal hydrographs (2.7 $m^3 s^{-1}$, with 3.4 $m^3 s^{-1}$ the average), and all days (3.9 $m^3 s^{-1}$, with 3.6 $m^3 s^{-1}$ the average). The daily amplitude of the non-diurnally classified days is actually larger than the diurnally classified ones. The overall discharge magnitude is similar to average both for diurnal (5.8 $m^3 s^{-1}$, average 5.3 $m^3 s^{-1}$) and all hydrographs (5.9 $m^3 s^{-1}$, average 5.3 $m^3 s^{-1}$), with the diurnal discharge being larger than the mean for phase 2. The lag time to peak discharge for diurnal hydrographs (4.46 hours) was shorter than average and for phase 2, but including all hydrographs was much longer (8.17 hours). Overall the air temperatures, both in terms of mean and daily maximum at LOMET were similar to average within 1°C.

The phase 3 runoff in 2011 occurred both before (phase 3a) and after (phase 3b), the phase 2 runoff period. The mean discharge of the phase 3a and 3b runoff for diurnal and all hydrographs was higher (3a) and lower (3b) than average but by not much more than 1 $m^3 s^{-1}$, with both lower than the phase 2 mean discharge. In terms of diurnal amplitude (using only diurnal hydrographs) the phase 3a runoff had a higher diurnal amplitude than average and the phase 2 runoff, but during phase 3b the diurnal amplitude was lower than average and phase 2. Using both diurnal and all hydrographs the lag time of phase 3a and 3b (around 9-10 hours) was higher than phase 2 and the seasonal average. The mean and maximum air temperature at LOMET of the phase 3a and 3b periods was higher than average, but by less than 1°C.

In general the phase 3 runoff tends to occur during average weather conditions, and results in close to average proglacial discharges and diurnal amplitudes. Therefore if air temperatures are similar or only a little above average, the hydrographs will be less likely to

be diurnal. Perhaps Miage Glacier proglacial runoff is on average not diurnal, but tends towards completely rising or falling hydrographs. Diurnal hydrographs are confined to conditions when the weather is particularly warm.

The reason why phase 3 runoff has been named saw-toothed can be seen in Figure 6.50. The increasingly warm air temperatures during days 211 to 213 in 2010 lead to a gradually rising hydrograph, then after the precipitation inputs have passed and the weather cools the runoff decreases. The cooler days of 215 and 216 give a steady hydrograph. Overall the air temperature signal is smoothed and lagged so the diurnal signal is not apparent. Warmer temperatures lead to gradually increasing discharges, but a decrease in air temperature leads to a sharp runoff decrease. In 2011, Figure 6.51 shows the rise in night-time air temperature on day 240 results in a rising hydrograph on day 241. In the following days the discharge does become diurnal but the minimum flow has a clearer trough than the maximum flow has a peak. This is difficult to explain without a glacier-hydrological model that could account for the lag times of each of the sources of water, but may be because each part of the system with a certain lag had a similar magnitude. This meant one part of the system did not dominate and give the peak for the day. Usually the daily peak is attributed to efficiently routed clean ice melt, especially if the lag time is short, but on Miage Glacier this is not as clear. It could also be due to the gradual release of water from an aquifer (possibly the layer of subglacial sediment) attenuating the input hydrograph.

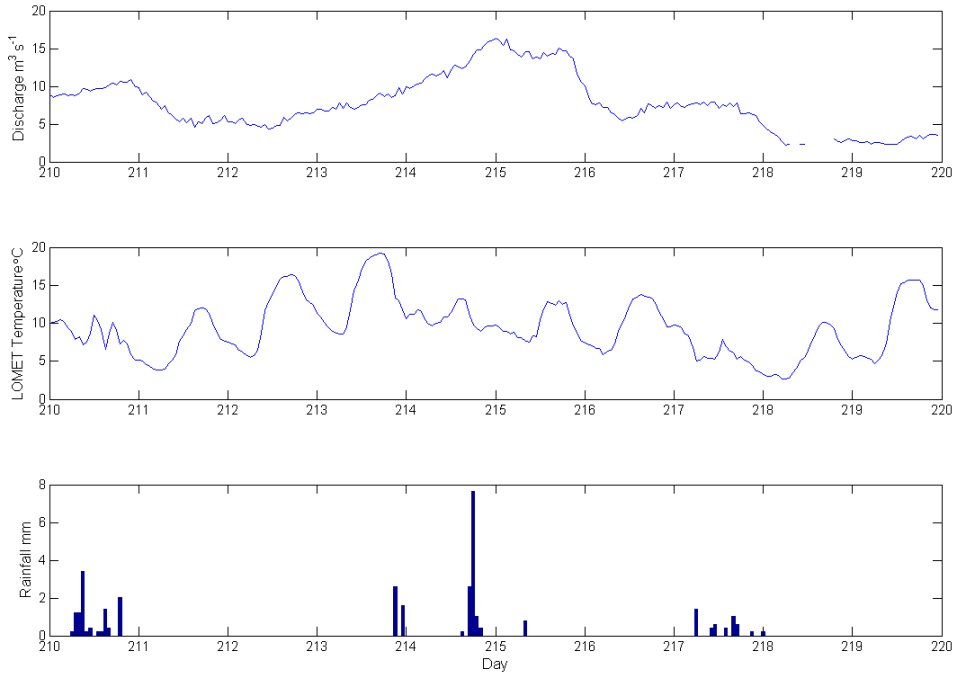

Figure 6.50 Close-up of the runoff, air temperature and rainfall (from LOMET) from days 210 to 220 in 2010.

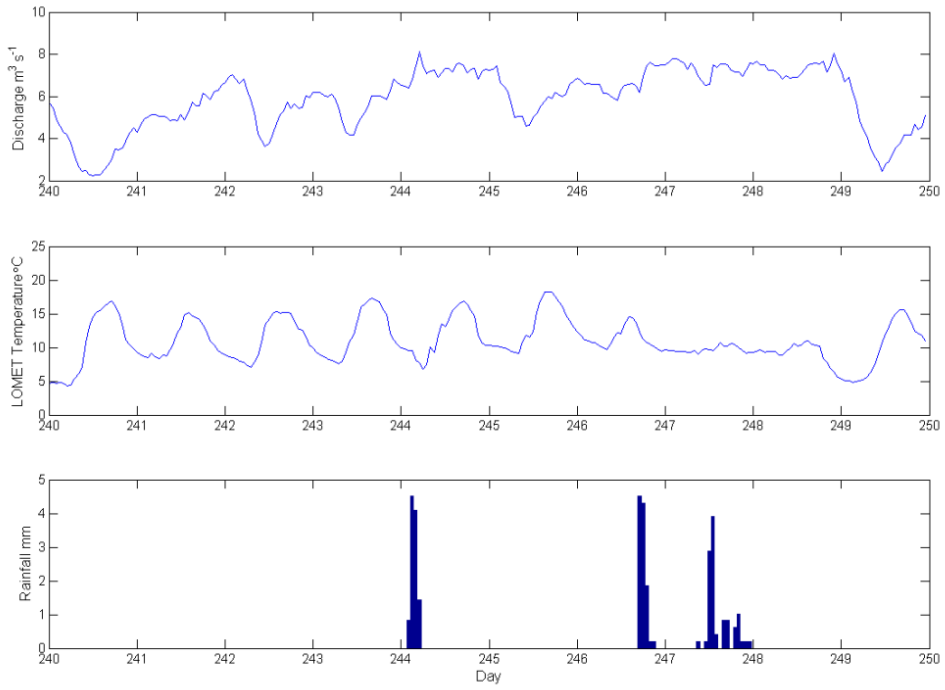

Figure 6.51 Close-up of the runoff, air temperature and rainfall (from LOMET) from days 240 to 250 in 2011.

It is possible the debris-cover, by providing a less peaked supraglacial hydrograph and a less efficient englacial/subglacial system is part of the reason why the diurnal melt peak is not as clear. It was mentioned by Covington *et al.* (2012) that smeared or multiple hydrograph peaks could be caused by multiple input points with different lag times. Since variations in debris thickness cause variations in the time of the supraglacial hydrograph peak (section 4.2.2), and the debris morphology leads to many, smaller input points (section 4.3), this may result in a flattened peak, especially if cooler weather means a larger proportion of runoff is from the debris-covered area. Saw-toothed hydrographs have not been mentioned on other glaciers, including Haut Glacier d'Arolla (Swift *et al.,* 2005) and Taillon Glacier (Hannah *et al.*, 1999). From the information available, there is not evidence of saw-toothed hydrographs on the Dokriani (Singh *et al.,* 1995), Lirung (Sakai *et al.,* 1997) or Gangotri Glaciers (Singh *et al.,* 2006b), although the Dokriani Glacier hydrograph was measured hourly for only one day, and the graphs of the Gangotri and Lirung Glacier runoff give only 3 or 4 consecutive days of hourly flow data under clear weather. They all do show periods of clearly diurnal runoff during clear weather, so perhaps Miage Glacier is an anomaly in showing a less clear diurnal signal under average weather conditions. It would be interesting to compare whole runoff records of other clean and debris-covered glaciers to determine whether the area or thickness of the debris cover, especially when compared to the area and altitude of clean ice, may control the existence of a less clear diurnal runoff signal.

6.3.2 Summary of main findings of proglacial runoff analysis

Overall the debris, by attenuating the input hydrograph, reducing the efficiency of the local subglacial drainage system, and possibly through the creation of many, smaller input points, may lead to:

1. The larger baseflow component during lower discharge periods identified in section 6.3.1.1.
2. Increased lag times from peak air temperature to peak runoff, as well as a period when conductivity rises in phase with discharge due to the increased solute load of sub-debris melt (section 6.3.1.2). Although melt from the tributary glaciers which has longer travel times and potentially a greater solute load (from an inefficient upglacier subglacial system or post-mixing chemical reactions), may also contribute to the discharge and solute peak.
3. The finding that large amplitude diurnal hydrographs were less common than expected and occurred only when conditions were warmer than average (phase 2) and snow no-longer covered the upglacier clean ice areas. The debris therefore has a similar influence as snow in attenuating the proglacial hydrograph.

Furthermore it was also found that:

1. There was not a clear decrease in the lag time between melt and runoff as the season progresses – possibly because the main channelized system opens early on Miage Glacier.
2. Under average weather conditions the runoff has a 'saw-toothed' appearance (phase 3 runoff) in which the hydrograph troughs are clearer than peaks. This may also be related to the debris cover or subglacial sediment, but more work is needed to understand the existence of a 'saw-toothed' runoff hydrograph.

7 The influence of debris on the water balance

The water balance is used to understand the magnitude of the input and output components and how they vary over time. In this section the inputs and outputs were quantified for the Miage Glacier catchment, with the storage estimated as the residual. This was done to understand the relative importance of meltwater and rainfall, and whether short term storage or release of water may influence the proglacial hydrograph. Inputs to the water balance include rainfall and glacial ablation from surface melt; from within the glacier (due to dissipation of strain energy); and from beneath the glacier (due to frictional and geothermal heat). Groundwater flow and condensation are also included as inputs. Outputs include evaporation, losses to groundwater and proglacial runoff, with the short term storage calculated as inputs minus outputs (Willis *et al.,* 1993). In the long term glacial ablation is thought of as a negative storage component (Jansson *et al.,* 2003), but since data was only available from the melt season it will be considered as an input to the system. In the second part of the chapter the overall influence of the debris on two of the water balance components, melt and evaporation will be quantified by comparing the results of the distributed model with a 'no debris' scenario.

7.1 Measured water balance

It is important to clarify how each of the water balance components were calculated. The inputs of surface glacial melt and rainfall are as calculated by the distributed surface energy balance model (see section 3.2.4 for details). Melt within and beneath the glacier was not considered as the quantity of water involved is likely to be at least an order of magnitude smaller than the other input components (Willis *et al.,* 2003). In terms of outputs, the evaporation was calculated within the distributed model, and proglacial runoff was measured at the northern lobe proglacial stream (see sections 3.2.4.1 and 3.4.1). Although evaporation from beneath the debris was calculated from the empirical lysimeter measurements, it was considered zero over ice and snow, and areas of bare rock outside the glacier. Evaporation of rainfall from bare rock is likely, and is probably of similar magnitude as from debris (Braun *et al.,* 1994), but it was not measured in this study, and the rate of decrease in evaporation with altitude in the Alps in the literature is very varied due to measurement uncertainties (Lang, 1981). Vegetation cover within the catchment is limited. Unfortunately the groundwater component was not measured during this study.

Evaporation of rainfall could have been calculated using the modelled latent heat flux but there were gaps in the surface relative humidity data (within which the latent heat was presumed zero) which affects the calculation of latent heat over debris. Furthermore, DEB-model does not completely capture the processes of evaporation from the debris. In DEB-model latent heat is only calculated when the relative humidity at the surface is 100 %, however evaporation of water stored within the debris could occur if the surface humidity was less than 100 % (as inferred from analysis of vapour flow within the debris, section 4.4.2). This implies evaporation of stored melt/rain water occurs more constantly than was modelled. During or after rainfall the location of the drying front will move to the debris surface (i.e. the air at the surface will be saturated), and it is under these conditions the latent heat flux is calculated in the model. It was therefore decided to use the bulk values of evaporation of rainfall measured by the lysimeter, and since any condensation onto the surface which percolated into the lysimeter would have reduced the quantity of evaporation calculated, it can be thought of as included within this measurement. Sublimation was assumed to be zero, as it tends to be common only on dry Arctic and low latitude glaciers (Benn and Evans, 1998).

The water balance components are given in Table 7.1. The errors given were calculated as follows. For melt the standard error of the estimate of sub-debris melt was used, as calculated from the difference between the modelled value and that measured at stakes across the glacier of 0.005 m w.e. d^{-1} (Table 4.2). This was converted into a percentage error of 23.8 % using the mean ablation over the entire glacier in the 2010 season of 0.02 m w.e. d^{-1}. Only the error of sub-debris stakes was used due to the short measurement periods of the dirty ice and snow stakes. The rainfall error was calculated from the standard error of the estimate of the difference between the total daily rainfall as calculated using the rainfall lapse rate and that measured at UPMET between days 167 and 219 in 2011. This equated to 4.52 mm d^{-1}, which was converted into the percentage error of 34.1 % using the average rainfall measured at UPMET (on rainy days only) of 13.3 mm d^{-1}. The standard error of the estimate was calculated including the days in which it rained at UPMET but not LOMET, this resulted in a large rainfall underestimate on those days and occurred because the rainfall in the model was lapsed using the rainfall at LOMET as the starting value. It rained at UPMET but not LOMET on 4 days within a 53 day record (7.5 % of the time). The proglacial runoff error was calculated from standard error of the estimate of the discharge as calculated from the rating curve (using the spot gaugings as the measured value) of 0.76 m^3 s^{-1}, which gave a percentage error of 14.6% using the average daily discharge in 2010 of 5.37 m^3 s^{-1}. The errors in the calculation of evaporation were more difficult to quantify, since the modelled value was empirically derived from the

lysimeter measurements. Ground-flush rain gauges are similar in design to the lysimeters and they tend to underestimate rainfall by 2-7 % (Marsh and Dixon, 2012), this would result in evaporation being overestimated, but this will be compensated by the presumption of zero evaporation over bare rock areas outside of the glacier. The error was therefore estimated as 10 %. Errors of inputs, outputs and storage were calculated cumulatively from their respective constituents.

Table 7.1 Table of the magnitude of water balance components in 2010 and 2011. Values are the total volume of water in 10^6 m^3 over the period of days given. Two time periods are given in 2011, since proglacial runoff data was only available for part of the season.

		2010		2011			
Days		**159-247, 250-253**	**Error (±)**	**165-255**	**Error (±)**	**165-169, 216-255**	**Error (±)**
Melt		23.35	5.55	23.72	5.64	11.99	2.85
Rainfall		13.13	4.47	16.78	5.72	8.37	2.85
Inputs		36.48	21.10	40.50	23.42	20.36	11.77
Runoff	**10^6 m^3**	43.76	6.40			30.15	4.41
Evaporation		0.42	0.04	0.64	0.06	0.31	0.03
Outputs		44.18	10.88			30.46	7.50
Storage		-7.70	6.35			-10.10	8.33
% melt of inputs		64.00		58.57		58.90	
% rainfall of inputs		36.00		41.43		41.10	
% evaporation of rainfall		3.16		3.83		3.71	

The magnitudes of the components calculated over the whole season (days 165-255 in 2011) will now be described. Total inputs were 4.02×10^6 m^3 larger in 2011 compared to 2010, mainly due to greater rainfall in 2011. This resulted in more evaporation in 2011, but the quantity of ablation in both years was almost identical. Glacial melt was a very consistent source of runoff between years, but precipitation was more variable. Inputs were composed mainly of melt, being 64 % in 2010 and 59 % in 2011 using annual totals, however the average of daily values was 76% in both 2010 and 2011. Evaporation was a small portion of rainfall being 3.2% in 2010 and 3.7% in 2011, using hourly totals, and 3.6% and 3.8% using average of daily values (although note the caveats mentioned above). These values were much lower than the lysimeter measurements due to the presumption of no evaporation from clean ice or bare rock areas.

The magnitude of the proglacial runoff component cannot be directly compared between seasons because of the different periods of measurement. However the average runoff in 2010 of 5.46 m^3 s^{-1} was lower than the average runoff in 2011 of 7.75 m^3 s^{-1}, although this is likely skewed since August was much warmer than July 2011, and the July runoff data was missing. In both years storage was a significant negative component of the water balance, indicating that more water left the glacier than entered it. Some of this

negative storage may be due to undercatch of rainfall at high elevations (see section 4.1.1.3), or of the melt of snow out with the glacier that was not modelled. However, the errors of the storage component (-7.7 ± 6.35 × 10^6 m^3 in 2010 and -10.10 ± 8.33 × 10^6 m^3 in 2011) are almost as large as the component itself.

Table 7.2 Water balance components by month in 2010 and 2011, the values are the daily average for the whole Miage Glacier catchment. Values are given in m^3 s^{-1} since the periods used vary in length.

	Days	Melt	Rain	Input	Runoff	Evap.	Output	Storage	% melt of inputs	% rainfall of inputs
2010					(m^3 s^{-1})				%	
June	159-181	2.68	1.69	4.37	3.19	0.036	3.22	1.15	61	39
July	182-212	3.35	1.71	5.06	5.98	0.055	6.03	-0.97	66	34
Aug	213-243	2.81	1.62	4.43	7.03	0.060	7.10	-2.66	63	37
Sep	244-253	2.32	1.18	3.50	3.73	0.045	3.78	-0.34	66	34
Season	159-253	2.90	1.62	4.52	5.45	0.051	5.50	-0.96	64	36
2011					(m^3 s^{-1})				%	
June	165-181	3.16	3.29	6.46	11.53	0.132	11.79	-3.57	49	51
July	182-212	2.69	1.97	4.66	-	0.088	-	-	58	42
Aug	213-243	3.26	1.55	4.82	7.62	0.046	7.67	-3.05	68	32
Sep	244-255	3.02	2.41	5.42	6.48	0.087	6.57	-1.15	56	44
Season	165-255	3.02	2.13	5.15	7.75	0.082	7.83	-2.60	59	41

The values of the average monthly water balance components are in Table 7.2. In the following discussion the average is the average of the component over the season. In 2010, July had the greatest inputs, caused primarily by an increase of ablation (15% above average), as well as a slight increase in rainfall. September had the lowest average inputs, due to a combination of 20% lower than average ablation and 27% lower than average rainfall. Evaporation was highest in August, which was not when rainfall was highest, but was due to evaporation being lower earlier in the season when rain fell on snow and evaporation was assumed zero. The higher July ablation was caused by particularly warm weather, with air temperatures at LOMET almost 3°C warmer than average. This was caused by a persistent North African anticyclone that resulted in a positive anomaly of mean monthly air temperatures in northern Italy of between +2°C and +4°C (Società Meteorologica Italiana, 2010). Conversely, September was 2°C cooler than average and had 13% less than average daily incoming shortwave radiation.

Runoff (and consequently outputs) were lowest in June, being 41% lower than average, even though rainfall was greater than average and melt was only 8% lower. This period corresponded with positive storage equating to 1.15 m^3 s^{-1}, which can also be seen as a region of positive storage during days 160 to 163 and 166 to 169 (Figure 7.3). The

snowpack was deep and continuous above 2289 m a.s.l. at the beginning of the 2010 field season, so it is likely a proportion of rainfall in June refroze or was stored within the snowpack or firn. Refreezing occurs when melt (and presumably rainfall) percolates through the cold firn in springtime (Reijmer and Hock, 2008) where the water forms ice layers and lenses in the percolation and wet-snow zones (Paterson, 1994). The most favourable conditions for superimposed ice formation are when liquid water contacts below freezing glacier ice at the base of the snowpack (Bøggild, 2007). Both refreezing and superimposed ice formation would reduce immediate runoff. Water could also be stored beneath the glacier, either in the distributed subglacial system or in a till aquifer beneath the glacier (Jansson *et al.,* 2003). Even though the errors of the storage component are large, the general trend of positive early season storage and negative storage during the rest of the season does correlate with results of other workers, for instance on South Cascade Glacier, USA (Tangborn *et al.,* 1975) and Storglaciären (Östling and Hooke, 1986). By mid-season the reorganisation of the drainage network and removal of the snowpack likely resulted in the reduction in storage.

In 2011, inputs were largest in June, due to a significant quantity of rainfall (54% higher than average, totalling 4.8×10^6 m^3 over the month, concentrated in two storms around day 169 and 173, Figure 7.2). The large rainfall magnitude meant this month had the highest evaporation, and was the only one in both years when rainfall was a higher percentage of runoff than ablation. Contrary to 2010, inputs were lowest in July, caused by ablation and rainfall being lower than average, ablation by 11%. This month was anomalously cool, being 1.8°C cooler than the seasonal average. The inputs in August weren't much greater than in July, even though it had the highest average ablation, as this was offset by a low average rainfall. This meant ablation was the greatest percentage of runoff of all months in both years. In terms of outputs they were greatest in June 2011, due to the large rainstorm mentioned above, this resulted in proglacial discharge being an average of 11.5 m^3 s^{-1} in June (although there were only 5 days of data). Proglacial runoff was high in August and September compared to 2010, due to both higher melt inputs, and in September higher rainfall. Storage was negative in all of the measured months, and the majority of days (Figure 7.4). Since the snowpack was noticeably thinner and less extensive than in 2010, it is suggested the capacity for storage of water in the snow was lessened.

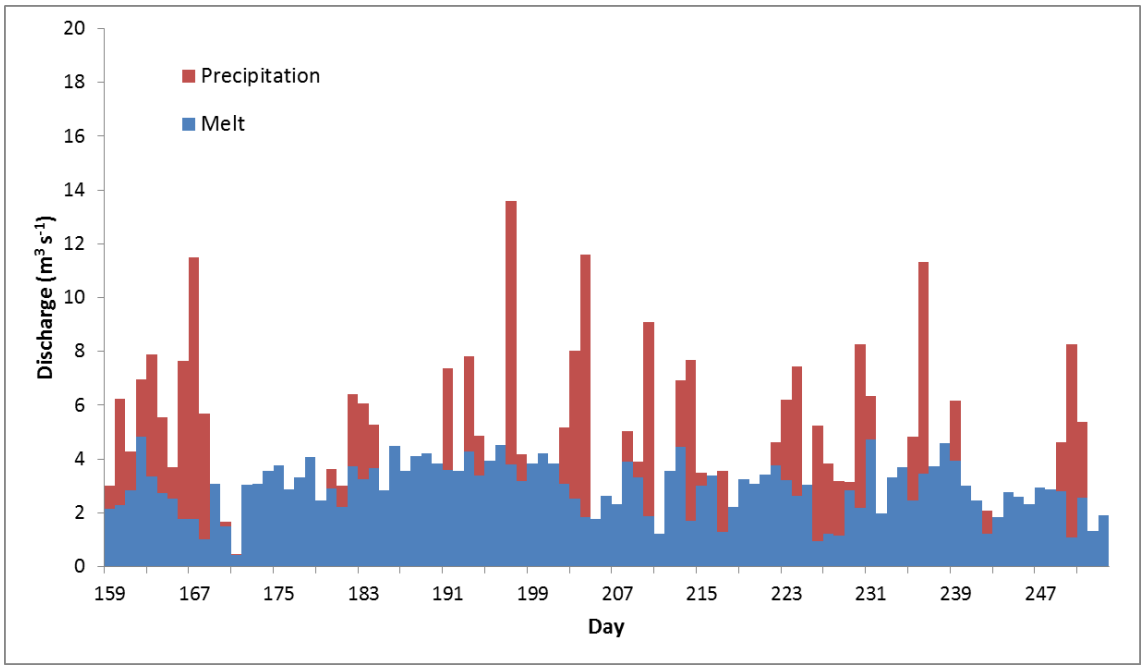

Figure 7.1 Daily modelled values of melt and precipitation for the Miage Glacier catchment in 2010.

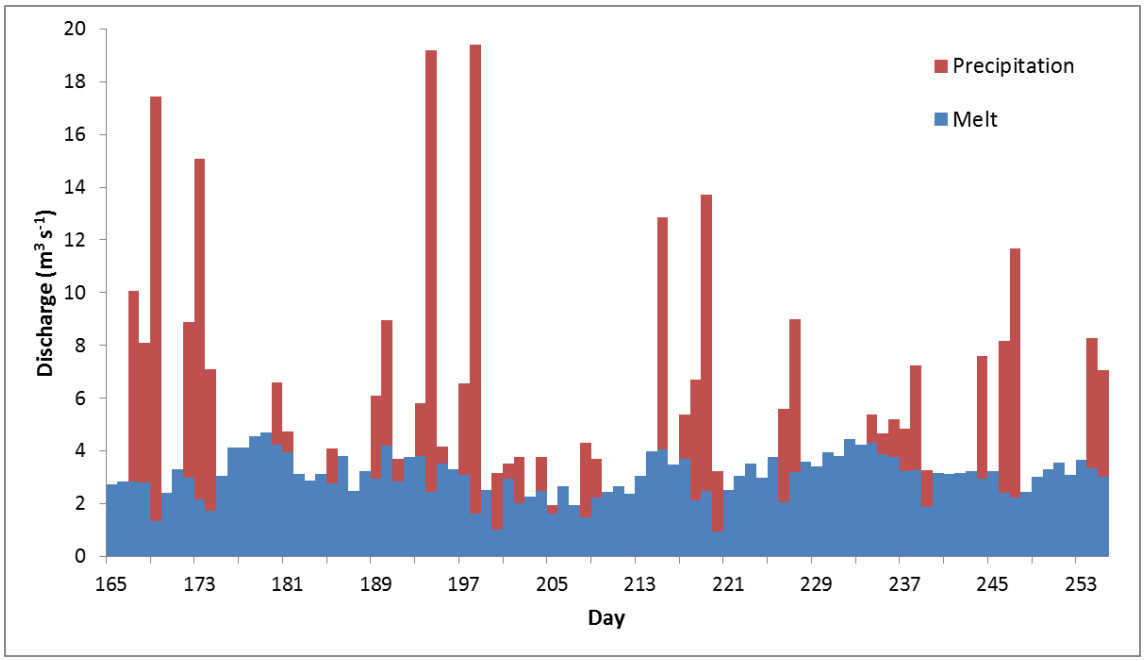

Figure 7.2 Daily modelled values of melt and precipitation for the Miage Glacier catchment in 2011.

The daily pattern of inputs can be seen in Figure 7.1 and Figure 7.2. The glacial melt provides a consistent baseflow over the summer, with most major peaks being rainfall dominated. The contrasting conditions in July (warm in 2010 and cool in 2011) show as regions of higher and lower melt respectively, and there were two periods when inputs were particularly low in 2010 when there was no rainfall and melt was very low (days 171 and 210). These periods result in recession flows in the proglacial hydrograph (see section

6.3). Rainfall appears more frequent but with a smaller magnitude in 2010, whereas in 2011 there were long dry periods, intersected by large rainfall events (e.g. days 169 and 198).

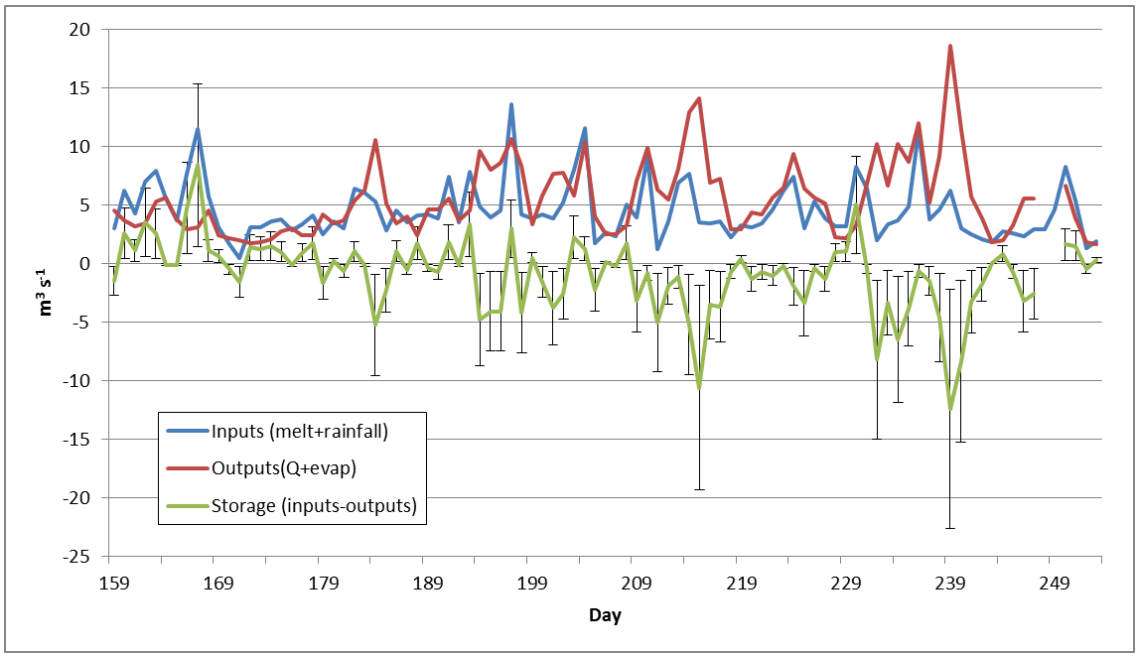

Figure 7.3 Water balance components for the Miage Glacier catchment in 2010. Error bars represent ±82.45 % of the storage value.

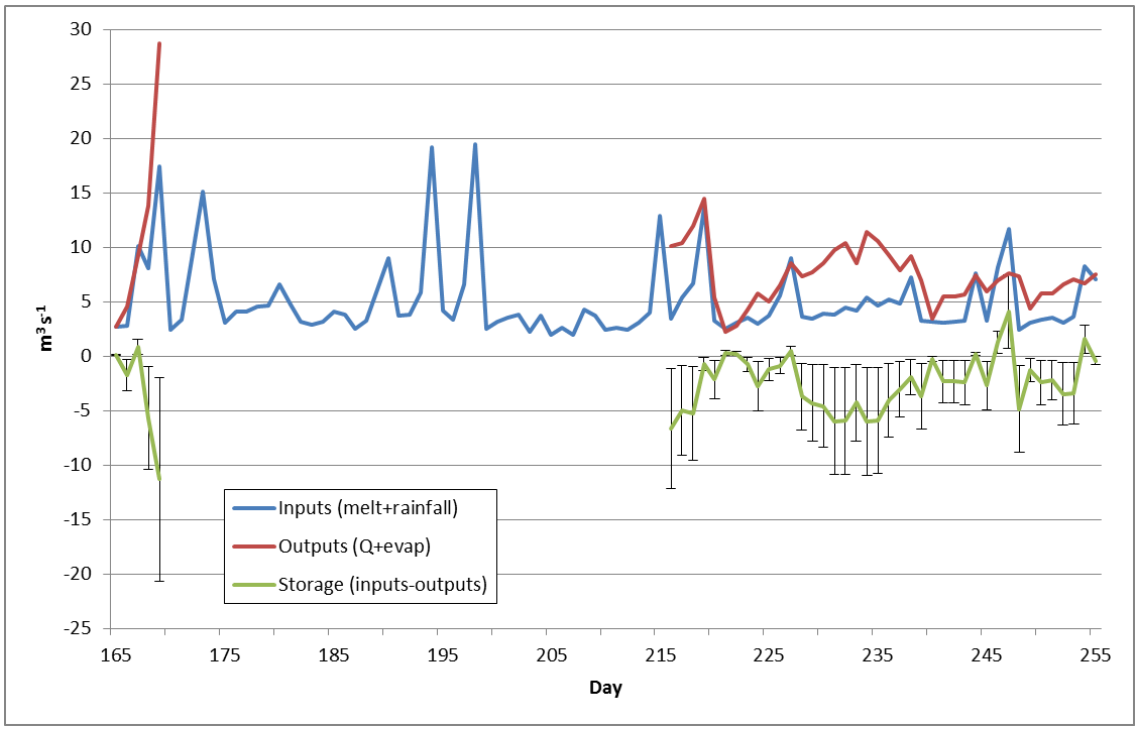

Figure 7.4 Water balance components for the Miage Glacier catchment in 2011. Error bars represent ±82.45 % of the storage value.

Although the general trends in water storage can be identified, the magnitude of the daily storage values can vary greatly between days. Part of this variation may be due to underestimation of the inputs – specifically rainfall. It can be seen clearly in Figure 7.1 and

Figure 7.2 that variations in rainfall result in the largest variations in the inputs to the glacier. Periods of very negative storage (for instance day 239 in 2010, Figure 7.3) could be the result of raingauge undercatch, or of rainfall occurring on the upper but not lower glacier (resulting in no measured rainfall at LOMET, and therefore no modelled rainfall). Weingartner *et al.* (2007) stated that problems in the determination of the water balance for mountainous areas were often due to inaccuracies in the determination of precipitation. In the distributed model the precipitation was determined solely by elevation, although factors such as the air mass characteristics and large scale pressure patterns are also important in shaping the rainfall patterns of individual events (Barry, 2008). Considering that precipitation provided 39 % of inputs to the glacier (mean of season long values in 2010 and 2011), and that the error associated with this component was large (34.1%), future efforts should be focussed on more accurately determining the quantity of rainfall across the catchment in order to improve the certainty of the determination of the storage component.

7.2 Modelling the influence of the debris on the melt and evaporation water balance components

The debris influences two parts of the water balance; evaporation and melt, and it therefore influences the proglacial runoff. To investigate this the melt model was run assuming the glacier was entirely debris-free (all cells were classed as clean ice, with snow cover as before), with the air temperature at UPMET and LOMET lowered by 2.4°C (the average difference between ICEMET and UPMET air temperature) to account for the cooler air temperatures over ice. It is more difficult to account for the differences in the wind field and air relative humidity so they have been handled in the same way as in the 'debris-covered' model. The existence of the snout at such a low elevation is only possible because of preservation of the ice by the thick debris cover. Without a mass balance model to evolve the glacier without a debris-cover it can be assumed its snout would lie at a similar elevation to nearby clean glaciers. The snout elevation of the nearby Brouillard and Freiney Glaciers was about 2267 m a.s.l. and 2200 m a.s.l. in 2005 respectively (mean of 10 heights taken from the 2005 ARPA DEM and 2005 aerial photograph) with the lowest elevation of Miage Glacier snout being 1735 m a.s.l. The area of Miage Glacier below 2233 m a.s.l. (mean of the Brouillard and Freiney snout positions), which would equate to that 'lost' without the debris-cover, would equal 2.5 km^2 in area, or 24% of the glacier outline in 2005. The 'no debris' model was only run for glacier cells above 2233 m a.s.l.

The 'no debris' model shows melt was highest on south facing slopes and the lowest elevation areas of the crevassed icefalls, although generally melt decreased with distance upglacier (Figure 7.5b). This is unlike the debris-covered model where the highest melt rates were found around 2500 m a.s.l. Melt was lower in the 'no debris' scenario compared to the 'debris-covered' one, with average daily melt across the glacier being 2.65 $m^3 s^{-1}$, compared to 2.90 $m^3 s^{-1}$, which equates to a reduction of 2.1 $\times 10^6$ m^3 of water over the season (-8.6% of total melt). This will be due to the reduction of the size of the ablation area in the 'no debris' scenario, as well as the lack of high ablation dirty ice areas, and the cooler air temperatures over ice compared to debris. Temporally (Figure 7.5a), the decrease in melt is greatest in spring, when snow cover dominates as the melt source, but the model does not take into account melt of proglacial snowcover which would add to spring runoff. The percentage reduction in daily average melt decreases to a mean of -7.9% from day 200 onwards which implies that even when ice melt dominates, melt is less without debris. Therefore, the debris increases total melt because the effects of the increased glacier area, higher air temperatures and increased melt rates where ice is dirty are greater than the decrease in ablation where debris is thick.

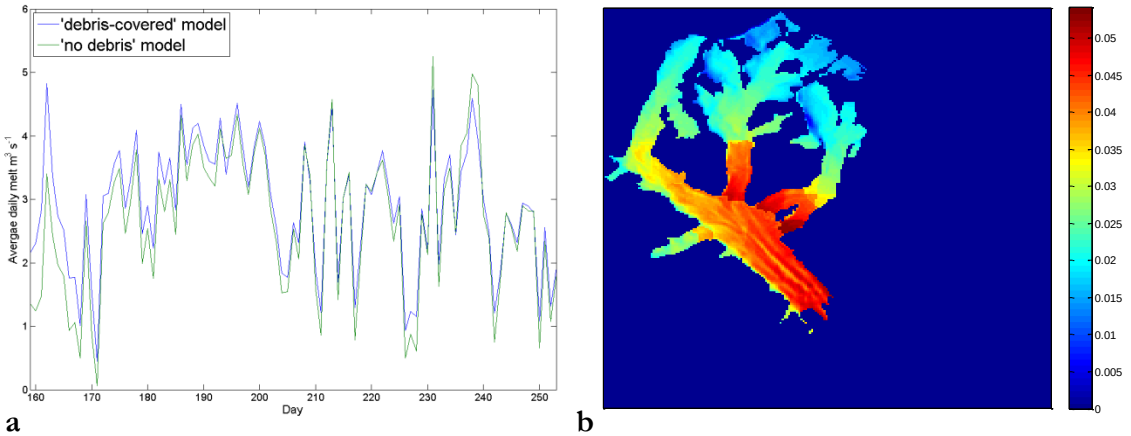

Figure 7.5 Results from the 'no debris' model, with a) the daily average melt of both the 'no debris' and 'debris-covered' models during 2010, and b) average daily ablation (in m w.e. d^{-1}) in 2010 with the 'no debris' model.

The evaporation of rainfall over debris is likely greater than over clean ice due to its warm surface, but it depends upon the debris permeability (section 4.4.1). However as evaporation of rainfall over ice was not modelled specifically this will not be considered further. What can be compared is the overall latent heat flux. The 'no debris' model shows evaporation prevails across the whole glacier (Figure 7.6) with values increasing upglacier because of the lower air temperatures, and therefore lower vapour pressure at altitude (Paterson, 1994). The values are also low on the main tongue but this model does not include the presence of strong downwards glacier winds caused by the cooling of air over the sloping glacier surface, common on alpine glaciers (Oerlemans, 2010). Strong katabatic

winds are generally absent on Miage Glacier (Brock *et al.,* 2010), and so evaporation lower on the glacier in the 'no debris' model may be underestimated. Total latent heat is more negative (greater evaporation) in the 'no debris' compared to the 'debris-covered' scenario, with the average latent heat for an hour being -45 W m^{-2} and -34 W m^{2} respectively, between days 215 to 256 in 2011. This equates to a 30% increase in the magnitude of evaporation when the debris is removed. Overall the increase in evaporation due to the constant availability of water at the ice surface overcomes the increase in evaporation of rainfall on debris due to the warmer surface temperature. However, the calculation of the vapour flux through the debris indicated that evaporation from beneath the surface of the debris may occur, but latent heat only occurred in the model when the debris surface was saturated. More work is required to understand evaporation of water from within the debris before the overall influence of the debris on evaporation can be ascertained.

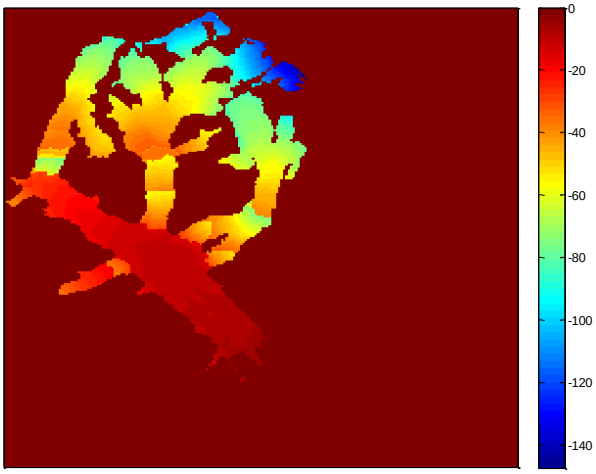

Figure 7.6 Average hourly latent heat flux across the glacier using the 'no debris' scenario in 2011, values are in W m^{-2}.

7.3 Summary

The main findings of this chapter are as follows:

1. Melt provides around 60% of the water balance inputs, with this input having a relatively small variability between years and throughout the season.
2. Rainfall provides a smaller proportion of the inputs to the glacier than melt but it has a much greater variability between years. Rainfall tends to result in the largest fluctuations in daily inputs.
3. Storage was negative on average in both years, but was positive for some days in June 2010. It is likely this was related to the considerable snow cover during this time.

4. Overall the debris increases the melt input compared to a 'no debris' model. This suggests that the larger glacier area, warmer air temperatures and increased melt where debris is thin, compensates for the decrease in ablation beneath thick debris.
5. Modelling suggests that the latent heat flux is reduced by the debris, since modelled evaporation only occurs when the debris is saturated. However, this does not take into account the possibility of evaporation of water from within the debris.

8 Spatial and temporal variations in glacier velocity

This chapter aims to examine the spatial and temporal variations in glacier velocity across the glacier and to interpret how these are influenced by variations in water inputs and the structure of the hydrological system. The velocities will be studied at a daily resolution to investigate the short-term glacier dynamics, as well as at an annual and seasonal time scale, to understand the overall patterns. The results will then be discussed in the context of the debris' influence on the glacier dynamics.

8.1 Results

The velocity variations during each of the study periods will be described first, followed by the annual and seasonal velocities. Horizontal velocities in cm d^{-1} for all points are given in Figure 8.1 and Figure 8.2, which are referred to throughout the rest of the chapter. To allow periods of faster or slower than average velocities to be identified easily, and so the magnitude of change is relative to the usual variability of a specific point, most daily velocity measurements are given as the difference from the point's average velocity in units of each point's standard deviation (calculated over the study period discussed). The standard deviation of all points (except SL1) was larger than the average distance error of the dGPS measurement technique (± 0.005 m). Velocity anomalies greater than ±1 σ are therefore interpretable. Actual velocities in cm d^{-1} are also given in June of both years. Velocity values which are an average over two or more days are given on both the day of the second GPS measurement, and any other days after the first GPS measurement, as the velocity will be equally relevant to all days. This gives the appearance of a 'stable' velocity on the graphs so care is required in their interpretation. Vertical velocities have been adjusted for downslope movement of the point, following the glacier's flowline (section 3.5.2). Vertical velocities greater than 0.6 cm d^{-1} (the mean root mean squared error of the dGPS height measurements was ± 0.006 m) are likely not due to measurement error. The position of the dGPS points on the glacier is shown in Figure 3.1.

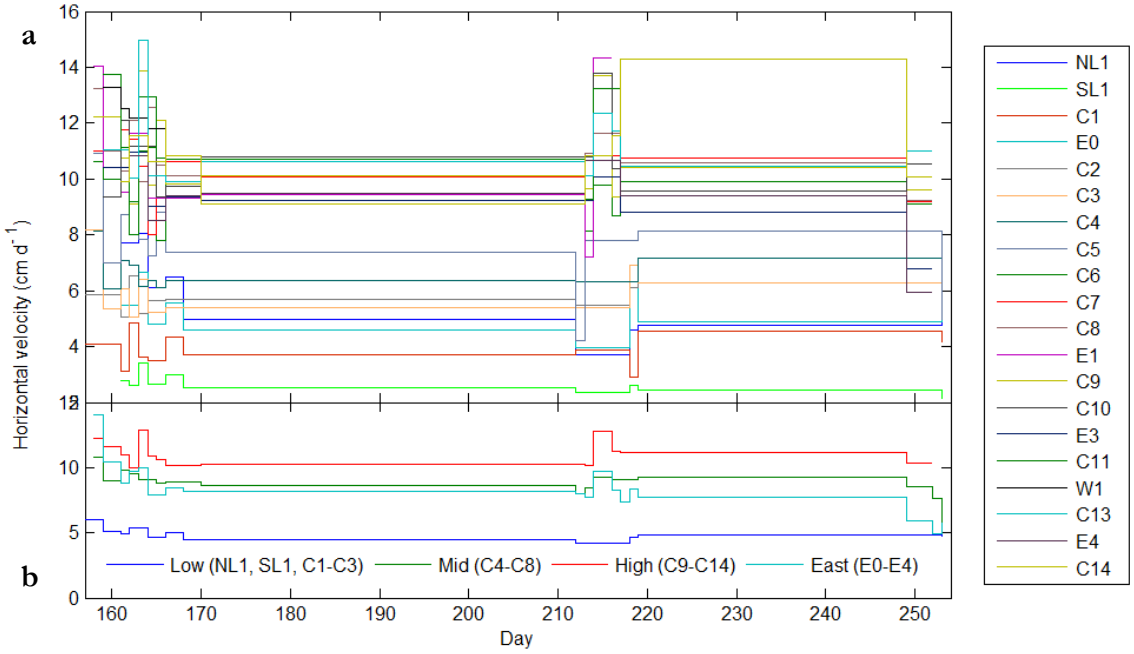

Figure 8.1 Horizontal velocities for a) individual points across the glacier and b) averaged over groups of points for different regions of the glacier, all measured in 2010.

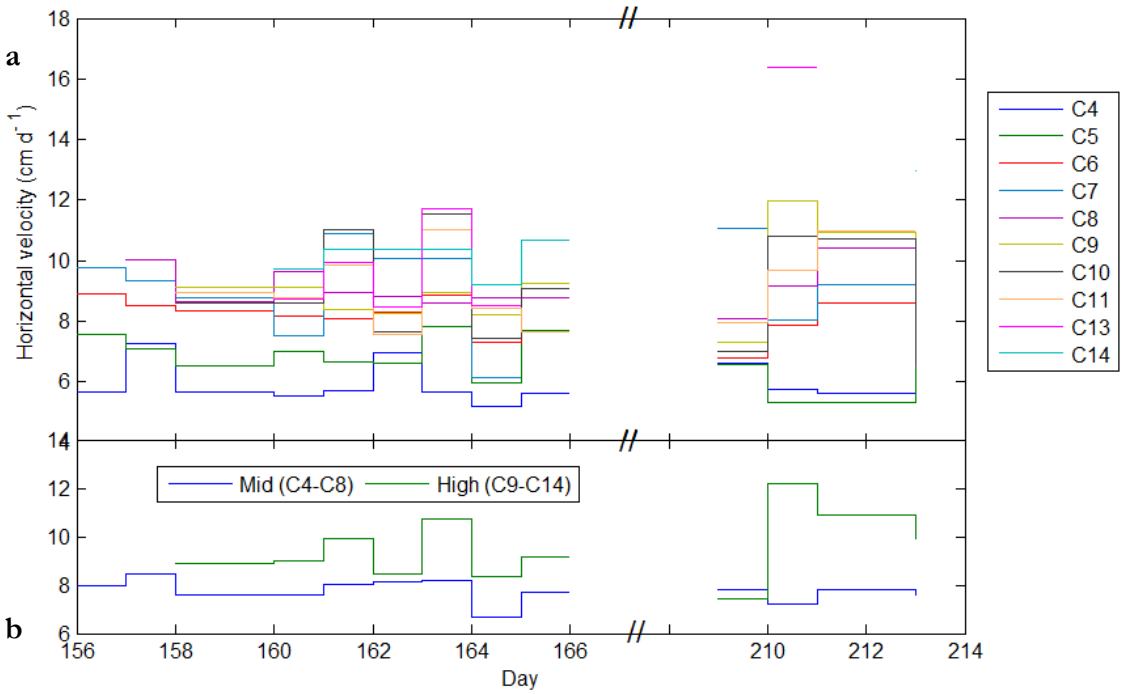

Figure 8.2 Horizontal velocities for a) individual points across the glacier and b) averaged over groups of points for different regions of the glacier, all measured in 2011. The graph is split on the x-axis since the mean velocities between the end of the June and start of the July/August fieldtrip could not be calculated (due to a change in reference position).

8.1.1 June 2010

The velocity variations during the June study period will now be described, with horizontal velocity anomalies given in Figure 8.3a (where the values given are the difference between the measurement and the June average velocity divided by the June standard deviation), and also in cm d^{-1} in Figure 8.4. Vertical velocities are given in Figure 8.3b.

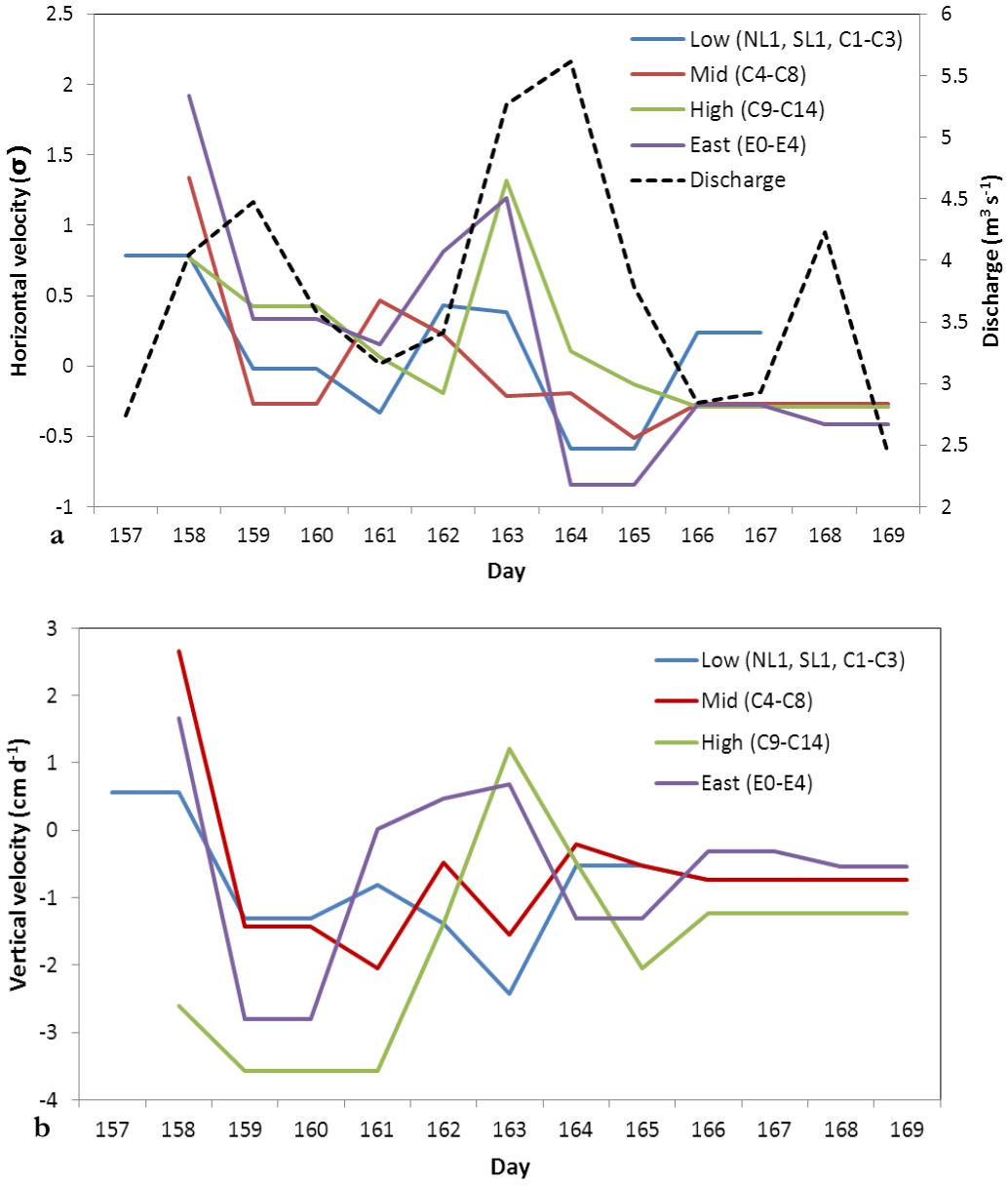

Figure 8.3 a) Averaged horizontal velocity anomalies in June 2010, with average daily proglacial discharge on the secondary axis, and b) averaged vertical velocities in June 2010, adjusted to remove the influence of surface slope.

The velocity of all points was faster than average on day 158. The points C3, C4, C5, C8 and E1 all experienced their highest horizontal velocity anomaly for June (all greater

than average by more than 1 σ), and C3, C4, C5 and C8 experienced their highest measured velocity of the season (Figure 8.1). Both C4 and C5 moved faster than average by more than 2 σ (8.1 cm d^{-1} and 10.9 cm d^{-1} respectively, Figure 8.4). The horizontal velocities of C6 and C7 were faster than usual, but not significantly. The vertical velocities of 5 points were greater than 0.6 cm d^{-1}, with C3, C6 and C7 exhibiting particularly significant vertical velocities (of 4.0 cm d^{-1}, 2.9 cm d^{-1} and 9.1 cm d^{-1} respectively, Figure 8.3b).

During days 159 and 160 the fastest points were higher up glacier (especially C11, with a line of slightly faster points C7-C9), with the mid-glacier (C3-C6) points being slower than average. None of the points had positive vertical velocities. Over days 160 to 163 the area of faster velocity between points C7 and C9 on day 160, appeared to move to between C4 and C7 on day 161, which transferred to the region below C2 (except SL1) on day 162, and then SL1, NL1 and E0 on day 163. This is shown in Figure 8.5 where orange and red dots are the points with faster than average velocities.

Figure 8.3a and Figure 8.4 show day 163 was characterised by fast horizontal velocities on the upper glacier above C9, with all points going significantly faster apart from E1, C10 and C11. C9 and C13 moved particularly quickly, at 13.9 cm d^{-1} and 15.0 cm d^{-1}, respectively (Figure 8.4). Most of the faster points had positive vertical velocities (C7, C9, C13, C14, E3 and E4) with all by more than 1 cm d^{-1}. The two points on the northern lobe (NL1 and E0) and one on the southern lobe (SL1) were significantly faster than usual. This pattern varies from day 158 when the entire glacier was faster, with the regions which were much slower on day 163 compared to day 158 being C8 and from C3-C5.

On day 164, C8 and W1 were the only points significantly faster and C8 had a positive vertical velocity of 2.4 cm d^{-1}. C6, C10, and C11 were faster than average (although for C10 and C11 this may be due to their measurement being an average from day 162 and 163 respectively). C6 also had a positive vertical velocity of 2.3 cm d^{-1}. On day 165 the glacier was generally slower than average, with only C5, C9 and W1 faster than usual. Only the lowermost points were measured on day 167 but none were significantly faster or slower than average. On day 169 all measured points (C6 and above) were slower than average, and none showed significant vertical uplift. This was despite a large rainstorm (Figure 4.24) resulting in high discharges on day 168 (4.23 m^3 s^{-1} on average), higher than the discharge on days 157 and 158 (2.74 m^3 s^{-1} and 4.05 m^3 s^{-1} respectively).

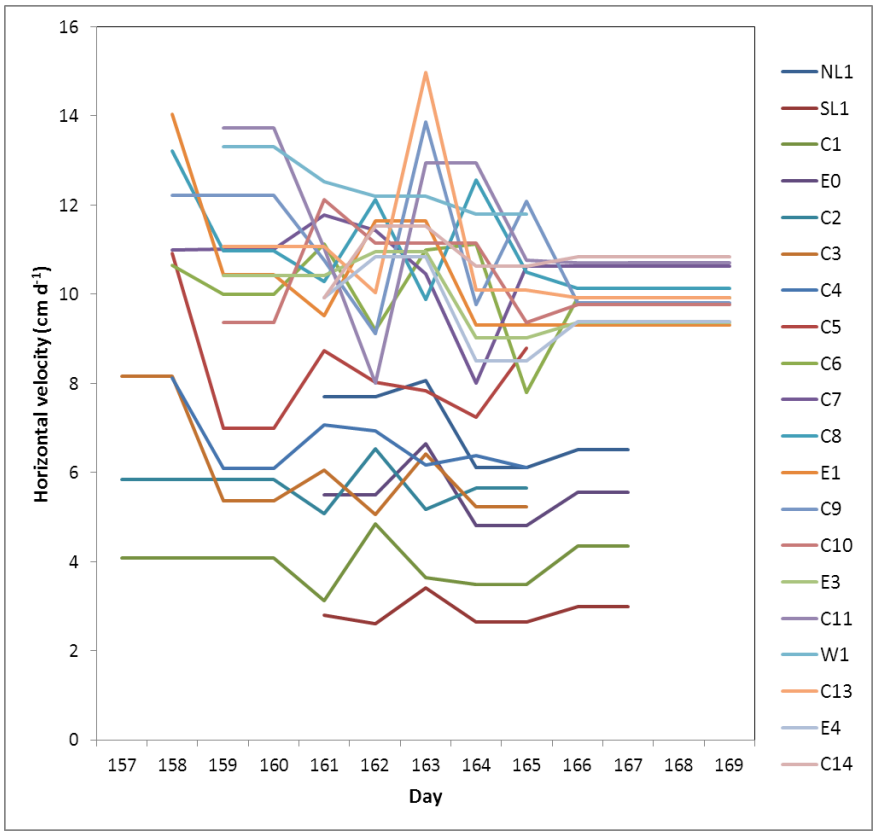

Figure 8.4 Horizontal velocities in cm d^{-1} for all measured points in June 2010.

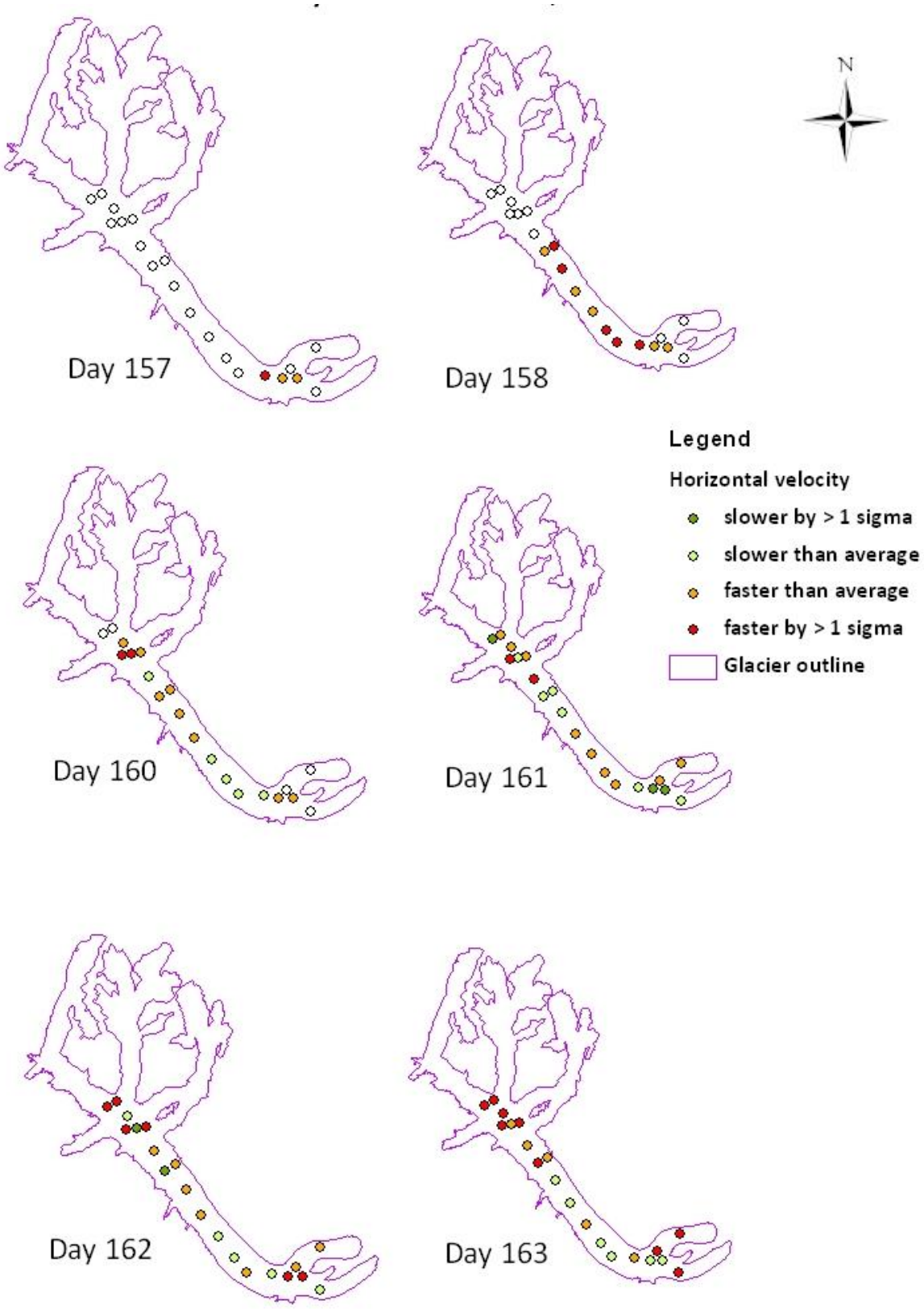

Figure 8.5 Spatial patterns in horizontal glacier velocities from day 158 to 163 June 2010. See Figure 3.1 for the naming of the GPS points.

8.1.2 June 2011

The glacier velocity results in June 2011 will now be described. Horizontal velocity anomalies are given in units of standard deviation calculated by finding the difference between the measurement and the June average velocity divided by the June standard deviation (Figure 8.6 and Figure 8.8a), although values in cm d^{-1} are also given (Figure 8.9). Vertical velocities are given in Figure 8.7 and Figure 8.8b.

On day 156, C5 and C6 moved significantly faster, and no points exhibited significant uplift. On day 157 all points measured were faster than average, with C4 and C8 being faster by almost 2 σ (7.2 cm d^{-1} and 10.0 cm d^{-1}, respectively). C8 had a large positive vertical velocity (1.6 cm d^{-1}).

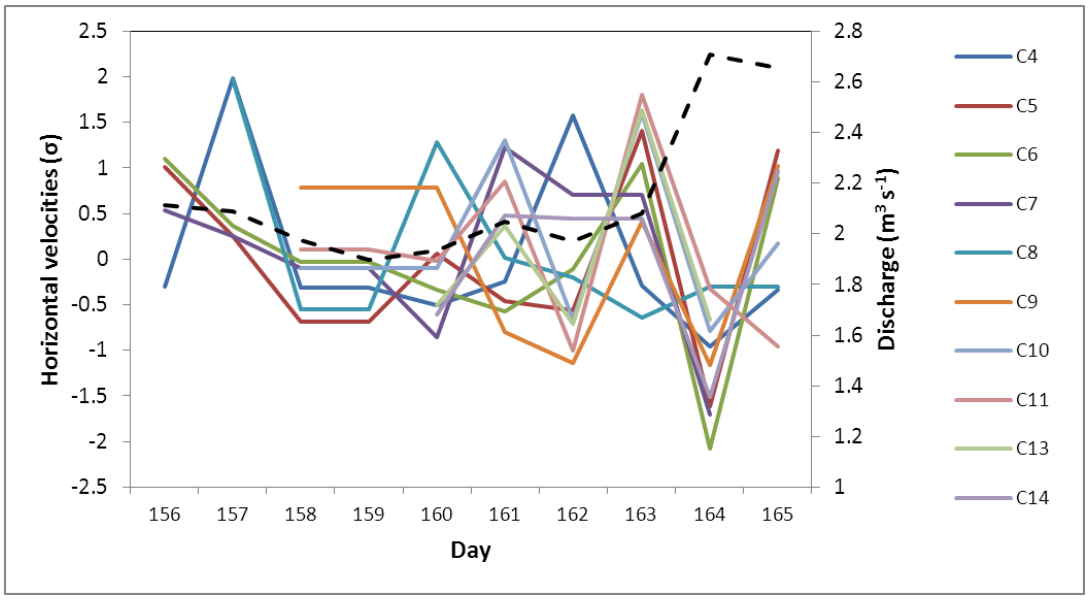

Figure 8.6 Net horizontal velocity anomalies and average daily proglacial discharge in June 2011. Discharge is shown in dashed black.

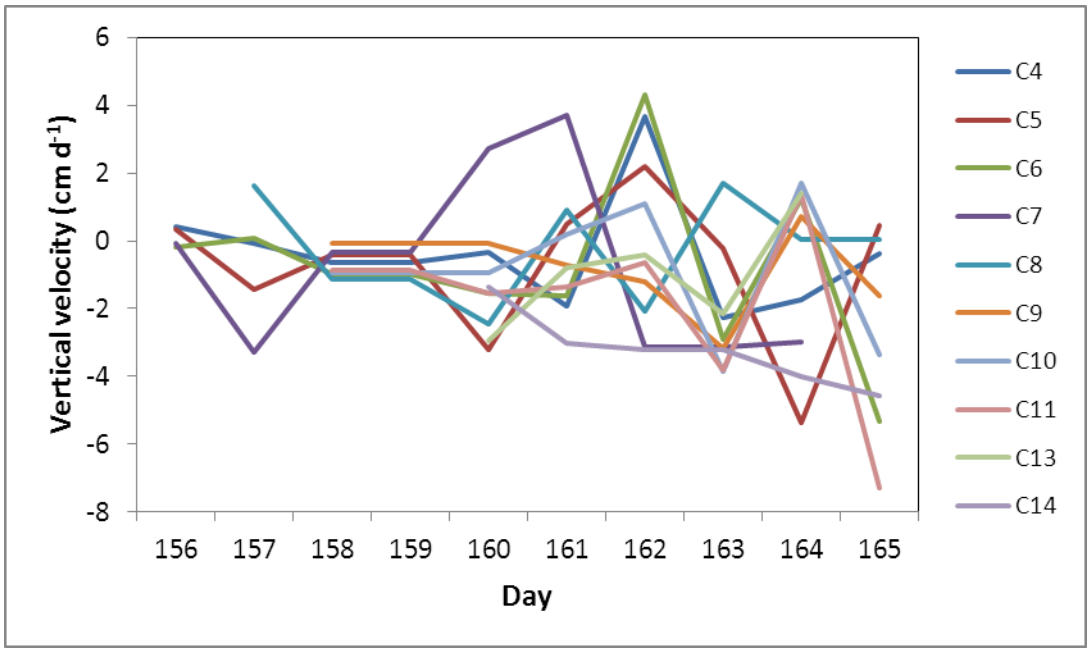

Figure 8.7 Vertical velocities adjusted for the influence of surface slope, June 2011.

On days 158 and 159 all points below C8 had a slower than average velocity, and on day 160 only C8 was significantly faster than average. The glacier velocities above C7 (except for C9) were faster than average on day 161 (C7 by 1.22 σ and C10 by 1.31 σ), and 4 points had positive vertical velocities (C5, C7, C8 and C10), with the uplift particularly large for C7 (3.7 cm d^{-1}). On this day the maximum air temperature (of 10.6°C) and peak discharge (of 2.1 m^3 s^{-1}) were the highest since day 157.

Most points on day 162 went slower than usual, except for C4, C7 and C14, with only C4 significantly faster (1.58 σ) and exhibiting a positive vertical velocity (3.67 cm d^{-1}). Despite slower than average velocities C5, C6 and C11 also experienced positive vertical velocities (Figure 8.7 and Figure 8.8b). Even though the maximum temperature on day 162 (of 10.1°C) was only slightly lower than the maximum temperature on day 161, the peak discharge was lower (2.0 m^3 s^{-1}), with the overnight discharge between day 161 and 162 falling steeply.

Figure 8.6 and Figure 8.8 show that on day 163 most of the glacier moved faster than average, with 5 of the points moving significantly faster (C5, C6, C10, C11 and C13), and only C4 and C8 slightly slower than usual. The region between C10 and C13 moved particularly quickly, with all points moving faster than 11 cm d^{-1} (Figure 8.9). Only C8 had a positive vertical velocity (1.7 cm d^{-1}).

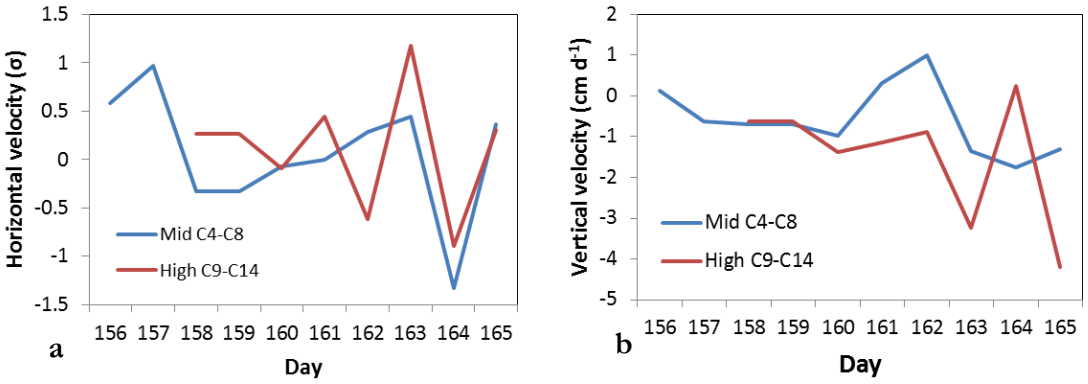

Figure 8.8 a) averaged net horizontal velocity anomalies and b) averaged vertical velocity for the middle and high GPS points, June 2011.

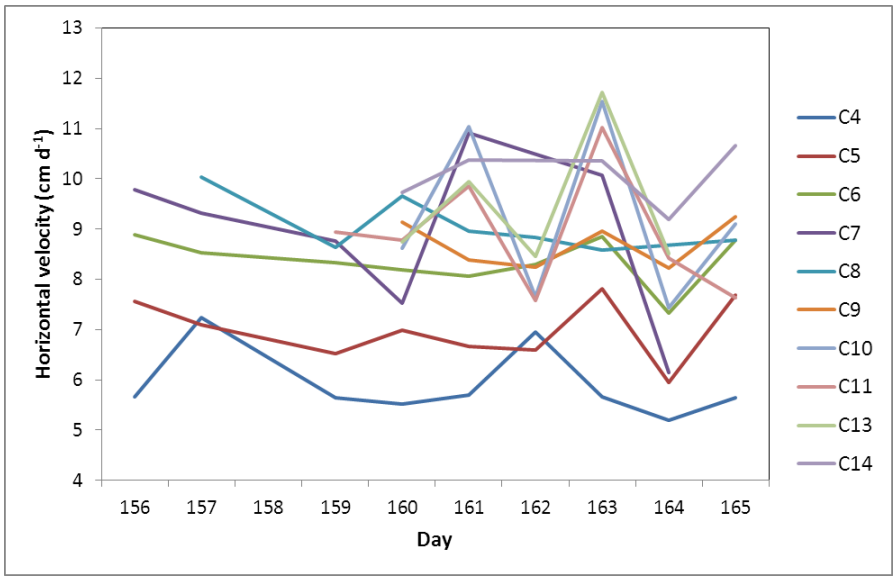

Figure 8.9 Horizontal velocities in cm d^{-1} in June 2011.

On day 164 all measured points were slower than average (C5, C6, C7, C9 and C14 significantly slower), even though the discharges rose during day 164. It was not as warm on day 164 as on day 163, but the air temperatures were still greater than they were before day 163. Despite slower velocities 4 points had a positive vertical velocity greater than 1 cm d^{-1} on day 164; C6, C10, C11 and C13.

On day 165 5 points travelled faster than usual (C5, C6, C9, C10, and C14), with the velocity anomaly apparently of a similar magnitude for all points involved (around 1 σ); no points went significantly slower.

8.1.3 July/August 2010

Next the glacier velocity in July and August 2011 variations will be described. Horizontal velocity measurements have been converted into a difference from average

velocity (the average velocity being the velocity measured between the end of June and the end of July), in units of the standard deviation derived from all daily measurements. Only upper glacier points will be mentioned due to the limited measurements of the lower glacier points.

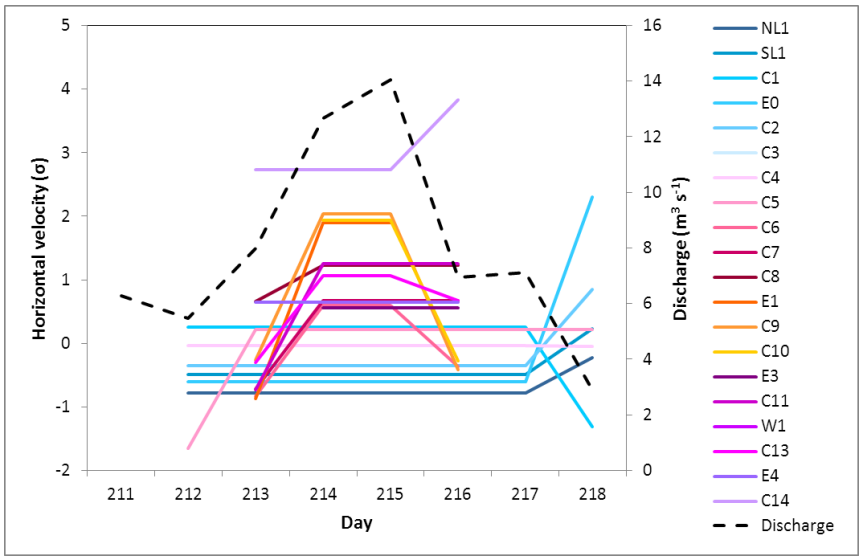

Figure 8.10 Net horizontal velocity anomalies and average daily proglacial discharge in July/August 2010.

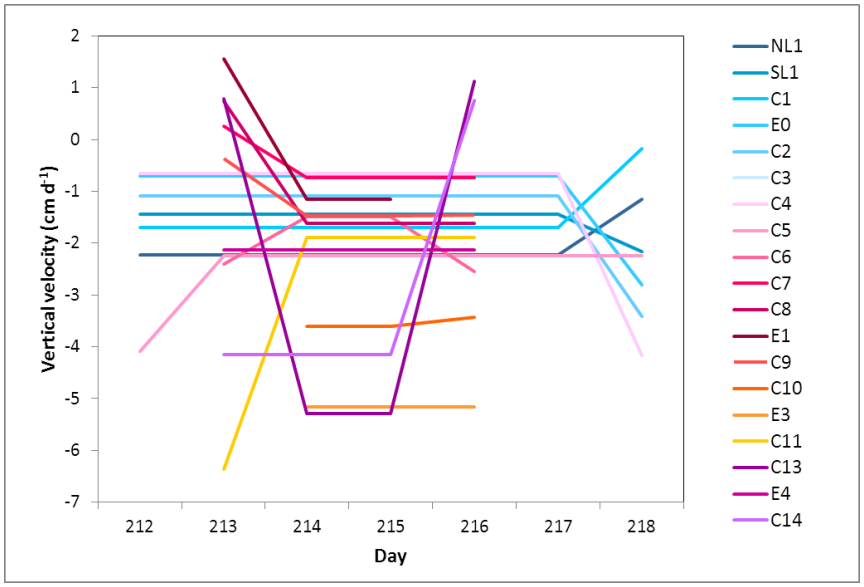

Figure 8.11 Vertical velocities corrected for surface slope in July/August 2010.

On day 213 most points (except C6) had a negative horizontal velocity anomaly (Figure 8.10), although none by more than -1 σ. Four points (Figure 8.11) had a positive vertical velocity on this day: C7, C8, E1 and C13. On days 214 and 215 all measured points from C5 upwards had faster than average horizontal velocities, and for 7 out of 12 points this was by more than 1 σ. These fast horizontal velocities were pronounced even in the season long record (Figure 8.1). All measured points had a negative vertical velocity, with

the upper glacier points having the most negative vertical velocities. On day 216, the region upglacier of C11 remained faster than average (C8, C11 and C14 were faster by more than 1 σ). Two points (C13 and C14) had a positive vertical velocity on day 216.

8.1.4 July/August 2011

The glacier velocity variations of C4 to C14 were measured during the July and August fieldtrip. The horizontal velocities are given as the difference from average (the velocity for that point between the first and last measurement in this field trip), in units of standard deviation (of all short duration measurements in the season), see Figure 8.12 and Figure 8.14a. Vertical velocities are in Figure 8.13 and Figure 8.14b.

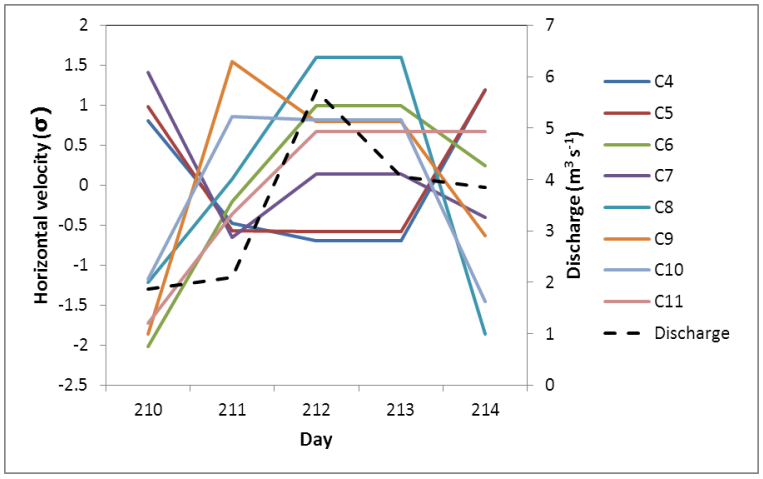

Figure 8.12 Horizontal velocity anomalies and average daily proglacial discharge, in July/August 2011.

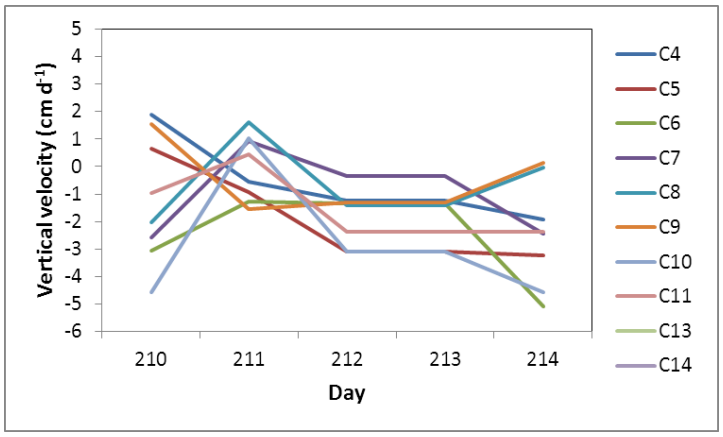

Figure 8.13 Vertical velocities adjusted for surface slope in July/August 2011.

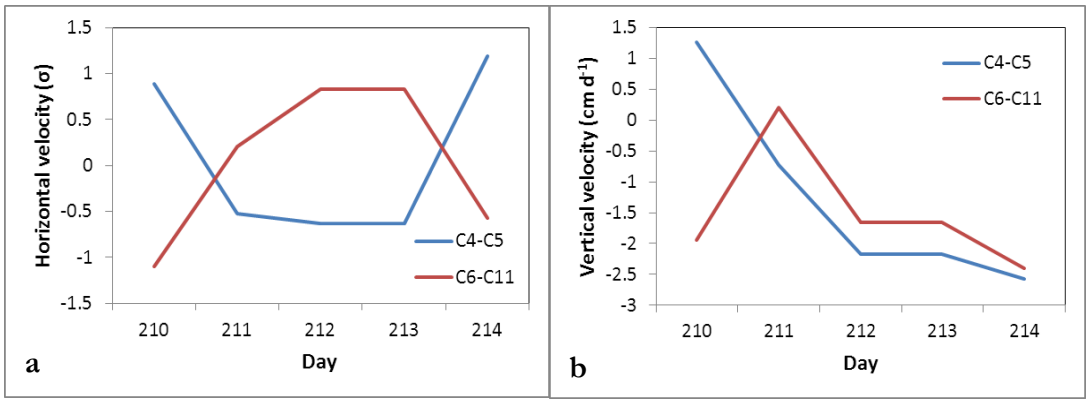

Figure 8.14 a) Averaged net horizontal velocity anomalies and b) averaged vertical velocities adjusted for surface slope, both in July/August 2011.

On day 211 all points from C8 to C10 went faster than usual (Figure 8.14a), with C9 travelling faster by 1.54 σ, and C13 moving at 16.4 cm d^{-1}, the fastest horizontal velocity measured for this point. Four points had a positive vertical velocity on this day, including C7, C8, C10 and C11 (Figure 8.14b), with uplift significant for C8 (1.6 cm d^{-1}) and C10 (1.0 cm d^{-1}). The lower glacier points moved slower than average on day 211 but the area of fast flow moved downglacier by days 212 and 213 as all points from C6 upglacier went faster than usual, including C8 which went faster by 1.6 σ. The area of faster velocities moved down to the points lower on the glacier (C4 to C6) by day 214, with both C4 (1.19 σ) and C5 (1.20 σ) significantly faster. Most points (except C4 to C6) were slower than average on day 214.

8.1.5 Seasonal overview

In order to identify the overall patterns of the glacier velocity variations on Miage Glacier, the annual and mean summer and winter velocities were calculated, as well as mean velocities for the June and July/August measurement periods. These results will be discussed first. Following this, the differences in the variability of the glacier velocity at any point on the glacier will be studied, by collating and analysing the daily measurements from the whole season. By comparing the magnitude and variability of the glacier velocities between different parts of the glacier and times of year, this will allow inferences to be made about the combined effect of the quantity and timing of melt and the likely hydrological structure on the glacier dynamics, and how this may be influenced by the debris cover (discussed in section 8.2.3).

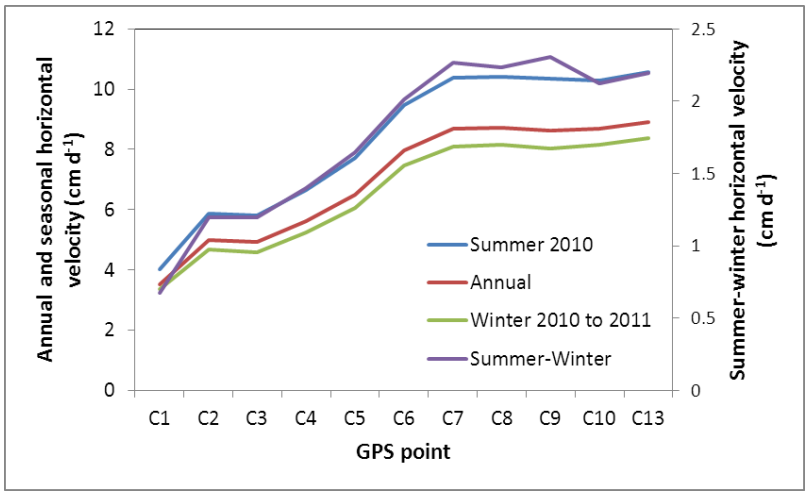

Figure 8.15 Annual, summer, winter (y-axis to left), and difference between summer and winter net horizontal velocities (y-axis to right) along the glacier centreline.

Table 8.1 Annual horizontal velocities calculated from point displacement between June 2010 and June 2011. The eastings and northings given are in UTM 32N and give the position of the point in June 2010.

Point	Easting	Northing	Horizontal velocity (m yr^{-1})
C1	0335028	5072094	12.87
C2	0334768	5072104	18.23
C3	0334474	5072151	17.93
C4	0334009	5072177	20.49
C5	0333789	5072446	23.72
C6	0333505	5072825	29.11
C7	0333175	5073230	31.69
C8	0332898	5073691	31.88
C9	0332534	5074076	31.48
C10	0332316	5074379	31.75
C13	0331845	5075012	32.53

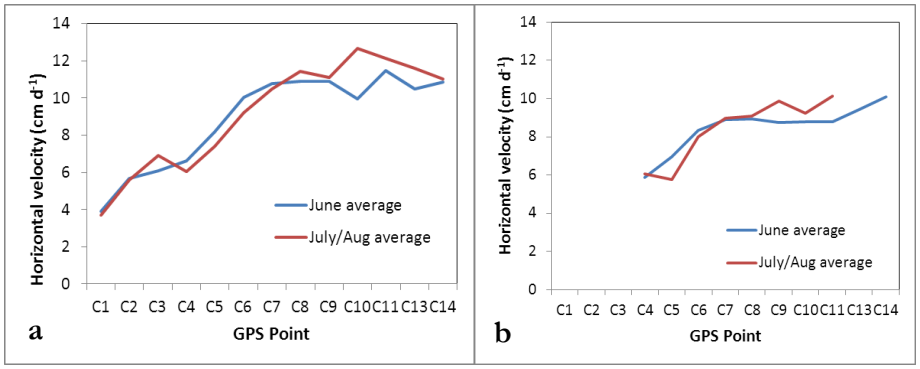

Figure 8.16 Average June and July/August net horizontal velocities in a) 2010 and b) 2011.

Annual average velocities were calculated from the displacements of the points between June 2010 and June 2011 (Figure 8.15 and Table 8.1), and show annual average

velocities between C7 and C13 were the highest on the glacier, and were similar at around 32 m yr^{-1}. The glacier becomes slower downglacier with the decrease sharpest between C7 and C5, although it also decreased between C5 and C3. Velocities of C3 and C2 were similar, but decrease again to C1, near the terminus of the small central lobe. Looking at the difference between summer and winter velocities (Figure 8.15), summer velocities (measured from June 2010 to September 2010) were faster than winter velocities over all measured points. The difference was greatest at C9 (29%), with most of the upper glacier down to C5 experiencing an increase in summer motion by over 27%. The difference decreases downglacier, most sharply from C2 to C1, so at C1 the difference is 20%. The differences in glacier velocity between the June and July/August fieldtrips can also be compared (Figure 8.16). This shows that both the 2010 and 2011 average velocities show similar relationships when June is compared with July/August. The region from C10 to C13 in 2010 and C9-C10 in 2011 was faster in July/August than in June, whereas the middle region of the main tongue from C6-C8 in 2010 and C5-C6 in 2011 was slower in July/August than in June.

The variability of the glacier velocity measurements for different parts of the glacier will now be described. It is clear that the upper glacier points have greater velocity variability than the lower glacier points. This was shown in the daily measurements (Figure 8.17 and Figure 8.18), where the difference in velocity on different days is much larger on the upper compared to the lower glacier. This results in the difference between the maximum and minimum daily velocity measured being greater upglacier (points C8 to C13 have a daily velocity range of between 4 and 5 cm d^{-1}, with this decreasing downglacier to below 2 cm d^{-1} for C1 and C2, although the range was also high for C5 (6.71 cm d^{-1})), Figure 8.19. The only day the lower glacier sped up by as much as the upper glacier points were observed to (by 2 to 3 cm d^{-1} more than average) was on day 158 in 2010 (Figure 8.3a and Figure 8.17). A similar increase in velocity of points C3, C4 and C5 was not measured again for the rest of the year, or at all in 2011.

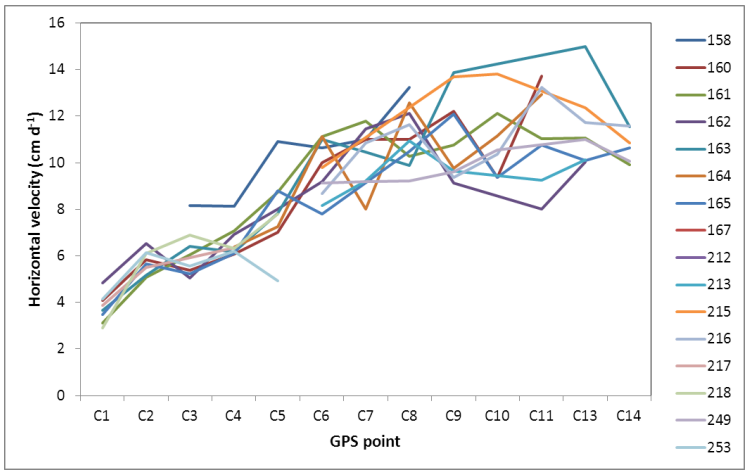

Figure 8.17 All daily net horizontal velocity measurements along the centreline in 2010.

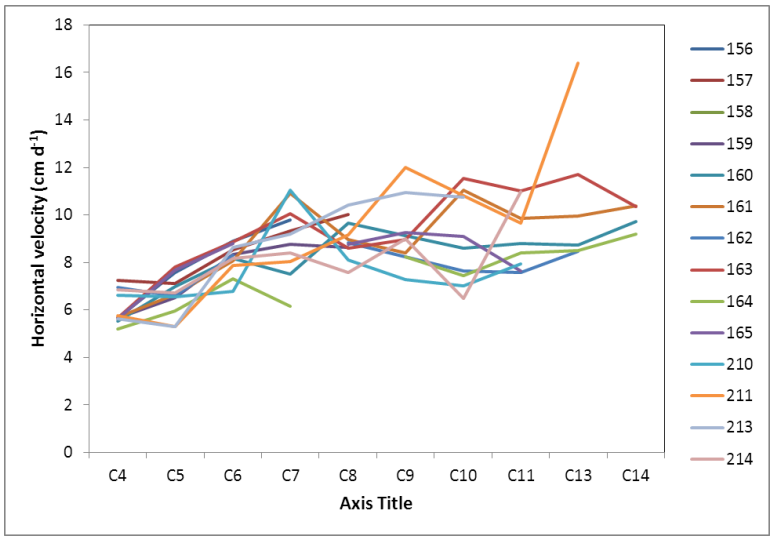

Figure 8.18 All daily net horizontal velocity measurements along the centreline in 2011.

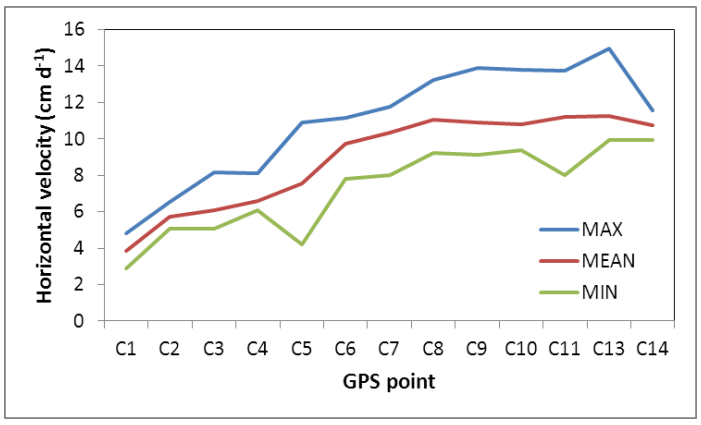

Figure 8.19 Maximum, mean and minimum net horizontal velocities for each GPS point in 2010.

8.2 Interpretation and discussion

In this section the glacier velocity measurements described above will be interpreted and the results discussed in terms of how the glacier dynamics are influenced by the water inputs and hydrological structure, and whether this may be influenced by the debris. Weather conditions and melt inputs are given in Figure 4.24.

8.2.1 June

In June 2010 there were two days in which glacier velocities were noticeably increased, on day 158 when all of the measured points moved faster than average, and day 163 when all of the points above C9 moved faster than average. Prior to the velocity measurements air temperatures were very warm: day 155 had a peak air temperature of 22.6°C at 15:00; the highest recorded temperature since the beginning of the year. The surrounding days were also warm with the maximum temperatures of day 154 and 156 being 19.6°C and 17.4°C respectively. These warm temperatures would have led to large melt inputs (there is no modelled melt until day 159) which resulted in the proglacial discharge increasing from day 157 to 159 (Figure 4.24). Unfortunately, the structure of the englacial and subglacial hydrological system was not known from dye tracing, because the first successful trace was not performed until day 160.

The fast glacier velocities over the entire glacier on day 158 suggests subglacial water pressures were elevated enough to increase the sliding velocity and suggests the glacier was underlain by an inefficient subglacial system, especially beneath the regions with the fastest velocities. At the very least, melt inputs overwhelmed the hydrological system, so water was transferred to areas surrounding the main drainage routes. Significant positive vertical velocities were also experienced by five points on this day. Areas of positive vertical velocities, especially those which have moved faster, can signify the glacier has been lifted off its bed by high water pressure (the 'hydraulic jack' mechanism). However, vertical strain variations can be a component of the vertical velocity and this was not accounted for (Mair *et al.,* 2002).

During days 160 to 163 the region of the fastest velocities appeared to move downglacier (Figure 8.5). If the leading edge of this wave of faster motion is marked by the transition from slower to faster than average velocities this would correspond with C7 on day 160, C4 on day 161, and C1 on day 162. This gives a wave front velocity of 56 m h^{-1} between days 160 and 161, and 43 m h^{-1} between days 162 and 163. Short term waves of areas of faster velocity moving down glacier were seen on Findelengletscher, Switzerland,

by Iken and Bindschalder (1986), and were associated with waves of high water pressure following the regions of higher velocity downglacier. They were caused by either high melt inputs or the release of stored water into a subglacial drainage system unable to transfer those inputs, resulting in high water pressures which increased basal sliding velocities. They calculated the speed of the waves by the distance the wave front or area of maximum water pressure moved downglacier, and these varied from 101-178 m h^{-1} for the period in May, and from 54-97 m h^{-1} for the period in June. Since these speeds are similar to those calculated for Miage Glacier, the wave of faster motion may also have been caused by pressurisation of the subglacial system. Willis (1995) suggested short term waves may be more likely if the moulins were located upglacier, because this could result in storage of late-season melt upglacier if conduits close early downglacier of the moulins. The main moulins for Miage Glacier exist upglacier, just above the region of thickest ice (section 4.3). However the drainage of supraglacial lakes (like that associated with S13) could also be a source of water. The release of a pulse of particularly ion and sediment rich water peaked on day 160 (section 6.2.2.1) – further evidence water temporarily covered a large proportion of the bed.

Melt inputs were low during days 159 to 161, although there was rainfall on day 161. The quantity of melt increased significantly during days 162 and 163 (from 2.8 m^3 s^{-1} on day 161 to 4.8 m^3 s^{-1} on day 163), which along with rainfall on day 162 led to discharges increasing to a peak of 7.96 m^3 s^{-1} at 23:00 on day 163, the highest so far this season (Figure 4.24). Glacier velocities were significantly faster on the upper glacier on day 163 (Figure 8.3a), but the mid-part of the glacier did not increase in velocity as seen during day 158. It is likely that below C5 the drainage system had increased in efficiency, meaning it could accommodate the melt without an increase in water pressure. The particularly fast velocities and vertical uplift of the upper glacier points indicates water pressures were high enough to increase sliding velocities. Considering that the S13_162 trace implied there was a main conduit system below C10 (section 5.1.1.1), the large melt water inputs must have overcome the conduit system below this point in order to increase sliding velocities at C9.

In June 2011, most points measured on day 156 and all on day 157 moved faster than average. Air temperatures increased substantially from day 152 to day 155 (mean LOMET air temperature -2.6°C and 7.0 °C respectively, the latter appears high in this short record but is actually relatively low (Figure 4.24). Melt inputs were not modelled this early in 2011 (Figure 4.24), but the warmer weather would have increased inputs compared to day 152, although there was also heavy rain on the morning of day 156 (not shown in Figure 4.24 since no rainfall data). There was not a significant increase in proglacial discharge however. For a small input increase to cause a significant increase in the velocity

of C5 and C6 on day 156 and C4 and C8 on day 157, there must have been a mainly inefficient subglacial hydrological system, so the water covered a large area of the bed and was able to increase sliding velocities. Similarly, although the increase in air temperatures (and presumably melt), and the corresponding increase in proglacial discharge on day 161 (Figure 4.24) was small in the context of the whole season, the horizontal velocities did increase at all points above C7. Dye tracing into S12 on this day revealed that there was a channelized system, and so the melt inputs must have been large enough to overcome this system in order to increase the glacier velocity. The loss of the water to the distributed system may mean the remaining discharge could be accommodated in the conduit system downglacier (so long as inputs from the lower glacier were not significant) meaning the lower glacier would not experience a velocity increase.

On day 163 the majority of the glacier moved significantly faster than average. The maximum discharge on day 163 was the highest recorded since day 155 at 21:00, and during the afternoon of day 163 was the first time the conductivity fell below average and the C-ratio increased above 0.75 (section 6.2.1.2), which suggests a significant input of dilute meltwater. For glacier velocities to have increased, the conduit system must not have been able to efficiently route the meltwater (at least down to C5), and so it was transported within the less efficient system where it increased sliding velocities. It is likely that the hydrological system adjusted to the rise in melt inputs since on day 164 all points moved slower than average despite the proglacial discharge continuing to rise.

If the system did become more efficient, then it still could not contain the steep increase in discharge between days 164 and 165, which resulted in velocities increasing again on day 165. Discharges increased from 2.3 $m^3 s^{-1}$ at 13:00 on day 164 to 3.4 $m^3 s^{-1}$ at 18:00 the same day, with the discharge remaining high into the morning of day 165. This increase in discharge was driven by rainfall, since although only 0.82 mm of rain fell at UPMET (none at LOMET) on day 164, if this fell evenly over half of the catchment it would equate to 1.08 $m^3 s^{-1}$.

Overall it is clear that measureable short term variations in velocity do occur on Miage Glacier in the spring time, even on the heavily debris-covered main tongue. These variations are closely related to changes in the quantity of melt inputs to the glacier (and hence weather patterns), but the continual evolution of the system was also apparent. For instance in June 2010 faster glacier velocities were experienced over the entire glacier on day 158, but on day 163 faster velocities were confined mainly to the upper glacier despite larger water inputs – thus suggesting the lower glacier hydrological system had increased in capacity between day 158 and 163.

8.2.2 July/August

Both July/August filedtrips were characterised by periods of significantly faster than average velocities, especially for the upper glacier. These increased velocities were noticeable even within the season long records (Figure 8.1 and Figure 8.2).

In 2010 days 214 and 215 experienced faster than average velocities at all points from C5 upwards. Melt inputs increased significantly from day 211 (1.2 $m^3 s^{-1}$) to day 213 (4.5 $m^3 s^{-1}$), with heavy rainfall in the afternoon of day 214 equating to 5.8 $m^3 s^{-1}$ (Figure 4.24). The large water inputs led to the peak discharge on day 214 of 16.4 $m^3 s^{-1}$ at 24:00 being the highest discharge measured so far this season, and the 12th highest discharge measured in 2010 (exceedance probability 0.54%). These large inputs were not able to be accommodated within the channelized network – leading to water spreading into a larger area of the bed and increasing sliding velocities. Since the glacier did not speed up on day 213 (which experienced hourly discharges up to around 10 $m^3 s^{-1}$, exceeded in 2010 9.3% of the time), this suggests the subglacial channel system was efficient enough to transport this magnitude of water by mid-summer.

In the mid-season of 2011, faster velocities were confined to the upper glacier on day 211, but by days 212 and 213 faster velocities extended from C6 upglacier. Melt inputs increased gradually from day 208 to day 211 (from 1.5 $m^3 s^{-1}$ to 2.6 $m^3 s^{-1}$), and there was rainfall at UPMET (not LOMET) over these days too, but there was no noticeable increase in proglacial discharge until day 212. Dye tracing suggested that prior to day 212 the conduit system was unable to evacuate water as efficiently as in June (section 5.2.1), with the lag between increasing inputs and discharge possibly pointing to storage of water within the distributed system, although logged stage data were not available. This would be expected to result in an increase in water pressures in the adjacent distributed system, and would have caused the observed increase in glacier velocities. The only part of the glacier to move faster than usual on day 214 was between C4 and C6 – implying a downward transfer of the water through the distributed system. Since the rest of the glacier moved slower than usual on day 214, and dye traces after day 212 indicated an increase in the efficiency of the conduit system (despite discharges remaining higher than prior to day 212), the hydrological system must have evolved to accommodate a larger discharge.

The efficiency of the channel network increased during the summer, so larger discharges could be accommodated without an increase in glacier velocity. The magnitude of the increase in velocities was similar in spring compared to summer (Figure 8.1 and Figure 8.2), but required much higher actual air temperatures and discharges to invoke a similar dynamic response in 2010. The average discharge of 4.0 $m^3 s^{-1}$ on day 158 2010 was

associated with higher than usual velocities over the entire glacier, but the average discharge on day 215 2010 when the upper glacier was faster than usual was 14.0 m^3 s^{-1}. However, in 2011 faster velocities occurred on the upper glacier on day 212 when the average proglacial discharge had risen to only 5.7 m^3 s^{-1}. This year the cold preceding conditions (Figure 5.24) were more important because they led to a decrease in channel efficiency identified by the S12 and S14 dye traces (section 5.2.1). The system was similar to its spring time configuration, meaning glacier velocities increased given a relatively small discharge increase. Cooler conditions on debris-covered glaciers may be more likely to result in a relative closure of the system, because the melt inputs which sustain the system are produced from debris-free regions higher up glacier.

8.2.3 Seasonal overview

In this section the annual and seasonal velocities are interpreted, along with the variability of velocities over the season. The spatial variation in these measurements will be discussed in terms of the likely effect of the glacier's morphology and debris cover.

On Miage Glacier the average annual velocity decreased with distance downglacier (Figure 8.15). On annual timescales glacier flow is driven by the glacier's climate and mass balance gradient, so glaciers with high accumulation and ablation rates have a steep mass balance gradient and correspondingly high velocities to enable the transfer of this mass. Conversely, glaciers with a shallow mass balance gradient flow more slowly. Variations from the balance velocity are due to the glacier's valley geometry and surface slope, and may be driven on smaller timescales by variation in the quantity and distribution of the water at the bed (Benn and Evans, 1998). Velocities were faster from C7 up-glacier because the confluence of the tributary glaciers occurs between C14 and C10, where the valley is relatively wide (747 m just below C14 where the main Miage Glacier, and Dome glacier combine), but downglacier of C10 the valley decreases in width (to 644 m at C10). This decrease in valley width continues to C7 where it is at its narrowest (561 m). For the ice to be evacuated through an increasingly narrow channel it must therefore maintain a high velocity, even though velocities usually decrease with distance from the equilibrium line (Benn and Evans, 1998). This may explain the consistent velocities along the main tongue. The glacier widens substantially between C6 and C5 (to 663 m), before narrowing slightly to C3 (607 m). This results in slower velocities at C5 of 6.50 cm d^{-1}, and at C3 of 5.80 cm d^{-1}. This area is associated with a clear region of compressional longitudinal strain between C4 and C7 but which is most apparent between C5 and C6 (Figure 8.20). The valley becomes wider again at C2 (around 700 m), and wider still at C1 (836 m), as it splits into

the two main, and one smaller central lobe. The annual velocity at C3 and C2 is almost the same, but the glacier slows to just 3.5 cm d^{-1} at C1. The area between C2 and C3, and especially between C1 and C2 also experiences compressional strain as the glacier slows and widens (Figure 8.20).

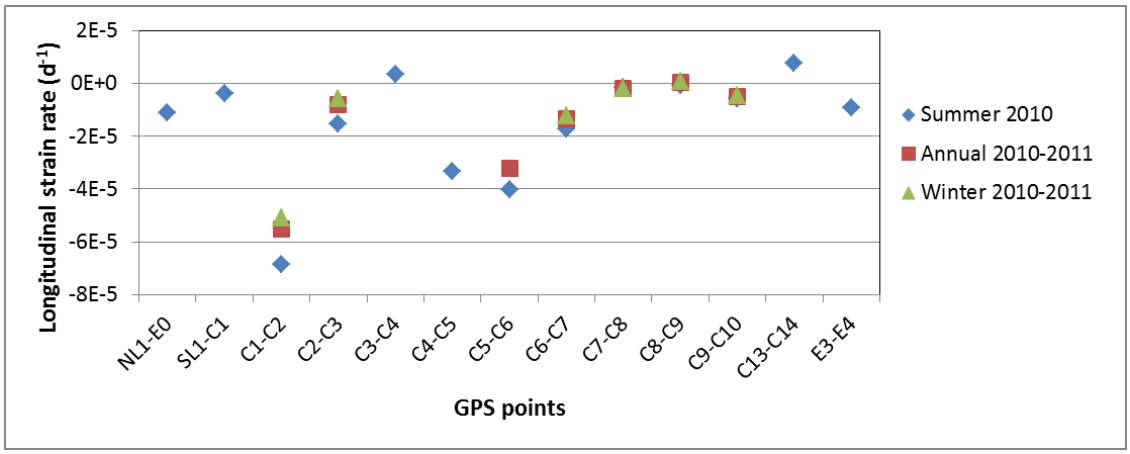

Figure 8.20 Annual, summer and winter longitudinal strain rates for the centreline (C1 to C14), northern lobe (NL1-E0), southern lobe (SL1-C1) and eastern moraine (E3-E4).

The pattern of decreasing glacier velocities with distance downglacier is similar to other (debris-covered) glaciers, such as Baltoro Glacier which has a region of particularly fast flow at the main confluence at Concordia of > 200 m a^{-1} (Mayer *et al,* 2006; Quincey *et al.,* 2009), which generally decreases downglacier despite local velocity increases at confluences or where the valley narrows. Decreasing downglacier velocities were found from feature tracking on Chaturangi Glacier from around 6 km from the terminus, and also on Gangotri Glacier, both in the Garhwal Himalayas, as well as on Khumbu Glacier, Nepal where velocities decrease from around 5 km from the terminus (Scherler *et al.,* 2008). For these glaciers the areas of faster velocities also had the most variability in velocity (which made feature tracking difficult), and Gangotri Glacier had evidence of higher summer compared to annual velocities (Scherler *et al.,* 2008). On Baltoro Glacier, summer velocities are higher than winter velocities, by as much as 65% at Concordia, decreasing to 35% upglacier from here (Quincey *at al.,* 2009).

Summer velocities on Miage Glacier were also larger than winter velocities to a larger extent on the upper glacier compared to the lower glacier (section 8.1.5). The detailed daily glacier velocity measurements carried out in June 2010 and 2011 show short term spring speed up-events occur on Miage Glacier, when weather conditions are such that relatively large meltwater inputs are introduced into a system that cannot efficiently transfer the water, for instance on days 158 and 163 in June 2010 (section 8.1.1, Figure 8.3a), and days 157 and 163 in June 2011 (section 8.1.2, Figure 8.6). These short term speed-ups explain the increased summer compared to winter velocities. The difference

between summer and winter velocities was quite small, perhaps because the majority of the spring snow melt occurred fairly early in 2011 (before June) meaning some of the increased velocities were attributed to the winter period, although they actually happened just prior to the first measurements. Large increases in velocity also occurred on the debris-covered Baltoro Glacier in summer 2005, just downstream of where a series of large moulins reached the bed downstream of Concordia. This happened following a particularly cold preceding winter and was attributed to increased meltwater reaching the bed when the hydrological system was less well developed, increasing the subglacial water pressure, and therefore sliding velocities (Quincey *et al.,* 2009). Short-term spring speed-up events are common to many glaciers however, and are unlikely attributed to the existence of a debris cover. They have been reported on the Underaargletscher, Switzerland (Flotron, unpublished, cited in Iken *et al.,* 1983, cited in Willis, 1995), Midtdalsbreen, Norway (Willis and Sharp, in prep., cited in Willis, 1995), Storglaciären, Sweden (Hooke *et al.,* 1983; 1989, cited in Willis, 1995), Haut Glacier d'Arolla, Switzerland (Mair *et al.,* 2003), and most recently on outlet glaciers of the Greenland ice sheet (Bartholomew *et al.,* 2010; Sole *et al.,* 2011).

In terms of the differences in average June and July/August velocities, the faster upglacier velocities may be caused by the change from snow to ice melt and warmer summer air temperatures enlarging the contributing area. This would increase the magnitude and amplitude of melt inputs in July/August compared to June into the upper glacier moulins, and increases the possibility of inputs overwhelming the channel system and increasing glacier velocities. This suggests that although the channel system usually evolves to evacuate an increasing input discharge over the summer, this does not entirely offset the increase in meltwater production. However, the mid-glacier points tend to increase in velocity when the hydrological system is less efficient and more of the upper glacier inputs reach the lower glacier in the distributed system. This is therefore more likely to occur in the springtime.

It was shown in section 8.1.5 that there was a greater variability of the daily velocity values on the upper rather than lower glacier. This is contrary to most glacier ablation areas where the 'the difference between maximum and minimum velocities over a variety of timescales gradually decreases upglacier' (Willis, 1995, p 96). The exception to this was near the terminus of Storglaciären where sliding speeds were faster upglacier. Variations in the water pressure had less effect on glacier velocities lower on the glacier, because the pressure of the subglacial hydrological system reached atmospheric pressure at the terminus. Surface motion variations of the lowermost stakes was due to the upglacier

variations in sliding speed transferring longitudinal stress to the lower glacier (Brzozowski and Hooke, 1981).

The dye tracing results suggest the subglacial hydrological system of the lower glacier was at least locally distributed, which would usually result in higher water pressures than a channelized system, although there is a main channel which the meltwater reaches eventually. Therefore, the reason lower glacier velocities are lower than those upglacier and have less variability is not because the hydrological system becomes more efficient and decreases the water pressure with distance downglacier. Instead, the decrease in ablation and supraglacial stream discharge due to the debris cover (section 4) results in local meltwater inputs being too small to increase the water pressure and therefore the sliding velocity, even in a relatively inefficient subglacial system. This means velocities are lower and have less variability because the inputs can be sufficiently evacuated even by a less efficient system. Some of the velocity variation of the lower glacier points may be due to the transfer of longitudinal stress from upglacier, especially considering the longitudinal stress is particularly compressional as the glacier flow changes direction in the region of C5 to C6.

The only time the lower glacier velocities experienced as large an increase in velocities as was seen on the upper glacier points was on day 158 in 2010 (Figure 8.17). This speed-up event was linked to the release of ion and sediment rich water when discharges fell on day 160 (section 6.2.2.1), and must have occurred before the hydrological system was channelized (the earliest dye trace which indicated an efficient channel was on day 160). Water from upglacier was likely transferred in an inefficient system, increasing the velocity of the entire glacier and resulting in the release of water that had been stored at the bed for some time. Substantial increases in the lower glacier velocity may only occur when the upper glacier meltwater is transferred to the lower glacier through a distributed system. Throughout the rest of the season, dye tracing suggests upglacier meltwater travels in a channelized system, meaning it is less likely to influence the velocity of the lower glacier.

The velocity variations of the upper glacier are high throughout most of the season, even though the system was traced as channelized throughout both years. Since the greatest meltwater inputs enter the glacier at the moulins close to C10 (e.g. S12 and S14), this region will have the largest increases in subglacial water pressure due to variations in meltwater input. In June 2010, the only points to have a significant relationship between horizontal velocity and maximum air temperature were upglacier (C8 with a p-value of 0.022 and R^2 of 36.6, E1 with a p-value of 0.017 and a R^2 of 39.7, and if the maximum air temperature was lagged by a day then the relationships were significant for C9 with a p-value of 0.022 and R^2 of 36.6, and for C11 with a p-value of 0.022 and R^2 of 39.9). Sliding velocities can still

increase when a channelized system exists, but inputs must increase at a rate greater than channel expansion, forcing meltwater into the surrounding distributed system where it increases water pressures.

The overall findings from this chapter concerning how the debris influences the dynamic response of the glacier to meltwater inputs are as follows:

1. The highest glacier velocities and greatest variability in velocities are found on the upper glacier, since the largest water inputs enter the glacier via the large moulins around C10.
2. Glacier velocities are lower and less variable on the lower glacier, because although the hydrological system here is not efficient, the smaller inputs from beneath the debris are less able pressurise the system. Speed-ups of the lower glacier are therefore rare.

These influences of the debris on the glacier hydrology, and consequently on the glacier velocity could impact on the overall glacier mass balance. Slow glacier velocities tend to encourage the build-up of englacially derived debris on the glacier surface, and therefore increase the thickness of the debris layer - in turn reducing melt inputs into the system. The overall influence of the hydrology may not be the most significant factor in reducing the velocity of the lower glacier, as the compressional flow, shallow glacier bed slope, shallow mass balance gradient, and especially a negative overall mass balance, will play the most significant role. However, it is possible the reduction in the magnitude and amplitude of melt inputs, and the reduction in the short term variability of the glacier dynamics caused by lower input discharges, may exacerbate the aforementioned processes and aid in the formation of a stagnating lower tongue.

9 Conclusions and outlook

This thesis has five aims which were: to understand the influence of the debris on the input hydrograph, to understand the influence of debris on the water routing through the glacier using dye tracing, to examine the temporal variations in bulk water routing using water chemistry and proglacial hydrograph analysis, to quantify the water balance of the glacier and to understand how the water inputs and hydrological structure influence the glacier dynamics. The research findings which address each of these aims will be summarised in turn within this chapter. Suggestions for future research will also be given within the appropriate sections.

9.1 Water inputs

The first aim was to understand how the debris influenced the form and discharge of the supraglacial streams, and how it influenced the inputs to the englacial system. It was found there were two main impacts the debris has on the supraglacial hydrograph: the first is where the debris is thick it reduces ablation, and secondly, it delays the onset and peak of daily ablation. The debris topography, whether concentrated in medial and lateral moraines, or in a hummocky form, changes the size and shape of the supraglacial catchments. Where the debris is thick the supraglacial stream water travels slowly, due to the shallow stream gradient and high debris concentration within the stream. Importantly, the discharge of these streams tends to be small, due to the small catchment sizes and low melt rates, and their diurnal discharge amplitude is reduced (based on the daily input melt signal).

There is a good understanding about how the change from snow to ice changes the supraglacial input hydrograph (Campbell *et al.,* 2006; Willis *et al.,* 2002), but despite the above knowledge, the same cannot be said for the presence of debris. A detailed catchment study would be needed to quantify and model the debris' influence on the input hydrograph. Preferably parallel areas of clean and debris covered ice at the same altitude would be chosen, where supraglacial streams would be instrumented to capture the differences in runoff. Resolving the uncertainty surrounding how meltwater reaches the supraglacial streams from the ice/debris interface would also be pertinent. The base of the debris is usually saturated (Nakawo and Young, 1981), but exactly how water travel times are affected is not known. Dye tracing, similar to performed through snow, would be the best way to achieve this. This work would be tied to a detailed distributed energy balance

melt model, with the aim to model the debris' influence on the runoff compared to clean ice, and create part of a water routing model for a debris-covered glacier.

The distributed melt model revealed that where the debris was thin and patchy the lower albedo meant ablation rates were higher than for clean ice. These areas of thin debris had the highest melt rates on the glacier and were found in between the moraines on the upper glacier, including the lower parts of the icefalls. The dirty ice cells had an average ablation of 0.047 m w.e. d^{-1} in 2010, more than double the average ablation beneath debris of 0.019 m w.e. d^{-1} (these values include the influence of snowcover for each cell). Reid and Brock (2010) mentioned the ablation of dirty ice could be modelled using a 'patchiness' parameter, representing the fraction of debris covered to clean ice over an area, but have yet to test this. To model the dirty ice area, the Miage Glacier melt model simply used an albedo mid-way between clean and debris-covered ice. This matched well enough with measured ablation, but stake data were limited. A further difficulty was the delimiting of the boundary between dirty ice and clean and debris-covered ice. This was carried out subjectively on the basis of aerial photography, with operator decision-making being critical to the creation of the exact boundary. A detailed study which measures melt beneath thin and patchy debris with a better spatial and temporal resolution than previously would be necessary (using a high resolution stake network, or small scale terrestrial LiDAR), followed by work to determine the most appropriate and accurate modelling methods. Making use of remote sensing data other than aerial photography (similar to Casey *et al.* (2012) who mapped debris cover mineralogy) to find specific spectral characteristics of dirty ice which allow it to be delimited accurately, would benefit distributed melt models.

Furthermore, the ablation rate of clean ice at higher elevations tended to be higher than ice beneath debris on the lower glacier, with melt occurring across most of the glacier by the middle of the day. Springtime snow melt rates were higher than sub-debris melt rates at a similar altitude. The quantity of water produced from the middle and upper regions of the glacier was relatively large, and clean and dirty ice melt had a greater diurnal melt rate amplitude as there was no lag due to conduction. The catchment sizes of supraglacial streams were usually large on the upper glacier: streams could be followed down-glacier for several hundred meters, and GIS catchment analysis suggested they were not constrained topographically, although the moraine system on the main tongue did focus meltwater into a few streams. Consequently, these supraglacial streams had fast velocities and large discharges.

The temporal variation in the source of melt was also investigated. Sub-debris melt provided a consistent 27-30% of melt which remained almost constant throughout the season apart from when it increased during particularly cold meteorological conditions. The

proportion of snowmelt was much larger in 2010, with it being replaced by clean ice melt as the season progressed. During the middle of the day debris-free areas had much higher melt rates than beneath the debris, although sub-debris melt continued later into the evening due to the time taken for heat to conduct through the debris.

One of the objectives within the water inputs aim was to measure the evaporation and condensation from the debris. Overall water vapour moved downward through the debris, driven by the large temperature gradient between the surface and the ice, although periods of upwards flow at the surface occurred when the upper layer had a low relative humidity. The upwards movement of liquid water may balance the downward vapour flow flux, although this was only implied by the vapour flow calculations and not measured. The water likely evaporates at the clast/granule interface. To fully understand the water flux within the debris, the liquid water flux could be monitored continuously using TDR (time demain reflectometry) sensors (Pfletschinger *et al.,* 2012). These work by measuring the relative dielectric permittivity in the area surrounding the sensor, since the permittivity is strongly influenced by the soil water content. These sensors tend to be used in natural soils (Mittelbach *et al.,* 2012), or in soil column experiments (Pfletschinger *et al.,* 2012), usually within sand or loam soils. Their applicability within course diamictic sediment, typical of supraglacial debris (Nicholson and Benn, in press), has yet to be tested.

The warm debris surface during the day meant evaporation rates of rainfall were high, although this was enhanced if percolation was inhibited by debris with a low permeability. Using volumetric lysimeters to measure evaporation worked well and could be multiplied and modified to test different debris thicknesses, grain sizes and types, although lysimeters only quantified evaporation of rainfall not melt. Currently the evaporation of rainfall over glaciers is not quantified within glacier runoff models (Arnold *et al.,* 1998; Hagg *et al.,* 2006 and Rana *et al.,* 1996), but it may determine how the proglacial runoff is affected by rainfall events, so should be a research priority to enable accurate prediction of future runoff from basins containing debris-covered glaciers.

The sensitivity of the model to air temperature and debris thickness changes was also investigated. An increase in air temperature resulted in the crevassed ice falls, and dirty and thinly debris-covered ice suffering the greatest ablation increases. However, the thickly debris-covered ice was much less sensitive to an air temperature increase. An increase in debris thickness resulted in certain cells switching from being classed as dirty to being classed as debris-covered ice, consequently increasing the debris-covered area. This resulted in a large increase in melt where debris cover was previously zero or very thin, but could result in a dramatic decrease in melt if the cell had a debris thickness just great enough to be modelled as debris-covered. Ablation was decreased for all debris thicknesses greater

than the threshold between dirty and debris-covered ice (0.01 m), although further refinements to the model to improve the transition from debris-covered to clean ice melt would be useful. If both air temperature and debris thickness were increased then the greatest ablation increase occurred where the debris was previously zero or very thin, but where the debris was moderately thin ablation still decreased overall because the thicker debris counteracted the increase in air temperature. Average daily melt was increased by 6.3% by a 1°C increase in air temperature, although this could be negated by an increase in debris cover (a 0.01 m increase reduced melt by 1.9%).

However, future predictions of the rate of debris thickness or area increase are only known for a few glaciers (e.g. Stokes *et al.,* 2007; Bolch *et al.,* 2008). How the debris evolves and results in the observed topography is also not well known, with the only mention of debris re-distribution being in Deline (2002) and Iwata *et al.* (2000). High resolution digital elevation models (either produced from LiDAR or using new and more cost-effective automatic photogrammetric techniques) could be used to look at glacier cross-sections and transects over time, revealing the glacier topography, its relation to the supraglacial hydrology, and how this changes. It would be important to determine the controls on expansion of the debris cover. Repeat imagery of selected glaciers over a 20-30 year time period would provide a record of changes in debris-covered area, which could be compared to possible controlling factors such as the glacier's structure, basin topography, debris geology and retreat rate. Once the controlling factors have been established they could be applied to predict future changes in debris-covered areas. As the upglacier expansion of the debris cover is associated with high ablation rates of dirty ice (Stokes *et al,* 2007), a greater understanding of dirty ice ablation would help quantify the increase in debris covered area.

As the change in mass of a debris-covered glacier is due to not just the climate and glacier dynamics, as on clean glaciers, but also the supply and thickness of the debris, a mass balance model for a debris-covered glacier needs to incorporate these feedback mechanisms. The work on Miage Glacier also linked the annual velocity of different parts of the glacier with the debris-covered and clean-ice regions and their associated glacier-hydrology. Currently, theoretical models have been produced which replicate the changes in a debris-covered glacier over time (Lefeuvre and Ng, 2012), but if they are to become predictive tools for the evolution of individual glaciers, then they will need to be verified using field data. The work done to understand the debris-cover evolution would be useful, but this would need to be combined with data on mass balance and annual velocity to provide the required data. This would necessitate either a longer term project working on a

few glaciers, or one that uses historical mass balance and remote sensing data to provide model inputs.

Melt modelling of Miage Glacier predicted that if temperatures were to increase mass loss would be greatest on crevassed ice falls and areas of thinly debris-covered or dirty ice. This corresponds with observations on other debris-covered glaciers where mass loss is greatest just upglacier of the continuous debris cover (e.g. Stokes *et al.,* 2007). This also matches observations of Miage Glacier, where mass loss of the Dome and Mont Blanc tributary glaciers has been evident recently. It is likely these tributaries will become detached from the main glacier in the future as warming continues. However, it would be important to measure and model glaciers with different structures. Glaciers similar to Miage Glacier with steep ice-falls may react differently to climate and debris-cover changes than those with shallower profiles. Furthermore, the influence of an increase in debris thickness or air temperature was lessened in areas of thicker debris, and so glaciers with a thicker average debris-cover will likely be influenced to a lesser degree, and vice versa. This modelling would be necessary to inform the likely response of debris-covered glaciers to climate change in the 21st century.

9.2 Dye tracing

The next aim was to understand the structure of the englacial and subglacial hydrological drainage system and how it evolved using dye tracing. Based on previous research on debris-free glaciers (Nienow *et al.,* 1998; Willis *et al.,* 2002), it was expected that the opening of the hydrological system would not occur until the snowline had passed the debris-covered region. Instead, the englacial and subglacial system emanating from the main moulins on the upper glacier was efficient and channelized from early in June, even when the upper glacier was still snow-covered. This probably occurred because of the large supraglacial streams, or occasionally because of supraglacial lake drainage. Conduit closure analysis suggested the main subglacial conduit network did close up over the winter. The conduit system remained efficient throughout the melt season, and was characterised by fast water velocities, low dispersion coefficients, and a travel time to the proglacial stream of around 3 hours. This network is believed to have become less efficient during July 2011, after anomalously cold weather conditions. The decrease in the efficiency of conduits in mid-summer is unusual and could be more likely because the input meltwater is from relatively high on the glacier, but equally the unusual weather conditions could have been critical.

On the contrary, the englacial and subglacial system emanating from the streams on the lower glacier was not consistently efficient. Usually dye trace velocities were slower and dispersion coefficients larger, and the time taken for meltwater to reach the proglacial stream was longer than for moulins higher upglacier. The less efficient hydrological system beneath the more thickly debris-covered lower glacier exists because the magnitude of water reaching the system from any given point is relatively small and has a subdued diurnal signal. Consequently, pressurisation of the system and its conversion to a channelized form is less likely, with peaked dye returns probably indicating the stream follows a crevasse which connects with the main subglacial channel system originating from the upper glacier. The multi-peaked nature of some traces, and their evolution towards fewer larger peaks, gave evidence the system was distributed, although it did evolve to use certain flow paths at the expense of other, less efficient routes. However, even by mid-summer the efficiency of parts of the network did not reach that of the upper glacier moulins. Previous work indicated the lower glacier is underlain by a layer of sediment (Pavan *et al.,* 1999, cited in Deline, 2002), which may partly inhibit conduit formation (Flowers, 2008), but the lower discharges of the input streams are likely the most significant factor

Observations on Miage Glacier suggest the hydrological system does not follow the 'clean glacier' model of the most efficient drainage being at lowest elevations, with the increase in efficiency occurring gradually further up-glacier as the season progresses. Instead, the most efficient part of the system emanated from the large moulins higher on the glacier, and this remained the case throughout the season. Quincey *et al.,* (2009) mentioned that on Baltoro Glacier particularly large streams entered the glacier via moulins near Concordia, a region at the top of the main tongue where the debris is limited to longitudinal moraines and is above the zone of continuous debris cover: tellingly this area also experienced the largest increases in glacier velocity. It is therefore likely a similar drainage structure could be present beneath other debris-covered glaciers.

Therefore to replicate the runoff from a debris-covered glacier, a runoff model would need to be specifically developed to take the influence of the debris into account. The model could be tested using the runoff hydrograph observed from Miage Glacier, as well as records from other debris-covered glaciers. This thesis has provided an initial understanding to allow the future construction of a runoff model for a debris-covered glacier. It could be envisaged that melt would be routed supraglacially in one of three parallel reservoirs: one fast reservoir to replicate flow over an ice or dirty ice surface (with water velocities in the region of 0.8 m s^{-1}, the mean supraglacial stream velocity for the three upper glacier streams measured), and two slow reservoirs, one replicating flow

through snow and the other through debris and within the smaller streams of the lower glacier. The velocity of flow through snow could be calculated using the equations by Colbeck (1978). Further work would be required to understand the flow of water within and beneath the debris, but flow velocities in the lower glacier supraglacial streams would be in the region of 0.2 ms^{-1} (mean of S5 and S7 supraglacial stream velocities).The englacial and subglacial system could be replicated using one fast (conduit) and one slow (distributed system) reservoirs, positioned in series so that flow into the distributed system would flow into the conduit system. Typical flow velocities for the conduit system would be 0.6 ms^{-1} (average trace velocity into the moulins around C10), and typical velocities for the distributed system would be 0.1 ms^{-1} (average trace velocity for S5 and S7, which gave traces most indicative of a distributed system (section 5.2.2)). Flow from the ice and dirty ice reservoirs would immediately enter the conduit system (as observed on the upper glacier), while flow from the debris reservoir would enter the distributed system before flowing to the conduit system. There were no measurements on Miage Glacier which gave information of the likely route of snowmelt, but evidence from other workers (e.g. Nienow *et al.,* 1998) suggests the flow would enter a distributed system prior to a conduit system.

The main difficulties in applying this to other debris-covered glaciers would be the need to account for supraglacial lake drainage, which is characteristic of the lower ablation zones of debris-covered glaciers (Röhl, 2008) (as predicting lake drainage will be difficult, and may need to be modelled stochastically), and determining the location of streams and moulins (due to the difficulties of locating them in the field (Hambrey *et al.,* 2008) or from remotely sensed data). It may be necessary to repeat the dye tracing of the glacier drainage network on other glaciers to check the general model of the hydrological system evolution (early opening of the main channel, coupled to a less efficient network under debris-covered areas) is just as applicable to other debris-covered glaciers in different stages of development. If this could be achieved it would signify the understanding of debris-covered glacier hydrology had a reached a par with clean glacier hydrology, where there is still debate regarding the most appropriate runoff models.

9.3 Bulk water routing

The next aim was to understand the temporal variations in bulk water routing. In order to determine whether supraglacial reactions of the water with sediment would affect the water chemistry samples were also taken from supraglacial streams. The results suggested that ion concentrations were low for streams on the upper glacier, although higher sulphate concentrations were possible due to springtime snowmelt. On the lower

glacier there was evidence for raised bicarbonate concentrations, caused by reactions of the meltwater with the debris, although there was no evidence that sulphate concentrations were increased, except in small ponds.

Generally, the proglacial water chemistry revealed that periods of relatively high melt or rainfall, and therefore high discharges, were associated with low ion concentrations, high SSC and a high C-ratio, indicative of quickflow dominating runoff. Whereas periods of relatively low inputs and low discharges were associated with high ion concentrations, low SSC and a low C-ratio, indicative of delayed flow dominating runoff. The exception to this was on day 160 when there was a pulse of ion and sediment rich water. Since both the bicarbonate and sulphate concentration rose with discharge it was thought this pulse was caused by high water pressures which caused water which had spent a long time at the bed to be flushed out by the rising discharges – possibly during the period of fast glacier velocities on day 158.

Seasonal totals of sulphate and bicarbonate were high compared to other temperate clean glaciers, but similar to other debris-covered glaciers. The high sulphate ion concentration, as well as the low variability of values over the season suggested that a significant part of runoff did flow through a distributed system throughout the season – confirming the findings from dye tracing. Unlike other studies (e.g. Hasnain and Thayyen, 1999a) there did not appear to be an increase in sulphate ions during periods of rainfall – on Miage Glacier it is thought that only bicarbonate ions are produced through supraglacial reactions with debris. Although part of the elevated bicarbonate concentrations may be from supraglacial reactions of melt with the debris, the proglacial concentrations were high enough during low flow periods to suggest that at least a proportion of the bicarbonate concentration was also produced during reactions at the bed in a distributed system.

After identifying the structure of the drainage network and how it evolved, the next objective was to understand how this related to the fluctuations (and specifically the timing) of the proglacial stream runoff. The proglacial runoff hydrograph is a product of the quantity and timing of the water produced across the glacier, with the quantity determined by the ablation rate for a certain position and surface cover and the timing determined by a combination of the daily supraglacial hydrograph and the efficiency of the englacial and subglacial channel system. Analysis of the proglacial hydrograph found it had a few notable features: the lag time between air temperature and runoff was longer than for other debris-free temperate glaciers, and it did not decrease over the season; the baseflow was a larger component of runoff during cool weather compared to other debris-free alpine glaciers and the percentage of diurnal-type hydrographs was smaller than expected. Interestingly the diurnal conductivity cycle often reached a minimum (associated with the dilute quickflow

peak reaching the proglacial stream) before the discharge peak, so the conductivity and discharge rose in phase for a few hours. This suggests dilute melt with a short travel time, originating from clean and dirty ice close to the upper glacier moulins, was not the greatest proportion of runoff. Rather the runoff peak is composed of sub-debris melt and melt from the tributary glaciers, which are likely to have a higher ion concentration (for sub-debris melt due to its higher bicarbonate concentration, and for the tributary melt from a possibly less efficient subglacial system or post-mixing chemical reactions) and longer lag times (supraglacially and/or subglacially). This explanation would correspond with the overall longer lag times.

Complete understanding of the runoff signal was not possible without a full runoff model, which is beyond the scope of this thesis, but the hydrograph was classified into different periods to investigate what may be causing the hydrograph characteristics. Miage Glacier proglacial runoff tends not to be dominated by diurnal hydrographs under average weather conditions, instead the hydrograph rises steadily and falls more rapidly, smoothing out the meteorological signal into a 'saw-toothed' pattern. This will be due to a combination of the lower glacier melt having a greater lag (from conduction of the temperature signal through the debris, and the slower englacial and subglacial system) and a large amount of runoff being produced relatively far from the proglacial stream (travel times from above the main moulins are less well known however). Diurnal runoff patterns happen only under particularly warm weather, and are especially clear when clean ice melt is the largest proportion of runoff and the peak in debris-covered ice melt occurs at the same time as the other melt components. Perhaps when air temperatures are particularly warm the quantity of melt from the more thinly debris-covered regions on the upper tongue increases, and as the lag due to heat conduction is shorter, the overall lag is reduced. These findings suggest that glaciers which become debris-covered, or which experience an increase in debris-covered area may experience a change in their daily runoff signal towards one which peaks later, has a larger baseflow and a less clear diurnal signal under average weather conditions.

As discussed, some of the characteristics of the Miage Glacier runoff may be due to the presence of the debris. However, to fully understand how the debris influences the runoff hydrograph, runoff measurements from other debris-covered and clean glaciers would be required. This data could be used in a comparative study, with identical analysis methods, to allow the identification and quantification of factors which influence the magnitude and timing of runoff, such as the glacier's climate regime, distribution and thickness of debris cover, and hydrological system efficiency. A database could be developed which could be enlarged as more data is collected. To identify the contribution

and timing of sub-debris melt within the hydrograph, partitioning of the runoff into different components would be useful. On Miage Glacier the debris increases the bicarbonate ion concentration (and hence the conductivity) of the supraglacial stream water, but a more detailed approach using a suite of ions, or even isotopic fingerprinting (as used by Bhatia *et al.* (2011)) would be beneficial. Fingerprinting of proglacial runoff could be used to partition downstream runoff into glacial and non-glacial sources (expanding on work such as Maurya *et al.* (2011)). This could identify areas most at risk of future water resource depletion as glaciers recede.

9.4 Water balance

To quantify the parts of the water balance four objectives were addressed. The first involved calculating the inputs through the creation of a distributed melt model, which included distributing measured precipitation across the glacier, and the second involved the calculation of outputs by measuring proglacial discharge and evaporation. Melt was the greatest component of the inputs to the glacier, with the quantity of water stable across the season and between years. The largest runoff peaks were composed of rainfall, with the quantity much more variable between years. The third objective was to calculate storage, which was negative throughout the season of both years, although it was thought that this may be partly due to an underestimation of rainfall. A period of positive storage was identified in June 2010, thought due to storage of water within the thick snowpack which existed at this time.

To address the fourth objective, which was to understand the overall influence of the debris on the magnitude of ablation and evaporation, the melt model was modified to replicate the glacier with no debris. Total ablation was greater when the glacier was debris-covered because ice existed at a lower altitude and so covered a larger area, and melt rates were increased by the warmer air temperatures and higher albedo where the debris was thin or ice dirty. The overall latent heat flux over debris was less negative than if the glacier was debris free, because (at least in the model) evaporation only happened when the surface was saturated, whereas liquid water was always available from a melting debris-free ice surface. It may be pertinent to investigate whether evaporation of water from lower layers in the debris (as suggested by the fluxes of water vapour within the debris) is a significant flux, and if so develop models to reproduce this.

Within different climatic regions other debris-covered glacier basins may not share a similar water balance. For instance, monsoonal regions will likely have a larger rainfall (and therefore evaporation) component, and so it will be even more important to

accurately measure and distribute modelled rainfall and evaporation. The consistency of the quantity of melt produced between years on Miage Glacier is notable though, and this may be transferable to other regions, with melt providing a more predictable water resource than rainfall.

9.5 Glacier velocity

The region of the fastest and most variable glacier velocities corresponded with the region close to the main moulins on the upper glacier. Particularly fast velocities occurred during warm weather conditions in June, but also in mid-summer. These fast glacier velocities were occasionally associated with vertical uplift which implies water had overwhelmed the conduit network and entered the surrounding distributed system where the water pressure was increased and basal sliding enhanced. Although the magnitude of the increase in glacier velocities during a specific event was not necessarily larger in the spring compared to summer, the discharges required to initiate the same dynamic response were larger later in the season. This suggests the capacity of the conduit system increased during the summer.

The horizontal glacier velocities of the lower part of the debris-covered tongue (especially below the bend) were slower than the rest of the glacier, due to the shallow bed slope and widening valley which led to compressional longitudinal flow. This area also exhibited a small daily velocity variability, and a small difference between summer and winter velocities, the opposite of the case found on clean glaciers where velocity variability increases downglacier (Willis, 1995). Even though the subglacial system is relatively inefficient, which usually results in a greater variability of velocities, because inputs at any given point are small they rarely increase to a level sufficient to pressurise the system and lead to an increase in glacier velocities. The exception to this is when the rest of the subglacial system is less efficient and water reaches the bed of the lower glacier from springtime inputs higher on the glacier. This was likely the cause of the speed up of the lower glacier on day 158 in 2010, as it was associated with a release of sediment and ion rich water, indicative of water with a long basal residence time becoming flushed out by rising water pressures in the distributed system. There is evidence from days 160 to 163 2010 of a wave of faster velocities moving downglacier, caused by the movement of water through the subglacial system which increased water pressures at the bed. However, once the main subglacial conduit system becomes more efficient, increases in velocity are rare on the lower glacier, and are confined to points around the upper glacier moulins.

9.6 Summary

The main conclusion from this thesis is that the debris does influence the glacier-hydrology of Miage Glacier. Through its influence on the magnitude and timing of ablation, and the supraglacial topography it decreases the discharge and velocity of supraglacial streams where the debris is thick. This impacts on the form and evolution of the englacial and subglacial network, which when coupled with the supraglacial influences changes part of the amplitude and timing of the hydrograph reaching the proglacial stream, as well as glacier velocity variations. The debris does not prevent clean ice, dirty ice and snow melt from reaching the proglacial stream quickly through a well-developed conduit system, or from causing large daily variations in glacier velocity when weather conditions are warm, but it does mean the areas of highest ablation rates are relatively far from the proglacial stream outlet. In the future it is likely the regions of crevassed and dirty ice will experience the greatest increases in ablation, but this could be negated if the debris thickness increases.

10 References

Adhikary, S. Nakawo, M., Seko, K. and Shakya, B. (2000) Dust influence on the melting process of glacier ice: experimental results from Lirung Glacier, Nepal Himalayas, *Debris-Covered Glaciers, IAHS Publication* (264) 43-52

Ageta, Y., Iwata, S., Yabuki, H., Naito, N., Sakai, A., Narama, C. and Karma (2000) Expansion of glacial lakes in recent decades in the Bhutan Himalayas, *Debris-Covered Glaciers, IAHS Publication* (264) 165-175

Anderson, S.P., Drever, J.I., Frost, C.D. and Holden, P. (2000) Chemical weathering in the forefield of a retreating glacier. *Geochim. Cosmochim. Acta* (64) 1173–1189

Andreas, E. L. (2002) Parameterizing scalar transfer over snow and ice: a review, *Journal of Hydrometeorology* (3) 417-432

Arnold, N., Richards, K., Willis, I. and Sharp, M. (1998) Initial results from a distributed, physically based model of glacier hydrology, *Hydrological Processes* (42) 191-219

Arnold, N., Willis, I., Sharp, M., Richards, K. S. and Lawson, W. J. (1996) A distributed surface energy-balance model for a small valley glacier. I. Development and testing for Haut Glacier d'Arolla, Valais, Switzerland, *Journal of Glaciology,* 42 (140), 77-89

Baker, D., Escher-Vetter, H., Moser, H., Oerter, H. and Reinwarth, O. (1982) A glacier discharge model based on results from field studies of energy balance, water storage and flow, *Hydrological Aspects of Alpine and High Mountain Areas, IAHS Publication* (138) 103-136

Baraer, M., Mark, B. G., McKenzie, J. M., Condom, T., Bury, K., Huh, K-I., Portocarrero, C., Gómez, J. and Rathay, S. (2012) Glacier recession and water resources in Peru's Cordillera Blanca, *Journal of Glaciology*, 58 (207) 134-150

Baretti, M. (1880) Il ghiacciaio del Miage. Versant italiano del gruppo Monte Bianco (Alpi Pennine). *Memoria della Reale Accademia de Scienze di Torino* (2) 3-36

Barnett, T. P., Adam, J. C. and Lettenmaier, D. P. (2005) Potential impacts of a warming climate on water availability in snow-dominated regions, *Nature* (438) 303-309

Barrett, A. P. and Collins, D. N. (1997) Interaction between water pressure in the basal drainage system and discharge from an Alpine glacier before and after a rainfall-induced subglacial hydrological event*, Annals of Glaciology*, 288-292

Barry, R. G. (2008) *Mountain Weather and Climate, 3rd Edition*, Cambridge University Press, Cambridge

Bartholomew, I., Nienow, P., Mair, D., Hubbard, A., King, M.A., Sole, A. (2010) Seasonal evolution of subglacial drainage and acceleration in a Greenland outlet glacier, *Nature Geoscience*, 3 (6) 408-411

Bartholomew, I. D., Nienow, P., Sole, A., Mair, D., Cowton, T., King, M. A. and Palmer, S. (2011) Seasonal variations in Greenland Ice Sheet motion: Inland extent and behaviour at higher elevations, *Earth and Planetary Science Letters* (307) 271–278

Beniston, M. (2003) Climatic change in mountain regions: a review of possible impacts, *Climatic Change* (59) 5-31

Benn, D. I. and Evans, D. J. A. (1998) *Glaciers and Glaciation*, Arnold, London

Benn, D. I., Gulley, J., Luckman, A., Adamek, A. and Glowacki, P. S. (2009) Englacial drainage systems formed by hydrologically driven crevasse propagation, *Journal of Glaciology*, 55 (191) 513-522

Benn, D. I., Wiseman, S. and Hands, K. A. (2001) Growth and drainage of supraglacial lakes on debris-mantled Ngozumpa Glacier, Khumbu Himal, Nepal, *Journal of Glaciology*, 47 (159) 626-638

Benn, D. I., Wiseman, S. and Warren, C. R. (2000) Rapid growth of a supraglacial lake, Ngozumpa Glacier, Khumbu Himal, Nepal, *Debris-Covered Glaciers, IAHS Publication* (264) 177-185

Bernath, A. (1991) Zum Wasserhaushalt im Einzugsgebiet der Rhône bis Gletsch, *Zürcher Geographische Schriften* (43) 383

Bhatia, M.P., Das, S. B., Kujawinski, E. B., Henderson, P., Burke, A. and Charette, M. A. (2011) Seasonal evolution of water contributions to discharge from a Greenland outlet glacier: insight from a new isotope-mixing model, *Journal of Glaciology*, 57 (205) 929-941

Bingham, R. G., Nienow, P. W., Sharp, M. J. and Copland, L. (2006) Hydrology and dynamics of a polythermal (mostly cold) High Arctic glacier, *Earth Surface Processes and Landforms* (31) 1463-1479

Bocchiola, D., Mihalcea, C., Diolaiuti, G., Mosconi, G., Smraglia, C. and Rosso, R. (2010) Flow prediction in high altitude ungauged catchments: A case study in the Italian Alps (Pantano Basin, Adamello Group), *Advances in Water Resources* (33) 1224–1234

Bøggild, C. E. (2007) Simulation and parameterization of superimposed ice formation, *Hydrological Processes* (21) 1561–1566

Bolch, T., Buchroithner, M., Pieczonka, T. and Kunert, A. (2008) Planimetric and volumetric glacier changes in the Khumbu Himal, Nepal, since 1962 using Corona, Landsat TM and ASTER data, *Journal of Glaciology*, 54 (187) 592-600

Bozhinskiy, A. N., Krass, M. S. and Popovnin, V.V. (1986) Role of debris cover in the thermal physics of glaciers, *Journal of Glaciology*, 32 (111) 255-266

Braun, L. N., Aellen, M., Funk, M., Hock, R., Rohrer, M. B., Steinegger, U., Kappenberger, G. and Müller-Lemans, H. (1994) Measurement and simulation of high alpine water balance components in the Linth-Limmern Head watershed (North-Eastern Switzerland), *Zeitschrift für Gletscherkunde und Glazialgeologie* (30) 161-185

Braun, L. N., Grabs, W. and Rana, B. (1993) Application of a conceptual precipitation-runoff model in the Langtang Khola Basin, Nepal Himalaya, *Snow and Glacier Hydrology, IAHS Publication* (218) 221-237

Brock, B.W. and Arnold, N. S. (2000) A spreadsheet-based point surface energy balance model for glacier and snowmelt studies. *Earth Surface Processes and Landforms,* 25 (6) 649–658

Brock, B., Mihalcea, C., Kirkbride, M., Diolaiuti, G., Cutler, M. and Smiraglia, C. (2010) Meteorology and surface energy fluxes in the 2005-2007 ablation seasons at Miage debris-covered glacier, Mont Blanc Massif, Italian Alps, *Journal of Geophysical Research* (115) D09106

Brock, B., Rivera, A., Casassa, G., Bown, F. and Acuna, C. (2007) The surface energy balance of an active ice-covered volcano: Villarrica Volcano, southern Chile, *Annals of Glaciology* (45) 104-114

Brock, B.W., Willis, I. C. and Sharp, M. J. (2000) Measurement and parameterization of albedo variations at Haut Glacier d'Arolla, Switzerland. *Journal of Glaciology,* 46 (155) 675–688

Brock, B. W., Willis, I. C. and Sharp, M. J. (2006) Measurement and parameterisation of aerodynamic roughness length variations at Haut Glacier d'Arolla, Switzerland, *Journal of Glaciology*, 52 (177) 281-297

Brown, G. H. (2002) Glacier meltwater hydrochemistry, *Applied Geochemistry* (17) 855-883

Brown, G. H., Sharp, M. J., Tranter, M., Gurnell, A. M. and Nienow, P. W. (1998) Impact of post-mixing chemical reactions on the major ion chemistry of bulk meltwaters draining the Haut Glacier d'Arolla, Valais, Switzerland. In Sharp, M., Richards, K. S. and Tranter, M. (eds.) *Glacier Hydrology and Hydrochemistry*, John Wiley and Sons Ltd, Chichester, p139-154

Brown, G. H., Tranter, M., Sharp, M. J. (1996) Subglacial chemical erosion – seasonal variations in solute provenance, Haut Glacier d'Arolla, Switzerland, *Annals of Glaciology* (22) 25-31

Brutsaert, W. (1982) *Evaporation Into the Atmosphere: Theory, History and Applications*, Springer, New York.

Brzozowski, J. and Hooke, R. L. (1981) Seasonal variations in surface velocity of the lower part of Storglaciären, Kebnekaise, Sweden. Geografiska Annaler 63 A (3-4) 233-240

Burton, G. (2000) *Chemical Storylines Second Edition*, Heinemann Educational Publishers, Oxford

Caiping, C. and Yangjian, D. (2009) The application of artificial neural networks to simulate meltwater runoff of Keqikaer Glacier, south slope of Mt. Tuomuer, western China, *Environmental Geology* (57) 1839-1845

Campbell, F. M. A., Nienow, P. W. and Purves, R. S. (2006) Role of the supraglacial snowpack in mediating meltwater delivery to the glacier system as inferred from dye tracer investigations, *Hydrological Processes* (20) 969-985

Carabelli (1961) [Seismic survey 1957] Rilevamenti di ghiacciai e studi glaciologici in occasione dell'anno geofisico (Ghiacciaio del Miage): eslanazione geofisca. *Bollentino del Comitato Glaciologico Italiano*, 9 (1) 87-94

Casati, D. (1998) *Studio della dinamica di un debris-covered glacier: il Ghiacciaio del Miage*. Tesi Laurea, Universita Milano, 249

Casey, K. A., Kääb, A. and Benn, D. I. (2012) Geochemical characterization of supraglacial debris via in situ and optical remote sensing methods: a case study in Khumbu Himalaya, Nepal, *The Cryosphere* (6) 85-100

Chikita, K., Jha, J. and Yamada, T. (1998) The basin expansion mechanism of a supraglacial lake in the Nepal Himalayas, *Journal of the Faculty of Science, Hokkaido University, Series 7, Geophysics*, 11 (2) 501-521

Chikita, K., Jha, J. and Yamada, T. (2001) Sedimentary effects on the expansion of a Himalayan supraglacial lake, *Global and Planetary Change* (28) 23-34

Chikita, K., Joshi, S. P., Jha, J. and Hasegawa, H. (2000) Hydrological and thermal regimes in a supra-glacial lake: Imja, Khumbu, Nepal Himalaya, *Hydrological Sciences*, 45 (4) 507-521

Clifford, N. J., Richard, K. S., Brown, R. A. and Lane, S. N. (1995) Scales of variation in suspended sediment concentration and turbidity in a glacial meltwater stream, *Geografiska Annaler,* 77 A (1-2) 45-65.

Chiuminatto, D. (2004) *Analisi delle relazione tra assetto strutturale e geomorfologico dei rilievi montuosi nel bacino glaciale del Miage e nella Bassa Val Veny (Monte Bianco)*, M.Sc. thesis, University of Turin

Colbeck, S. C. (1978) Physical aspects of water flow through snow, *Advances in Hydroscience* (11) 165-206

Collins, D. N. and Young, G. J. (1979) Hydrochemical separation of components of discharge in Alpine catchments, *Proceedings of the Western Snow Conference* (47) 1-9

Conway, H. and Rasmussen, L. A. (2000) Summer temperature profiles within supraglacial debris on Khumbu Glacier, Nepal, *Debris-Covered Glaciers, IAHS Publication* (264) 89-97

Copland, L., Sharp, M. J. and Nienow, P. W. (2003) Links between short-term velocity variations and the subglacial hydrology of a predominantly cold polythermal glacier, *Journal of Glaciology*, 49 (166) 337-348

Covington, M. D., Banwell, A. F., Gulley, J., Saar, M. O., Willis, I. and Wicks, C. M. (2012) Quantifying the effects of glacier conduit geometry and recharge on proglacial hydrograph form, *Journal of Hydrology* (414-415) 59-71

Deline, P. (2002) *Etude géomorphologique des interactions écroulements rocheux/glaciers dans la haute montagne alpine (verant sud-est du Massif du Mant Blanc),* PhD thesis

Deline, P. (2005) Change in surface debris cover on Mont Blanc massif glaciers after the 'Little Ice Age' termination, *The Holocene*, 15 (2) 302-309

Deline, P. (2009) Interactions between rock avalanches and glaciers in the Mont Blanc massif during the late Holocene, *Quaternary Science Reviews* (28) 1070-1083

DHV Consultants (1999) *How to establish stage discharge rating curve*, DHV Consultants, New Delhi

Diaz, F., Jimenez, C. C. and Tejedor, M. (2004) Influence of the thickness and grain size of tephra mulch on soil water evaporation, *Agricultural Water Management* (74) 47-55

Dingman, S. L. (2002) *Physical Hydrology Second Edition*, Prentice Hall, New Jersey

Diolaiuti, G., Citterio, M., Carnielli, T., D'Agata, C., Kirkbride, M. and Smiraglia, C. (2006) Rates, processes and morphology of freshwater calving at Miage Glacier (Italian Alps), *Hydrological Processes* (20) 2233-2244

Diolaiuti, G., D'Agata, C., Meazza, A., Zanutta, A. and Smiraglia, C. (2009) Recent (1975-2003) changes in the Miage debris-covered glacier tongue (Mont Blanc, Italy) from analysis of aerial photos and maps, *Geogr. Fis. Dinam. Quat.* (32) 117-127

Diolaiuti, G., Kirkbride, M. P., Smiraglia, C., Benn, D. I., D'Agata, C. and Nicholson, L. (2005) Calving processes and lake evolution at Miage glacier, Mont Blanc, Italian Alps, *Annals of Glaciology* (40) 207-214

Fairchild, I.J., Bradby, L., Sharp, M., Tison, J.-L. (1994) Hydrochemistry of carbonate terrains in alpine glacial settings, *Earth Surface Processes and Landforms* (19) 33–54

Farinotti, D., Usselmann, S., Huss, M., Bauder, A. and Funk, M. (2011) Runoff evolution in the Swiss Alps: projections for selected high-alpine catchments based on ENSEMBLES scenarios, *Hydrological Processes*, 26 (13) 1909–1924

Fetter, C. W. (1988) *Applied Hydrogeology, Second Edition*, Merrill Publishing Company, Ohio

Flotron, A. (unpublished) *Jährliche Berichte über die Ergebnisse der Gletschermessungen im Auftrag der Kraftwerke Oberhasli,* Annual Reports

Flowers, G. E. (2008) Subglacial modulation of the hydrograph from glacierized basins, *Hydrological Processes* (22) 3903-3918

Flowers, G. E. and Clarke, G. K. C. (2002a) A multicomponent coupled model of glacier hydrology 1. Theory and synthetic examples, *Journal of Geophysical Research*, 107 (B11) 9-1 - 9-17

Flowers, G. E. and Clarke, G. K. C. (2002b) A multicomponent coupled model of glacier hydrology 2. Application to Trapridge Glacier, Yukon, Canada, *Journal of Geophysical Research*, 107 (B11) 10-1 - 10-16

Forbes, J. D. (1843) *Travels through the Alps of Savoy and others parts of the Pennine chain,* Black, Edinburgh

Ford, D. and Williams, P. (1989) *Karst Geomorphology and Hydrology*, Unwin Hyman Ltd., London

Foster, L., A., Brock, B. W., Cutler, M. E. J. and Diotri F. (2012) A physically based method for estimating supraglacial debris thickness from thermal band remote sensing data, *Journal of Glaciology*, 58 (210) 677-691

Fountain, A. G. (1993) Geometry and flow conditions of subglacial water at South Cascade Glacier, Washington State, U.S.A.; an analysis of tracer injections, *Journal of Glaciology*, 39 (131) 143-156

Fountain, A. G., Schlichting, R. B., Jansson, P. and Jacobel, R. W. (2005) Observations of englacial water passages: A fracture-dominated system, *Annals of Glaciology* (40) 25-30

Fountain, A. G. and Tangborn, W. (1985) Overview of contemporary techniques, *Techniques for Prediction of Runoff from Glacierized Areas, IAHS Publication* (149) 1-41

Fox, A. M., Willis, I. C. and Arnold, N. S. (2008) Modification and testing of a one-dimensional energy and mass balance model for supraglacial snowpacks, *Hydrological Processes* (22) 3194–3209

Fujii, Y. (1977) Field experiment on glacier ablation under a layer of debris cover, *Seppyo, Special Issue* (39) 20-21.

Gardelle, J., Berthier, E. and Arnaud, Y. (2012) Slight mass gain of Karakoram Glaciers in the early twenty-first century, *Nature Geoscience* (5) 322-325

Garvaglia, V., Pelfini, M. and Motta, E. (2010) Glacier stream activity in the proglacial area of debris covered glacier in Aosta Valley, Italy: an application of dendroglaciology, *Geogr. Fis. Dinam. Quat.* (33) 15-24

Giardino, M., Mortara, G. and Bonetto, F. (2001) Proposta per la realizzazione di un catalogo aerofotografico dei ghiacciai italiani, *Supplementi di Geografia Fisica e Dinamica Quaternaria* (5) 89-98.

Gomez, B. and Small, R. J. (1985) Medial moraines of the Haut Glacier d'Arolla, Valais, Switzerland: Debris supply and implications for moraine formation, *Journal of Glaciology*, 31 (109) 303-307

Gottlieb, L. (1980) Development and applications of a runoff model for snow-covered and glacierized basins, *Nordic Hydrology* (11) 255-272

Grifoll, J., Gastó, J. M., and Cohen, Y. (2005) Non-isothermal soil water transport and evaporation, *Advances in Water Resources* (28) 1254-1266

Gulley, J. (2009) Structural control of englacial conduits in the temperate Matanuska Glacier, Alaska, USA, *Journal of Glaciology*, 55 (192) 681-690

Gulley, J. and Benn, J. I. (2007) Structural control of englacial drainage systems in Himalayan debris-covered glaciers, *Journal of Glaciology*, 53 (182) 399-412

Gulley, J. D., Benn, D. I., Müller, D. and Luckman, A. (2009) A cut-and-closure origin for englacial conduits in uncrevassed regions of polythermal glaciers, *Journal of Glaciology*, 55 (189) 66-80

Haeberli, W. (1986) Factors influencing the distribution of rocky and sedimentary beds, Eidy. Tech. Hochshule, Zürich Wasserbau, *Hydrol. Glaziol. Mitt.* (90) 48-49

Hagg, W., Braun, L. N., Weber, M. and Becht, M. (2006) Runoff modelling in glacierized Central Asian catchments for present-day and future climate, Nordic Hydrology, 37 (2) 93-105

Hagg, W., Mayer, C., Lambrecht, A. and Helm, A. (2008) Sub-debris melt rates on southern Incheck Glacier, central Tian Shan, *Geografiska Annaler*, 90 (1) 55-63

Hambrey, M. J., Quincey, D. J., Glasser, N. F., Reynolds, J. M., Richardson, S. J. and Clemmens, S. (2008) Sedimentological, geomorphological and dynamic context of debris-mantled glaciers, Mount Everest (Sagarmatha) region, Nepal, *Quaternary Science Reviews* (27) 2361–2389

Han, H., Wang, J., Wei, J. and Liu, S. (2010) Backwasting rate on the debris-covered Koxkar glacier, Tuomeur mountain, China, *Journal of Glaciology*, 56 (169) 287-296

Hannah, D. M. and Gurnell, A. M. (2001) A conceptual, linear reservoir runoff model to investigate changes in cirque glacier hydrology, *Journal of Hydrology* (246) 123-141

Hannah, D. M., Gurnell, A.M. and McGregor, G. R. (1999) A methodology for investigation of the seasonal evolution in proglacial hydrograph form, *Hydrological Processes* (13) 2603-2621

Harrison, S., Glasser, N., Winchester, V., Haresign, E., Warren, C. and Jansson K. (2006) A glacial lake outburst flood associated with recent mountain glacier retreat, Patagonian Andes, *Holocene*, 16 (4) 611-620

Hasnain, S. I., Jose, P. G., Ahmad, S. and Negi, D. C. (2001) Character of the subglacial drainage system in the ablation area of Dokriani glacier, India, as revealed by dye-tracer studies, *Journal of Hydrology* (248) 216-223

Hasnain, S. I. and Thayyen, R. J. (1994) Hydrograph separation of bulk melt-waters of Dokriani Bamak glacier basin, based on electrical conductivity, *Current Science*, 67 (3) 189-13

Hasnain, S. I. and Thayyen, R. J. (1999a) Controls on the major-ion chemistry of the Dokriani glacier meltwaters, Ganga basin, Garhwal Himalaya, India, *Journal of Glaciology*, 45 (149) 87-92

Hasnain, S. I. and Thayyen, R. J. (1999b) Discharge and suspended-sediment concentration of meltwaters, draining from the Dokriani Glacier, Garhwal Himalaya, India, *Journal of Hydrology*, 218 (3-4) 191-198

Hewitt, I. J. and Fowler, A. C. (2008) Seasonal waves on glaciers, *Hydrological Processes* (22) 3919–3930

Hock, R. (1999) A distributed temperature-index ice- and snowmelt model including potential direct solar radiation, *Journal of Glaciology*, 45 (149) 101–111

Hock, R. and Holmgren, B. (2005) A distributed surface energy-balance model for complex topography and its application to Storglaciären, Sweden, *Journal of Glaciology*, 51 (172) 25-36

Hodgkins, R., Tranter, M. and Dowdeswell, J. A. (1998) The hydrochemistry of runoff from a 'cold-based' glacier in the high Arctic (Scott Turnerbreen, Svalbard), *Hydrological Processes* (12) 87-103

Hodson, A., Porter, P., Lowe, A. and Mumford, P. (2002) Chemical denudation and silicate weathering in Himalayan glacier basins: Batura Glacier, Pakistan*, Journal of Hydrology* (262) 193-208

Hodson, A. J., Gurnell, A. M., Washington, R., Tranter, M., Clark, M.J. and Hagan, J. O. (1998) Meteorological and runoff time-series characteristics in a small, high-Arctic glaciated basin, Svalbard, *Hydrological Processes* (12) 509-526

Hooke, R. Le B. (1984) On the role of mechanical energy in maintaining subglacial water conduits at atmospheric pressure, *Journal of Glaciology* (30) 180–187.

Hooke, R. Le B., Brzozowski, J. and Bronge, C. (1983) Seasonal variations in surface velocity, Storglaciären, Sweden, Geografiska Annaler (65A) 263-277

Hooke, R. Le B., Calla, P., Holmlund, P., Nilsson, M. and Stroeven, A. (1989) A three year record of seasonal variations in surface velocity, Storglaciären, Sweden*, Journal of Glaciology* (35) 235-247

Hubbard, B. and Clemmens, S. (2008) Recent high-resolution surface velocities and elevation change at a high-altitude, debris-covered glacier: Chacraraju, Peru*, Journal of Glaciology*, 54 (186) 479-486

Hubbard, B. and Glasser, N. (2005) *Field Techniques in Glaciology and Glacial Geomorphology,* John Wiley and Sons Ltd, Chichester

Hubbard, B., Heald, A., Reynolds, J. M., Quincey, D., Richardson, S. D., Luyo, M. Z., Portilla, N. S. and Hambrey, M. J. (2005) Impact of a rock avalanche on a moraine-dammed proglacial lake: Laguna Safuna Alta, Cordillera Blanca, Peru, *Earth Surface Processes and Landforms*, 30 (10) 1251-1264

Hubbard, B. P., Sharp, M. J., Willis, I. C., Nielsen, M. K. and Smart, C. C. (1995) Borehole water-level variations and the structure of the subglacial hydrological system of Haut Glacier d'Arolla, Valais, Switzerland, *Journal of Glaciology*, 41 (139) 572-583

Huss, M., Farinotti, D., Bauder, A. and Funk, M. (2008) Modelling runoff from highly glacierized alpine drainage basins in a changing climate, *Hydrological Processes* (22) 3888–3902

Iken, A. and Bindschadler, R. A. (1986) Combined measurements of subglacial water pressure and surface velocity of Findelengletscher, Switzerland: conclusions about drainage system and sliding mechanism, *Journal of Glaciology,* 32 (110) 101-119

Iken, A., Röthlisberger, H., Flotron, A. and Haeberli, W. (1983) The uplift of Unteraargletscher at the beginning of the melt season – a consequence of water storage at the bed? *Journal of Glaciology* (29) 28-47

Iwata, D., Aoki, T., Kadota, T., Seko, K. and Yamaguchi, K. (2000) Morphological evolution of the debris cover on Khumbu Glacier, Nepal, between 1978 and 1995, *Debris-covered glaciers, IAHS Publication* (264) 3-11

Jacobs, T., Wahr, J., Pfeffer, W. T. and Swenson, S. (2012) Recent contributions of glaciers and ice caps to sea level rise, *Nature* (482) 514-518

Jansson, P., Hock, R. and Schneider, T. (2003) The concept of glacier storage: a review, *Journal of Hydrology* (282) 116-129

Kamb, B. (1987) Glacier surge mechanism based on linked cavity configuration of the basal water conduit system, *Journal of Geophysical Research*, 92 (B9) 9083-9100

Kattelmann, R. and Watanabe, T. (1997) Draining Himalayan glacial lakes before they burst, *Destructive Water: Water-Caused Natural Disasters, their Abatement and Control*, *IAHS Publication* (239) 337-343

Kayastha, R. B., Takeuchi, Y., Nakawo, M. and Ageta, Y. (2000) Practical prediction of ice melting beneath various thickness of debris cover on Khumbu Glacier, Nepal, using a positive degree-day factor, *Debris-Covered Glaciers, IAHS Publication* (264) 71-81

Kellerer-Pirklbauer, A., Lieb, G. K., Avian, M. and Gspurning, J. (2008) The response of partially debris-covered valley glaciers to climate change: the example of the Pasterze Glacier (Austria) in the period 1964-2006, *Geografiska Annaler, 90 A* (4) 269-285

Keystone Aniline Corporation (2002) *Keyacid Rhodamine WT Liquid*, Keystone Aniline Corporation, Chicago

Khan, M. I. (1989) *Ablation on Barpu Glacier, Karakoram Himalaya, Pakistan: a study of melt processes on a faceted, debris-covered ice surface,* M.Sc. thesis, Department of Geography, Wilfrid Laurier University, Waterloo, Ontario

Kilpatrick, F. A. and Cobb, E. D. (1985) *Measurement of discharge using tracers*, United States Government Printing Office, Washington

Kilpatrick, F. A. and Wilson, J. F. (1989) *Measurement of time of travel in streams by dye tracing*, United States Government Printing Office, Washington

Kirkbride, M. P. (1995) Ice flow vectors on the debris-mantled Tasman Glacier, 1957-1986, *Geografiska Annaler*, 77A (3) 147-157

Kirkbride, M. P. and Dugmore, A. J. (2003) Glaciological response to distal tephra fallout from the 1974 eruption of Heckla, south Iceland, *Journal of Glaciology*, 49 (166) 420-428

Kirkbride, M. P. and Spedding, N. (1996) The influence of englacial drainage on sediment-transport pathways and till texture of temperate valley glaciers, *Annals of Glaciology* (22) 160-166

Kirkbride, M. P. and Warren, C. R, (1997) Calving Processes at a grounded ice cliff, *Annals of Glaciology* (24) 116-121

Kirkbride, M. P. and Warren, C. R. (1999) Tasman Glacier, New Zealand: 20th-century thinning and predicted calving retreat, *Global and Planetary Change* (22) 11-28

Kite, G. (1993) Computerized streamflow measurements using slug injection, *Hydrological Processes* (7) 227-233

Klok, E. J., Greuell, J. W. and Oerlemans, J. (2003) Temporal and spatial variation of the surface albedo of Morteratschgletscher, Switzerland, *Journal of Glaciology* (48) 505-518

Knight, P. G. (1999) *Glaciers*, Stanley Thornes Publishers Ltd., Cheltenham

Komori, J. (2008) Recent expansion of glacial lakes in the Bhutan Himalayas, *Quaternary International* (184) 177-186

Konovalov, V. (2000) Computations of melting under moraine as a part of a regional modelling of glacier runoff, *Debris-Covered Glaciers, IAHS Publication* (264) 109-118.

Kumar, K., Miral, M. S., Joshi, S., Pant, N., Joshi, V. and Joshi, L. M. (2009) Solute dynamics of meltwater of Gangotri glacier, Garhwal Himalaya, India, *Environmental Geology* (58) 1151-1159

Kundzewicz, Z.W., L.J. Mata, N.W. Arnell, P. Döll, P. Kabat, B. Jiménez, K.A. Miller, T. Oki, Z. Sen and I.A. Shiklomanov (2007) Freshwater resources and their management. In: M.L. Parry, O.F. Canziani, J.P. Palutikof, P.J. van der Linden and C.E. Hanson (eds.) *Climate Change 2007: Impacts, Adaptation and Vulnerability. Contribution of Working Group II to the Fourth Assessment Report of the Intergovernmental Panel on Climate Change,* Cambridge University Press, Cambridge, 173-210

Lambrecht, A., Mayer, C., Hagg, W., Popovnin, V., Rezepkin, A., Lomidze, N. and Svanadze, D. (2011) A comparison of glacier melt on debris-covered glaciers in the northern and southern Caucasus, *The Cryosphere* (5) 525–538

Lang, H. (1980) Theoretical and practical aspects in the computation of runoff from glacier areas. In: *Int. Symp. Computation and Prediction of Runoff from Glacierized Areas. Tbilisi, 1978 UNESCO/IAHS*, Academy of Sciences USSR, Geophysical Committee, Section Glaciology (38) 187-194

Lang, H. (1981) Is evaporation an important component in high alpine hydrology? *Nordic Hydrology* (12) 217-224

Lang, H. (1985) Höhenabhängigheit der Niederschläge. In B. Sevrah (ed.) *Die Niederschlag in der Schweiz* (Berträge zur Geologie der Schweiz – Hydrologie, No. 31) Bern: Kummerly and Frey, 149-157

Lappegard, G. and Kohler, J. (2005) Determination of basal hydraulic systems based on subglacial high-pressure pump experiments, *Annals of Glaciology* (40) 37-42

Lefeuvre, P. –M. and Ng, F. S. L. (2012) Uncovering glacier dynamics beneath a debris mantle, *Geophysical Research Abstracts* (14) EGU presentation, 25/04/12

Lefrançois, J., Grimaldi, C., Gascuel-Odoux, C. and Gilliet, N. (2007) Suspended sediment and discharge relationships to identify bank degradation as a main sediment source on small agricultural catchments, *Hydrological Processes* (21) 2923–2933

Lemke, P., J. Ren, R.B. Alley, I. Allison, J. Carrasco, G. Flato, Y. Fujii, G. Kaser, P. Mote, R.H. Thomas and T. Zhang (2007) Observations: Changes in Snow, Ice and Frozen Ground. In: Solomon, S., D. Qin, M. Manning, Z. Chen, M. Marquis, K.B. Averyt,

M. Tignor and H.L. Miller (eds.) *Climate Change 2007: The Physical Science Basis. Contribution of Working Group I to the Fourth Assessment Report of the Intergovernmental Panel on Climate,* Cambridge University Press, Cambridge, 337-383

Lesca, C. (1974) Emploi de la photogrammétrie analytique pour la determination de la vitesse supérficielle des glaciers et des profondeurs relatives, *Bollentino del Comitato Glacologico Italiano* (22) 169-186

Lister, H. (1953) Report on glaciology at Breiđamerkurjökull 1951, *Jökull* (3) 23-31

Loomis, S.R. (1970) Morphology and ablation processes on glacier ice. In Bushnell, V. C. and Ragle, R.H. (eds.) *Icefield Ranges Research Project; Scientific Results. Vol. 2.* Montréal, Que., Arctic Institute of North America; NewYork, American Geographical Society, 27-31

Lundquist, D. (1982) Modelling runoff from a glacierized basin, *Hydrological Aspects of Alpine and High Mountain Areas, IAHS Publication* (138) 131-136

Mair, D., Hubbard, B., Nienow, P., Willis, I. and Fischer, U. H. (2008) Diurnal fluctuations in glacier ice deformation: Haut Glacier d'Arolla, Switzerland, *Earth Surface Processes and Landforms* (33) 1272-1284

Mair, D., Nienow, P., Willis, I. and Sharp, M. (2001) Spatial patterns of glacier motion during a high-velocity event: Haut Glacier d'Arolla, Switzerland, *Journal of Glaciology*, 47 (156) 9-20

Mair, D. W. F., Sharp, M. J. and Willis, I. C. (2002) Evidence for basal cavity opening from analysis of surface uplift during a high-velocity event: Haut Glacier d'Arolla, Switzerland, *Journal of Glaciology*, 48 (161) 208-216

Mair, D., Hubbard, B., Nienow, P., Willis, I. and Fischer, U. H. (2008) Diurnal fluctuations in glacier ice deformation: Haut Glacier d'Arolla, Switzerland, *Earth Surface Processes and Landforms* (33) 1272-1284

Mair, D., Willis, I., Fischer, U. H., Hubbard, B., Nienow, P. and Hubbard, A. (2003) Hydrological controls on patterns of surface, internal and basal motion during three "spring events": Haut Glacier d'Arolla, Switzerland, *Journal of Glaciology*, 49 (167) 555-567

Maisch, M., Haeberli, W., Hoelze, M. and Wenzel, J. (1999) Occurance of rocky and sedimentary glacier beds in the Swiss Alps as estimated from glacier inventory data, *Annals of Glaciology* (28) 231-235

Marsh, T. and Dixon, H. (2012) The UK water balance – how much has it changed in a warming world? *Proceedings of the BHS Eleventh National Symposium Dundee 2012*

Marshall, J. and Holmes, J. W. (1988) *Soil Physics*, Cambridge University Press, Cambridge, Massachusetts

Marty, C., Philipona, R., Frohilich, C. and Ohmura, A. (2002) Altitude dependence of surface radiation fluxes and cloud forcing in the Alps: results from the alpine surface radiation budget network, *Theoretical and Applied Climatology*, 72 137-155

Masetti, M., Diolaiuti, G., D'Agata, C. and Smiraglia, C. (2009) Hydrological characterization of an ice-contact lake: Miage lake (Monte Bianco, Italy), *Water Resource Management* (24) 1677–1696

Mattson, L. E. (2000) The influence of a debris cover on the mid-summer discharge of Dome Glacier, Canadian Rocky Mountains, *Debris-Covered Glaciers, IAHS Publication* (264) 25-33

Mattson, L. E. and Gardner, J. S. (1991) Energy exchanges and ablation rates on the debris covered Rakhiot Glacier, Pakistan. *Z. Gletscherkd. Glazialgeol.*, 25 (1) 1989, 17-32.

Mattson, L. E., Gardener, J. S. and Young, G. J. (1993) Ablation on debris covered glaciers: an example from the Rakhiot Glacier. Punjab, Himalaya, *Snow and Glacier Hydrology, IAHS Publication* (218) 289-296

Maurya, A. S., Shah, M., Deshpande, R. D., Bhardwaj, R. M., Prasad, A. and Gupta, S. K. (2011) Hydrograph separation and precipitation source identification using stable water isotopes and conductivity: River Ganga at Himalayan foothills, *Hydrological Processes* (25) 1521-1530

Mayer, C., Lambrecht, A., Belò, M., Smiraglia, C. and Diolaiuti, G. (2006) Glaciological characteristics of the ablation zone of Baltoro glacier, Karakoram, Pakistan*, Annals of Glaciology* (43) 123-131

Mehta, A. J. and McAnally, W. H. (2008) Fine grained sediment transport. In: García, M. H. (ed.) *Sedimentation Engineering, Processes, Measurements, Modeling and Practice*, American Society of Civil Engineers, Virginia

Mihalcea, C., Brock, B. W., Diolaiuti, G., D'Agata, C., Citterio, M., Kirkbride, M. P., Cutler, M. E. J. and Smiraglia, C. (2008a) Using ASTER satellite and ground-based surface temperature measurements to derive supraglacial debris cover and thickness patterns on Miage Glacier (Mont Blanc Massif, Italy), *Cold Regions Science and Technology* (52) 341-354

Mihalcea, C., Mayer, C., Diolaiuti, G., D'Agata, C., Smiraglia, C., Lambrecht, A., Vuillermoz, E. and Tartari, G. (2008b) Spatial distribution of debris thickness and melting from remote-sensing and meteorological data, at debris-covered Baltoro glacier, Pakistan, *Annals of Glaciology* (48) 49-75

Mihalcea, C., Mayer, C., Diolaiuti, G., Lambrecht, A., Smiraglia, C. and Tartari, G (2006) Ice ablation and meteorological conditions on the debris-covered area of Baltoro glacier, Karakoram, Pakistan, *Annals of Glaciology* (43) 292-300

Mittelbach, H., Lehner, I., Seneviratne, S. I. (2012) Comparison of four soil moisture sensor types under field conditions in Switzerland, *Journal of Hydrology* (430-431) 39-49

Nakawo, M., Morohoshi, T. and Uehara, S. (1993) Satellite data utilization for estimating ablation of debris covered glaciers, *Snow and Glacier Hydrology, IAHS Publication* (218) 75-83

Nakawo, M. and Takahashi, S. (1982) A simplified model for estimating glacial ablation under a debris layer, *Hydrological Aspects of Alpine and High Mountain Areas, IAHS Publication* (138) 137-145

Nakawo, M., Yabuki, H. and Sakai, A. (1999) Characteristics of Khumbu Glacier, Nepal Himalaya: recent change in the debris-covered area, *Annals of Glaciology* (28) 118-122

Nakawo, M. and Young, G. J. (1981) Field experiments to determine the effect of a debris layer on ablation of glacier ice, *Annals of Glaciology* (2) 85-91

Nakawo, M. and Young, G. J. (1982) Estimate of glacier ablation under a debris layer from surface temperature and meteorological variables, *Journal of Glaciology,* 28 (98) 29-34

Nicholson, L. and Benn, D. I. (2006) Calculating ice melt beneath a debris layer using meteorological data, *Journal of Glaciology*, 52 (178) 463-470

Nicholson, L., Benn, D. I. (in press) Properties of natural supraglacial debris in relation to modelling sub-debris ice ablation, *Earth Surface Processes and Landforms*, doi: 10.1002/esp.3299

Nienow, P. W., Sharp, M. and Willis, I. C. (1996) Velocity-discharge relationships derived from dye-tracer experiments in glacial meltwaters: implications for subglacial flow conditions, *Hydrological Processes* (10) 1411-1426

Nienow, P. W., Sharp, M. and Willis, I. C. (1998) Seasonal changes in the morphology of the subglacial drainage system, Haut Glacier d'Arolla, Switzerland, *Earth Surface Processes and Landforms* (23) 825-843

Obleitner, F. (2000) The energy budget of snow and ice at Breidamerkurjökull, Vatnajöull, Iceland, *Boundary-Layer Meteorology* (97) 385-410

Oerlemans, J. (2010) *The Microclimate of Valley Glaciers*, Utrecht Publishing and Archiving Services, Universiteitsbibliotheek Utrecht

Oke, T. R. (1987) *Boundary Layer Climates, 2nd Edition,* Methuen and Co. Ltd., London

Oke, T. R. (1978) *Boundary Layer Climates,* Methuen and Co. Ltd., London

Östling, M., and Hooke, R. L. (1986) Water storage in Storglaciären, Kebnekaise, Sweden, *Geografiska Annaler* (A68) 279–290

Östrem, G. (1959) Ice melting under a thin layer of moraine, and the existence of ice cores in moraine ridges*, Geografiska Annaler*, 41 (4) 228-230

Östrem, G. (1964) Ice-cored moraines in Scandinavia, *Geografiska Annaler*, 46 (3) 282-337

Paterson, W. S. B. (1994) *The Physics of Glaciers*, 3rd Edition, Pergamon Press, Oxford

Pavan, M., Smiraglia, C. and Merlanti, F (1999) *Prospezione geofisca sul ghiacciaio del Miage (Alpi accidentali)*, Poster, Genova, 1

Pellicciotti, F., Brock, B. W., Strasser, U., Burlando, P., Funk, M. and Corripio, J. (2005) An enhanced temperature-index glacier melt model including the shortwave radiation balance: development and testing for Haut Glacier d'Arolla, Switzerland, *Journal of Glaciology*, 51 (175) 573-587

Pellicciotti, F., Helbing, J., Rivera, A., Favier, V., Corripio, J., Araos, J., Sicart, J. E-. and Carenzo, M. (2008) A study of the energy balance and melt regime on Juncal Norte Glacier, semi-arid Andes of central Chile, using melt models of different complexity. *Hydrological Processes,* 22 (19) 3980-3997.

Pfletschinger, H., Engelhardt, I., Piepenbrink, M., Königer, F., Schuhmann, R., Kallioras, A. and Schüth, C. (2012) Soil column experiments to quantify vadose zone water fluxes in arid settings, *Environmental Earth Sciences* (65) 1523–1533

Philip, J. R. and de Vries, D. A. (1957) Moisture movement in porous materials under temperature gradients, *Transactions, American Geophysical Union*, 38 (2) 222-231

Popovnin, V. V. and Rozova, A. V. (2002) Influence of sub-debris thawing on ablation and runoff of the Djankuat Glacier in the Caucasus, *Nordic Hydrology*, 33 (1) 75-94

Purdie, H. L., Brook, M. S. and Fuller, I. C. (2008) Seasonal variation in ablation and surface velocity on a temperate, maritime glacier: Fox Glacier, New Zealand, *Arctic, Antarctic and Alpine Research*, 40 (1) 140-147

Quincey, D. J., Copland, L., Mayer, C., Bishop, M., Luckman, A., Belò, M. (2009) Ice velocity and climate variations for Baltoro Glacier, Pakistan, *Journal of Glaciology*, 55 (194) 1061-1071

Quincey, D. J., Richardson, S. D., Luckman, A., Lucas, R. M., Reynolds, J. M., Hambrey, M. J. and Glasser, N. F. (2007) Early recognition of glacial lake hazards in the Himalaya using remote sensing datasets, *Global and Planetary Change* (56) 137-152

Rainwater, F.H. and Guy, H.P. (1961) *Some observations on the hydrochemistry and sedimentation of the Chamberlain Glacier area, Alaska*, US Geological Survey Professional Paper 414-c

Raiswell, R. and Thomas, A. G. (1984) Solute acquisition in glacial melt waters I. Fjallsjökull (south-east Iceland): bulk melt waters with closed-system characteristics, *Journal of Glaciology*, 30 (104) 35-43

Ramsey, J. G. (1967) *The folding and fracturing of rocks*, Mc-Graw Hill, New York

Rana, B., Fukushima, Y., Ageta, Y. and Nakawo, M. (1996) Runoff modelling of a river basin with a debris-covered glacier in Langtang Valley, Nepal Himalaya, *Bulletin of Glacier Research* (14) 1-6

Rana, B., Nakawo, M., Fukushima, Y. and Ageta, Y. (1997) Application of a conceptual precipitation-runoff model (HYCYMODEL) in a debris-covered glacierized basin in the Langtang Valley, Nepal Himalaya*, Annals of Glaciology* (25) 226-231

Reda, I. and Andreas, A. (2008) *Solar Position Algorithm for Solar Radiation Applications, National Renewable Energy Laboratory, Technical Report NREL/TP-560-34302*, U.S. Department of Energy, Oak Ridge

Reid, T. D., Carenzo, M., Pellicciotto, F. and Brock, B. W. (in press) Including debris cover effects in a distributed model of glacier ablation, *Journal of Geophysical Research,* doi:10.1029/2012JD017795

Reid, T.D. and Brock, B.W. (2010) An energy-balance model for debris-covered glaciers including heat conduction through the debris layer, *Journal of Glaciology* (56) 903–916

Reijmer, C. H. and Hock, R. (2008) Internal accumulation on Storglaciären, Sweden, in a multi-layer snow model coupled to a distributed energy- and mass-balance model, *Journal of Glaciology*, 54 (184) 61-72

Reynolds, J. M. (2000) On the formation of supraglacial lakes on debris-covered glaciers, *Debris-Covered Glaciers, IAHS Publication* (264) 153-161

Reznichenko, N., Davies, T., Shulmeister, J. and McSaveney, M. (2010) Effects of debris on ice-surface melting rates: an experimental study, *Journal of Glaciology*, 56 (197) 384-394

Richards, K. (1982) *Rivers: Form and Process in Alluvial Channels*, Methuen and Co. Ltd., London

Richards, K., Sharp, M., Arnold, N., Gurnell, A., Clark, M., Tranter, M., Nienow, P., Brown, G., Willis, I. And Lawson, W. (1996) An integrated approach to modelling hydrology and water quality in glacierized catchments, *Hydrological Processes* (10) 479-508

Richardson, S. D. and Reynolds, J. M. (2000) Degradation of ice-cored moraine dams: implications for hazard development, *Debris-Covered Glaciers, IAHS Publication* (264) 187-197

Rivera, A., Bown, F., Mella, R., Wendt, J., Casassa, G., Acun□ a, C., Rignot, E., Clavera, J. and Brock, B. (2006) Ice volumetric changes on active volcanoes in southern Chile, *Annals of Glaciology* (43) 111-122

Rivera, A., Corripio, J. G., Brock, B., Clavero, J. and Wendt, J. (2008) Monitoring ice-capped active Volcán Villarrica, southern Chile, using terrestrial photography

combined with automatic weather stations and global positioning systems, *Journal of Glaciology*, 54 (188) 920-930

Röhl, K. (2008) Characteristics and evolution of supraglacial ponds on debris-covered Tasman Glacier, New Zealand*, Journal of Glaciology*, 54 (188) 867-880

Röthlisberger, H. (1972) Water pressure in intra- and subglacial channels, *Journal of Glaciology*, 11 (62) 177- 203

Roy, V. (2005) *Sun_position MATLAB function*, MATLAB File Exchange, http://www.mathworks.com/matlabcentral/fileexchange/4605 , 28/06/12

Ruffles, L.M. (1999) *In situ investigations of subglacial hydrology and basal ice at Svartisen Glaciological Observatory, Norway,* Unpublished PhD thesis, University of Wales, Aberystwyth

Saito, H., Šimůnek, J. and Mohanty, B. P. (2006) Numerical analysis of coupled water, vapor, and heat transport in the vadose zone, *Vadose Zone Journal* (5) 784-800

Sakai, A., Takeuchi, N., Fujita, K. and Nakawo, M. (2000) Role of supraglacial ponds in the ablation process of a debris-covered glacier in the Nepal Himalayas, *Debris-Covered Glaciers, IAHS Publication* (264) 119-130

Sakai, A. Fujita, K. and Kubota, K. (2004) Evaporation and percolation effect on melting at debris-covered Lirung Glacier, Nepal Himalayas, 1996, *Bulletin of Glaciological Research* (21) 9-15

Sakai, A., Fujita, K., Aoki, T., Asahi, K., and Nakawo, M. (1997) Water discharge from the Lirung Glacier in Langtang Valley, Nepal Himalayas, 1996, *Bulletin of Glacier Research* (15) 79-83

Scanlon, B. R. (1992) Evaluation of liquid and vapor water flow in desert soils based on chlorine 36 and tritium tracers and nonisothermal flow simulations, *Water Resources Research*, 28 (1) 285-297

Scherler, D. and Strecker, M. R. (2012) Large surface velocity fluctuations of Biafo Glacier, central Karakoram, at high spatial and temporal resolution from optical satellite images, *Journal of Glaciology*, 58 (209) 569-580

Scherler, D., Leprince, S. and Strecker, M. R. (2008) Glacier-surface velocities in alpine terrain from optical satellite imagery – accuracy improvement and quality assessment, *Remote Sensing of Environment* (112) 3806-3819

Schuler, T. V. and Fischer, U. H. (2009) Modeling the diurnal variation of tracer transit velocity through a subglacial channel*, Journal of Geophysical Research* (144) F04017

Shepherd, A., Hubbard, A., Nienow, P., King, M., McMillan, M. and Joughin, I. (2009) Greenland ice sheet motion coupled with daily melting in late summer, *Geophysical Research Letters* (36) L01501

Shreve, R. L. (1972) Movement of water in glaciers, *Journal of Glaciology*, 11 (62) 205-214

Singh, P., Arora, M. and Goel, N. K. (2006a) Effect of climate change on runoff of a glacierized Himalayan basin, *Hydrological Processes* (20) 1979-1992

Singh, P., Haritashya, U. K. and Kumar, N. (2008) Modelling and estimation of different components of streamflow for Gangotri Glacier basin, Himalayas, *Hydrological Sciences Journal*, 53 (2) 309-322

Singh, P., Haritashya, U. K., Kumar, N. and Singh, Y. (2006b) Hydrological characteristics of the Gangotri Glacier, central Himalayas, India*, Journal of Hydrology*, 327 (1-2) 55-67

Singh, P., Haritashya, U. K., Ramasastri, K. S. and Kumar, N. (2005) Diurnal variations in discharge and suspended sediment concentration, including runoff-delaying characteristics, of the Gangotri Glacier in the Garhwal Himalayas, *Hydrological Processes* (19)1445-1457

Singh, P., Ramasastri, K. S and Singh, U. K. (1995) Hydrological characteristics of the Dokriani Glacier in the Garhwal Himalayas, *Hydrological Sciences* (40)243-257

Small, R. J. and Clark, M. J. (1974) The medial moraines of the lower Glacier de Tsidjiore Nouve, Valais, Switzerland. *Journal of Glaciology*, 13 (68) 255-263.

Smiraglia, C., Diolaiuti, G., Casati, D. and Kirkbride, M. P. (2000) Recent areal and altimetric variations of Miage Glacier (Monte Bianco massif, Italian Alps), *Debris-Covered Glaciers, IAHS Publication* (264) 227-233

Società Meteorologica Italiana (2010) Luglio 2010: tra i più caldi mai registrati al Nord Italia, *Nimbus*, Società Meteorologica Subalpina, Castello Borello, Bussoleno, http://www.nimbus.it/clima/2010/100804CaldoLuglio2010.pdf, 22/08/12

Società Meteorologica Italiana (2011) Prima metà di aprile: caldo record al Nord Italia, *Nimbus*, Società Meteorologica Subalpina, Castello Borello, Bussoleno, http://www.nimbus.it/clima/2011/110419RecordCaldoAprile.htm, 22/08/12

Sole, A.J., Mair, D.W.F., Nienow, P.W., Bartholomew, I.D., King, M.A., Burke, M.J. and Joughin, I. (2011) Seasonal speed up of a Greenland marine-terminating outlet glacier forced by surface melt-induced changes in subglacial hydrology, *Journal of Geophysical Research F: Earth Surface*, 116 (3) art. no. F03014

Steinpórsson, S. and Óskarsson, N. (1983) Chemical monitoring of Jökulhlaup water in Skeidará and the geothermal system in Grímsvötn, Iceland, Jokull (33) 73–86

Stenborg, T. (1969) Studies of the internal drainage of glaciers, *Geografiska Annaler*, 51A (1-2) 13-41

Stokes, C. R., Popovnin, V., Aleyhikov, A., Gurney, S. D. and Shahgedanova, M (2007) Recent glacier retreat in the Caucasus Mountains, Russia, and associated increase in

supraglacial debris cover and supra-/proglacial lake development, *Annals of Glaciology* (46) 195-203

Sugiyama, S., Naruse, R. and Murav'yev, Y. D. (2005) Surface strain anomaly induced by the storage and drainage of englacial water in Koryto glacier, Kamchatka, Russia, *Annals of Glaciology* (40) 232-236

Swift, D. A., Nienow, P. W., Hoey, T. B. and Mair, D. W. F. (2005) Seasonal evolution of runoff from Haut Glacier d'Arolla, Switzerland and implications for glacial geomorphic processes, *Journal of Hydrology* (309) 133-148

Syverson, K.M. and Mickelson, D. (1995) Ablation of debris-covered ice and the formation of pitted outwash plains at Burroughs Glacier, south eastern Alaska. In Engstrom, D.R. (ed.) *Proceedings of the Third Glacier Bay Science Symposium, 1993,* Anchorage, AK, U.S. Department of the Interior, National Park Service, 66-74.

Takeuchi, Y., Kayastha, R. B. and Nakawo, M. (2000) Characteristics of ablation and heat balance in the debris-free and debris-covered areas on Khumbu Glacier, Nepal Himalayas, in the pre-monsoon season, *Debris-Covered Glaciers, IAHS Publication* (264) 53-61

Tangborn, W. and Rana, B. (2000) Mass balance and runoff of the partially debris-covered Langtang Glacier, Nepal, Debris-Covered Glaciers, *IAHS Publication* (264) 99-108

Tangborn, W. V., Krimmel, R., and Meier, M. (1975) A comparison of glacier mass balance by glaciological, hydrological, and mapping methods, South Cascade Glacier, Washington, *General Assembly of Moscow, IAHS Publication* (104) 185–196

Thompson, A. M., Kim. K. and Vandermuss, A. J. (2008) Thermal characteristics of stormwater runoff from asphalt and sod surfaces, *Journal of the American Water Resources Association*, 44 (5) 1325-1336

Thomson, M. H., Kirkbride, M. P. and Brock, B. W. (2000) Twentieth century surface elevation change of the Miage Glacier, Italian Alps, *Debris-Covered Glaciers, IAHS Publication* (264) 219-225

Tranter, M. and Raiswell, R. (1991) The composition of the englacial and subglacial component in bulk meltwaters draining the Gornergletscher, Switzerland, *Journal of Glaciology*, 37 (125) 59-66

Tranter, M., Brown, G. H., Hodson, A. J. and Gurnell, A. M. (1996) Hydrochemistry as an indicator of subglacial drainage system structure: a comparison of Alpine and sub-Polar environments, *Hydrological Processes* (10) 541-556

Tranter, M., Brown, G. H. and Sharp, M. J. (1993a) The use of sulphate as a tracer for the delayed flow component of alpine glacial runoff, *Tracers in Hydrology, IAHS Publication* (215) 89-98

Tranter, M., Brown, G., Raiswell, R., Sharp, M. and Gurnell, A. (1993b) A conceptual model of solute acquisition by Alpine glacial meltwaters, *Journal of Glaciology*, 39 (133) 573-581

Tranter, M., Sharp, M. J., Brown, G. H., Willis, I. C., Hubbard, B. P., Nielson, M. K., Smart, C. C., Gordon, S., Tulley, M. and Lamb, H. R. (1998) Variability in the chemical composition of in situ subglacial meltwaters. In Sharp, M., Richards, K. S. and Tranter, M. (eds.) *Glacier Hydrology and Hydrochemistry*, John Wiley and Sons Ltd, Chichester, p219-236

Valbusa, U. (1924) Il ghiacciaio della Brenva (M. Bianco) dal 20 Aprile 1923 al 15 Giugnio 1924, *Journal of the Italian Alpine Club* (43) 270–281

Vatne, G. (2001) Geometry of englacial water conduits, Austre Brøggerbreen, Svalbard, *Norsk geogr. Tidsskr.* (55) 85-93

Walder, J. S. (1986) Hydraulics of subglacial cavities, *Journal of Glaciology* (32) 439-445

Ward, R. C. and Robinson, M. (2000) *Principles of Hydrology Fourth Edition*, McGraw-Hill, Berkshire

Watanabe, O., Iwata, S. and Fushimi, H. (1986) Topographic characteristics in the ablation area of the Khumbu Glacier, Nepal Himalaya, *Annals of Glaciology* (8) 177-180

Weertman, J. (1973) Can a water-filled crevasse reach the bottom surface of a glacier? *Symposium on the Hydrology of Glaciers, IAHS Publication* (95) 139-145

Weingartner, R., Viviroli, D. and Schädler, B. (2007) Water resources in mountain regions: a methodological approach to assess the water balance in a highland-lowland-system, *Hydrological Processes* (21) 578-585

Werder, M. A., Schuler, T. V. and Funk, M. (2010) Short term variations of tracer transit speed on alpine glaciers, *The Cryosphere* (4) 381–396

Willis, I. C. (1995) Intra-annual variations in glacier motion: a review, *Progress in Physical Geography*, 19 (1) 61-106

Willis, I. C. and Sharp, M. J. (in prep.) Short-term horizontal velocity variations of Midtdalsbreen, Hardangerjokulen, Norway, *Journal of Glaciology*

Willis, I. C., Arnold, N. S. and Brock, B. W. (2002) Effect of snowpack removal on energy balance, melt and runoff in a small supraglacial catchment, *Hydrological Processes* (16) 2721-2749

Willis, I. C., Lawson, W., Owens, I., Jacobel, B. and Autridge, J. (2009) Subglacial drainage system structure and morphology of Brewster Glacier, New Zealand, *Hydrological Processes* (23) 384-396

Willis, I. C., Richards, K. S., and Sharp, M. J. (1996) Links between proglacial stream suspended sediment dynamics, glacier hydrology and glacier motion at Midtdalsbreen, Norway, *Hydrological Processes* (10) 629-648

Willis, I. C., Sharp, M. J. and Richards, K. S. (1990) Configuration of the drainage system of Midtdalsbreen, Norway, as indicated by dye-tracing experiments*, Journal of Glaciology*, 36 (122) 89-101

Willis, I. C., Sharp, M. J. and Richards, K. S (1993) Studies of the water balance of Midtdalsbreen, Hardangerjökulen, Norway. II. Water storage and runoff prediction, *Zeitschrift für Gletscherkunde und Glazialgeologie* (27/28) 117-138

Willis, I. C., Fitzsimmons, C. D., Melvold, K., Andreassen , L. M. and Giesen, R. H. (2012) Structure, morphology and water flux of a subglacial drainage system, Midtdalsbreen, Norway, *Hydrological Processes* , DOI: 10.1002/hyp.8431

Wilson, J. F., Cobb, E. D., Kilpatrick, F. A. (1986) *Fluorometric procedures for dye tracing*, United States Government Printing Office, Washington

World Glacier Monitoring Service (WGMS) (2011) *Glacier Mass Balance Bulletin No. 11 (2008–2009).* Zemp, M., Nussbaumer, S. U., Gärtner-Roer, I., Hoelzle, M., Paul, F., and Haeberli, W. (eds.), ICSU(WDS)/IUGG(IACS)/UNEP/UNESCO/WMO, World Glacier Monitoring Service, Zurich, Switzerland, 1-102

Xu, J., Grumbine, R. E., Shrestha, A., Eriksson, M., Yang, X., Wang, Y. and Wilkes, A. (2009) The Melting Himalayas: Cascading Effects of Climate Change on Water, Biodiversity, and Livelihoods, *Conservation Biology*, 23 (3) 520-530

Zhang, Y., Fujita, K., Liu, S., Liu, Q. and Nuimura, T. (2011) Distribution of debris thickness and its effect on ice melt at Hailuogou glacier, southeastern Tibetan Plateau, using in situ surveys and ASTER imagery, *Journal of Glaciology*, 57 (206) 1147-1157

Zhang, Y., Liu, S. and Ding, Y. (2007) Glacier meltwater and runoff modelling, Keqicar Baqi glacier, southwestern Tien Shan, China, *Journal of Glaciology*, 53 (180) 91-98

Zhang, Y., Liu, S. and Xu, J. (2008) Glacier change and glacier runoff variation in the Tuotuo River basin, the source region of Yangtze River in western China, *Environmental Geology* (56) 59-68